The Modulation of Structural Components in Metallosupramolecular Assemblies and Metal-Organic Frameworks

A Thesis Submitted in Partial Fulfilment of the Requirements for the Degree of

Doctor of Philosophy** in **Chemistry

David Young

2016

Contents

Acknowledgements

I am very grateful to my supervisor Prof. Paul Kruger for his excellent support, motivation and the tremendous scientific freedom given to me throughout this work. In addition to this, the support of the Kruger research group in general has been a great inspiration. I would like to thank all past and present members, for introducing me to the field of metallosupramolecular chemistry and keeping me inspired throughout my time as a PhD student. Everyone who has been part of this group has helped make it a fun and friendly place to work.

I would also like to thank Dr Chris Fitchett for his help with crystallography and ideas on organic synthesis. My thanks extend to his research group and in particular to Will Kerr with whom I have bounced ideas off regularly throughout the course of my studies.

I don't think the department could function without Dr Matt Polson, and I am grateful for all the help he has given me in the handling of dangerous chemicals, synthetic chemistry and single crystal and powder X-ray crystallography. Dr Amelia Albrett and Dr Marie Squire are also immensely important to this department and I would like to thank them for going above and beyond in helping with mass spectrometry and NMR spectroscopy. I would like to extend my thanks to Wayne Mackay, Rob McGregor and the department technical staff, for promptly fixing anything that required fixing.

I am grateful for the help of Prof. Shane Telfer and Dr Hui Yang at Massey University in respect to gas sorption measurements. Giving up time on a new instrument is never easy and I would like to thank them for being so welcoming and excited about the results too.

I wish to acknowledge the University of Canterbury, for providing a doctoral scholarship, and to the MacDiarmid Institute for additional top up funding while writing up. The Marsden fund has also provided funding for some of the chemicals used in this thesis, and allowed me to attend multiple conferences.

Finally I would like to extend my thanks to my friends and family who have helped me throughout this process. Discussions not relating to chemistry in the tearoom, staff club or at your houses and flats have been instrumental in me keeping my sanity and your friendship is greatly appreciated.

Abstract

This thesis details the design and preparation of novel metallosupramolecular assemblies and metal-organic framework materials. This is achieved through the investigation of three families of ligand systems in combination with transition metal salts through solid state analysis. Experiments seeking to determine the effect of modulation of the structural components within these families are examined in each case.

The first of such families consist of ligands containing the N^1-acylamidrazone functional group in its neutral state and is described in Chapter 2. In addition to the coordination properties of these ligands being investigated, the hydrogen bonding motifs with a range of counter ions are described. The systematic variation of these anions allows for the modulation of the resultant supramolecular architectures.

Chapter 3 describes a series of complexes based upon ligands containing the N^1-acylamidrazone functional group in a twofold deprotonated state. Deprotonation of these ligands produces an additional bidentate coordination domain which allows the ligand to bridge metal ions. This leads to the formation of a series of octanuclear metal-organic macrocycles when reacted with zinc(II) carboxylate salts. It is shown that the modulation of the carboxylate co-ligands can be achieved with the retention of a conserved macrocyclic motif. The crystal packing of the macrocycles with respect to the carboxylate co-ligands are analysed. The use of these compounds as building units in the synthesis of metal-organic frameworks is investigated.

The second family of ligands is based upon 2,2':6',2"-terpyridine-4,4"-dicarboxylic acid derivatives. A series of nine ligands, each containing an aromatic functional group at the 4'-position were synthesised. Seven of these were used in the synthesis of metal-organic frameworks with zinc(II) and were observed to form isoreticular frameworks based upon a zeolitic **gis-c** topology. The conserved topology and similarity of the size of the internal cavities mean the differences in properties can be attributed to the functional group at the 4'-position of the ligand. The effect of the appended functional group on the structure and their sorption properties of nitrogen, hydrogen, methane and carbon dioxide gases is discussed.

The third family of ligands are based upon the phenolic oxime coordination group and are described in Chapter 5. This functional group is known to reproducibly form a pseudomacrocyclic ring around coordinated metal ions due to hydrogen bonding of the oxime proton to the phenolate oxygen atom. The functionalisation of the periphery of these complexes with carboxylic acid functional groups for their use as metalloligands in the synthesis of MOFs is investigated.

This study is primarily concerned with the solid-state structural chemistry of metallosupramolecular assemblies and metal-organic frameworks. Particular attention is paid, however, to solution-based measurements such as NMR spectroscopy for elucidation of dynamic behaviour, and thermogravimetric analysis and gas uptake studies for potential void-containing materials. Twenty three ligands (twenty of which have not previously been reported) have been prepared and characterised during the course of this study. Forty two coordination complexes are also reported along with their single crystal X-ray crystal structures.

Abbreviations

NMR: Nuclear Magnetic Resonance

COSY: Correlation Spectroscopy

HSQC: Heteronuclear Single Quantum Coherence

IR: Infrared

MP: Melting Point

UV/Vis: Ultraviolet/Visible

ESI-MS: Electrospray Ionisation Mass Spectrometry

PXRD: Powder X-ray Diffraction

CP: Coordination Polymer

SOF: Supramolecular Organic Framework

MOF: Metal-Organic Framework

SBU: Secondary Building Unit

MBB: Molecular Building Block

MOM: Metal-Organic Macrocycle

TGA: Thermogravimetric Analysis

Atom Colouring Scheme

Black: Carbon

White: Hydrogen

Blue: Nitrogen

Red: Oxygen

Mustard: Sulphur

Green: Chlorine, Copper

Purple: Iron

Pale Green: Nickel

Yellow: Zinc

Mahogany: Bromine

Cream: Cadmium

Chapter 1

Introduction

1.1 Supramolecular Chemistry

Supramolecular chemistry is concerned with the weak interactions between molecules, leading to the formation of multi-component molecular assemblies. This idea breaks away from the classical idea of molecular chemistry where the design of a structure is based upon a single molecule held together by strong covalent bonds. For this reason it is described as "*chemistry beyond the molecule*".[1] The first examples of synthetic supramolecular assemblies involved host-guest systems in which a small guest molecule or ion could be trapped within a larger host by non-covalent intermolecular interactions such as ion-dipole interactions or hydrogen bonding (Figure 1.1). Synthetically, this field of chemistry was pioneered in the 1960s by Cram,[2] Lehn,[3] and Pederson[4] and for this they were awarded the Nobel Prize in Chemistry in 1987. These host-guest studies were the foundation for the design and synthesis of more complex supramolecular structures such as bio-inspired assemblies,[5] catenanes,[6] rotaxanes,[7] helicates,[8] knots[9] and anion receptors.[10]

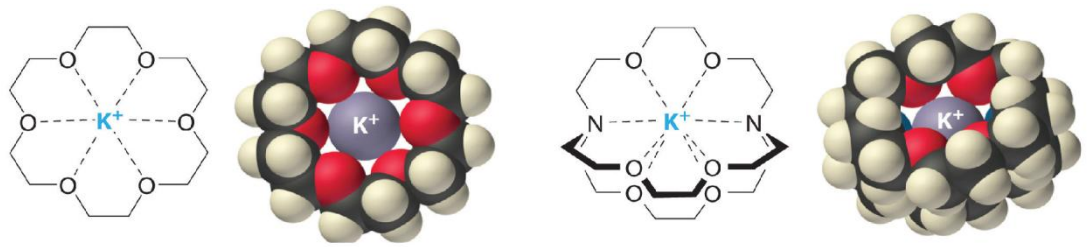

Figure 1.1: *Schematic and space-fill representation of a potassium ion guest encapsulated by the crown ether host 18-crown-6 (left) and by the cryptand 2,2,2-cryptand (right). Figure adapted from Averill.*[11]

Supramolecular assemblies are said to self-assemble; that is they come together spontaneously due to the stabilising interactions designed into the molecules. The synthesis of such assemblies is convergent as the components assemble into a single, stable structure. The weak, reversible bonds responsible for the formation of the assembly lead to an error checking mechanism in the formation of supramolecular species leading to a thermodynamic minimum of the system.[12] When mixed in a fixed ratio, concentration, pH and temperature the same thermodynamic product should always be produced.[13] Although the non-covalent interactions are generally weak, structural rigidity can be imparted into the system by tailoring the specific interaction or incorporating multiple interactions.[14]

Supramolecular interactions include hydrogen bonding, π-π stacking, electrostatic interactions and Van der Waals forces. Metal-to-ligand coordination bonds also fit this classification, but due to increased interest by inorganic chemists, they are defined as metallosupramolecular systems and will be described separately.

Although supramolecular interactions are individually much weaker than covalent bonds, employing large numbers of them allows for the formation of very robust assemblies of individual molecules. An understanding of the strength and directionality of these non-covalent interactions is key to the designed synthesis of materials based upon these systems. The field of crystal engineering has emerged as a result of controlling these interactions to form pre-determined structures based upon weak interactions.[15] In such systems the strongest interactions between species are most likely to form and hence have the most control over the final assembly. For this reason functional groups must be chosen carefully. This increasingly important field is defined as "the understanding of intermolecular interactions in the context of designing new solids with desired physical and chemical properties".[16] The importance stems from the realisation that the properties of materials are not only based on the discrete covalent molecular structure, but additionally on how these molecules are arranged in space.

1.1.1 Hydrogen bonding

The hydrogen bond is amongst the most common and ubiquitous interaction in supramolecular chemistry. It is the very interaction nature uses for selective base pairing within DNA and to generate the secondary structure of proteins.[17] In the designed synthesis of materials, hydrogen bonding has many beneficial attributes such as its strength and directionality. These features lead to predictability in the arrangements of molecules capable of forming this useful interaction.

The strength of a hydrogen bond depends on the nature of the atoms involved. A conventional hydrogen bond, where both the hydrogen bond donor (D) and the acceptor (A) atoms are largely electronegative (for example O-H···N), can have bond strengths between 20 and 40 kJ/mol, whereas weaker hydrogen bonds occuring between less electronegative atoms such as in the non-conventional C-H···O case have typical bond strengths between 2

and 20 kJ/mol.[18] In the 1990's Desiraju intensively investigated weak intermolecular forces such as C-H···X and C-H···π and the roles they play in the design of organic solids.[19-20] Although weak, these interactions are part of the spectrum of hydrogen bonding and often impact the crystal packing of molecules. Stronger interactions between molecules can be made from multiple hydrogen bonding interactions working in tandem.

A key feature of the hydrogen bond is its directionality. Strong hydrogen bonding interactions tend to have D-H···A angles of approximately 180° (D = hydrogen bond donor, A = hydrogen bond acceptor). The relative positioning of hydrogen bond donor and acceptor sites in a covalent molecule gives directionality to the interactions and hence control over the final supramolecular structure. This directionality can be seen in the cyclic rosette assembly shown in Figure 1.2.

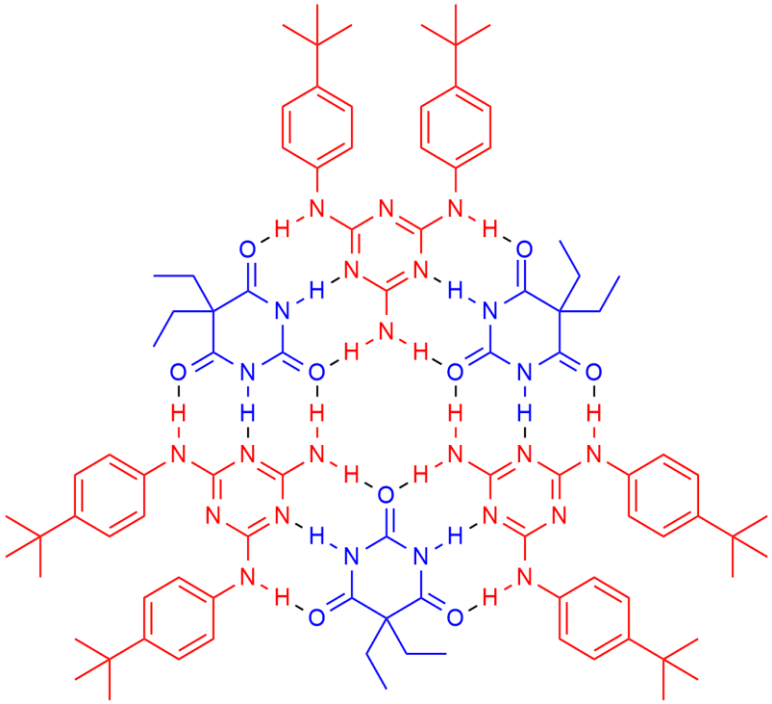

Figure 1.2: *Cyclic rosette structure of 5,5-diethylbarbituric acid (blue) and N,N'-bis(4-tert-butylpheny1)melamine (red).[21] The 120° angle between hydrogen bonding sites on the different molecules encode information into the final hexagonal assembly.*

In the field of crystal engineering, the designed synthesis of supramolecular structures, a hierarchy of hydrogen bonds can be used to predict the architecture of the final assembly. The strongest hydrogen bond donor (or set of donors) will recognise the strongest hydrogen

bond acceptor (or set of acceptors). This is followed by pairing of the second strongest donor and acceptor and so on.

The description of hydrogen bonding patterns can often be simplified by the use of graph set nomenclature.[22-23] This notation allows complicated networks of hydrogen bonds to be reduced to singular or combinations of four simple interaction descriptors. These include discrete (D), rings (R), chains (C) and intramolecular or self (S) hydrogen bonding interactions. These can be further classified by specifying the number of hydrogen bond donors (as a subscript) and acceptors (as a superscript) and the size of the ring or chain (in parenthesis) where relevant. Combinations of interactions can be reduced into hierarchical combinations of these descriptors. If one type of interaction necessitates another interaction, such as in a chain of rings, the latter interaction is appended in square brackets to the chain designation. Where groups of interactions are present yet not required for each other they can be arranged into different levels. The first level contains individual interactions, and subsequent levels contain combinations of higher level interactions. Graph set notation of hydrogen bonding interactions for a range of compounds is shown in Figure 1.3.

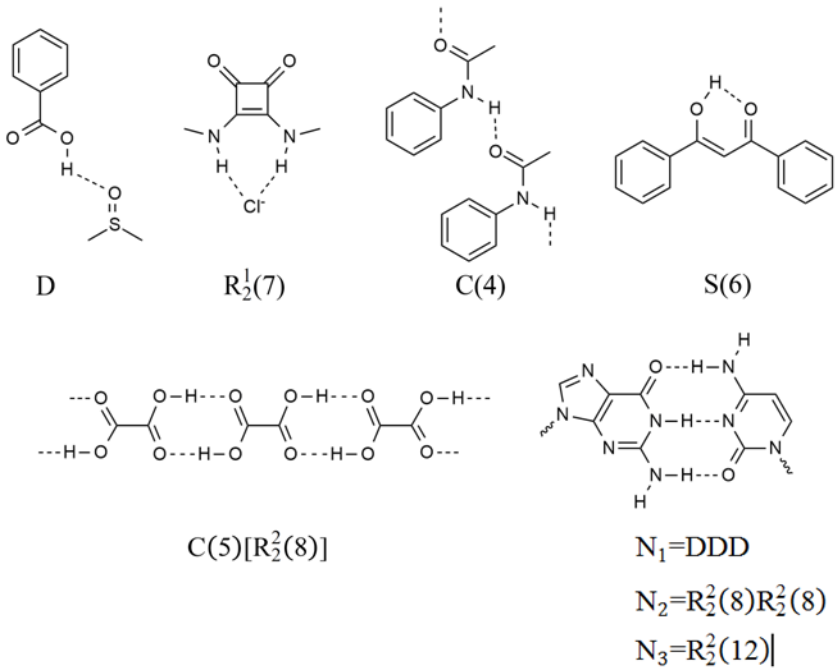

Figure 1.3: *Graph set notation of a range of hydrogen bonding interactions. Examples are representative only.*

Where relevant, this notation will be used to describe hydrogen bonding patterns in this thesis. It will be used as a way of simplifying the hydrogen bonding networks within related structures to clarify and denote similar interactions for ease of comparison. It will not used as an absolute method of rigorous structural analysis.

1.1.2 π-Interactions

Attractive interactions between the π-systems of aromatic molecules have been shown to have both a stabilising and ordering effect on molecules.[24-25] There are two general types of π-interactions: face-to-face stacking, and edge-to-face interactions (Figure 1.4).

Although the term face-to-face may imply a perfect overlap of π-systems, it is common for a partially offset overlap arrangement to minimise the π electron repulsion and maximise the π-σ attraction between systems.[25] It has been found that a 20° offset with plane to plane distances below 3.8 Å maximises attractive forces. Strictly edge-to-face interactions should not be considered stacking, as no stacking is taking place. Indeed they are related to hydrogen bond interactions where a slightly electron deficient hydrogen atom of one ring interacts with the electron rich π-cloud of a perpendicular system.

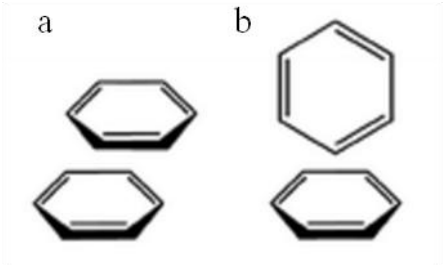

Figure 1.4: *Face to face (a) and edge to face (b) π-interactions of benzene.*

Parallel-offset and edge-to-face dimers are the most stable π-interactions and nearly isoenergetic.[26] These interactions are generally weaker than hydrogen bonding and have low interaction energies of 4-8 kJ/mol, although stronger stacking energies of up to 50 kJ/mol for larger heteroaromatic systems are possible.[25,27]

1.2 Metallosupramolecular Chemistry

The terms 'metallosupramolecular chemistry' is used to describe systems which include metal-to-ligand coordination bonds in combination with or instead of other weaker interactions to create supramolecular structures.[28] The intermediate bond strength of the coordination bond can be used to impart the same structural stability as multiple weak interactions working in tandem.

Metallosupramolecular chemistry involves the use of at least two different species; a metal ion and a ligand. The difference between this and a Werner type metal complex is the way in which these species assemble to create new architectures. Like hydrogen bonds, the directionality of coordinate bonds is an important feature and geometries that are hard to create using purely organic constituents are trivial to realise using metal ions. The varied, yet rigid, geometries of metal ions are useful building blocks in the formation of supramolecular assemblies with a designed shape.[29]

Metallosupramolecular assembly allows the introduction of useful properties imparted by metal ions such as magnetism, spin crossover, catalytic, electrochemical and/or photophysical responsive behaviour.[30] In addition to adding functionality to the resultant systems, metal ions can encode structural information in the supramolecular assembly by taking into account the preferred coordination number, geometry and affinity for different coordinate bond donors. Common geometries for first row transition metals with coordination numbers from four to six are shown in Figure 1.5. Of particular note is that metal ions commonly allow the introduction of angles not often seen in organic chemistry such as 90°.

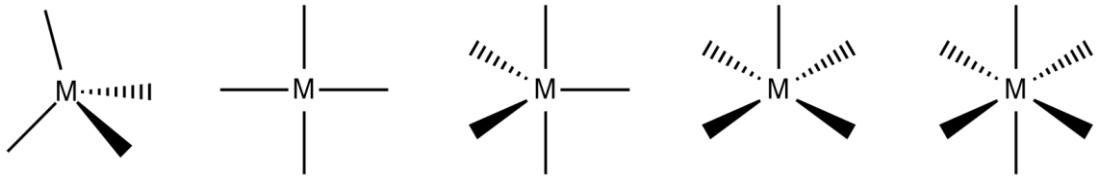

Figure 1.5: *Examples of commonly encountered metal geometries. From left to right; tetrahedral, square planar, trigonal bipyramidal, square pyramidal and octahedral.*

A compromise must be made between the strength of the coordinate bond and reversibility, to both maximise the robustness of the resulting assembly and to allow for equilibration to a single product under synthetically achievable conditions. To achieve a balance of predictable geometries, reversibility of coordination, stability and cost, nitrogen-containing heterocycles and/or carboxylic acids are commonly used in combination with first row transition metals in their divalent oxidation state.

1.2.1 Structural Descriptors

Metal ions do not always adopt the idealised geometries shown in Figure 1.5. Distortions to these can exist due to restraints imposed by the ligand system such as chelate rings, peripheral supramolecular interactions, or effects from the metal itself. Several methods have been devised to quantify the deviation from ideal geometry as a numerical parameter in the cases of 5-coordinate and 4-coordinate geometries. These two structural descriptors are particularly relevant for the contents of this thesis and are useful for describing the differences between multiple, similar structures.

Five-coordinate metal complexes commonly exist in one of two idealised geometries; square pyramidal or trigonal bipyramidal. To distinguish between these two geometries the single structural parameter tau (τ_5) was proposed by Addison *et al.* in 1984.[31] It is defined in Equation 1.1, where β is the largest angle between substituents around a central five-coordinate atom (angle BMC, Figure 1.6), and α is the second largest angle in the coordination sphere that does not involve the substituents used to form β (angle DME, Figure 1.6).

$$\tau_5 = \frac{(\beta-\alpha)}{60} \qquad \textit{(Equation 1.1)}$$

In an ideal square pyramidal geometry, $\beta = \alpha = 180°$ and $\tau_5 = 0$. In an ideal trigonal-bipyramidal geometry, α becomes 120° and $\tau_5 = 1$. Distorted geometries can described as variants of the ideal cases mentioned above and as they have α angles between 180° and 120°, they have τ values between 0 and 1.

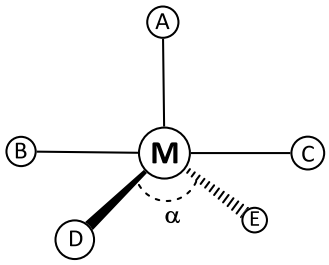

Figure 1.6: *Five coordinate geometry around metal ion M. In an ideal square pyramidal geometry, α = 180°. For a perfect trigonal-bipyramidal geometry, α = 120°.*

This parameter is useful as it allows geometries of five-coordinate metal ions to be easily characterised and compared as will be discussed throughout this thesis. As each distorted geometry is on a continuum between square pyramidal and trigonal bipyramidal this parameter gives an indication of how similar a distorted geometry is to the idealised case.

Likewise, four-coordinate geometries can also be given a structural descriptor.[32] Common idealised four-coordinate geometries include square-planar and tetrahedral. The parameter for the structural description of a four coordinate complex is defined in Equation 1.2. Again β represents the largest angle between two substituents, and α the second largest. Thus, for a perfect tetrahedral complex β+α = 109.5+109.5 = 219, and τ_4 = 1. For a purely square planar complex, β+α = 180+180 = 360, and τ_4 = 0. Distortions to each idealised geometry, including seesaw geometry (τ_4 = 0.43), result in a parameter that falls within this range.

$$\tau_4 = \frac{360-(\beta+\alpha)}{141} \qquad \textit{(Equation 1.2)}$$

1.2.2 Discrete Metallosupramolecular Assemblies

Metal-directed self-assembly has proven to be a powerful tool in the synthesis of discrete assemblies. Many systems based on two-dimensional shapes and regular polygons have been synthesised.[33] The design of such assemblies is the same as that for other supramolecular assemblies where the information encoded into the metal ions and ligands is used to generate a predefined architecture. Each component of the structure can be

simplified into a geometrical shape based upon the positioning of functional groups responsible for supramolecular interactions. This can result in the simplification of complex arrangements of molecules into common geometrical two and three-dimensional discrete assemblies (Figure 1.7).

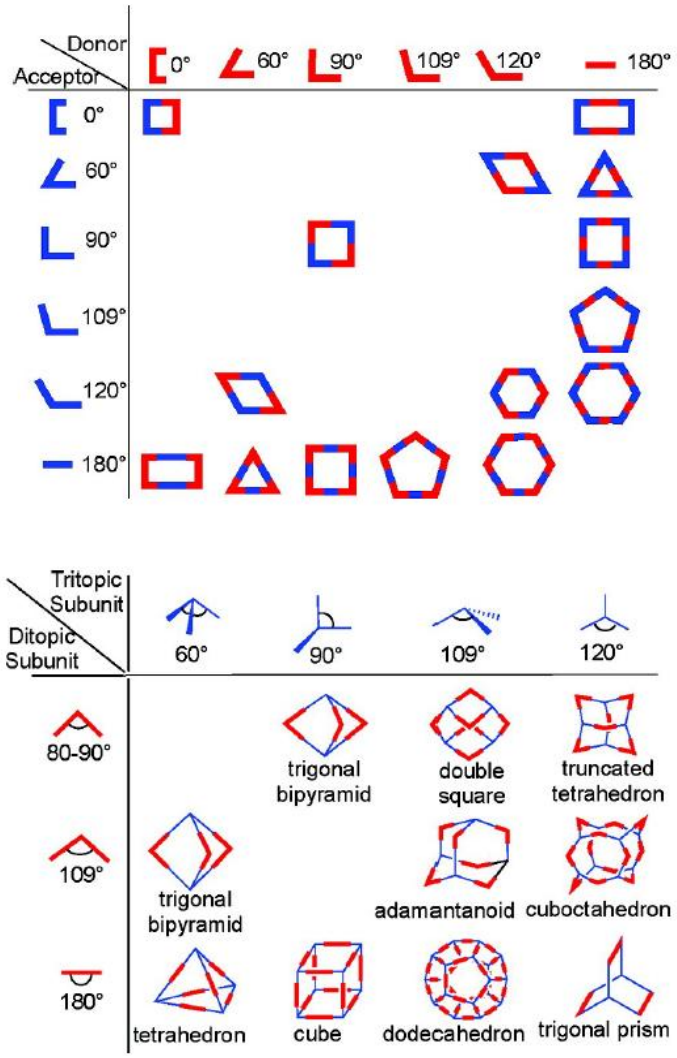

Figure 1.7: *Two and three-dimensional discrete assemblies can be formed by the combination of various individual molecular components. Commonly observed geometries in molecular components are represented by red and blue linkers. Figure adapted from Stang et al.*[34]

Discrete assemblies are favoured due to both enthalpic (maximum number of metal coordination and ligand binding sites interact) and entropic (the smaller the assembly, the more species are formed) considerations.

1.2.3 Infinite Assemblies

On a simple level the design principles of discrete and infinite assembles share a common methodology. The major exception being the geometry of the components used to create the assembly. As with discrete assemblies, the often complex shape of molecules can be reduced to simplify the analysis of the resulting structures by denoting each part of the assembly a node or spacer. This approach, first described by Wells[35] and later by Robson[36-37] is a simple way of interpreting the topology of supramolecular assemblies. Discrete systems can be formed when at least one component is convergent and/or monotopic subunits are used. Infinite systems are created from higher connected nodes and linkers with divergent points of propagation.

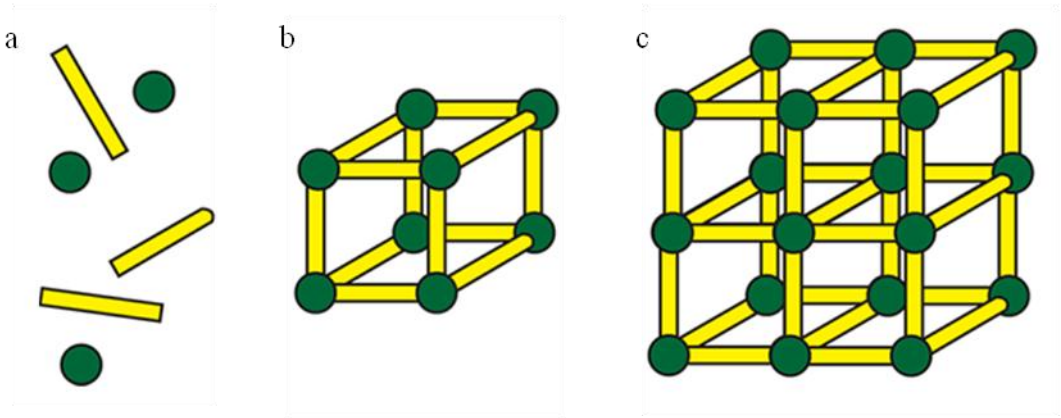

Figure 1.8*: a) Random orientation of nodes (green) and linkers (yellow). b) Self-assembled discrete supramolecular cube created through convergent trigonal pyramidal nodes and ditopic linear linkers. c) Infinite three-dimensional primitive cubic network created through the self assembly of octahedral nodes and linear ditopic linkers. Figure adapted from Stang et. al.*[38]

Where the nodes and linkers assemble through coordination bonds, infinite metallosupramolecular assemblies are often termed coordination polymers (CPs). These species can be one, two or three-dimensional and need not be crystalline.[39] A further clarification of coordination network is useful, which includes only two and three-dimensional or cross-linked one-dimensional coordination polymers arranged in a repeating array. This subset of coordination polymers is implied to be crystalline.

Typically in coordination polymer chemistry, the linker is defined by the organic ligand, and the node by an inorganic component. In this way, the coordination geometry of the

metal ions can be directly realised in the topology of the resulting assembly. Commonly used nodes in CPs include single metal ions, inorganic metal clusters, metal-organic macrocycles and metal-organic polyhedra.[40-41] Common linkers include ligands containing divergent carboxylate, pyridyl, nitrile, pyrazolate and imidazolate coordination groups separated by or appended to phenyl rings.

The carboxylate group is perhaps the most common of these coordinating groups, and can adopt many potential coordination modes. These range from monodentate to bridging polydentate (Figure 1.9). The bridging ability means polymeric species can be obtained from ligands containing only one carboxylate functional group. One series of infinite assemblies comprised of ligands containing a single carboxylate group is metal formate frameworks of the form $[M_3(HCO_2)_6]$ (M= Mn, Fe, Co, Ni, Zn, or Mg).[42] In this case the formate ligand adopts the *syn, syn, anti-* coordination mode.

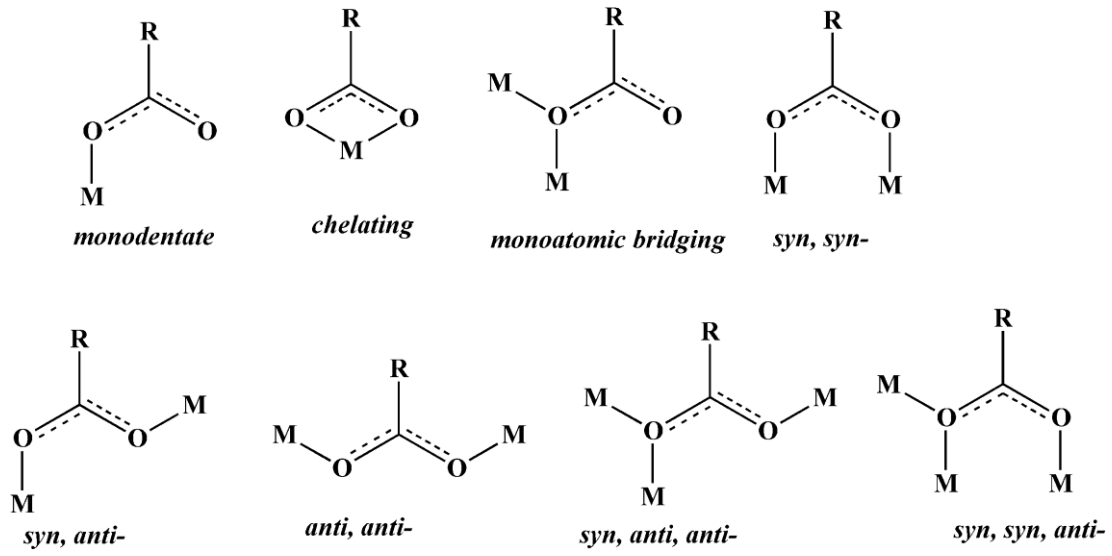

Figure 1.9: *Potential coordination modes of the carboxylate functional group. Figure adapted from Marinho et al.*[43]

1.2.4 Topology

The structure of coordination networks can be described by their topology, just as discrete metallosupramolecular assemblies are described by their shape. Coordination bonds are not the only supramolecular interaction capable of forming infinite networks. As described previously, other interactions such as hydrogen bonding and π-π stacking can be used to impart structural information into an assembly. Although commonly used for CPs, purely organic infinite supramolecular assemblies can be defined by topological descriptors too. Whether the linkers are defined as ligands linked to metal ions in coordination polymers (CPs), or supramolecular interactions as in the case of supramolecular organic frameworks (SOFs), the terminology used to describe them is the same.

Crystals, by their very nature, are composed of repeating units. The regularity of these units means the molecules in the crystal lattice are arranged in a repeating array. Each atom, ion and molecule within the crystal experiences interactions with its neighbours. The nature of these interactions can be covalent, ionic, coordinate, hydrogen bonding or π-π stacking. Information on the arrangement of these molecules and the interactions holding them together is not given by the symmetry of the unit cell. Topological descriptors, first being studied in mathematics, can be used to simplify the connections of molecules into their underlying nets. This leads to a simplified description of how molecules interact with each other. This topological approach can be used to describe any two-dimensional or three-dimensional network of interactions and is regularly used in the fields of crystal engineering, and coordination polymer chemistry.

Topological descriptors rely on the deconstruction of a crystal structure into the constituent parts as either nodes or linkers. Describing atoms or molecules as nodes, and the interactions as linkers is common in supramolecular frameworks. Describing metal ions or clusters as nodes and ligands linking them together is common in coordination polymer chemistry. There are many ways to describe network topology. These methods usually rely on the node connectivity, and the number of nodes required to complete a circuit to describe the underlying topology. The point symbol and the three letter Reticular Chemistry Structure Resource (RCSR) code are the most useful and widely used; these will be described here.

Networks can be described by the use of a point symbol, which takes the form $(A^d \cdot B^e \cdot C^f)$, where A, B and C are the lengths of each circuit and d, e and f are the number of unique occurrences of each circuit in the structure. The length of each circuit indicates the number of nodes that must be traversed to reach, and including the starting point. A three-connected node has three possible unique paths from each node back to itself, a four-connected node has six unique shortest paths, and a six-connected node has fifteen. The point symbols for a selection of topologies are given in Figure 1.10.

This offers many unique descriptors for networks, however, some networks of different topologies have the same point symbol, an example of which is the diamondoid and Lonsdaleite topologies. Both contain four-connected tetrahedral nodes, and each of the 6 paths leading from each node back to itself contain 6 nodes in total, hence both have a point symbol of 6^6. A way around this is to describe a topology after a known mineral, a library of which is contained within the RCSR.[44] By convention a three letter code relating to the mineral is used, and in the above example the diamondoid and lonsdaleite nets can be distinguished via the codes **dia** and **lon** respectively.

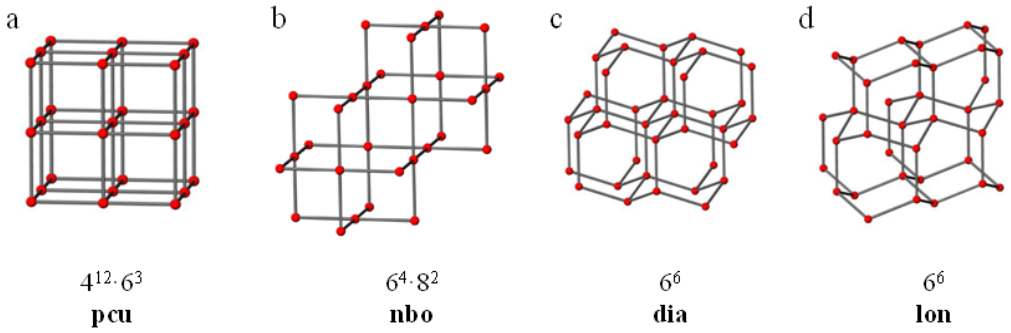

Figure 1.10: *Some common topologies and their associated point symbols and RCSR three letter codes.*

These three letter codes are used even when there is no confusion as they allow rapid identification of known network topologies. Extensions to these codes can be added to give extra information such as whether it is a binary net (b) or indicate the degree of catenation

(c). These extensions are placed after the three letter code and take the form of **dia-b** for a binary diamondoid topology (such as in ZnS) or **dia-c** for a catenated diamondoid network.

1.2.5 Interpenetration

Coordination polymers can often contain internal cavities which are commonly occupied by solvent molecules. The size of these regions can be increased by a change in topology and/or extensions of the linkers. The growth of another framework within this space is increasingly likely as the size of the internal cavities increase. Interpenetration is a term used to describe this catenation of infinite networks.[45] The interweaving of independent and chemically unconnected networks means that they cannot be separated without breaking chemical bonds. Interpenetration arises from the driving force towards close packing in solids. By maximising the interactions between networks, the overall energy of the system is lowered. As interpenetration occurs by the filling of void space, it may only occur if the pore volume in an individual network is sufficiently large to accommodate one or more additional nets. The use of elongated organic linkers in attempts to synthesise networks with large pores can be a challenging task, as the formation of an interpenetrated phase may be preferred, reducing the potential void volume of the material.

All networks can be defined as *n*-fold interpenetrated. An *n* value of 1 indicates a single net that is not interpenetrated and a value of 2 describes two interpenetrated nets. An example of a three-fold interpenetrated net is shown in Figure 1.11.

The interpenetration of networks can be further described in terms of dimensionality, where several modes of interpenetration are possible; 2-dimensional networks can interlock to form a denser 2-dimensional sheet with no extension into the perpendicular dimension (2D to 2D interpenetration), or the interpenetrating sheets can be inclined with respect to each other, to give an overall 3-dimensional network consisting of interlocked 2-dimensional components (2D to 3D interpenetration).

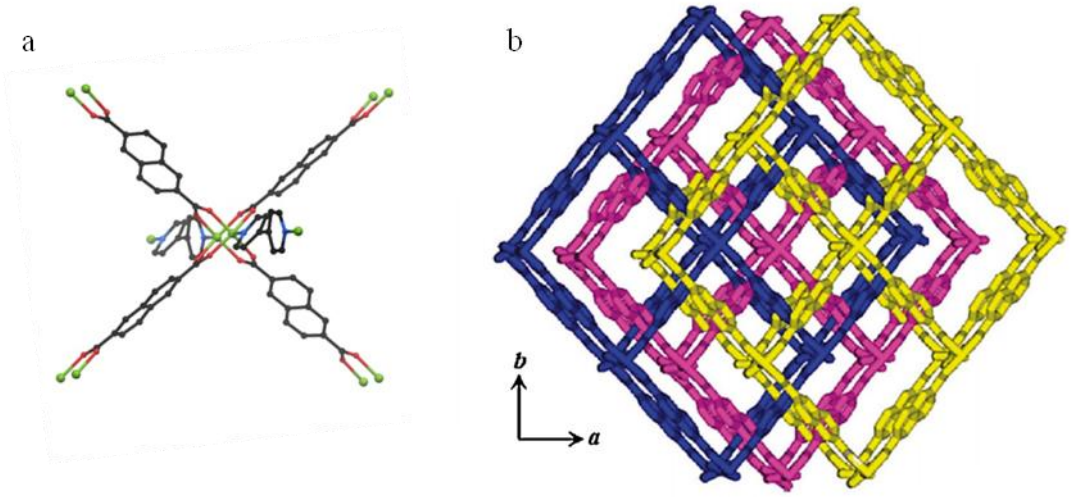

Figure 1.11: *Octahedral node (a) used in the formation of a 3-fold interpenetrated pillared coordination polymer(b) with* ***pcu-c3*** *topology.*[46]

The degree of interpenetration of a given framework can be controlled by modification of the constituent parts such as the length of linkers[47] or inclusion of bulky thermo labile protecting groups.[48] Synthetic conditions such as the temperature and concentration,[49] solvent,[50] and reaction time[51] can also be used. As this phenomenon requires internal cavities for another net to grow, it was often thought that interpenetration was of limited value because it decreased the total amount of accessible pore volume in a network material. It is now realised that interpenetration can add many interesting features to coordination networks such as increased stability,[52] tailored dimensions of internal cavities[53] and introduction of dynamic behaviour.[54] It should be noted that for a given network, its porosity, stability and possibility of interpenetration is closely related to its network topology.

1.3 Metal-Organic Frameworks

A sub-class of coordination polymers, metal-organic frameworks (MOFs) are defined as being three-dimensional coordination polymers that contain potential voids.[39] The term 'potential' is used here to define dynamic frameworks that may not show porosity in their initial state and not to include coordination polymers that irreversibly collapse upon

removal of solvent or guest molecules contained within their pores. To sustain permanent porosity, the structures must be constructed of robust building units. The organic components are inherently stable due to being constructed of strong covalent bonds. It is the coordination bond that is the weak point of most assemblies. Several strategies have been used to increase the stability such as use of negatively charged ligands and inert metals or metal clusters as the nodes of the framework. Negatively charged ligands are also desirable because not only do they increase the strength of the coordinate bond, but render extra-framework anions unnecessary, increasing the amount of possible void space within the structure.

1.3.1 Secondary building units

The term secondary building unit (SBU) was introduced to describe the structural components that comprise a MOF.[55] These are not simply the reagents used in the reaction, as the starting entities may not maintain their structure during the reaction or may assemble into entirely new structural motifs. Due to the strength of the covalent bond, organic molecules generally retain their structure under typical solvothermal conditions and have a known SBU shape. Due to bridging nature of some ligand systems, metal ions can assemble *in situ* into inorganic metal clusters which represent the nodes of the assembly. Some of these inorganic secondary building units are stable as clusters with monotopic carboxylate groups, yet others have not been realised in their discrete form.[41] The points of extension from organic SBUs are the coordination bond donor sites, such as carboxylate, pyrazolate or pyridyl groups. For the inorganic SBUs these are the coordination bond acceptor sites.

Some of the most common inorganic SBUs include the dimetallic paddlewheel $[M(RCO_2)_4L_2]$ and the basic zinc(II) acetate cluster $[Zn_4O(RCO_2)_6]$ (Figure 1.12). These form the basis for the HKUST-1 (Hong Kong University of Science and Technology) and IRMOF (IR stands for isoreticular) series respectively.[56] The starting materials for each of these inorganic SBUs is commonly copper(II) or zinc(II) nitrate, highlighting the *in situ* nature of the clusters formation.

Dimetallic paddlewheels are comprised of two metal ions bridged by four *syn*, *syn*-carboxylate groups. Each carboxylate group can be thought of as a point of extension from

this SBU when polycarboxylate ligands are used allowing the generation of a planar four-coordinate node. The apical sites on each metal ion usually contain a water or other neutral monotopic ligand, however, if they contain polytopic ligands such as 4,4'-bipyridine, the SBU can be described as an octahedral node (Figure 1.11). Basic zinc(II) acetate has an octahedral SBU geometry; six linear di-carboxylate ligands are arranged in an octahedral environment around a tetranuclear zinc μ_4-O core.

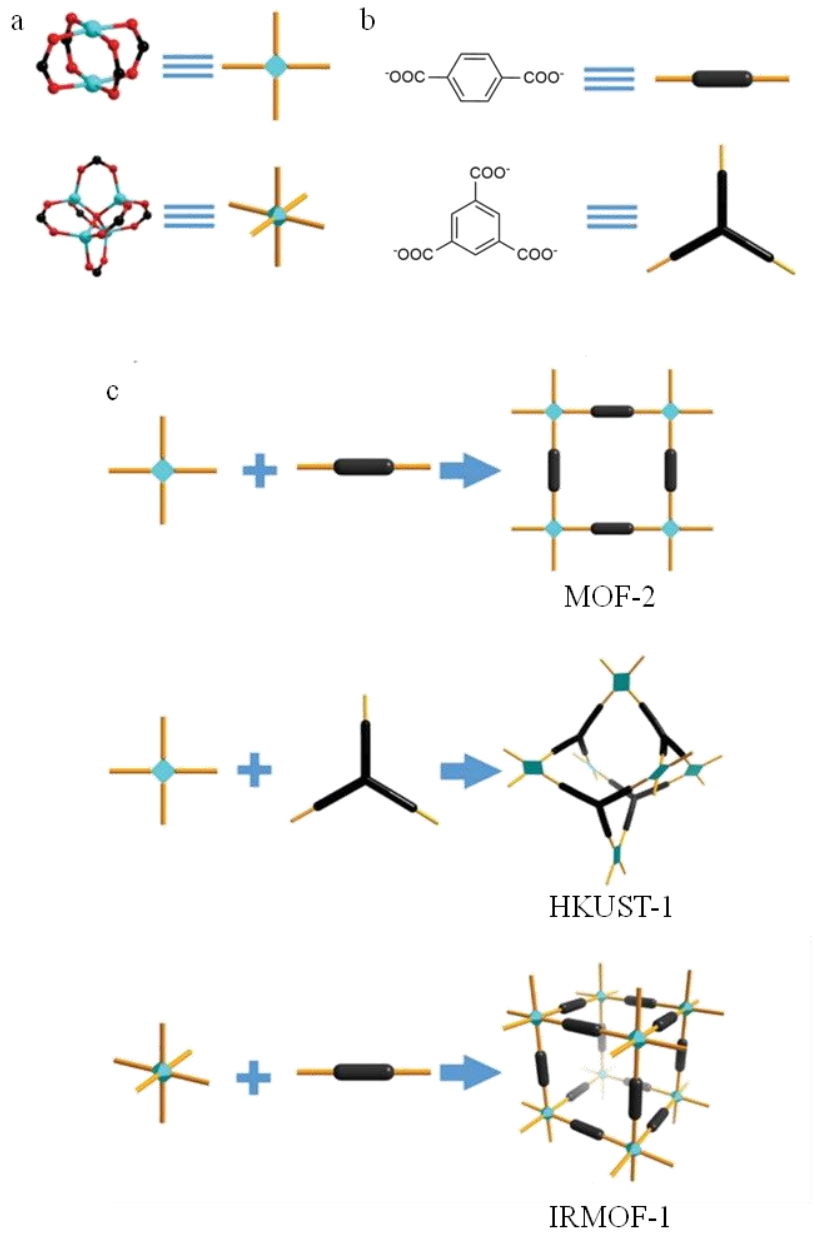

Figure 1.12: *Examples of inorganic (a) and organic (b) secondary building units and their schematic representations. The connection of each through their points of extension leads to metal-organic frameworks. Figure adapted from Zhou et al.*[57]

The secondary building units need not be discrete entities. Several well known MOFs are based upon infinite secondary building unit, including the well known MOF-74.[58] The designed synthesis of SBUs to create discrete polyhedra and infinite networks of a predetermined shape or topology has been described extensively by O'Keeffe and Yaghi in numerous reviews.[33,56,59] SBUs often impart increased stability to MOFs due to the multiple coordination bonds contained within.

1.3.2 Isoreticular Frameworks

Isoreticular frameworks are defined as materials based upon the same topological net and of similar composition. Although this is a general term, it is commonly used to describe one particular series of MOFs. In this series, each of the structures is based upon octahedral $[Zn_4O(RCO_2)_6]$ secondary building units bridged by linear ditopic carboxylate linkers. Variation in the size of the linker allows for modulation of the pore dimensions in the resultant **pcu** framework. Figure 1.13 shows how the internal cavity of a framework can be tuned by increasing the length of dicarboxylic acid used to synthesis the MOF.

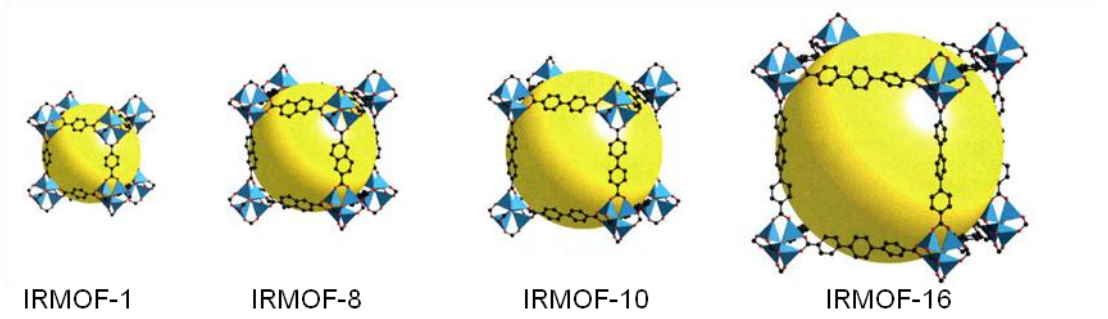

***Figure 1.13**: Single crystal X-ray structures of IRMOF-1, IRMOF-8, IRMOF-10 and IRMOF-16 showing the effect of linker length on the pore size (yellow spheres) within a framework. IRMOF = isoreticular metal-organic framework. Figure adapted from Yaghi et al.[56]*

It is not just the pore volume that can be modulated this way though. Functionality can be systematically changed within a series of frameworks with the same pore dimensions. This allows the effect of particular functional group on a particular property to be studied, independent of framework topological effects. Several ligands that have been used to introduce functionality to the IRMOF series are shown in Figure 1.14.[56,60]

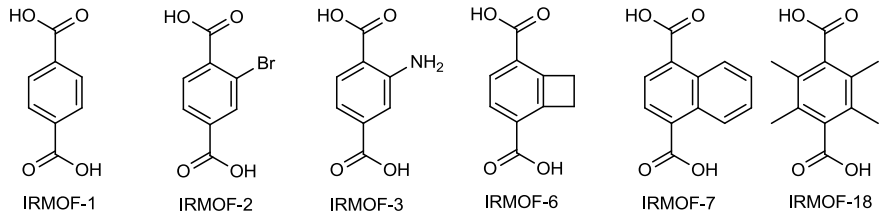

Figure 1.14: *Some representative ditopic carboxylate linkers used in the synthesis of members of the IRMOF series. Labels relate each ligand to its respective IRMOF descriptor.*

Although extensively studied, the IRMOF series is by no means the only framework to have its constituents systematically modulated to provide novel and interesting properties. MOF-74 is another framework for which the modulation of structural components has been investigated. This framework contains infinite rod-like SBUs connected via tetra-anionic 2,5-dioxidobenzene-1,4-dicarboxylate (dobc) linkers. The topology of MOF-74 is seen to be conserved with respect to variation of the metal ion, and use of magnesium,[61] manganese,[62] iron,[63] cobalt,[64] nickel,[65] copper,[66] zinc,[58] or even mixed metal ions[67] produce isoreticular frameworks. The linkers have also been extended from a single phenyl spacer to up to eleven, creating one dimensional channels with diameters ranging from 10 Å to 85 Å (Figure 1.15).[68] Other notable series such as those of UiO-66,[69] NOTT,[70] PCN[71] have also been studied with respect to systematic modulation of structural components. The reader is directed to the references for details on the nature of these frameworks and ways in which modulation was achieved.

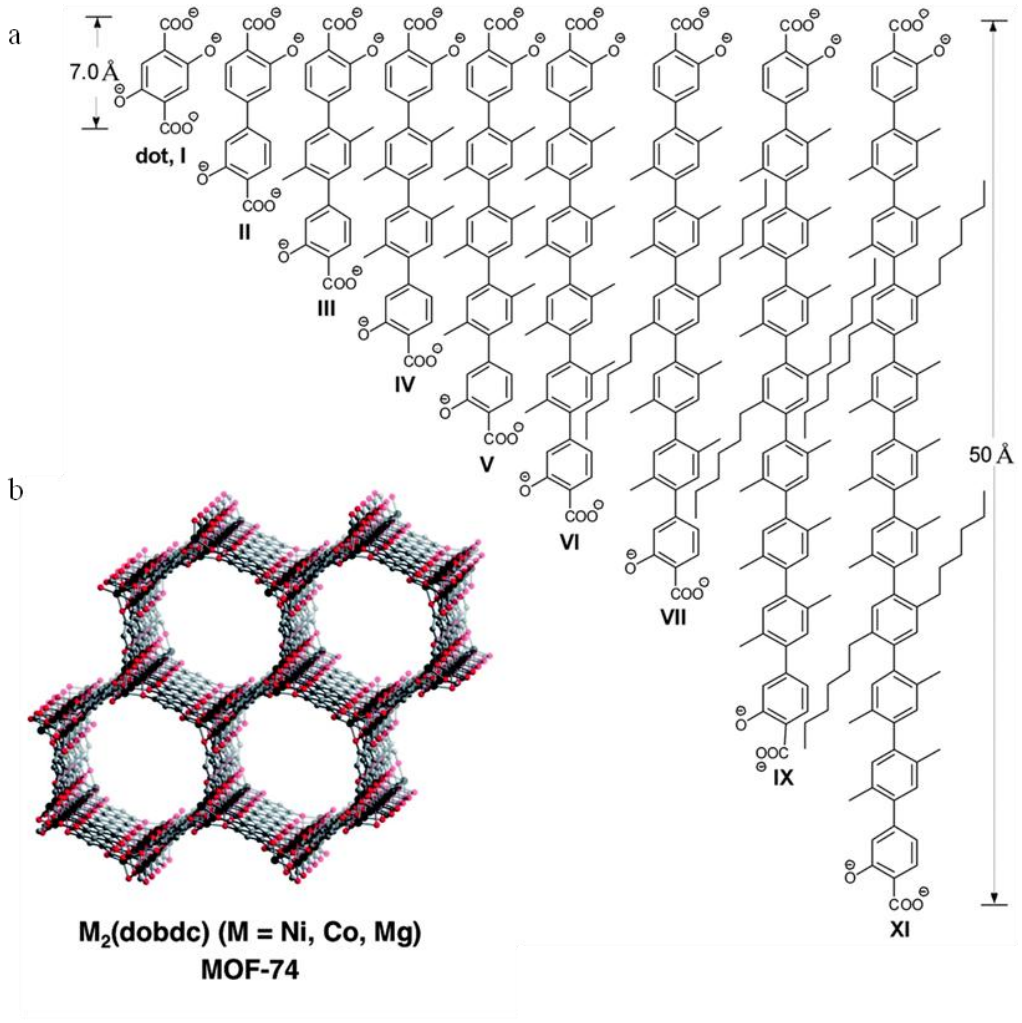

Figure 1.15: *a) Ligands used in the synthesis of MOF-74 and isoreticular derivatives. Increasing the length of the linker results in larger channel apertures. b) One dimensional hexagonal channels in MOF-74. Figures adapted from Zhou et al.*[57] *and Yaghi et al.*[72]

1.3.3 Metalloligands

In a similar way to the organic functionality seen in Figure 1.14, metal centres can be embedded in a framework through the use of metalloligands. These can be either thought of as an organic linker that contains an inorganic component, or as a discrete complex that contains pendant coordination bond donor sites.[73-74] The metal ion may play an important role in the directing of the pendant coordination sites, although this is not a requirement. As with their organic counterparts, the pendant coordination groups are usually limited to

carboxylate, pyridyl or pyrazolate groups. Metalloligands can be incorporated directly in the synthesis of MOFs and used exactly as an organic component would be, or created through post synthetic metalation of the framework. Only the former will be described here and the reader is directed to a review on post-synthetic metalation of MOFs for the latter.[75]

To avoid confusion between metalloligands and metallic nodes, metalloligands will be classified here when they are used in an analogous way to a purely organic ligand in the synthesis of a MOF *i.e.* the only structural information they encode into the framework is via coordination bond donors. Metalloligands are related to organic linkers in the sense that they are essentially complexes used in the self assembly of infinite species instead of organic components. As such, similar considerations for organic linkers apply to metalloligands; they must remain structurally intact throughout the construction process and be soluble in common organic solvents in order to ensure the feasibility of the subsequent framework formation.[76]

MOFs containing such linkers can manifest the properties of the individual metalloligand building blocks (e.g., chirality, catalysis, sensing, magnetism, or luminescence). From a purely structural point of view, metalloligands may also provide many features unattainable through purely organic counterparts such as unique geometries, chirality, size and ionisation. Examples of some metalloligands used in the synthesis of coordination polymers and MOFs are shown in Figure 1.16. The use of metalloligands in the syntheiss of CPs and MOFs allow the inclusion of added functionality, more than can be achieved from organic features alone.

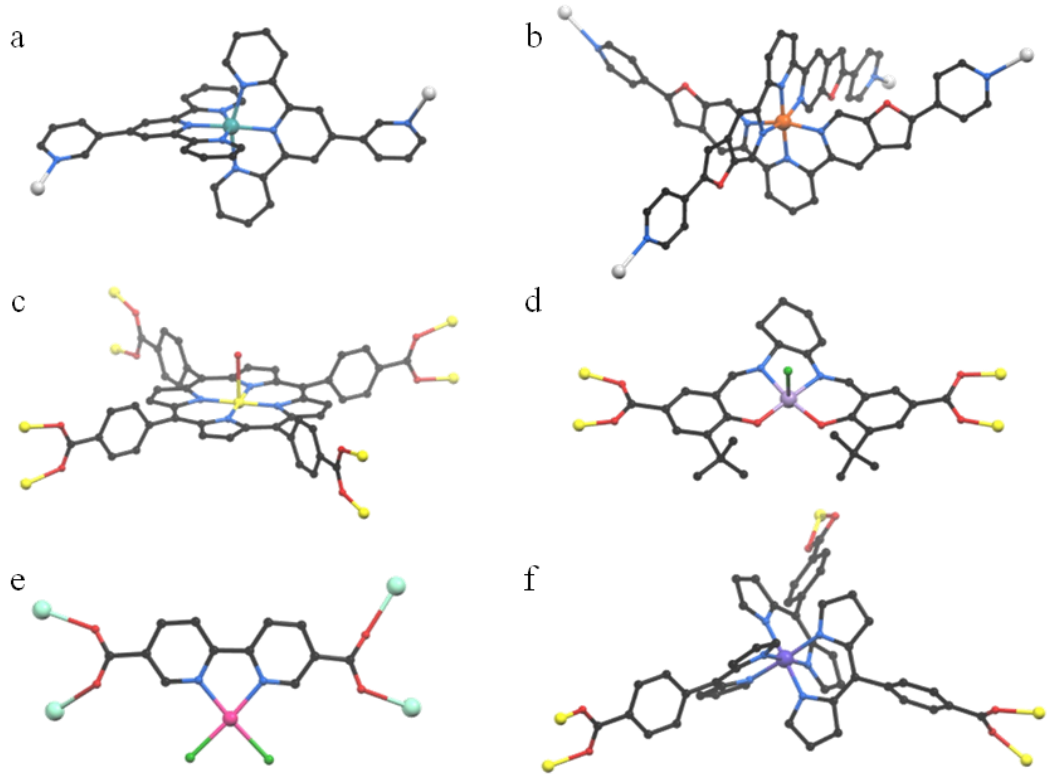

Figure 1.16: *Examples of metalloligands used in the synthesis of coordination polymers and metal-organic frameworks. a) Ruthenium(II) terpyridine complex with two pendant 3-pyridyl donor groups acts as a linear linker in the formation of a silver(I) coordination polymer.*[77] *b) Iron(II) terpyridine complex with four pendant 4-pyridyl donor groups acts as a tetrahedral linker in the formation of a silver(I) coordination polymer.*[78] *c) Zinc(II) porphyrin complex with four pendant carboxylate groups acts as a square planar linker in the formation of a pillared paddlewheel MOF.*[79] *d) Manganese(III) salen complex with two pendant carboxylate groups acts as a linear linker in the formation of a MOF with* ***pcu*** *topology.*[80] *e) Palladium(II) bipyridine complex with two pendant carboxylate groups acts as a linear linker in the formation of a samarium MOF.*[81] *f) Cobalt(III) dipyrrin complex with three pendant carboxylate groups acts as a triangular linker in the formation of a MOF with infinite zinc(II) SBUs.*[82]

If the central metal ion of the complex is not coordinatively saturated by the organic components of the metalloligand, it can be accessible to guest moieties. This may lead to useful functions such as catalysis, sensing or enhanced gas sorption. Due to the use of coordinating solvents in the synthesis of MOFs, such as DMF, DMA or NMP, often a post-synthetic desolvation step will be performed to achieve this. Typical procedures include heating the framework under vacuum, necessitating the framework be thermally stable and stable to removal of solvent within the internal void space. Incorporation of open metal sites in the linking struts of MOFs is advantageous because they are not hidden in

inaccessible locations such as the metal centres in nodal clusters. It has been shown that hydrogen and other gases are readily adsorbed near open metal sites.[83-89]

Two of the most studied metalloligands are based upon salen and porphyrin complexes. Metal complexes prepared from derivatives of salen ligands have enjoyed wide utility as constituents of coordination polymers and MOFs and many examples exist.[90-95] The chiral catalytic behaviour of the salen unit combined with the high surface area and heterogeneity of MOFs have shown good catalytic behaviour. In the case of the zinc porphyrin tetracarboxylate node (Figure 1.16c) it is important to note that only the carboxylate coordinate bond donors encode structural information into the framework.[79] The central metal ion is not involved in a structural way to the actual framework, created by the four carboxylate groups. In such cases where a metalloligand encodes structural information through both coordination bond donor and acceptor sites, it will be termed an auxiliary node.[79] This type of building unit will be discussed in Chapter 4. A range of different metals can be used in the porphyrin to generate a family of structures which have been shown to be effective Lewis acid catalysts.[96-98] The benefit of including open metal sites into framework materials is the ability to turn homogenous catalysts into heterogeneous catalysts and still maintain high surface areas.

1.3.4 Soft Porous Crystals

Potentially porous coordination polymers can be classified into three categories.[99] The first category includes materials that collapse irreversibly upon guest removal and is in fact non-porous. The second includes robust and rigid frameworks that retain crystallinity when the guests are not present within the cavities. The third, predicted in 1998, are defined as exhibiting flexible or dynamic behaviour in response to external stimuli and are often called soft porous crystals.[100] This generation of materials is defined as having a highly ordered network structure that is capable of undergoing structural transformations. The bistable or multistable materials show reversible transformations between states, with at least one state showing porosity (shown through gas or guest adsorption). The flexibility required for structural transformations can be introduced through either interpenetration of multiple

networks or linker and node design. A schematic of potential dynamic processes can be seen in Figure 1.17.

Figure 1.17: *Dynamic mechanisms in MOFs can be caused by displacement or shearing deformations. Examples of each are shown using the* ***pcu-c*** *net. Figure adapted from Kitagawa et al.*[101]

The interpenetration of chemical networks is not a static phenomenon, dynamic processes can occur between catenated networks. The relative displacement between frameworks can have drastic effects on the properties of the interpenetrated compound. The internal surface area and pore volume may change greatly and functional sites may be hidden from potential guests.

Examples of MOFs that exhibit shearing flexibility are dehydrated chromium and aluminium MIL-53 (Material of Institut Lavoisier) frameworks.[102] These frameworks are based upon benzene-1,4-dicarboxylate and infinite one-dimensional inorganic SBUs which form a three dimensional frameworks containing one dimensional potentially porous diamond-shaped channels. Upon the removal of solvent from within the pore structure, the framework distorts to adopt a closed, narrow pore state with limited porosity (Figure 1.18). Upon exposure to a gas with a strong affinity for the framework such as CO_2, above a certain pressure the framework opens and shows a higher sorption capacity. The shearing deformation in this case stems from distortions in the coordinate bond between the carboxylate ligand and the metal ions in the inorganic SBUs.[103]

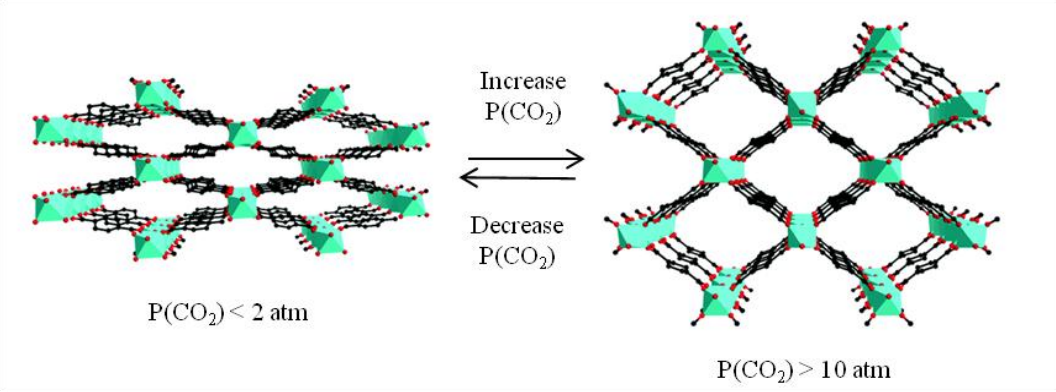

Figure 1.18: *Dynamic behaviour in MIL-53. Increasing pressure of CO_2 leads to a phase change from a narrow pore to an open pore form. Figure adapted from Zhou et al.*[57]

1.3.5 Gas Sorption

Storage and separation of target gases are typical applications of porous materials. Gas sorption within porous solids is attractive because of the increased capacity for a gas to be stored in a given volume of solid than can be stored in an empty container, even at high pressures. This leads to a higher storage density, a benefit in many applications. The benefit of physisorption of gases within porous materials is the low interaction energy of the gas with the material, leading to fast, and reversible kinetics. Other chemisorption storage methods, such as metal hydrides for hydrogen or carbamates for carbon dioxide, show strong binding, but significant energy must be spent on removal of the gaseous component.[104] Generally materials that have a more open pore system (larger surface area) adsorb more gas, and the materials that have a more confined pore system have higher heats of adsorption.

Whilst a comprehensive review of the gas sorption behaviour of porous materials is beyond the scope of this thesis, additional information can be found in several reviews.[105-107] A brief introduction to the sorption behaviour of nitrogen, hydrogen, methane and carbon dioxide is, however, presented. The sorption behaviour of these gases in a series of MOFs is discussed in Chapter 4.

1.3.5.1 Nitrogen Adsorption

Although the direct capture of nitrogen gas is not industrially relevant, nitrogen isotherms are commonly run on porous materials at cryogenic temperatures to determine their surface area.[108] Within the MOF community, this is most commonly performed through the Brunauer-Emmett-Teller (BET) equation.[109] For these materials it is considered more accurate than the Langmuir equation as it takes into account multilayer adsorption. The latter tends to over-estimate the surface areas of porous materials as only a monolayer of adsorbed gasses is assumed. Details on calculating BET surface areas can be found in Appendix 3.

1.3.5.2 Hydrogen Adsorption

There is significant interest in the use of hydrogen gas as a fuel source. This is due to the clean burning nature of hydrogen which, when burnt in oxygen, produces water as the only by-product.[110] For this to be a useful source of energy, the advancement of technologies that can help store and transport hydrogen is required. In recent years several materials have been proposed as potential solutions to this and include porous carbon,[111] zeolites,[112] and metal-organic frameworks.[113] These materials depend on the physisorption of gas within the material and hence the adsorption capacity depends on the surface area and features of the material.

The adsorption of large volumes of hydrogen is inherently difficult due to the small molecular dimensions and the weak interactions of hydrogen with adsorbents. This leads to marked temperature dependence for hydrogen physisorption with low hydrogen uptake capacities at ambient temperature. A positive side to the low interaction energy is the fast adsorption and desorption kinetics compared to species that chemisorb hydrogen such as metal hydrides.

It has been proposed that the ideal binding energy should be approximately 15 kJ/mol.[114] This would raise the working temperature of such materials from cryogenic temperatures to around room temperature. To increase the functional temperature of physisorbtion in metal organic frameworks, the strength of interactions with hydrogen gas must be increased. To increase adsorption enthalpies and hence adsorption at higher temperatures several

strategies have been developed. These include the synthesis of materials that, counter intuitively, contain very small pores.[115] This can be achieved by using small linkers or control of topologies or degrees of interpenetration. In these cases multiple adsorption sites per gas molecule act in concert to increase the binding energy between the gas and material, critical for hydrogen adsorption. Another strategy is the incorporation of open metal sites within frameworks. Open metal sites within frameworks have been shown to enhance the binding of hydrogen as the molecules directly interact with these sites.[83-85] The metal-hydrogen interactions have been confirmed by neutron powder diffraction experiments.[83-85] The strategies for introducing open metal sites in the MOFs have traditionally focused on the removal of coordinating solvent from metal clusters or the use of the metalloligand building blocks that contain open metal sites, such as porphyrin or salen units. The attachment of organometallic complexes to the aromatic components of the linkers, and the use of anionic frameworks with free metallic counter cations have also been investigated.[113]

The problem of hydrogen storage is the inherent weight of the storage material in comparison to the weight of the fuel source, decreasing the energy density of the system. As such, the uptake of materials considered for hydrogen storage materials is often quoted as a weight percentage.[113] This indicates the mass of hydrogen that can be stored inside a given weight of a particular material.

The appeal of MOFs for this task is their modular nature. Their size, shape and functionality can be tuned relatively easily to investigate these ideas and create new materials with novel properties. The inclusion of particular functional groups and open metal centres has been shown to facilitate modulation of the binding strength within series of frameworks.[116]

1.3.5.3 Methane Adsorption

Methane, like hydrogen, is another potential future fuel source. It is considered advantageous to hydrogen because it is naturally abundant, and although it still produces pollution, it is relatively environmentally friendly compared to conventional liquid hydrocarbon fuels. Among all hydrocarbons, methane has the highest hydrogen to carbon ratio and combustion of methane produces the smallest amount of carbon dioxide for each

unit of heat that is released.[116] However, because of its gaseous nature the density of energy stored is lower than other liquid hydrocarbons, hence the need for a suitable storage medium. As it is important to increase the total volumetric density of methane, adsorption values are often quoted as such. Many different porous materials have been examined and evaluated as potential methane storage media. Like hydrogen, research has focused on porous materials such as activated carbons, zeolites and MOFs.[117] Unlike hydrogen, the interaction energy between methane and the surface of MOFs is already large enough to give reasonable adsorption around room temperature.

Recently, the Advanced Research Projects Agency – Energy (ARPA-E) of the U.S. Department of Energy (DOE) updated the new methane storage target to guide the research on adsorbent based methane storage. This is a volumetric storage capacity of 350 cm^3(STP)/cm^3 at room temperature for the entire storage system.[118] The volumetric storage target is significantly higher than the previous one set in the year 2000 of 180 cm^3(STP)/cm^3 at 35 atm.[119]

The size and shape of the pores and the functionality included within, have an effect of the adsorption of methane in microporous materials. Computationally, it was calculated that MOFs with pore diameters of 4 or 8 Å show the highest calculated methane storage.[120] This corresponds to exactly one or two molecules across (CH_4 kinetic diameter 3.8 Å), maximising framework-gas interactions. More recently, from a large data set comprised of a mixture of experimental and theoretical data it has been shown that optimal pore diameter of ~11 Å for methane storage is a better guideline.[121] Like hydrogen, the sorption of methane has been shown to be strongest at open metal sites within frameworks.[86-88]

Storage materials that deliver natural gas to an engine require a minimum inlet pressure to operate. If the binding enthalpy is too high, then too much CH_4 will be retained at low pressures, decreasing the usable capacity. Alternatively, if the binding enthalpy is too low, then too little CH_4 will be adsorbed at higher pressures. It has been shown that the ideal enthalpy of adsorption for real world applications is 18.8 kJ/mol.[105] MOFs typically have values of 12-25 kJ/mol which encompass this ideal value, meaning they are suitable for methane storage applications. HKUST-1, a MOF containing coordinatively unsaturated copper(II) sites has subsequently been incorporated into a working vehicle.[107]

1.3.5.4 Carbon Dioxide Adsorption

Carbon dioxide is a significant contributor to global warming, and gigatonnes are produced every year.[122] Although the desired outcome would be to cease industrial production of this gas, this is not a foreseeable target, and new technologies that can sequester carbon dioxide from industrial flues or the atmosphere must be produced. In contrast to the gasses described previously, carbon dioxide has a high quadrupole moment and is therefore adsorbed by polar media such as MOFs to a greater degree than non-polar gasses. MOFs typically adsorb higher amounts of carbon dioxide with respect to nitrogen, hydrogen and methane due to the polar nature of both this gas and the frameworks. This selective adsorption of gases is characteristic of MOFs and enables potential applications such as separation of CO_2 from natural and flue gas.[123]

The variability in the structural characteristics (pore size and shape) dominates CO_2 adsorption effects and thus precludes generalisations about whether certain functional groups are optimal for sorption of this gas.[124] Analysis of a range of MOFs have shown that compounds containing fluoro and chloro functional groups frequently show better selectivity for CO_2 over N_2 and CH_4 compared to frameworks containing other functional groups.[125] This is attributed to the increase in polarity, resulting in an increased affinity for the high quadrupole moment of carbon dioxide. Similar effects are seen in other fluorinated materials such as gels and membranes.[126-127] Early work on CO_2 separation and storage focused on incorporation of Lewis basic sites in frameworks such as amino groups to mimic the current amine scrubbing technology. However, this analysis showed that although amine functional groups performed better than alkyl groups, the increase in adsorption is not as dramatic as expected. This may be due to the predominance of aromatic amine functional groups in MOFs. In these cases the partial charge on the nitrogen atom is not as strong as in alkyl amines which are the current predominant mode of carbon dioxide fixation as amine scrubbers.[128] Although interesting to note, these comparisons are generalisations based upon a selection of MOFs containing a wide variety of pore structures. It does not show the direct influence of a particular functional group on the sorption behaviour of a particular material. To investigate the effect of functional group on sorption behaviour, a series of isostructural frameworks would need to be created, differing only in an appended functional group.

1.3.5.5 Heat of Adsorption

Of vital importance to practical gas sorption applications is the isosteric heat of adsorption (Q_{st}), a measure of the strength of the interactions between the gas molecules and the internal surface of a porous material. For non-polar molecules, such as N_2, these interactions rely on comparatively weak van der Waals forces. If the adsorbate is polar, like CO_2, stronger bonds such as hydrogen bonds or dipole-dipole interactions may play a role and increase the adsorption potential. Stronger interactions can be induced by either modulation of the size of the pores or by introduction of strong binding sites.

The modulation of the size of the pores has been elegantly shown in the SIFSIX series of MOFs by Zaworotko and co-workers.[53,129] A series of three MOFs were created that differed by the size of the square one-dimensional microporous channels (Figure 1.19a, b, c). As the pore size in the frameworks decreases the enthalpy of adsorption of CO_2 (kinetic diameter 3.76 Å) increases as each gas molecule interacts with the surface of the MOF to a greater extent. As the channel width of the SIFSIX series decreases in the order SIFSIX-2-Cu (13.05 Å) > SIFSIX-2-Cu-i (5.15 Å) > SIFSIX-2-Zn (3.84 Å), the enthalpy of adsorption increases in the order SIFSIX-2-Cu (22 kJ/mol) < SIFSIX-2-Cu-i (32 kJ/mol) < SIFSIX-2-Zn (45 kJ/mol). The approximately constant Q_{st} values with increased loading shown in Figure 1.19d indicate that all points within the microporous structure adsorb equally well.

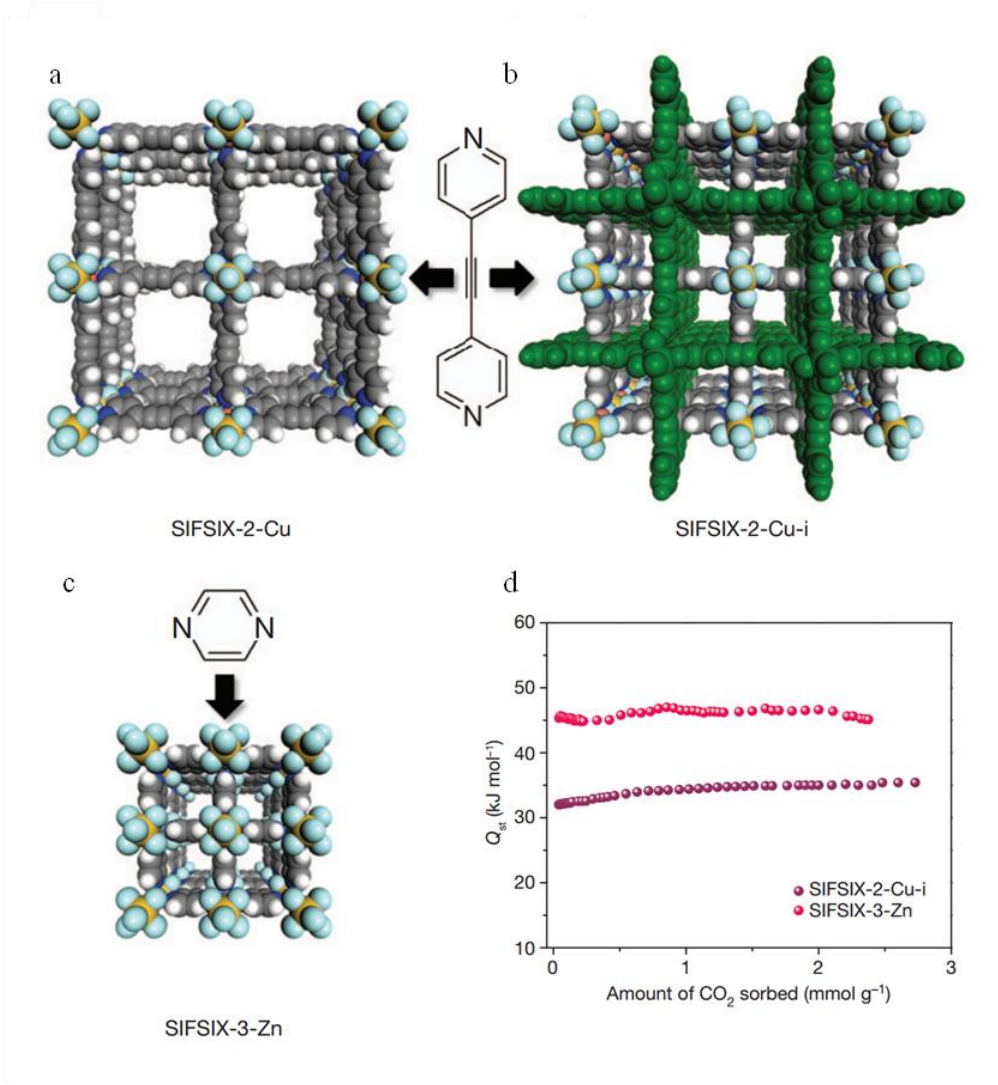

Figure 1.19: *Modulation of the channel dimensions in the SIFSIX series of MOFs directly affects the enthalpy of adsorption of CO_2. The smaller the width of the channels the stronger the interactions are with the adsorbate. a) SIFSIX-2-Cu. b) SIFSIX-2-Cu-i, an interpenetrated phase of (a). c) SIFSIX-3-Zn. d) Isosteric heats of adsorption for CO2 within two members of the SIFSIX family. Figure adapted from Zaworotko et al.*[53]

At zero-loading, this parameter gives an indication of the strength of the strongest binding sites within the material, which, depending on its magnitude, can subsequently be attributed to certain adsorption sites, such as exposed metal sites or amine functionalities. How this parameter changes with increased loading reveals the filling mechanism of the material. Open metal sites show remarkable increases in the enthalpy of adsorption in MOFs. However, this increased affinity is only present during filling of the MOF. Ni-MOF-74 (Ni_2(dobdc)) shows a high Q_{st} at zero loading for methane of 22 kJ/mol, however after

adsorption of approximately 100 cm^3/g, this drops off to 18 kJ/mol as all the open metal sites in the framework have been filled (Figure 1.20).[130] In contrast, MOF-5 exhibits a constant, but much weaker, binding energy of 12.3 kJ/mol as there is very little energetic difference between the potential binding sites.[131] The stronger binding energy of Ni-MOF-74 compared to MOF-5 is consistent with the shapes of the adsorption isotherms, for which the former compound has the steepest rise at low pressures, the latter exhibits a gradual adsorption isotherm. Activated carbon (AX-21, Figure 1.20) shows a gradual decline in Q_{st} with increasing adsorption due to its wide distribution of pore sizes. As the smaller pores, with stronger interactions with methane molecules fill up, the enthalpy of adsorption gradually decreases.

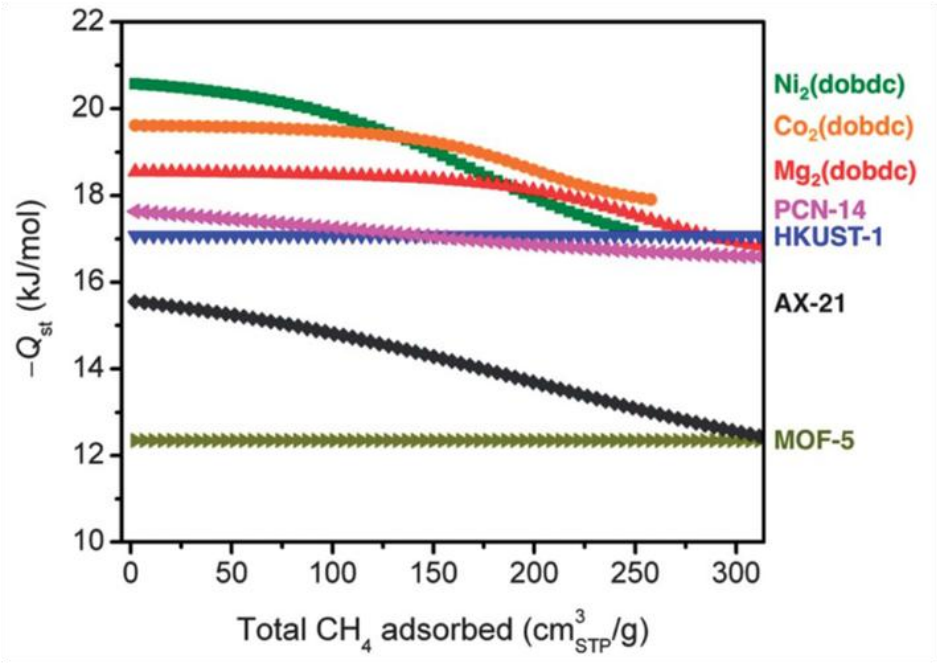

Figure 1.20: *Enthalpy of Adsorption in a series of MOFs and activated carbon. Figure adapted from Long et al.*[72]

It is worthwhile to note, that although HKUST-1 contains open metal sites, the octahedral cages within the structure are the primary adsorption sites due to their ideal size for methane.[132]

1.4 The Present Study

The overall objective of this thesis is to design and prepare novel metallosupramolecular assemblies and metal-organic framework materials. This will be achieved by the combination of metal ions with designed ligands systems. Although this aim is extremely broad in scope, it will be limited to three such systems, none of which have been studied with respect to their supramolecular interactions prior to the commencement of this thesis. The synthesis of novel supramolecular systems is important for many applications, the discussion of which is beyond the scope of this thesis but include the bottom up synthesis of nanotechnology, anion recognition/transport and sensing, magnetic materials, gas sorption and extractive metallurgy among others.[133] The metallosupramolecular assemblies presented herein will be discussed in the context of relevant potential applications where appropriate.

The systematic variance of the constituent parts of the prepared metallosupramolecular assemblies is integral to this work. The modular nature of the assemblies created will be investigated with regard to the structural and functional properties of each system where applicable. This will involve the systematic variance of metal ions and organic ligands within the presented systems. The rationale behind the choice of metal ions used will be outlined where relevant, and discussed in the appropriate section. The modulation of the organic ligand components will be performed by targeted organic synthesis using relevant synthetic techniques. Modulation of components is important in materials science as it allows for increased understanding of the system as well as tuning of the properties of the material.

The solid-state structures ascertained through single crystal X-ray diffraction of the metallosupramolecular assemblies will be the major focus of this research. The comparison of a library of similar structures allows for definitive conclusions about reproducible structural motifs which could be used in the rational design of metallosupramolecular assemblies containing similar organic building units for specific applications. Where relevant, other techniques such as luminescence and gas sorption measurements will be discussed and related back to the modulation of structural components.

Chapter 2 details the preparation of a family of N^1-acylamidrazone derivatives. The structure of these ligands is investigated through ^1H NMR spectroscopy and X-ray diffraction. The coordination chemistry of these ligands is then investigated with a strong focus on the reproducible hydrogen bonding motifs they form with counter ions in the solid state. The systematic modulation of these anions allows for the modulation of supramolecular architectures.

In Chapter 3 it is proposed that the N^1-acylamidrazone based ligands could adopt a bridging coordination mode upon twofold deprotonation. This led to the formation of a series of octanuclear metal-organic macrocycles when reacted with zinc(II) carboxylate salts. Modulation of the carboxylate co-ligands was achieved and the crystal packing analysed. It was proposed these could act as molecular building blocks in the synthesis of MOFs, and investigations into this were carried out.

Chapter 4 switches focus to 2,2':6',2''-terpyridine-4,4''-dicarboxylic acid derivatives. A series of ligands, differing by an appended functional group in the 4'-position were synthesised, and their use as scaffolds for the incorporation of a variety of functional groups in MOFs was investigated. A series of isoreticular frameworks based upon a zeolitic topology were produced and their gas sorption properties studied. The effect of the appended functional group on the structure and gas sorption properties will be discussed.

Chapter 5 looks at ways of including functionality in the form of open metal sites into MOFs. The linear structure and high stability of phenolic oxime complexes show promise for this purpose. Several metalloligands were synthesised and their use in the synthesis of MOFs were investigated.

A brief summary of these results will be presented in Chapter 6. This will be followed by a discussion of future work including the incorporation of such systems into potential applications.

Chapter 2

Hydrogen Bonding Motifs in Complexes Containing N^1-Acylamidrazone Based Ligands

2.1 Introduction

Intermolecular interactions have been widely studied in the field of crystal engineering due to their ability to produce designed structures based upon reproducible motifs.[16] One of the most common interactions used in synthetic supramolecular chemistry is the hydrogen bond due to its strength and directionality. A wide range of functional groups containing hydrogen bond donors and acceptors are commonly used for the formation of supramolecular assemblies. Of particular note and relevance to this chapter are the related amide, urea and squaramide functional groups which are known to be strong hydrogen bond donors.[10,134-135]

The N^1-acylamidrazone functional group has not been studied in the context of its supramolecular chemistry despite it being commonly produced as an intermediate in the synthesis of 1,2,4-triazoles; a heterocyclic motif widely used in medicinal, coordination and materials chemistry.[136-137] This intermediate, as the name suggests, is derived from acyl, amide and hydrazone functional groups, and like its constituents it is expected to form many potential hydrogen bonding interactions. With this in mind systems based upon this intermediate were investigated. The N^1-acylamidrazone functional group can be synthesised from nitrile groups in two ways; through the formation and then acylation of an amidrazone, or through the formation and then reaction of an alkyl imidate with a hydrazide derivative (Scheme 2.1). Substituted amidrazone molecules follow the IUPAC naming conventions of $RC(N^3H_2)=N^2\text{-}N^1H_2$.[138]

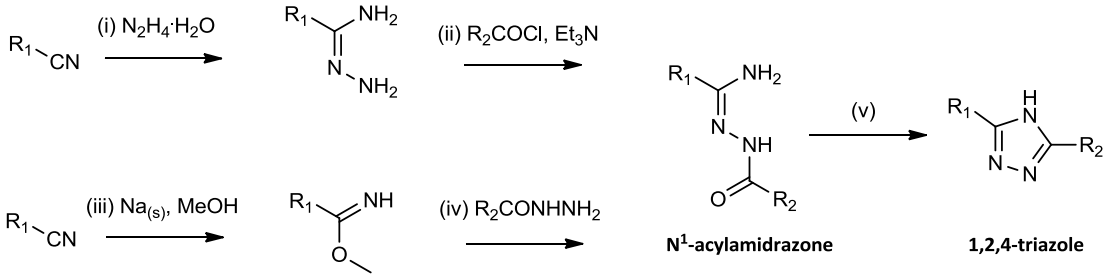

Scheme 2.1: *Synthesis of 1,2,4-triazoles from nitrile groups via N^1-acylamidrazones. Reactions i-iv are typically conducted at room temperature. Typical reaction conditions for cyclisation (v) include refluxing in ethylene glycol, use of dehydrating agents or microwave irradiation.*

When adjacent to a 2-pyridyl moiety the N^1-acylamidrazone functional group is expected to act as a tridentate ligand (Scheme 2.2). The coordination sphere is comprised of a pyridyl nitrogen atom in addition to the N^2 nitrogen atom of the amidrazone and the oxygen atom of the acyl group. Conjugation of the N^1-acylamidrazone functional group with the pyridyl ring enforces planarity in the ligand and hence meridional coordination geometry is expected around a 6-coordinate metal ion. As a consequence of this coordination mode, the protons on the hydrazide amide-like nitrogen atom, N^1, and the primary imidamide nitrogen atom, N^3, are arranged in a way reminiscent of the squaramide functional group (Figure 2.1).

Although the $C=N^2$ bond can exist in two isomeric forms in the free ligand, *i.e.* N^1 can be *cis* or *trans* to N^3, the sole crystal structure of a neutral molecule containing this functional group (reported as an intermediate of a 1,2,4-triazole) exhibits a *cis* geometry which allows for the formation of the squaramide like hydrogen bonding pocket.[139] When coordinated in the aforementioned tridentate binding mode, it requires this isomeric form. The rotation about the amide bond must also be in the correct orientation for coordination. This again enforces the correct orientation for anion binding.

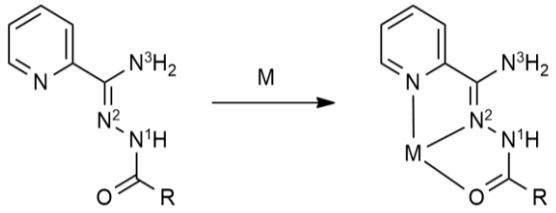

Scheme 2.2: *Tridentate coordination to metal centres requires certain geometries of the N^1-acylamidrazone functional group.*

The use of the hydrogen bonding pocket on the non-coordinating side of the N^1-acylamidrazone functional group has not been investigated. This pocket, created from amide-like protons (on N^1 and N^3, respectively) is expected to be a good hydrogen bond donor due to the arrangement of protons and the electron withdrawing nature of the attached 2-pyridyl ring. Upon coordination to an electropositive metal centre in a tridentate fashion the ability to bind anions is expected to greatly increase. In addition, the position of the amide oxygen atom will be locked creating a pair of hydrogen bond donors with a

similar geometry to that of squaramides; a functional group commonly used to bind anions.[10,134-135] The presence of a metal ion will result in a positively charged assembly that makes anions ideal targets for the hydrogen bond acceptors of this functional group.

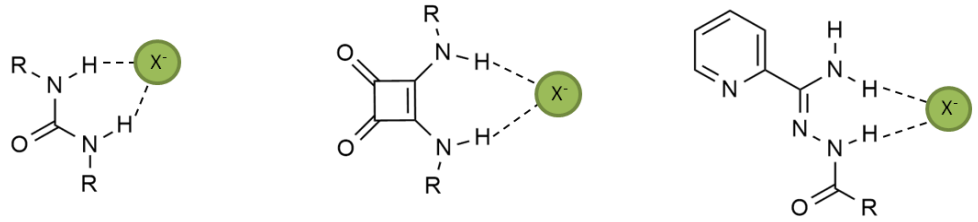

Figure 2.1: *Hydrogen bonding pockets of urea, squaramide and pyridin-2-yl(N^1-acylamidrazone) based ligands. Urea and squaramide functional groups commonly adopt R_2^1 (6) and R_2^1 (7) hydrogen bonding interactions, respectively, with monoatomic anions. Due to the size and geometry of the N^1-acylamidrazone functional group, it is expected to act in a similar way to squaramide and form R_2^1 (7) arrangements too.*

To investigate both the coordination chemistry and the hydrogen bonding interactions of this functional group, a series of ligands based upon it were synthesised. The simplest derivative pyridin-2-yl(N^1-acetylamidrazone) (H_2**L2.1**, Scheme 2.3) was synthesised through both methods of N^1-acylamidrazone synthesis mentioned in Scheme 2.1. As this ligand is the simplest synthesised in this chapter, it will be used as the basis upon which to make comparisons with other analogues. This ligand has been reported in the literature, but only as an intermediate in the synthesis of 2-(5-methyl-1,2,4-triazol-3-yl)pyridine, hence, the coordination and supramolecular properties of it have not been investigated.[140-142] The simplicity of this ligand compared with the few containing this functional group reported previously allows only the coordination and hydrogen bonding modes of the desired functionality to be studied.

The second derivative, pyridin-2-yl(N^1-amidoamidrazone) (H_2**L2.2**, Scheme 2.3) was synthesised to study the affect of the N^1-acylamidrazone hydrogen bonding pocket relative to that of a urea-like binding pocket within the same molecule. This ligand has not previously been reported in the literature, although the related thioacyl equivalent, synthesised through a similar procedure has.[143-146] Metal complexes of this ligand have shown biological activity and the coordination modes of the thiosemicarbazide moiety investigated with regard to soft metals such as gold and mercury.[147-149]

The ligand dipyridin-2-yl(N^1,$N^{1'}$-succinylbisamidrazone) (H_4**L2.3,** Scheme 2.3), was synthesised and contains two N^1-acylamidrazone functional groups. This will be used to investigate the effect of linking two such coordination domains together. Although this ligand was novel when first synthesised, recent publications have since reported the structure and magnetic properties of copper(II) and dysprosium(III) complexes.[150-151]

A derivative containing a carboxylic acid functional group, (H_3**L2.4**, Scheme 2.3) was also investigated. This ligand was synthesised as it is similar to previously reported ligands used within the group.[152] It was synthesised through a slightly modified method to those mentioned above. Pyridyl-2-amidrazone was reacted with succinic anhydride to form the ligand which allowed the incorporation of the free acid group.

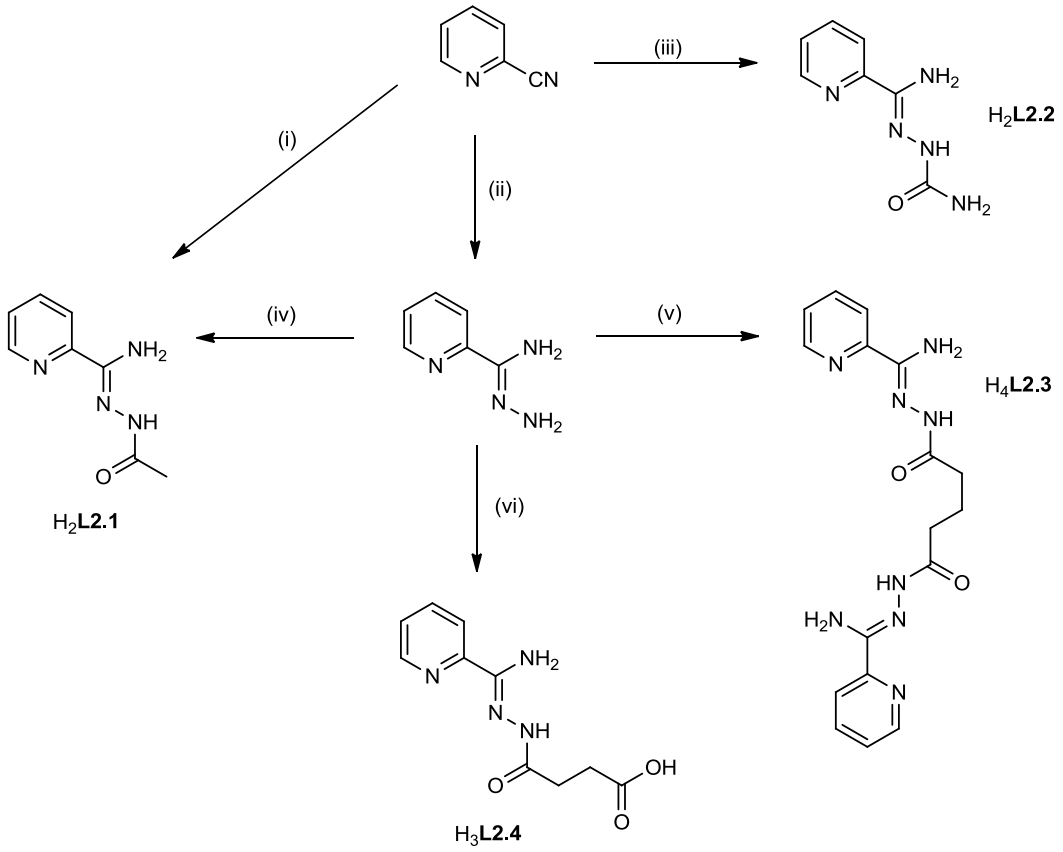

Scheme 2.3: *Synthesis of H_2**L2.1**-H_3**L2.4**. Reagents and conditions: (i) Sodium, methanol, acetylhydrazide. (ii) hydrazine hydrate, ethanol. (iii) semicarbazide hydrochloride, ethanol, triethylamine. (iv) Acetyl chloride, dichlormethane, triethylamine. (v) succinyl chloride, dichloromethane, triethylamine. (vi) succinic anhydride, ethylacetate.*

In addition to the pyridyl derivatives shown in Scheme 2.3, 2-pyrazinyl and 2-pyrimidinyl derivatives of H_2**L2.1**, named H_2**L2.5** and H_2**L2.6,** respectively, were synthesised using analogous procedures starting from 2-cyanopyrazine or 2-cyanopyrimidine. The more electron poor nature of these diazine derivitives with respect to pyridine is expected to make the acetyl amidrazones protons more acidic. Also, the potential extra metal coordination site could be incorporated into structures.

This chapter deals with the hydrogen bonding networks formed from the reaction of a variety of ligands containing N^1-acylamidrazone functional groups with transition metal salts. These interactions are examined through X-ray crystallography and described with graph set nomenclature.[22-23] Although the results presented here are only characterised and analysed by their structure, relevant examples may have potential applications in the fields of magnetochemistry.[153-154]

2.2 Ligand Synthesis

To examine the properties of this functional group, a simple derivative, H_2**L2.1**, was synthesised. Although the coordination chemistry of H_2**L2.1** has not previously been studied, ligands containing other similar functional groups have been in their neutral[150] and mono-deprotonated state[155,156] and magnetic properties of the resultant complexes studied. In each case the ligand adopts a meridional NNO coordination mode about an octahedral or square-based pyramidal metal ion. The free ligand structure of two illustrative examples, H_2**L2.1** and H_4**L2.3**, will be discussed below.

2.2.1 Synthesis and Structure of H_2L2.1

The ligand H_2**L2.1** can be synthesised via the reaction of acetyl hydrazide with methyl picolinimidate, prepared *in situ* from 2-cyanopyridine and sodium methoxide (Scheme 2.4). This procedure has the advantage over the other synthetic route to N^1-acylamidrazones as it does not generate triethylammonium chloride, a substance that can be difficult to remove from the final product highlighting its potential as an anion binder.

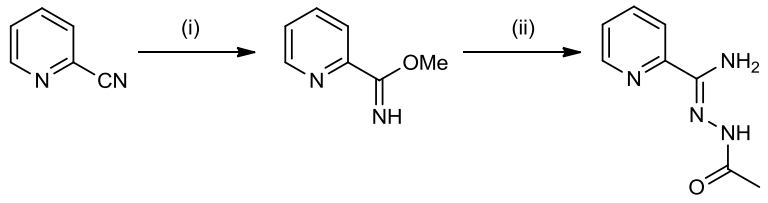

Scheme 2.4: *Synthesis of pyridin-2-yl(N^1-acetylamidrazone) (H_2**L2.1**). Reagents and conditions: (i) $Na_{(s)}$, MeOH, room temperature. Product used in-situ; (ii) acetylhyrazide, EtOH, reflux.*

The presence of a carbonyl stretch in the IR spectrum (1651 cm^{-1}) indicated the product had not cyclised to the 1,2,4-triazole under these conditions. Mass spectroscopy showed the presence of a [$C_8H_{10}N_4O+H^+$] peak at 179.0930 m/z (requires 179.0933 m/z) substantiating this. The ^{1}H NMR spectrum showed two environments for the hydrazide, 1° imidamide and methyl protons indicative of the hindered rotation of the hydrazide amide bond.[157] These can be seen at *circa* 9.8, 6.6, and 2.0 ppm for the amide, amine and methyl proton environments, respectively (Figure 2.2). These conformers exist in an approximate 3:2 ratio in DMSO at 25 $^{\circ}$C. Increasing the temperature of the sample to above 358 K led to the coalescence of signals at which point the rotation of the acetyl group becomes faster than the NMR time scale. Upon cooling back down to room temperature, an identical spectrum to that obtained before heating was observed, indicating that the ligand does not undergo cyclisation under these conditions.

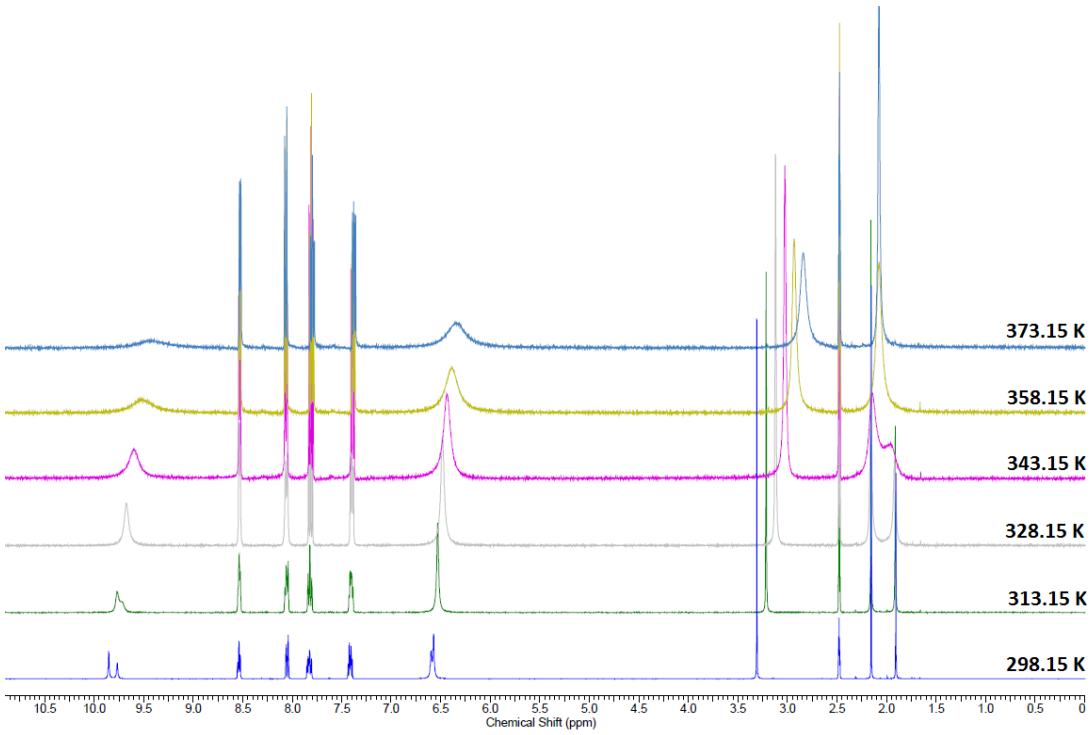

***Figure 2.2**: ^{1}HNMR spectra of H_2**L2.1** in d_6-DMSO at a range of temperatures. Coalescence of the amide (9.8 ppm), amine (6.6 ppm) and methyl (2.0 ppm) group protons can be observed above 358 K.*

Recrystalisation of H_2**L2.1** from methanol afforded crystals which were suitable for single crystal X-ray diffraction. The crystal data were solved and refined in the orthorhombic space group *Pbca* (R-factor 4.36%) with one H_2**L2.1** molecule in the asymmetric unit (Figure 2.3). The structure showed the ligand adopts the Z-stereoisomer around the C=N^2 (C7-N9) bond and antiperiplanar geometry around the hydrazide amide bond (N10-C11) (Figure 2.3a).

Each ligand is connected to three equivalent molecules via two non-equivalent sets of hydrogen bonds resulting in the formation a two dimensional sheet with a honeycomb (**hcb**) topology (Figure 2.3b). The unique interaction is a centrosymmetric $R_4^4(10)$ interaction comprised of the hydrogen bond donor H8A and acceptor N1. The other unique interaction, which occurs twice per molecule is defined as $N_1 = R_1^2(5)R_2^1(7)$, $N_2 = R_2^2(10)$ from hydrogen bond donors H8B and H10, and acceptors N9 and O12.

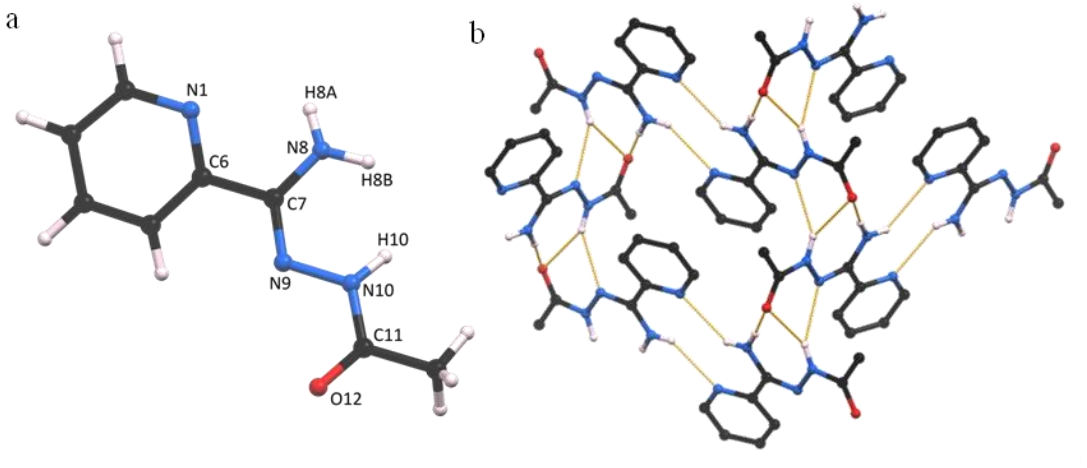

Figure 2.3: *a) Single crystal X-ray structure of* H_2***L2.1****. b) Hydrogen bonding interactions in the structure of* H_2***L2.1*** *create a two-dimensional framework. C-H bonds omitted for clarity. Selected bond lengths(Å) and angles(°); C7-N8 1.346(3), C7-N9 1.297(2), N9-N10 1.400(3), N10-C11 1.336 (3), C11-O12 1.234(3), N1-C6-C7-N8 11.8(3).*

This hydrogen bonding network is thought to contribute to the observed low solubility of H_2**L1** in common solvents. IR spectroscopy, NMR spectroscopy, mass spectrometry and single crystal X-ray crystallography confirmed that H_2**L1** was produced and exists in the non-cyclised form.

2.2.2 Synthesis and Structure of H_4L2.3

The ligand H_4**L2.3** was prepared via a similar synthetic pathway to H_2**L2.1** and can be thought of as effectively two H_2**L2.1** ligands connected at the methyl group. This ligand shows a similar splitting of the amidrazone and alkyl protons in the ^{1}H NMR spectrum due to the hindered rotation about the amide bond. Poor solubility in d_6-DMSO meant the spectrum was not as well resolved as H_2**L2.1**.

Recrystallisation of the analytically pure compound from a DMSO/methanol mixture afforded crystals suitable for single crystal X-ray diffraction. The structure was solved and refined in the monoclinic space group $P2_1/c$ (R-factor 7.58 %). The model obtained showed the expected structure of compound H_4**L2.3** confirming the ligand had not undergone cyclisation to the 1,2,4-triazole under recrystallisation conditions (Figure 2.4). The long

molecule is centred on an inversion centre making only half of each ligand crystallographically unique.

Analysis of the bond lengths showed that H_4**L2.3** exists in the same tautomeric form in the solid state as H_2**L2.1**. In addition to this, it also adopts the same rotomeric form about the hydrazide amide bond and pyridyl-amidrazone bond as H_2**L2.1** despite having a different crystal packing arrangement.

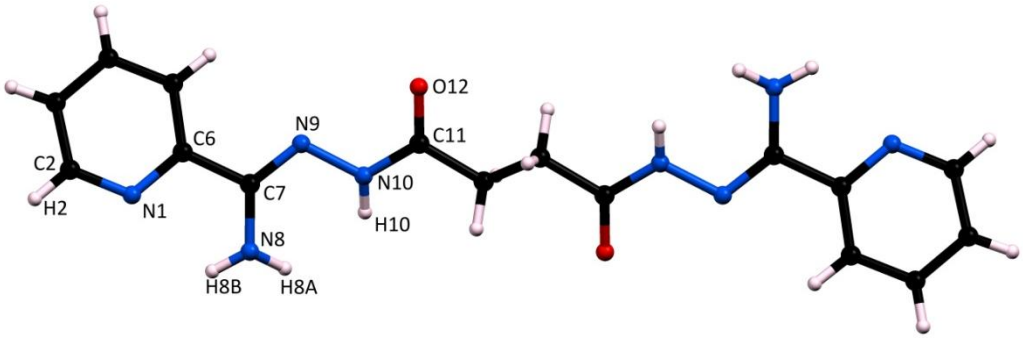

Figure 2.4: *Single crystal X-ray structure of compound H_4**L2.3**. Selected bond lengths(Å) and angles(°);C7-N8 1.346(5), C7-N9 1.303(5), N9-N10 1.405(5), N10-C11 1.339(5), C11-O12 1.239(4), N1-C6-C7-N8 12.9(5).*

The orientation of the N^1-acylamidrazone functional group allows for the hydrogen bonding pocket described in Figure 2.1. This interacts with the amide oxygen atom of a neighbouring molecule in a $R_2^1(7)$ arrangement, the same type of interaction seen in squaramide derivatives with monatomic hydrogen bond acceptors. These interactions allow the formation for a one dimensional hydrogen bonded polymer (Figure 2.5a). The link between molecules is comprised of two sets of these interactions.

The ligand adopts the well known herringbone arrangement with an angle of 77.73°. This arrangement is mediated by weak C-H···N hydrogen bonds of the pyridyl nitrogen atom and an α-CH of a pyridine ring. Although classed as a nonconventional hydrogen bond, this hydrogen bond donor is commonly seen as its position on the electron poor heterocycle means electron density is pulled away from the hydrogen atom strengthening the interaction. The arrangement of these nonconventional hydrogen bonds can be described as N_1=C(3)C(16), N_2=R_4^4(38).

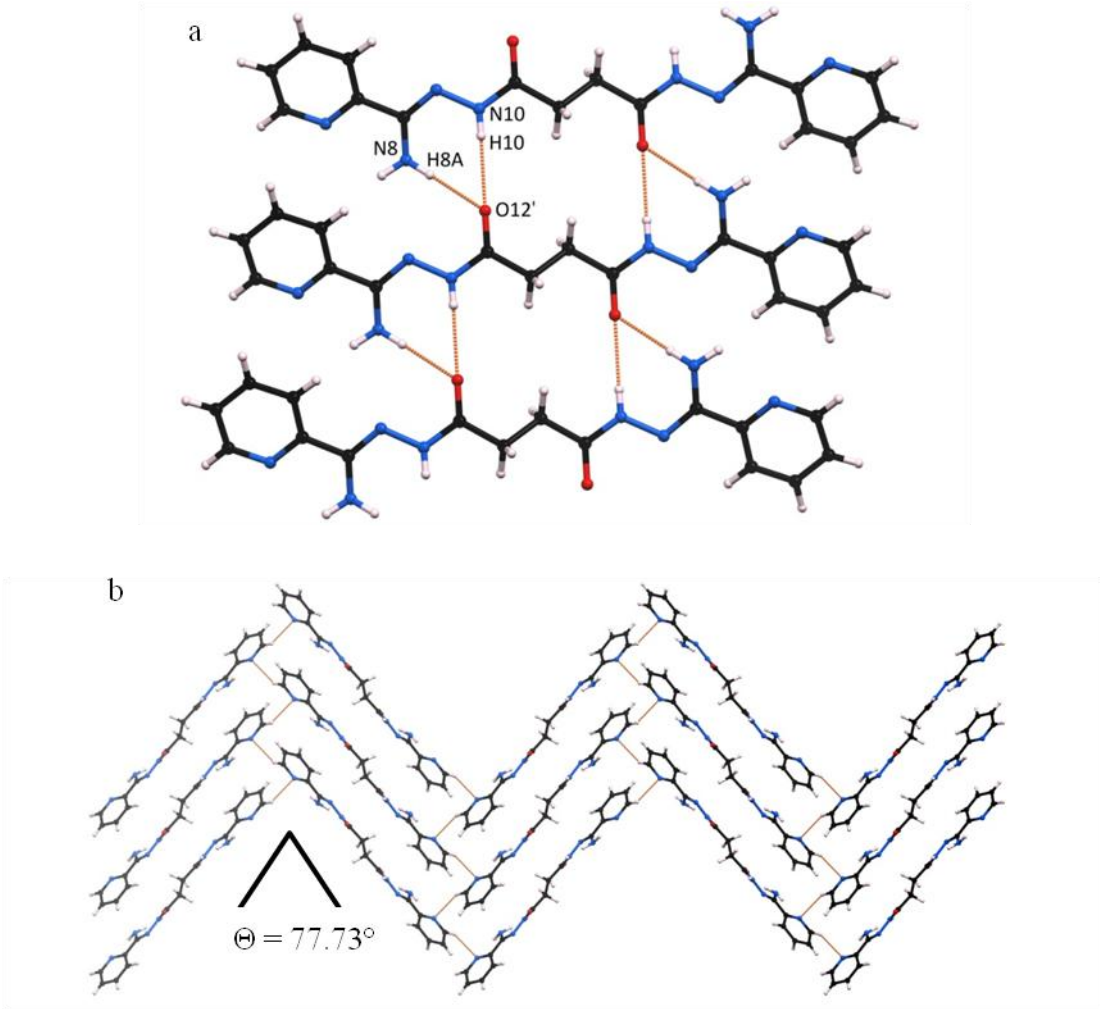

Figure 2.5: *Crystal packing of H_4**L2.3** showing the a) the $R_2^1(7)$ hydrogen bonding interactions of the acylamidrazone functional group and (b) the N_1=C(3)C(16), $N_2=R_4^4(38)$ α-CH to pyridyl nitrogen hydrogen bonding interactions and herringbone packing arrangement.*

Of particular note is the orientation of the amide. As with H_2**L2.1**, solution NMR showed evidence of a mixture of rotomers due to the hindered rotation about the amide bond. The crystal structures, of H_2**L2.1** and H_4**L2.3** show that in the solid state only a single rotomer exists.

2.2.3 Summary

The ligands H_2**L2.1** and H_2**L2.3** were shown to self recognise in the solid state. In each case $R_2^1(7)$ type hydrogen bonding interactions (that seen in squaramide derivatives) between protons of the amidrazone and oxygen atom of the acyl functional group were observed. Introduction of more effective hydrogen bond acceptors than an amide-like oxygen atom will be required to disrupt this interaction and form non-self recognition interactions. The same tautomer of the amidrazone functional group and same rotomer (about both the amide and pyridyl-amidrazone bonds) was observed in each case.

2.3 Reactions with Metal(II) Carboxylate Salts

Carboxylate anions are known to be good hydrogen bond acceptors. Due to the presence of two electronegative elements in this functional group there are multiple ways in which they can interact with multiple hydrogen bond donors. The two most common are shown in Figure 2.6 with urea as an example of a two-fold hydrogen bond donor.

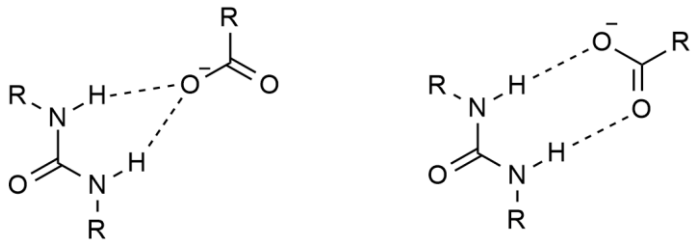

Figure 2.6: *Typical hydrogen bonding interactions of carboxylate anions with urea, a two-fold hydrogen bond donor. The left example corresponds to a* $R_2^1(6)$ *interaction and the right a* $R_2^2(8)$ *interaction.*

Ladder-like architectures have a long history in supramolecular chemistry.[158] Although the most famous is probably that created by base pairing within the helical nature of DNA, other synthetic examples of this topology have been created. The reaction of H_2**L2.1** with a series of metal carboxylate salts produced a series of compounds with ladder-like architectures assembled by hydrogen bonding motifs.

2.3.1 Synthesis of [Zn(H_2L2.1)$(AcO)_2$] (2.1)

H_2**L2.1** was combined with a stoichiometric amount of zinc(II) acetate in methanol. Following evaporation of the pale yellow solution, colourless needle-like crystals suitable for single crystal X-ray diffraction formed and were isolated by filtration. The data were solved and refined in the monoclinic space group *Cc* (R-factor 3.57 %). The asymmetric unit contained a complete discrete [Zn(H_2**L2.1**)$(AcO)_2$] neutral complex (Figure 2.7). The neutral ligand adopts a tridentate coordination mode. The two acetate co-ligands coordinate via mono-dentate coordination modes (Figure 1.9), leading to the zinc(II) ion having an overall 5-coordinate geometry (τ_5 = 0.25).

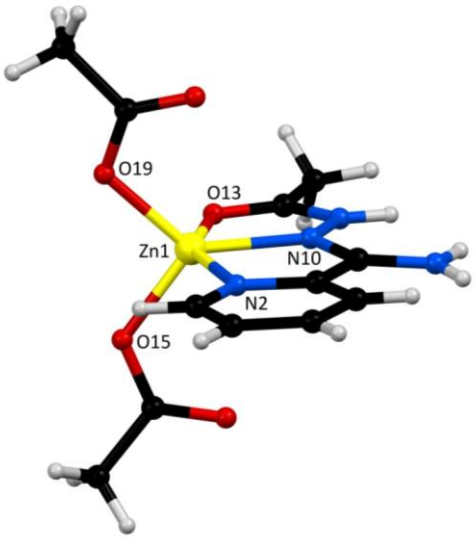

Figure 2.7: *Asymmetric unit of* ***2.1****. Selected bond lengths (Å) and angles (°): Zn1-N2 2.178(5), Zn1-N10 2.045(3), Zn1-O13 2.242(5), Zn1-O15 1.972(4), Zn1-O19 1.970(4), N2-Zn1-O13 149.3(2), N10-Zn1-O19 134.2(2), O15-Zn1-O19 95.8(2).*

Analysis of the hydrogen bonding interactions showed the complexes assemble in a ladder-like fashion (Figure 2.8). In this analogy the rungs of the ladder are comprised of the coordinated H_2**L2.1** ligands and the side rails are the hydrogen bonding interactions between the coordinated acetate co-ligands and H_2**L2.1**. There are two distinct types of side rail; one is a $R_2^1(7)$ squaramide-like interaction (H9A, H11, O17), the other can be described simply as a D interaction (H9B, O21). For simplicity the large rings created by higher levels of this interaction will not be described. Each of these interactions is given a

different colour in the schematic description of this architecture shown in Figure 2.8c. The steps of the ladder have a head-head type arrangement with the pyridyl ring of adjacent steps on the same face of each ladder. Alternate arrangement of the $R_2^1(7)$ and the D interactions mean that each step in the ladder is evenly spaced. Each supramolecular ladder is bisected by a glide plane.

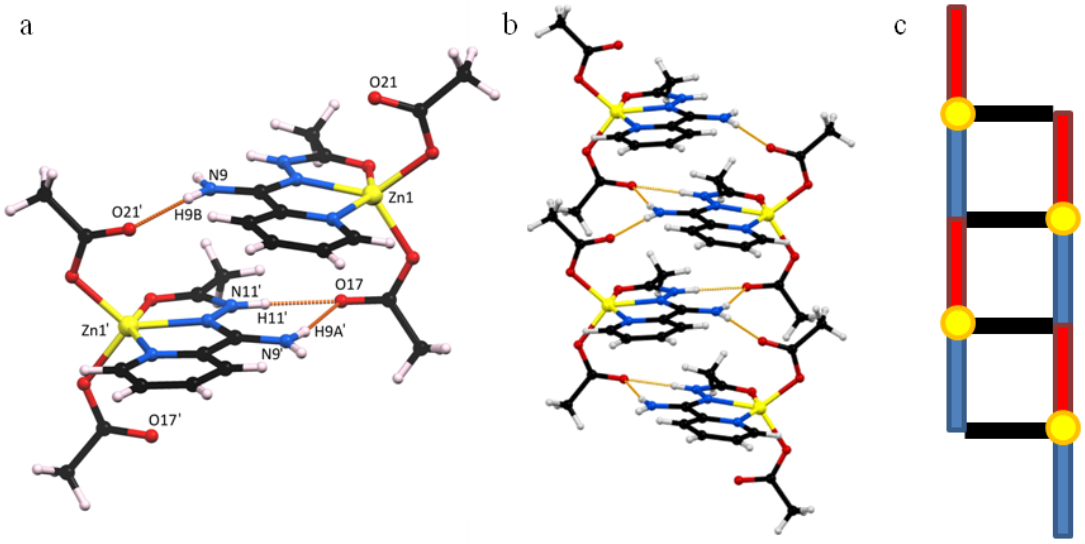

Figure 2.8: *Hydrogen bonding interactions in* ***2.1****. There are two types of hydrogen bonding interactions between complexes; one utilises the amidrazone pocket (H9A,H11-O17), the other uses the proton of the 1° imidamide nitrogen atom (H9B-O21). These interactions allow for the formation of a supramolecular polymer with a ladder-like architecture and glide plane symmetry. a) Interactions between symmetry equivalent complexes. b) Formation of one-dimensional ladder motif. c) Schematic of the ladder motif showing each type of hydrogen bonding interaction in a different colour; blue is the* $R_2^1(7)$ *squaramide-like interaction, red is a single D type interaction. Black steps represent the pyridyl end of* H_2***L2.1*** *coming out of the page, yellow circles represent the positions of zinc(II) ions.*

The ladders pack in a checker-board type arrangement with alternating ladders and solvent accessible channels. As each ladder is neutral, it is assumed that solvent methanol is contained within these channels. Despite attempts it was not possible to model this solvent and therefore the SQUEEZE routine within PLATON was used to suppress the contribution of the disordered solvent electron density to the assigned atoms.[159] This showed a total of 68 electrons were removed from the 190 $Å^3$ (11 %) solvent accessible void volume of the unit cell. This equates to 17 electrons per zinc(II) ion, or about one molecule of methanol (18 electrons). This contrasts the degree of solvation indicated by elemental analysis for which the best fit was obtained with 1.5 molecules of water per complex. The difference is

attributed to the different handling conditions before each technique leading to the loss of methanol followed by rehydration from atmospheric water.

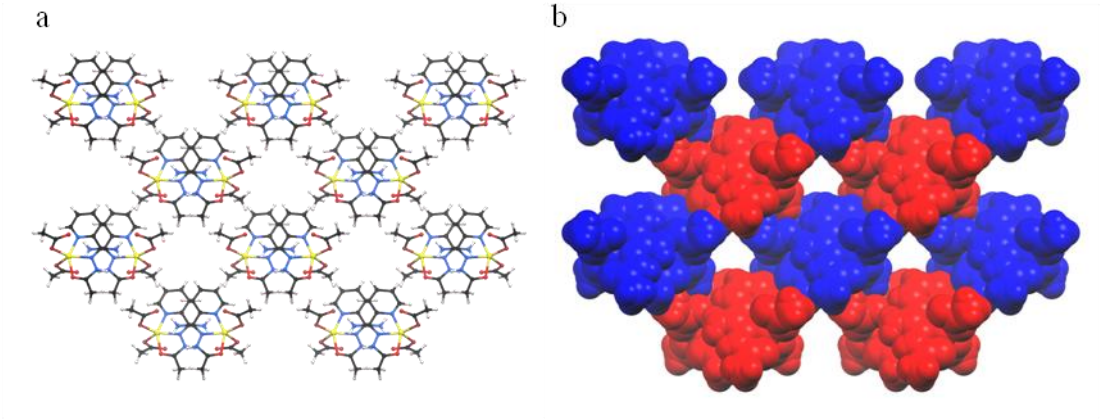

Figure 2.9: *a) The supramolecular ladder structure of* ***2.1*** *propagates along the crystallographic c-axis (into page). b) Each ladder is arranged such that small one-dimensional channels exist between ladders and propagate down the same axis. Each one-dimensional ladder is shown as either red or blue.*

Despite the solvent channels running parallel to the direction of the one-dimensional ladder motif, crystals of **2.1** were incredibly stable. After sitting for several years out of solution open to the atmosphere, they were shown to retain crystallinity by powder X-ray diffraction (Figure 2.10).

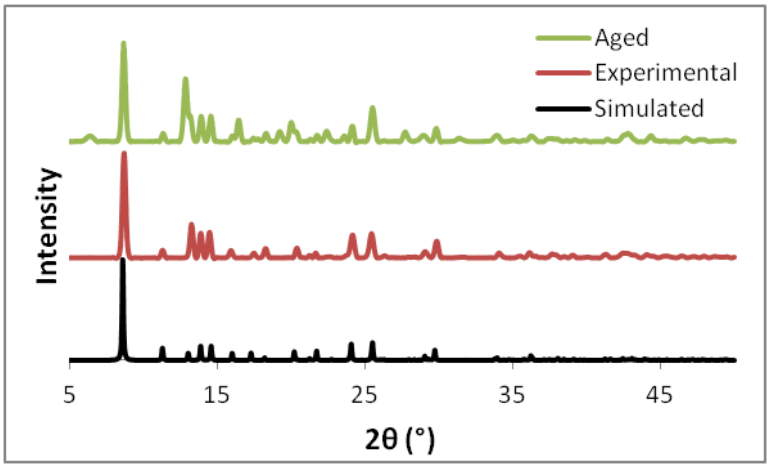

Figure 2.10: *PXRD patterns of* ***2.1****. Simulated pattern is shown in black, freshly synthesised in red and a sample aged open to the atmosphere for two years in green.*

2.3.2 Synthesis of $[Zn(H_2L2.1)(EtCO_2)_2]\cdot MeOH$ (2.2)

Combining stoichiometric amounts of zinc(II) propionate and H_2**L2.1** followed by evaporation of the resultant solution led to the crystallisation of **2.2**. The crystal was solved and refined in the monoclinic space group *Cc* (R-factor 4.82 %). The asymmetric unit contained a complete discrete $[Zn(H_2\mathbf{L2.1})(EtCO_2)_2]$ neutral complex (Figure 2.11). The neutral ligand adopts a tridentate coordination mode. The metal had a similar coordination geometry (τ_5 = 0.21) and had an analogous packing structure to **2.1**. The flexible propionate residues on the sides of the ladders showed no sign of disorder and are in the anti-conformation and have torsion angles of (1(1) and 9(1)°).

As before, each ladder has a head-head type arrangement of steps and centred on a glide plane. The same $R_2^1(7)$ and D hydrogen bonding interactions occur between rungs in the ladder. The same checker-board type arrangement of ladders exist, however in **2.2** the solvent within the channels could be located crystallographically and was seen to be a full occupancy methanol solvent molecule per complex supporting the assignment in **2.1**. This solvent was observed to have a D hydrogen bonding interaction with a coordinated carboxylate oxygen atom. Elemental analysis again showed a better fit of 1.5 water molecules per complex instead of a methanol solvent molecule. The difference is again attributed to the handling conditions before each measurement.

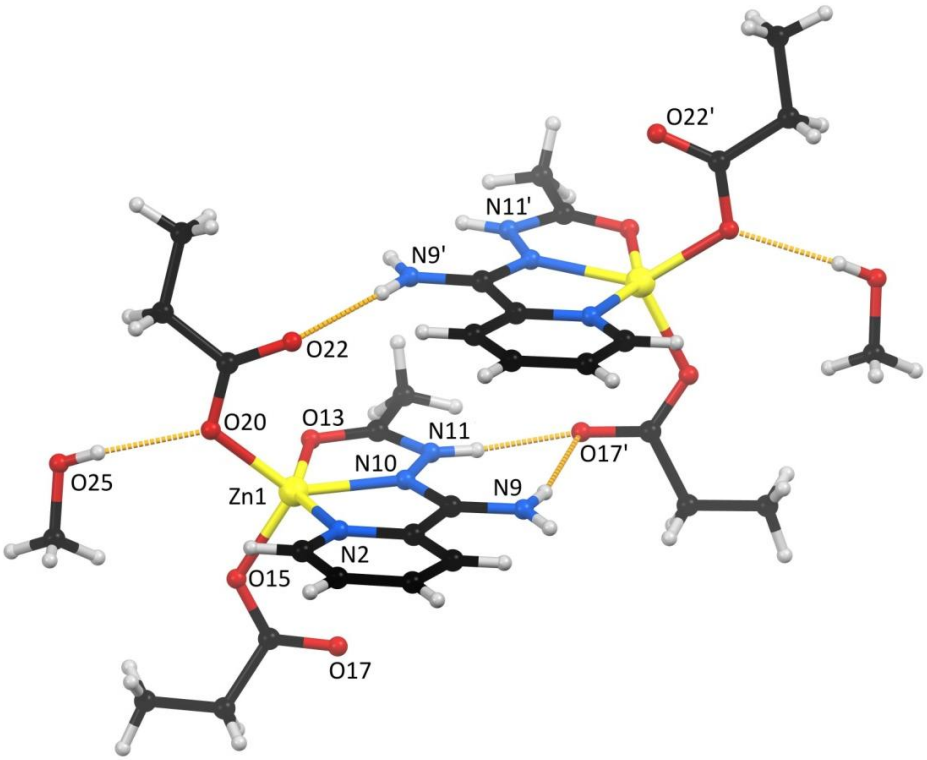

Figure 2.11: *Two complexes of* ***2.2*** *showing the hydrogen bonding interactions between selected complexes and solvent methanol. Selected bond lengths (Å) and angles (°): Zn1-N2 2.191(7), Zn1-N10 2.039(5), Zn1-O13 2.236(5), Zn1-O15 1.979(6), Zn1-O20 1.956(5), N2-Zn1-O13 149.7(2), N10-Zn1-O20 137.0(2), O15-Zn1-O20 97.9(2).*

The isostructural nature of **2.2** with respect to **2.1** indicates that the small change from acetate to propionate co-ligands does not affect the overall structure of the assembly.

2.3.3 Synthesis of [Zn(H_2L2.1)(ClAcO)$_2$] (2.3)

Combining stoichiometric amounts of zinc(II) chloroacetate and H_2**L2.1** produced crystals suitable for single crystal X-ray diffraction. These were solved and refined in the monoclinic space group *Cc* (R-factor 6.27 %). The asymmetric unit contained one complete [Zn(H_2**L2.1**)(ClAcO)$_2$] complex which has an analogous structure to **2.1** and **2.2** (Figure 2.12). The zinc(II) ion has a slightly more square pyramidal geometry than the previous two complexes (τ_5 = 0.16). As with **2.2**, the added flexibility of the carboxylate residue was not disordered, but has slightly larger dihedral angles (12(1) and 23(1)°). The solvent present

within the channels between ladder-like assemblies was unable to be located crystallographically and the SQUEEZE routine within PLATON was used to remove the contribution of this to the remaining atoms.[159] The electron density found within the solvent accessible void volume of the unit cell (12 %) corresponds to 18 electrons per zinc(II) ion, equivalent to one molecule of methanol (18 electrons). This is consistent with what was observed crystallographically in **2.2**. Elemental analysis showed 0.5 water molecules per zinc (5 electrons) and the difference is attributed to different handling procedures before each experiment.

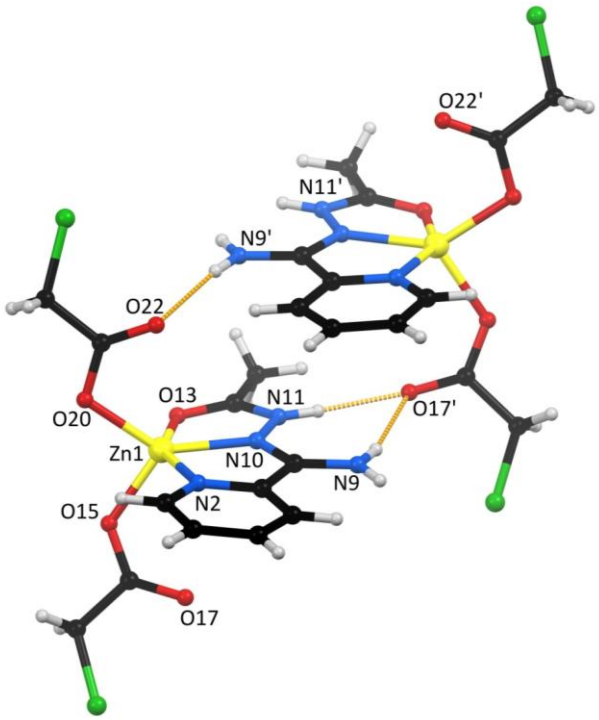

***Figure 2.12**: Two complexes of **2.3** showing the hydrogen bonding interactions between selected complexes. Selected bond lengths (Å) and angles (°): Zn1-N2 2.171(8), Zn1-N10 2.034(8), Zn1-O13 2.207(7), Zn1-O15 1.967(8), Zn1-O20 1.976(7), N2-Zn1-O13 150.2(3), N10-Zn1-O20 140.9(3), O15-Zn1-O20 91.0(3).*

2.3.4 Synthesis of [Zn(H_2L2.1)(BzO)$_2$] (2.4)

Zinc(II) benzoate and H_2**L2.1** were combined in methanol. Following evaporation of the solvent, crystals suitable for single crystal X-ray diffraction formed, and were solved and refined in the triclinic space group *P*-1 (R-factor 5.00 %). The asymmetric unit contained a complete neutral complex of the form [Zn(H_2**L2.1**)(BzO)$_2$] (Figure 2.13). The ligand

H_2**L2.1** coordinates to the zinc(II) ion in a tridentate coordination mode, and the benzoate co-ligands via monodentate coordination modes. The 5-coordinate zinc ion can be described as having distorted trigonal bipyrimidal geometry (τ_5= 0.16). The structure of this discrete complex is very similar to compounds **2.1**-**2.3**.

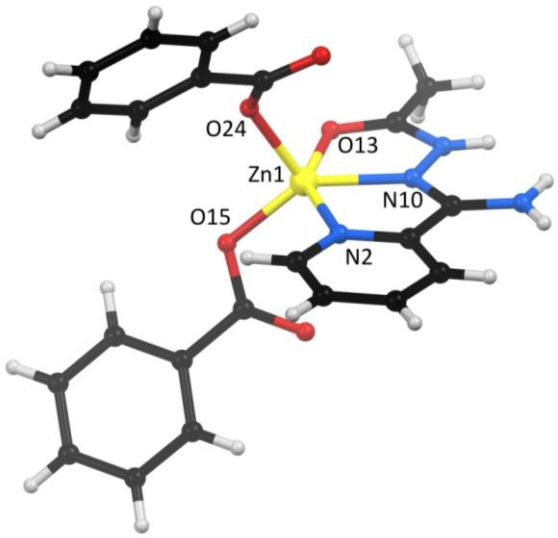

Figure 2.13: *Asymmetric unit of* ***2.4****. Selected bond lengths (Å) and angles (°): Zn1-N2 2.198(3), Zn1-N10 2.033(3), Zn1-O13 2.218(2), Zn1-O15 1.948(3), Zn1-O24 1.965(3), N2-Zn1-O13 149.5(1), N10-Zn1-O15 139.7, O15-Zn1-O24 99.7(1).*

Despite having a similar coordination sphere to **2.1**-**2.3**, an altogether different ladder-like structure to that seen in **2.1**-**2.3** is produced (Figure 2.14). This ladder is still based upon R_2^1 (7) and D hydrogen bonding interactions between the non-coordinating oxygen atoms of the carboxylate co-ligand and the hydrogen atoms of coordinated H_2**L2.1**. The main difference in the ladder of **2.4**, is that the H_2**L2.1** 'rungs' now take a head-tail type configuration instead of the head-head arrangement seen previously. Because of this arrangement, the ladders no longer have glide plane symmetry, but rather contain an inversion centre between each rung. Because of this type of arrangement, the distance between rungs is no longer strictly even. Every second gap is either comprised of a pair of R_2^1(7) interactions or a pair of D interactions. This contrasts **2.1**-**2.3** in which one of each type of interaction was seen per step.

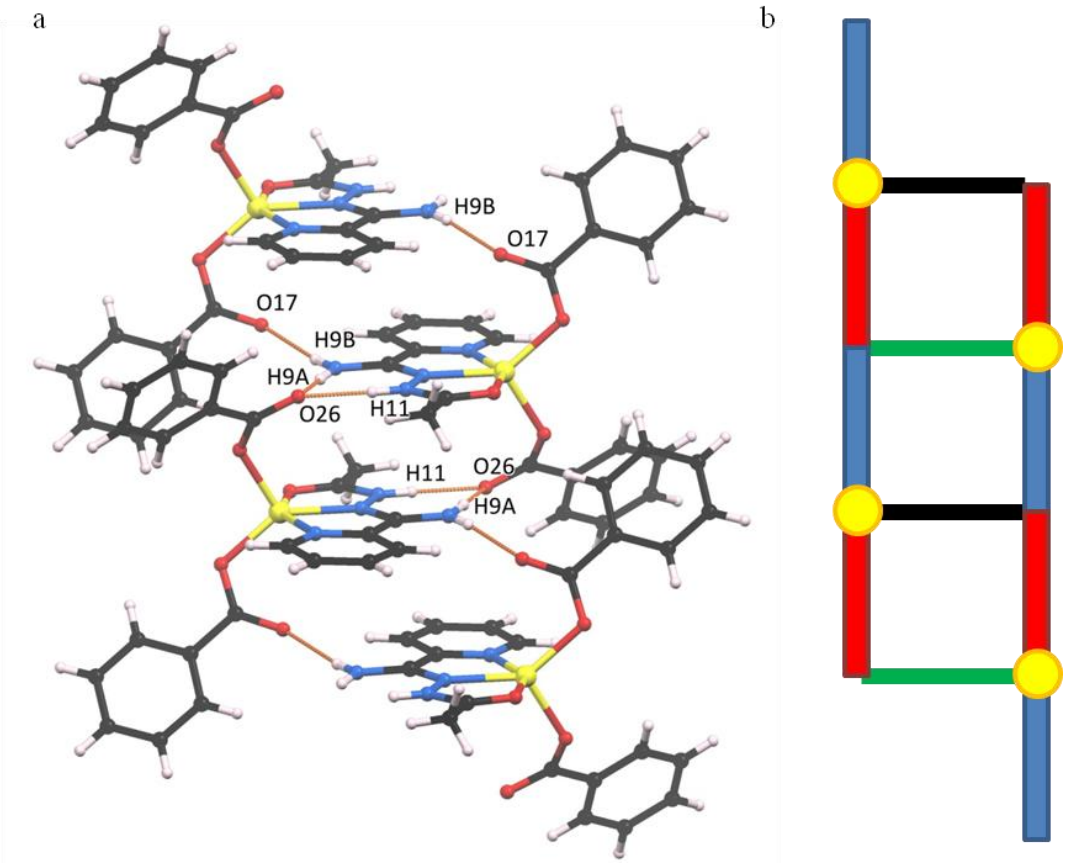

Figure 2.14: *Packing of **2.4** showing hydrogen bonding between complexes and the resultant ladder-like topology. Alternate steps in the ladder have different interactions, and the 'steps' of the ladder are in a head-tail arrangement. b) A simplified representation of the ladder-like topology. Blue represents* $R_2^1(7)$ *interaction, red a D interaction between a coordinated carboxylate anion and* H_2***L2.1***. *Black rungs represent the pyridyl end of the ligand coming out of the page, green represents it going into the page, yellow circles represent zinc(II) ions.*

Despite having different interactions in alternating steps, the distance between the steps remains relatively constant; interplanar distances between steps are 3.252(8) Å for the R_2^1 (7) (blue) and 3.276(8) Å for D (red) (*c.f.* **2.1** 3.310(7) Å between rungs).

The packing arrangement of **2.4** contains no room for solvent molecules to exist within the crystal lattice (Figure 2.15).

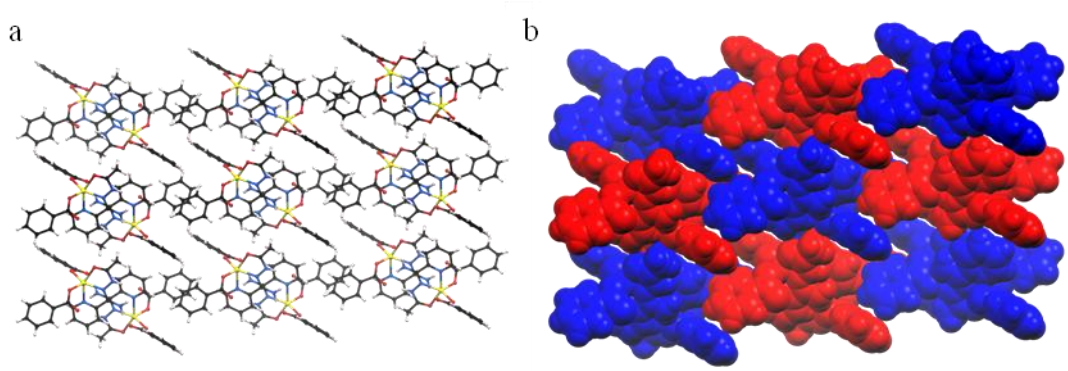

Figure 2.15: *Packing of* ***2.4*** *viewed along the crystallographic a-axis. The one-dimensional ladder-like supramolecular architecture is along the same axis. Space fill diagram showing that no void space exists between ladders.*

As the reaction conditions and the type of metal ion were kept constant, the apparent cause for this change in arrangement is the steric bulk of the benzoate groups compared to the smaller aliphatic acetate, propionate and chloroacetate groups of **2.1**, **2.2** and **2.3**.

2.3.5 Synthesis of [Zn(H_2L2.1)(*p*-MeBzO)$_2$] (2.5)

In an analogous procedure to **2.4**, a mononuclear zinc complex containing H_2**L2.1** and *p*-toluate ligands was prepared. This was solved and refined in the triclinic space group *P*-1 (R-factor 3.77 %) and contained one complex of the form [Zn(H_2**L2.1**)(*p*-MeBzO)$_2$] in the asymmetric unit. The ligand H_2**L2.1** coordinates in a tridentate fashion and the *p*-toluate co-ligands coordinate in a mononuclear fashion leading to an overall five-coordinate zinc(II) geometry (τ_5 = 0.05).

These discrete complexes were seen to assemble in a ladder like fashion, with a head-tail arrangement similar to that seen in **2.4**. However, a $R_2^2(9)$ rather than a $R_2^1(7)$ interaction exists in the squaramide-like pocket of the acylamidrazone ligand (Figure 2.16). This is due to a slight twist of one carboxylate group allowing it to act as a bifurcated hydrogen bond acceptor, similar to what was postulated in Figure 2.6. Despite this, the step distance in the ladder-like assembly is not significantly shortened or distorted. The overall architecture to

that seen in Figure 2.14b is retained with the exception of the blue steps which correspond to $R_2^2(9)$ rather than a $R_2^1(7)$ interactions. The red steps still correspond to D interactions.

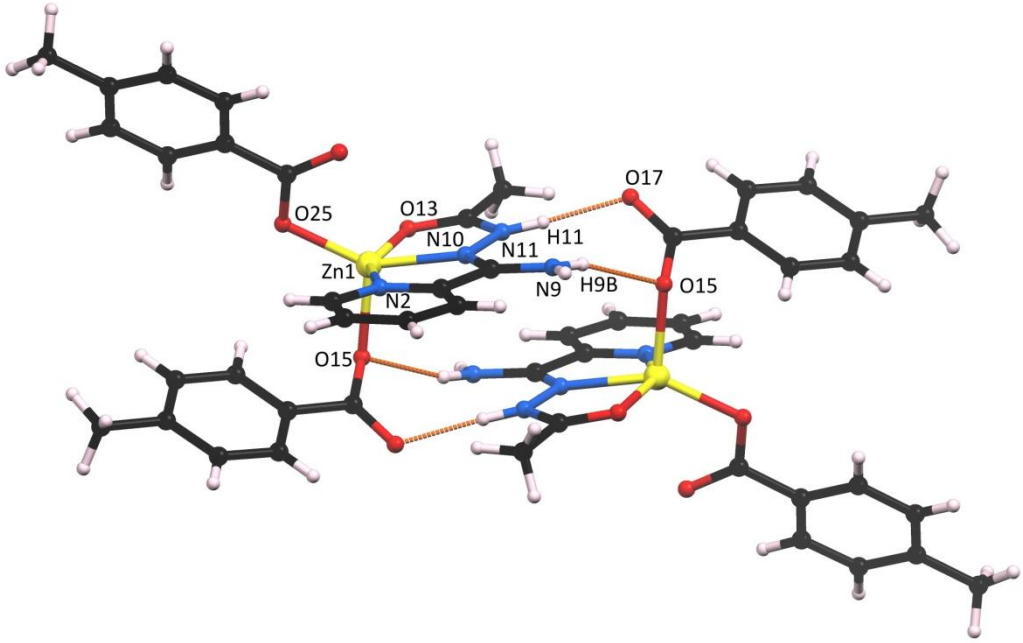

Figure 2.16: *Unit cell of* ***2.5*** *showing bifurcated hydrogen bonding between coordinated carboxylate co-ligand and* H_2***L2.1*** *of an adjacent complex. Selected bond lengths (Å) and angles (°): Zn1-N2 2.178(2), Zn1-N10 2.045(2), Zn1-O13 2.136(1), Zn1-O15 2.020(2), Zn1-O25 1.977(2), N2-Zn1-O13 150.42(6), N10-Zn1-O25 147.20(7), O15-Zn1-O25 110.17(6).*

It is unclear why this change of hydrogen bonding of carboxylate groups is observed, but highlights the versatile nature of the hydrogen bond donating site and its similarity to squaramide which is also capable of forming bifurcated hydrogen bonds.[160]

2.3.6 Synthesis of [Cd(H_2L2.1)($AcO)_2$] (2.6)

To check whether the ladder motif is formed with other metal carboxylate salts, cadmium(II) acetate was reacted with H_2**L2.1** in a stoichiometric ratio. Evaporation of this methanolic solution led to the formation of colourless crystals suitable for single crystal X-ray diffraction. These were solved and refined in the triclinic space group *P*-1 (R-factor 3.56 %). The asymmetric unit was comprised of a single [Cd(H_2**L2.1**)$(OAc)_2$] neutral complex (Figure 2.17a). The H_2**L2.1** ligand coordinates in the tridentate fashion seen

previously. The two acetate co-ligands coordinate in a bidentate chelating coordination mode (Figure 1.9), making the cadmium(II) ion seven-coordinate. Again each complex assembles into ladders formed via hydrogen bonding interactions. The acetate oxygen atoms participating in the hydrogen bonding (O15 and O19) have slightly longer coordination bond lengths than those that are not (O17 and O21). Despite having the relatively non-bulky acetate group, the head-tail ladder type arrangement seen in **2.4** is observed in this compound. The steps are arranged so that alternate steps have two $R_2^1(7)$ or two D hydrogen bond interactions (Figure 2.17b).

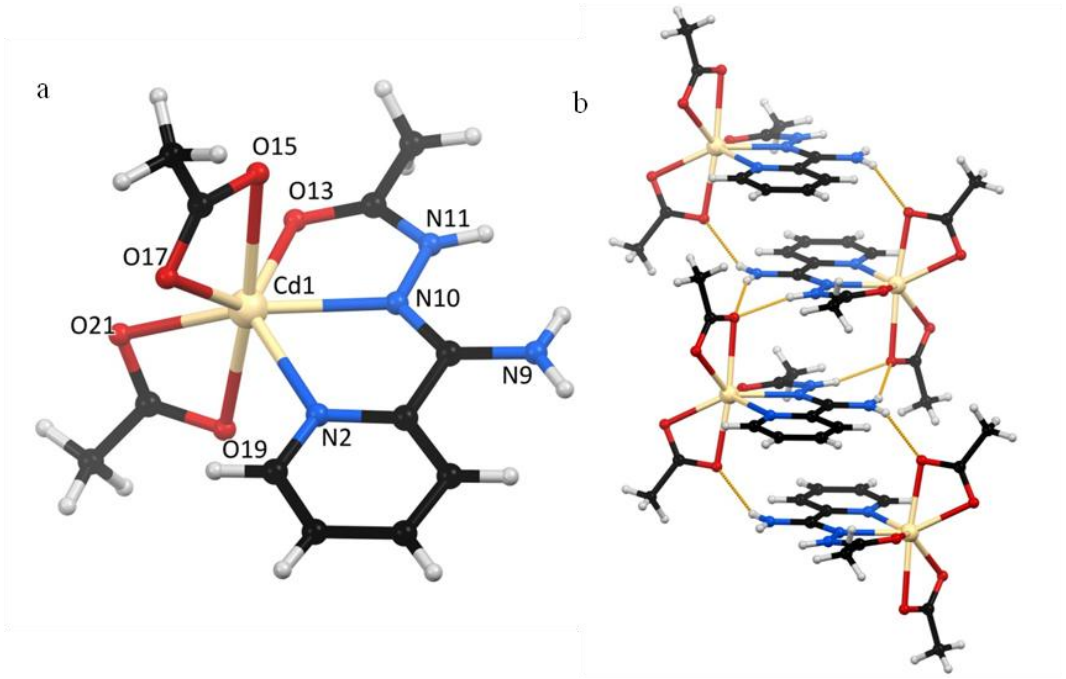

Figure 2.17: *a) Asymmetric unit of* ***2.6****. b) Head to tail ladder architecture with alternate steps comprised of either two* $R_2^1(7)$ *or two D interactions. Selected bond lengths (Å) and angles (°): Cd1-N2 2.414(3), Cd1-N10 2.305(3), Cd1-O13 2.389(2), Cd1-O15 2.480(3), Cd1-O17 2.304(2), Cd1-O19 2.369(3), Cd1-O21 2.344(3), N2-Cd1-O13 134.0(1).*

In this case, the head to tail arrangement is attributed to the bidentate coordination mode of the carboxylate ligand.

2.3.7 Summary

The reaction of H_2**L2.1** with zinc(II) and cadmium(II) carboxylate salts produced a series of neutral complexes with the general formula [M(H_2**L2.1**)(RCO_2)$_2$]. These were all seen to assemble into one-dimensional ladder-like architectures via hydrogen bonding between the coordinated H_2**L2.1** ligand (hydrogen bond donor) and co-ligand carboxylate oxygen atoms (hydrogen bond acceptor). The nature of this ladder was influenced by both the choice of carboxylate, and the choice of metal ion. The rungs of the ladders are defined as the H_2**L2.1** ligands and side rails of the ladder are created by either $R_2^1(7)$, $R_2^2(9)$ or D hydrogen bond interactions.

Small aliphatic carboxylate co-ligands such as acetate, propionate and chloroacetate produced head-head type ladders with zinc(II) (**2.1**-**2.3**). The side rails between each step is comprised of a $R_2^1(7)$ interaction on one side and a D hydrogen bonding motif on the other. The ladders are centred on a glide plane of the *Cc* space group. Larger aromatic carboxylate co-ligands such as benzoate and *p*-toluate produced head-tail type ladders in which the space between every step is centred on an inversion centre of the *P*-1 space group (**2.4**-**2.5**). In **2.4** the side rails between each step of the ladder is either comprised of two $R_2^1(7)$ or two D hydrogen bonding motifs. In **2.5** the side rails are either comprised of two $R_2^2(9)$ or two D hydrogen bonding motifs. When cadmium(II) acetate was used in place of zinc(II) acetate, a structure similar to that seen for **2.4** was seen, despite only containing a small aliphatic carboxylate co-ligand.

2.4 Reactions with Copper(II) Halide Salts

Investigations into the hydrogen bonding properties of coordinated H_2**L2.1** indicated that it formed interactions with coordinated carboxylate anions. To study the interactions of this and related ligands with halide anions, the ligands H_2**L2.1** and H_2**L2.2** were selected and reacted with copper(II) halide salts. Halide anions are known to be potent hydrogen bond acceptors and are expected to interact very strongly with the squaramide-like hydrogen bonding pocket of this ligand in $R_2^1(7)$ type interactions. The urea-like moiety of H_2**L2.2** is expected to compete with this binding pocket in the form of $R_2^1(6)$ interactions.

2.4.1 Synthesis of $[Cu_2(H_2L2.1)_2Cl_2(\mu\text{-}Cl)_2]$ (2.7)

Green crystals of $[Cu_2(H_2\mathbf{L2.1})_2Cl_2(\mu\text{-}Cl)_2]$ (**2.7**) suitable for single crystal X-ray diffraction analysis were obtained by cooling a hot methanolic solution of H_2**L2.1** and one equivalent of copper chloride to room temperature. The complex crystallised in the monoclinic space group $P2_1/c$ (R-factor 3.58 %), and contains half of a dinuclear species in the asymmetric unit. Each half is related by inversion symmetry (Figure 2.18). The copper(II) cation can be defined as having a coordination number of six if the Cu1-Cl16 bond length of 3.0587(7) Å is included in the coordination sphere. The geometry around each copper(II) can then be described as a octahedron with severe Jahn-Teller distortion. This N_2OCl_3 coordination sphere contains a meridional neutral tridentate H_2**L2.1** ligand**,** and a chloride anion in the equatorial plane; and two chloride anions in the axial positions. The Jahn-Teller distortion is quite pronounced in the axial coordination sites with Cu1-CI16 and Cu-O15' bond lengths of 3.0587(7) and 2.8511(6) Å, respectively, compared to bond lengths in the equatorial plane of 2.031(2), 1.921(2), 2.034(2) and 2.2132(9) Å for Cu1-N2, Cu1-N10, Cu1-O13 and Cu1-CI15, respectively. These bond lengths and angles are comparable to other copper(II) complexes containing similar N_2OCl_3 coordination spheres in the literature.[161-162] Chloride ion Cl15 acts as a bridging ligand between the equatorial and axial sites of Cu1 and Cu1' in the dimeric complex. Chloride ion Cl16 acts as a monodentate ligand and binds in only the axial position of Cu1. The box created through Cu1-Cl15-Cu1'-Cl15' is almost perfectly rectangular.

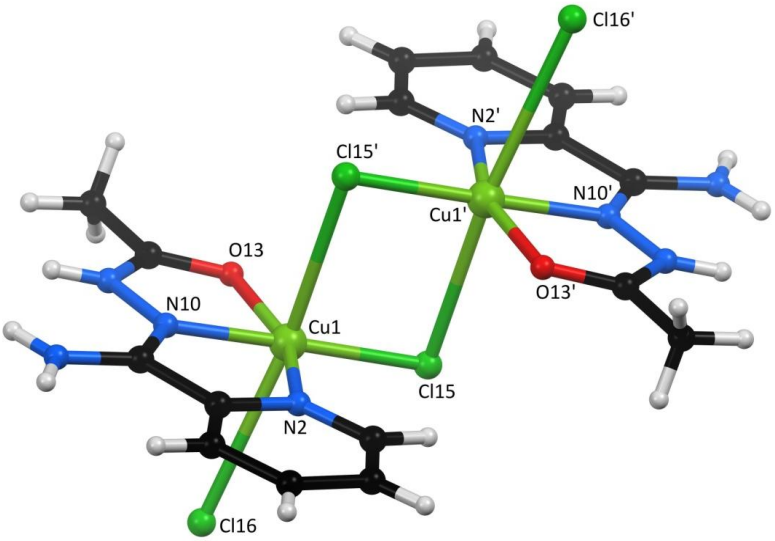

Figure 2.18: *Complete complex of* ***2.7****. The copper(II) ion is in a Jahn-Teller distorted octahedral geometry. Selected bond lengths (Å) and bond angles (°): Cu1-N2 2.031(2), Cu1-N10 1.921(2), Cu1-O13 2.034(2), Cu1-Cl15 2.2132(9), Cu1-Cl15' 2.8511(6), Cu1-Cl16 3.0587(7), N2-Cu1-N10 79.32(9), N10-Cu1-O13 79.93(8), Cl15-Cu1-Cl15' 90.37(3), Cu1-Cl15-Cu1' 89.63(3) .*

The chloride anion that only binds in the axial position, Cl16, occupies the hydrogen bonding pocket of the N^1-acylamidrazone of a neighbouring complex in a $R_2^1(7)$ arrangement. This creates a similar step to that seen in the ladder architecture of **2.4** (blue side rail, Figure 2.14b). As there are two Cl16 atoms per complex, the effect is the formation of a one-dimension hydrogen bonded polymer (Figure 2.19). There is little overlap of the planar ligands between dinuclear complexes.

Each dinuclear unit of this polymer is linked to four equivalent units via D hydrogen bonds from the other 1° imidamide proton of the amidrazone functional group (two per complex) and hydrogen bond accepting of the non-bridging chloride anion Cl16 (two per complex). These six hydrogen bonding interactions lead to a non-porous primitive cubic net (**pcu**) topology. The bridging chloride ion Cl15 and the amide-like oxygen atom O13 do not act as a hydrogen bond acceptors.

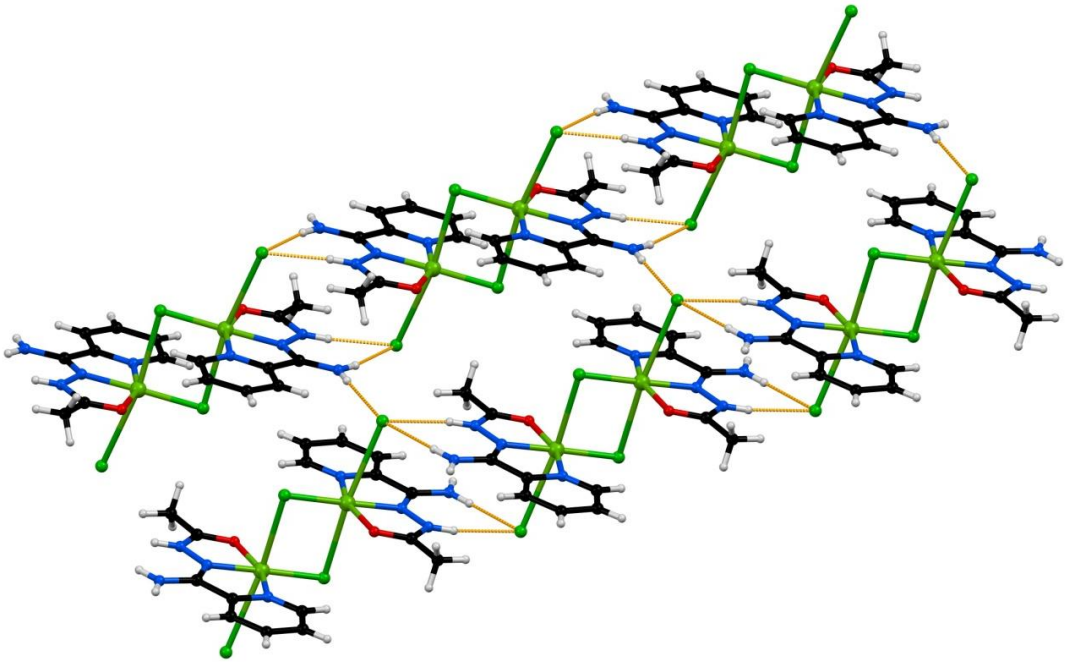

Figure 2.19: *Packing of **2.7** showing hydrogen bonds in orange. Each dinuclear complex is linked via a pair of $R_2^1(7)$ interactions, in a similar way to that seen in **2.4**. Further D hydrogen bonding interactions between Cl16 and H9 are present.*

2.4.2 Synthesis of $[Cu_2(H_2L2.1)_2Br_2(\mu\text{-}Br)_2]$ (2.8)

Cooling of a hot methanolic solution containing H_2**L2.1** and copper(II) bromide yielded large green crystals suitable for single crystal X-ray crystallography. The structure was solved and refined in the monoclinic space group $P2_1/c$ (R-factor 2.90 %). Complex **2.8** consists of a dimeric copper(II) complex, only half being crystallographically unique (Figure 2.20). Complex **2.8** is isomorphous to **2.7** with a slight elongation in the distance between copper(II) centres due to the longer Cu-Br bond lengths (Cu-Cu 3.7563(6) Å *c.f.* **2.7** 3.5980(6) Å).

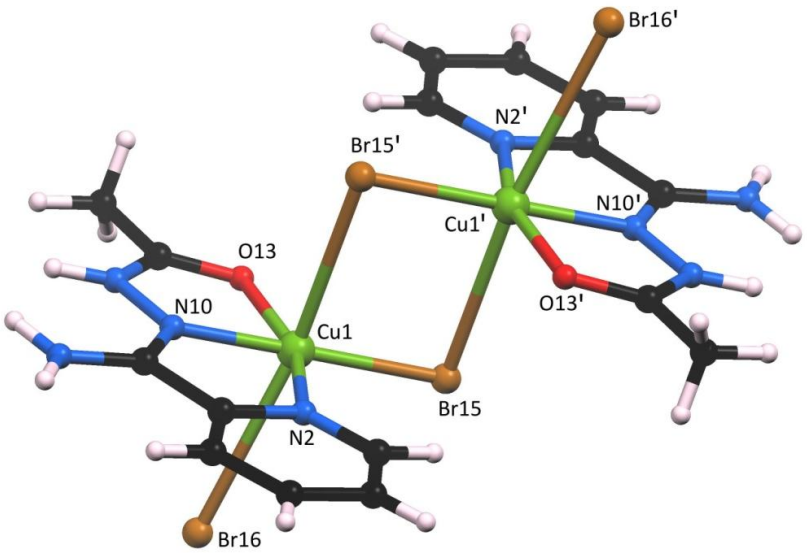

Figure 2.20: *Complete dinuclear complex* ***2.8****. The copper(II) is in a Jahn-Teller distorted octahedral geometry. Selected bond lengths (Å) and bond angles (°): Cu1-N2 2.029(2), Cu1-N10 1.918(3), Cu1-O13 2.027(2), Cu1-Br15 2.3478(6), Cu1-Br15' 2.9912(5), Cu1-Br16 3.1582(5), N2-Cu1-N10 79.52(9), N10-Cu1-O13 79.94(9), Br15-Cu1-Br15' 91.43(2), Cu1-Br15-Cu1' 88.57(2).*

Hydrogen bonding between the dimeric complexes exists as in **2.7**. This shows the overall crystal packing, does not depend on whether chloride or bromide anions are present. The modulation of anions, whilst still retaining the same crystal structure is an important feature of supramolecular chemistry as it allows the properties to be tuned. If something completely different was observed with such slight differences, with no predictability, there would be no opportunity to tune the properties of the resultant compound.

2.4.3 Synthesis of [Cu(H_2L2.2)Cl_2] (2.9)

The related ligand, H_2**L2.2** was trialled to see if the additional urea-like hydrogen atoms pocket would compete with those of the N^1-acylamidrazone for the halide anions.

Green crystals of [Cu(H_2**L2.2**)Cl_2] (**2.9**) grew upon cooling a hot methanolic solution containing copper(II) chloride and H_2**L2.2** to room temperature. These crystallised in the monoclinic space group $P2_1/c$ (R-factor 3.64 %) and contained a complete neutral

mononuclear complex in the asymmetric unit (Figure 2.21). As expected, the ligand coordinates in a tridentate fashion about a copper(II) ion. This ion adopts a five-coordinate square pyramidal geometry (τ_5 = 0.07), with chloride anions occupying the remaining two sites. The halide ions do no adopt bridging coordination modes, contrasting what was seen in **2.7** and **2.8** and consequently only a mononuclear complex is formed.

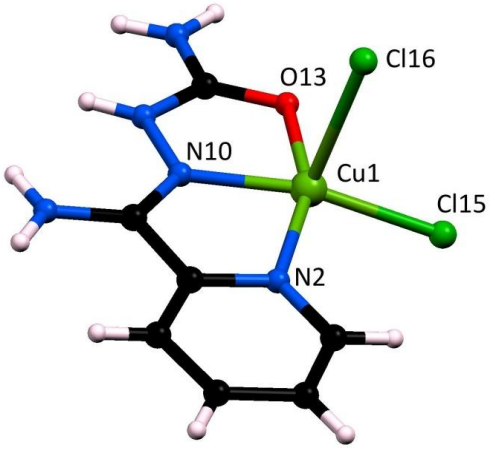

Figure 2.21: *Asymmetric unit and complex of* ***2.9****. Selected bond lengths (Å) and bond angles (°):Cu1-N2 2.023(2), Cu1-N10 1.923(2), Cu1-O13 2.011(1), Cu1-Cl15 2.2055(5), Cu1-Cl16 2.5959(5), N2-Cu1-O13 157.13(6), N10-Cu1-Cl15 161.44(5).*

Analysis of the hydrogen bonding network shows that Cl16, a coordinated chloride anion, acts as a hydrogen bond acceptor to the amidrazone hydrogen bond donors in a $R_2^1(7)$ arrangement (Figure 2.22). No anion is present in the urea-like pocket. This preference indicates that the acylamidrazone functional group is indeed a potent hydrogen bond donor. The chloride ion Cl15 does not adopt any significant hydrogen bonding interactions. The urea functionality is involved in a centrosymmetric $R_2^2(8)$ cyclic urea dimer hydrogen bonding motif, the most enthalpicly stable of all self-recognising urea interactions.[163] Interestingly, Cl15 does not act as a hydrogen bond acceptor.

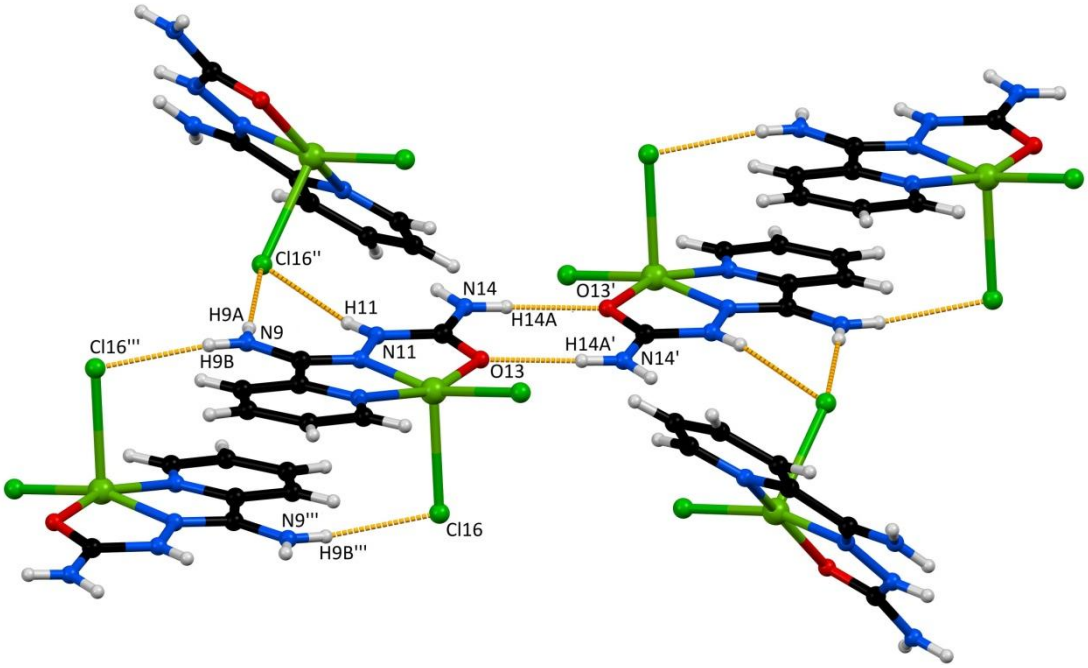

Figure 2.22: *Hydrogen bonding interactions in* ***2.9****.*

2.4.4 Synthesis of [Cu(H_2L2.2)Br_2] (2.10)

Addition of a hot methanolic solution of copper bromide to a hot methanolic solution of H_2**L2.2** followed by cooling to room temperature led to the formation of large green plate like crystals within a few hours. These were suitable for single crystal X-ray diffraction and were solved and refined in the space group *P*-1 (R-factor 3.20 %). The asymmetric unit contained a single five-coordinate copper complex (Figure 2.23). The ligand H_2**L2.2** coordinates via the tridentate binding mode seen in the previous examples, and two bromide anions coordinate to complete a distorted square-based pyramid coordination geometry (τ_5= 0.04).

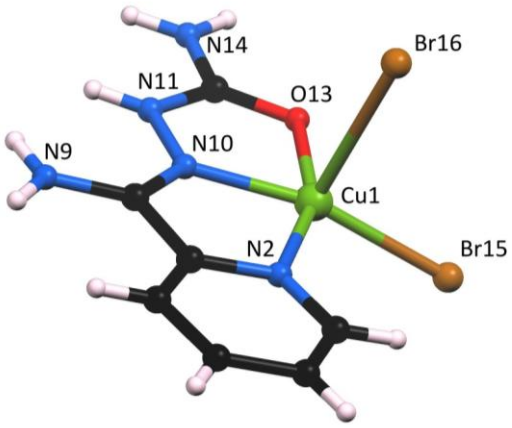

Figure 2.23: *Asymmetric unit of* ***2.10****. Selected bond lengths (Å) and bond angles (°):Cu1-N2 2.017(3), Cu1-N10 1.927(3), Cu1-O13 2.015(2), Cu1-Br15 2.3388 (5), Cu1-Br16 2.8563(7), N2-Cu1-O13 158.9(1), N10-Cu1-Br15 161.48(9).*

Compound **2.10** has a similar mononuclear complex sturcture to **2.9**, however, it does not adopt the same crystallographic packing motif (Figure 2.24). The urea functionality is again seen to form a centrosymmetric cyclic dimer $R_2^2(8)$ hydrogen bonding motif. In this case an additional interaction between H14A and Br15' buttresses the ureas' binding mode. In this way both halide ions are involved in hydrogen bonding interactions contrasting **2.9**.

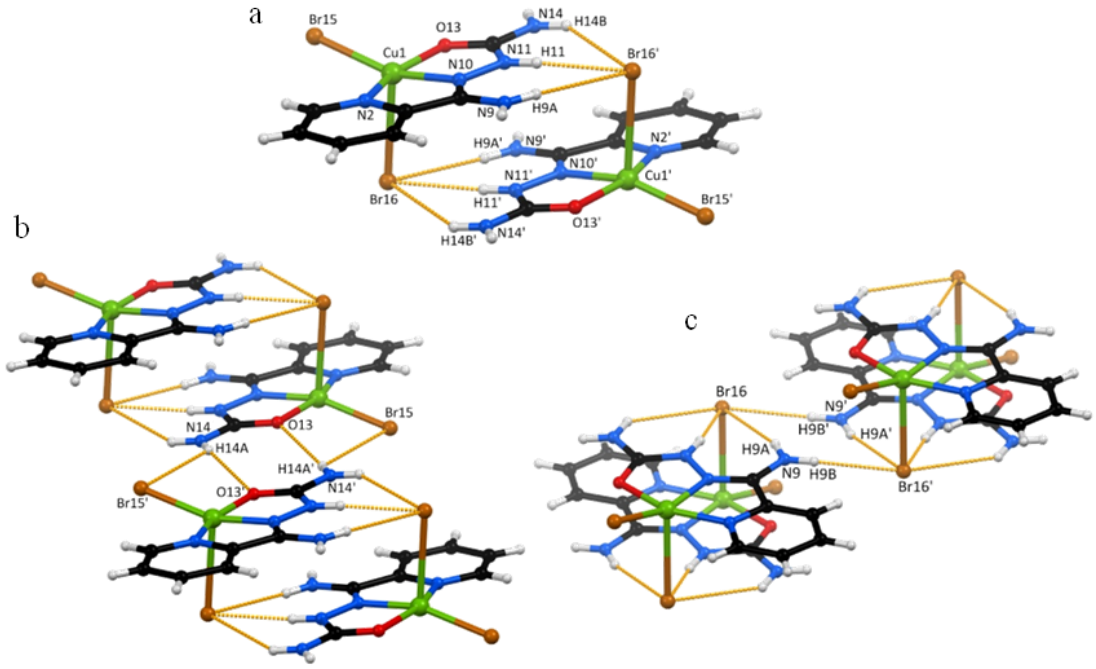

Figure 2.24: *Hydrogen bonding motifs in* ***2.10****. a) A pair of* $N_1 = R_2^1(7)R_2^1(6)$, $N_2 = R_2^1(9)$ *interactions between coordinated* H_2***L2.2*** *and Br16 are present instead of just a* $R_2^1(7)$ *interaction as seen previously for the chloride anion. b) Bifurcated* $R_1^2(4)$ *hydrogen bonding interactions buttress the* $R_2^2(8)$ *cyclic urea dimer hydrogen bonding motif. c)* $R_4^2(8)$ *hydrogen bonding between H9A, H9B and Br16.*

Rather than binding a coordinated halide in the N^1-acylamidrazone binding pocket in a $R_2^1(7)$ arrangement as seen in **2.9**, the halide is bound in a tridentate manner to the acetyl amidrazone, and urea moiety ($N_1 = R_2^1(7)R_2^1(6)$, $N_2 = R_2^1(9)$). This interaction is probably a consequence of the size of the bromide anion relative to the chloride.

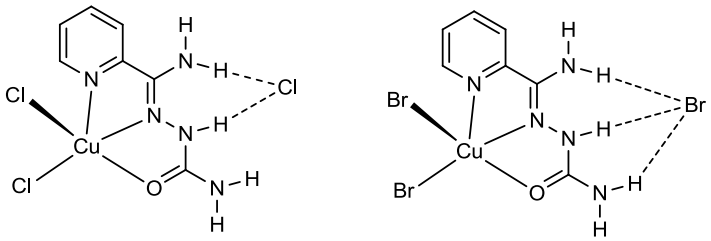

Figure 2.25: *Representation of the hydrogen bonding modes of coordinated* H_2***L2.2*** *with halide ions in* ***2.9*** *(left) and* ***2.10*** *(right).The arrangement in* ***2.9*** *is* $R_2^1(7)$*, the classic squaramide hydrogen bonding interaction. The arrangement in* ***2.10*** *is a combination of the squaramide and urea type hydrogen bonding interactions and is defined as a* $N_1 = R_2^1(7)R_2^1(6)$, $N_2 = R_2^1(9)$ *interaction.*

2.4.5 Summary

The ligands H_2**L2.1** and H_2**L2.2** were each reacted with copper(II) chloride and copper(II) bromide and the hydrogen bonding interactions of the resulting four complexes analysed. The complexes involving H_2**L2.1**, **2.7** and **2.8**, crystallised as isostructural dimeric complexes. The hydrogen bonding motifs observed were conserved despite the change of halide anion. Complexes containing H_2**L2.2**, **2.9** and **2.10**, crystallised in a similar mononuclear fashion, but displayed different hydrogen bonding motifs. This difference was attributed to the size difference of chloride and bromide anions. In complex **2.10**, the coordinated ligand H_2**L2.2** was able to act as a tridentate hydrogen bond donor to a coordinated bromide anion.

The coordinated N^1-acylamidrazone ligand was again seen to form reproducible hydrogen bonding interactions with halide anions. In complex **2.9** this functional group was seen to bind a chloride anion in preference to a nearby urea-like functional group highlighting its strong anion binding nature. In all cases the halide anion with the longest Cu-X bond length was seen to occupy the hydrogen bonding pocket of the coordinated N^1-acylamidrazone ligand.

2.5 Reactions with Metal(II) Perchlorate Salts

In the previous cases, the hydrogen bonding interactions of coordinated N^1-acylamidrazone based ligands and coordinated anions were investigated. As a point of difference, perchlorate, an anion with a much lower charge density and hence weaker coordination and hydrogen bond acceptor ability was chosen to study. This section deals with the reaction of the N^1-acylamidrazone based ligands H_2**L2.1** and H_2**L2.3** with metal perchlorate salts, and an analysis of the resultant hydrogen bonding motifs.

2.5.1 Synthesis of $[Cu(H_2L2.1)_2](ClO_4)_2 \cdot H_2O$ (2.11)

Green crystals of $[Cu(H_2$**L2.1**$)_2] \cdot 2(ClO_4) \cdot H_2O$ suitable for X-ray diffraction analysis were obtained from evaporation of a methanolic solution of copper(II) perchlorate and two equivalents of H_2**L2.1**. The complex crystallises in the triclinic space group *P*-1 (R-factor

3.38 %) and contains one bis-tridentate complex, two perchlorate anions and a water molecule in the asymmetric unit (Figure 2.26). Two neutral ligands coordinate to form a distorted octahedral N_4O_2 coordination sphere around the copper(II) ion.

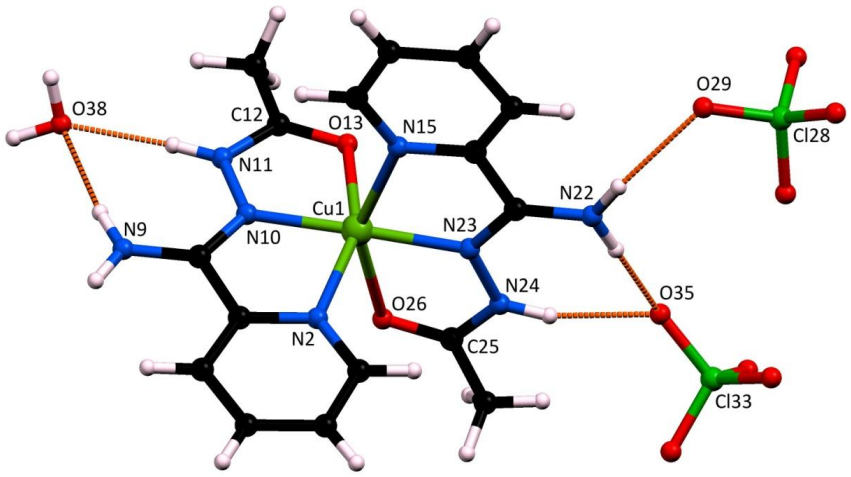

Figure 2.26: *Asymmetric unit of* ***2.11****. Selected bond lengths (Å) and bond angles (°): Cu1-N2 2.095(2), Cu1-N10 1.926(1), Cu1-O13 2.119(2), Cu1-N15 2.198(2), Cu1-N23 1.967(1), Cu1-O26 2.365(2), N11-C12 1.346(3), C12-O13 1.245(2), N24-C25 1.339(3), C25-O26 1.242(2), N2-Cu1-N10 78.23(7), N10-Cu1-O13 78.43(7), N2-Cu1-O13 155.52(7), N15-Cu1-N23 76.59(7), N23-Cu1-O26 74.36(7), N15-Cu1-O26 150.32(6).*

The ligand was deemed to be in the neutral state due to the observation of two perchlorate anions, the presence of the amide protons in the difference map and analysis of hydrogen bonding interactions. Hydrogen bond acceptors are found in both crystalographically unique N^1-acetylamidrazone hydrogen bonding pockets; a water molecule in one, a perchlorate anion in the other. Each of these are in $R_2^1(7)$ arrangements. A further perchlorate anion forms a discrete (D) hydrogen bond with the 1° imidamide proton of this functional group.

Each complex has hydrogen bonding interactions with a symmetry equivalent complex to form a close packed supramolecular dimer (Figure 2.27). The proton not involved in the amidrazone hydrogen bonding pocket on N9 acts as a hydrogen bond donor to coordinated O26. This interaction is centred around an inversion centre and is similar to that found in alternate steps of the head-tail ladder chains of **2.4**, **2.5** and **2.6**. As this interaction only

creates a finite supramolecular species it will be denoted as a step stool interaction rather than a ladder. The discrete nature of this interaction arises because only H9A acts as a hydrogen bond donor to an adjacent complex, and not the chemically equivalent H22A.

Due to the acetyl oxygen hydrogen bond acceptor being closer to the metal centre in this complex than the carboxylate co-ligand hydrogen bond acceptor of the ladder-like assembly of **2.4**, the ligands/steps of the stool are located closer together (metal-metal distance 6.7855(9) Å *c.f.* **2.4** 7.720(1)).

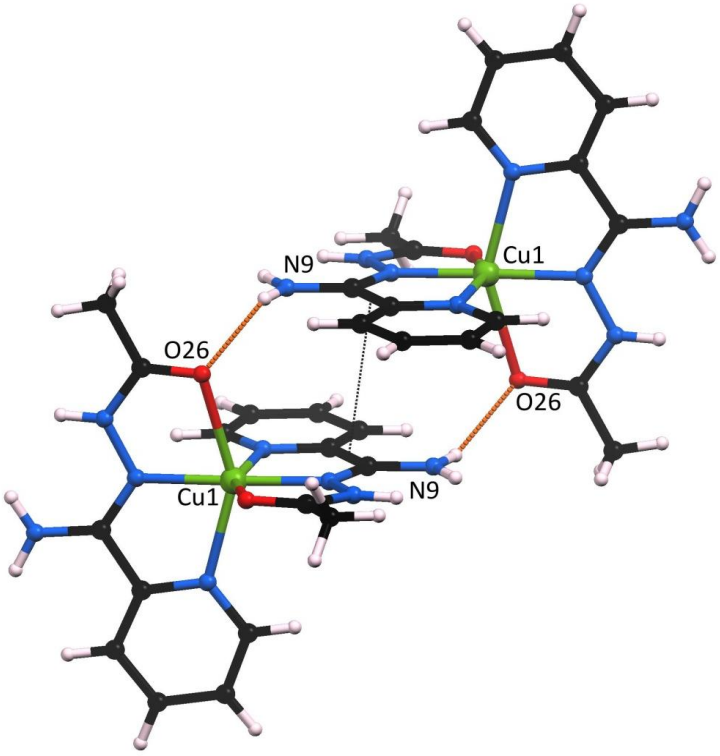

Figure 2.27: *Step stool hydrogen bonding interaction in* ***2.11****. Hydrogen bonds are shown in orange, π-π stacking interaction in black. Anions and solvent molecules have been omitted for clarity.*

2.5.2 Synthesis of $[Fe_2(H_4L2.3)_2](ClO_4)_4 \cdot 2MeCN \cdot 0.2H_2O$ (2.12)

Upon diffusion of *m*-xylene into a dark red solution of iron(II) perchlorate and H_4**L2.3** in acetonitrile small, red rod-like crystals formed. These were suitable for single crystal X-ray diffraction and were solved and refined in the monoclinic space group *C*2/*c* (R-factor 5.63 %). The asymmetric unit contained half of a $[Fe_2(H_4\mathbf{L2.3})_2]^{4+}$ cation, two perchlorate anions, an acetonitrile molecule and a partial occupancy water molecule (Figure 2.28a). The

flexible, ditopic nature of the ligand H_4**L2.3** allows it to bridge between two metal centres to create a dinuclear double helicate structure. Only half of the helicate structure is crystallographically unique (Figure 2.28b).

Perchlorate anions act as hydrogen bond acceptors within both of the crystallographically unique amidrazone hydrogen binding pockets and form N_1= $R_2^1(7)R_1^2(4)$, N_2=$R_2^2(9)$ interactions. The acetonitrile nitrogen atom is a hydrogen bond acceptor in a D interaction to the amine nitrogen of a amidrazone functional group. The partial occupancy water molecule does not appear to be involved in any hydrogen bonding interactions, and as such it was not modelled with any hydrogen atoms. The coordinate bond lengths at 120 K indicate that the iron(II) centres are in the high spin state.[154]

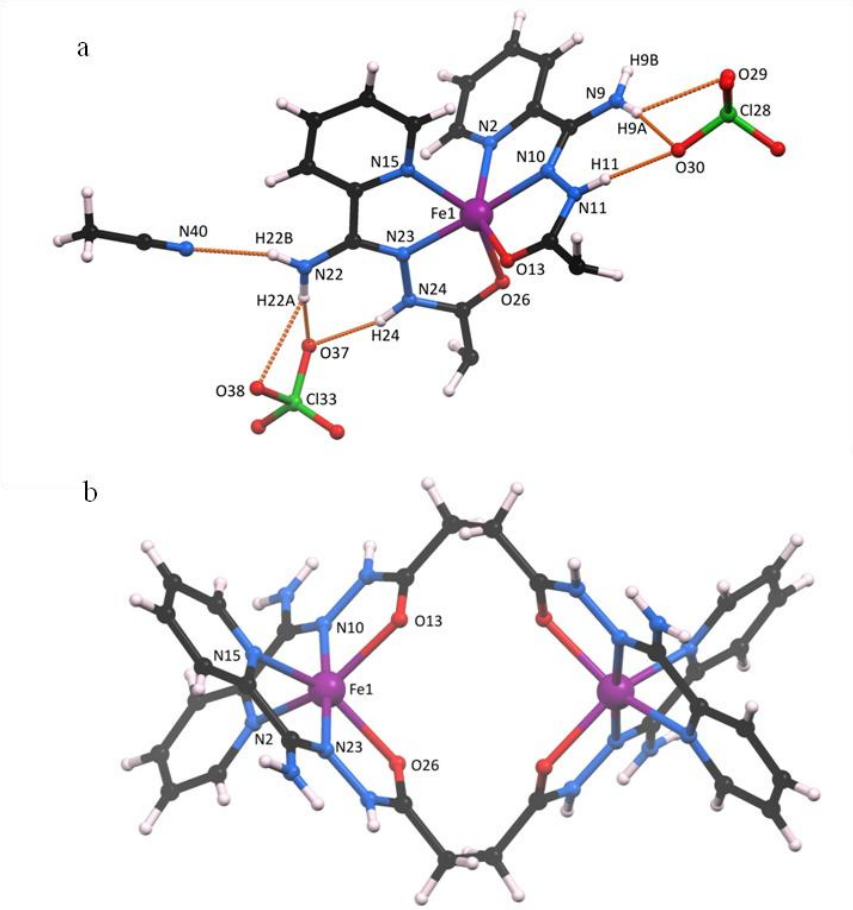

***Figure 2.28**: a) Asymmetric unit of **2.12** showing hydrogen bonding interactions of the ligands with perchlorate anions and solvent acetonitrile. Solvent water and disorder of one perchlorate anion omitted for clarity. b) Structure of **2.12** showing just a Δ isomer. The helicate is centred on a two-fold rotation axis and only half of the complex is crystallographically unique. Selected bond lengths (Å) and bond angles (°): Fe1-N2 2.198(3), Fe1-N10 2.089(3), Fe1-O13 2.170(3), Fe1-N15 2.165(3), Fe1-N23 2.072(4), Fe1-O26 2.213(2), N2-Fe1-O13 146.6(1), N15-Fe1-O26 147.4(1).*

The same 'step stool' type hydrogen bonding motif observed in **2.11** is seen in **2.12**. An infinite chain is not observed as the acetonitrile solvent occupies the amine-like hydrogen bond donor required for this. However, due to each complex containing two octahedral metal ions, they are linked together into a series of stools. As each of these types of interactions is centred over an inversion centre, the chirality of each of the helicates alternate across the series.

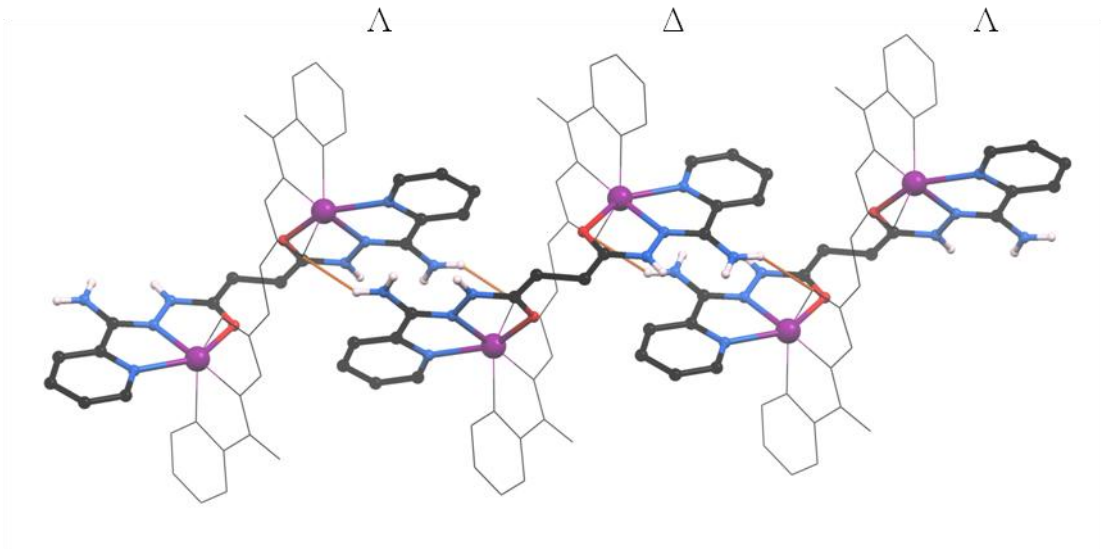

Figure 2.29: *Packing of helicates in* ***2.12*** *showing the step stool interactions between neighbouring complexes. This centrosymmetric interaction means that the helicates are arranged in an alternating pattern of Λ and Δ isomers.*

2.5.3 Summary

The reaction of metal perchlorate salts with N^1-acylamidrazone ligands produced complexes containing bis-ligated octahedral metal centres. In compound **2.11**, a water molecule was seen to out-compete a perchlorate anion for the hydrogen binding pocket seen to bind anions so well in previous examples. In both **2.11** and **2.12** hydrogen bonding interactions between complexes created step stool like hydrogen bonded dimers in a similar way to portions of the ladder architecture of **2.4** (red side rail, Figure 2.14b).

2.6 Reaction with Nickel(II) salts

In every case observed so far, a hydrogen bond acceptor has been observed in the squaramide-like hydrogen bonding pocket of the coordinated N^1-acylamidrazone based ligand. This relies on the protonation state of the amide. Deprotonation, a feature commonly observed in coordinated amides, can occur which would dramatically change the ability of the ligand to form strong hydrogen bonds. Nickel(II) was chosen as a metal to investigate the effect of deprotonation on the hydrogen bonding motifs in N^1-acylamidrazone based ligands.

2.6.1 Synthesis of $[Ni(H_2L2.1)_2]Cl_2 \cdot 2MeOH$ (2.13)

Combining nickel(II) chloride with two equivalents of H_2**L2.1** in methanol, followed by slow evaporation of the solvent led to the formation of crystals suitable for single crystal X-ray diffraction. These were solved and refined in the triclinic space group *P*-1 (R-factor 3.17 %) and contained a single complex, two chloride counter ions and two methanol solvent molecules within the asymmetric unit (Figure 2.30). From the stoichiometry of reagents it was expected that a bis-ligated complex would be produced, as indeed, was the case. The nickel(II) is in a distorted octahedral geometry, due to the two five-membered chelate rings of each ligand. As is the case with unsymmetrical tridentate ligands, each complex is chiral, although both enantiomers are present within each crystal.

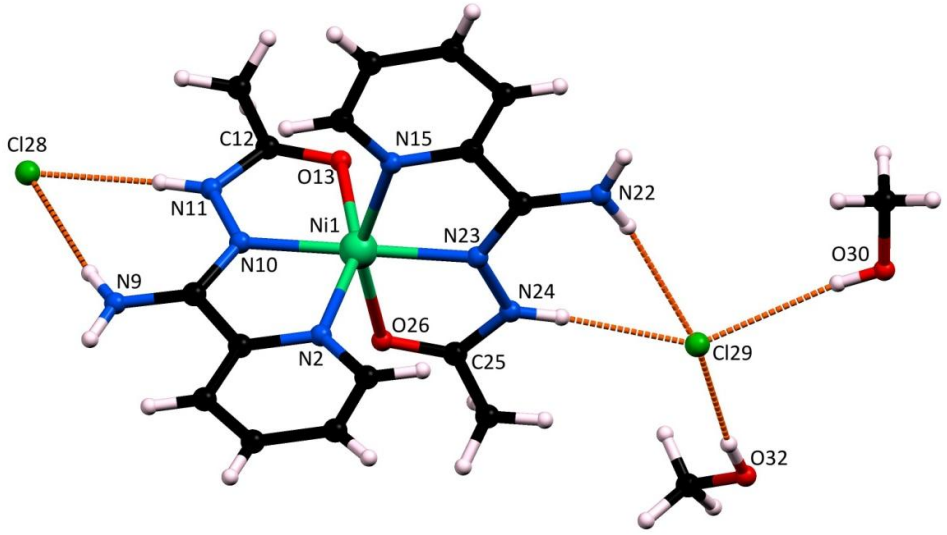

Figure 2.30: *Asymmetric unit of* ***2.13****. Selected bond lengths (Å) and bond angles (°): Ni1-N2 2.089(1), Ni1-N10 1.973(2), Ni-O13 2.138(1), Ni1-N15 2.087(2), Ni1-N23 1.982(2), Ni1-O26 2.149(1), N2-Ni1-O13 154.60(6), N15-Ni1-O26 154.15(6).*

The chloride counter ions occupy the N^1-acetylamidrazone hydrogen bonding pocket of both of the crystallographically unique H_2**L2.1** ligands in $R_2^1(7)$ arrangements. This is not surprising as chloride anions are potent hydrogen bond acceptors and coordinated N^1-acylamidrazone functional groups are good hydrogen bond donors. Both of the solvent methanol molecules have D hydrogen bonding interactions with one chloride anion (Cl29).

2.6.2 Synthesis of [Ni(HL2.5)$_2$] (2.14)

The proton on N^1 in the N^1-acyclamidrazone functional group is the most acidic in the ligand system and becomes more acidic on coordination of the oxygen atom. As a strategy to investigate the impacts of this on hydrogen bonding, a complex containing a deprotonated N^1-acyamidrazone ligand was prepared and the hydrogen bonding motifs observed.

When nickel(II) acetate was combined with two equivalents of H_2**L2.5** in methanol, and allowed to stand for several days, green crystals suitable for single crystal X-ray diffraction were produced. These were solved and refined in the orthorhombic space group *Pbcn* (R-

factor 3.08 %) and contained half of a neutral mononuclear complex in the asymmetric unit (Figure 2.31). No anions or solvent molecules are present within the structure which indicated that each ligand must be mono-deprotonated. Analysis of the difference map indicated that no proton is present on the hydrazide amide-like nitrogen atom N11. A slightly longer C12-O13 bond length (1.291(2) Å *c.f.* **2.13** 1.253(2) Å), and shorter N11-C12 (1.327(2) Å *c.f.* **2.13** 1.342(2) Å) is observed in **2.14** than in the previous complexes containing a neutral H_2**L2.1** ligand, supporting the assignment of a deprotonated functional group.

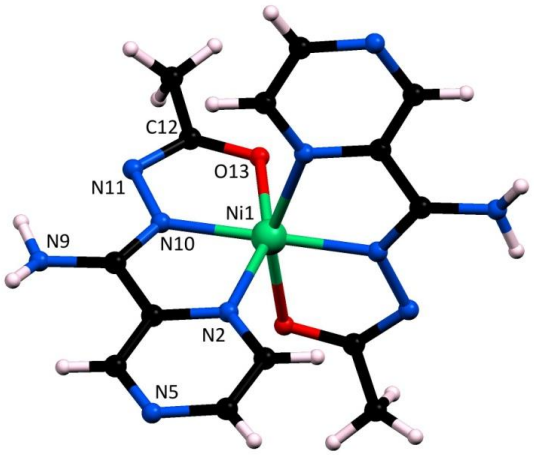

Figure 2.31: *Complete complex of* ***2.14****. Only one half is crystallographically unique. Selected bond lengths (Å) and bond angles (°): Ni1-N2 2.132(2), Ni1-N10 1.956(2), Ni-O13 2.188(1), N2-Ni1-O13 155.18(5).*

Due to deprotonation, the hydrogen bond donor pocket mentioned in all previous examples within this chapter no longer exists. As the complex is neutral, no anions are present leading to the the acetyl oxygen atom being the best hydrogen bond acceptor in the system. Indeed, hydrogen bonding interactions between complexes do exist, the hydrogen bond donor being H9A, a proton from the 1° imidamide group of the amidrazone functionality (Figure 2.32).

A new hydrogen bond donating pocket incorporating H9A and H6 is formed. The nonconventional hydrogen bond donor, H6, is an α-CH proton on a coordinated pyrazinyl ring, greatly increasing its ability to hydrogen bond through both inductive and resonant

effects. This effectively acts as the pocket described previously, and allows the formation of a 'step stool' like complex again based upon a $R_2^1(7)$ interaction. As each mononuclear complex is capable of forming four of these type of interactions, two hydrogen bond donating pairs and two hydrogen bond acceptors per complex, it can be thought of a square node in the construction of a supramolecular network. As no solvent or anions are present, the extent of this is not stunted as in **2.11** and **2.12** and a non-porous square-grid (**sql**) type hydrogen bonded framework with distances of 7.01917(8) Å between adjacent metal centres is created.

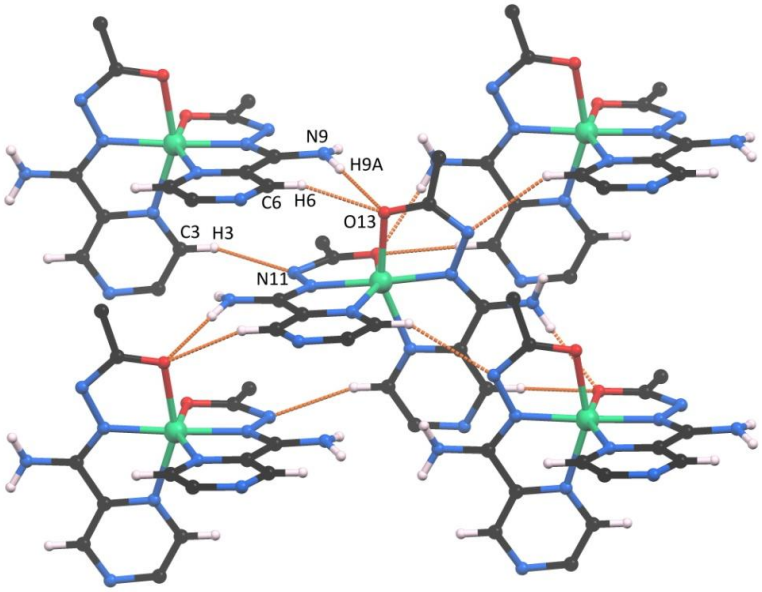

Figure 2.32: *Each mononuclear complex in* ***2.14*** *interacts with four equivalent complexes via one* $R_2^1(7)$ *interaction (H9A, H6-O13) and one D interaction (H3-N11). These pairs of interactions create a square-grid (**sql**) type supramolecular assembly, a portion of which is shown here.*

2.6.3 Summary

Two bis-ligated octahedral nickel(II) complexes were created using N^1-acylamidrazone based ligands. Compound **2.13** contained two neutral ligands H_2**L2.1** which formed hydrogen bonding interactions to chloride counter ions. These interactions stem from the squarmaide-like hydrogen bonding pocket of the ligand and adopt the $R_2^1(7)$ arrangement, commonly seen for this type of system within this report. The chloride anions are better

hydrogen bond acceptors than the coordinated amide-like oxygen and hence the latter is not seen to form hydrogen bonding interactions with the hydrogen bonding pocket.

Compound **2.14** contained two monodeprotonated H**L2.5** ligands. Due to the removal of this proton, the squaramide-like hydrogen bonding site observed in the previous examples is no longer present. The neutral complex does not require anions and hence the best hydrogen bond acceptor is the coordinated amide oxygen. A new $R_2^1(7)$ squaramide-like binding pocket was created from the amine-like nitrogen atom and an α-CH proton from the pyrazine ring. A further α-CH proton from the pyrazine ring is involved in a D hydrogen bonding interaction with the now deprotonated amide-like nitrogen atom.

The protonation state is key to forming the hydrogen bonding pocket in complexes of N^1-acylamidrazone based ligand and the hydrogen bonding motifs it forms.

2.7 Conclusions and Future Work

The N^1-acylamidrazone functional group has, in addition to its known tridentate coordination properties, proven to be a robust and strong hydrogen bond donor to a variety of hydrogen bond acceptors. These include carboxylates, halides, perchlorates and water molecules. The binding mode of this is similar to that of squaramide derivitives and has been shown to commonly adopt $R_2^1(7)$ hydrogen bond arrangements.

In particular, it appears that coordinated carboxylate and coordinated and free halide anions have a strong affinity for this functional group, as in all cases where these ions were present, they were found within this hydrogen bonding site. The directionality encoded in this binding site relative to the metal centre is useful in the construction of mono and bis-ligated complexes and a variety of reproducible hydrogen bonding motifs were observed.

Due to the proximity to the metal centre, the identity of the anion is expected to have a subtle influence on the properties of the metal centre. Potential applications may include anion sensing, or subtly influencing the electronic properties of the coordinated metal ion. Further work into establishing the strength of this hydrogen bonding interaction in the solution state by NMR or UV/Vis spectroscopy is recommended.

Chapter 3

Modulation of Co-ligands in Octanuclear Metal-Organic Macrocycles

3.1 Introduction

3.1.1 Metal-Organic Macrocycles

Metal ions are widely used in the formation of supramolecular structures due to their propensity to adopt a preferred geometry; the reversibility of coordination bond formation; and the catalytic, redox, magnetic and/or photo-physical properties they can impart on the final structure.[30,38] Metal-organic macrocycles (MOMs) are a class of supramolecular systems containing both metal ions and organic ligands arranged in a cyclic array.

One of the requirements of macrocyle formation is incorporation of components with angular, bridging coordination modes. These can be provided by either the ligand or metal ions. A cis-substituted palladium(II) ion is a common angular metallic motif, although more complex clusters are often used (Figure 3.1). Angular ligand geometries are commonly provided by carboxylate, oxo or halide moieties, or in more complex cases heterocyclic polydentate chelating ligands. Rigid ligand systems and metal ions with predictable coordination geometries are generally favoured and a rational choice of such components will often allow prediction of the resultant structure. Formation of discrete macrocycles is attributed to their entropic advantage over a polymeric species.[164]

Commonly, these species incorporate one particular transition metal ion with either; a bridging carboxylate and/or hydroxide or oxo ions; or a single ligand type; and are formed through a self-assembly process. The incorporation of multiple types of metallic centres, types of ligands and combinations of carboxylate and hydroxide ions not only increases the complexity of the resultant system but renders the self assembly of the corresponding parts more complex. A selection of MOMs are shown in Figure 3.1.

In addition to the aesthetic beauty of these macrocyclic structures, the ability to hold metal-ions in defined orientations relative to each other allows for many interesting chemical and physical properties. In particular, this property is important in magnetochemistry, and a significant driving force in the synthesis of metal-organic macrocycles has come from this field. The earliest reports of such systems acknowledged this and the potentially interesting magnetic properties of the cyclic arrays of paramagnetic iron(III)[165] and copper(II)[166] metal ions were studied. The field continued to develop with this in mind, and a lot of research

into single molecule magnet materials has been based upon macrocyclic complexes.[167] Indeed, the largest single molecule magnet, a Mn_{84} torus, can be described as a metal-organic macrocycle.[168] Recently, other properties of metal-organic macrocycles have been investigated such as pore properties,[169] guest binding,[170] catalysis,[171] and their use as nodes in coordination polymers.[172] By definition the array of metal ions in a metal-organic macrocycle must be arranged in a cyclic structure. Although in many cases the metal ions form planar arrangements, this does not have to be the case. Other interesting cyclic arrangements of ions have been observed such as saddles[173] and Möbius strips.[174]

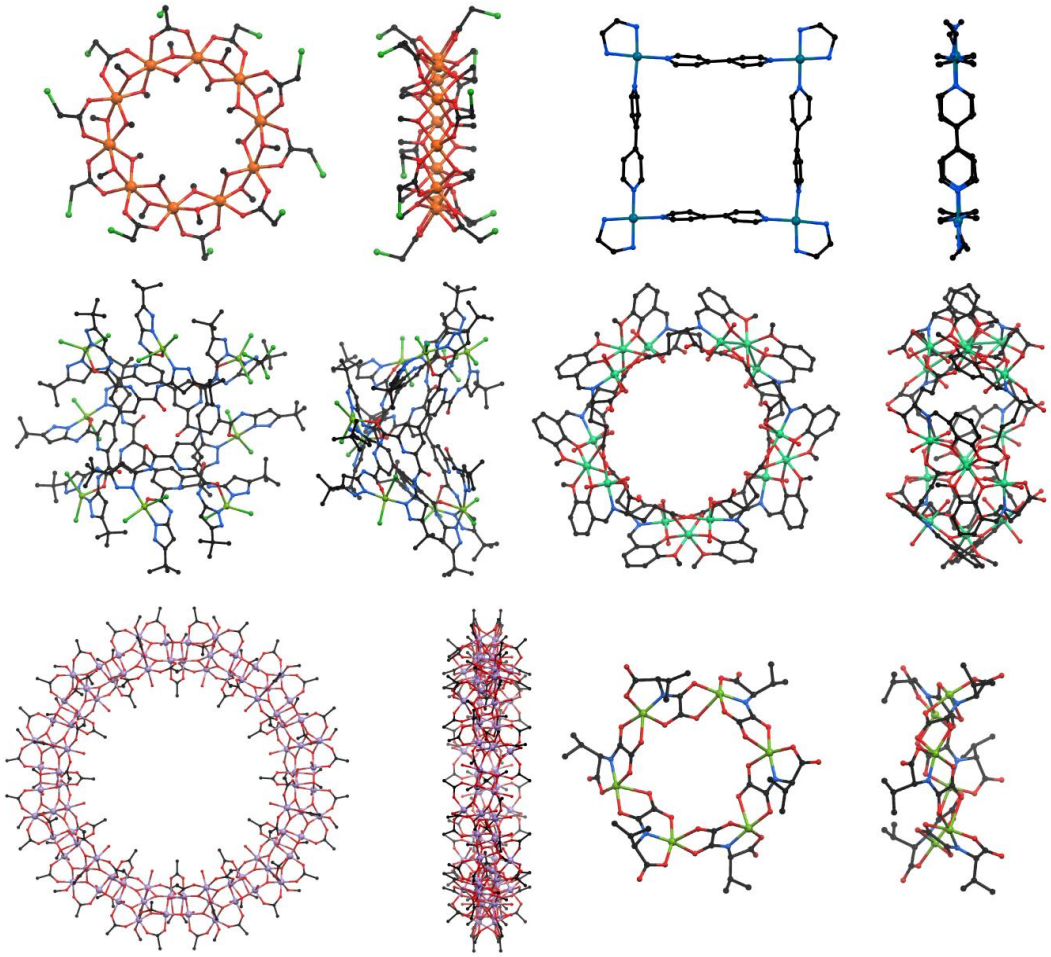

Figure 3.1: *Front and side projections of a selection of metal-organic macrocycles. Clockwise from top left; decanuclear ferric wheel* $[Fe_{10}(ClAcO)_{10}(MeO)_{20}]$,[165] *tetranuclear palladium box* $[Pd_4(en)_4(bipy)_4]$,[175] *pentadecanuclear nickel wheel* $[Ni_{15}(evan)_{10}(H_2O)_{20}]$,[169] *chiral hexanuclear copper(II) wheel* $[Cu_6(R\text{-}valma)_6]^{6-}$,[176] *manganese single molecule magnet* $[Mn_{84}O_{72}(AcO)_{78}(MeO)_{24}(MeOH)_{12}(H_2O)_{42}(OH)_6]$,[168] *octanuclear copper(II) saddle shaped metal-organic macrocycle* $[Cu_8(tpb)_8Cl_{16}.]$.[173] *Hydrogen atoms omitted for clarity. en = ethylenediamine, bipy = 2,2'-bipyridine, evan = 2-(((2-hydroxy-3-methoxyphenyl)imino)methyl)glutaric acid, R-valma = (R)-2-(carboxyformamido)-3-methylbutanoic acid, tpb = tetrakis(5-(tert-butyl)-1H-pyrazol-3-yl)-[4,4'-bipyridine]-2,2',6,6'-tetracarboxamide.*

Metal-organic macrocycles are often reported as single structures. However, modulation of structural components such as ligands[177] and metal ions[178,179,180] have been shown to have novel effects on the structure and properties.

3.1.2 Molecular Building Blocks

Carboxylate clusters have particular significance in metal-organic framework (MOF) chemistry where they have been employed as secondary building units to yield multidimensional frameworks. This is based upon their ability to act as nodes with organic dicarboxylate or polycarboxylate linkers. One of the challenges of the topological prediction of such frameworks arises because of the *in situ* formation of inorganic SBUs with the organic linkers. This often leads to unpredictable, non-porous or mixed phase framework structures. Although some degree of prediction can be obtained by judicious choice of metal ions, coordination group of the ligand, solvent and pH, the result can often be judged as random.[181] This is due to the many different local energy minima of potential structures. The general lack of control over the character of solids produced from the traditional synthetic methods is directly related to the fact that the starting entities do not maintain their structure during the reaction, leading to poor correlation between reactants and products.[182-183]

To overcome these difficulties, a stepwise approach of node formation and isolation, followed by ligand substitution can be employed. The synthesis of pre-formed nodes with known geometries decreases the number of potential products and greatly increases the chance of prediction of the resultant network topology. Pre-formed nodes must have three properties for them to be of use:[76]

1. The precursor should remain intact throughout the construction process.

2. The precursor should have a defined coordination geometry.

3. The precursor should be soluble in common organic solvents.

These properties mean the building blocks can be readily dissolved, withstand the elevated temperatures and pressures usually required in MOF synthesis and will create a framework

with an *a priori* topology. An important goal in the field of MOFs is to be able to design the topological structure with accuracy and reproducibility. In this way, tailor made solids with predetermined structures and properties starting from well characterised inorganic and organic species can be produced.[184]

These preformed nodal units are defined as molecular building blocks (MBBs), and are in effect premade SBUs with anion or solvent sites that can be replaced with ditopic ligands to form network structures. To distinguish these from metalloligands, MBBs will be defined as units that only encode structural information based upon coordination bond acceptor sites. The use of such units vastly simplifies the amount of possible products of a MOF synthesis and hence the resultant network topology will be limited.

For this strategy to work, molecular building blocks must be identified. These must be discrete polymetallic coordination clusters that contain open metal sites, coordinated solvent or anions arranged in a regular array on the periphery of the cluster. Either through coordination or solvent/anion exchange these clusters can be linked together with ditopic coordination bond donors to form a framework material. Replacement of neutral species such as solvent molecules, coordinated to metal sites in the assemblies is easier than anionic species due to weaker coordinate bonds, and can often be achieved at room temperature.[172] A extensive series of such poly-carboxylate clusters exist, only some of which have been used in the synthesis of MOFs.[41]

The difference between molecular building blocks and secondary building units is exemplified in the use of pentanuclear zinc(II) benzotriazole nodes and their use in the synthesis of framework materials (Figure 3.2). In such clusters, coordinated anion co-ligands are arranged in an tetrahedral manner about the cluster, and benzotriazole ligands in an octahedral arrangement. Coordinated anions may include chloride, acetylacetonate, formate, acetate and nitrate.[76,185] Dissolution of these compounds in a DMA solution containing a linear dicarboxylic acid derivative, such as benzene-1,4-dicarboxylic acid, results in exchange of the coordinated anions, and the formation of a framework material (Figure 3.2b).[76] Because of the pre-defined geometry of the anions in the cluster, the resultant framework is based upon a tetrahedral node and indeed a diamondoid (**dia**) topology net is formed. This approach has also been applied to a variety of other

ditopic,[76,186] tritopic,[187] and tetratopic[188] carboxylate linkers to create a variety of pre-determined network topologies.

In this case, the coordination cluster can also be assembled as a SBU *in situ* by the use of a ditopic benzotriazole ligand. In this case, the octahedral arrangement of benzotriazole units lead to the formation of an octahedral SBU, and a framework based upon the primitive cubic net is produced (Figure 3.2c).

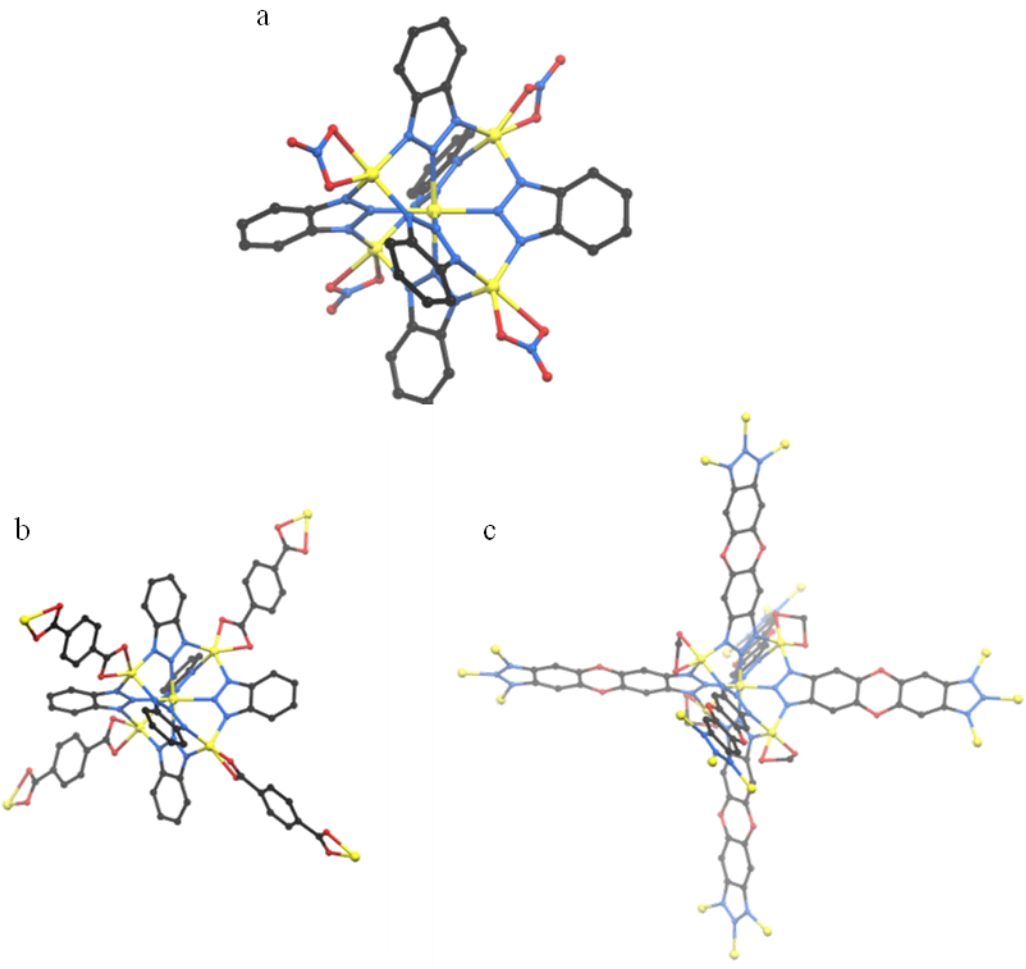

Figure 3.2: *a) Neutral pentanuclear zinc(II) coordination cluster [$Zn_5(bzt)_6(NO_3)_4$].[76] Coordinated nitrate anions are in a tetrahedral arrangement around the cluster. Benzotriazole (bzt) ligands are in an octahedral arrangement around the cluster. b) Upon reaction with dicarboxylic acid derivitives such as benzene-1,4-dicarboxylic acid, exchange of coordinated anions occures and a* ***dia*** *framework based upon a tetrahedral node is produced.[76] c) Use of a ditopic benzotriazole ligand in the synthesis of the coordination cluster results in a framework based upon an octahedral SBU.[189] Note formate anions are coordinated to zinc(II) in this case. Hydrogen atoms omitted for clarity.*

3.1.3 This study

The previous chapter investigated the hydrogen bonding properties of complexes containing a series of N^1-acetylamidrazone based ligands. The neutral and mono-deprotonated states of the coordinated ligand presented there are not the only two possible states, a further twofold deprotonated state also exists. In this case, in addition to the deprotonation of N^1 in the amidrazone functional group, deprotonation of N^3 (1° imidamide-like nitrogen atom) occurs (Figure 3.3a). This protonation state is potentially capable of bridging two metal centres. One metal ion will occupy the tridentate coordination domain exhibited previously, and another in the same pocket that was previously demonstrated to be an anion binder. The two hydrogen atoms formerly seen to act as hydrogen bond donors are lost to leave two nitrogen atoms with formal negative charges. It is this site which is defined as the new bidentate coordination domain. There has been only a single report of this bridging behaviour in the literature, and in this case other coordination bond donors are present, supporting the coordination domain (Figure 3.3b).[190]

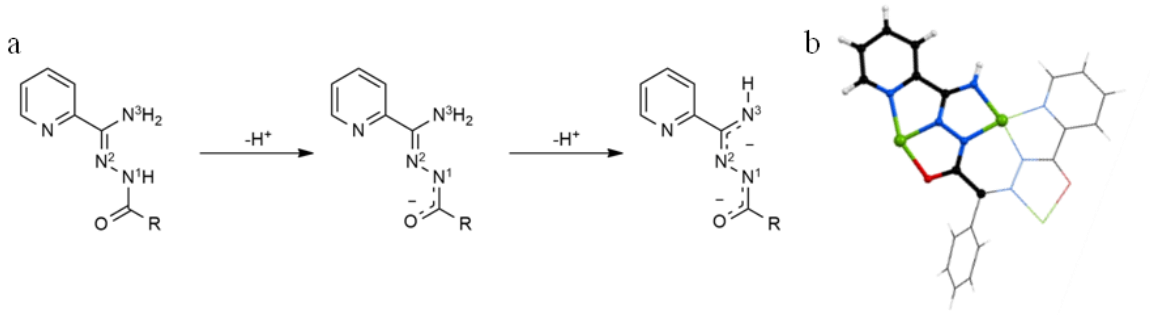

Figure 3.3: *a) Deprotonation of the N^1-acylamidrazone functional group can occur twice. The most acidic proton is that of N^1 followed by N^3. This leads to the formation of an additional bidentate coordination domain. b) This bridging behaviour has only been seen in once in the literature.[190] A single fragment of this nonanuclear copper(II) grid complex $[Cu_9(pph–2H)_2(pph–3H)_3]^{5+}$ is shown here and the N^1-acylamidrazone fragment highlighted. Of the five ligands in this structure only three adopt this bridging mode. pph = N'-(2-phenyl-2-(2-picolinoylhydrazono)acetyl)picolinohydrazonamide*

This chapter will examine the coordination chemistry of this di-anionic mode through coordination with transition metal ions. The ligand H_2**L2.1**, used in the previous chapter will be used again to investigate the coordination behaviour of the former hydrogen

bonding pocket. Further related ligands will be introduced throughout this chapter where relevant.

3.2 Synthesis of Metal-Organic Macrocycles

The two coordination domains in two-fold deprotonated pyridin-2-yl(N^1-acylamidrazone) ligands are not antiparallel with respect to each other. This angular arrangement of coordination sites leads to the possibility of metal-organic macrocycle formation.

The shape of these metal-organic macrocycles results in poor and inefficient crystal packing. Although some of the non macrocycle electron density could be assigned to solvent/antisolvent molecules, some could not and hence the SQUEEZE routine within PLATON was used to suppress the contribution of this to the atoms of the macrocycle in some cases.[159] For cases where this is used, the quoted R-factor refers to the modified data. The degree of solvation present for each macrocycle includes only the solvent that could be observed via crystallography. This is sometimes inconsistent to that observed via elemental analysis and TGA due to the high volatility of such solvent and different sample treatment prior to analysis.

3.2.1 Synthesis of $[Zn_8(L2.1)_4(AcO)_8]\cdot 4H_2O$ (3.1)

Combining a colourless methanolic solution of H_2**L2.1** and a colourless methanolic solution containing two equivalents of zinc(II) acetate produced a yellow solution which, upon diffusion of diethyl ether deposited yellow plate crystals suitable for single crystal X-ray diffraction. The diffraction data were solved and refined in the tetragonal space group *I*-42*d* (R-factor 5.68 %) in which the main residue in the asymmetric unit contained two chemically distinct zinc(II) ions bridged by two acetate moieties and a two-fold deprotonated **L2.1** ligand (Figure 3.4a). A solvent water molecule was also located and refined with full occupancy. Upon the action of the four-fold rotoinversion axis of the space group, a neutral metal-organic macrocycle of the form $[Zn_8(\mathbf{L2.1})_4(AcO)_8]$ with S_4 point group symmetry is generated (Figure 3.4b).

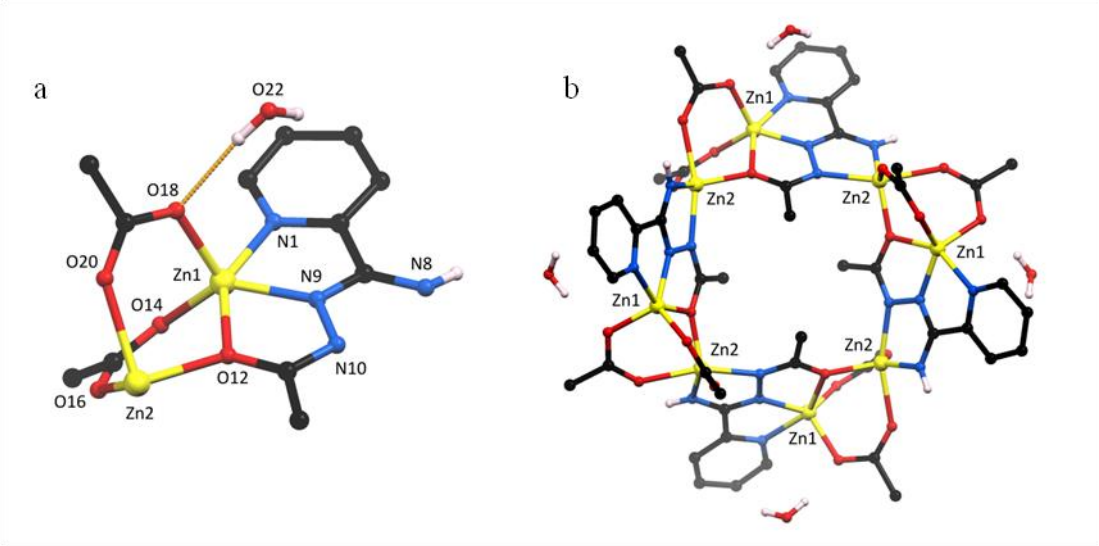

Figure 3.4: *a) Asymmetric unit of compound **3.1**. b) Complete macrocyclic structure of compound **3.1** and solvent water molecules. CH hydrogen atoms have been omitted for clarity. Selected bond lengths (Å) and angles (°): Zn1-N1 2.211(6), Zn1-N9 1.983(6), Zn1-O12 2.187(6), Zn1-O14 1.966(6), Zn1-O18 1.979(6), Zn2-O12 1.968(5), Zn2-O16 2.005(6), Zn2-O20 2.235(5), Zn2-N8' 1.978(7), Zn2-N10' 2.140(6), N1-Zn1-O12 149.2(2), N9-Zn1-O14 131.0(3), N8'-Zn2-O16 131.8(2), N10'-Zn2-O20 162.8(2).*

The ligand **L2.1** binds one zinc ion (Zn1) in the NNO tridentate binding domain (N1, N9, O12) as seen in the previous chapter. In addition to this, the ligand coordinates to two further zinc ions (both equivalent Zn2); one via the twofold deprotonated bidentate chelating amidrazone moiety (N8 and N10) and the other via the bridging oxygen atom (O12) of the amide group. This multi-metallic coordination mode allows the ligand to bridge in an angular fashion and hence allows for the construction of a macrocycle.

The ligand was assigned a formal negative two charge due to the two fold deprotonation required for the formation of the bidentate coordination domain. The overall charge of the macrocycle is therefore neutral. A single proton on N8 was seen in the difference map, and analysis of the bond lengths in **L2.1** indicated that there is significant delocalisation of the charge over the N^1-acetylamidrazone functional group.

The two chemically distinct zinc ions have distorted N_2O_3 five-coordinate geometry (τ_5(Zn1)= 0.30, τ_5(Zn2)= 0.51). Zn1 can be described as having distorted square-based pyramidal geometry, whereas Zn2 is distorted even more towards trigonal bipyramidal geometry. The acetate groups coordinate in a *syn, syn* bridging bidentate mode between Zn1

and Zn2 (Figure 1.9), the same coordination mode observed in the dinuclear metal carboxylate paddlewheel motifs.

The shortest cycle in the structure encompassing all zinc(II) ions is comprised of four -[Zn_1-N-N-Zn_2-O]- repeating units, creating a 20-membered ring (Figure 3.5a). Despite the size of this ring, there is no solvent accessible volume within the macrocycle due to the steric bulk of the methyl substituent of **L2.1** directed into the potential internal cavity. The zinc(II) ions and **L2.1** ligands are arranged in a saddle-like shape within the macrocycle. This is highlighted in Figure 3.5b-d.

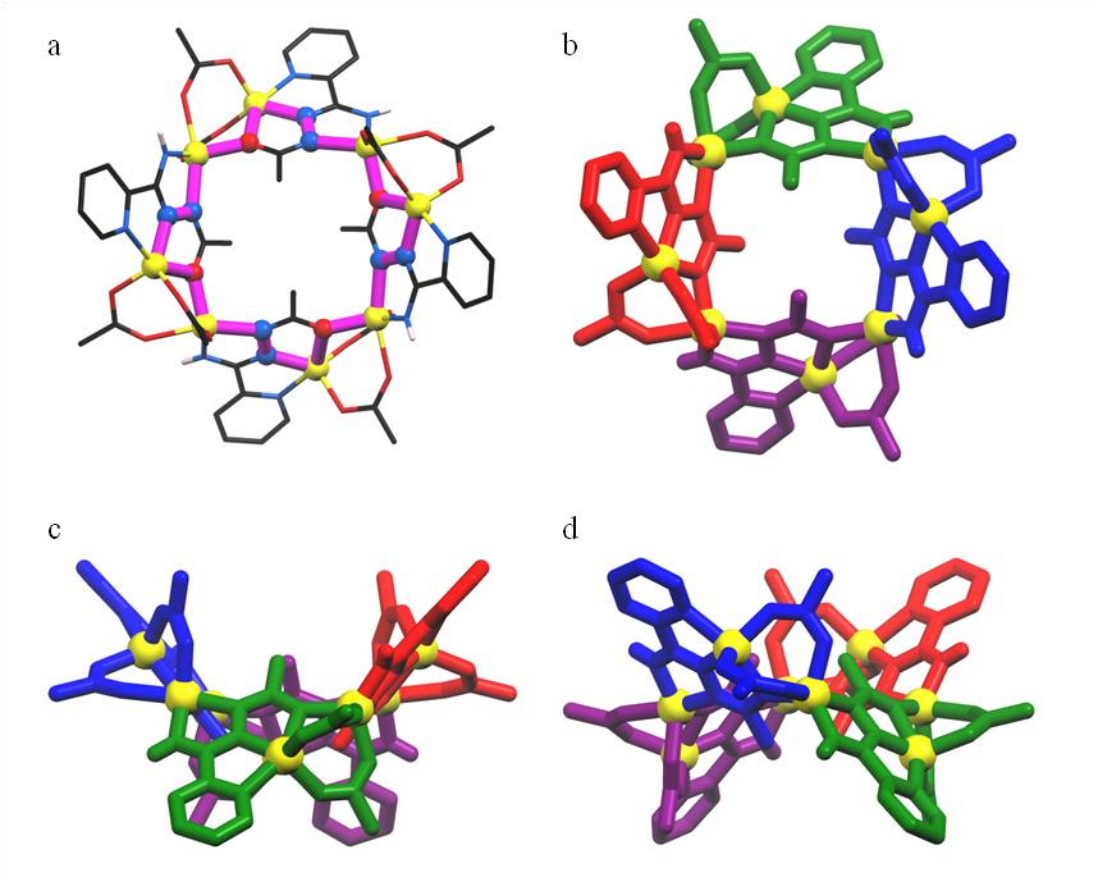

Figure 3.5: *a) Crystal structure of the macrocycle of* ***3.1****. The -[Zn_1-N-N-Zn_2-O]- cyclic repeating units are highlighted in magenta. The S_4 point group of each macrocycle is best visualised by highlighting the symmetry equivalent non-metallic components in different colours. Views along the crystallographic c-axis (b) and at arbitrary angles between the a and b-axes (c and d) shown the saddle -like orientations of the zinc(II) ions and* ***L2.1*** *ligands within the macrocycle.*

The **L2.1** ligands are arranged around the macrocycle in a fashion reminiscent of the 1,3-alternate configuration of a calix[4]arene. The angle between the mean planes created by opposite ligands is θ_{saddle} = 81.3(1)° highlighting the saddle shape of the macrocycle. There are two distinct positions for the acetate co-ligands around the periphery of the macrocycle. One position is arranged in the plane of the macrocycle, the other is approximately perpendicular to this ring. The four residues in the plane of the macrocycle are arranged in a square-planer type arrangement, whilst the four perpendicular have a distorted tetrahedral arrangement.

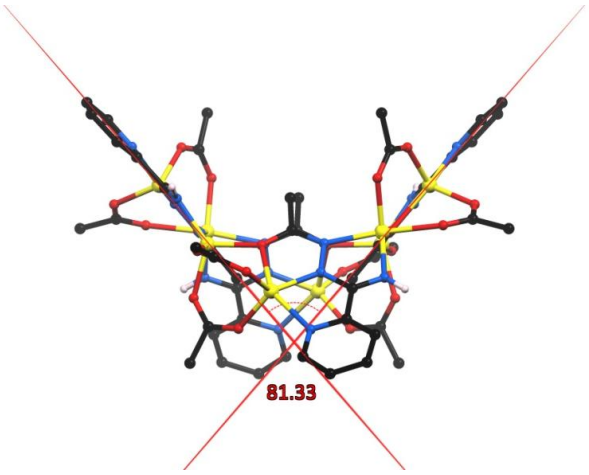

Figure 3.6: *The angle between the mean planes of the 13 non-hydrogen atoms of opposite* ***L2.1*** *ligands is 81.3(1)°.*

Each metal-organic macrocycle is connected to four adjacent molecules via hydrogen bond pairs from the remaining proton on the deprotonated 1° imidamide nitrogen atom to a carboxylate oxygen atom (H8···O20 2.374(6) Å, NH-O 158.9(4)°) (Figure 3.7). Due to the symmetry of the macrocycle, these connections create a hydrogen bonded diamondoid network compressed about the crystallographic c-axis. Despite the assignment of four water molecules of solvation within this lattice being assigned crystallographically, and confirmed by elemental analysis, solvent accessible void space does exist within the cavities between stacked macrocycles. The four-fold rotoinversion axis is centred on this cavity making the assignment of the minimal electron density in this region ambiguous. However, very little residual electron density was contained in this region and as SQUEEZE routine did not improve the model appreciably it was not used.

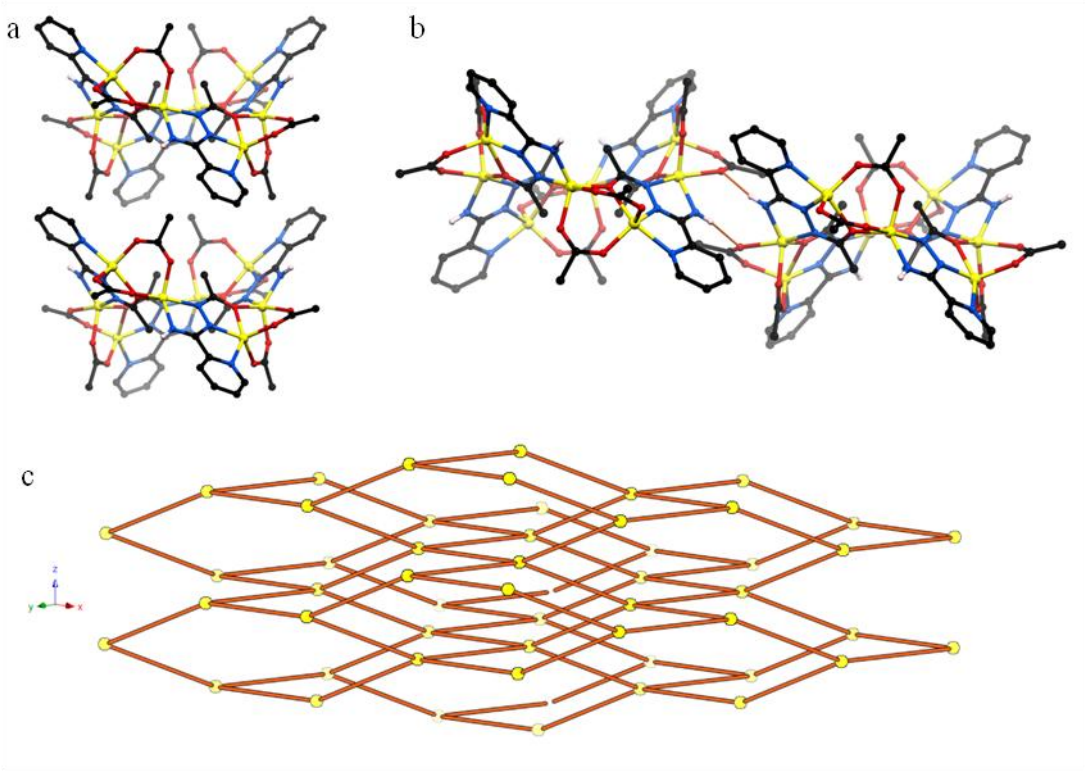

Figure 3.7: *a) Inefficient packing of macrocycles within the structure of **3.1**. A consequence of the bulk of the acetate groups allows for void space between stacked macrocycles. b) Hydrogen bonding interactions between neighbouring macrocycles shown in orange. c) Hydrogen bonding interactions of S_4 symmetry macrocycles create a diamondoid hydrogen bonding network. Macrocycles are represented by yellow balls and the hydrogen bonding interactions by orange rods.*

Due to the insolubility of **3.1** in all common laboratory solvents, attributed to the hydrogen bonding network, solution based characterisation methods were unable to be performed. Crystalline samples were stable for short periods out of solution, and powder X-ray diffraction in combination with elemental analysis was used to clarify that the bulk phase was indeed pure.

Complexes, clusters and frameworks containing d^{10} metal ions show promising prospects in photochemistry, photosensors and as electroluminescent displays. Due to the insolubility of **3.1**, only solid state luminescence measurements were performed. PXRD was performed on the sample to confirm phase purity (Figure 3.8a). The experimental pattern matched the pattern simulated from single crystal X-ray diffraction which confirmed the sample of **3.1** was indeed pure. Upon excitiation at λ_{ex} = 441 nm compound **3.1** showed an emission maximum at λ_{em} = 519 nm (Figure 3.8b). Solid state luminescent measurements were

carried out on H_2**L2.1** as a comparison, but the free ligand was found to not be luminescent. As no emission bands for the free ligand can be observed, the origin of the emission band for this emission is attributed to a metal-to-ligand charge transfer (MLCT).[191]

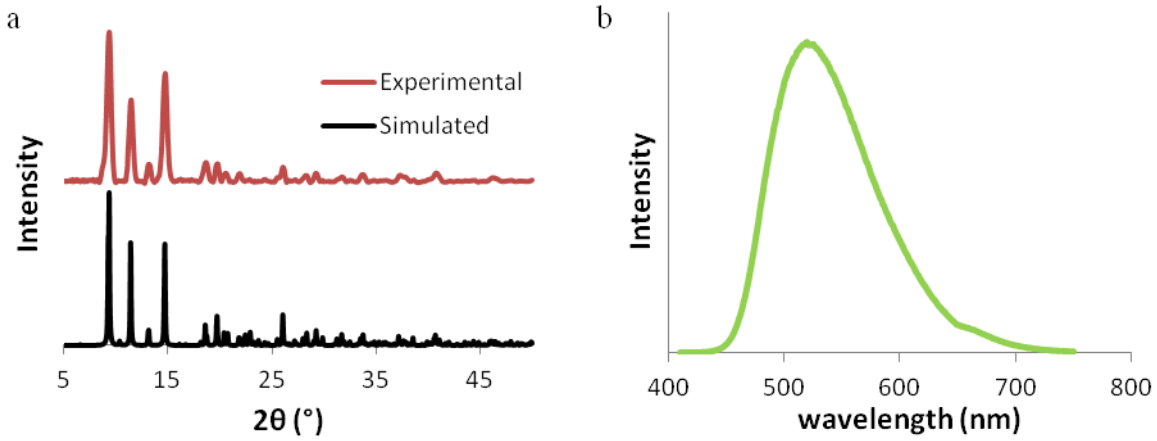

Figure 3.8: *a) PXRD pattern of* ***3.1*** *compared to that simulated from single crystal X-ray diffraction. b) Solid state state emission spectrum of* ***3.1****. Excitation at 396 nm leads to an emission at 519 nm. No luminescence was detected for the free ligand* H_2***L2.1****.*

Macrocycle **3.1** contains three unique parts; the ligand, the metal and the carboxylate residue. Each part of this assembly can potentially be modified to examine the effect on the overall structure. Modulation of the carboxylate residues will be described in the following sections.

3.2.2 Synthesis of $[Zn_8(L2.1)_4(EtCO_2)_8]\cdot 1.5H_2O$ (3.2)

An analogous procedure to that described for **3.1**, utilising zinc propionate was under taken to test whether the carboxylate moiety had a structure directing role in the synthesis of the metal-organic macrocycle. Combining a colourless methanolic solution of H_2**L2.1** and two equivalents of colourless zinc(II) propionate gave a yellow solution which, upon diffusion of diethyl ether deposited yellow plate crystals suitable for single crystal X-ray diffraction. The diffraction data was solved and refined in the tetragonal space group *I*-42*d* (R-factor 3.75%) and contained, as in **3.1**, one quarter of a metal-organic macrocycle in the asymmetric unit (Figure 3.9). The overall macrocyclic structure is analogous to that

described for **3.1** with the exception of propionate rather than acetate co-ligands. The solvent water molecule observed in the asymmetric unit was modelled with partial occupancy and is located further from the macrocycle. Due to these features, the hydrogen atoms of the water molecule could not be located and were not included within the structure model.

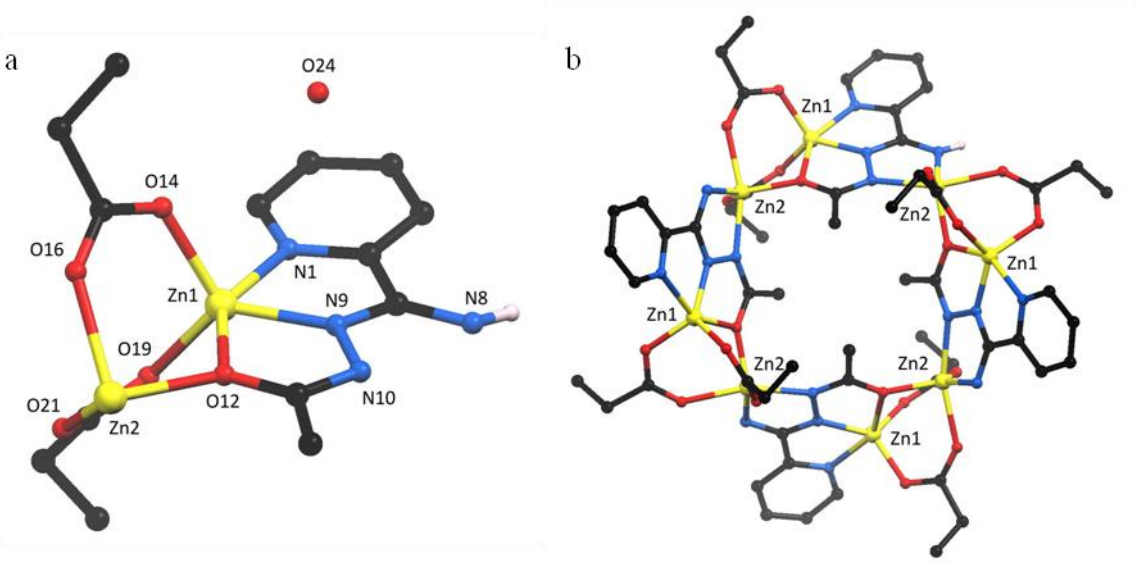

Figure 3.9: *a) Asymmetric unit of **3.2** with heteroatom labelling scheme. b) Complete structure of the macrocyclic structure of **3.2** viewed along the crystallographic c-axis. Solvent and CH atoms have been omitted for clarity.*

The bridging modes of the di-anionic **L2.1** and carboxylate co-ligands are the same as in **3.1** however, subtle changes in the angles of the ligands with respect to core of the macrocycle give rise to distorted bonding environments around the two unique Zn(II) centres (τ_5(Zn1)= 0.38, τ_5(Zn2)= 0.48), and a slightly smaller saddle angle (θ_{saddle} = 80.2(1)°). The flexible coordination environment of d^{10} metal ions such as zinc(II) is due to there being no preference in coordination geometry as there is no stabilisation by the crystal field.

Despite the addition of a flexible propionate residue to the exterior of the macrocycle, the symmetry of the overall structure remains (S_4 point symmetry) and the propionate residues were located in a single crystallographic environment. This is surprising as the terminal

carbon of these residues are directed within the solvent filled cavity and have no significant interactions with other groups.

The hydrogen bonding network seen in **3.1** is conserved in **3.2**. However, the added steric bulk of the propionate residue compared to the acetate leads to a reduction in the void volume between stacked macrocycles. The solvent accessible void space between two stacked macrocycles is reduced from 173 $Å^3$ in **3.1** to 27 $Å^3$ in **3.2** (calculated by PLATON, 1.2 Å probe radius). As with **3.1**, the minimal electron density within this cavity was not assigned and as the SQUEEZE routine did not improve the model appreciably, it was not used. Less aqueous solvent is seen within the diamondoid network crystallographically and via elemental analysis which is attributed to the combination of increased hydrophobicity and steric bulk of the propionate co-ligand with respect to acetate.

Despite the longer chain carboxylate residue, the macrocycle remained insoluble in common laboratory solvents hampering solution characterisation. Investigation into the effect of the carboxylate co-ligand on the macrocycle was continued with other carboxylate residues.

3.2.3 Synthesis of $[Zn_8(L2.1)_4(i\text{-}BuCO_2)_8]$ (3.3)

A longer and bulkier carboxylate group was used in an attempt to increase solubility of the metal-organic macrocycle. Combining a colourless methanolic solution of H_2**L2.1** and two equivalents of colourless zinc(II) isovalerate produced a bright yellow solution which, upon diffusion of diethyl ether deposited yellow plate crystals suitable for single crystal X-ray diffraction. The diffraction data were solved and refined in the monoclinic space group *C*2/*c* (R-factor 12.90%) and contains one complete macrocycle (of similar composition to **3.1** and **3.2**) in the asymmetric unit (Figure 3.10). The central 20-membered ring in the macrocycle is distorted so no four-fold rotoinversion or even two-fold rotation axis exist within the centre of the macrocycle. The deviation in the dihedral angle of the Zn2-Zn4-Zn6-Zn8 plane is 29.23(3)°. Despite the flexibility of the isovalerate moiety, electron density corresponding to only one orientation per residue was located.

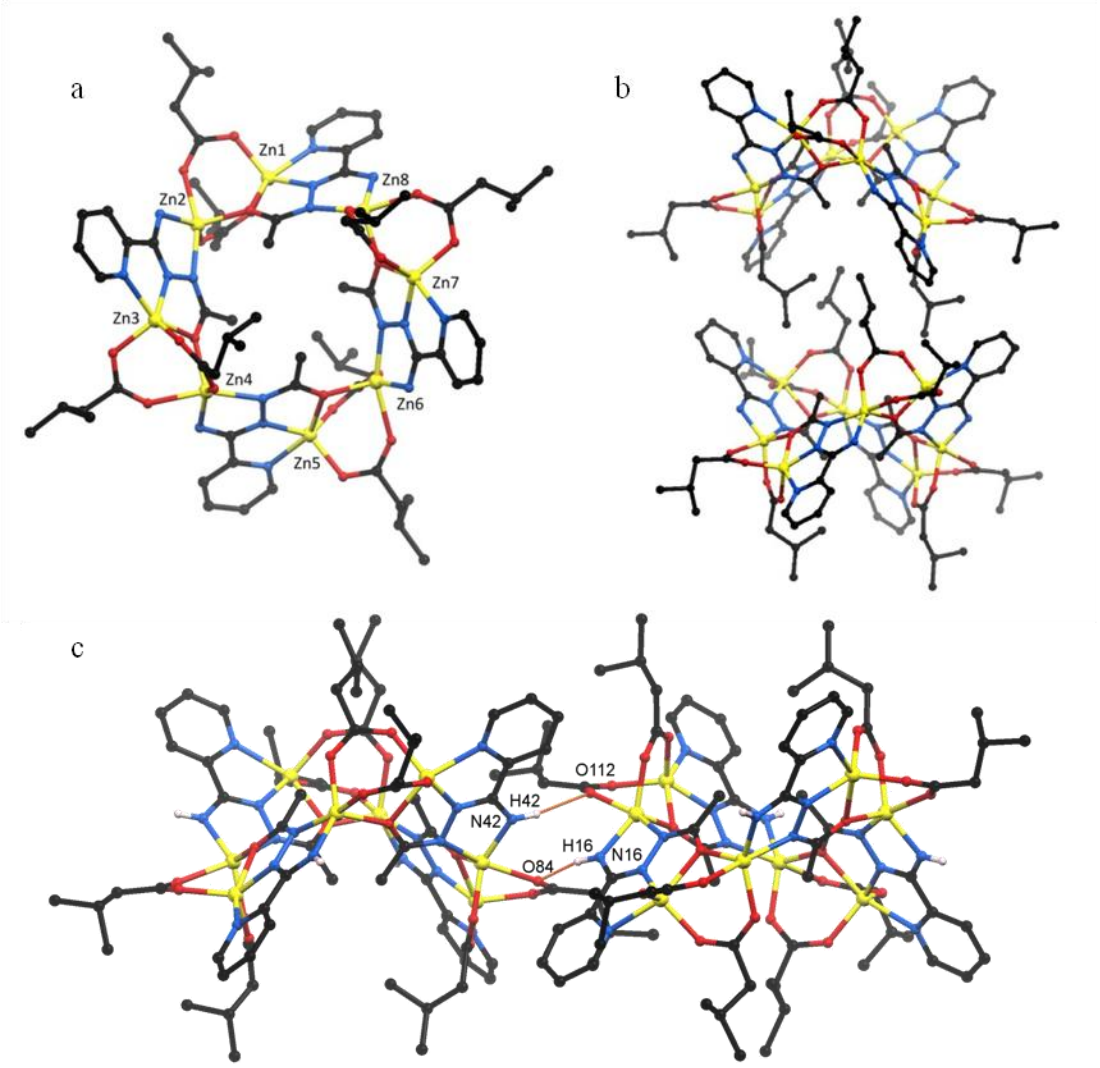

Figure 3.10: *a) Asymmetric unit of **3.3**. b) Stacking of **3.3** showing interdigitation of isovalerate residues between stacked macrocycles. c) Two hydrogen bonds link **3.3** with each of its four neighbours. Each macrocycle is linked to the four others via crystallographic non-equivalent pairs of hydrogen bonds. Hydrogen atoms (when not showing hydrogen bonding interactions) are omitted for clarity.*

Each macrocycle forms a pair of hydrogen bonds to 4 adjacent MOMs in a similar fashion to **3.1** and **3.2** (H16···O84 2.314 Å, NH···O 157.58°; H29···O63 2.334 Å, NH···O 161.52°; H42···O112 2.304 Å, NH···O 162.60°; H55···O91 2.290 Å, NH···O 163.84°). However, due to the distortions of the central macrocyclic ring, the hydrogen bond array forms a planar two-dimensional square grid (**sql**) instead of a diamondoid (**dia**) supramolecular network. In essence the distortion of the S_4 point symmetry of the macrocycle to C_1 means each unit acts as a square planar node instead of a tetrahedral one.

Adjacent grids are stacked directly on top of each other. Each layer is not offset relative to the next and layers interact via interdigitation of the hydrophobic isovalerate residues. The square channels along the c-axis created by this stacking of grids contain diffuse electron density. This is likely to be loosely bound solvent molecules consistent with the sample losing crystallinity rapidly upon removal from the mother liquor and no solvent being evident from microanalysis. After attempts at modelling this disordered solvent were unsuccessful, the decision was made to use the SQUEEZE routine in PLATON to remove the solvent contribution to the diffraction due to this electron density.[159]

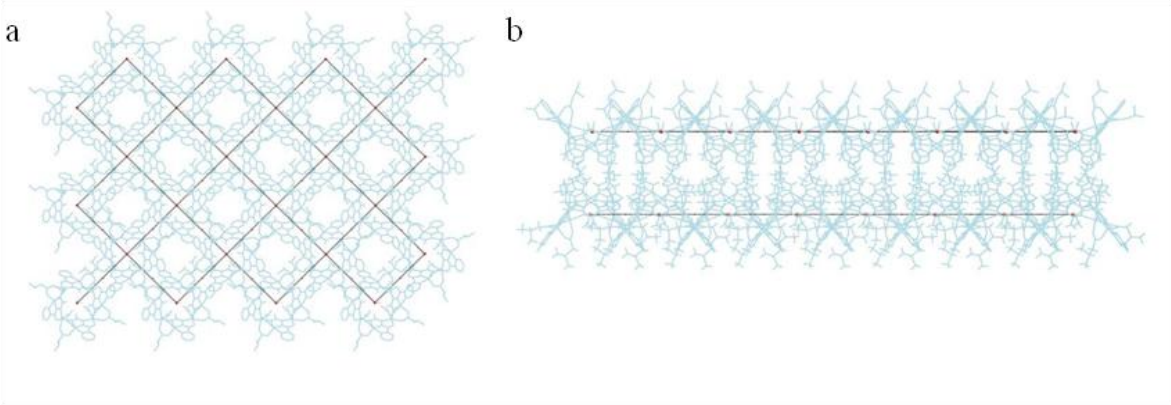

Figure 3.11: *Packing of* ***3.3*** *with an overlaid schematic representation of a two-dimensional square grid formed by hydrogen bonding interactions between each macrocycle. Each node is centred on a macrocycle. a) View along the crystallographic c-axis. (b) View along an arbitrary axis 90° to the c-axis.*

The SQUEEZE routine removed residual electron density corresponding to 216 electrons per macrocycle, approximately 5 molecules of diethyl ether per macrocycle (210 electrons). The fact that no solvent was observed in the TGA or in elemental analysis supports the notion the removed solvent was the volatile diethyl ether.

3.2.4 Synthesis of $[Zn_8(L2.1)_4(t\text{-}BuCO_2)_8]\cdot 2Et_2O$ (3.4)

As the above macrocycle still remained insoluble in common laboratory solvents, a bulkier isomeric carboxylate co-ligand to isovalerate was used; pivalate. This co-ligand contains a tertiary butyl group, a moiety commonly used in coordination chemistry to increase solubility of complexes in organic solvents.[192-193]

Combining a colourless methanolic solution of H_2**L2.1** and two equivalents of zinc(II) pivalate gave a bright yellow solution which, upon diffusion of diethyl ether deposited yellow plate crystals suitable for single crystal X-ray diffraction. The diffraction data were solved and refined in the monoclinic space group *C*2/*c* (R-factor 3.10 %) and contains two crystallographically distinct **L2.1**, four zinc(II) ions, and 8 pivalate moieties in the asymmetric unit. The two fold rotation axis of the space group generates a metal-organic macrocycle of analogous structure to those described previously in this chapter (Figure 3.12). The reduction in symmetry of the macrocycle with respect to **3.1** and **3.2** (C_2 point symmetry *c.f.* **3.1**, **3.2** S_4) arises from the uneven twisting of the central 20-membered macrocyclic ring, facilitated by the flexible coordination geometry of the zinc ions (τ_5(Zn1) = 0.40, τ_5(Zn2) = 0.45, τ_5(Zn3) = 0.36, τ_5(Zn4) = 0.39). Tertiary butyl groups are often seen to be rotationally disordered when no significant inter-molecular interactions exist; indeed, two of the four tertiary butyl groups in the asymmetric unit of **3.4** are disordered over two positions.

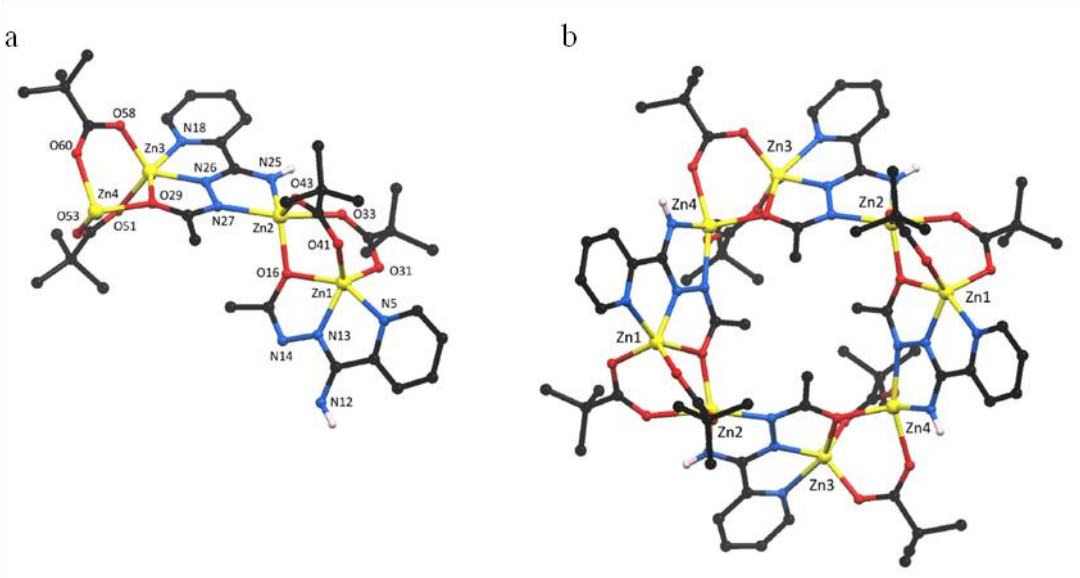

Figure 3.12: *a) Asymmetric unit of **3.4** with heteroatom labelling scheme. b) Complete macrocycle generated from 2-fold rotation axis with metallic numbering scheme. Disorder of tertiary butyl groups and CH hydrogen atoms and solvent diethyl ether molecules have been omitted for clarity.*

The macrocycles stack directly on top of each other with the same orientation as in **3.1**-**3.3**. Again, the carboxylate residues prevent close packing, but the added bulk of the pivalate

residue compared with acetate and propionate in **3.1** and **3.2**, directed above and below each macrocycle does not significantly change the inter-macrocycle stacking distance.

The two symmetrically inequivalent **L2.1** ligands experience different intermolecular interactions within the crystal lattice. The residue containing the pyridyl nitrogen atom N5 is involved in centrosymmetric π-π stacking with a neighbouring macrocyle, which, because of the two-fold symmetry, creates a one-dimension chain motif along the c-axis (Figure 3.13). In contrast to this, the other **L2.1** residue, containing pyridyl nitrogen atom N18, has no significant interactions.

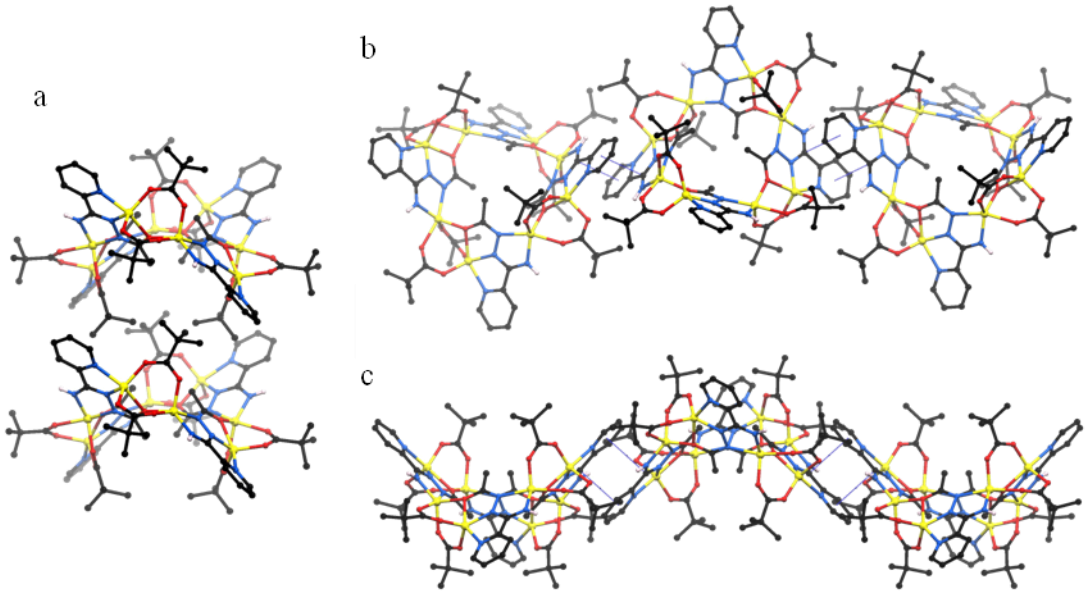

Figure 3.13: *a) Stacking of macrocycles in **3.4**. The steric bulk of pivalate residues prevent close packing on macrocycles. One dimensional chain of macrocycles formed via 3.390(7) Å π-π stacking interactions of equivalent **L2.1** ligands.*

An obvious feature of the supramolecular interactions of **3.4** with respect to **3.1**-**3.3**, is the lack of hydrogen bonds from the coordinated, deprotonated 1° imidamide nitrogen atoms (protons H12, H25) to carboxylate groups on neighbouring molecules. From structural comparison of the crystal structures it seems that the bulk of the pivalate group is responsible for this and the required close approach of macrocycles from the required angle

is no longer possible. The π-π stacking interactions of **L2.1** occur at a more remote position relative to the pivalate residues and are therefore not affected by the bulkiness of this group.

Residual electron density exists in channels between the metal-organic macrocycles. Initial attempts at modelling this suggested the presence of two diethyl ether molecules, however, these could not be modelled satisfactorily and the SQUEEZE routine within PLATON was performed.[159] This found a possible solvent accessible void volume of 262 $Å^3$ and an electron count of 82 per complete macrocycle. This is consistent with the inclusion of two diethyl ether molecules (84 electrons). Elemental and TGA analysis did not show any solvent being present, consistent with the volatility of the ether, the channel-like structure of the solvent regions and the more rigorous drying conditions before the latter two measurements. Despite of the suppression of the hydrogen bonding interactions between macrocycles, compound **3.4** remained insoluble in common laboratory solvents.

3.2.5 Synthesis of $[Zn_8(L2.1)_4(n\text{-}PenCO_2)_8]$ (3.5)

The steric bulk of the carboxylate residue was shown to not alter the overall solubility of the macrocycle, so a longer chain carboxylate was used to study the effect on crystal packing and hence solubility. Hexanoate was chosen as a potential co-ligand.

Combining a colourless methanolic solution of H_2**L2.1** and two equivalents of colourless zinc(II) hexanoate gave a yellow solution which, upon diffusion of diethyl ether deposited yellow block crystals suitable for single crystal X-ray diffraction. The diffraction data were solved and refined in the chiral hexagonal space group $P6_2$ (R-factor 7.31 %). The asymmetric unit contains two crystallographically independant halves of a MOM. Each half macrocycle is centred on a two-fold rotation axis such that only half of each of the two crystallographically distinct macrocycles is unique (Figure 3.14). Each macrocycle displays slightly distorted coordination geometry around the zinc ions (τ_5(Zn1) = 0.28, τ_5(Zn2) = 0.71, τ_5(Zn3) = 0.25, τ_5(Zn4) = 0.48, τ_5(Zn5) = 0.32, τ_5(Zn6) = 0.63, τ_5(Zn7) = 0.40, τ_5(Zn8) = 0.43) and displays different orientations of flexible hexanoate chain. Surprisingly the best model for **3.5** includes no disorder in the eight unique hexanoate residues in the asymmetric unit.

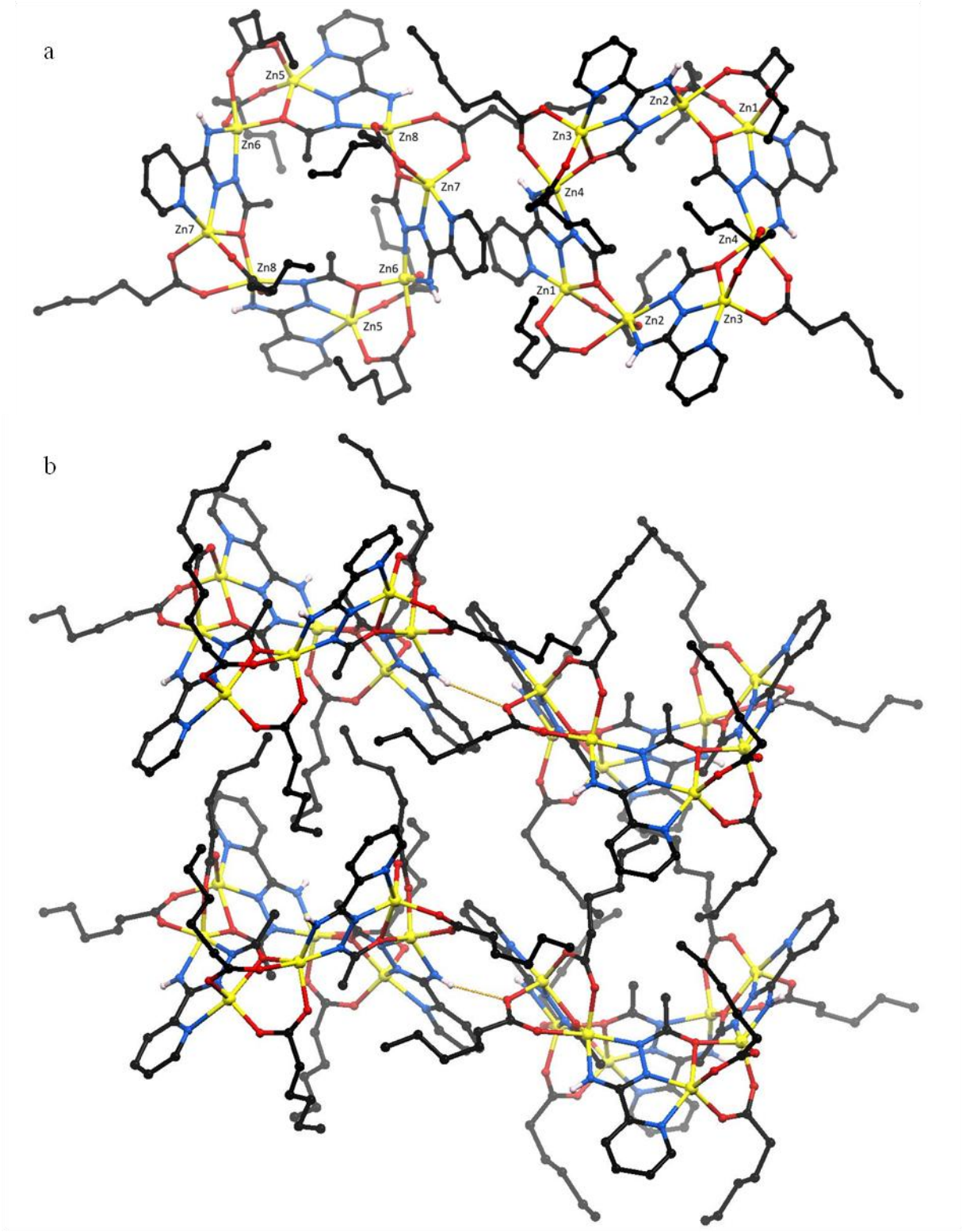

Figure 3.14: *a) Two independant metal-organic macrocycles in* ***3.5****. b) Each macrocycle has four single hydrogen bonding interactions with four non-equivalent neighbouring macrocycles. Only one of such interactions per macrocycle is shown. Hexanoate alkyl chains occupy the space between macrocycles. CH hydrogen atoms omitted for clarity.*

The crystallographically independent macrocycles interact with neighbours in similar ways and hence can be treated as the same shaped node in topological analysis of the resultant binary framework. Each macrocycle has hydrogen bonds to four adjacent (non-crystallographically equivalent) macrocycles; two hydrogen bond donors, and two acceptors which due to the shape of the directionality of these bonds allows it to be described as a tetrahedral node. When extended in three dimensions the hydrogen-bonded framework can be described by the three-dimensional quartz (**qtz-b**) net; a rare topology compared to the related **dia** net (Figure 3.15).[194] The binary descriptor is added to distinguish between the two crystallographically inequivalent macrocycles. In contrast to the uniform chair-conformation of six membered rings in the **dia** net, there are two different rings in the **qtz** net: the distorted boat-conformation of six-membered rings and the saddle eight-membered rings. Interestingly, no interpenetration of this framework is observed, contrasting many published metal-organic systems with **qtz** topology. This is attributed to the steric bulk of the macrocyclic nodes of the supramolecular framework. Subtle deviations in the linker structure have been shown to allow for formation of chiral quartz type topologies instead of the more common achiral diamondoid from achiral building units. [195]

The quartz network contains large channels along the crystallographic *c*-axis (Figure 3.15). These contained diffuse residual electron density which could not be modelled satisfactorily and hence the SQUEEZE routine was carried out.[159] Despite finding electron density corresponding to 748 electrons in the 3406 $Å^3$ void space of the unit cell, no significant solvent was seen in the TGA or elemental analysis leading to the opinion that this solvent is volatile diethyl ether (electron density corresponds to 18 diethyl ether molecules, or 3 per macrocycle). Observation of diethyl ether in the crystals structures but not via microanalysis or TGA of some of the following examples gives credence to this conclusion.

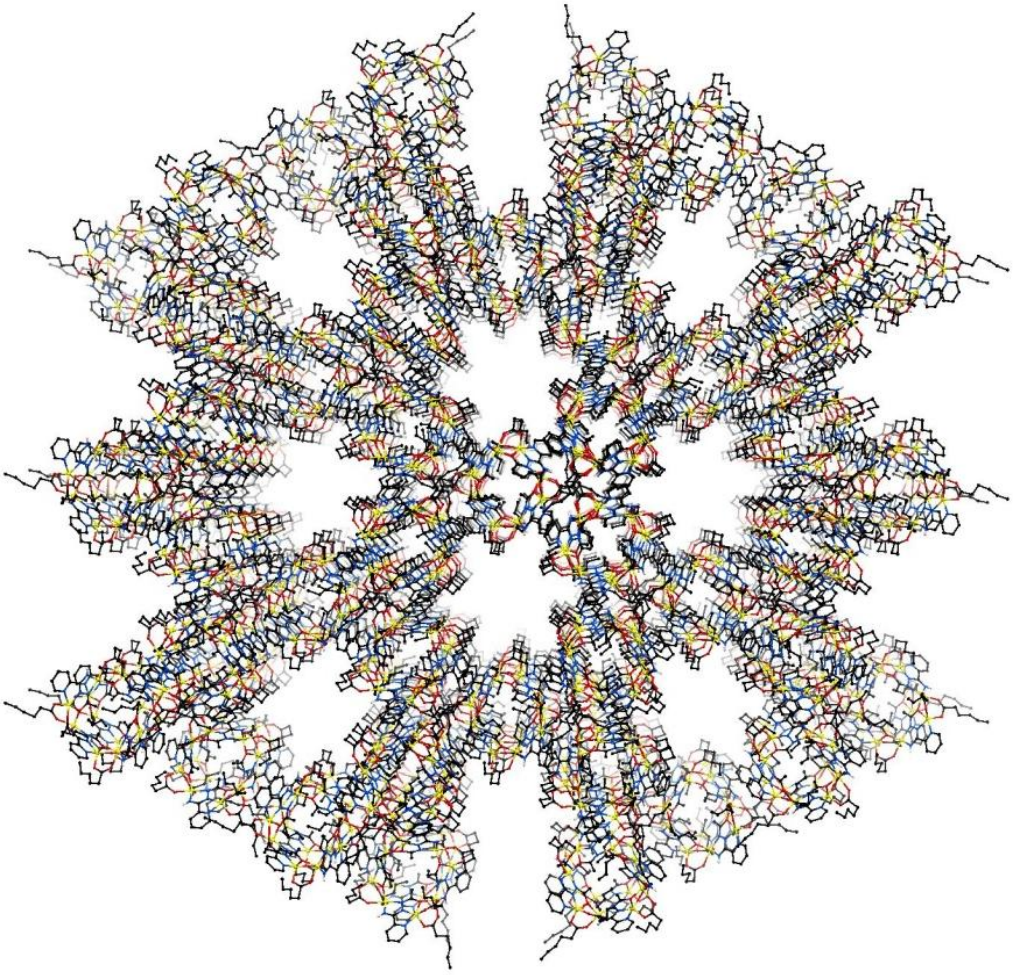

Figure 3.15: *Extended* ***qtz-b*** *hydrogen-bond network of* ***3.5,*** *showing hexagonal channels along the crystallographic c-axis within structure.*

A shorter c-axis is possible with this unit cell due a pseudo-translation; however, variations in the mean plane saddle angles of **L2.1** (76.1(2)° and 75.5(2)° in one macrocycle verses 83.6(3)° and 67.8(2)° in the other) and significant disorder of hexanoate chains prevent a suitable model being formed. When the longer c-axis is used in the model no disorder in the hexanoate chains and better thermal parameters for atoms in **L2.1** residues were observed and hence was deemed to be the best choice.

3.2.6 Synthesis of $[Zn_8(L2.1)_4(p\text{-}MeBzO)_8]\cdot Et_2O\cdot H_2O$ (3.6)

The same macrocyclic motif has been shown to be conserved with variation of aliphatic carboxylate residues. To test whether this would be the case with rigid aromatic carboxylate co-ligands, a *p*-toluate derivative was devised using similar reaction conditions to those mentioned previously.

The decreased solubility of zinc(II) *p*-toluate with respect to aliphatic zinc(II) carboxylate salts meant that gentle heating and stirring overnight in the presence of H_2**L2.1** was required for complete dissolution in methanol and formation of a yellow solution. Upon diffusion of diethyl ether into this solution, yellow block crystals formed. These were solved and refined in the tetragonal space group *I*-4 (R-factor 4.53 %). The asymmetric unit contained two quarter macrocycles of the same general formula as described for **3.1**-**3.5** (Figure 3.16). Each of these macrocycles is centred on a four-fold rotoinversion axis. The rigid carboxylate groups prevent close packing of macrocycles and significant void space exists between molecules. Within this space one disordered diethyl ether molecule and a water molecule could be located and modelled, however, due to the large cavities and diffuse residual electron density within, the rest of the electron density was subject to the SQUEEZE routine.[159]

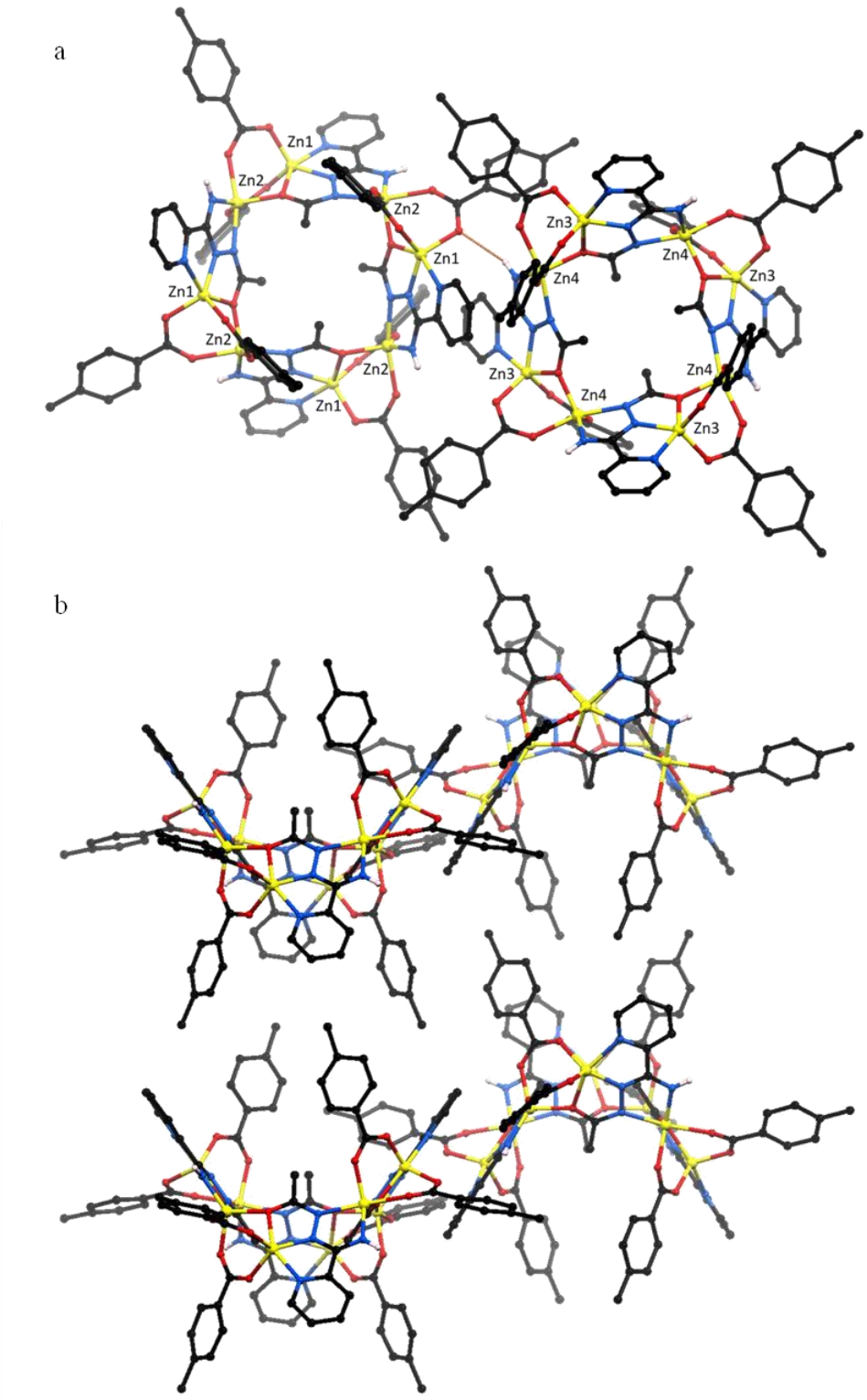

Figure 3.16: *a) Two crystallographically unique macrocyles in* ***3.6****. Hydrogen bonding between macrocycles shown in orange. b) The p-toluate residues prevent close stacking between macrocycles. Solvent and CH hydrogen atoms omitted for clarity.*

The two crystallographically distinct macrocycles have two different modes of inter-molecular interactions. The macrocycle containing zinc ions Zn1 and Zn2, acts as a four-fold hydrogen bond acceptor, via O41, a coordinated carboxylate oxygen atom. The macrocycle containing zinc ions Zn3 and Zn4 acts as a four-fold hydrogen bond donor via the proton on the deprotonated 1° imidamide nitrogen atom N25. The chemically equivalent imidamide nitrogen atom, N12, on the other macrocycle is not involved in hydrogen bonding with adjacent macrocycles and the proton is directed into the cavities of the structure. No electron density was found that could be attributed to a hydrogen bond acceptor and hence the proton, seen in the difference map, was left to point into the void. In addition to the hydrogen bonding between MOMs, a π-π stacking interaction between **L2.1** ligands exist. The crystal packing arrangement of these two crystallographically inequivalent macrocycles leads to a supramolecular binary diamondoid network (**dia-b**) due to the extension of these hydrogen bonds.

The same macrocyclic motif was observed to form with aromatic carboxylate co-ligands in addition to the aliphatic examples **3.1**-**3.5**. The solubility of **3.6** is similar to previous examples and a solvent capable of dissolving crystals of **3.6** was not found.

3.2.7 Synthesis of $[Zn_8(L2.1)_4(BnCO_2)_8]$ (3.7)

When zinc(II) phenylacetate and H_2**L2.1** were combined in methanol and subject to the same crystallisation conditions as described for **3.1**-**3.6**, crystals suitable for single crystal X-ray diffraction were obtained. These were solved and refined in the chiral hexagonal space group $P6_2$ (R factor 6.36 %). The asymmetric unit contains two half metal-organic macrocycles with the same general structure to those described previously. Each half macrocycle is centred around a two-fold rotation axis such that only half of each is crystallographically unique (Figure 3.17). Of the eight crystallographically unique phenylacetate residues, three were modelled as being disordered over two positions.

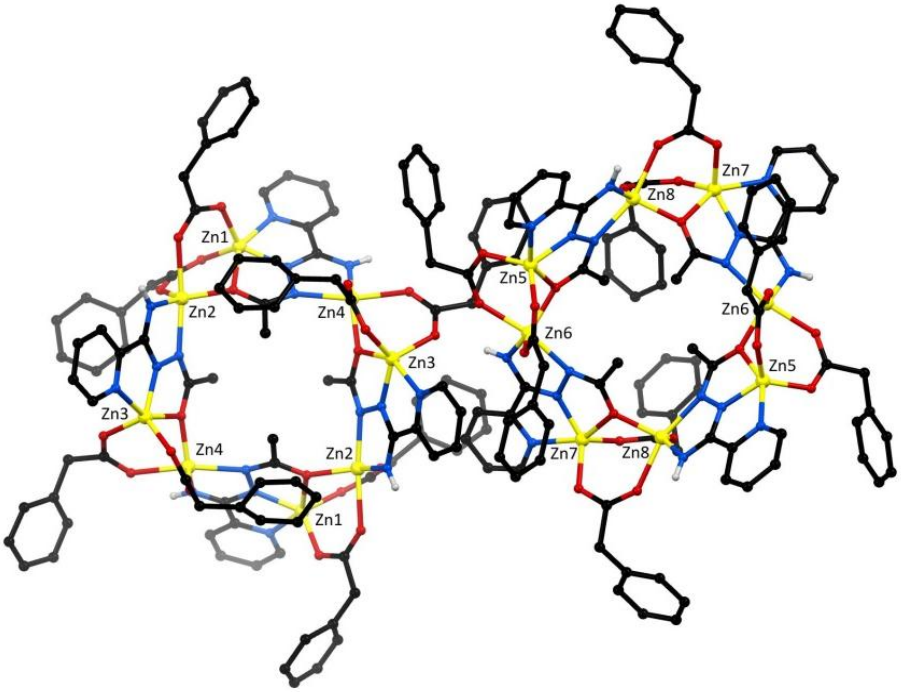

Figure 3.17: *The two crystallographically unique macrocycles in* ***3.7*** *with metallic labelling scheme. In addition to the different relative positions of the flexible phenylacetate residues on each macrocycle, the core of the macrocycle twists which is reflected in the* τ_5 *values of each zinc ion (*τ_5*(Zn1)= 0.35,* τ_5*(Zn2)= 0.54,* τ_5*(Zn3)= 0.34,* τ_5*(Zn4)= 0.50,* τ_5*(Zn5)= 0.48,* τ_5*(Zn6)= 0.50,* τ_5*(Zn7)= 0.28,* τ_5*(Zn8)= 0.40). CH hydrogen atoms have been omitted for clarity.*

Hydrogen bonding exists between the deprotonated 1° imidamide proton of **L2.1** and a coordinated carboxylate oxygen atom of a phenylacetate co-ligand to form a one-dimensional chain. Parallel chains are arranged in flat layers. Each layer is offset to neighbouring layers by a 60^{o} angle, a consequence of the screw axis of the space group. This generates hexagonal channels perpendicular to these layers, which contained diffuse electron density that despite attempts was unable to be modelled (Figure 3.18). Hence the SQUEEZE routine in PLATON was performed and the solvent contribution of the crystal structure was removed.[159] This found a solvent accessible volume of 4440 Å^3 containing 1021 electrons per unit cell, or four molecules of diethyl ether per macrocycle. Crystals of **3.7** were unstable out of solution and rapidly lost crystallinity when removed from solution.

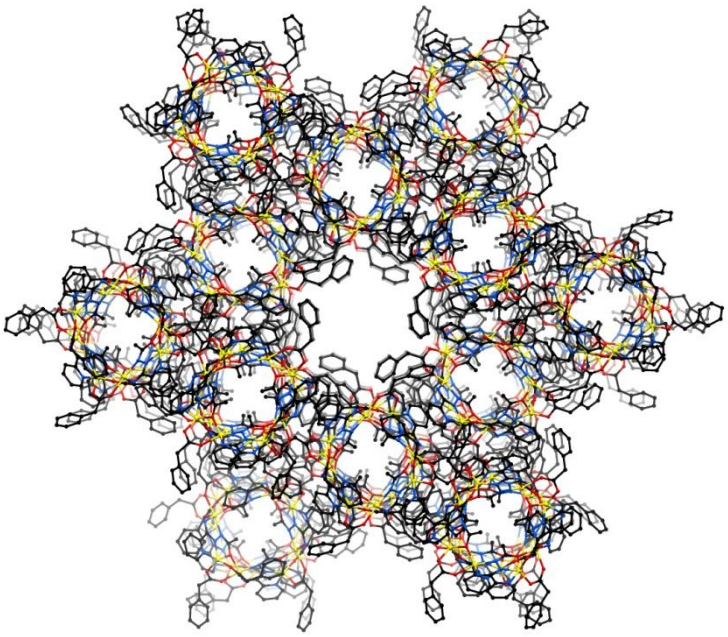

Figure 3.18: *Hexagonal one-dimensional channels in **3.7** viewed along the crystallographic c-axis. Disorder of phenylacelate co-ligands and hydrogen atoms have been omitted for clarity.*

3.2.8 Synthesis of $[Zn_8(L2.1)_4(p\text{-}ClBnCO_2)_8]\cdot 0.5Et_2O$ (3.8)

Metal-organic macrocycles of the general form $[Zn_8\mathbf{L1}_4(RCO_2)_8]$, where R contains only carbon and hydrogen atoms have been synthesised. The ligand *p*-chlorophenylacetic acid, a potential anti-cancer agent,[196] was chosen as a potential co-ligand because of its similarity to phenylacetate in **3.6** and it containing a halogen atom.

The introduction of aryl halides was attempted by reacting H_2**L2.1** with two equivalents on zinc(II) *p*-chlorophenylacetate in methanol. Upon the diffusion of diethyl ether, crystals of sufficient quality for single crystal X-ray diffraction were produced. The data were solved and refined in the space group *I*-4 (R-factor 3.77 %). The asymmetric unit contained two quarter macrocycles of the same general formula as described for the above examples (Figure 3.19). Compound **3.8** shares the same space group and crystal packing arrangement as **3.6** (*p*-toluate co-ligand). As in **3.6**, the two crystallographically distinct macrocycles adopt different hydrogen bonding modes; one acts as a four-fold hydrogen bond donor, the other a four-fold hydrogen bond acceptor. However, due to twisting of macrocycles relative to each other, no π-π stacking is observed between **L2.1** residues. Despite this twisting the

same hydrogen bonding network and thus **dia-b** hydrogen bond framework is formed. A partial occupancy diethyl ether molecule was located crystallographically within this framework and was modelled appropriately. Unlike the rigid *p*-toluate residues in **3.6**, the flexible nature of of *p*-chlorophenylacetate, allows the two crystallographically distinct macrocycles to adopt very different shapes. The flexible co-ligands are able to adapt to the space around each macrocycle decreasing the potential void space within the crystal lattice. This structure did not contain any potential solvent accessible void space that could not be modelled and hence was not subject to the SQUEEZE routine. Contrasting the phenylacetate derivitive **3.7**, the *p*-chlorophenylacetate co-ligands in **3.8** are not disordered.

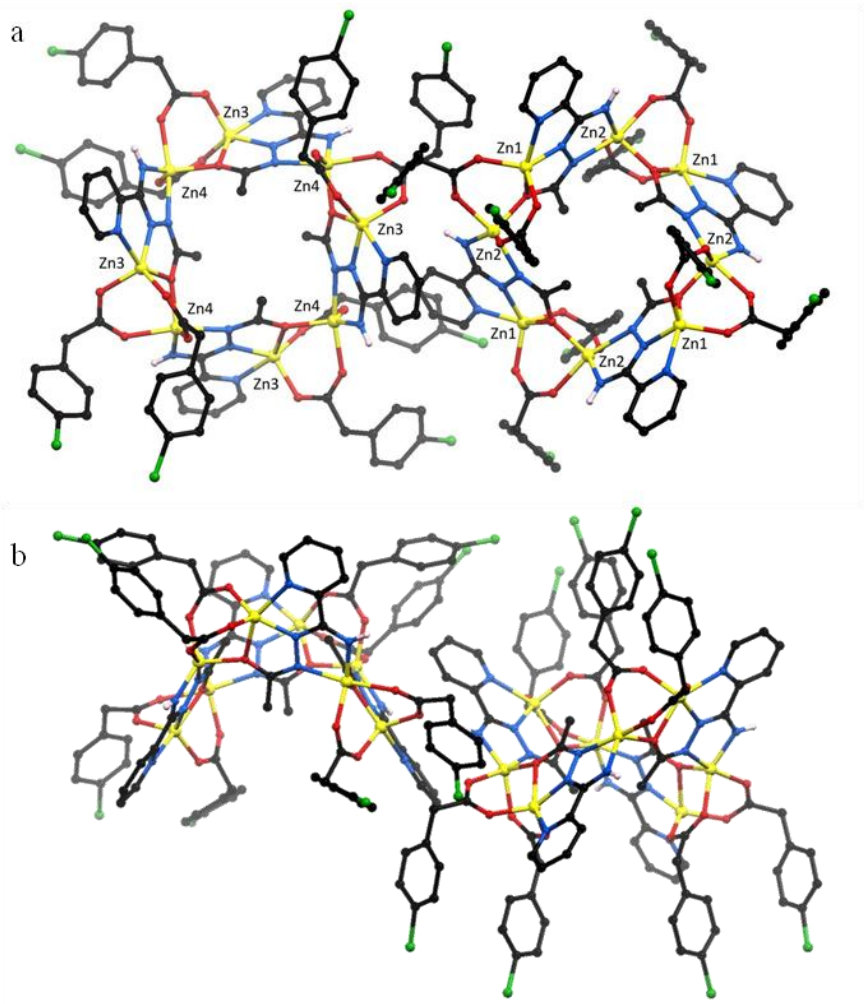

Figure 3.19: *a) Two crystallalographically unique macrocycles in **3.8** viewed down the crystallographic c-axis. Each macrocycle is centered on a four-fold rotoinversion axis, and hence only a quarter of each is crystallographically unique. b) The flexibility of the p-chlorophenylacetate residues allow for each macrocycle to adopt very different shapes relative to each other. Solvent, CH atoms omitted for clarity.*

In addition to hydrogen bonding between the imidamide protons of one macrocycle to carboxylate oxygen atoms on an adjacent non-equivalent macrocycle, a secondary interaction between the imidamide protons on the latter macrocycle and a chloro atom Cl61 on a symmetry equivalent macrocycle exists. Due to the lower electronegativity of chlorine with respect to oxygen, this interaction is expected to be much weaker than the former. This is supported by a similar **dia-b** topology being present in **3.6** despite the lack of this additional interaction.

3.2.9 Synthesis of $[Zn_8(L2.1)_4(Ph(CH)_2CO_2)_8]\cdot 3Et_2O$ (3.9)

Biologically relevant carboxylate molecules could also be attached to the periphery of the metal-organic macrocycles. Trans-cinnamic acid and derivatives have been shown to inhibit seed growth and germination[197] and being similar in structure to other carboxylates mentioned in this chapter was tested as a potential co-ligand for the metal-organic macrocyclic motif.

Combining a colourless methanolic solution of H_2**L2.1** and two equivalents of colourless zinc(II) *trans*-cinnamate gave a bright yellow solution which, upon diffusion of diethyl ether deposited yellow plate crystals suitable for single crystal X-ray diffraction. The data was solved and refined in the tetragonal space group $I4_1/a$ (R-factor 5.69 %). The asymmetric unit contained one quarter of a complete MOM and a partial occupancy solvent diethyl ether molecule (Figure 3.20). One of the *trans*-cinnamate residues was disordered over two positions due to rotation about the single bond between the carboxylate group and alkene bond, and was modelled appropriately. The conjugated carboxylate residues remain relatively flat, with only slight deviations from planarity (17.0(6)° for the ordered co-ligand, 13(2)° and 9(2) for two orientations of the disordered co-ligand).

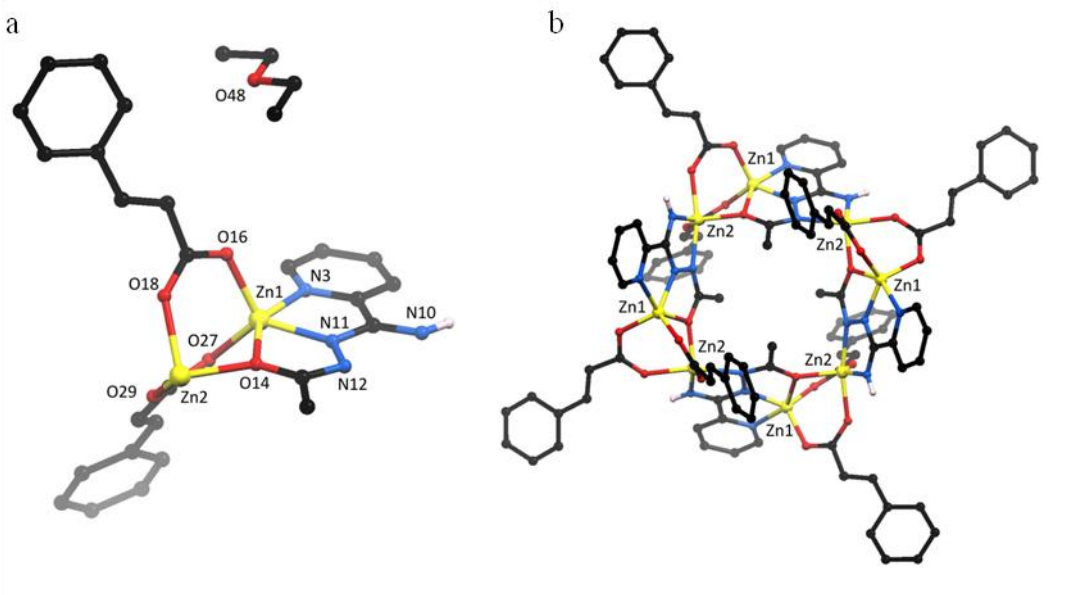

Figure 3.20: *a) Asymmetric unit of **3.9** with heteroatomic labelling scheme. b) Complete macrocycle in **3.6** generated by four-fold rotoinversion axis. Disorder of cinnamate residues, CH hydrogen atoms and solvent in complete macrocycle have been omitted for clarity.*

In lieu of hydrogen bonds between complexes, **3.9** includes four offset π-π stacking interactions (3.395(6) Å) between **L2.1** ligands of neighbouring complexes. These are orientated in the same fashion as the interactions seen in **3.4**, however, because of the four fold symmetry of **3.9** they propagate in four directions rather than just two, a three-dimensional diamondoid (**dia**) network topology is produced.

Within this diamondoid network, one partial occupancy diethyl ether molecule could be located crystallographically. Despite the large remaining void space within the crystal lattice no other solvent could be seen and the SQUEEZE routine within PLATON was carried out.[159] This showed that cavities of 298 $Å^3$ exist between stacked macrocycles, containing 63 electrons each, potentially corresponding to a further one and a half diethyl ether molecules per cavity. No solvent was observed through elemental analysis.

3.2.10 Synthesis of $[Zn_8(L2.1)_4(Ph(CH_2)_2CO_2)_8]\cdot 6Et_2O$ (3.10)

The saturated derivative of the co-ligand used in **3.9**, hydrocinnamic acid was also trialled as a comparison. H_2**L2.1** was combined with a colourless solution of zinc(II)

hydrocinnamate and upon diffusion of diethyl ether yellow crystals were produced. The data was solved and refined in the tetragonal space group $I4_1/a$ (R-factor 3.12%). Macrocycle **3.10** crystallises in the the same space group, and has the same **dia** supramolecular packing arrangement as **3.9** (Figure 3.21). Due to this similarity, the analysis of crystal structure of **3.10** will be brief, and will be limited to the differences and comparisons.

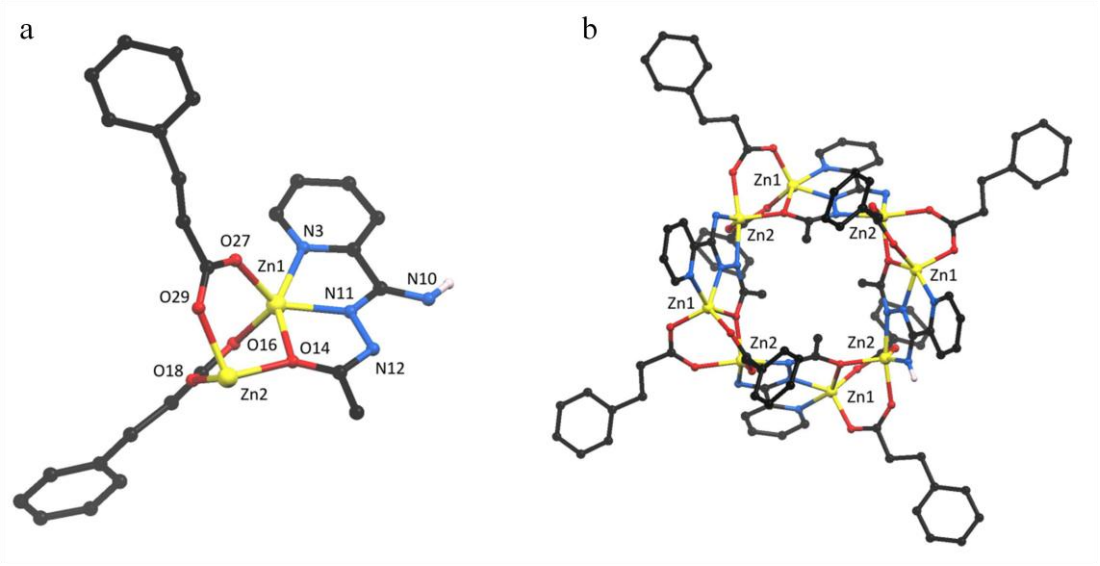

Figure 3.21: *a) Asymmetric unit of **3.10** with heteroatomic labelling scheme. (Right) Complete macrocycle in **3.10** generated by four-fold rotoinversion axis. CH hydrogen atoms and solvent have been omitted for clarity.*

In contrast to **3.9**, no disorder was observed in the carboxylate residues in **3.10**. It is thought that the smaller energy barrier for rotation in the unsaturated hydrocinnamate co-ligand allows the energy minima to be found, where as in the unsaturated derivative the rotation is more hindered, therefore does not reach its energy minima and is trapped in two positions as the sample was cooled down for diffraction.

In **3.9**, the cinnamate residues remain fairly flat because of their conjugated nature. The unsaturated hydrocinnamate residues on the other hand are twisted away from planarity (31.7(3)° and 92.6(3)° c.f. **3.9** 17.0(6)°, 13(2)°, 9(2)°). The hydrocinnimate co-ligand in **3.10** with the largest torsion angle corresponds to carboxlyate residue that is disordered in **3.9**.

Two positions of diethyl ether molecules could be located in **3.10** compared to only one in **3.9** making it likely that the residual electron density removed from the model of **3.9** corresponds to the predicted diethyl ether solvent molecules. The two positions of diethyl ether fill potential voids between macrocycles so that none remained and hence the SQUEEZE routine was not used in this case.

3.2.11 Intermolecular Interactions in 3.1-3.10

The reaction of H_2**L1** with ten different zinc(II) carboxylate salts resulted in a conserved macrocyclic motif of the general formula $[Zn_8(\mathbf{L2.1})_4(RCO_2)_8]$ being formed. Despite this similar discrete MOM structure, **3.1**-**3.10** showed varied inter-molecular interactions, in which different crystal packing topologies were seen. The major supramolecular interactions can be divided into three major classes which will be defined as A, B and C. A denotes a $R_2^2(8)$ pair-wise hydrogen bonding between deprotonated 1° imidamide protons and carboxylate oxygen atoms. B denotes an offset π-π stacking between **L2.1** ligands. C denotes a single D hydrogen bond between a deprotonated 1° imidamide proton and carboxylate oxygen atom. Each macrocycle fits into a single class, except **3.6** which exhibits a combination of single hydrogen bonding and offset π-π stacking. Representative examples of each class, along with class descriptors for all macrocycles are shown in Figure 3.22.

As different interactions give rise to the same conserved macrocyclic motif it is implied that the close packing of crystallisation is not the driving force for the macrocycles formation. Despite this, the insolubility of all macrocycles prevented solution studies and could only be examined in their crystalline form.

In all cases the insolubility was attributed the the supramolecular network structure of the respective macrocycles. Compounds that contain macrocycles with S_4 point symmetry include **3.1**, **3.2**, **3.6**, **3.8**, **3.9**, **3.10** and all adopt supramolecular diamondoid networks through the classes of interactions termed A, B or C. The macrocycles with C_2 point symmetry **3.4**, **3.5** and **3.7** adopt either linear architectures (**3.4**, **3.7**) or a quartz topology (**3.5**). Macrocycle **3.3**, which has C_1 point symmetry adopts a square-grid type supramolecular network.

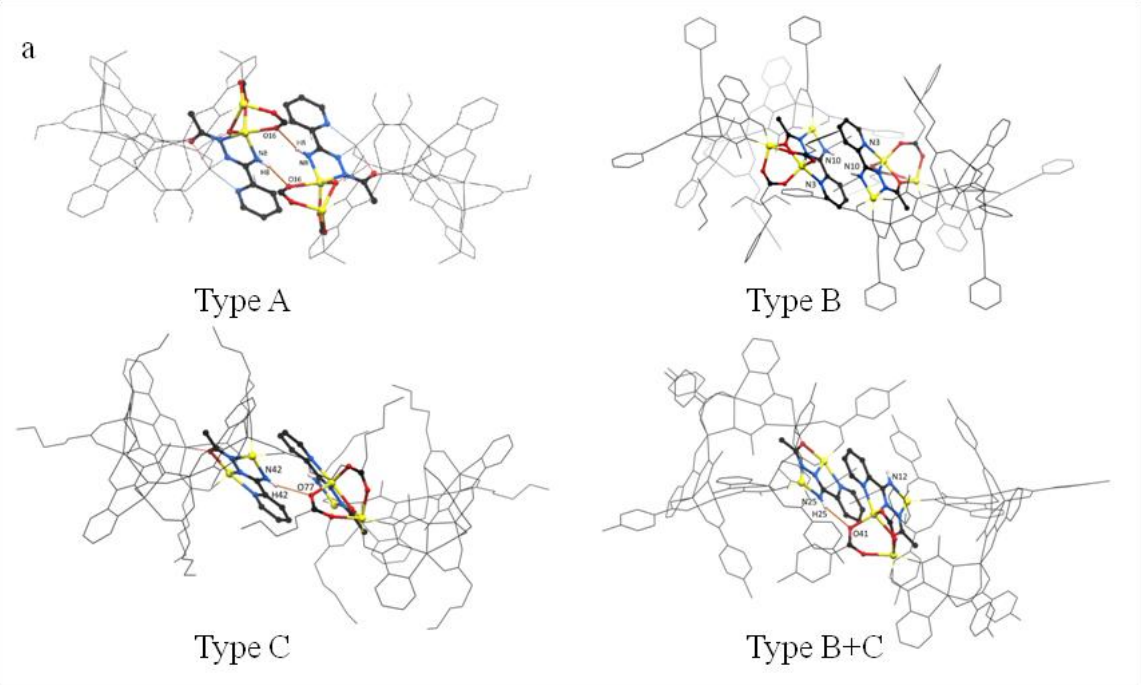

b

Macrocycle	3.1	3.2	3.3	3.4	3.5	3.6	3.7	3.8	3.9	3.10
Interaction	A	A	A	B	C	B + C	C	C	B	B

Figure 3.22: *Intermolecular interactions in metal-organic macrocycles **3.1**-**3.10**. a) Representative examples from, clockwise from top left, are **3.2**, **3.10**, **3.6** and **3.5**. Type A interactions are $R_2^2(8)$ pair-wise hydrogen bonding between a deprotonated 1° imidamide proton and carboxylate oxygen atom. Type B involves off-set π-π stacking of coordinated **L2.1** ligands. Type C is similar to type A but only a single D hydrogen bond is formed. b) Interactions of **3.1**-**3.10**.*

3.2.12 Flexibility of Carboxylate Co-ligands

Increasing the flexibility of the peripheral carboxylate substituent of the macrocycle was expected to reduce the overall maximum S_4 symmetry of the macrocycle. Although this was generally the case, and increasing the number of rotable bonds from 0 in **3.1** (acetate) to 4 in **3.5** (hexanoate) did lead to the formation of macrocyles with lower point symmetry, no obvious trends in symmetry with respect to flexibility of the carboxylate were observed (Figure 3.23). A quarter of macrocycle **3.10** is crystallographically unique, the smallest fraction possible, yet has one of the most flexible carboxylate residues trialled (hydrocinnamate) with three rotable bonds (blue).

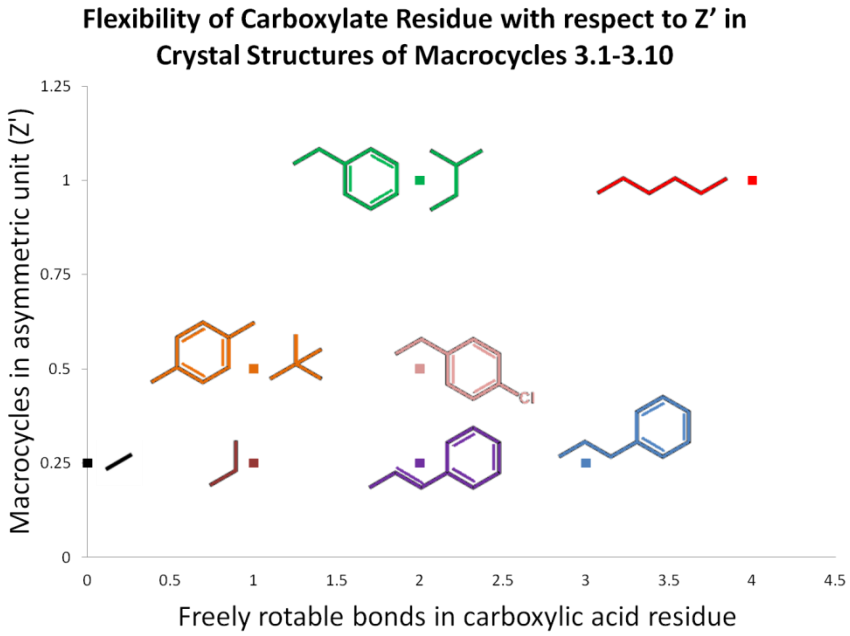

Figure 3.23: *Flexibility of carboxylate residues with respect to Z' in the crystal structures **3.1-3.10**. Each data point has been labelled with the R group of macrocycles of the general form [Zn_8(**L2.1**)$_4$(RCO_2)$_8$]. Disorder of carboxylate residues is not taken into account.*

This is only a rough approximation as the disorder of the trans-cinnamate residue in **3.9** is not taken into account**.** The difference in symmetry of each macrocycle can therefore be attributed to the metal ions geometry, the saddle angles and supramolecular interactions A, B and C.

3.2.13 Zinc(II) Ion Geometry in Macrocycles

Each of the metal ions in the macrocycles **3.1**-**3.10** is five coordinate and has a N_2O_3 coordination environment. This generalisation belies the fact that there are two chemically different coordination environments for the metal ions within each macrocycle. The two different coordination environments of the zinc(II) ions can be defined as Zn-A and Zn-B, with Zn-A being the zinc(II) ion in the tridentate coordination site of **L2.1** and Zn-B being the zinc(II) ion in the bidentate binding site (Figure 3.24a). In macrocycles with S_4 point symmetry (a quarter of a MOM in the asymmetric unit), the highest possible symmetry for this structure, there is only one crystallographically unique type of each zinc(II) ion, *i.e.* one

Zn-A and one Zn-B ion. In macrocycles with lower crystallographic symmetry, up to eight inequivalent ions may be present per macrocycle, four Zn-A and four Zn-B environments. The τ_5 parameter was calculated for each crystallographically unique metal ion in metal-organic macrocycles **3.1**-**3.10** and segregated in either Zn-A or Zn-B categories. The weighted average τ_5 parameter for Zn-A ions is 0.35, whilst for the Zn-B position it is 0.48. A distribution of value for the τ_5 parameters for both Zn-A and Zn-B positions can be seen in Figure 3.24b.

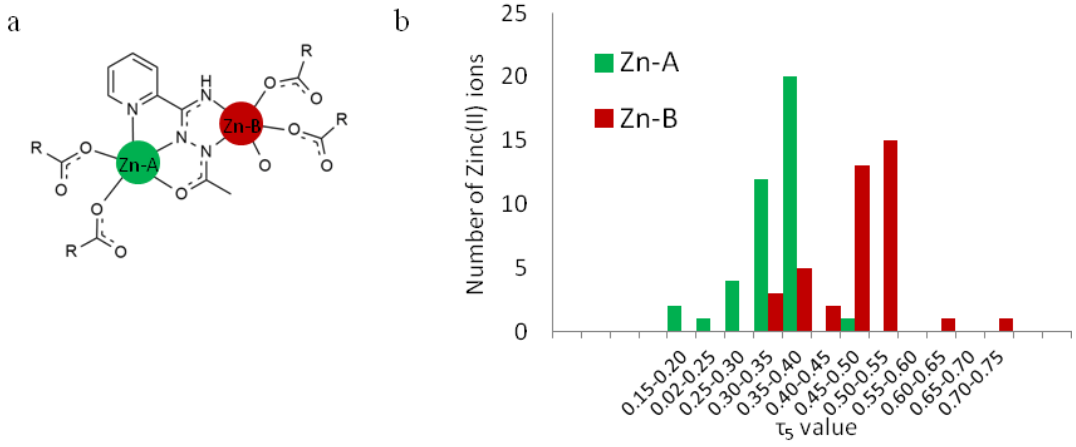

Figure 3.24: *a) Two chemically different zinc(II) ions exist within the octanuclear metal-organic macrocycles* ***3.1***-***3.10****. These are defined as Zn-A and Zn-B. b) The geometry parameter* τ_5 *differs for each of these zinc(II) positions. The position Zn-A exhibits more square pyramidal character than position Zn-B.*

From this analysis, it can be seen that for other metals to be used in the synthesis of similar metal-organic macrocycles, they must favour distorted square based pyramidal geometries. The inclusion of paramagnetic metal ions such as copper(II) in this system may be interesting magnetically.

3.2.14 Saddle Angles

Each metal-organic macrocycle adopts a shape similar to that of the 1,3-alternate configuration of a calix[4]arene. This is due to the relative angle of **L2.1** ligands around the macrocyclic core. Comparison between the mean plane saddle angles of macrocycles **3.1**-**3.10** highlights the subtle differences in each structure more clearly. Each

crystallographically independent macrocycle has two possible saddle angles (θ_{saddle}). The angles, defined as the angle between the mean plane created by the non-hydrogen atoms of each **L2.1** ligand, range from 61.22(3)° in **3.10** to 110.5(2)° in **3.3** indicating that there is significant flexibility in the shape of the macrocycle. The zinc(II) ion in the bidentate binding domain of **L2.1** (Zn-B position, Figure 3.24a) is located on the corners of the square central ring of the macrocycle and hence is responsible to for the saddle angle of **L2.1** ligands. As the ligands bend outwards (larger θ_{saddle}) the geometry of this particular zinc ion becomes more square-pyramidal (lower τ_5(Zn-B)).

a

Macrocycle	θ_{saddle} (°)
3.1	81.3(1)
3.2	80.2(1)
3.3	107.1(2)
	110.5(2)
3.4	85.89(3)
	86.48(4)
3.5	67.8(2)
	75.5(2)
	76.1(2)
	83.6(3)
3.6	65.65(8)
	72.85(8)
3.7	70.0(2)
	73.7(2)
	75.2(3)
	79.1(2)
3.8	62.3(1)
	68.7(1)
3.9	66.31(5)
3.10	61.22(3)

b

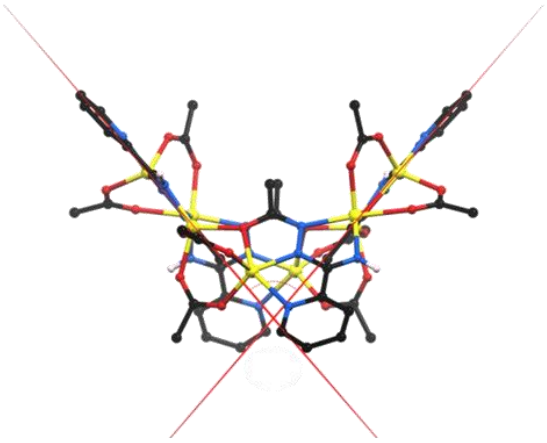

c

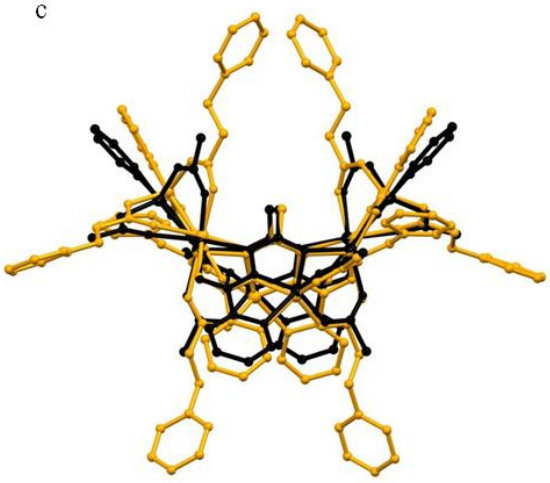

***Figure 3.25**: a) Saddle angles in metal-organic macrocycles **3.1**-**3.10**. The saddle angle is defined as the angle between the mean planes of non-hydrogen atoms of opposite **L2.1** ligands. Each crystallographically unique macrocycle can therefore be described by a maximum of two saddle angles. b) Saddle angles in **3.1** shown as red planes perpendicular to the page. c) Overlaid macrocycles **3.1** (black) and **3.10** (gold) showing a larger saddle angle in the former.*

Generally, all macrocycles containing a phenyl ring on the carboxylate co-ligand exhibit smaller saddle angles than their aliphatic counterparts. No trend could be found between the saddle angles of the macrocycles and the intermolecular interactions.

3.2.15 Analysis of Bond Lengths

Upon two-fold deprotonation of the free ligand H_2**L2.1** to **L2.1** within the macrocycles of the form $[Zn_8(\mathbf{L2.1})_4(RCO_2)_8]$, changes in the bond lengths of the N^1-acetylamidrazone functional group are expected to be observed (Scheme 3.1). Indeed, this is the case and analysis of the bond lengths determined by X-ray crystallography in the series of macrocycles show consistent deviations from that of the free ligand (Table 3.1).

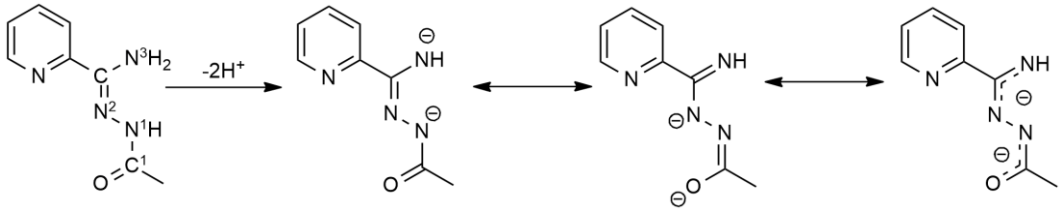

Scheme 3.1: *Deprotonation of free ligand H_2**L2.1** to **L2.1** within macrocycles of the general formula $[Zn_8(\mathbf{L2.1})_4(RCO_2)_8]$ is expected to change the bond lengths within the N^1-acetylamidrazone functional group. Bonds C-N^3, C^1-N^1 are expected to decrease, while C-N^2 and C^1-O are expected to increase.*

Bond length/ Compound	C-N^3	C-N^2	N^2-N^1	C^1-N^1	C^1-O
H_2**L2.1**	1.346(3)	1.297(3)	1.400(3)	1.336(3)	1.234(3)
3.9	1.315(4)	1.308(4)	1.400(4)	1.298(4)	1.295(4)
3.10	1.315(2)	1.317(2)	1.400(2)	1.307(2)	1.293(2)

Table 3.1: *Bond lengths of the N^1-acetylamidrazone functional group in the free ligand H_2**L2.1** and the two-fold deprotonated ligand **L2.1** in the metal-organic macrocycles **3.9** and **3.10**. These macrocycles are chosen as comparisons as they have the lowest standard uncertainty on bond lengths. Atom labelling corresponds to that shown in Scheme 3.1.*

The N^1-acetlyamidrazone bond lengths for the free ligand H_2**L2.1** and representitive macrocycles **3.9** and **3.10** are given in Table 3.1. Despite the low bond precision of the

carbon and nitrogen bond lengths in some of the macrocycle crystal structures (**3.3**, **3.5**, **3.7**), general trends emerge. The most noticeable change between the free ligand H_2**L2.1** and the dianionic bridging **L2.1** is the lengthening of the carbonyl bond (C^1-O), a consequence of the deprotonation of the amide-like functionality. This bond is not long enough to be a purely single bond indicating partial double bond character.

In addition to this, the coordinated ligand must be deprotonated further to balance the charge in the neutral macrocycle and provide the secondary coordination domain. This occurs at the imidamide-like site of the ligand, and the similarity of the C-N^2 and C-N^3 bond lengths in macrocycle **3.1**-**3.10** indicate that the resultant formal negative charge is delocalised over this functional group.

The N^1-N^2 bond length remains constant with the twofold deprotonation and coordination at approximately 1.400 Å in H_2**L1** and **L2.1** within **3.1**-**3.10.** This implies that there is no delocalisation of charge from the imidamide side of the ligand (bonds C-N_2 and C-N_3), to the amide side (bonds N_1-C_1 and C_1-O).

3.2.16 Summary

A range of metal-organic macrocycles have been synthesised and characterised by single crystal X-ray diffraction. These macrocycles adopt the general formula $[Zn_8(\mathbf{L2.1})_4(RCO_2)_8]$ and are comprised of three parts; zinc(II) ions, twofold deprotonated **L2.1** ligands and carboxylate co-ligands. There are two chemically inequivalent positions for the zinc(II) ions, one being more square pyramidal than the other. Analysis of bond lengths in the macrocycle shows the formal negative charges are delocalised in either the imidamide or the amide-like regions of the N^1-acetylamidrazone functional group.

The highest point symmetry for these macrocycles is the S_4 point group, although in some cases distortions in the structure prevent this and C_2 or C_1 point symmetry is observed. The parent macrocycle **3.1**, based upon acetate co-ligands retains crystallinity when removed from the mother liquor and shows solid state luminescence. The other samples were not seen to retain crystallinity upon removal from solvent. This is attributed to the large solvent accessible cavities and channels within the crystal lattice due to inefficient packing of the

saddle shaped macrocycles. These cavities were often seen to contain volatile diethyl ether molecules by X-ray crystallographically. The fact that no solvent was observed through elemental analysis or TGA supported the assumption that in the cases where these volitile anti-solvent molecules could not be located crystallographically, they were present.

Intermolecular interactions between macrocycles relied on the interactions of the **L2.1** ligands. The intermolecular interactions of the **L2.1** functional group could be reduced to three descriptors. These are based upon either hydrogen bonding of the remaining 1° imidamide proton to carboxylate co-ligands or π-π stacking interactions between **L2.1** ligands. All macrocycles were seen to adopt a single or combination of these interactions. Topological descriptors could be given to the two and three-dimensional supramolecular frameworks based on these interactions.

3.3 Carboxylate Replacement in Metal-Organic Macrocycles

The conservation of the core macrocyclic motif with modulation of the peripheral carboxylate residues shows the nature of carboxylate co-ligand does not have a structure directing role. This is a promising feature if these macrocycles were to be used as molecular building blocks (MBBs) in the synthesis of MOFs, as a variety aliphatic or aromatic dicarboxylate co-ligands could be used to link these units together.

There are eight carboxylate co-ligands around the periphery of each metal-organic macrocycle. Taking the carboxylate groups as points of extension, the macrocycle can be represented by a distorted gyrobifastigium (Figure 3.26). This polyhedron, a Johnson solid (J_{26}) can be thought of as two triangular prisms joined on their square faces with one having a 90° twist relative to the other. This polyhedron, although rare in chemistry, has been shown to be capable of forming porous frameworks based upon shared vertices.[198]

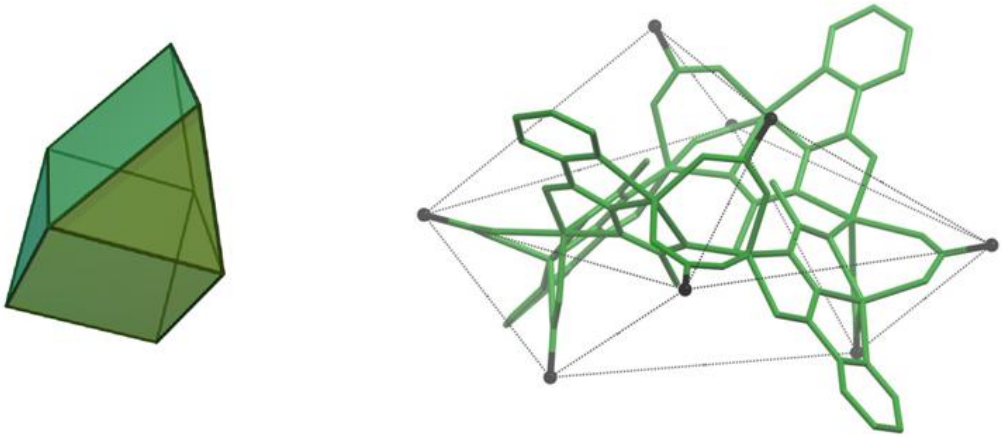

Figure 3.26: *Gyrobifastigium polyhedron and schematic of metal-organic macrocycle* ***3.1*** *with carboxylate potential points of extension highlighted in black. The name of this polyhedron is derived from it being described as twisted (gyro) two (bi) sloped roofs (fastigium).*

In addition to an eight vertices gyrobifastigium, the metal-organic macrocycles could be expected to act as a four coordinate MBB if angular dicarboxylate ligands were used (Figure 3.27). This utilises the four half paddlewheel-like moieties around the macrocycle. Several one-dimensional coordination polymers based upon the paddlewheel unit have been synthesised using approximately 90° angular dicarboxylic acid ligands such as 2,8-dicarboxy-Trögers base (87.7(1)°)[199] (Figure 3.27a), succinate (79.5(4)°)[200] and (R)-2,2'-dimethoxy-1,1'-binaphthalene-6,6'-dicarboxylic acid (86(1)°).[201] The four potential sites for extension from the macrocycle could lead to networks with four coordinate nodes being synthesised and each linker comprised of two angular dicarboxylate residues. It is hypothesised that a tetrahedral node would result, but just as with the hydrogen bonding supramolecular assemblies of **3.1** (**dia**) and **3.3** (**sql**), a square grid framework is possible too. The angle between carboxylates in **3.1**-**3.10** is slightly larger than the 90° seen in idealised paddlewheels, and ranges from 97(1)° in **3.3** to 113.8(7)° in **3.4** (Figure 3.27d). Several strategies for the replacement of monotopic carboxylate ligands, in particular acetate, can be imagined, and will be described within this section.

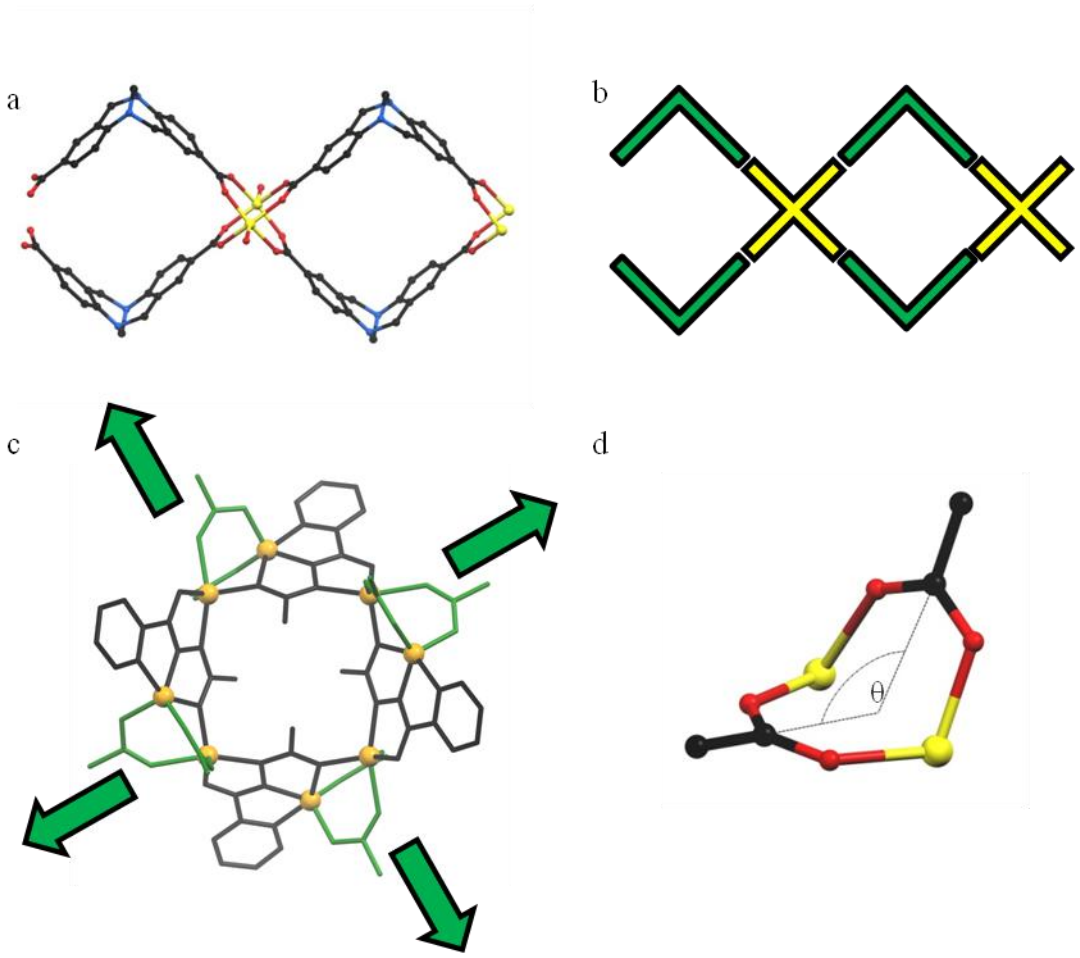

Figure 3.27: *a) Two angular dicarboxylic acid ligands such as 2,8-dicarboxy-Trögers base can be used as a linear linker in combination with a dinuclear zinc(II) paddlewheel building unit. b) Schematic representation of paddlewheels (yellow) being linked with angular dicarboxylate ligands (green) to form one-dimensional coordination polymers. c) Four half paddlewheel units exist around the metal-organic macrocycles reported here allowing them to potentially act as four coordinate nodes. d) The angle between carboxylate groups and the centroid of the zinc(II) ions in MOMs* ***3.1****-****3.10*** *is slightly larger than 90°. Values range from 97(1)° in* ***3.3*** *to 113.8(7)° in* ***3.4****.*

3.3.1 Azeotropic Co-ligand Exchange

The replacement of monotopic bridging carboxylate co-ligands with ditopic carboxylate ligands via azeotopic co-ligand exchange was reported by Christou *et al.* in 2013.[202] In this case single molecule magnet manganese(III) clusters containing three acetate co-ligands were assembled into tetrahedral cages via co-ligand replacement with a fumaric acid (Figure 3.28). This was achieved by mixing a preformed trinuclear cluster containing three acetate co-ligands with 1.5 equivalents of the dicarboxylic acid in acetonitrile. Toluene was then added and the solvent was removed *in vacuo*. Five more cycles of dissolution in

acetonitrile, addition of toluene and solvent removal were carried out to remove all acetic acid as its toluene azeotrope. Finally, the residue was dissolved in acetonitrile and layered with toluene to afford crystals of the fumarate co-ligand species. No indication that incomplete substitution had occurred, although only a 35 % yield based upon the manganese(III) cluster was reported.

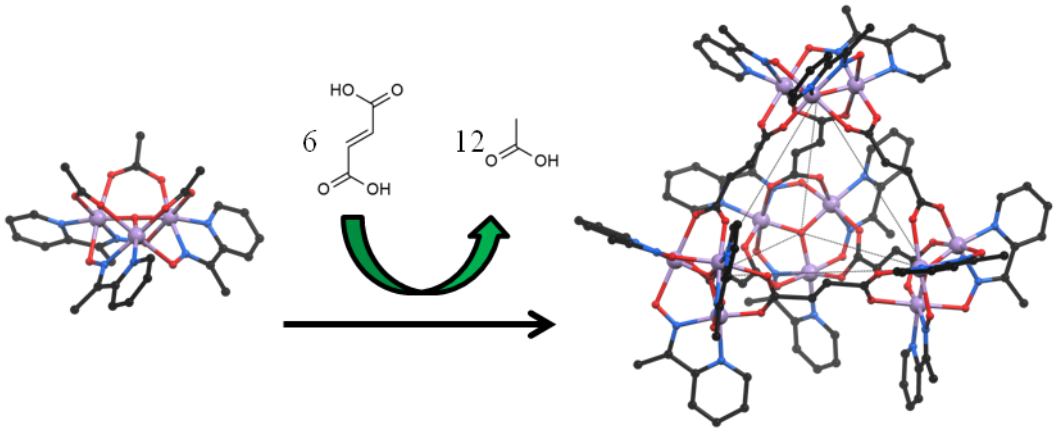

Figure 3.28: *Azeotropic carboxylate exchange in a Mn(III) trinuclear cluster to form a metal-organic tetrahedron. Acetic acid is removed as its toluene azeotrope.*[202]

Similar methods have been used for acetate replacement with other monotopic carboxylate, phosphinate and sulfonate ligands in Mn_{12} single molecule magnet clusters.[203-208]

The main point of difference to this method if the macrocycle **3.1** is to be used is that the product likely to form would not be a discrete species, but rather a polymeric one. The gyrobifastigium arrangement of carboxylate residues is not capable of forming discrete species by replacement of all co-ligands. The crystallisation of such a species is therefore going to be very different. It is assumed that the partial linker exchange will hinder the crystallisation process of the overall MOF.

As a test case of this methodology on the metal-organic macrocyles presented here, the monotopic carboxylic acid trichloroacetic acid was chosen to potentially replace the eight acetate co-ligands. This acid was selected because macrocycle formation could not be achieved starting from zinc(II) trichloroacetate. Upon addition of a methanolic solution of this zinc(II) salt to a solution of H_2**L2.1**, the solution did not turn bright yellow as in the

cases described previously for **3.1**-**3.10**. Diffusion or addition of diethyl ether into this colourless solution did not result in the formation of a solid. The lower pKa of this acid means it should deprotonate in preference to the excess free acetic acid in solution (generated from the deprotonation of H_2**L2.1**) and therefore preferentially act as a ligand. Its low volatility also means it will not be removed in the azeotropic induced exchange process. Finally it contains heavy atoms that are easily observed through single crystal X-ray diffraction. This will give a handle on the occupancy if partial exchange occurs. It is worth noting that ligand substitution of the metal-organic macrocycle is unlikely to occur, but rather a general carboxylate exchange in a soluble precursor species. This is due to the insolubility of the final MOM.

3.3.1.1 Synthesis of $[Zn_8(L2.1)_4(Cl_3CCO_2)_{0.8}(AcO)_{7.2}]$ (3.11)

To a methanolic solution of H_2**L2.1** was added two equivalents of zinc(II) acetate in methanol. A bright yellow solution resulted from the two colourless solutions. Upon addition of a colourless solution of trichloroacetic acid the yellow solution immediately lost its colour. Toluene was then added and the solvent was removed in vacuo. Eight cycles of dissolution in methanol, addition of toluene and solvent removal were carried out. Finally, diethyl ether was left to diffuse in to the now yellow solution. Small yellow plate-like crystals grew from this and were isolated by filtration and defined as **3.11**. The data were solved and refined in the tetragonal space group *I*-42*d* (R-factor 5.23 %). This is the same space group as that of the parent macrocycle **3.1**, which contains only acetate co-ligands. The structure was determined to be that of a macrocycle of the general formula $[Zn_8(\mathbf{L2.1})_4(RCO_2)_8]$. Only one quarter of the macrocycle is crystallographically unique. As with macrocyles **3.1**-**3.10**, there are two inequivalent carboxylate positions around the periphery of the macrocycle. One is arranged in the plane of the macrocyclic ring, the other approximately perpendicular to this ring. Analysis of the difference map showed that only the carboxylate perpendicular to the plane of the macrocycle exhibited partial replacement with the new trichloroacetate moiety. Letting the occupancies of the three chlorine atoms to refine together yet freely resulted in a value of 19.851 % which was rounded up to 20 % in the final model. This equates a total replacement of 10 % of the total carboxylate co-ligands. An interesting feature of this is the specific partial replacement of one position of

the co-ligand which hints at the fact that this position is more likely to undergo ligand substitution. This result is surprising as it is the other acetate co-ligand that has longer coordination bond lengths in **3.1**. It is not known why substitution is location specific.

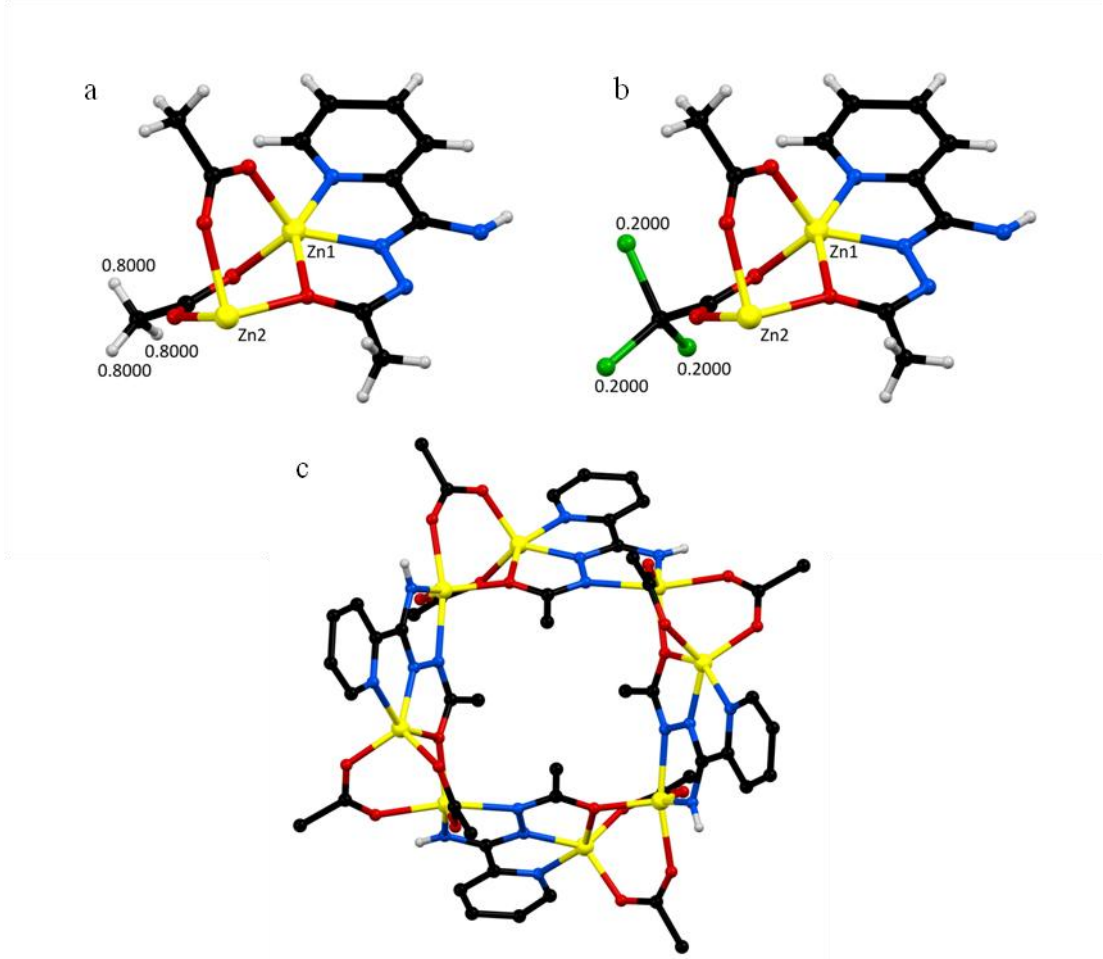

Figure 3.29: *Asymmetric unit of **3.11** containing the major (a) and minor (b) components. Occupancy of each component is labelled and unspecified atoms are implicitly full occupancy. The full macrocycle in **3.11** with only the major component co-ligand is shown (c). CH atoms in (c) omitted for clarity.*

The intermolecular interactions in this structure are similar to that of the parent acetate macrocycle **3.1**, and likewise **3.11** adopts the A descriptor introduced in Figure 3.22. Potential solvent within the structure could not be modelled, and was subject to the SQUEEZE routine.[159]

Partial and site selective exchange of one monocarboxylate with another was achieved via azeotropic removal of acetic acid. The synthesis of polymeric structure via this method was

not thought to be worth pursuing due to the low replacement factor and potential crystallisation problems and instead other prospective methods were developed.

3.3.2 Solvothermal Co-ligand Exchange

Another potential way to attempt carboxylate exchange to form a polymeric species is through solvothermal methods. As all macrocycles were insoluble in all solvents, a pre-synthesised macrocycle is not an applicable reagent, but rather the constituent parts, H_2**L2.1**, zinc(II) acetate and a dicarboxylic acid based co-ligand were combined in DMF following a typical synthesis of metal-organic frameworks. It was hoped the macrocyclic motif would assemble with the dicarboxylate ligands as a SBU. Several flexible and rigid linear and angular dicarboxylic acid derivatives were used. These included succinic acid, glutaric acid, subaric acid, terephthalic acid, isophthalic acid, 4,4'-oxydibenzoic acid and 2,8-dicarboxy-Trögers base. Although this synthetic method did not lead to the desired product, the same coordination polymer based upon **L2.1** was produced in each case. A representative example will be described below.

3.3.2.1 Synthesis of $[Zn_2(L2.1)_2]\cdot$DMF (3.12)

Adding colourless zinc(II) acetate to a colourless solution of H_2**L2.1** in DMF resulted in a bright yellow solution. When the dicarboxylic acid succinic acid was added, the solution noticeably paled and after complete dissolution of the carboxylic acid was colourless/very pale yellow. Upon heating for half an hour the solution reverted to a bright yellow colour, which is attributed to the increased pH of the solution due to the decomposition of DMF. Heating at 90 °C overnight led to the formation of colourless block crystals. These were filtered from the still yellow solution and and were of sufficient quality for single crystal X-ray diffraction. They were solved and refined in the monoclinic space group $P2_1/c$ (R-factor 4.50 %). The overall structure, defined as **3.12**, is that of a one-dimensional coordination polymer comprised of $[Zn_2($**L2.1**$)_2]$ repeating units (Figure 3.30). There are two chemically distinct zinc(II) ions. One is in an N_4O_2 octahedral coordination environment created by the tridentate coordination domain of two, twofold deprotonated **L2.1** ligands. The other zinc(II) is in a N_4 tetrahedral coordination geometry created by the bidentate binding

domain of two **L2.1** ligands. As the ligand necessitates two-fold deprotonation for this bridging coordination mode, there is no net charge on the coordination polymer. There is disorder of the tetrahedral zinc(II) ion over two positions due to flexing of the **L2.1** ligands.

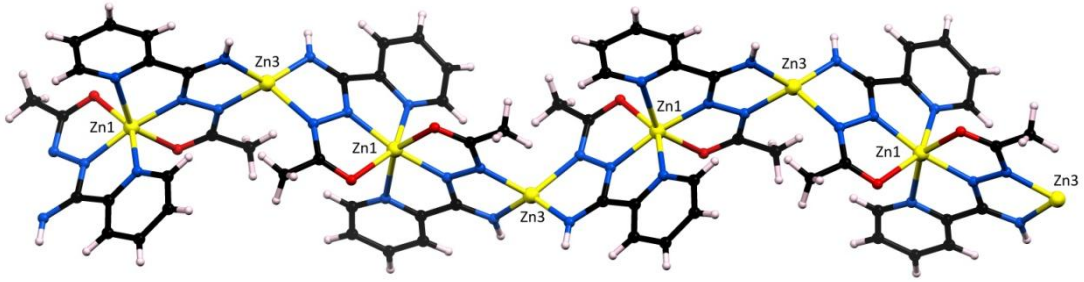

Figure 3.30: *Polymeric chain of* ***3.12****. Solvent DMF and disorder of* ***L2.1*** *ligand and tetrahedral zinc(II) omitted for clarity.*

.

Although one disordered DMF solvent molecule molecule was observed crystallographically, the remaining electron density could not be modelled and the SQUEEZE routine was used.[159] This showed the presence of 39 electrons per formula unit, consistent with another molecule of DMF (40 electrons).

The structure did not contain the proposed metal-organic macrocycle or even any carboxylate co-ligands. The fact that the mother liquor remains yellow is indicative of zinc(II) and **L2.1** still being in solution.

As the building unit was not preformed, the macrocyclic structure is not generated or retained throughout the synthesis and an altogether different structure was produced. Further methods for increasing the solubility of the macrocycle by appending functional groups to H_2**L2.1** so the macrocycle could be used in a preformed state were trialled next.

3.3.3 Increasing the Solubility of H_2L2.1

Despite attempts to increase the solubility of the macrocycles **3.1**-**3.10** by addition of longer and bulkier carboxylate co-ligands, the macrocycles remained insoluble. Potential functionalisation of the ligand H_2**L2.1** with a solubilising group could be a way to prepare

soluble macrocycles. To do this, a solubilising group was added to the periphery of the ligand component of the macrocycle. Introduction of tertiary butyl groups has been shown to be an effective method to create more soluble ligands and coordination compounds.[192-193] Commonly the incorporation of tertiary butyl groups on 2-substituted pyridine rings usually involve starting from 4-*tert*-butylpyridine and functionalising the 2-position via formylation, acetylation or cyanation to afford the desired functionality. Another route is to start with the desired functionality in the 2-position, and introduce the *tert*-butyl group to the 4-position via the Minisci reaction (reaction iii).[209] Traditionally the general alkylation of pyridine was undertaken with toxic alkyl mercury reagents, however, in this reaction it proceeds via the radical decomposition of pivalic acid in the presence of ammonium persulfate. The alkylation occurs at both the 4 and 6 positions of 2-substituted pyridines, leading to a possible four species in the reaction mixture (including starting material). Strong acid can be used to suppress the extent of substitution in the 6-position, and the readily soluble desired product can be purified by column chromatography. This is a quick and easy synthetic method that precludes the use of the toxic reagents. The intermediate 4-*tert*-butylpyridine-2-carbonitrile has not previously been synthesised via this methodology.

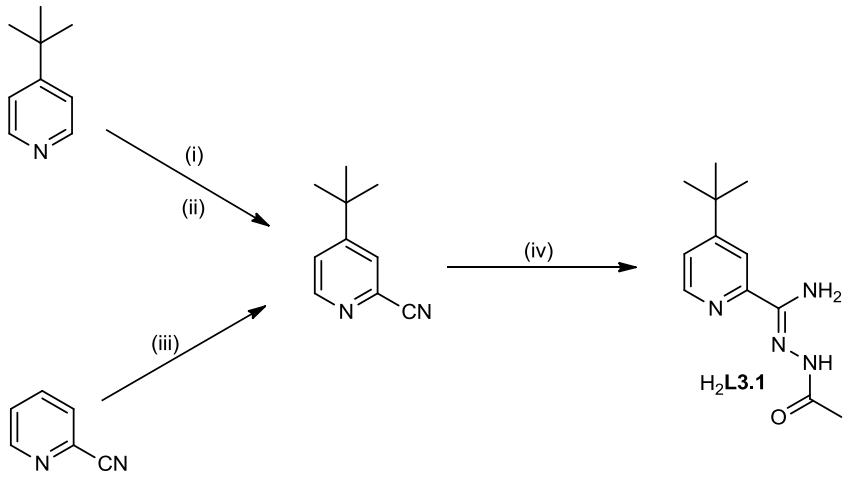

Scheme 3.2: *The two possible routes to synthesise 4-tert-butylpyridine-2-carbonitrile and subsequent reaction to form desired ligand H_2**L3.1**.Reagents and conditions; i) 3% H_2O_2, acetic acid, reflux. ii) trimethylsilyl cyanide, triethylamine, acetonitrile.[193] iii) Ammonium persulfate, sulfuric acid, silver nitrate, then water, disodium carbonate.[210] iv) Sodium, methanol, then acetylhydrazide, reflux.*

Like H_2**L2.1**, the ligand H_2**L3.1** showed the presence of isomers due to rotation about the amide bond in solution. This ligand was significantly more soluble than its parent, and was even shown to dissolve in hot diethyl ether.

When H_2**L3.1** was combined with two equivalents of a zinc(II) monocarboxylate salt, a yellow solution resulted consistent with that seen for H_2**L2.1**. However, upon diffusion of diethyl ether, no solid was formed. Analysis of the reaction solution by mass spectrometry and NMR spectroscopy (in deuterated methanol) did not shed light on the species produced. When combined with zinc(II) acetate and a dicarboxylic acid co-ligand, no identifiable product was produced.

3.4 Ligand Extension in Metal-Organic Macrocycles

Another potential way to prepare MOFs from this series of macrocycles is through their *in situ* formation in the presence of ligands that contain two N^1-acetylamidrazone functional groups. An analogous procedure for a literature example involving dibenzotriazole ligands is shown in Figure 3.2c.

In Section 2.3, the reaction between H_2**L2.1** and one equivalent of a zinc(II) carboxylate salt was investigated. In each case the products were shown to be discrete, five-coordinate complexes. It is proposed that the macrocycles, formed by the reaction of H_2**L2.1** and two equivalents of a zinc(II) carboxylate salt, assemble via an intermediate similar to the discrete, 5-coordinate complexes observed in this previous section. Ligands containing two N^1-acetylamidrazone functional groups are assumed to form dinuclear, discrete complexes (molecular model of potential intermediate shown in Figure 3.31). Upon assembly of the macrocyclic structure through the bridging mode of this functional group with an additional zinc(II) ions, these dinuclear, discrete species will assemble into a MOF rather than individual discrete MOMs. As the pyridyl ring of **L2.1** is on the periphery of the macrocycle, this is an ideal position for the connection of an additional coordinating group.

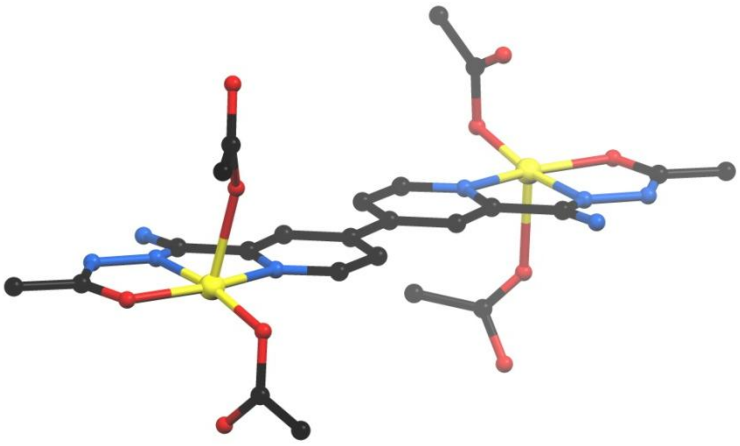

Figure 3.31: *Molecular model of a dinuclear, discrete zinc(II) complex from a ligand that contains two N^1-acetylamidrazone functional groups. This is similar to the discrete complexes reported in Section 2.3. Metal-organic macrocycles are thought to be synthesised from intermediates similar to these.*

The saddle-like shape of the **L2.1** ligands in each macrocycle presented in Section 3.2 will mean the points of extension from each macrocycle will be arranged in a tetrahedral fashion around the macrocyclic core (Figure 3.32). As the ligand is responsible for framework formation, and not the carboxylate co-ligands these could be potentially used to tune the pore properties within the framework. The carboxylate ligands will be directed into the potential cavities of the frameworks, and modulation of the potential pore volume could be performed by increasing the steric bulk of these carboxylate co-ligands.

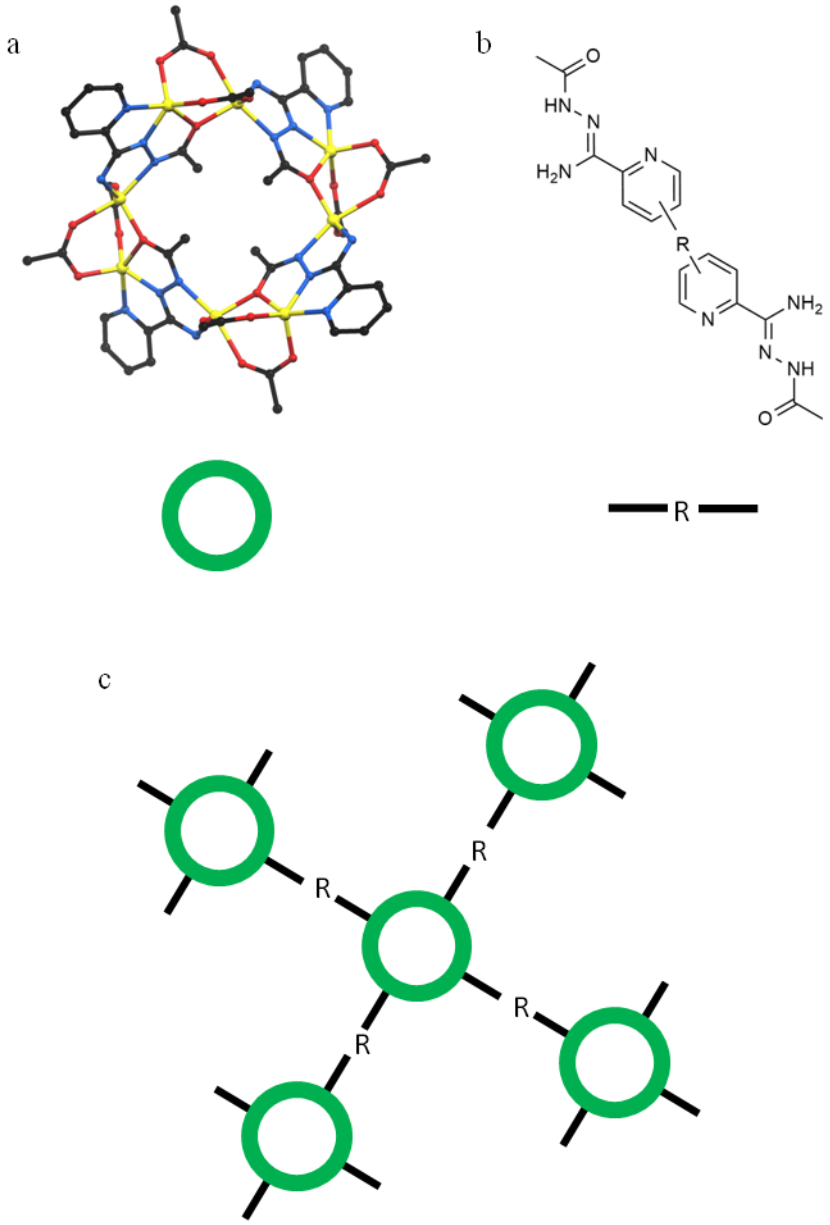

Figure 3.32: *Connection of macrocycles (a), by ligands containing two N^1-acetylamidrazone based functional groups (b) could produce polymeric species (c).*

3.4.1 Synthesis of Extended Ligands

To examine whether this method of MOF formation is applicable to the synthesis of MOFs several novel ligands containing up to two N^1-acetylamidrazone groups were synthesised. These include 4-phenylpyridin-2-yl(N^1-acetylamidrazone) (H_2**L3.2**), 4,4'-bis(pyridin-2-yl(N^1-acetylamidrazone)) (H_4**L3.3**), 1,3-di(4-(pyridin-2-yl(N^1-acetylamidrazone))propane (H_4**L3.4**), and 2,5-di(N^1-acetylamidrazone)pyrazine (H_4**L3.5**) (Scheme 3.3).

Ligand H_2**L3.2** was synthesised from commercially available 4-phenylpyridine-2-carbonitrile in a manner similar to that of H_2**L2.1**. It will be used to test the effect of added aromatic functionality on the 4-position of the pyridine ring during the synthesis of macrocycles. In particular this ligand can be thought of as an analogue to H_4**L3.3** that only contains one N^1-acetylamidrazone functional group.

Ligand H_4**L3.3**, synthesised from 4,4'-bipyridine via cyanation of the 1,1'-dimethoxy derivative with sodium cyanide, contains two N^1-acetylamidrazone coordination domains. These are rigidly spaced, but can freely rotate about the pyridine rings. As with other biaryl systems, the dihedral angle is expected to be small due to conjugation between rings so the tridentate coordination domains are likely to be approximately *cis* or *trans* to one another. It can be thought of as two H_2**L2.1** ligands connect at the 4-position of the pyridyl ring or H_2**L3.2** with two N^1-acetylamidrazone functional groups.

Ligand H_4**L3.4**, synthesised from 1,3-bis(4-pyridyl)propane, is effectively two H_2**L2.1** ligands connect by a flexible propyl chain linker at the 4-position of the pyridine rings. Rotation of N^1-acetylamidrazone functional groups about this flexible chain is expected. Despite attempts to use the same cyanation reaction as that used in the synthesis of H_4**L3.3**, the 2-cyanopyridine product did not form. Instead another synthetic preparation, using benzoyl chloride and trimethylsilyl cyanide was used.

Ligand H_4**L3.5** was synthesised from 2,5-dimethylpyrazine and contains two coordination domains locked in a trans arrangement to each other. This ligand differs from the others as it contains a pyrazinyl rather than a pyridine coordinating group. The ligand H_2**L2.5**, which also contains a pyrazinyl coordinating group, will be used to investigate the effect this might have on the macrocyclic structure.

All ligands were prepared in moderate yields, and due to their relative insolubility in common solvents, were easily purified. To an even greater extent than other N^1-acylamidrazone based ligands, H_4**L3.3**-H_4**L3.5** remained insoluble in common laboratory solvents which precluded the collection of ^{13}C NMR spectra for H_4**L3.3**-H_4**L3.5** and ^{1}H NMR spectrum for H_4**L3.5**.

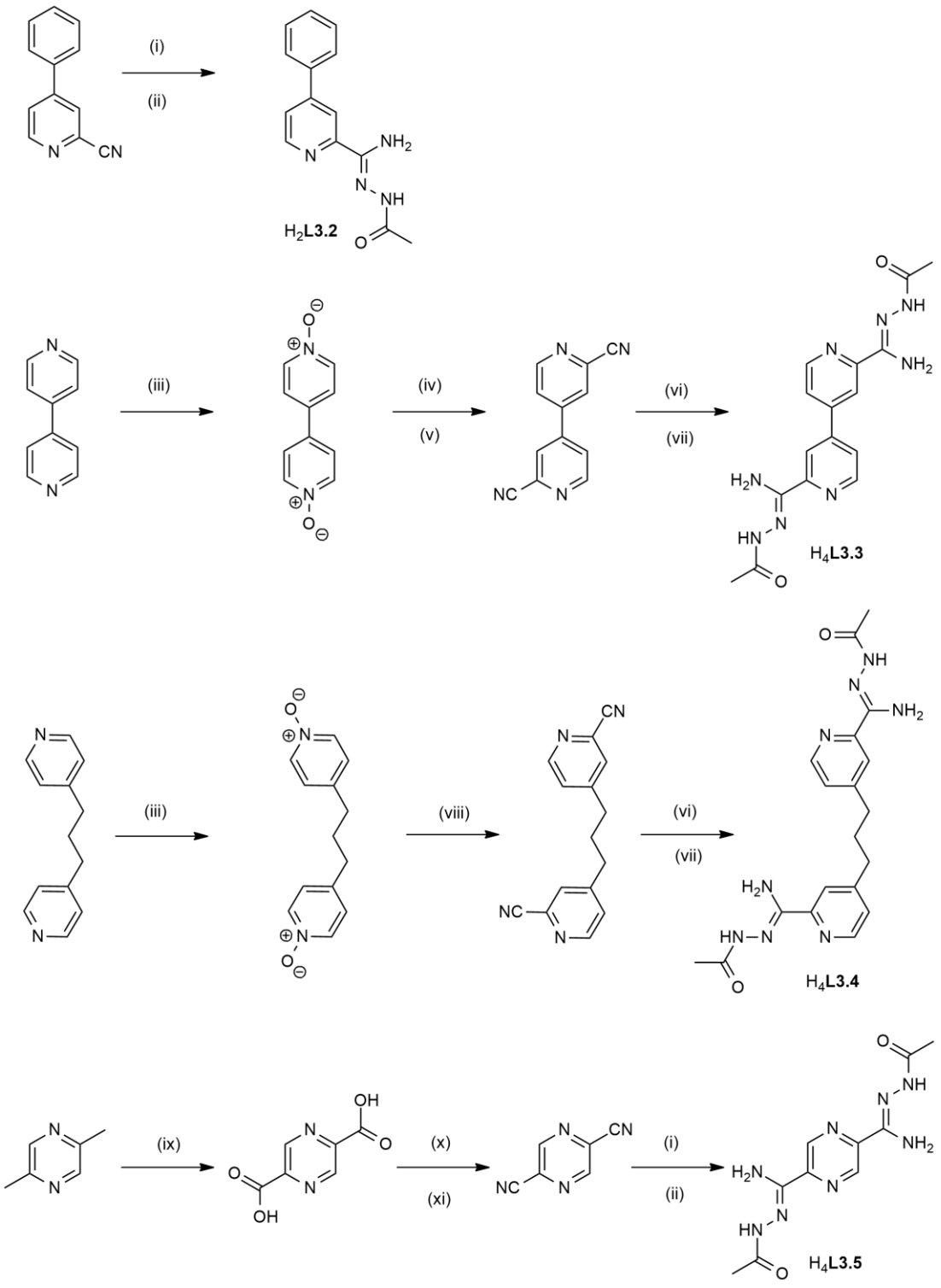

Scheme 3.3: *Synthesis of the novel ligands 4-phenylpyridin-2-yl(N^1-acetylamidrazone) (H_2**L3.2**), 4,4'-bis(pyridin-2-yl(N^1-acetylamidrazone)) (H_4**L3.3**), 1,3-di(4-(pyridin-2-yl(N^1-acetylamidrazone))propane (H_4**L3.4**) and 2,5-di(N^1-acetylamidrazone)pyrazine (H_4**L3.5**). Reagents and conditions: i) Sodium, methanol. ii) acetylhydrazide, ethanol, reflux. iii) Oxone, H_2O. iv) Dimethyl sulfate, perchloric acid. v) Sodium cyanide, H_2O. vi) Hydrazine, ethanol reflux. vii) Acetyl chloride, triethylamine, dichloromethane. viii) Benzoyl chloride, trimethylsilyl cyanide, DCM. ix) $KMnO_4$, H_2O reflux. x) $SOCl_2$, DMF reflux then ammonia. xi) $SOCl_2$, reflux.*

3.4.2 Synthesis of Complexes

It was hypothesised that ligands H_4**L3.3**, H_4**L3.4** and H_4**L3.5** would form linked macrocycles. This potential three-dimensional polymeric compound would assemble as the macrocycle assembles. The ligands designed as mimics of these that only contain a single N^1-acetylamidrazone functional group, H_2**L3.2** and H_2**L2.5**, are expected to be able to form a metal-organic macrocycle in the same manner as that seen for H_2**L2.1** in macrocycles **3.1**-**3.10**.

3.4.2.1 Synthesis of $[Zn_8(L3.2)_4(AcO)_8]$ (3.13)

To ascertain if added steric bulk on the pyridyl ring of H_2**L2.1** would influence the formation of the macrocyclic structure, the ligand H_2**L3.2** was synthesised from commercially available 4-phenylpyridine-2-carbonitrile and acetylhydrazide. It can be thought of as being effectively H_2**L2.1** with a phenyl ring attached at the 4-position of the pyridine ring.

To a colourless solution of H_2**L3.2** in methanol was added a colourless solution of zinc(II) acetate. Diethyl ether was allowed to diffuse into the resulting yellow solution and after one week, yellow block crystals were isolated from the colourless solution. These were solved and refined in the monoclinic space group *C*2/*c* (R-factor 7.02 %). The asymmetric unit contained two **L3.2** ligands, four zinc(II) ions and four acetate co-ligands (Figure 3.33a). Upon the action of the two-fold rotation axis, a complete metal-organic macrocycle with the formula $[Zn_8(\mathbf{L3.2})_4(AcO)_8]$ and the same core structural macrocyclic motif as **3.1**-**3.10** was produced. The peripheral phenyl rings are not co-planar with the rest of the ligand with torsion angles of 33.43° and 20.71° for the two crystallographically distinct residues. The saddle shape of the macrocycle is emphasised due to the extra length of the ligand, and close packing is severely limited (Figure 3.33c).

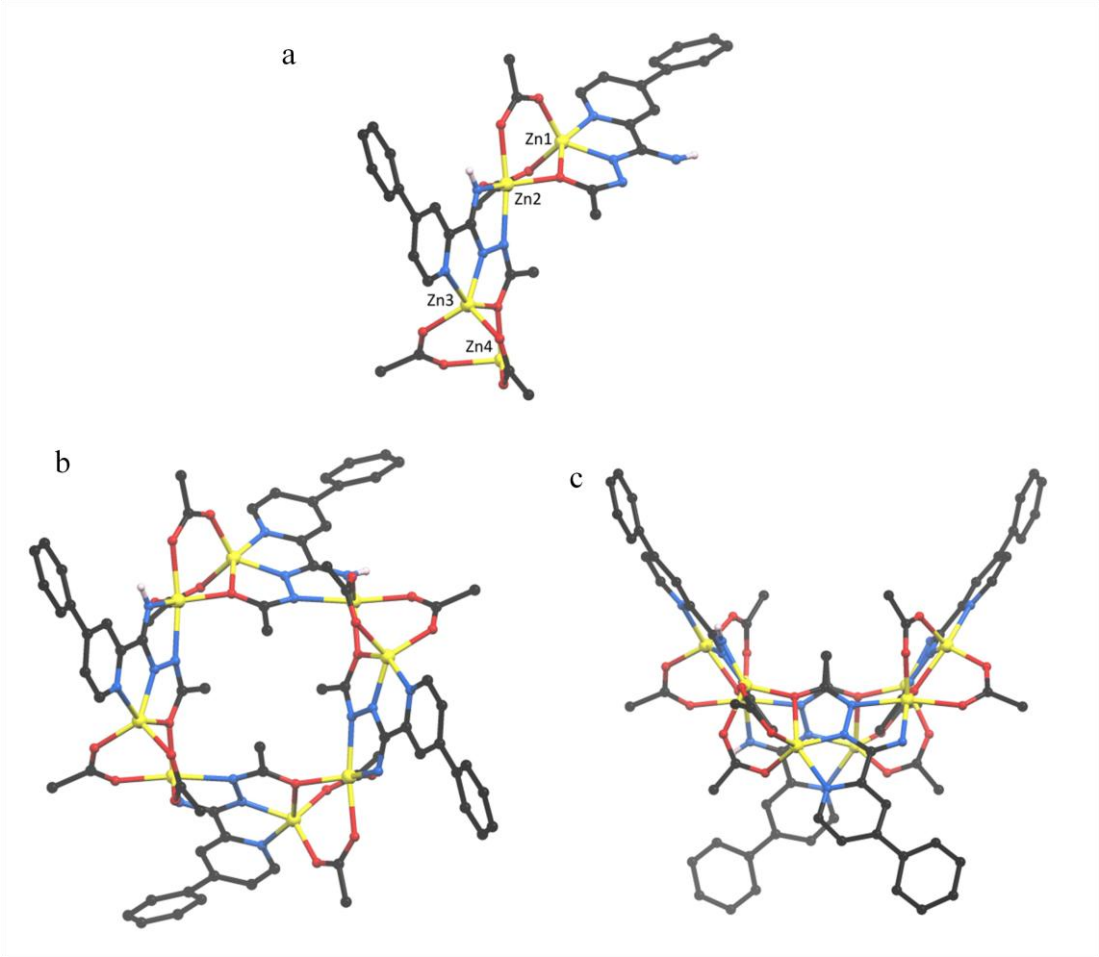

Figure 3.33: *a) Asymmetric unit of **3.13**. CH atoms omitted for clarity. b) View down the crystallographic b-axis of **3.13**. View of **3.13** perpindicular to the b-axis. CH hydrogen atoms omitted for clarity. Potential solvent has been removed by the SQUEEZE routine within PLATON.*[159]

The saddle angles, as defined in Figure 3.25, and do not contain the added phenyl ring of ligand **L3.2**, in **3.13** are 71.59(7)° and 61.76(7)° which are within the range of saddle angles found for **3.1**-**3.10** (61.22(3)°-110.5(2)°).

Although some solvent was seen crystallographically (two methanol and one diethyl ether molecule per macrocycle), modelling of said solvent did not lead to a convergent structure model and consequently the SQUEEZE routine within PLATON was employed.[159] This showed a volume of 2470 $Å^3$ containing 658 electrons (624 electrons for the described solvent) consistent with the solvent assignment. The two fold symmetry of the macrocycle allows for two different interactions with neighbouring cycles from the four ligands. One

interaction involved hydrogen bonding between an imidic acid proton donor and a coordinating carboxylate oxygen acceptor on another macrocycle. This is the same type of interaction seen in previous structures and can be described as a type-C interaction (Figure 3.22). The other two ligands interact with other ligands via π-π stacking interactions of the peripheral phenyl rings on the ligand (centroid to closest atom 3.47(1) Å). As the phenyl rings were not present on macrocycles **3.1**-**3.10** this type of interaction was not given a descriptor.

This structure confirmed that modification in the 4-position of the pyridyl ring of H_2**L2.1** with an aromatic substituent did not alter the structural properties of the macrocycle and hence connections to make a framework in the 4-position of the pyridyl ring would be a good place to start, in particular, with H_4**L3.3**.

3.4.2.2 Synthesis of $[Cu_2(H_4L3.3)(ClO_4)_2(H_2O)_2(Me_2CO)_2](ClO_4)_2 \cdot 2Me_2CO$ (3.14)

Upon reaction of H_4**L3.3** with zinc(II) carboxylate salts, insoluble products were observed to form immediately. Crystals of a copper(II) complexes could, however, be obtained.

When colourless H_4**L3.3** and blue copper(II) perchlorate were combined in acetone, a green solution resulted. Diffusion of benzene into this solution led to the formation of crystals suitable for single crystal X-ray diffraction. These were solved and refined in the triclinic space group *P*-1 (R-factor 3.89 %). The asymmetric unit contained half of one neutral H_4**L3.3** ligand, a copper(II) ion, a coordinated water molecule, a coordinated, disordered acetone molecule, a coordinated perchlorate anion and a free acetone molecule and a disordered free perchlorate anion (Figure 3.34). The H_4**L3.3** ligand is centred over an inversion centre, meaning the tridentate coordination domains are *trans* to each other. A small dihedral angle of 0.8(3)° exists between the central pyridine rings.

The octahedral copper(II) ion is located within the tridentate coordination site of the ligand with solvent and an anion taking up the remaining three coordination sites. The non-coordinating perchlorate anion is located in the N^1-acylamidrazone hydrogen bonding pocket described in the preceding chapter. It adopts a $R_2^2(9)$ hydrogen bonding arrangement.

The octahedral copper(II) ion is six coordinate and exhibits Jahn-Teller distortion. The equatorial plane of the octahedron is comprised of the NNO tridentate binding domain of the ligand and the coordinated water molecule. The axial sites include the coordinated perchlorate anion and an acetone molecule. The carbon atoms of this acetone molecule are disordered over two positions.

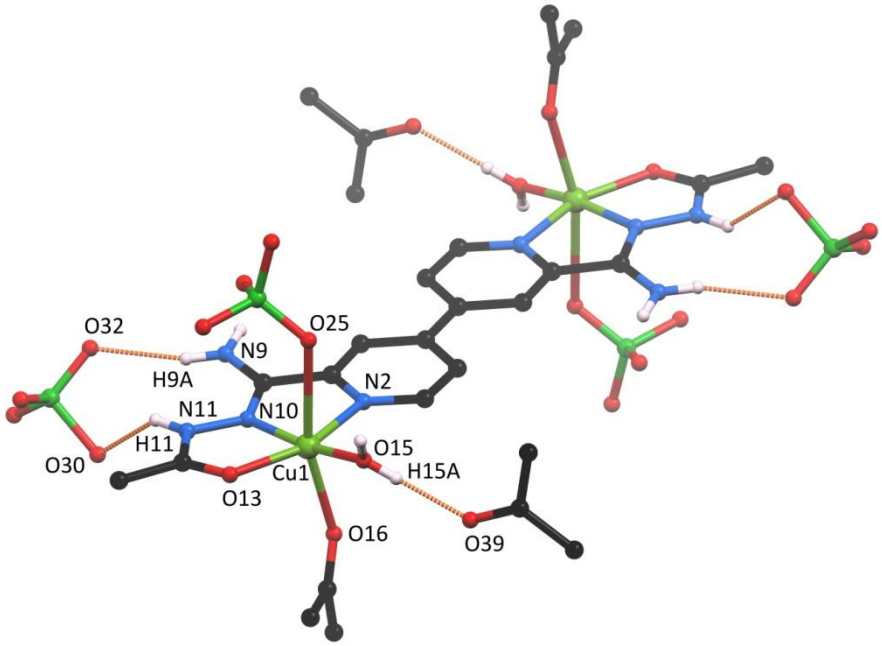

Figure 3.34: *Complete complex and surrounding anions and solvent molecules of* ***3.14****. One perchlorate anion coordinates to Cu1, the other occupies the amidrazone hydrogen bonding pocket in a* $R_2^2(9)$ *arrangement. Disorder of hydrogen bonding anion, coordinated acetone molecule and CH hydrogen atoms omitted for clarity. Selected bond lengths (Å) and angles (°): Cu1-N2 2.020(2), Cu1-N10 1.920(2), Cu1-O13 2.006(2), Cu1-O15 1.928(2), Cu1-O16 2.270(2), Cu1-O25 2.698(1), N2-Cu1-O13 159.11(7), O16-Cu1-O25 165.27(7).*

The structure of this complex differs from **2.10**, the complex formed from the reaction of H_2**L2.1** and copper(II) perchlorate, due to the relative stoichiometry of coordination site to metal ion.

3.4.2.3 Synthesis of $[Cu_2(H_4L3.3)(MeCN)_4](ClO_4)_4 \cdot 2PhH$ (3.15)

The reaction of H_4**L3.3** with copper perchlorate in acetonitrile followed by the diffusion of benzene into the green solution led to the formation of green block crystals. These were solved and refined in the monoclinic space group $P2_1/c$ (R-factor 5.92 %). In this case a similar dinuclear complex to **3.14** formed, however the coordination environments, and the relative orientation of the ligand differ (Figure 3.35). The ligand is not situated on a symmetry element and each crystallographically distinct copper(II) ion has a five-coordinate square pyramidal geometry (τ_5(Cu1)=0.03, τ_5(Cu2)=0.07). In each case the basal plane is comprised of the tridentate coordination site of the ligand and one solvent acetonitrile molecule, and the apical position another acetonitrile. The coordinate bond length of the apical acetonitrile molecules are longer than that of those in the basal plane (2.249(3) and 2.197(3) Å *c.f.* 1.971(3) and 1.966(3) Å). Anti-solvent benzene molecules interact with the main residue by π-π stacking interaction with the pyridine rings of the ligand.

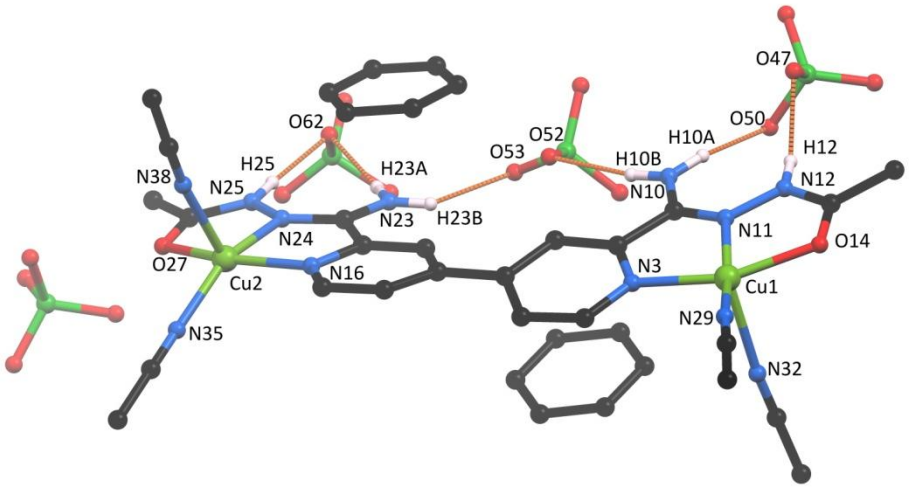

Figure 3.35: *Asymmetric unit of* ***3.15****. Each copper(II) ion adopts a five-coordinate square pyramidal geometry. CH hydrogen atoms omitted for clarity. Selected bond lengths (Å) and angles (°): Cu1-N3 2.033(2), Cu1-N11 1.910(3), Cu1-O14 2.017(2), Cu1-N29 1.971(3), Cu1-N32 2.249(3), Cu2-N16 2.027(3), Cu2-N24 1.917(3), Cu2-O27 2.017(3), Cu2-N35 1.966(3), Cu2-N38 2.197(3), N3-Cu1-O14 158.7(1), N11-Cu1-N29 163.2(1), N16-Cu2-O27 158.2(1), N24-Cu2-N35 156.6(1).*

The fact that the two coordination domains are *cis* to each other in this example, yet *trans* in **3.14** highlight the flexibility of the ligand. Although either orientation is suitable for the

formation of a framework material, a combination of both would not generate the required orientations for these macrocycles to act as tetrahedral nodes in a diamondoid framework.

3.4.2.4 Synthesis of $[Zn_2(H_4L3.4)(AcO)_4]\cdot 2H_2O$ (3.16)

H_4**L3.4** effectively contains two H_2**L2.1** ligands linked at the pyridyl end by a propane spacer. When combined with four equivalents of zinc(II) acetate in hot methanol a yellow solution formed consistent with the observation in the synthesis of the macrocycles **3.1-3.10**. Heating for a further six hours allowed all of the insoluble ligand to be brought into solution. This bright yellow solution was then filtered and diethyl ether was allowed to diffuse in. The resultant colourless needle crystals were of sufficient quality for single crystal X-ray diffraction. These were solved and refined in the orthorhombic space group $Pna2_1$ (R-factor 7.43 %). The asymmetric unit contained one neutral H_4**L3.4** ligand, two zinc(II) ions, four coordinated acetate anions and two free water molecules (Figure 3.36). Each zinc(II) centre is five-coordinate (τ_5(Zn1)=0.32, τ_5(Zn2)=0.30). Although a somewhat similar coordination geometry to the mononuclear zinc(II) carboxylate complexes that were seen to assemble in ladder-like architectures as in Section 2.3, the orientation of the carboxylates around the metal ion in **3.16** is different to these previous examples. In that section both non-coordinating oxygen atoms of the carboxylate residue are directed the same way; over the H_2**L2.1** ligand. In this case, they point in opposite directions, one over the ligand and one away. This in effect means only 'step stool' interactions can form, rather than the infinite ladder architecture as the hydrogen bonding motif responsible for the infinite ladders requires the carboxylate co-ligands non-coordinated oxygen atom to be directed over the N^1-acetylamidrazone ligand.

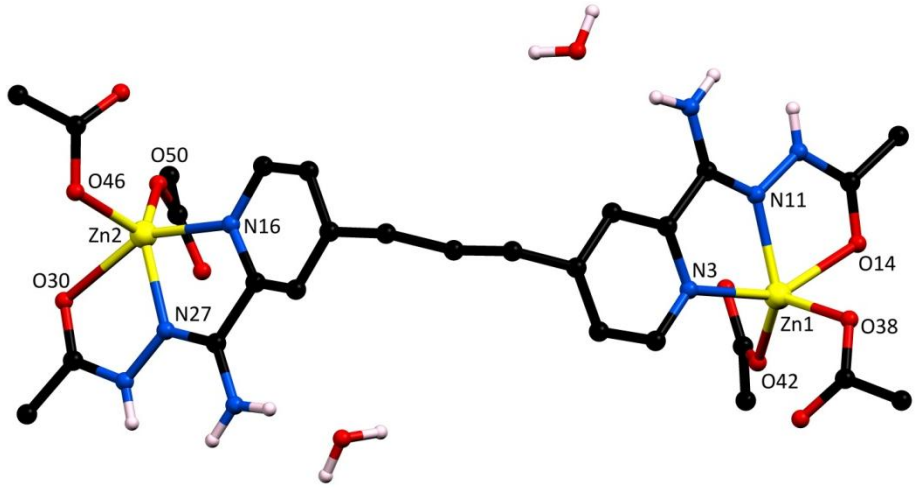

Figure 3.36: *Asymmetric unit of* ***3.16****. Disorder of the propyl chain and CH hydrogen atoms omitted for clarity. Selected bond lengths (Å) and angles (°): Zn1-N3 2.131(8), Zn1-N11 2.043(8), Zn1-O14 2.259(8), Zn1-O38 1.948(8), Zn1-O42 1.953(8), Zn2-N16 2.13(1), Zn2-N27 2.03(1), Zn2-O30 2.279(8), Zn2-O46 1.945(8), Zn2-O50 1.955(8), N3-Zn1-O14 149.5(3), N11-Zn1-O42 130.4(3), N16-Zn2-O30 149.7(3), N27-Zn2-O50 131.6(4).*

It is interesting to note that under the same conditions used to form the metal-organic macrocyclic structures **3.1**-**3.10** (diffusion of diethyl ether into a methanolic solution), this ligand formed something more similar to the complex **2.1** (obtained via evaporation of methanolic solution). This is despite adding four equivalents of zinc(II) acetate per H_4**L3.6** ligand. The decreased solubility of this complex probably plays a role in its crystallisation from solution before the macrocycle can form.

3.4.2.5 Synthesis of $[Zn_8(L2.5)_4(BnCO_2)_8]\cdot Et_2O\cdot 3MeOH$ (3.17)

Ligand H_2**L2.5** is an analogue of H_2**L2.1** that contains a pyrazine instead of a pyridine ring. To test whether this slight difference has an effect of the formation of the macrocycle, H_2**L2.5** was combined with a zinc(II) carboxylate salt in a manner similar to that used in the formation of macrocycles metal-organic macrocycles **3.1**-**3.10**. This was done as a test to determine the influence of a pyrazine ring before proceeding with ligand H_4**L3.5**).

Upon combination of colourless methanolic solutions of H_2**L2.5** and zinc(II) phenylacetate a bright yellow solution was formed. Diffusion of diethyl ether into this led to the formation of orange crystals that were of sufficient quality for single crystal X-ray diffraction. These

were solved and refined in the monoclinic space group *C*2/*c* (R-factor 7.09 %). The asymmetric unit contains four zinc(II) ions, two **L2.5** ligands, four phenylacetate co-ligands, 3 non-coordinated methanol molecules and a diethyl ether molecule. The main residue is arranged in a neutral metal-organic macrocyclic motif with the formula $[Zn_8(\mathbf{L2.5})_4(BnCO_2)_8]$ with crystallographic C_2 point symmetry. Although apparently similar to the previously observed macrocycles **3.1**-**3.10**, this metal-organic macrocycle adopts a very different form. Instead of two chemically inequivalent zinc(II) ions, there are three in this macrocyclic structure. Each macrocycle contains two octahedral (Zn4), four 5-coordinate (Zn1, Zn3), and two tetrahedral (Zn2) zinc(II) ions instead of eight 5-coordinate ions. These have coordination spheres of O_6, N_2O_3 and N_4, respectively.

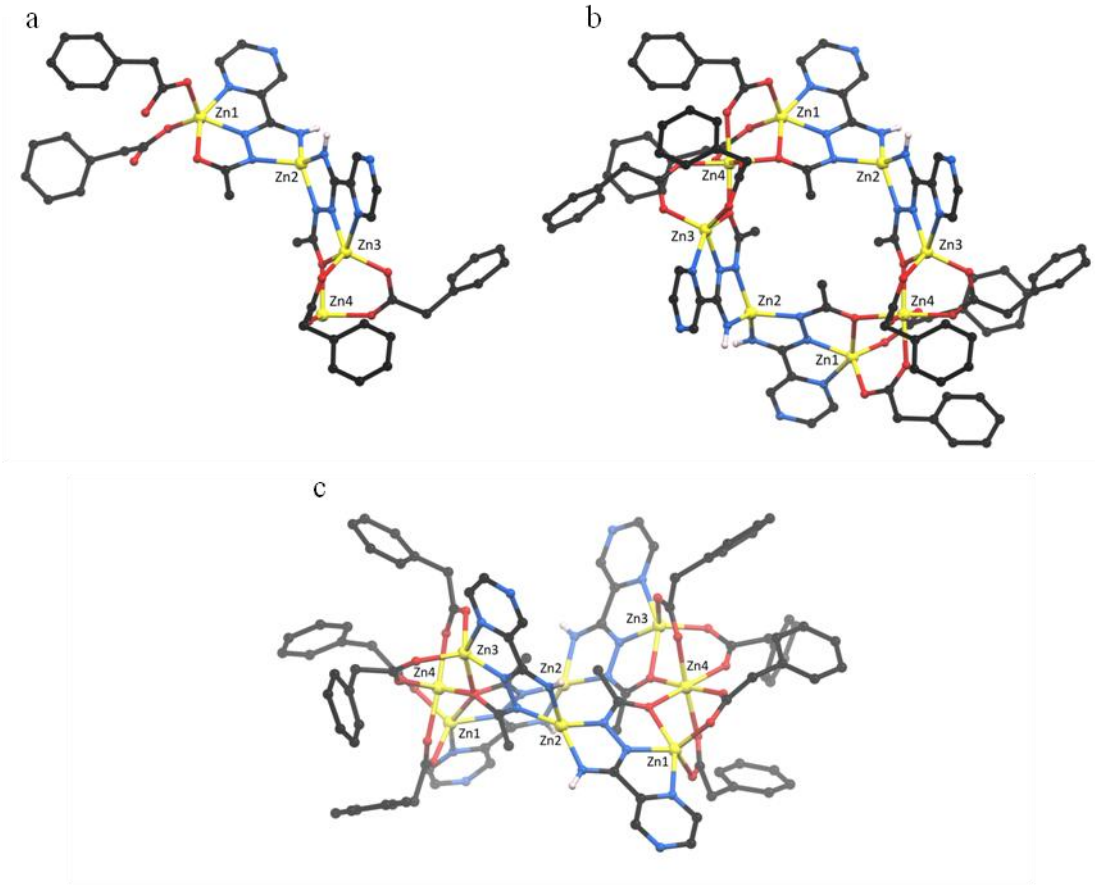

Figure 3.37*: a) Asymmetric unit of* ***3.17****. b) Complete macrocyclic unit of* ***3.17****. c) The macrocycle not only contains the same general formula as the previously described macrocycles, but also adopts a saddle shaped architecture. Solvent molecules and CH hydrogen atoms omitted for clarity.*

In contrast to **3.6**, the macrocycle containing **L2.1**, zinc(II) and phenylacetate co-ligands, the phenylacetate ligands in **3.17** are not disordered. In the arrangement of the macrocycles **3.1**-**3.10** the highest possible point symmetry is S_4 whereas in this macrocycle the highest potential symmetry of this arrangement is D_2 although only the C_2 symmetry is observed in the crystalline state. Unlike macrocycles **3.1**-**3.10** which, in their highest symmetry point group (S_4) are not chiral, the macrocycles of **3.17** are intrinsically chiral (D_2). It is not known why this combination of substituents adopts a different saddle shaped MOM to those seen in **3.1**-**3.10**.

The intermolecular interactions of this macrocycle with its closest neighbours stem from the bridging ligand **L2.5**, not the carboxylate co-ligands. The two crystallographically inequivalent **L2.5** ligands exhibit different intermolecular interactions. One ligand exhibits a combination of two hydrogen bonds and π-π stacking interactions (Figure 3.38a). In this the hydrogen bonds are in a $R_2^2(12)$ arrangement. The other adopts a pair of pyrazinyl α-CH nonconventional hydrogen bonding interactions with coordinated carboxylate oxygen atoms (Figure 3.38b). In this case the hydrogen bond acceptors do not exist in this configuration in the original macrocycles **3.1**-**3.10**. As with the previous macrocycles, **3.17** remained insoluble in common solvents.

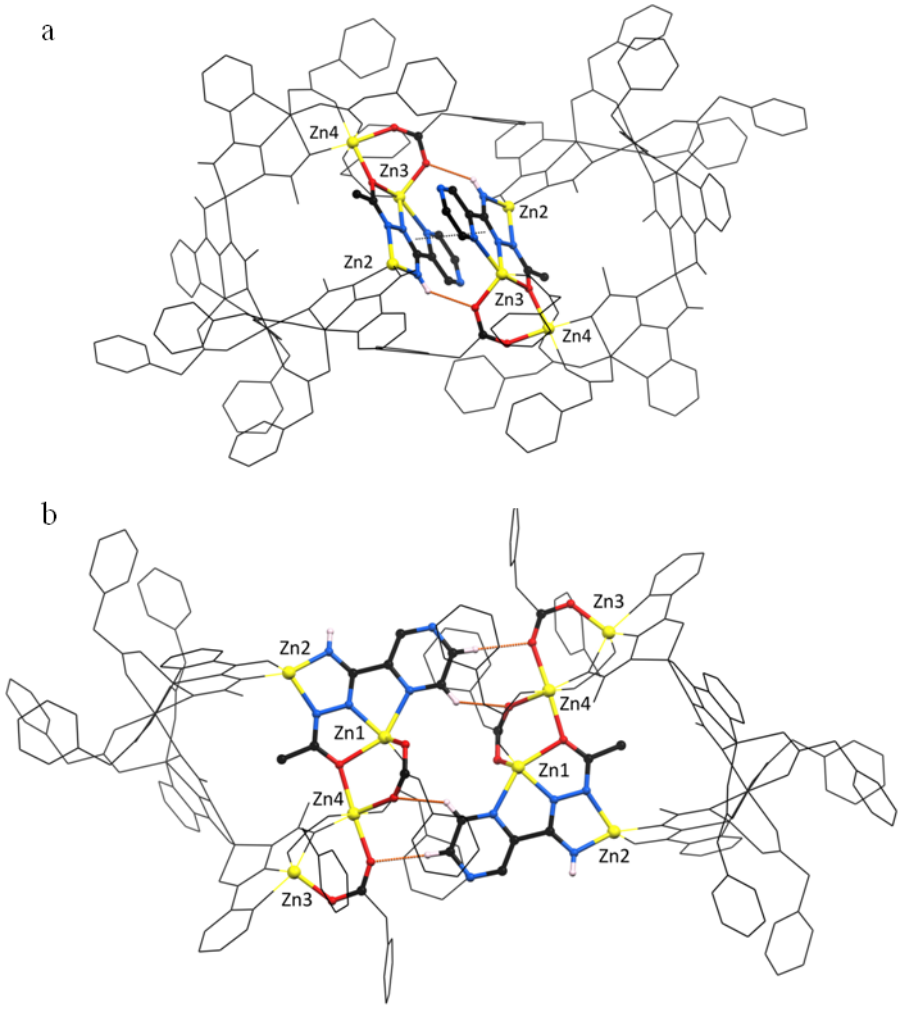

Figure 3.38: *Intermolecular interactions in* ***3.17****. The two crystallographically inequivalent* ***L2.5*** *ligands adopt different intermolecular interactions. One adopts a centrosymmetric* $R_2^2(8)$ *hydrogen bonding and π-π stacking motif (a). The other adopts a pair of pyrazinyl α-CH hydrogen bonding interactions to coordinated carboxylate residues (b).*

The pyrazinyl ligand containing two N^1-acetylamidrazone functional groups, H_4**L3.5**, was insoluble in all common solvents, and in the presence of zinc(II) carboxylate salts created another insoluble, inseparable phase. Reaction with other transition metal ions also produced a mixture of organic and metal-organic insoluble phases that could not be characterised.

3.4.3 Summary

A series of ligands containing two N^1-acetylamidrazine functional groups were synthesised. This involved the synthesis of dipyridyl and pyrizinyl dinitrile based ligands. For H_4**L3.3** this was achieved by sodium cyanide and for H_4**L3.4** trimethylsilyl cyanide was used. In H_4**L3.5** this involved the dehydration of an amide. All of these ligands displayed solubility problems on their own, but eventually dissolved in the presence of metal ions (except H_4**L3.5**). Other ligands such as H_2**L3.2** and H_2**L2.5** were used to ascertain the impact of the changes required to generate ligands with multiple binding domains in H_4**L3.3**-H_4**L3.5**.

Conditions for the ligands containing two N^1-acetylamidrazone functional groups to form macrocyclic compounds were not found. Only complexes containing the neutral ligands could be produced, and macrocycle formation was not observed to occur. Instead dinuclear complexes were formed with copper(II) and zinc(II). These were characterised by single crystal X-ray diffraction. The ligands H_2**L3.2** and H_2**L2.5**, designed to be mimics of H_4**L3.3** and H_4**L3.5** respectively that contain only one N^1-acetylamidrazone functional group did form macrocyclic compounds. Ligand H_2**L3.2** produced a metal-organic macrocycle of similar composition and form to those described in Section 3.2. The appended phenyl rings of the ligand emphasise the saddle shape of the compound. Ligand H_2**L2.5** produced a metal-organic macrocycle that had similar composition, but an altogether different arrangement of ligands and metal ions to those discussed previously. This macrocycle contained zinc(II) ions with coordination numbers four, five and six.

3.5 Conclusions and Future Work

Ten metal-organic macrocycles have been synthesised from zinc(II) carboxylate salts and H_2**L2.1**. The macrocycles are of the general formula $[Zn_8(\mathbf{L2.1})_4(RCO_2)_8]$, the ligand having undergone twofold deprotonation allowing the formation of an additional bridging bidentate coordination domain. This new coordination domain has only been observed once before in the literature. Each macrocycle adopts a saddle-like shape due to the relative orientations of the **L2.1** ligands. The saddle angles range from 61.22(3)° to 110.5(2)° within the series of macrocycles. Each macrocycle has a potential maximum S_4 point symmetry, which although was observed in six cases (**3.1**, **3.2**, **3.6**, **3.8**, **3.9**, **3.10**), lower

symmetry was observed in others. Other macrocycles exhibited C_2 point symmetry **(3.4**, **3.5**, **3.7**) or C_1 point symmetry (**3.3**). There is no correlation between the flexibility of the carboxylate co-ligand and the point symmetry of the macrocycle.

Although insoluble in common solvents, the inefficient packing of the saddle-shaped macrocycles led to large solvent filled cavities and channels in the structures making them lose crystallinity rapidly out of solution. Volatile diethyl either molecules were commonly observed within these regions through X-ray crystallography. Despite this, the parent macrocycle **3.1**, containing acetate co-ligands, was stable out of solution, and solid state luminescent measurements were performed. The macrocycle was shown to be emissive, in contrast to the free ligand H_2**L2.1**. Upon excitation at 441 nm, an emission was observed at 519 nm. The majority of the other compounds did not retain crystallinity when removed from solution and hence their desolvated structure could not be confirmed. For this reason only luminescent measurements of **3.1** are reported.

Analysis of the bond lengths of **L2.1** within the macrocycles showed that the two formal negative charges within the ligand were delocalised not throughout the N^1-acetylamidrazone functional group, but rather in the amide-like region, and at the imidamide-like region. No evidence of partial azo character between the nitrogen atoms of the hydrazone functionality was observed.

It was thought that these macrocycles could act as nodes in the formation of MOFs due to either carboxylate co-ligand exchange or by using ligands that contained two N^1-acetylamidrazone functional groups. Although both of these methods were trialled, neither proved successful. The lack of success with the former is attributed to the insolubility of the MOMs, breaking the third attribute required for MBBs outlined in Section 3.1.2. The insolubility of ligands and neutral complexes containing two N^1-acetylamidrazone functional groups is thought to hinder the latter method.

Chapter 4

2,2':6',2''-Terpyridine-4,4''-dicarboxylic Acid: A Robust Scaffold for the Incorporation of Functional Groups in Zinc(II) MOFs with Zeolitic Topology

4.1 Introduction

4.1.1 Synthesis and Structure of Terpyridine

2,2':6',2''-terpyridine (hereafter referred to as terpyridine or terpy) and its derivatives are common ligands in coordination chemistry due to their strong tridentate binding mode and relative ease of synthesis and functionalisation.

The high stability of transition metal complexes of terpyridine is due to the combination of the chelate effect of the tridentate binding domain, and strong bonding due to metal-ligand (d-π*) back donation. As the most common coordination number for transition metals is six, complexes are often found in the form $[M(terpy)_2]^{n+}$ with the metal ion in a pseudo-octahedral geometry. In this case, the terpyridine ligands bind in the exceedingly stable and reproducible tridentate meridional coordination mode. The two terpy units are arranged perpendicular to each other leading to a distorted octahedral coordination geometry of the central metal ion and the complex having D_{2d} symmetry (Figure 4.1).

With metal ions that do not favour a six-coordinate geometry, or when a strict 1:1 stoichiometry is imposed, another species is commonly seen, $[M(terpy)S_A]^{n+}$ (S = solvent or anion; A = 1, 2, 3). The terpy ligand adopts the tridentate binding mode as before, but the remaining coordination sites of the metal ion are occupied by solvent molecules or anions. The geometry of these complexes depend on the metal ion, with platinum(II) and palladium(II) species adopting four-coordinate square planar geometries with A = 1, and copper(II) and zinc(II) complexes often adopting five-coordinate trigonal bipyramidal or square-based pyrimid geometries with A = 2. Figure 4.1 shows both octahedral bis-terpyridine and five-coordinate mono- terpyridine complexes.

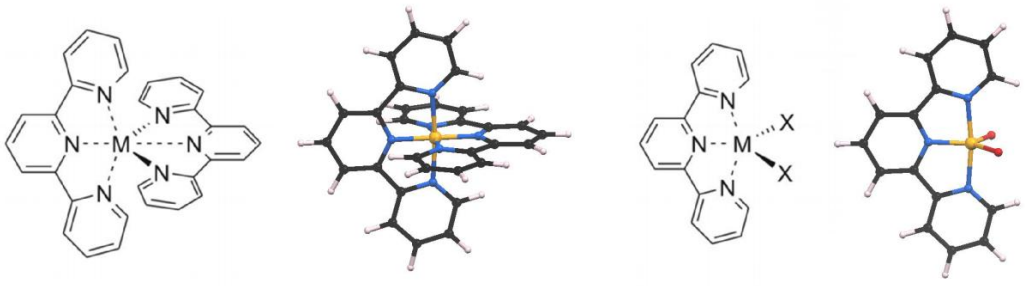

Figure 4.1: *Two common types of first row transition metal terpyridine complexes are the 1:2 stoichiometry $[M(terpy)_2]^{n+}$ complexes, and the 1:1 stoichiometry $[M(terpy)S_2]^{n+}$ complexes. Metal ions that favour octahedral geometries such as iron(II), cobalt(II), and cobalt(III) most commonly adopt the 1:2 stoichiometry.*

Distortions from idealised octahedral or trigonal bipyramidal geometry created by the two five-membered chelate rings can be seen in the above figure. The meridional tridentate binding mode shown in both examples is the most common binding motif of terpyridine, however, bidentate and monodentate coordination modes of derivatives to monovalent coinage metals are also known.[8]

As with other poly-pyridyl ligands, terpyridine complexes can have novel redox properties involving ligand radical products,[211] show interesting magnetic and spin crossover behaviour,[212] and those of the late second and third row elements are often strongly luminescent.[213-214] The properties and applications of such complexes have been well studied in the literature, and been the focus of many reviews.[212-213,215-224]

Octahedral complexes of bis-terpyridine are advantageous to the more common tris 2,2'-bipyridine analogue[225] not only due to their high stability, but that the former does not give rise to enantiomers.

4.1.2 Terpyridine in Metallosupramolecular Chemistry

Many derivatives of terpyridine have been amenable to the field of metallosupramolecular chemistry and have been used to create, among others, metal-organic macrocycles,[226] wheels,[227] helicates,[228] grids,[229] cages,[230-232] catenanes,[233] rotaxanes,[234-235] knots,[236] molecule wires,[237] and dendrimers.[238]

In supramolecular chemistry, it is often desired to design regular shaped assemblies such as molecular triangles, rectangles, squares or hexagons. However, substitution with further coordination groups at the 4 and 4"-positions of terpyridine does not lead to the formation of suitable 180° linear linkers or 120° triangular corners. A search of the CSD shows a distribution of C4-M-C4" angles for terpyridine based ligands coordinated to first row transition metals, with all angles being smaller than the 180° required for idealised geometries (Figure 4.2).[239] The distribution of angles can be attributed to the size of the metal ion (type, oxidation state) and the functional groups located on the periphery of the ligand. The angle mediated by the two five membered chelate rings, is approximately 150°. Because of this, functionalisation of the peripheral pyridine rings has not been used to

create many supramolecular structures with this angle designed into the structure. Instead focus has been on utilisation of the robust tridentate binding mode and/or functionalisation of the 4'-position. In octahedral bis-terpyridine complexes the two 4'-positions are approximately 180° to each other.

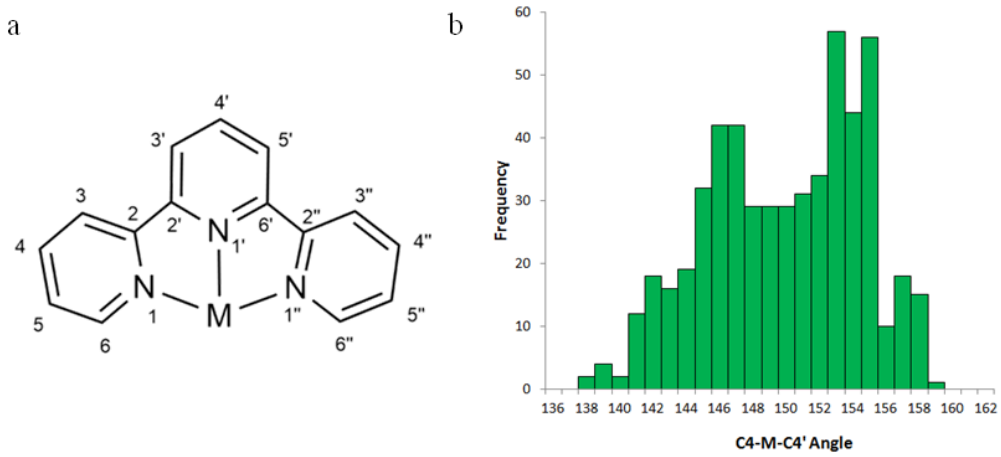

Figure 4.2: *a) Structure of coordinated terpyridine, with IUPAC labelling scheme. b) Histogram showing the C4-M-C4'' angle of a range of first row transition metal terpyridine complexes.*

Despite the wealth of discrete metallosupramolecular architectures, the use of terpyridine derivatives in the construction of coordination polymers and/or metal-organic frameworks is limited. This is further reduced when considering only polymers made via functionalisation of the side pyridine rings. Because of the strength and reproducibility of the coordination mode, it is an ideal building unit for such structures. Several examples do exist however, and units of these are shown in Figure 1.16.

4.1.3 This study

Carboxylate groups are ubiquitous in coordination polymer chemistry due to their strong coordinate bond and anionic nature. When this study began, terpyridine-4,4''-dicarboxylic acid derivatives had not been represented in the supramolecular literature, in contrast to the multiple reports of 2,2'-bipyridine-4,4'-dicarboxylic acid derivatives.[240] This is possibly due

to the fact that a convenient, moderately yielding synthetic route had not been established until 2011.[241] In early 2016 two groups reported MOFs based upon these ligands.[242-243]

When coordinated to a metal ion in a bis-tridentate fashion, a terpyridine-4,4"-dicarboxylic acid derivative would be expected to form a tetra-carboxylate metalloligand (Figure 4.3a). The angles between carboxyl groups on the same terpyridine ligand are at approximately 150° and depend on the size of the central metal ion, allowing fine tuning of the potential nodes geometry. A mono-terpyridine complex can also be envisioned to act as an auxiliary node, with two coordinate bond donors and two coordinate bond acceptors (Figure 4.3b).

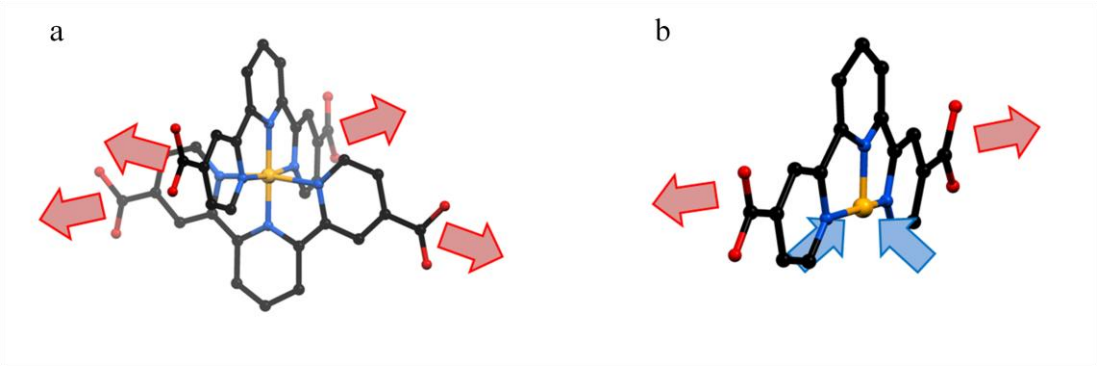

Figure 4.3: *Models of potential $[M(tdc)_2]^{n+}$ tetra-carboxylic acid metalloligand (a) and potential $[M(tdc)X_2]^{n+}$ dicarboxylic acid, dicoordination bond acceptor auxiliary node (b) for the synthesis of coordination polymers. Red and blue arrows represent coordination bond donors and acceptors, respectively. tdc = terpyridine-4,4"-dicarboxylic acid.*

Although some headway was made with bis-terpyridine complexes, these will not be reported here and this chapter will focus on the synthesis and characterisation of MOFs containing a 1:1 ratio of terpyridine-4,4"-dicarboxylic acid to metal ion. The synthesis of ligands and crystallographic characterisation of the resultant frameworks will be discussed. The activation and subsequent gas sorption properties of the MOFs will be presented.

4.2 Ligand Synthesis

Since its discovery via ferric chloride dehydrogenation of pyridine,[244] many synthetic methods have been devised for, and are applicable to the synthesis of terpyridine.[245] The two most common synthetic methods are the coupling of pyridine rings or formation of the central pyridine ring.

Common coupling methods involve the Suzuki,[246] Negishi[247] and Stille[248] reactions. Although these reactions are compatible with a range of functional groups and allow non-symmetrical terpyridine products they suffer from poor yields and are often system dependent.

The ring formation methods are more common and include, among others, the Kröhnke,[249] Potts,[250] Sauer[251] and Tohda[252] methods for the synthesis of substituted terpyridines. Together, these methods are tolerant of a wide range of functional groups and substitution patterns. Of these methods, the Kröhnke method is perhaps the most commonly employed. This is due to the fact that it is a moderately yielding one-pot protocol, which does not need to be carried out under an inert atmosphere, uses simple reagents and environmentally benign solvents. It is based on an aldol condensation of 2-acetylpyridine (or substituted derivative) with an aryl aldehyde in basic media to give an α, β unsaturated ketone (Scheme 4.1). Michael addition of a suitable enolate (traditionally an α-pyridinium ketone) then affords a 1,5-diketone which, followed by ring closure with ammonia, results in a dihydropyridine which rapidly oxidises to the desired terpyridine.

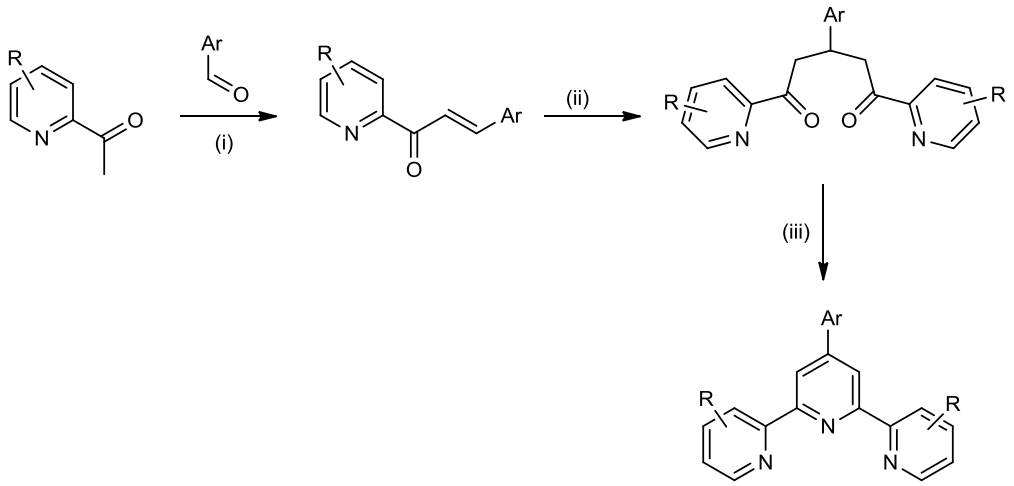

Scheme 4.1: *Synthesis of terpyridine derivatives using the Kröhnke methodology. (i) Strong base such as KOH or KOBu^t. (ii) A second equivalent of 2-acetylpyridine, or derivative, and base. (iii) Ammonia solution, followed by aerobic oxidation.*

Although substituents on the peripheral pyridine rings are optional, this synthesis necessitates the incorporation of a substituent at the 4'-position of the central pyridine ring. Realistically, this must be aromatic in nature to stabilise the intermediate, which, although seemingly limiting the scope of potential products, allows for the formation of a large family of related 4'-arylterpyridines. There is a wide range of commercially available aromatic aldehydes, from which families of related terpyridine ligands can be prepared with relative ease.

The Kröhnke methodology has been shown to be tolerant to the addition of ester functional groups on 2-acetylpyridine.[241,253] As such, it was chosen as the method of choice for the synthesis of a range of 4'-substituted terpyridine-4,4''-dicarboxylic acid derivatives. It was thought that these ligands, when combined with suitable transition metal ions, could be used as either tetracarboxylate metalloligands or dicarboxylate auxiliary nodes as shown in Figure 4.3, to be further used in the synthesis of coordination polymers and MOFs.

The incorporation of heteroatoms into coordination polymers and metal-organic frameworks has been shown to fine tune their pore properties and affect their gas sorption behaviour.[254] Indeed one of the main justifications for the continued research into MOFs

over cheaper, and often more robust zeolitic and other porous materials is the ability to tune them with particular functional groups of interest. With this in mind, a range of different heterocyclic aldehydes and functionalised benzaldehyde derivatives were chosen to be used in the Kröhnke synthesis with methyl 2-acetylisonicotinate to form a series of 4'-aryl-2,2':6',2''-terpyridine-4,4''-dicarboxylic acid derivatives. It was hoped that these functional groups would modify the adsorption isotherms of resultant MOFs by changing the properties of the internal surface area of potential frameworks. Further discussion on why particular functional groups were chosen will be elaborated further within the description of each resultant framework.

Following the Kröhnke methodology, the ligands 4'-phenyl-2,2':6',2''-terpyridine-4,4''-dicarboxylic acid (H_2**L4.1**), 4'-(*o*-tolyl)-2,2':6',2''-terpyridine-4,4''-dicarboxylic acid (H_2**L4.2**), 4'-(4-chlorophenyl)-2,2':6',2''-terpyridine-4,4''-dicarboxylic acid (H_2**L4.3**), 4'-(4-nitrophenyl)-2,2':6',2''-terpyridine-4,4''-dicarboxylic acid (H_2**L4.4**), 4'-(2-thienyl)-2,2':6',2''-terpyridine-4,4''-dicarboxylic acid (H_2**L4.5**), 4'-(3-thienyl)-2,2':6',2''-terpyridine-4,4''-dicarboxylic acid (H_2**L4.6**), 4'-(4-pyridyl)-2,2':6',2''-terpyridine-4,4''-dicarboxylic acid (H_2**L4.7**), 4'-(2-furanyl)-2,2':6',2''-terpyridine-4,4''-dicarboxylic acid (H_2**L4.8**), 4'-(4-N,N-dimethylaminophenyl)-2,2':6',2''-terpyridine-4,4''-dicarboxylic acid (H_2**L4.9**), were prepared in modest yields from isonicotinic acid (Scheme 4.2). All ligands were characterised by mass spectrometry and NMR and IR spectroscopy. Each of these, apart from the furanyl derivative H_2**L4.8**,[253] has not previously been reported in the literature. It was found that the purity of aldehyde was a major influencing role in the yield of the reaction, to the extent that some unpurified aldehydes gave no products at all. Due to this, all aldehyde derivatives were subject to relevant purification procedures before use.[255]

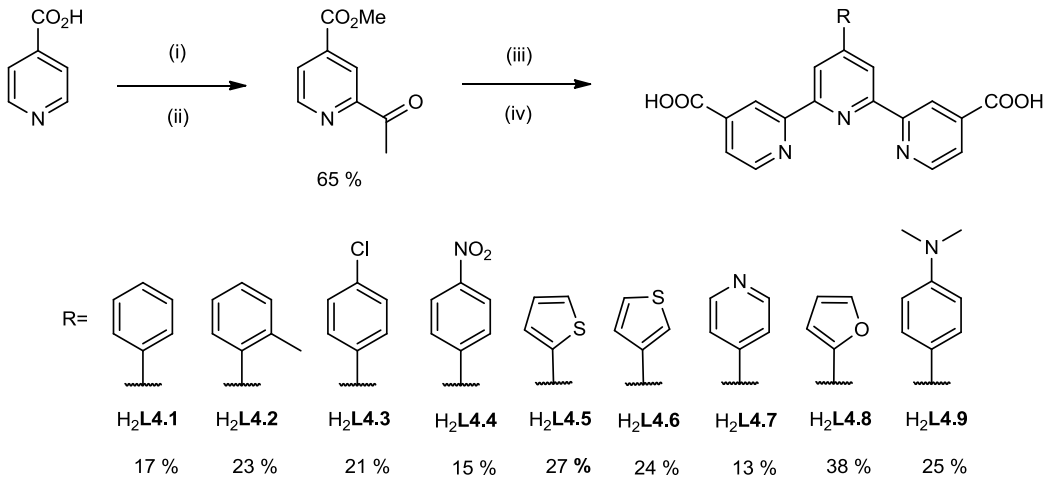

Scheme 4.2: *Synthesis of terpyridine-4,4''-dicarboxylic acid derivatives from isonicotinic acid. (i) H_2SO_4, methanol. (ii) tBuOOH, iron(II) sulfate, paraldehyde, trifluoroacetic acid, acetonitrile. (iii) RCHO, KOH, ethanol, ammonia. (iv) HCl, water.*

All terpyridine ligands H_2**L4.1**-H_2**L4.9** displayed limited solubility in common laboratory solvents, especially those with electron withdrawing substituents such as H_2**L4.3**, H_2**L4.4** and H_2**L4.7**. In these three cases, solubility was so poor, the collection of ^{13}C NMR spectra was precluded, even after long acquisition times as a sample could not be made sufficiently concentrated in d_6-DMSO.

4.3 Synthesis of MOFs

Carboxylate based MOFs are commonly synthesised under solvothermal conditions.[256] Although strictly this means heating sealed samples to temperatures above the boiling point of the solvent, it was found that such extreme temperatures were not required for the synthesis of the following series of MOFs. In this case, the ligand was dissolved in DMF with a little nitric acid to aid dissolution. To this solution was added a DMF solution of zinc nitrate, which in some cases had water added to it. The combined solutions were mixed thoroughly then sealed in screw-capped vials and heated at 90 °C for 24 hours. This time frame was arbitrary, and in some cases, crystals started to form after several hours. The

addition of water to some samples was not necessary for crystallisation, although, where applicable did produce the crystals with the best single crystal diffraction pattern.

The formation of MOFs at elevated temperatures in DMF is attributed to the slow break down of this solvent at high temperatures.[257] This increases the pH of the solution, allowing deprotonation of the carboxylic acid functional groups and subsequent coordination leading to a polymeric structure. As a polymeric solid is being formed, there is no need for slow cooling or other common crystallisation techniques, and the MOF crystallises out at the elevated temperature.

The pores within this series of MOFs contained disordered solvent molecules that, in all cases, was unable to be modelled. These are likely to contain a combination of H_2O, DMF or breakdown products thereof. As such, the SQUEEZE routine within PLATON was applied to suppress the contribution of the disordered solvent electron density to the framework atoms.[159] The quoted R-factors for each structure in this chapter refer to the modified data.

4.3.1 Synthesis of [Zn(L4.1)] (4.1)

The first ligand to be used in the synthesis of zinc(II) based coordination polymers was the 4'-phenyl derivative, H_2**L4.1**. Upon heating an aqueous DMF solution containing this ligand, zinc nitrate and nitric acid at 90 °C for 24 hours, orange crystals formed. Single crystal X-ray diffraction showed these crystallised in the tetragonal space group $I4_1/acd$ (R-factor 5.06 %). The asymmetric unit contained a single zinc(II) ion and **L4.1** ligand (Figure 4.4). The ligand coordinates to the zinc via the tridentate binding mode of terpyridine described previously. The deprotonated carboxylate groups interact with symmetry equivalent zinc(II) ions via a monodenate coordination mode. Each zinc(II) atom is 5-coordinate and has a distorted square-based pyrimidal geometry (τ_5 = 0.15). The equatorial plane is comprised of N2, N16, N18 and O7; from the meridionally chelating terpyridine ligand and an oxygen atom from a monodentate carboxylate group of an adjacent ligand. In the apical position is another monodentate carboxylate group oxygen atom, O24. The phenyl substituent is slightly twisted with respect to the central pyridine ring (C14-C13-C26-C31 torsion 11.0(6)°).

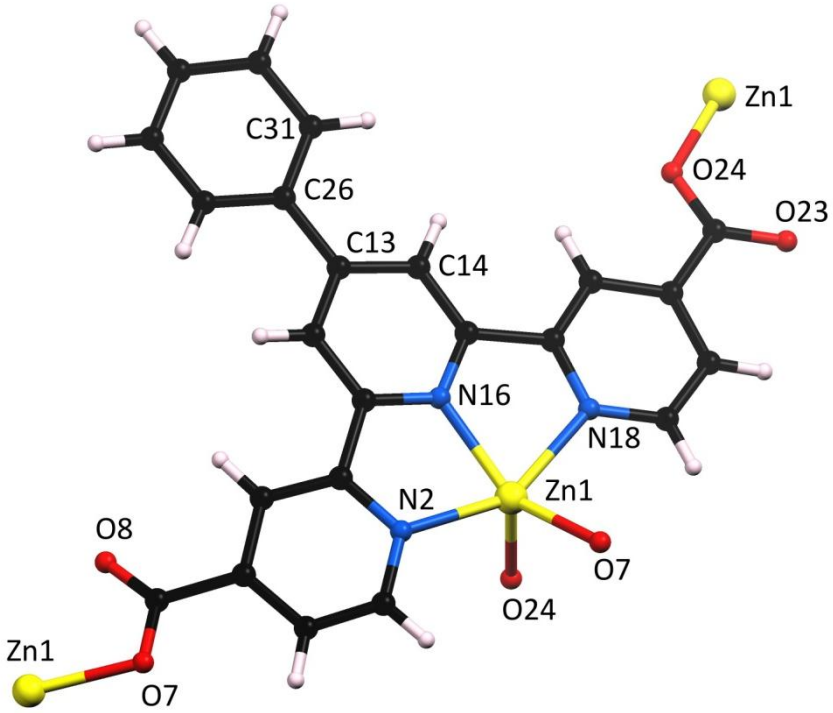

Figure 4.4: *Asymmetric unit of* ***4.1****. Each* ***L4.1*** *ligand coordinates to a single zinc(II) ion via the tridentate terpyridine binding site. The carboxylate groups of the same ligand bridge to a further two crystallographically equivalent zinc(II) centres. Selected bond lengths (Å) and angles (°); Zn1-N2 2.139(3), Zn1-N16 2.056(2), Zn1-N18 2.191(3), Zn1-O7 1.990(2), Zn1-O28 1.973(2), N2-Zn1-N18 151.6(1), O7-Zn1-N16 142.5(1), C14-C13-C26-C31 11.0(6).*

Each unit of the coordination polymer can be treated as an auxiliary node, linked to four other metal centres by the carboxylate residues of the ligand. The four links can be broken down into sets of two; two links occur via pyridine-to-carboxylate linkages, and two via carboxylate-to-pyridine linkages in an analogous way to that described in Figure 4.3b. This results in a three dimensional coordination network (Figure 4.5).

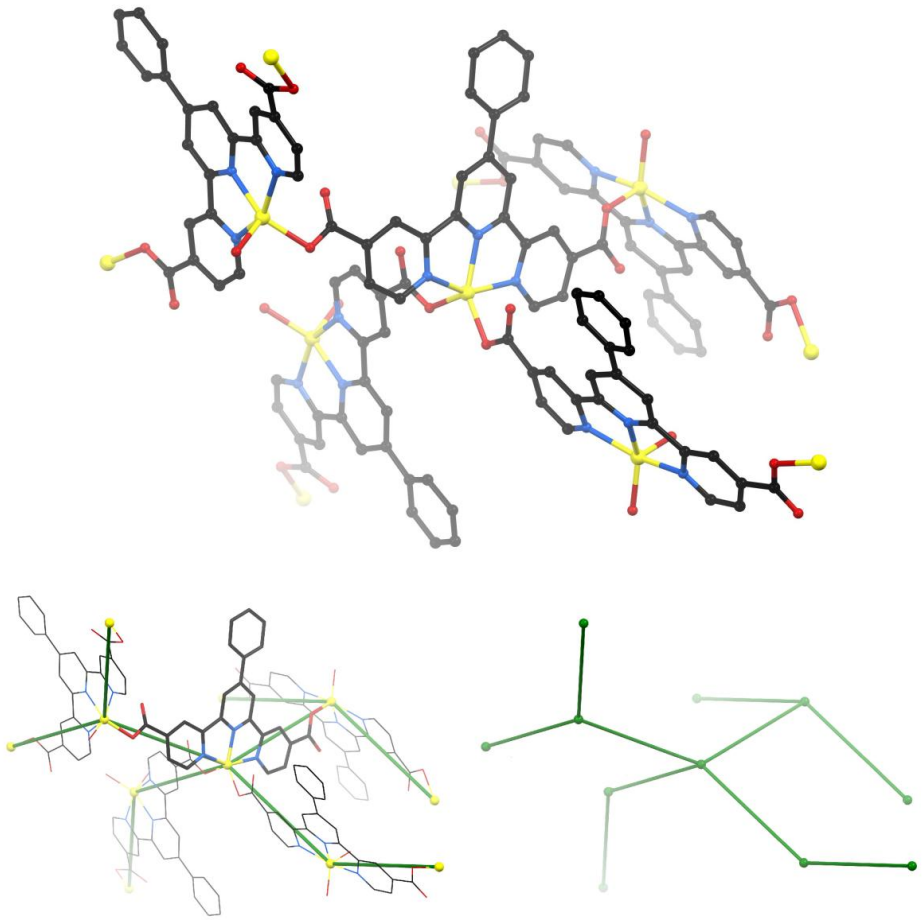

Figure 4.5: *Deconstruction of the crystal structure of* ***4.1*** *into a schematic representation of its underlying topology. The coordination network of* ***4.1*** *is created through coordinate bonding of 4-carboxypyridine residues of the* ***L4.1*** *ligand.*

There are many nets based upon four connected nodes. The most common are the diamondoid (**dia**) and the square grid (**sql**) topologies. Analysis of this resultant four-connected framework showed it has a Schläfli symbol of ($4^3 \cdot 6^2 \cdot 8$) and can be described as having the same overall topology of gismondine (**gis**), an alumino-silicate zeolite. The metal-organic nodes in this case are much bigger than the inorganic zeolitic analogue and allow for interpenetration. Several non-interpenetrated coordination polymers have been reported with this topology,[258-259] only one of which displays porosity.[260] The large channels along the *a* and *b*-axes usually observed in **gis** frameworks are no longer present and are filled with another identical framework (Figure 4.6).

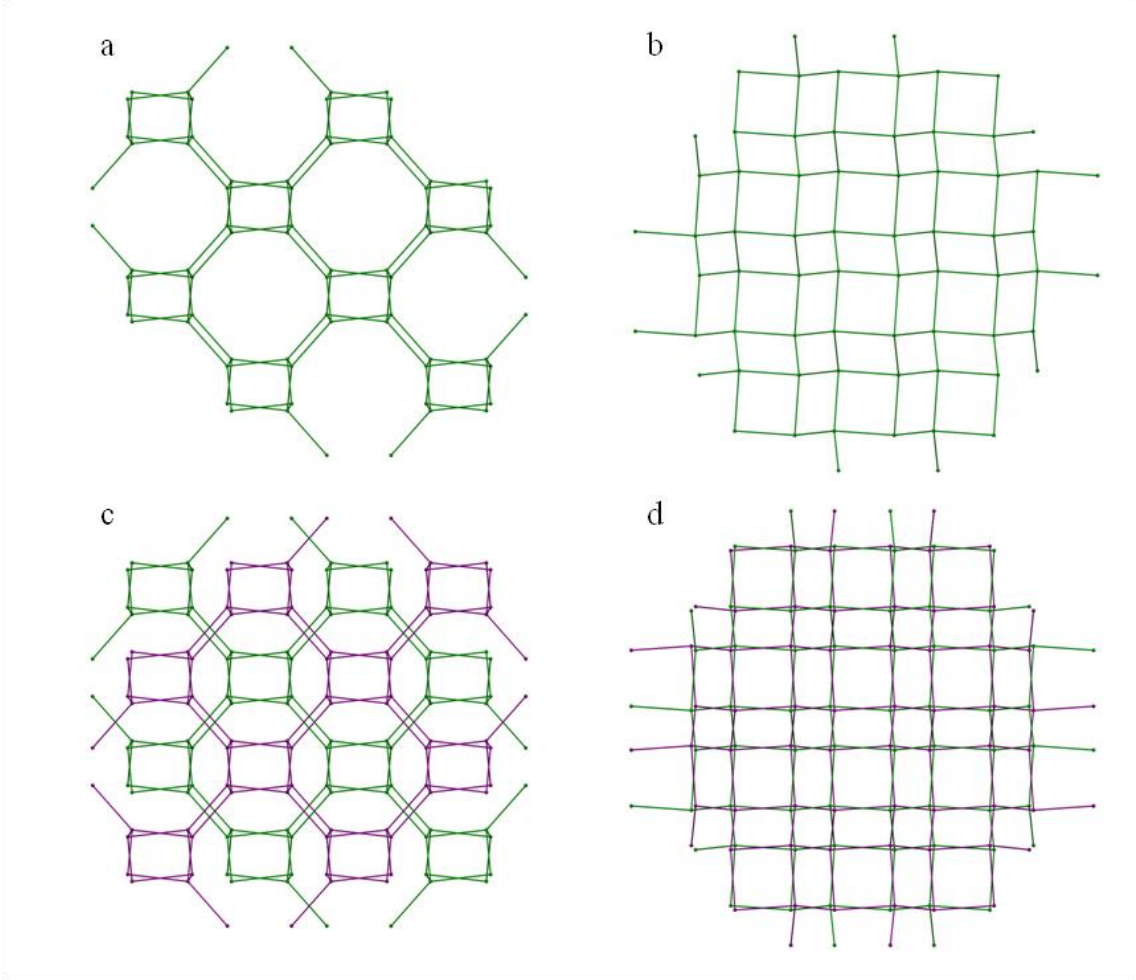

***Figure 4.6** : Schematic representation of the underlying topology of **4.1**. Views along the b (a) and c-axes (b) showing the **gis** zeolitic topology. The large cavities within the framework allow for interpenetration with another identical net shown in purple (c and d).*

The catenated nets interact via π-π stacking interactions of [Zn(**L4.1**)] units (Figure 4.7). These interactions are based around a 2-fold rotation axis. This operation allows the stacked zinc(II) ions bulky coordination spheres to be separated by approximately 120°, and hence a close face to face π-π stacking distance of 3.645(3) Å can be achieved.

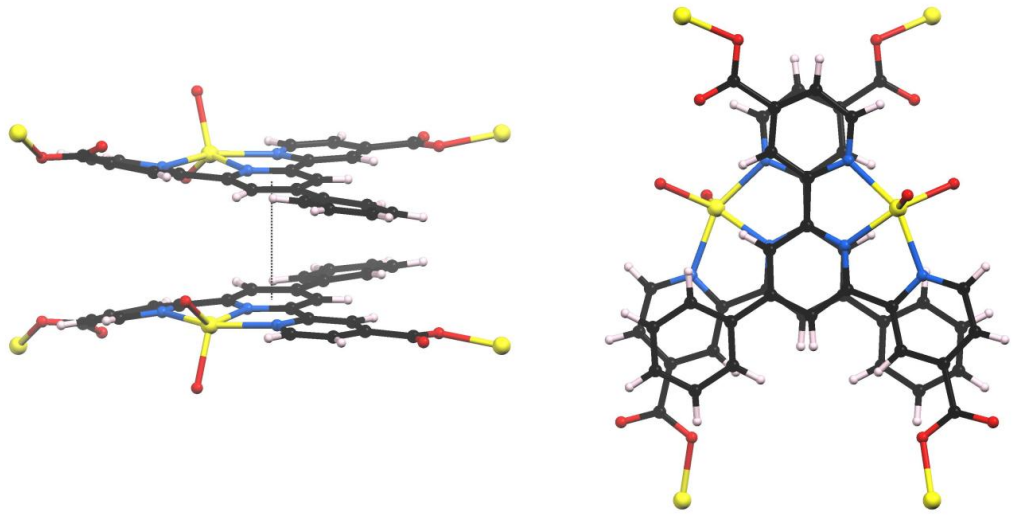

Figure 4.7: *The interpenetrating nets of* ***4.1*** *interact via a π-π stacking interaction. Each crystallographically equivalent, but not chemically linked, residue shown is related to the other by a two-fold rotation perpendicular to the direction of the stacking interaction. The distance between centroids of the two central pyridine rings is 3.645(3) Å.*

Despite the interpenetration of the framework, significant void space exists within the crystal structure. This is mainly located in large, square channels that run down the crystallographic *c*-axis (Figure 4.8). Smaller sinusoidal channels weave along the *a* and *b*-axes. Due to high symmetry of the framework and/or the lack of suitable ordering interactions of the solvent within the framework, no sensible solvent model could be found for the electron density within these channels. The SQUEEZE routine within PLATON was used to suppress the contribution of the disordered solvent electron density to the framework atoms.[159] This procedure indicated that there are a total of 2253 electrons contained within the 9151 $Å^3$ (40 %) solvent accessible volume of the unit cell. As the framework is neutral, these are likely to correspond to DMF (or decomposition products thereof) or water solvent molecules. Indeed, elemental analysis showed that there was approximately one molecule of DMF and one molecule of formic acid per zinc centre (corresponding to 2048 electrons per unit cell).

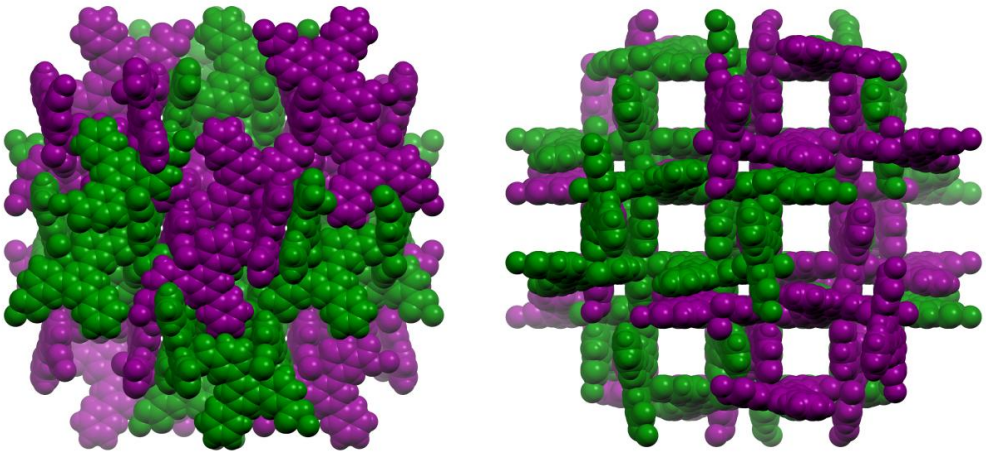

Figure 4.8: *Packing of the interpenetrated* ***gis*** *networks of* ***4.1*** *along the b (left) and c-axes (right). Despite the interpenetration, large channels exist along the c-axis. Smaller sinusoidal channels are present along the b-axis, but cannot be visualised here.*

The internal surfaces of the square channels running down the *c*-axis are centred on crystallographic four-fold rotoinversion axes, and bounded by one of the four-connected circuits inherent to the **gis** topology. The dimensions of this circuit, from node to node (zinc to zinc) are 8.9925(8) Å. From this, the phenyl rings at the 4'-position of the terpyridine ligands that create the circuit flare out, making the point immediately to either side of the circuit the tightest point of the channel at 8.856(7) Å diameter. At the widest point the channel is bounded by the phenyl rings and the girth of the channel and is 13.052(8) Å.

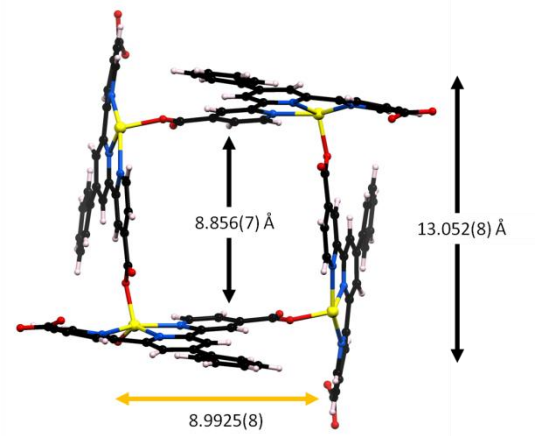

Figure 4.9: *Dimensions of the channel running down the crystallographic c-axis of* ***4.1****. At the narrowest point, the diameter is 8.856(7) Å and at the widest point it is 13.052(8) Å. The distance between zinc(II) ions is 8.9925(8) Å.*

This periodic widening and narrowing creates an undulation in the channels along the crystallographic *c*-axis which can be visualised in Figure 4.10. Smaller sinusoidal channels weave through the structure along the *a* and *b*-axes connect the larger undulating channels.

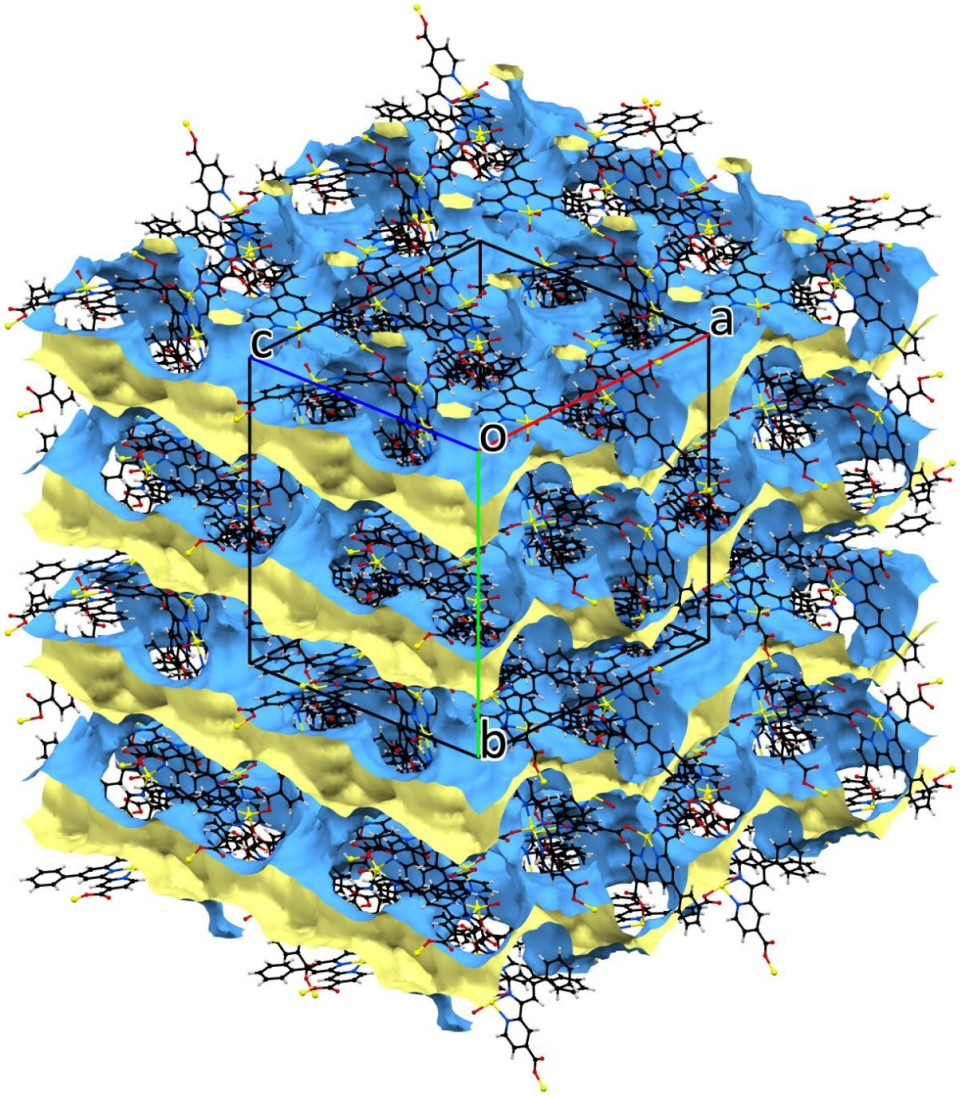

Figure 4.10: *Crystal structure of* ***4.1*** *with overlaid solvent accessible surface created using a 1.2 Å probe. Internal surface area of framework is rendered in cream. Undulations in the large channels running in the crystallographic c-axis can be seen. The small sinusoidal channels running along the a and b-axes can be seen to weave through the structure.*

These small sinusoidal channels are too small for guest molecules to traverse and the framework is described as only having one-dimensional channels.

4.3.2 Synthesis of [Zn(L4.2)] (4.2)

The interpenetration of **4.1** seems to be reliant on the π-π stacking interaction of the terpyridine ligand. This type of interaction necessitates a relatively planar conformation of both the terpyridine core and aryl substituent at the 4'-position. It was thought that replacement of the phenyl group with an *o*-tolyl group would, due to the added steric bulk, twist this substituent out of the plane of the terpyridine ligand and decrease the favourability of the π-π stacking interaction. The outcome of this small modification was intended to prevent interpenetration of the resultant network.

When H_2**L4.2** was heated in an aqueous DMF solution containing zinc nitrate and nitric acid at 90° C for 24 hours, pale yellow crystals formed. Single crystal X-ray diffraction showed these crystallised in the tetragonal space group $I4_1/acd$ (R-factor 4.24%). The asymmetric unit contained a single zinc(II) ion, coordinated by a **L4.2** ligand (Figure 4.11). The remainder of the five-coordinate coordination sphere of the metal is taken up by carboxylate groups of symmetry equivalent [Zn(**L4.2**)] moieties. The geometry around the zinc(II) ion is approximately square pyramidal (τ_5 = 0.14).

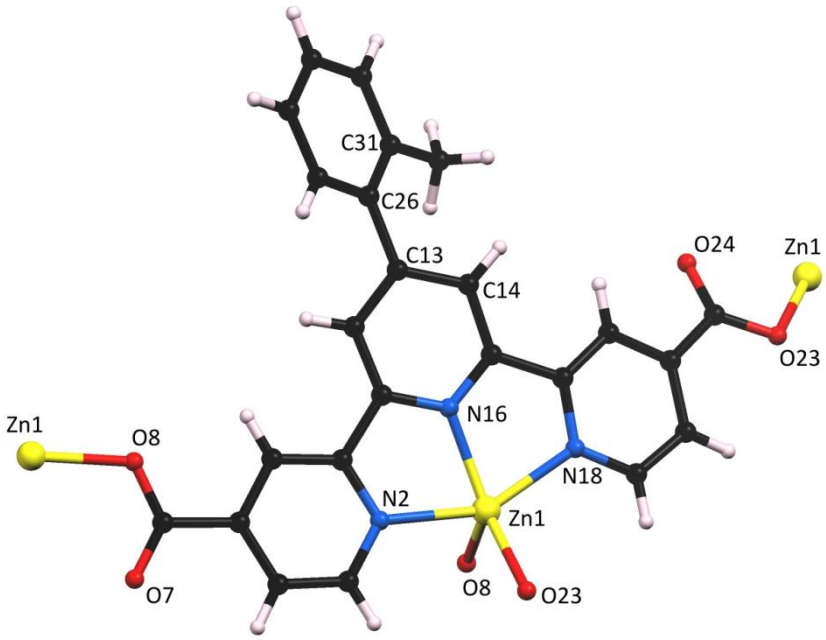

Figure 4.11: *Asymmetric unit of* ***4.2****. Each* ***L4.2*** *ligand coordinates to a single zinc(II) ion via the tridentate terpyridine binding site. The carboxylate groups of the same ligand bridge to a further two crystallographically equivalent zinc(II) centres. Selected bond lengths (Å) and angles (°); Zn1-N2 2.179(2), Zn1-N16 2.058(2), Zn1-N18 2.132(2), Zn1-O8 1.970(2), Zn1-O23 2.006(2), N2-Zn1-N18 151.62(9), N16-Zn1-O23 143.51(8), C14-C13-C26-C31 36.3(4).*

The same three-dimensional ($4^3 \cdot 6^2 \cdot 8$) **gis** network topology seen in **4.1** is again seen in **4.2**. Despite the replacement of the phenyl ring with an *o*-tolyl residue, the framework is again observed to be interpenetrated. The chemically independent frameworks pack in a similar way, except the larger torsion angle of the aryl substituent to the terpyridine core (36.3(4)° *cf.* **4.1** 11.0(6)°) results in a slightly larger inter-framework distance of 3.732(4) Å. By necessity the methyl groups are directed away from the stacking interaction. The large torsion angle of the *o*-tolyl residues deny co-planarity to two of the four rings involved in potential π-π stacking interactions.

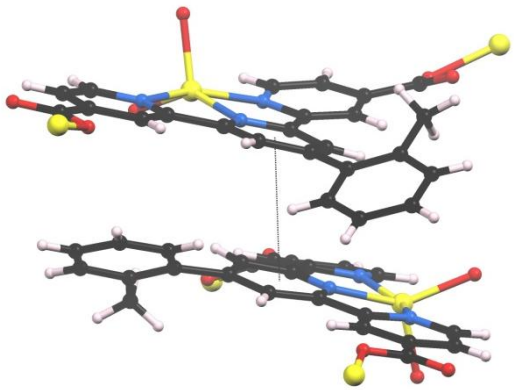

Figure 4.12: *Despite the increased torsion angle of the o-tolyl substituent, interpenetrating nets in* ***4.2*** *interact with each other via π-π stacking interactions as in* ***4.1****. Only two of the four rings of each ligand are approximately co-planar with rings of an interpenetrated equivalent and therefore are capable of forming π-π stacking interactions. The distance between the two central pyridine rings is 3.732(4) Å.*

The hypothesised prevention of interpenetration was not achieved as the torsion angle and the steric bulk of the methyl group is obviously not great enough. The torsion angle of the *o*-tolyl residue was significantly lower than expected. In other complexes of 4'-(*o*-tolyl)terpyridines reported in the CSD[239] the torsion angles are much higher, and range between 46 and 66° (Figure 4.13).

Although the desired outcome of a non-interpenetrated framework was not achieved, a framework which is isoreticular to **4.1** was produced.

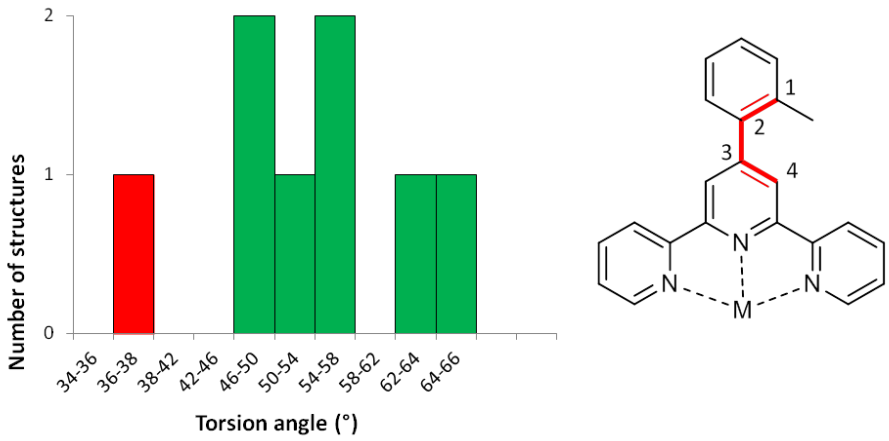

Figure 4.13: *Torsion angles of an o-tolyl ring relative to the central pyridine ring of terpyridine in coordination complexes. Green bars represent results from the CSD (EJEYEY, EJEYOI, MAHQOD, XIPNEP, XIPNIT and YIGNIN), the red bar represents compound* ***4.2*** *reported here.*

The solvent channels running along the crystallographic *c*-axis are not obstructed by the methyl group of the twisted *o*-tolyl residue and remain approximately the same diameter (Figure 4.14).

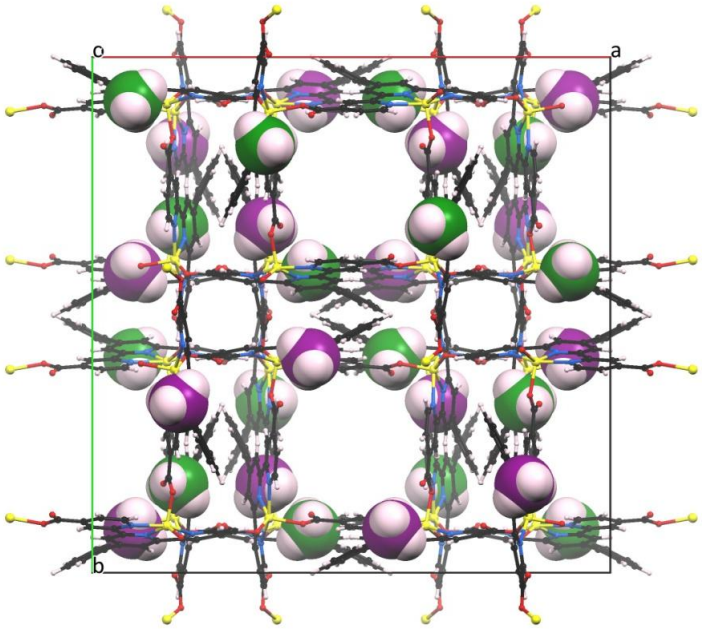

Figure 4.14: *Unit cell of* ***4.2*** *viewed along the crystallographic c-axis. Methyl groups have been highlighted in green and purple depending on which of the interpenetrated nets they belong to. The methyl groups do not block the diameter of the crystallographic channels running parallel to the crystallographic c-axis.*

The channel contents of **4.2** were not able to be appropriately modelled crystallographically and as such the SQUEEZE routine was applied.[159] This suggested a total of 1962 electrons per unit cell (61 electrons per formula unit). In combination with elemental analysis the channels were assigned to contain a DMF and formic acid solvent molecule per formula unit (64 electrons). The solvent accessible void space calculated by PLATON was seen to decrease to 7999 $Å^3$ (35 %) with the introduction of the *o*-tolyl group (*cf.* **4.1** 9051 $Å^3$, 40 %).

4.3.3 Synthesis of [Zn(L4.3)] (4.3)

As mentioned previously, the incorporation of useful functional groups within the pores of coordination polymers and MOFs is one of their most attractive attributes. It has previously been reported that mono-halogenated terephthalic acid derivatives have a positive effect on gas sorption behaviour in analogues of IRMOF-1.[261] In order to test whether similar effects could be observed in this system, the ligand 4'-(4-chlorophenyl)-2,2':6',2"-terpyridine-4,4"-dicarboxylic acid (H_2**L4.3**) was prepared.

When H_2L**4.3** was heated in DMF with zinc nitrate and nitric acid, crystals suitable for single crystal X-ray diffraction were formed. These were solved and refined in the tetragonal space group $I4_1/acd$ (R-factor 4.49 %). The asymmetric unit contained a single twofold deprotonated ligand and a zinc(II) metal ion. The ligand adopts a tridentate binding mode around the metal ion and the carboxylate groups coordinate to crystallographically related zinc(II) ions (Figure 4.15).

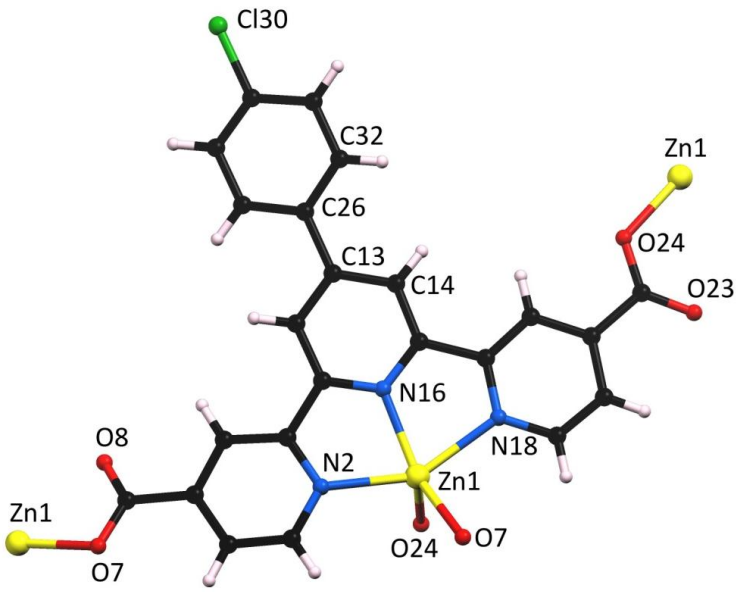

Figure 4.15: *Asymmetric unit of* ***4.3****. Selected bond lengths (Å) and angles (°); Zn1-N2 2.177(2), Zn1-N16 2.059(2), Zn1-N18 2.219(2), Zn1-O7 2.001(2), Zn1-O24 1.972(2), N2-Zn1-N18 74.67(9), O7-Zn1-N16 147.92(9), 17.2(5), C14-C13-C26-C32 17.2(5).*

Compared to **4.1** and **4.2**, the zinc(II) ion in **4.3** adopts a slightly less distorted square pyramidal coordination geometry (τ_5 = 0.05).

The overall structure is conserved, and a three-dimensional **gis-c** topology polymer is observed, indicating the chloro-group did not affect the crystallisation process. The framework is interpenetrated in the same manner as shown previously, and catenated nets interact via the previously mentioned π-π stacking motif. The 4-chlorophenyl substituent adopts a torsion angle of 17.2(5)° with respect to the central pyridine ring of the coordinated terpyridine. As with the previous structures, the non-framework electron density provided no indication to what was in the solvent accessible void space of 8718 A^3 (38 %). As such the SQUEEZE routine was used to suppress the contribution of the disordered solvent electron density to the framework atoms. This found 72 electrons per zinc(II) ion, approximately equivalent to one DMF and one formic acid molecule (64 electrons) which were assigned by elemental analysis of the as synthesised sample.

As with the phenyl substituent in **4.1**, the 4-chlorophenyl substituent in **4.3** makes up the walls of the channels running parallel to the crystallographic *c*-axis. This means they do not

decrease the size of the channels running along the *c*-axis. The increased steric bulk of the ligand was not seen to decrease the solvent accessible void space appreciably (38 % *c.f.* **4.1** 39 %).

4.3.4 Synthesis of [Zn(L4.4)] (4.4)

When the 4-nitrophenyl derivative, H_2**L4.4** was combined with zinc nitrate and nitric acid in DMF at 90 °C for 24 hours, orange crystals suitable for single crystal X-ray diffraction were obtained. These were solved and refined in the tetragonal space group $I4_1/acd$ (R factor 8.83%). The asymmetric unit contained a single ligand and a zinc(II) ion. The zinc(II) ion is coordinated by the tridentate terpyridine component of **L4.4** in addition to two carboxylate groups from neighbouring, equivalent [Zn(**L4.4**)] units. In contrast to the previous structures, one carboxylate group appears to adopt an unsymmetrical bidentate chelating coordination mode to the zinc(II) ion. The Zn1-O7 bond length of 1.988(4) Å remains consistent with that seen in **4.1** (1.990(2) Å), however, close approach of O8 to Zn1 (2.556(5) Å) means it could be argued that a change in coordination mode is observed. This exceeds the combined ionic and atomic radii of zinc(II) and oxygen (0.73 and 1.40 Å, respectively)[262] and will not be considered a coordinate bond. This keeps consistency with the other structures in this chapter, and Zn1 will be defined as having a 5-coordinate square pyramidal coordination geometry (τ_5 = 0.06).

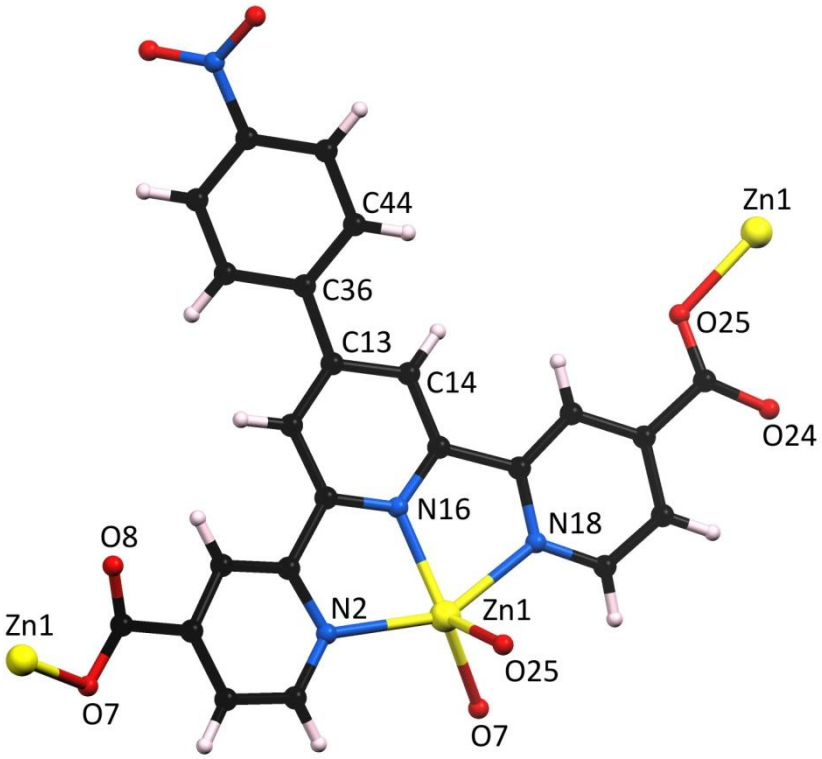

Figure 4.16: *Asymmetric unit of* ***4.4****. Disorder of the nitrophenyl and carboxy-group have been omitted for clarity. The model shown has 50 % occupancy. Selected bond lengths (Å) and angles (°); Zn1-N2 2.179(4), Zn1-N16 2.069(4), Zn1-N18 2.195(5), Zn1-O7 1.988(4), Zn1-O25 1.989(4), N2-Zn1-N18 150.8(2), N16-Zn1-O7 147.2(2), C14-C13-C36-C44 22(1).*

The 4-nitrophenyl substituent is disordered over two positions. The torsion angles of the two nitrophenyl ring positions and the central pyridine ring are 22(1)° and -26(1)°. This rotation does not hinder the π-π stacking between complexes in interpenetrated networks, and the same mode of interpenetration is observed. The twist of the substituent in the 4'-position of terpyridine in the framework directly affects the angle of the carboxylate-group attached to the pyridine ring it experiences π-π interactions with. Because it has both positive and negative torsions (it is rocking both ways), the non-coordinated oxygen of the carboxylate group is also disordered over two positions. The occupancy factors of the nitrophenyl disorder and the carboxy disorder are directly related.

Each [Zn(**4.4**)] unit can again be described as a node and upon analysis of the underlying network formed by coordinate bonds, an interpenetrated three dimensional coordination polymer with **gis-c** topology is observed. The addition of a bulky nitro group leads to a

decrease in the solvent accessible void volume, leaving just 7251 $Å^3$ (32 %), *cf.* **4.1** 9151 $Å^3$ (40 %). This corresponds to a volume decrease of 59 $Å^3$ per formula unit compared to **4.1**, consistent with the introduction of three additional non-hydrogen atoms. As the nitro groups are directed along the *c*-axis, the channels running down the same axis remain the same approximate diameter. No solvent could be modelled within the channels of **4.4** and were therefore subject to the SQUEEZE routine.[159] This indicated a presence of 57 electrons per formula unit, less than what was assigned from elemental analysis (74 electrons from DMF, formic acid, water).

4.3.5 Synthesis of [Zn(L4.5)] (4.5)

Thiophene heterocycles are rarely seen in metallosupramolecular chemistry despite having an interesting array of coordination modes.[263] A notable exception to this is when they are employed as structural units rather than coordinating groups, as in IRMOF-20.[264] This framework showed superior gravimetric uptake of hydrogen gas compared with other frameworks in the IRMOF series, HKUST-1 and Zn-MOF-74. For this reason 2-thienyl was chosen as a functional group to include in this series of frameworks.

When H_2**L4.5** was combined with zinc nitrate and nitric acid in DMF at 90 °C, crystals suitable for single crystal X-ray diffraction were produced. These were solved and refined in the tetragonal space group $I4_1/acd$ (R-factor 5.39%). The asymmetric unit contained a **L4.5** ligand and a zinc(II) ion (Figure 4.17). The zinc(II) has a similar 5-coordinate coordination sphere to the zinc(II) ions described for other members of this series, albeit with slightly more trigonal bipyramidal character (τ_5 = 0.20).

The 2-thienyl substituent showed rotational disorder about the bond to the 4'-position of the terpyridine. Two different thienyl rings could not be modelled, and instead a single distorted 5-membered ring with equal partial occupancy carbon/sulfur atoms at the 2 and 5-positions was assigned. Each part was confined to the same plane with a torsion angle of 3.4(5)°. The smaller torsion is expected in this case as five membered rings tend to exhibit a higher degree of planarity with aryl rings than bi-aryl systems due to less repulsion between *ortho*-hydrogen atoms. The greater atomic radius of sulfur and formal single bond character causes the bond between the heteroatom and the α-carbon atoms to be about 0.3 Å longer

than the other bonds in the heterocycle. As a consequence of the disorder model, the bond lengths of this thienyl ring deviate from what would be expected for a regular, non-disordered thiophene heterocycle (C26-C27 and C27-C28 are abnormally long).

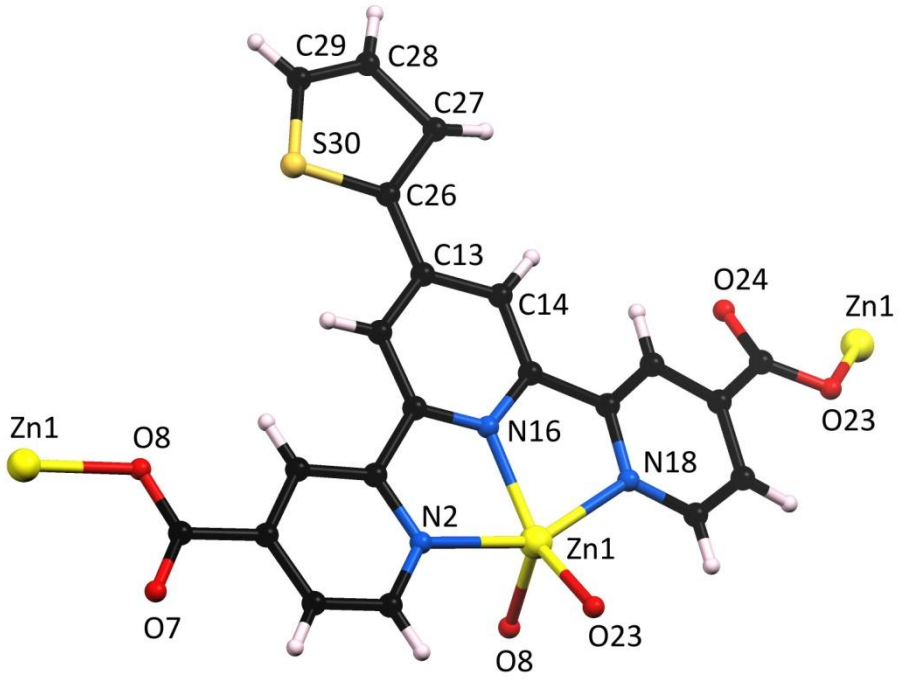

***Figure 4.17**: Asymmetric unit of **4.5**. Abnormal C26-C27 and C27-C28 bond lengths are due to disorder model of 2-thienyl substituent which has been omitted for clarity. Selected bond lengths (Å) and angles (°); Zn1-N2 2.191(3), Zn1-N16 2.060(2), Zn1-N18 2.140(2), Zn1-O8 1.970(2), Zn1-O23 1985(2), C26-C27 1.643(4), C27-C28 1.545(6), C28-C29 1.326(8), C29-S30 1.635(5), C26-S30 1.718(4), N2-Zn1-N18 151.6(1), N16-Zn1-O23 139.3(1), C14-C13-C26-C27 3.4(5).*

Each [Zn(**L4.5**)] unit is again linked to neighbouring units to form an interpenetrated **gis** framework with channels running down the crystallographic *c*-axis. Due to the nature of the framework, these retain a consistent cross-sectional area as in the previous examples. An appropriate solvent model could not be found for the electron density contained within these channels and the SQUEEZE routine was used.[159] The solvent accessible void volume within the unit cell is calculated to be 9075 $Å^3$ (39 %). There are 68 electrons per formula unit which was assigned to DMF and formic acid (64 electrons), consistent with elemental analysis.

4.3.6 Synthesis of [Zn(L4.6)] (4.6)

For the same reasons mentioned in the previous section, 3-thienyl was chosen to be substituent at the 4'-position of terpyridine-4,4''-dicarboxylic acid.

When H_2**L4.6** was combined with zinc nitrate and nitric acid in DMF at 90 °C, crystals suitable for single crystal X-ray diffraction were produced. These were solved and refined in the tetragonal space group $I4_1/acd$ (R-factor 4.94%). The asymmetric unit contained a single **L4.6** ligand and a zinc(II) ion (Figure 4.18). These are linked into a three dimensional interpenetrated framework with **gis** topology as described previously. Again, rotational disorder over two positions of the thiophene heterocycle exists. As with **4.5**, this could not be resolved into two separate rings. Instead a single ring containing equal partial occupancy carbon/sulfur atoms at the 3 and 4-positions with distorted bond lengths was modelled.

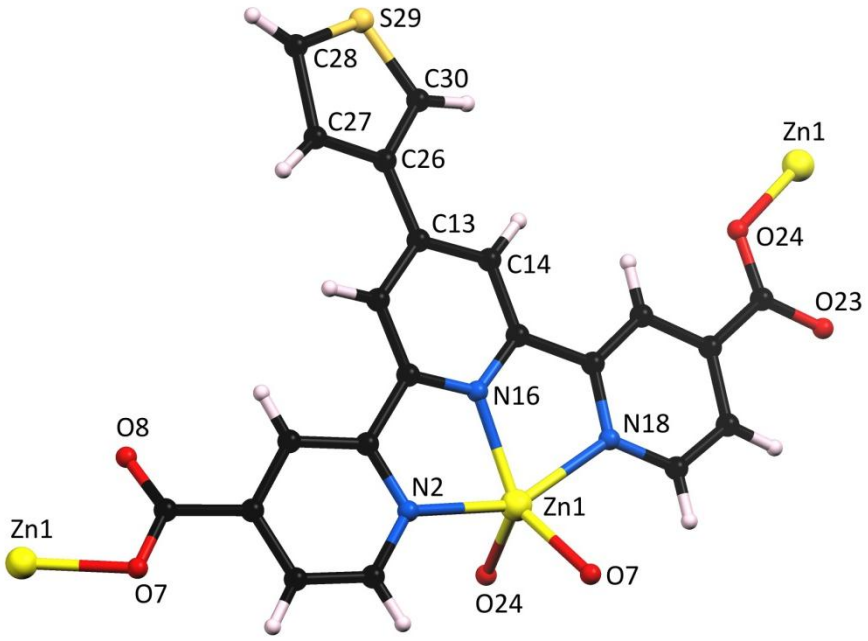

Figure 4.18: *Asymmetric unit of* ***4.6****. Abnormal C27-C28 bond length is due to the disorder model of 3-thienyl substituent which has been omitted for clarity. Selected bond lengths (Å) and angles (°); Zn1-N2 2.149(3), Zn1-N16 2.052(3), Zn1-N18 2.192(3), Zn1-O7 1.988(2), Zn1-O24 1.980(2), C26-C27 1.379(6), C27-C28 1.636(5), C28-S29 1.490(4), S29-C30 1.670(6), N2-Zn1-N18 151(8), O7-Zn1-N16 140.4(1), C14-C13-C26-C30 2.4(6).*

Again the 5-membered heterocycle was approximately planar with respect to the pyridine it is attached to (dihedral angle 2.4(6)°). The contents of the channels were unable to be modelled appropriately and as such the SQUEEZE routine within PLATON was used.[159] This indicated the presence of 73 electrons per formula unit, more than the amount indicated by the degree of solvation assigned from elemental analysis of DMF and water (48 electrons). The drying conditions for the single crystal were different to the sample sent for elemental analysis and this may be the cause of the difference.

4.3.7 Synthesis of [Zn(L4.7)] (4.7)

The synthesis of MOFs containing Lewis basic sites such as amines and heterocyclic nitrogen atoms is still a significant challenge because they tend to coordinate to metal ions instead of remaining intact inside MOF channels. Lewis basic sites inside the confined MOF channels have been shown to be beneficial for CO_2 adsorption, selective catalytic organic transformations, and the capture of biologically important species.[254] For this reason, a derivative of terpyridine-4,4"-dicarboxylic acid containing a 4-pyridyl group on the 4'-position was synthesised (H_2**L4.7**).

H_2**L4.7** and zinc nitrate were dissolved in DMF with a small amount of nitric acid. Upon heating to 90 °C red block crystals formed and were removed from the still hot solution. The crystals were of suitable quality for single crystal X-ray diffraction and were solved and refined in the space group $I4_1/acd$ (R-factor 6.07 %). The asymmetric unit contains one **L4.7** ligand and one zinc(II) ion (Figure 4.19). The remaining coordination sites on the metal centre are taken up by carboxylate groups on two crystallographically equivalent [Zn(**L4.7)**] units. This, as described for the previous compounds, creates a three-dimensional, interpenetrated framework with **gis-c** topology. The zinc(II) ion adopts a square pyramidal coordination geometry (τ_5 = 0.14). The 4-pyridyl residue is non-coordinating, and is disordered over two positions due to rotation about the C13-C26 bond. Dihedral angles of 11.8(7)° and -19.4(1)° exist for the two positions of the disordered ring relative to the central pyridine ring of the ligand. Unlike **4.4**, the twisting of this substituent does not cause disorder in the non-coordinating oxygen atom of a nearby carboxylate group.

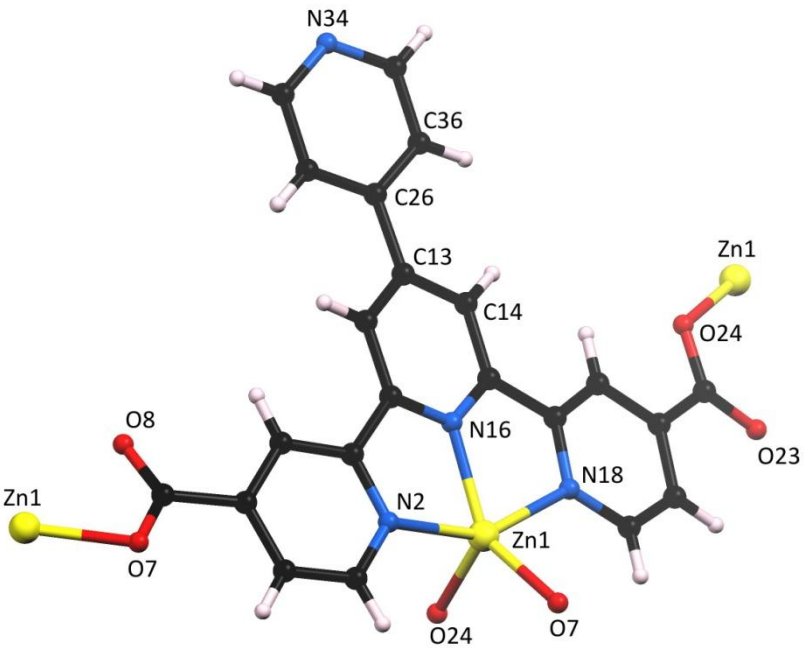

Figure 4.19: *Asymmetric unit of* ***4.7****. Disorder of the non-coordinating 4-pyridyl substituent is omitted for clarity. Selected bond lengths (Å) and angles (°): Zn1-N2 2.130(3), Zn1-N16 2.067(3), Zn1-N18 2.181(4), Zn1-O7 1.986(3), Zn1-O24 1.970(3), N2-Zn1-N18 151.4(1), N16-Zn1-O7 143.0(1), C14-C13-C26-C36 11.8(7).*

Large solvent channels are present along the crystallographic *c*-axis. The solvent contained within could not be modelled and hence the SQUEEZE routine was used to suppress contributions from this. The solvent accessible void volume was calculated to be 8936 A^3 per unit cell (39 %), a similar fraction to that seen in **4.1** (also 39 %). This was found to contain 64 electrons per zinc(II) ion, a count much lower than that corresponding to formic acid, two molecules of DMF and one and a half molecules of water (79 electrons) assigned from elemental analysis.

4.3.8 Summary

A series of seven isoreticular, three-dimensional framework materials were synthesised from ligands H_2**L4.1**-H_2**L4.7** and characterised by single crystal X-ray diffraction. The compounds **4.1**-**4.7** crystallised in the tetragonal space group $I4_1/acd$, and have very similar unit cell dimensions. Each compound is comprised of [Zn**L**] auxiliary nodes, connected via

monodentate coordination of carboxylate groups on the terpyridine ligand. The zinc(II) ion in each case was observed to be in a distorted square pyramidal geometry, with τ_5 = 0.15, 0.14, 0.05, 0.04, 0.06, 0.20, 0.14 for **4.1**-**4.7**, respectively. The resultant three-dimensional frameworks are based on the zeolitic gismondine topology. Although interpenetrated, all compounds exhibit large one-dimensional channels along the crystallographic *c*-axis. The solvent accessible void volume was found to be between 32 and 40 % of the unit cell depending on the functional group of the ligand. The differing aryl and heterocyclic functional groups line the walls of these channels and do not affect the diameter of the channel significantly. The likely content of these channels was determined to be mixtures of solvent DMF, formic acid and water through elemental analysis.

4.4 Activation of MOFs

For use in practical applications, these polymers must retain their porosity upon removal of solvent. To assess the stability of compounds **4.1**-**4.7** with regard to desolvation, each sample was removed from the mother liquor, washed with DMF and left to soak in acetone for 48 hours, the acetone was regularly refreshed during this time. The samples were then kept under high vacuum for 18 hours to remove the exchanged solvent. The activated samples were analysed by PXRD, TGA, IR spectroscopy and microanalysis.

4.4.1 PXRD Analysis

PXRD patterns simulated from the single crystal X-ray diffraction data, from samples taken directly from the mother liquor and from activated samples were compared. This showed that all samples retained crystallinity and did not undergo any phase changes as a result of activation. An illustrative set of overlaid PXRD patterns for compound **4.3** can be seen in Figure 4.20. Patterns for all compounds can be found in Appendix 2.

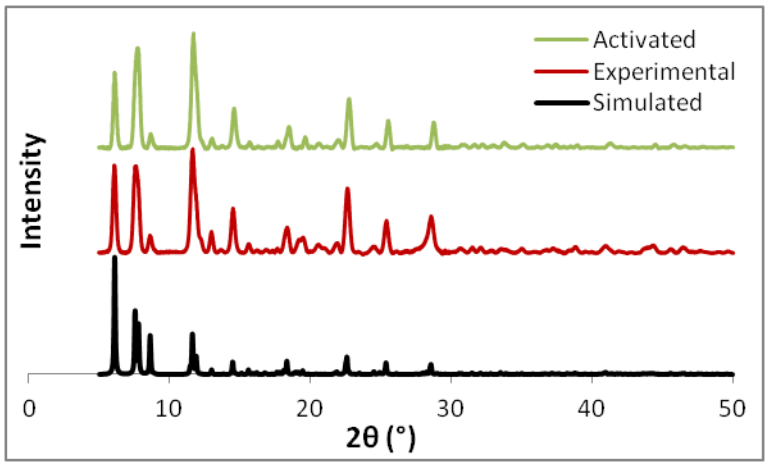

Figure 4.20: *PXRD patterns derived from simulated data, freshly synthesised compound and activated compound for* ***4.3****.*

4.4.2 Thermogravimetric Analysis

Knowing that crystallinity was retained post-activation, thermogravimetric analysis (TGA) was used to confirm all solvent had been removed. The weight of compounds **4.1**-**4.7** with respect to temperature was measured from room temperature to 800 °C (Figure 4.21). The weight of all compounds remained approximately constant until ~320 °C, at which point a stepped decline was observed until reaching a residual weight of less than 20 % consistent with full decomposition to zinc oxide.

Compounds **4.3** and **4.4** show lower residual percentage weights due to higher initial molecular weights relative to zinc oxide.

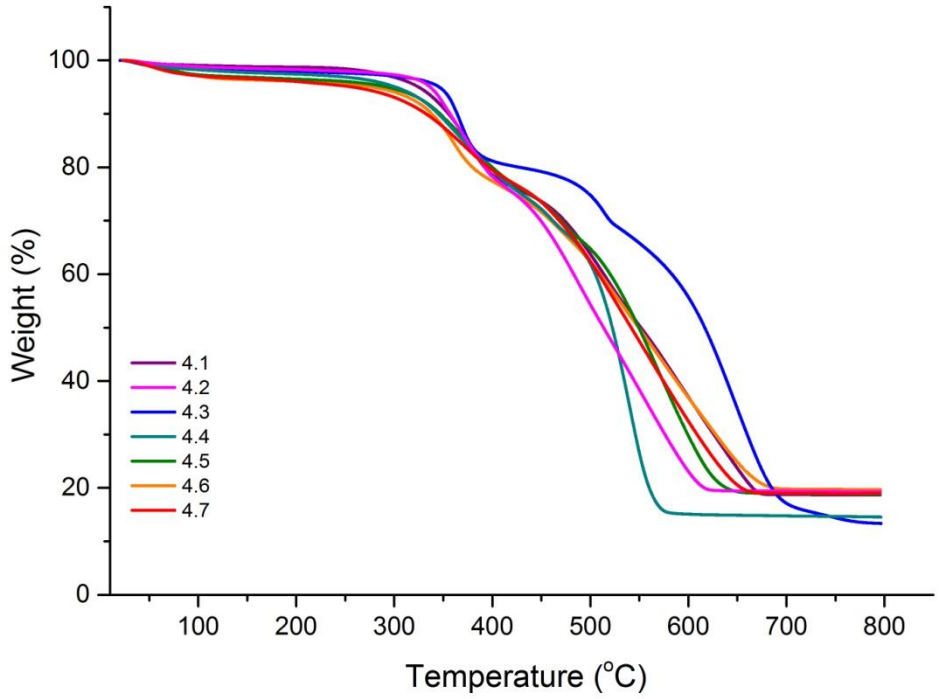

Figure 4.21: *Thermogravimetric analysis curves of activated compounds* ***4.1****-****4.7****.*

The thermal decomposition curve for **4.3** appears more gradual than the other samples in the 400-500 °C temperature range. Compound **4.3** contains a chlorophenyl functional group. The thermal decomposition of such groups is known to proceed via rupture of the C-Cl bond, the phenyl radical decomposing quickly, while the chlorine atom abstracts a hydrogen atom from another aromatic ring to form hydrogen chloride gas.[265] This likely reacts with the zinc(II) ions of the framework producing zinc chloride, which takes longer to decompose to zinc oxide than zinc carboxylate salts.[266]

The thermal decomposition curve for **4.4** appears steeper than the other samples from 500-550 °C. This may be due to the homolysis of the nitro-group and rapid mass loss due to the formation of gaseous NO_2 and NO.[267]

The experimental weight of compounds at the relevant step temperatures can be compared to calculated values of the expected decomposition products (Table 4.1). The first step is

likely to correspond to decarboxylation of the ligand. Calculated values for the weight of the dry frameworks minus two equivalents of CO_2 per formula unit match the experimentally determined weight at 375 °C, the plateau at the bottom of the first step. The final weight loss is due to decomposition of the ligand, leaving only zinc oxide as a white powder. Zinc oxide is calculated to be 16-18 % of the total weight of a dry, empty framework, which is in agreement with the 13-20 % values observed at 775 °C.

	Calculated weight (%)			Experimental weight (%)	
Compound	[ZnL]	[ZnL] - $2CO_2$	[ZnO]	375 °C	775 °C
4.1	100	81	18	79	19
4.2	100	81	17	79	19
4.3	100	82	16	82	13
4.4	100	83	16	80	15
4.5	100	81	17	80	19
4.6	100	81	17	78	20
4.7	100	81	18	80	19

Table 4.1: *Calculated weights of expected thermal decomposition products from desolvated compound* ***4.1-4.7*** *and experimental weights at 375 and 775 °C. The weight at 375 °C corresponds to the completion of the first decomposition step; decarboxylation. The weight at 775 °C corresponds to full decomposition of the framework to zinc oxide.*

4.4.3 IR Spectroscopic Analysis

IR spectroscopy was performed on activated samples (Figure 4.22). Potential guests inside the framework left over from the synthesis and solvent exchange steps contain functional groups that are easily visualised by IR spectroscopy.[268] No DMF or formic acid was observed in any of the samples. A small peak that could correspond to the carbonyl stretch of acetone is present in **4.3** at 1715 cm^{-1}, however, other stretches characteristic of acetone were not observed. This indicated that no solvent containing a carbonyl functional group remained within the pores of compounds **4.1**-**4.7** post activation consistent with TGA results. The stretches related to the coordinated carboxylate groups of the framework adsorb at lower frequency than these solvents and do not potentially obscure them. The asymmetric and symmetric stretching of the coordinated carboxylate groups can be seen at

approximately 1555 and 1360 cm^{-1}, respectively. It is well known that the difference in these stretches can give an indication of the coordination geometry of the carboxylate group.[269] In this case, the difference of 195 cm^{-1} confirms the monodentate coordination mode observed via single crystal X-ray crystallography. Stretches related to the chloro-group of **4.3** and the nitro group of **4.4** were identified and are highlighted in Figure 4.22.

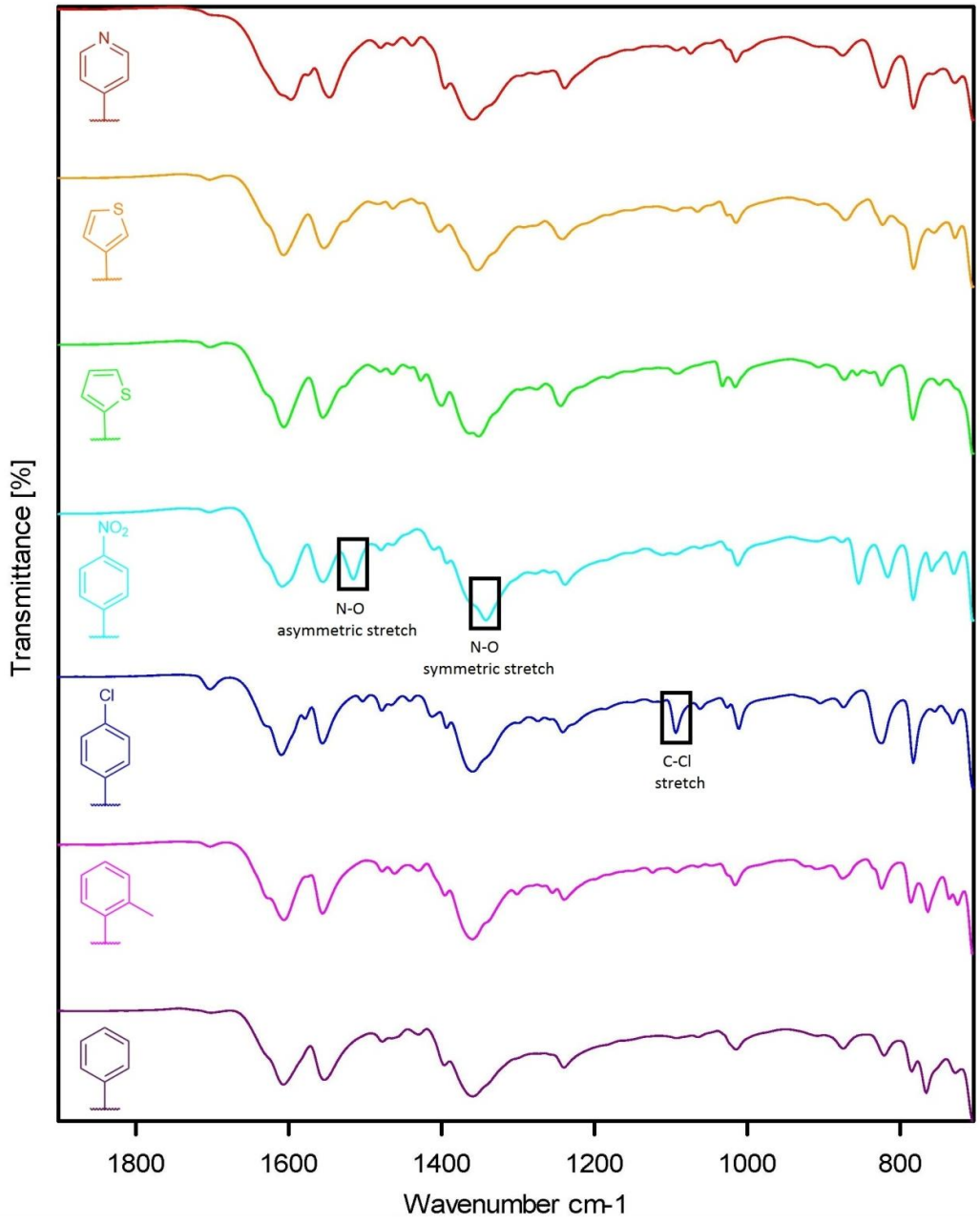

Figure 4.22: *IR spectra of activated frameworks* ***4.1-4.7*** *(bottom to top) in the range 700 to 1900 cm^{-1}. No DMF, formic acid or acetone was identified in the spectra. Strong peaks at 1555 and 1360 cm^{-1} correspond to coordinated carboxylate asymmetric and symmetric stretches respectively. Absorbance related to chloro and nitro functional groups have been highlighted in relevant spectra.*

4.4.4 Elemental Analysis

Elemental analysis was performed on all seven activated samples (Section 7.3). This confirmed that no DMF or formic acid was present within the framework. The best fit of these results was obtained when between one and two water molecules were assigned per [Zn**L**] unit for the frameworks. It is unclear whether this has not been removed in the activation procedure, or the sample has undergone rehydration from the atmosphere post-activation. The latter is considered more likely.

4.5 Gas Sorption Behaviour of 4.1-4.7

Crystallographic analysis of the frameworks **4.1**-**4.7** showed that large, square solvent channels of approximately 9 x 9 Å (diagonal approx. 12.6 Å) exist along the crystallographic *c*-axis. The results of the SQUEEZE routine within PLATON on this series of compounds indicated that the unit cell was comprised of up to 40 % void volume, indicating that the compounds could display porosity upon removal of the encapsulated solvent.

As all frameworks were shown to be stable upon removal of internal solvent, gas sorption measurements could be undertaken. The conserved topology and similarity of channel sizes, means the differences in gas sorption can therefore be attributed to the functionality in the 4'-position of the terpyridine ligand. The nature of this group is expected to subtly influence the nature of the channels in the frameworks due to their variety in size and polarity. Each aryl group is parallel to the channel and therefore the π-face of the substituent may interact with the adsorbate in the channel. It should be noted that although the zinc(II) centres adopt five-coordinate square pyramidal geometries in **4.1**-**4.7**, there are no open metal sites accessible to adsorbed gas molecules.

4.5.1 Nitrogen Adsorption

The adsorption of nitrogen at low temperatures is commonly measured in porous materials to determine their internal surface area. Within the MOF literature the BET method is often used in preference to the Langmuir method and generally considered a better approximation.[108]

A nitrogen gas isotherm was measured at 77 K on activated samples of **4.1**-**4.7** (Figure 4.23). A type-1 isotherm was observed in compounds **4.1**-**4.3** and **4.5**-**4.7** characteristic of microporous materials (pore diameter <2 nm). The BET surface area of each of these was calculated to be within the range of 690-900 m^2/g (Table 4.2). Apparent slight hysteretic behaviour was observed in **4.1**, **4.5** and **4.6**. Slight hysteresis can often be observed due to incomplete equilibration of the system. The instrument moves on to a subsequent pressure point before the adsorbed and non-adsorbed gas reach equilibrium. The slow diffusion rate of nitrogen and hence time to reach equilibrium, is due to the combination of the low thermal energy of the gas at 77 K and the one-dimensional microporous channels of the framework causing diffusion limited uptake. On the desorption isotherm, there isn't quite enough time for all the gas to desorb to the equilibrium value and hence marginally higher uptake values are reported, resulting in the appearance of hysteresis.

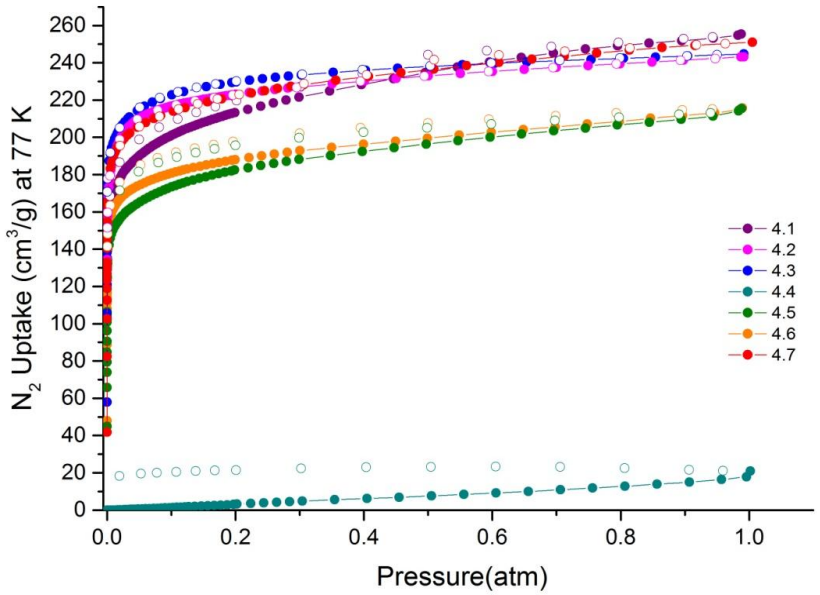

Figure 4.23: *Nitrogen adsorption (filled symbols) and desorption (open symbols) isotherms for compounds* ***4.1****-****4.7*** *at 77 K. All compounds except* ***4.4*** *show typical type-1 isotherms, characteristic of microporous materials. Slight adsorption of* ***4.4*** *is attributed to surface adsorption.*

There is almost no nitrogen adsorption for compound **4.4** at 77 K. The gradual gradient is indicative of the structure being non-porous, and the minimal uptake observed is attributed to adsorption on the surface of the crystals. The BET surface area of **4.4** was calculated to be 30 m^2/g, significantly less than that expected of a microporous structure and the results obtained for the other six members of the series. As each MOF is isoreticular and activated according to the same procedure, the difference in sorption behaviour is presumably due to the nitrophenyl functional group contained within the framework. Apparent lack of porosity could stem from one or a combination of the following four reasons;

1. The framework irreversibly collapses upon activation.
2. The activation procedure did not remove all of the solvent within the frameworks pores.
3. Strong adsorption and low thermal energy of the gas mean that it clusters on the surface of the crystal blocking the one-dimensional channels.
4. A gating mechanism due to deformation of the interpenetrated frameworks does not allow adsorption of nitrogen at 1 atm.

The first issue seems unlikely due to PXRD showing crystallinity is retained post activation. Subsequent adsorption measurements of other gases show high uptake which confirm that framework collapse has not occurred. The second issue is also unlikely as **4.4** was subject to the same activation procedure as the rest of the series and TGA, IR spectroscopy and elemental analysis showed all DMF/acetone solvent molecules had been removed under the activation conditions. The likely cause of limited adsorption of nitrogen at 77 K is therefore due to blocking or gating mechanism.

To test whether a blocking or gating mechanism is more likely, a nitrogen isotherm at a 195 K was measured (Figure 4.24). At this higher temperature, the potential surface blocking effects are minimised due to weaker interactions between the gas and the framework. If blocking is the cause of the limited adsorption, an isotherm consistent with the rest of the series should be observed. If limited uptake is observed again, then surface blocking effects can be ruled out and a gating mechanism is likely responsible for the limited uptake.

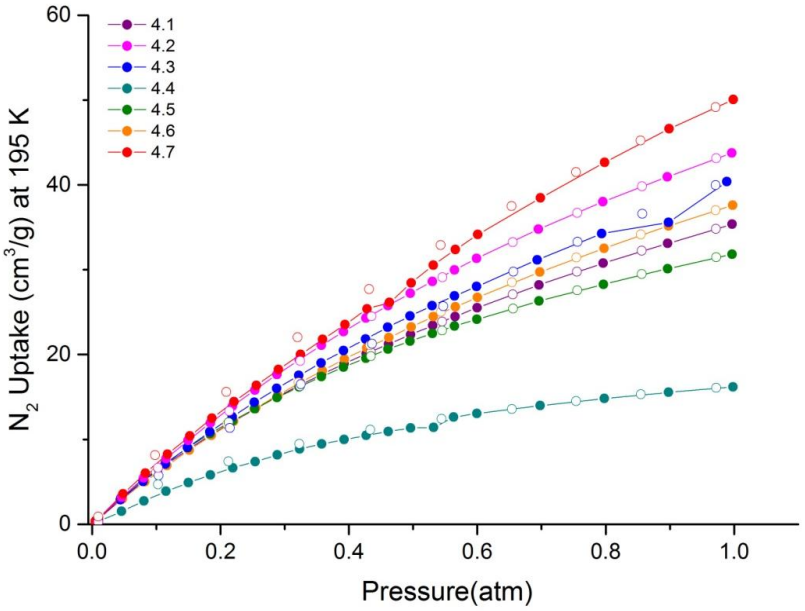

Figure 4.24: *Nitrogen adsorption (filled symbols) and desorption (open symbols) isotherms for compounds* ***4.1****-****4.7*** *at 195 K.*

The limited adsorption of nitrogen by **4.4** at 77 and 195 K indicate that gas sorption in this framework is likely governed by a gating mechanism. A stepped adsorption isotherm for carbon dioxide at 195 K and 273 K, described later, supports this proposed gating mechanism theory.

Gating mechanisms are often observed in interpenetrated or flexible frameworks and can be due to displacement or shearing transformations.[101] Due to the nature of the **gis-c** topology, displacement of interpenetrated frameworks can only occur along the crystallographic *c*-axis, which does not disrupt the one-dimensional pore structure of the framework. More likely a shearing transformation occurs, facilitated by the flexible coordination geometry of the five-coordinate zinc(II) ion and monodentate coordination mode of carboxylate groups (Figure 4.25). This deformation has the effect of reducing the pore aperture of the framework, and may occur to such an extent that the kinetic diameter of nitrogen exceeds the dimensions of the pore.

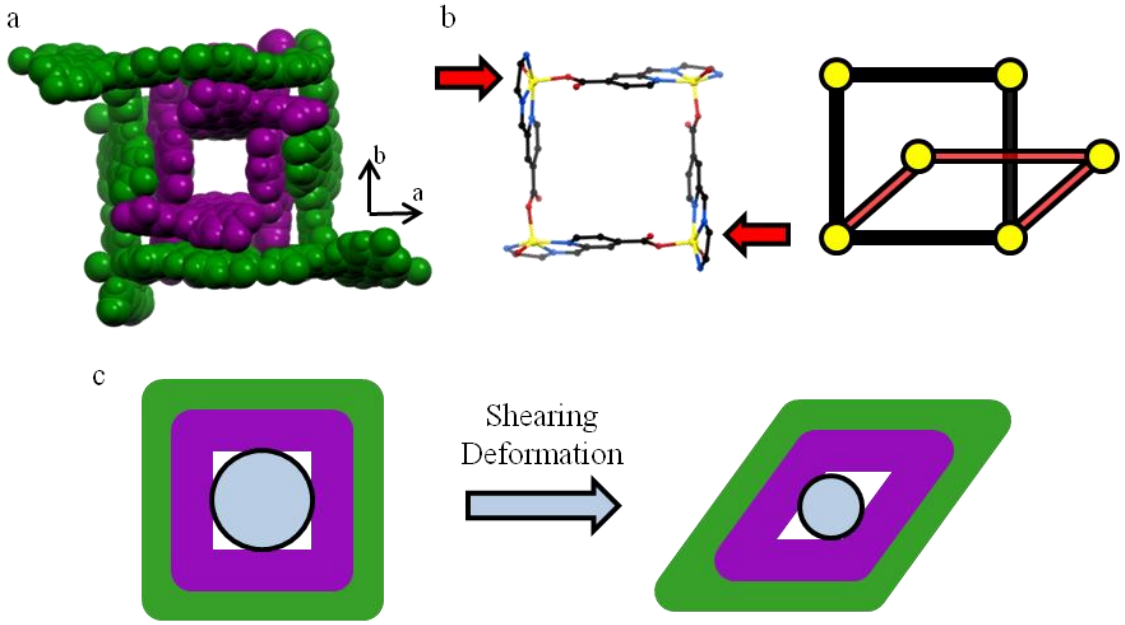

Figure 4.25: *Possible gating mechanism for compound* ***4.4****. a) Interpenetration in the reported series of MOFs with* ***gis-c*** *topology does not allow displacement deformations along the crystallographic a or b-axes. Displacement along the c-axis does not result in blocking of the one-dimensional channels along the same axis. b) Shear deformations, due to distortions of zinc(II) coordination spheres is more likely. c) Schematic illustration of possible framework transformation during activation. This deformation causes the aperture of the channel, represented here by a blue circle, to shrink.*

The reason why **4.4** adopts a gating mechanism while the others do not is unknown, but could arise due to either the strong electron withdrawing properties or the steric bulk of the nitro functional group. Electron withdrawing substituents on aromatic rings are known to increase the strength of π-π interactions,[25] which may increase the stability of an unknown closed state. The steric bulk of the functional group may also block access to the pores in an unknown closed state of the framework. Further studies on other isoreticular frameworks containing similarly π-deficient substituents such as 4-(trifluoromethyl)phenyl and 4-cyanophenyl or bulky groups such as 4-(N,N-dimethylamino)phenyl and 4-isopropylphenyl could be carried out to determine whether the gating mechanism is electronic or steric in nature. Variable pressure PXRD studies could also be performed to ascertain if a shearing phase transition occurs at low pressures.[270]

Gating mechanisms often mean that below a certain pressure (the gate pressure), there is no, or limited, adsorption. Upon reaching the gate pressure, the closed state is switched to an open state as gas-frameworks interactions overcome intra-framework interactions and

adsorption is observed. Examples of MOFs where adsorption properties are governed by gating mechanisms have been reported in the literature.[271-272]

Compounds **4.5** and **4.6**, which contain the five-membered heterocycles 2-thienyl and 3-thienyl, respectively, exhibited slightly lower surface areas than those containing six-membered aryl or heterocyclic rings. The interpenetrated frameworks **4.1**-**4.3** and **4.5**-**4.7**, have similar surface areas to the interpenetrated form of IRMOF-1 (Table 4.2).[273]

Compound	Formula	Gas	T (K)	P (atm)	Uptake (cm^3/g)	BET Surface Area (m^2/g)	Ref.
4.1	[Zn(**L4.1**)]	N_2	77	1	255.3	810	
			195	1	35.4		
4.2	[Zn(**L4.2**)]	N_2	77	1	243.2	900	
			195	1	43.8		
4.3	[Zn(**L4.3**)]	N_2	77	1	244.7	900	
			195	1	40.4		
4.4	[Zn(**L4.4**)]	N_2	77	1	20.9	30	
			195	1	16.2		
4.5	[Zn(**L4.5**)]	N_2	77	1	215.4	690	
			195	1	31.8		
4.6	[Zn(**L4.6**)]	N_2	77	1	215.7	730	
			195	1	37.6		
4.7	[Zn(**L4.7**)]	N_2	77	1	251.0	860	
			195	1	50.1		
IRMOF-1	$[Zn_4O(BDC)_3]$					2304	[274]
IRMOF-1 (interpenetrated)	$[Zn_4O(BDC)_3]$					760	[273]
IRMOF-8	$[Zn_4O(NDC)_3]$					4461	[275]
Zn-MOF-74	$[Zn_2(dobdc)]$					783	[276]
HKUST-1	$[Cu_2(BTC)_{4/3}]$					1507	[276]
NOTT-112	$[Cu_2(tdcbpb)_{2/3}]$					3800	[277]

Table 4.2: *Maximum uptake of nitrogen gas by activated samples of compounds **4.1**-**4.7** at 77 K and 1 atm. The BET surface area, calculated from the low pressure region of the isotherm is included and compared to literature examples. BDC = benzene-1,4-dicarboxylate, NDC = napthalene-2,6-dicarboxylate, dobdc = 2,5-dioxidobenzene-1,4-dicarboxylate, BTC = benzene-1,3,5-tricarboxylate, tdcbpb = 1,3,5-tris(3',5'-dicarboxy[1,1'-biphenyl]-4-yl)benzene*

4.5.2 Hydrogen Adsorption

Hydrogen gas isotherms were measured for compound **4.1**-**4.7** at 77 K. While compounds **4.1**-**4.3** and **4.5**-**4.7** showed high uptake of this gas at 1 atm, compound **4.4** showed only surface adsorption (Figure 4.26). Reproduction of the isotherm for **4.4** showed similarly low hydrogen uptake and, as mentioned before, subsequent measurement of other gases indicated that framework collapse was not a factor influencing this phenomenon. The gating mechanism suggested for the limited uptake of nitrogen at 77 and 195 K is likely responsible for the limited uptake of hydrogen. Due to the small size of H_2 (kinetic diameter of 2.89 Å) and the observation of only surface adsorption, the potential pore aperture of the closed state must be very small.

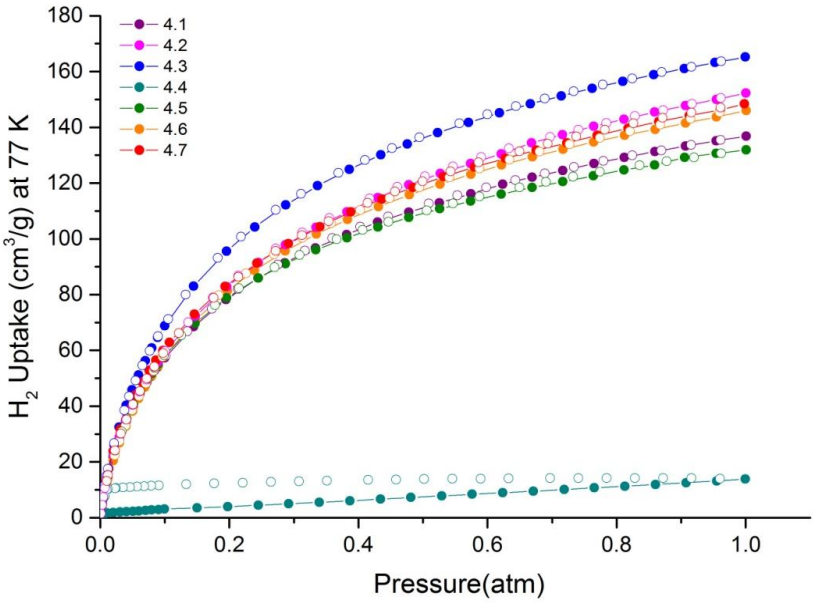

Figure 4.26: *Hydrogen adsorption (filled symbols) and desorption (open symbols) isotherms for compounds* ***4.1***-***4.7*** *at 77 K. All compounds except* ***4.4*** *show typical type-1 isotherms, characteristic of microporous materials.*

Functional groups do not seem to affect the uptake capacity at low pressures appreciably and isotherms for compounds **4.1**-**4.3**, **4.5**-**4.7** exhibit relatively similar shaped type-1 isotherms. It has been shown through both calculations and experimental data that a linear relationship exists between the hydrogen storage capacities of MOFs and their specific surface areas.[113] This is shown to hold true for this series of MOFs too.

These compounds show moderate hydrogen adsorption capacities, greater than 1% by weight at 77 K and 1 atm corresponding to approximately 3 gas molecules per formula unit (Table 4.3). It is not relevant to compare these values to the US Department of Energy (DOE) targets for hydrogen storage systems. The 2017 storage targets are 5.5 wt % at an operating temperature of between -40 to 60 °C under a maximum pressure of 100 atm.[278] These conditions, while suitable for applications, are vastly different to the conditions used for measuring hydrogen adsorption in the series of MOFs reported here. As hydrogen adsorption capacity decreases sharply with increasing temperature, low temperature isotherms were measured to get accurate uptake results. The experimental conditions used were 77 K and 1 atm as these are commonly used in the literature. Comparison with previously reported frameworks that have reported hydrogen isotherms measured under similar conditions reveal that compounds **4.1**-**4.3** and **4.5**-**4.7** show good hydrogen gas uptake.[113] Table 4.3 displays the gravimetric uptake of hydrogen by this series of compounds and some well known MOFs.

Compound	Formula	Gas	T (K)	P (atm)	Uptake (cm^3/g)	Wt%	Gas per f.u.	Ref.
4.1	[Zn(**L4.1**)]	H_2	77	1	136.9	1.22	2.8	
4.2	[Zn(**L4.2**)]	H_2	77	1	152.3	1.35	3.2	
4.3	[Zn(**L4.3**)]	H_2	77	1	165.2	1.47	3.7	
4.4	[Zn(**L4.4**)]	H_2	77	1	13.8	0.12	0.3	
4.5	[Zn(**L4.5**)]	H_2	77	1	131.9	1.17	2.7	
4.6	[Zn(**L4.6**)]	H_2	77	1	146.0	1.30	3.0	
4.7	[Zn(**L4.7**)]	H_2	77	1	148.4	1.32	3.1	
IRMOF-1	$[Zn_4O(BDC)_3]$	H_2	77	1	-	1.32	5.0	60
IRMOF-1 (interpenetrated)	$[Zn_4O(BDC)_3]$	H_2	77	1	-	2.0	8.0	279
IRMOF-8	$[Zn_4O(NDC)_3]$	H_2	77	1	-	1.5	6.9	60
Zn-MOF-74	$[Zn_2(dobdc)]$	H_2	77	1	-	1.77	2.9	276
HKUST-1	$[Cu_2(BTC)_{4/3}]$	H_2	77	1	-	2.54	5.1	276
NOTT-112	$[Cu_2(tdcbpb)_{2/3}]$	H_2	78	1	-	2.30	11.3	277

Table 4.3: *Maximum uptake of hydrogen gas by activated samples of compounds* ***4.1-4.7*** *at 77 K and 1 atm. The gravimetric uptake value is compared to literature examples. BDC = benzene-1,4-dicarboxylate, NDC = 2,6-naphthalenedicarboxylate, dobdc = 2,5-dioxidobenzene-1,4-dicarboxylate, BTC = benzene-1,3,5-tricarboxylate, tdcbpb = 1,3,5-tris(3',5'-dicarboxy(1,1'-biphenyl)-4-yl-)benzene.*

Despite having much lower surface areas, a similar hydrogen uptake capacity to IRMOF-1 is observed for compounds **4.1**-**4.3** and **4.5**-**4.7**. It should be noted that NOTT-112 shows one of the highest adsorption capacities at high pressure (10 wt% at 76 atm and 77 K).[277]

4.5.3 Methane Adsorption

Methane adsorption isotherms were measured for activated compounds **4.1**-**4.7** at 273 and 298 K. At 273 K, all compounds were shown to adsorb methane gas (Figure 4.27). All compounds displayed type-1 isotherm behaviour with no appreciable hysteresis. Saturation was not reached at 1 atm, the maximum pressure measured as indicated by the near constant gradient of the isotherm at this pressure. The compound with the highest uptake was **4.7**, the 4-pyridyl functionalised derivative. This showed an uptake of 26.2 cm^3/g, corresponding to a 28.3 v/v uptake. Again, compound **4.4** showed the lowest uptake. The gradient of this isotherm is also lower than the rest of the series at 1 atm, indicating that it may be reaching saturation in a closed or partially closed state, and again has not reached its open state.

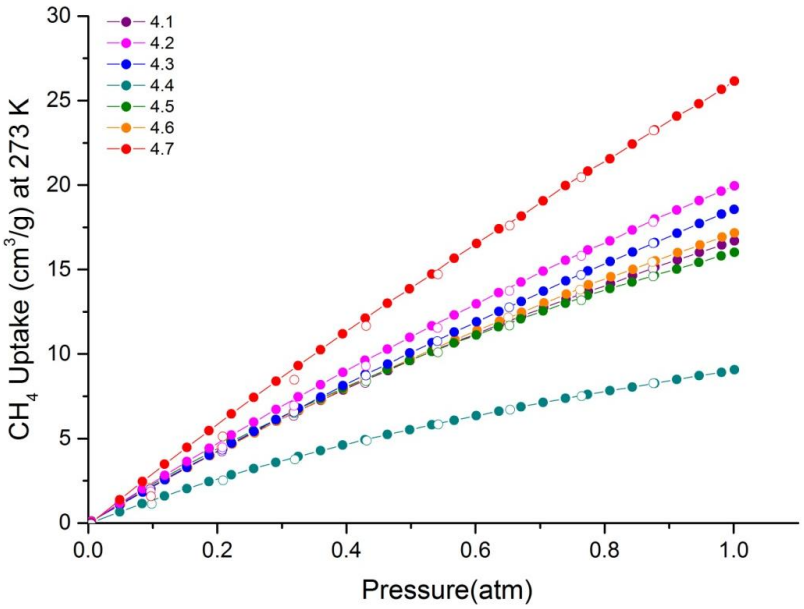

Figure 4.27: *Methane adsorption (filled symbols) and desorption (open symbols) isotherms for compounds* ***4.1***-***4.7*** *at 273 K.*

At 298 K all compounds were again shown to adsorb methane gas (Figure 4.28). Uptake values at this temperature are approximately half of what was observed at 273 K. The uptake of methane with respect to functional group at this temperature follows the same trend as that seen at 273 K, with one notable exception, the dramatic relative drop of **4.7**. At 273 K it displayed substantially higher uptake than the remainder of the series, while at 298 K it displayed average adsorption. This may be because at lower temperatures, the pyridine-methane interactions play a more significant role in the adsorption.[280] At both temperatures, **4.2** and **4.3** showed consistently good methane uptake.

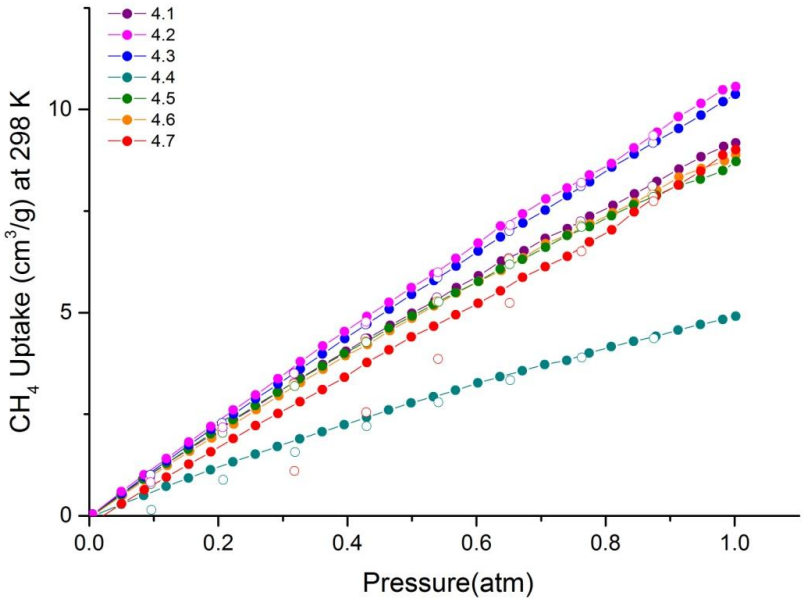

Figure 4.28: *Methane adsorption (filled symbols) and desorption (open symbols) isotherms for compounds* ***4.1****-****4.7*** *at 298 K.*

Due to the applications of methane storage, maximum capacities are often quoted at high pressures. A pressure of 34.5 atm has been widely used as a standard for evaluating adsorbents for storage, as this represents the maximum pressure achievable by most inexpensive single-stage compressors.[72] As the pressure of these experiments was limited to 1 atm, finding comparable literature values was difficult. A copper MOF, based upon the ligand 4,4′-(hexafluoroisopropylidene)-bis(benzoic acid) (H_2hfipbb) showed a similar uptake to the series reported here at 1 atm and 273 K of 17.2 cm^3/g (27.8 v/v).[281]

Adsorption at both 273 and 298 K results in linear isotherms (Henry's adsorption isotherms), indicating the uptake is proportional to the pressure of the gas. This is typically observed at low surface coverage, where the molecule-surface binding dominates and the molecule-molecule interactions are negligible consistent with the low volumetric uptake of less than 30 cm^3/g. Higher uptakes are expected at higher pressures of methane.

At both 273 and 298 K, activated compound **4.4** shows adsorption, albeit at a lower volume than the rest of the series. It is thought that this compound adopts a closed state upon activation, where only limited sorption is possible. Like N_2 and H_2, CH_4 does not trigger a change from the closed to open state of the framework. Higher pressures of CH_4 may be required for this to occur.

The isosteric heats of adsorption (Q_{st}) of compounds **4.1**-**4.7** were calculated from the methane adsorption isotherms at 273 and 298 K (Figure 4.29, Table 4.4). The Q_{st} values for methane at zero coverage (at the onset of adsorption) are in the range 17.9-25.5 kJ/mol. This is at the high end for MOFs,[117] especially considering no open metal sites are present.

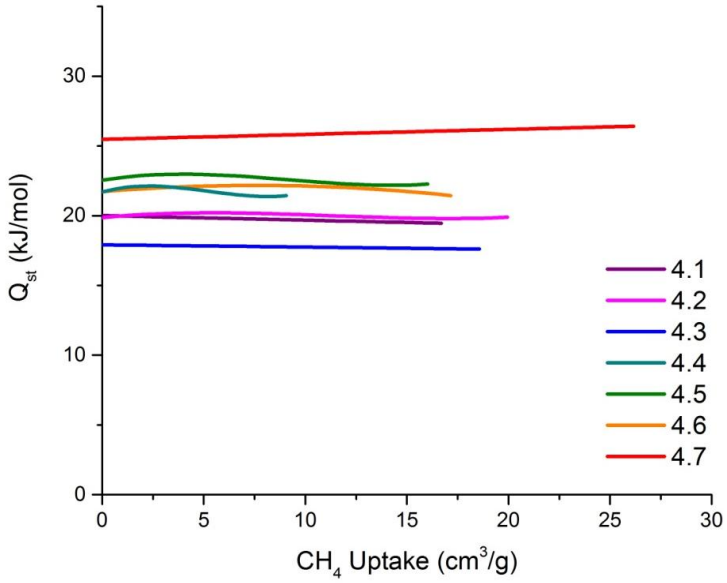

Figure 4.29: *Plot of the isosteric heat of adsorption versus uptake of methane in compounds* ***4.1****-****4.7****.*

The high heat of adsorption in this series of MOFs is attributed to the fit of methane (kinetic diameter 3.8 Å) within the pores. The channels in the MOFs are approximately 9 x 9 Å and

so, in a two dimensional cross-section, would fit four methane molecules, one in each corner. In corners, molecules can interact with two potential surfaces, increasing binding interactions. As saturation was not reached within at the measured temperatures below 1 atm, no decrease in Q_{st} is observed as the channels are still taking up methane in their preferential adsorption sites. The relatively flat plot of Q_{st} versus uptake indicates that surface-methane interactions are much more important than methane-methane interactions in this pressure range.

Compound	Formula	Gas	T (K)	P (atm)	Uptake (cm^3/g)	v/v	Q_{st} (kJ/mol)	Ref.
4.1	[Zn(**L4.1**)]	CH_4	273	1	16.7	17.8	20.0	
			298	1	9.2	9.8		
4.2	[Zn(**L4.2**)]	CH_4	273	1	19.2	22.0	19.9	
			298	1	10.6	11.7		
4.3	[Zn(**L4.3**)]	CH_4	273	1	18.6	21.2	17.9	
			298	1	10.4	11.9		
4.4	[Zn(**L4.4**)]	CH_4	273	1	9.1	10.6	21.7	
			298	1	4.9	5.8		
4.5	[Zn(**L4.5**)]	CH_4	273	1	16.0	17.2	22.5	
			298	1	8.7	9.4		
4.6	[Zn(**L4.6**)]	CH_4	273	1	17.2	18.4	21.7	
			298	1	8.9	9.5		
4.7	[Zn(**L4.7**)]	CH_4	273	1	26.2	28.3	25.5	
			298	1	9.0	9.7		
Cu-MOF	$[Cu(Hhfipbb)_2]$	CH_4	273	1	17.2	27.8	24.1	[281]
			298	1	10.5	17.0		
IRMOF-1	$[Zn_4O(BDC)_3]$	CH_4					12.2	[131]
Zn-MOF-74	$[Zn_2(dobdc)]$	CH_4					18.3	[130]
Ni-MOF-74	$[Ni_2(dobdc)]$	CH_4					20.2	[130]
HKUST-1	$[Cu_2(BTC)_{4/3}]$	CH_4					21.1	[282]

Table 4.4: *Maximum uptake of methane gas by activated samples of compounds **4.1**-**4.7** at 273 and 298 K and 1 atm. The isosteric heat of adsorption at zero coverage is calculated from virial fitting of both 273 and 298 K isotherms for each compound. The Q_{st} value is compared to literature examples. Calculations based on crystal density derived from XRD and containing no solvent. H2hfipbb = 4,4'-(hexafluoroisopropylidene)-bis(benzoic acid), BDC = benzene-1,4-dicarboxylate, dobdc = 2,5-dioxidobenzene-1,4-dicarboxylate, BTC = benzene-1,3,5-tricarboxylate.*

4.5.4 Carbon Dioxide Adsorption

The carbon dioxide adsorption isotherms of **4.1**-**4.7** were measured at 195 K, 273 K, and 298 K. All compounds showed sorption behaviour, however, subtle differences were observed between samples. Compounds **4.1**-**4.7** showed good adsorption at 195 K, with high volumetric uptakes at low pressure and negligible hysteresis (Figure 4.30). Care must be taken when measuring carbon dioxide isotherms at 195 K. At this temperature, the gas undergoes deposition to become a solid at pressures approaching 1 atm. To avoid effects relating to this, isotherms were measured up to a maximum pressure of 0.6 atm.

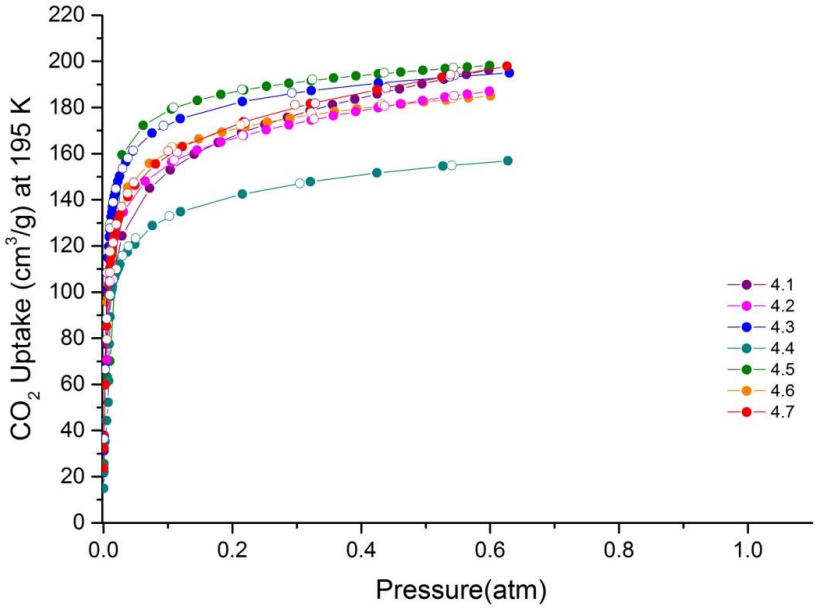

Figure 4.30: *Carbon dioxide adsorption (filled symbols) and desorption (open symbols) isotherms for compounds* ***4.1***-***4.7*** *at 195 K.*

The adsorption of carbon dioxide at 195 K is rapid and results in a steep gradient in the adsorption section of the isotherm. After this, each isotherm starts to plateau at approximately 0.15 atm indicating that filling of the micropores is complete. Subsequent increases in adsorption are attributed to surface adsorption. Compounds **4.1**-**4.3** and **4.5**-**4.7** show very similar maximum uptake volumes at 0.6 atm, all slightly higher than **4.4.** This compound still shows a high volumetric uptake which is indicative of the sample being microporous and therefore in its 'open' state. The fact that this behaviour is only seen with carbon dioxide supports the proposition that a gating mechanism plays a part in the low

nitrogen, hydrogen and methane uptake volumes. Gases with dipoles or quadrupoles are known to initiate pore opening mechanisms at lower pressures than non-polar gases.[102,272] This may be due to the stronger gas-framework interactions being able to overcome the intra-framework interactions.[283] The lower maximum uptake may be due to the overall reduced void space within the framework due to the bulky nitrophenyl substituent.

Although all appear to be type-1, **4.4** and **4.5** exhibit stepped isotherms for CO_2 adsorption at 195 K. The steps occur at very low pressures and are best visualised using a logarithmic pressure scale (Appendix 5). Compounds **4.1**-**4.3** and **4.6**-**4.7** display type-1 isotherms within the pressure range measured. It is not clear whether a step would be observed if lower pressures could be measured.

At 273 K, all samples again show uptake of carbon dioxide, although lower values were measured, an expected consequence of the higher measurement temperature (Figure 4.31). At this temperature compounds **4.1**-**4.3** and **4.6**-**4.7** show type-1 isotherms. The isotherms indicate that the adsorption is more gradual, consistent with the lower gradient of the micropore filling region of the isotherm. The chlorophenyl functionalised **4.3** shows the highest uptake, followed by **4.6** and **4.7** with almost identical shaped isotherms, and then the less polar **4.1** and **4.2** absorbing lower amounts.

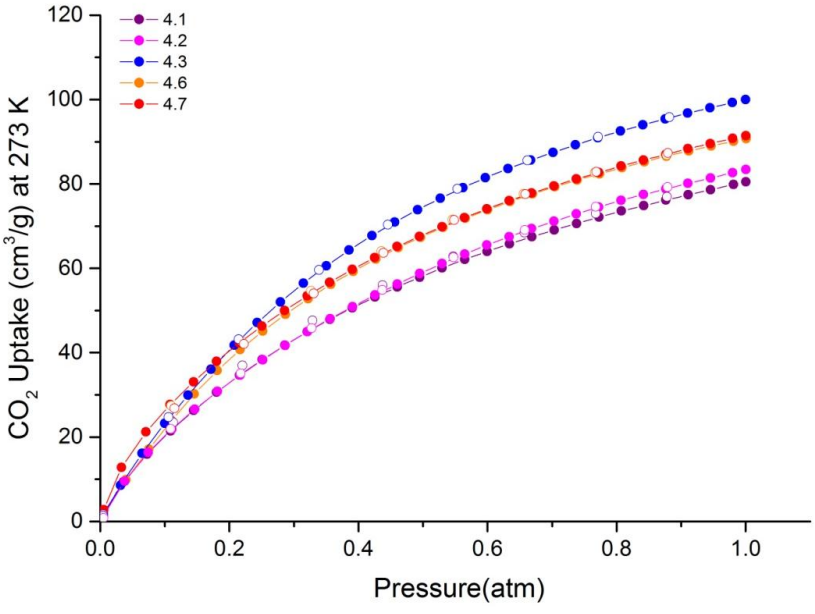

Figure 4.31: *Carbon dioxide adsorption (filled symbols) and desorption (open symbols) isotherms for compounds* ***4.1***-***4.3*** *and* ***4.6***-***4.7*** *at 273 K.*

Compounds **4.4** and **4.5** show type-4 isotherms with hysteretic behaviour (Figure 4.32). Although this type of isotherm is traditionally associated with mesoporous materials (pore diameter 20-100 Å),[284] larger than the 9 Å diameter observed from X-ray crystallography, it can also be indicative of structural changes within a microporous material.[99] The total uptake of these two compounds at 1 atm, is approximately equal to that seen in the non-hysteretic samples (Table 4.5).

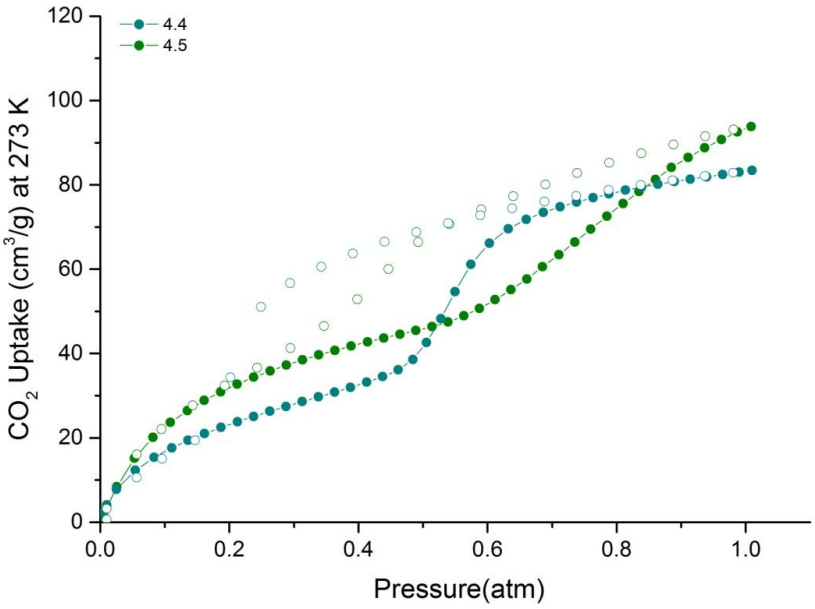

Figure 4.32: *Carbon dioxide adsorption (filled symbols) and desorption (open symbols) isotherms for compounds* ***4.4****-****4.5*** *at 273 K.*

The first adsorption step for **4.4** corresponds to the adsorption of 0.8 molecules of carbon dioxide per formula unit (0.46 atm). At 1 atm, 1.9 molecules are adsorbed per formula unit. For compound **4.5**, the steps in adsorption correspond to 1.0 molecules of carbon dioxide at 0.51 atm, and 2.0 molecules at 1 atm. The fact that the steps correspond to half filling of the microporous compounds could be symptomatic of the gating mechanism.

It is postulated that upon activation, compound **4.4** adopts a closed, non-porous state. In the presence of low pressure CO_2 the framework opens to let one molecule of CO_2 per formula unit into the one dimensional channels. The high quadrupole moment of CO_2 allows this

gas to overcome the intra-framework interactions and prise the channel open. This corresponds to an intermediate sorption state, which requires a higher pressure of CO_2 to transform the framework into its open state and show similar adsorption to the rest of the series.

A similar mechanism for **4.5** can be imagined except that it starts from the intermediate sorption state. This is based on the observation of adsorption of other gases and the steeper initial gradient for the adsorption of CO_2 at 273 K. Once one molecule of CO_2 per formula unit is present within the framework, the strong framework-gas interactions lock it in the intermediate state until higher pressures are reached making it show a stepped isotherm, rather than the gradual isotherms seen for **4.1**-**4.3** and **4.6**-**4.7**.

At 298 K, all compounds displayed gradual uptake of carbon dioxide (Figure 4.33). Contrasting the observations at 195 and 273 K, all compounds displayed type-1 isotherms at this temperature. At 1 atm, there was a range of maximum uptake values, **4.3** showing the highest adsorption (61.1 cm^3/g), and **4.4** showing the lowest (31.8 cm^3/g).

The two samples that exhibited hysteretic behaviour at 273 K, **4.4** and **4.5**, display the lowest total uptake at 1 atm. In the low pressure range, these samples show similar uptake to the rest of the series, but start to plateau at a much lower pressure. This suggests they are only reaching an intermediate adsorption state. Potentially a stepped increase in adsorption would be observed for these two compounds at 298 K at pressures above 1 atm. For samples that showed type-1 isotherm behaviour at 273 K, the same trend of maximum uptake is retained at 298 K.

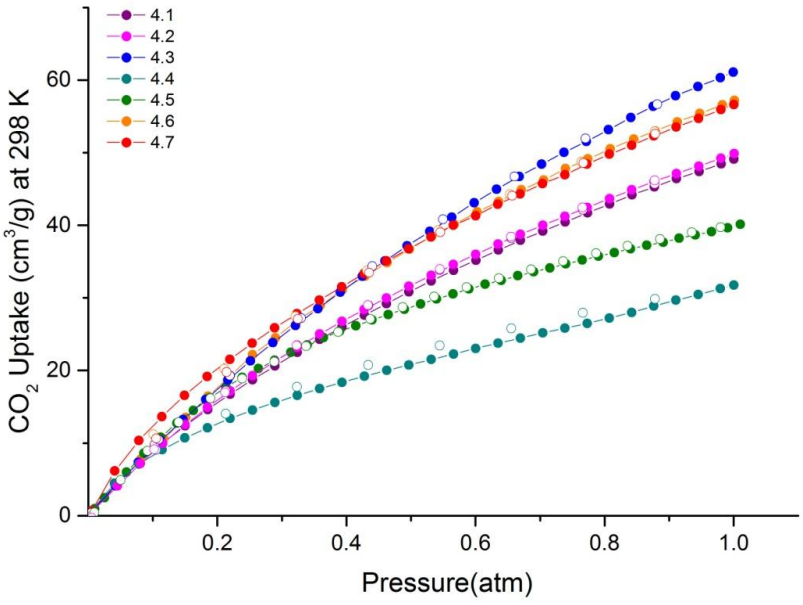

Figure 4.33: *Carbon dioxide adsorption (filled symbols) and desorption (open symbols) isotherms for compounds* ***4.1****-****4.7*** *at 298 K.*

The step observed in the CO_2 adsorption isotherms for **4.4** and **4.5** varies with temperature, occurring at higher pressures at higher temperatures. This feature has been reported for other dynamic frameworks.[270] The stepped nature of these isotherms is likely caused by shearing deformations from a 'closed' state where only limited adsorption is possible, to an 'open' state which likely resembles the structure obtained from X-ray crystallography. Similar shaped isotherms have been reported for flexible networks with one dimensional channels switching from closed pore (CP) to open pore (OP) states.[102,285] The temperature dependence of the hysteretic behaviour of **4.4** and **4.5** is an interesting observation, and warrants further investigation.

The fact that **4.4** showed similar maximum carbon dioxide uptake at 1 atm to the rest of the series for isotherms measured at 195, 273 and 298 K (measured after, before and after the nitrogen isotherm at 77 K respectively), indicates that **4.4** adsorbs other gases very poorly indeed. The size of the gas cannot be blamed for this affect, as although nitrogen gas has a larger kinetic diameter than carbon dioxide (3.64 vs 3.30 Å), slight adsorption of methane is observed (kinetic dimeter of 3.80 Å) whilst hydrogen is not (kinetic diameter of 2.89 Å). A

more logical argument is to assume it is related to the high quadrupole moment of carbon dioxide overcoming the intra-framework interactions and opening the one-dimension channels, allowing gas to fill the porous framework. Recent reports have shown similar behaviour of limited nitrogen adsorption at 77 K, yet moderate to high carbon dioxide uptake at higher temperatures.[286-287]

The isosteric heats of adsorption (Q_{st}) of compounds **4.1**-**4.3** and **4.6**-**4.7** were calculated from the carbon dioxide adsorption isotherms at 273 and 298 K. The Q_{st} values for CO_2 at zero coverage (at the onset of adsorption) are in the range of 27.5-31.5 kJ/mol which is higher than that observed for the adsorption of methane. The increased binding energy of carbon dioxide compared to methane is attributed to the polar nature of this gas. These values are typical for MOFs without free alkyl amines, or open metal sites.[288]

The heat of adsorption of CO_2 decreases with an increase in loading. As the pores are filled with gas the strongest binding sites are occupied, and the enthalpy of adsorption for subsequent gas molecules decrease.

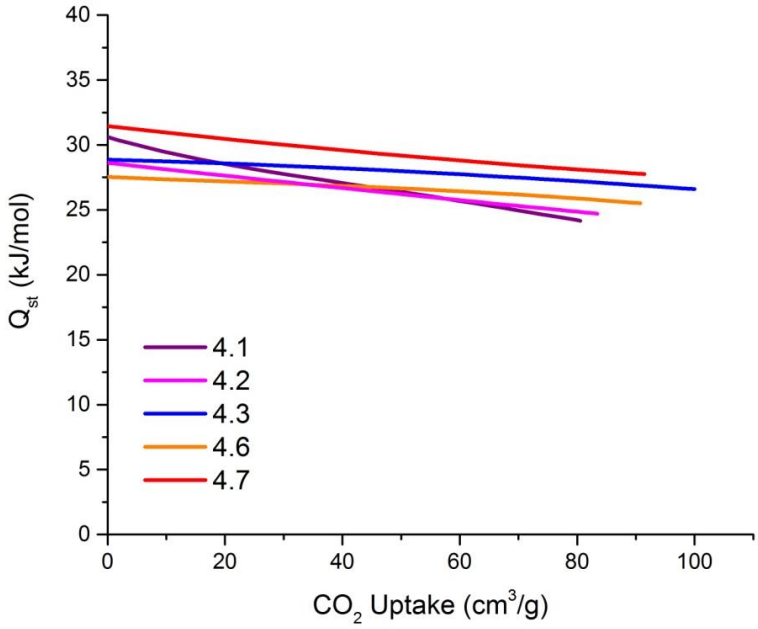

Figure 4.34: *Plot of the isosteric heat of adsorption of carbon dioxide in compounds* ***4.1***-***4.3*** *and* ***4.6***-***4.7****.*

Compound	Formula	Gas	T (K)	P (atm)	Uptake (cm^3/g)	V/v	Q_{st} (kJ/mol)	Ref.
4.1	[Zn(**L4.1**)]	CO_2	195	0.6	196.3	209.4	30.6	
			273	1	80.5	85.9		
			298	1	49.1	52.4		
4.2	[Zn(**L4.2**)]	CO_2	195	0.6	187.0	206.5	28.6	
			273	1	83.4	92.1		
			298	1	49.9	55.0		
4.3	[Zn(**L4.3**)]	CO_2	195	0.6	195.0	222.8	28.9	
			273	1	100.0	114.3		
			298	1	61.1	69.8		
4.4	[Zn(**L4.4**)]	CO_2	195	0.6	157.0	184.4	-	
			273	1	83.4	98.0		
			298	1	31.8	37.3		
4.5	[Zn(**L4.5**)]	CO_2	195	0.6	198.2	213.2	-	
			273	1	93.8	101.0		
			298	1	40.1	43.2		
4.6	[Zn(**L4.6**)]	CO_2	195	0.6	185.0	198.7	27.5	
			273	1	90.7	97.4		
			298	1	57.2	61.4		
4.7	[Zn(**L4.7**)]	CO_2	195	0.6	197.9	214.1	31.5	
			273	1	91.4	98.9		
			298	1	56.6	61.2		
IRMOF-1	$[Zn_4O(BDC)_3]$	CO_2	296	1	47.0		34	[274]
Ni-MOF-74	$[Ni_2(dobdc)]$	CO_2	-				42	[289]
HKUST-1	$[Cu_2(BTC)_{4/3}]$	CO_2	-				35	[290]

Table 4.5: *Maximum uptake of carbon dioxide by activated samples of compounds **4.1-4.7** at 195 K and 0.6 atm, and 273 and 298 K at 1 atm. The isosteric heat of adsorption at zero coverage is calculated from virial fitting of both 273 and 298 K isotherms for each compound. The Q_{st} value is compared to literature examples. Calculations based on crystal density derived from XRD containing no solvent. BDC = benzene-1,4-dicarboxylate, dobdc = 2,5-dioxidobenzene-1,4-dicarboxylate, BTC = benzene-1,3,5-tricarboxylate.*

For carbon dioxide capture applications, there must be a high selectivity for CO_2 over other components of the gas mixture. This selectivity can originate from three main mechanisms. The first is size based selectivity where only molecules with a small enough kinetic

diameter are able to diffuse into the pores. This has many drawbacks such as the small pores may limit the diffusion of gases through the framework, and potential adsorbates may have very similar sizes, *e.g.* nitrogen and carbon dioxide. The second is based on chemisorption: the reaction of CO_2 with amines to form carbamates, however, this suffers from the high energy cost of removing CO_2 and regenerating the starting material. The third and more practical separation method is based on the affinities of certain adsorbates with the material. MOFs are suitable for this as they have high surface areas and can be functionalised with polar groups easily.

For CO_2/N_2 separation relevant to post-combustion CO_2 capture, the high quadrupole moment of this gas can be used to selectively remove it from the system. Existing power plants generate a flue gas that is at atmospheric pressure and typically has a CO_2 concentration of less than 15 %.[291] The adsorptive selectivity for CO_2 from a gas mixture can be estimated from the experimental single-component gas adsorption isotherms. The selectivity factor is defined as the molar ratio of the adsorbed quantities at the relevant partial pressures of the gases.[288] For ease of comparison with literature values, a hypothetical flue gas comprising of 75 % nitrogen and 15 % carbon dioxide at 298 K will be used. Although, realistically the temperature of this gas would be closer to 350 K, uptake of both gases decreases at higher temperatures and hence adds greater uncertainty to each measurement. As the thermal energy of the gas molecules increase the difference in binding energies of CO_2 and N_2, which remain reasonably constant with temperature becomes less significant and the selectivity should consequently decrease.

In Table 4.6 the selectivity factors calculated from individual single-component isotherms for carbon dioxide and nitrogen are reported. Compounds **4.1**-**4.3** and **4.5**-**4.6** display values in the range of 30-50 indicating high selectivity. Compound **4.4** shows an astonishing selectivity factor, twenty fold greater than the rest of the series. It can be seen from comparison of nitrogen uptakes that this arises from the atypically low adsorption of nitrogen gas at 298 K. Due to the low absorbance of nitrogen at this temperature, small deviations in this measurement can greatly affect the selectivity factor. This means these values should only be seen as an approximation. More intensive calculation methods, such as those based on the Ideal Adsorbed Solution Theory (IAST)[292] or breakthrough experiments, would provide more accurate results. As this equation does not take into

consideration the competition of gas molecules for the pore surface, it is not expected to be a perfect predictor of actual behaviour in a mixed gas experiment. It does, however, provide an indication and a parameter that can be compared to a wide range of MOFs. The series of MOFs presented here appear to be more selective for CO_2 over N_2 than MOF-177 and are at least as selective as Ni-MOF-74.

Compound	**Formula**	**T (K)**	**CO_2 Uptake at 0.15 atm (wt%)**	**N_2 Uptake at 0.75 atm (wt%)**	**Selectivity**	**Ref.**
4.1	[Zn(**L4.1**)]	298	2.4	0.16	50	
4.2	[Zn(**L4.2**)]	298	2.4	0.22	30	
4.3	[Zn(**L4.3**)]	298	2.53	0.23	39	
4.4	[Zn(**L4.4**)]	298	2.06	0.01	1067	
4.5	[Zn(**L4.5**)]	298	2.77	0.28	30	
4.6	[Zn(**L4.6**)]	298	2.59	0.28	30	
4.7	[Zn(**L4.7**)]	298	3.15	-	[a]	
Ni-MOF-74	$[Ni_2(dobdc)]$	298	16.9	2.14	30	[288]
HKUST-1	$[Cu_2(BTC)_{4/3}]$	293	11.6	0.41	101	[288]
MOF-177	$[Zn_4O(BTB)_3]$	298	0.6	0.39	4	[293]

Table 4.6: *Gravimetric uptake and selectivity factors for activated compounds **4.1**-**4.7** compared to literature values. dobdc = 2,5-dioxidobenzene-1,4-dicarboxylate, BTC = benzene-1,3,5-tricarboxylate, BTB = 1,3,5-benzene-tribenzoate. [a] Unfortunately the nitrogen adsorption isotherm for 4.7 was not measured at 298 K, and hence a selectivity factor for this temperature could not be calculated.*

Based on this sorption data, it is obvious that activated **4.4** is a selective sorbent for carbon dioxide. The very low adsorption of non-polar gases by **4.4** stands out as one of its most interesting properties. The adsorption process for this compound is probably influenced by a gating mechanism and further work to examine the mechanism of this behaviour is suggested.

4.5.5 Effect of Aging on Gas Sorption Behaviour

One of the major drawbacks of MOFs, particularly those composed of labile metal ions such as zinc(II), is their stability with respect to water. To be of wider use they must not only by thermally stable, but hydrolytically stable.

To test the stability of this series of compounds three samples (**4.1**, **4.5**, **4.6**) were left out in the lab atmosphere post-activation for two weeks. The adsorption of carbon dioxide at 273 K was then re-measured after a further activation step (Figure 4.35). It can be seen that the maximum uptake at 1 atm has approximately halved after this time. Compound **4.5** has also lost its hysteresis. This decrease in uptake is attributed to the humidity in the air causing framework collapse due to hydrolysis of the zinc-carboxylate bond. The stability of the terpyridine-zinc coordination is assumed. Unfortunately, further analysis on aged samples was not performed to determine the breakdown products.

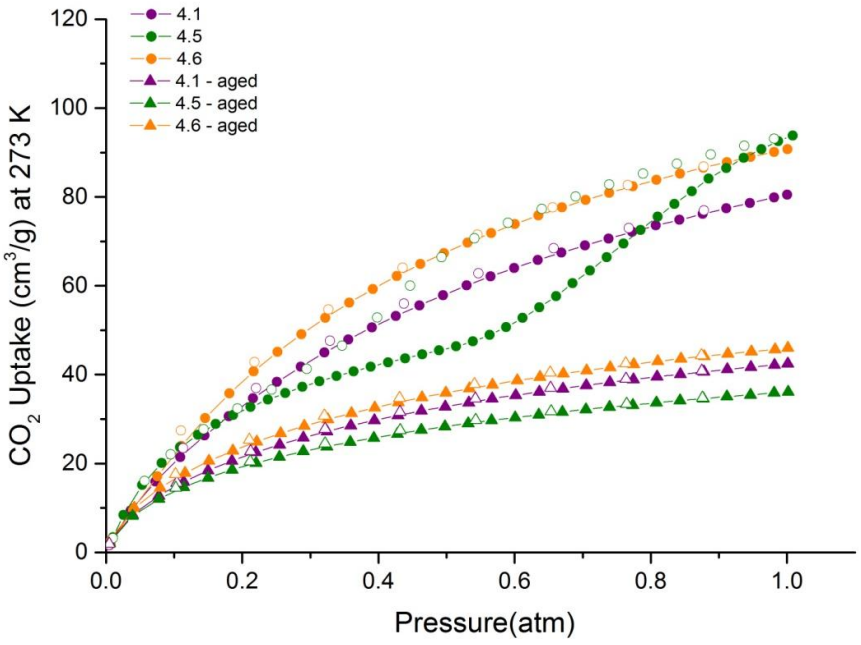

Figure 4.35: *Carbon dioxide adsorption (filled symbols) and desorption (open symbols) isotherms for samples of* ***4.1****,* ***4.5*** *and* ***4.6*** *that have been activated directly after removing from solution (circles) and samples that have been left open to the atmosphere in a lab environment for two weeks post activation (triangles). To reactivate the samples after aging, they were heated under vacuum at 100 °C for 18 hours.*

The uniform decrease in adsorption ability shows these are not stable out of solution once they have been activated. The loss of hysteresis is interesting, as it shows that the phenomenon is dependent on a pristine structure.

4.5.6 Summary of Gas Sorption Behaviour

Low temperature nitrogen experiments showed compound **4.1**-**4.3** and **4.5**-**4.7** to be microporous, with surface areas of approximately 800 m^2/g. Compound **4.4** showed very little uptake, the shape and magnitude of the isotherm indicating the sample was not microporous. Although one reason for the low uptake of nitrogen at 77 K could be because at this low temperature the gas has very little thermal energy and clusters on the crystal surface blocking the one-dimensional microporous channels, a gating mechanism was proposed as **4.4** also showed poor adsorption of nitrogen at the higher temperature of 195 K.

The six samples that showed nitrogen uptake also showed hydrogen uptake at cryogenic temperatures. The uptakes were approximately 1.4 % by weight at 77 K and 1 atm, comparable to other MOFs reported in the literature. Again, compound **4.4** showed minimal uptake which is attributed to the gating mechanism described for nitrogen adsorption.

The samples adsorbed methane at both 273 K and 298 K at pressures below 1 atm. Surprisingly compound **4.4** showed moderate uptake of this gas. The calculated heat of adsorption of compounds **4.1**-**4.7** is between 17.9 and 25.5 kJ/mol which is similar to frameworks that contain open metal sites. The high Q_{st} is attributed to the size of the channels within the framework allowing for efficient packing of gas molecules.

All compounds showed high carbon dioxide adsorption at 195 K indicating all samples were microporous. At 273 K, five samples showed typical type-1 isotherms, and two samples showed type-4 hysteretic isotherms. The type-4 isotherm behaviour is attributed to a gating mechanism. Compounds **4.1**-**4.3** and **4.6**-**4.7** showed moderate heats of adsorption, between 37.5 and 31.5 kJ/mol, comparable with other MOFs. All samples show good selectivities for this gas over N_2. Compound **4.4** showed an unprecedented selectivity of 1067 for CO_2 over N_2 due to its low absorbance of the latter.

Three compounds were examined to determine the effects of atmospheric air on this series of MOFs. After being allowed to sit out of solution post activation in a laboratory environment all three samples showed reduced CO_2 uptake at 273 K. This may be due to hydrolysis of zinc(II)-carboxylate bonds caused by humidity in the air.

Generally the aryl functional group in the 4'-position of the terpyridine-4,4"-dicarboxylic acid ligand showed little effect on the gas sorption behaviour of the resultant MOF. The notable exception to this is the 4-nitrophenyl functional group contained within **4.4** for which a gating mechanism was proposed. Although it remains unclear why this behaviour is observed for this sample, methods for the elucidation of this effect have been proposed.

4.6 Conclusions and Future Work

A series of ligands based upon the 2,2':6',2"-terpyridine-4,4"-dicarboxylic acid central core were synthesised via the Kröhnke methodology. A substituent was included in the 4'-position and in each case this was from a commercially available aromatic aldehyde. Modest yields were reported for this series of nine compounds.

Ligands H_2**L4.1**-H_2**L4.7** were reacted with zinc(II) nitrate in DMF to yield highly crystalline materials named **4.1**-**4.7**, respectively. Single crystal X-ray diffraction allowed their structures to be elucidated. All compounds crystallised in the same tetragonal space group and were shown to adopt isoreticular, interpenetrated frameworks based upon the **gis** topology. Despite being interpenetrated, significant potential void space was observed in the form of one-dimensional channels directed along the crystallographic *c*-axis. Although electron density was observed in these channels, the contents were not able to be modelled. Elemental analysis of as-synthesised compounds indicated that it is likely to be a mixture of solvents including DMF, formic acid and water.

The frameworks were shown to be stable to desolvation by a combination of PXRD, TGA, IR spectroscopy and elemental analysis. This allowed gas sorption measurements on the evacuated frameworks to be performed. The conserved topology, and similarity of channel sizes, means the differences in gas sorption behaviour can therefore be attributed to the functionality in the 4'-position of the terpyridine ligand. Nitrogen, hydrogen, methane and

carbon dioxide isotherms were measured at a range of temperatures up to 1 atm. Generally these compounds showed high surface areas, moderate gravimetric hydrogen adsorption, high heats of adsorption for methane and good selectivity for carbon dioxide over nitrogen. Interestingly, **4.4** showed little adsorption of nitrogen or hydrogen, which in concert with observing high CO_2 uptake led to a gating mechanism being proposed. Stepwise adsorption of carbon dioxide supported this. The structure of the closed form of this compound is unknown and further work into the gating mechanism is suggested. The synthesis of derivatives of terpyridine-4,4"-dicarboxylic acid containing electronic or sterically similar functional groups to that of **4.4** such as 4-cyanophenyl or 4-isopropylphenyl may also help determine the basis for this behaviour. Further experiments including variable pressure X-ray diffraction is suggested.

The series of terpyridine ligands can easily be extended due to the robust nature of the Kröhnke terpyridine synthesis. Extension of this isoreticular series of MOFs is envisioned and other functional groups, perhaps tailored for specific applications could be incorporated into the framework. These could include redox active groups, hydrophobic groups or fluorophores. Using bulkier residues at the 4'-position of terpyridine could prevent interpenetration of the framework which is likely to have a massive effect of the gas sorption behaviour of the resultant structure. Although this was attempted with the *o*-tolyl functional group, the torsion angle was not great enough to induce this effect. An even bulkier group such as mesitylene or anthracene derivative could achieve this. Potential functional groups are shown in Figure 4.36.

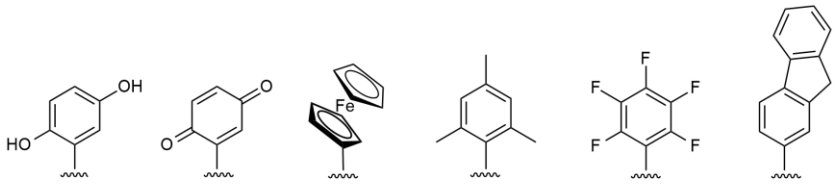

Figure 4.36: *Potential functional groups that could be included in terpyridine based MOFs.*

A combination of ligands could also be used in the synthesis of MOFs to incorporate more than one type of functionality within the pore structure. It has been shown that such multivariate MOFs can have properties significantly better than the sum of their parts.[294]

The conserved topology with respect to the functional group of the terpyridine ligand means there are no competing phases in mixed ligand systems. Due to the π-π stacking interaction between interpenetrated frameworks in this series of MOFs, the arrangement of different ligands within the framework may display interesting ordering behaviour (Figure 4.37).

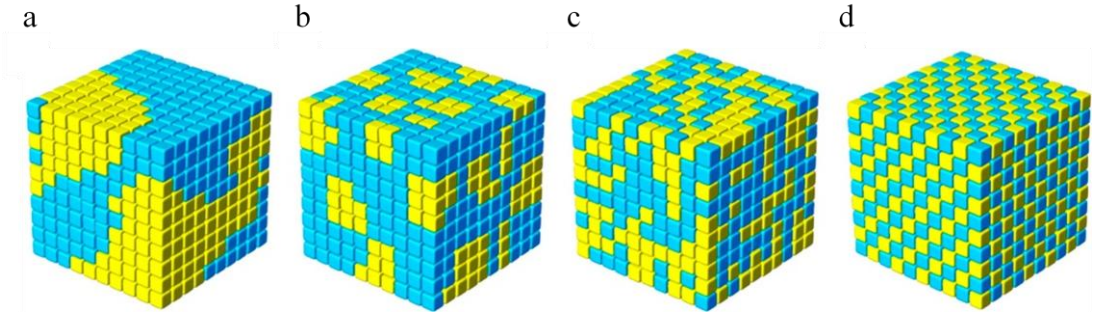

Figure 4.37: *Potential linker arrangement in multivariate MOFs. a) Large clusters, b) small clusters, c) random, d) alternating. Figure adapted from Yaghi et al.*[295]

Chapter 5

Phenolic Oximes: Towards Engineering Open Metal Sites in MOFs

5.1 Introduction

5.1.1 Phenolic Oximes in Chemistry

Oximes (an abbreviation of oxy-imine) are derived from aldehydes or ketones by their reaction with hydroxylamine. In this way, aldehyde groups create aldoximes, and keto groups ketoximes. These functional groups are amphiprotic in nature, having a slightly basic nitrogen atom and a mildly acidic hydroxyl group.[296] Phenolic oximes are defined as a phenol ring with an *ortho*-substituted aldoxime or ketoxime group.

Metal complexes of phenolic oxime based ligands have attracted renewed scientific interest over the past decades in the field of magneto-chemistry. The multiple bridging sites of the deprotonated functional group has led to the formation of many polynuclear first row transition metal clusters with interesting magnetic properties.[297] In particular, trivalent metal ions such as iron(III)[298-305] and manganese(III)[306-312] or a mixture thereof[313] have been focused on due to their slow magnetic relaxation and single molecule magnet behaviour. The nuclearity of these complexes ranges from two to ten.

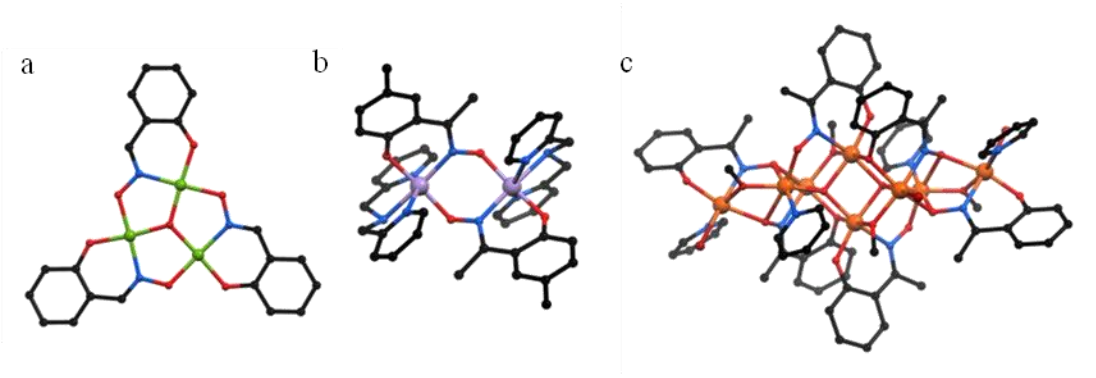

Figure 5.1: *Examples of polynuclear phenolic oxime based complexes. a) Trinuclear $[Cu_3(Hsalox)_3O]^+$ cation.[314] b) Dinuclear $[Mn_2(mhap)_2(dpa)_2]^{2+}$ cation.[307] c) octanuclear $[Fe_8O_2(OMe)_4(hap)_6Br_4(py)_4]$ complex.[302] H_2salox = salicylaldoxime, H_2mhap = 5-methyl-2-hydroxyacetophenoxime, dpa = di-(2-picolyl)-amine), H_2hap = 2-hydroxyacetophenoxime.*

Currently the main application for phenolic oxime based ligands is, however, in extractive metallurgy.[315] This relies on their selective coordination to copper(II) ions in acidic conditions due to the formation of an exceedingly stable $[CuL_2]$ type complexes. In these, a

pseudo-macrocyclic ring is created via hydrogen bonding around the metal ion which is thought to be the reason for their high stability. This ring, created by inter-ligand, intra-complex S(5) hydrogen bonding between the oxime proton of one ligand and the phenolate oxygen atom of the other (Figure 5.2a), is selective for copper(II) over other common metals found in ore due to the size of this metal ion and its fit within this pseudo-macrocyclic ring.[316] This binding mode is exceedingly stable for copper(II) even at low pH (Figure 5.2b).[317] It is estimated that between 20% and 30% of the world's copper is recovered using hydrometallurgical methods involving phenolic oxime extractants.[318]

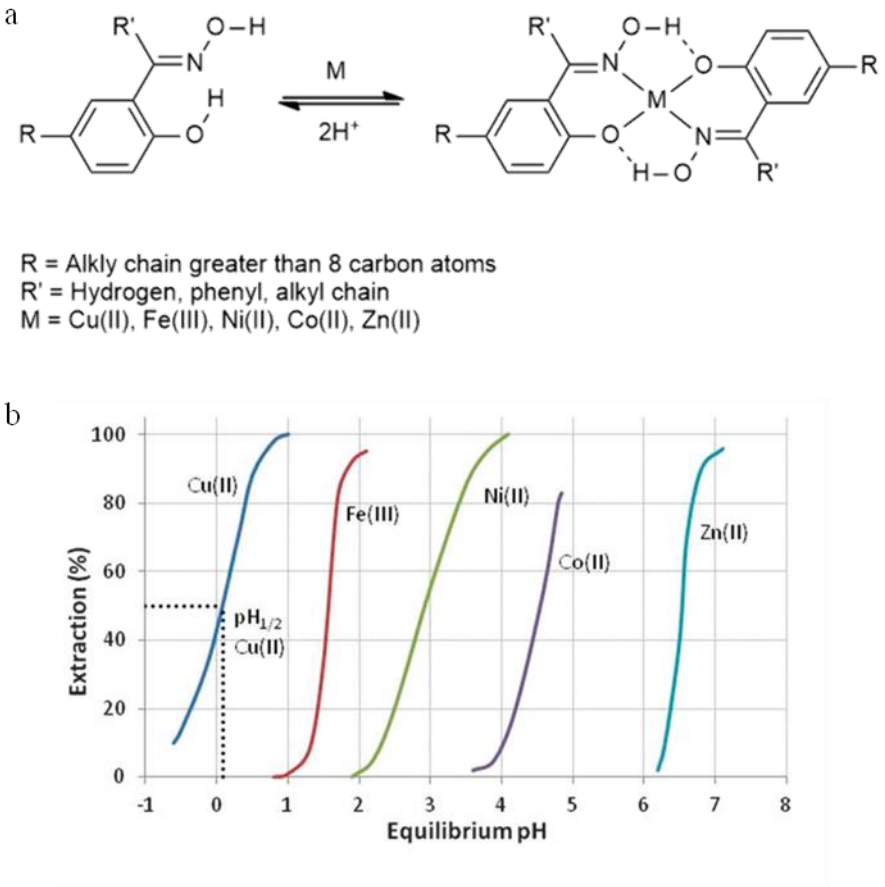

Figure 5.2: *Phenolic oxime complexes of selected transition metal ions. a) Bis-ligated complexes allows for the formation of a pseudo-macrocyclic ring around the metal ion. Substituents on the ligands are non-polar to increase hydrophobicity so the resultant neutral complex can be extracted into organic solvents. b) The pH dependance of metal ion extraction for a variety of cations with AcorgaP50 (R= C_9H_{19}, R'= H) a commercial phenolic oxime extractant. Metal ions with low $pH_{1/2}$ values, indicate they are capable of recovering metals from highly acidic feed solutions. Conversely, a weak extractant for metal cations is only capable of recovering metals at higher pH values. Graph adapted from Love* et al.[317]

The extraction process relies on the addition of sulfuric acid to copper containing ore to afford an aqueous solution containing a mixture of metal sulfate salts.[317] Treatment of this solution with a phenolic oxime ligand appended with non-polar functional groups leads to selective separation of dissolved copper from this aqueous mixture into an organic solvent layer. The neutral phenolic oxime copper(II) complex is soluble in hydrocarbon solvents, typically kerosene. It is therefore transferred out of the aqueous phase into the organic phase and is physically separated from the other metal ions which remain in the acidic aqueous solution. Subsequent treatment of the copper complex with strong acid releases free copper(II) ions back into aqueous solution which are then precipitated by electrolysis (Figure 5.3). The extractant ligand can then recycled back into the aqueous ore/sulfuric acid solution to repeat the process.

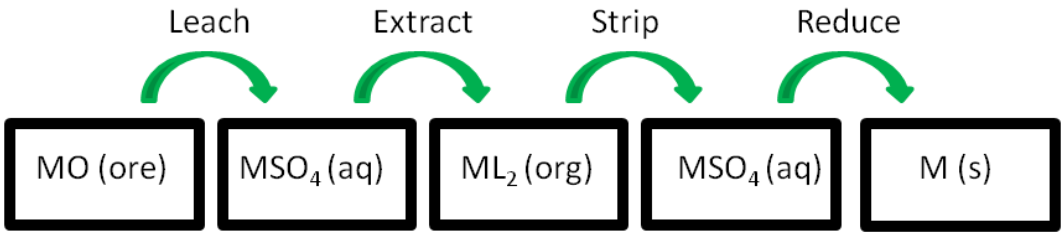

Figure 5.3: *Schematic representation of the extraction of metal ions from ore using organic soluble based extractants such as alkylated phenolic oximes. For copper extraction M = Cu, L = phenolic oxime ligand. Concentrated sulfuric acid is used to strip copper(II) from the extractant.*

On an industrial timeframe and scale, hydrolysis of commercial oxime based extractants under the aqueous/acidic conditions is possible and can diminish yields. To counter this additional hydroxylamine is be added to regenerate the active ligand. This can be done at the leaching, extracting or stripping phase of the process.[315]

Although shown as a mono-nuclear, square-planar complex in Figure 5.2a bis-phenolic oxime copper(II) complexes can exist as five-coordinate square based pyridyl dimers or coordination polymers due to the bridging potential of the coordinated phenolate oxygen atom. This can be prevented by the addition of bulky functional groups to the ligand.[319]

The strength of the pseudo-macrocyclic hydrogen bonding interactions can be tailored by the addition of functional groups in the 6-position of the phenolic oxime based ligand,[319]

and although these do not significantly affect the copper(II) binding strength to be industrially relevant,[320] they show that additional functionality can be included in these systems without detriment to the coordination motif.

In the mid 90s, Linert *et al.* showed the spin state of bis-phenolic oxime nickel(II) complexes were dependent on the solvent.[321] The magnetic susceptibilities of the nickel(II) ion, and chemical shift of the aldoxime protons of [Ni(Hsalox)$_2$] (H_2saldox = salicylaldoxime) in $CDCl_3$ were shown to change with increasing DMSO concentrations. This indicated an equilibrium between the diamagnetic square planar complex and the paramagnetic octahedral solvate [Ni(saldox)$_2$(DMSO)$_2$]. In effect the complex is able to act as a sensor for coordinating solvents, the output being a magnetic response. It has been shown that addition of other donor molecules such as dioxane, pyridine and cyclic amines also elicit a similar response.[322-324]

The properties of phenolic oxime complexes make them ideal targets to be incorporated into MOFs.

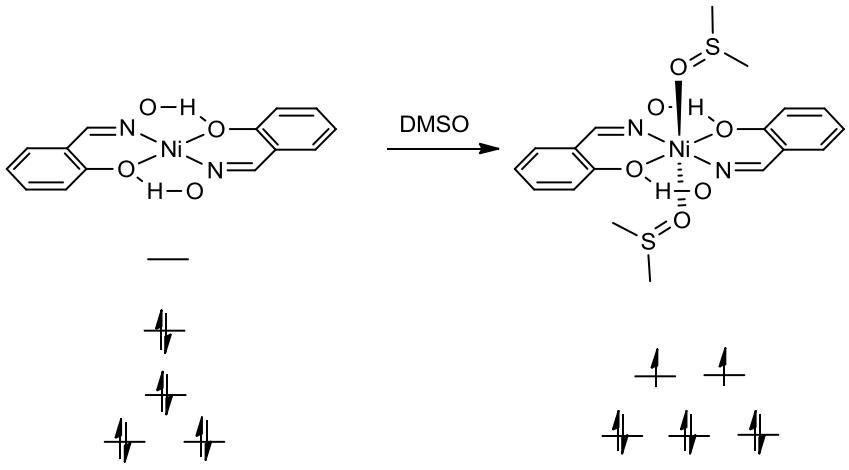

Figure 5.4: *Spin state of of bis-phenolic oxime nickel(II) complexes in solution can be modified by addition of coordinating analytes. such as DMSO.*[321]

5.1.2 Incorporation of phenolic oximes in MOFs

Examination of the structure of the extractant complex, and the extractive metallurgy process highlight several key properties of copper(II) phenolic oxime complexes that make

them ideal candidates as metalloligand building units in the synthesis of MOFs. Copper(II) complexes of phenolic oximes have a strong, reproducible coordination mode; are stable to harsh acidic conditions; have an anti-parrallel arrangement of ligands around a metal centre; a range of functional groups can be appended to the ligand; and potentially contain open metal sites of the resultant square-planar complex.

The strength and reproducibility of the coordination mode, even in acidic conditions means that as a metallo-ligand, copper(II) phenolic oxime complexes will not degrade and retain their structure in the typically acidic conditions used for MOF synthesis. The anti-parallel arrangement of ligands mean they can be used in the formation of linear bridging struts between metallic nodes. Due to this linear, planar structure it is proposed that phenolic oxime based ligands functionalised with carboxylic acid moieties could act as linear dicarboxylate linkers in the synthesis of MOFs.

Organic linkers such as terephthalic acid[325] or metalloligand 1,2-cyclohexanediamine-N,N′-bis-(3-tert-butyl-5-(carboxyl)salicylide[326] have their divergent coordinating groups anti-parallel and in the same line (Figure 5.5a). This arrangement is unachievable in phenolic oxime complexes due to the offset nature of the coordination site. As such, potential divergent coordination sites can be anti-parallel, but will be offset relative to each other (Figure 5.5c). Ligands with offset carboxylate groups can still act as linear linkers, the offset nature being accounted for by an undulating pattern of linkers within the MOF. Examples of this behaviour include fumaric acid,[327] 2,6-napthalenedicarboxylic acid in IRMOF-8,[56] and trans-4,4′-stilbene dicarboxylic acid[328] (Figure 5.5b). Compared to these, phenolic oxime complexes functionalised with carboxylic acid residues are expected be offset by a greater degree, however, this feature is not envisioned to be an issue in the construction of porous materials based upon such systems.

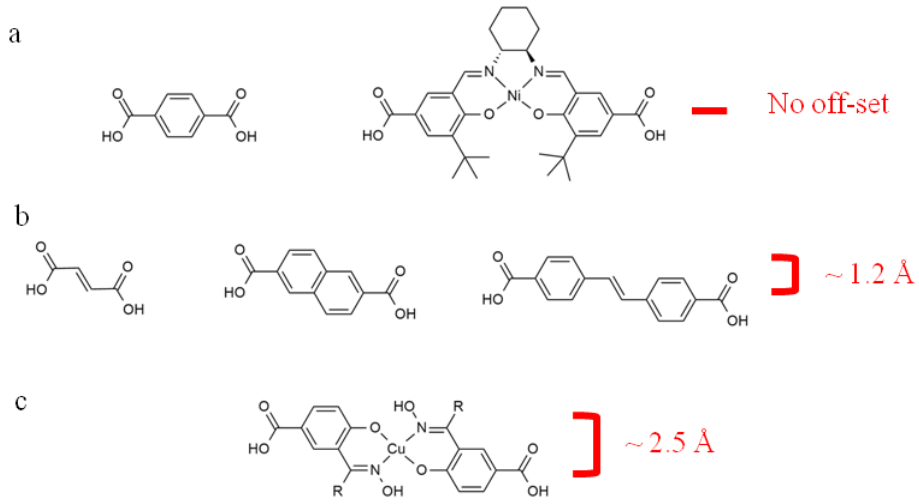

Figure 5.5: *Examples dicarboxylic acid ligands used in the construction of metal-organic frameworks showing no off-set (a), and approximately 1.2 Å off-set (b) between carboxylic acid moieties. c) Proposed phenolic oxime ligand with an estimated 2.5 Å off-set of carboxylic acid moieties.*

The phenolic oxime can also be modified in other ways to add more functionality to the potential framework. These could be included to tailor the properties of resultant MOFs and could include alkyl, nitro, amine, halogen and other functional groups.

Open metal sites are introduced into framework materials in two main ways. The first is through the removal of coordinated solvent molecules from the metallic nodes of the MOF. These are normally removed thermally, in vacuo or by washing with supercritical CO_2. Only when the framework retains its porosity when these solvents are removed it is classed as having open metal sites. This method has proved successful in several families of MOFs including the copper(II) paddlewheels of HKUST-1[329-330] and the one-dimensional metal oxide chains of the MOF-74 series.[58] The second is to include metal ions within the organic linkers of the framework. This metallo-ligand approach has the advantage of not only allowing some degree of predictability in having open metal sites, it means the metal ions are located in solvent accessible areas of the framework instead of hidden in the nodes or corners. Some well known metallo-ligands that have been incorporated into frameworks are based upon salen[91,326,331] and porphyrin[97-98,332-333] complexes.

It has been shown that gas, and in particular carbon dioxide,[334] hydrogen,[335] olefins,[336] and oxygen gas[89] are preferentially adsorbed near open metal sites in MOFs vastly increasing

their storage capacity. As it interacts with the gas, the choice of metal ion within isostructural frameworks directly affects the sorption properties.[334] Open metal sites within frameworks have also been used as heterogeneous Lewis acid catalysts[331,337] drug delivery delivery systems,[338-339] and hydrocarbon separation.[340]

Metals with more than one open metal site, *i.e.* a ion with octahedral geometry that after activation two axial solvent molecules are removed generating two solvent accessible sites per metal ion, have the advantage of having a higher open metal site density than equivalent structures with a single open metal site. The higher open metal site density means performance is enhanced.

With these features in mind, ligand systems based on derivatives containing carboxylic acid functional groups were synthesised and their use as metalloligands in the synthesis of frameworks investigated.

5.2 Synthesis of Ligands

The reproducible nature and exceedingly high stability of the bis-phenolic oxime complex with first row transition metals, particularly copper(II), lends itself to being applied in the synthesis of metal-organic frameworks.

Paraben (4-hydroxybenzoic acid) is a common chemical, ubiquitous as the precurser to various alkyl parabens used in the preservative industry.[341] As with other phenols, it can be easily formylated or acetylated in the *ortho*-position to yield 5-carboxysalicylaldehyde and 5-carboxy-2-hydroxyacetophenone, respectively. These can be reacted with hydroxylamine to form a phenolic oxime based ligand (Scheme 5.1). The reactivity of phenols in the 2-position with regard to electrophilic aromatic substitution means that further functionalisation is possible, and hence a large series of dicarboxylic acid metalloligands can be established. Possible functional groups that can be incorporated this way include nitro, amino, and halo groups.

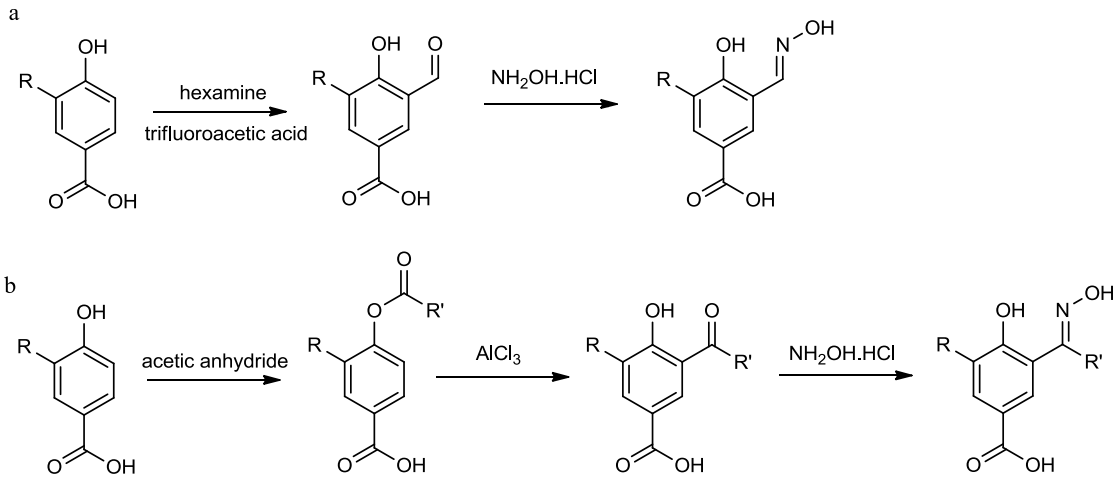

Scheme 5.1: *General synthesis of 5-carboxy-phenolic oximes. a) Aldoximes can be synthesised from formylation of paraben and derivatives followed by reaction of hydroxylamine hydrochloride. b) Ketoximes can be synthesised via the synthesis of a phenolic ester of paraben followed by a Lewis acid catalysed Fries rearrangement and reaction with hydroxylamine hydrochloride. Potential R groups could include added functionality required in the MOF or solubilising groups.*

The choice of potential functional groups that can be incorporated into the phenolic oxime is vast due to the activity of the 2-position of the phenol ring. Functionalisation of the 6-position also alters the strength of the pseudo macrocyclic ring due to buttressing hydrogen bonds. The solubility of the resultant metallo-ligand can also be tailored through substituent effects in this position.

Both aldoxime and ketoxime based ligands were synthesised as part of this study. Functional groups were also included to assess their role in the construction of MOFs. The novel ligands 4-hydroxy-3-(1-(hydroxyimino)ethyl)benzoic acid (H_3**L5.1**), 4-hydroxy-3-((hydroxyimino)methyl)benzoic acid (H_3**L5.2**) and 3-bromo-4-hydroxy-5-((hydroxyimino)methyl)benzoic acid (H_3**L5.3**) were synthesised following the procedures detailed in Scheme 5.1 (Figure 5.6).

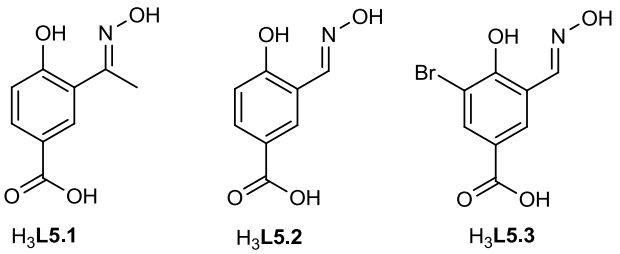

Figure 5.6: *Ligands used in the synthesis of metalloligands and coordination polymers within this chapter.*

Although a range of metal salts could be used in the formation of metallo-ligands based upon phenolic oxime derived ligands, focus was be directed towards nickel(II) and copper(II) ions due to their properties as mononuclear complexes being extensively studied in terms of their magnetic properties and stability, respectively.

5.3 Synthesis of Metalloligands

5.3.1 Synthesis of $[Ni(H_2L5.1)_2]$ (5.1)

Addition of a green DMF/H_2O solution of nickel nitrate to a pale yellow solution of H_3**L5.1** in DMF resulted in a pale green solution which was sealed in a screw capped vial and heated to 100 °C for 24 hours. Green plate-like crystals suitable for single crystal X-ray diffraction formed at this temperature and were solved and refined in the triclinic space group *P*-1 (R-factor 3.45 %). The asymmetric unit contained half of the expected $[Ni(H_2$**L5.1**$)_2]$ neutral complex with the nickel(II) ion located on an inversion centre. As expected, the nickel ion is in a square planar geometry (τ_4 = 0.00), and the oxime hydrogen atom (H7) has an intramolecular S(5) hydrogen bonding interaction with the coordinated phenolate oxygen atom (O2) to create a pseudo-macrocyclic ring around Ni1 (H7-O2' 1.827 Å) (Figure 5.7).

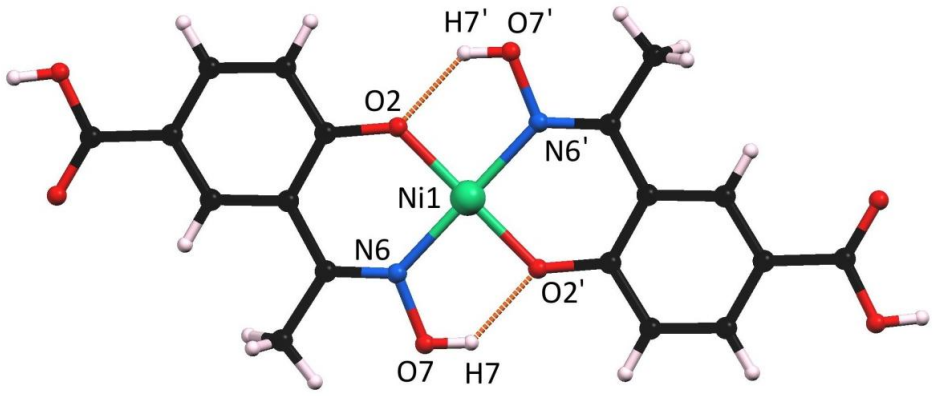

Figure 5.7: *Structure of complex **5.1**. Ni1 is centred on an inversion centre. Selected bond lengths (Å) and angles(°): Ni1-O2 1.8223(13), Ni1-N6 1.8957(16), O2-Ni1-N6 92.17(6), O2-Ni1-N6' 87.83(6).*

The free carboxylic acid groups of the complex participate in $R_2^2(8)$ centrosymmetric hydrogen bonding motifs with neighbouring complexes (Figure 5.8). These hydrogen bonded chains interact with neighbouring chains via offset π-π stacking interactions. The hydrogen bonded chains are slipped 3.464 Å relative to hypothetical perfectly stacked complexes. The distance between the mean plane of each complex is 3.317 Å indicating that there is some π-π stacking interactions between chains. No other significant interactions between stacks of one-dimensional chains are observed.

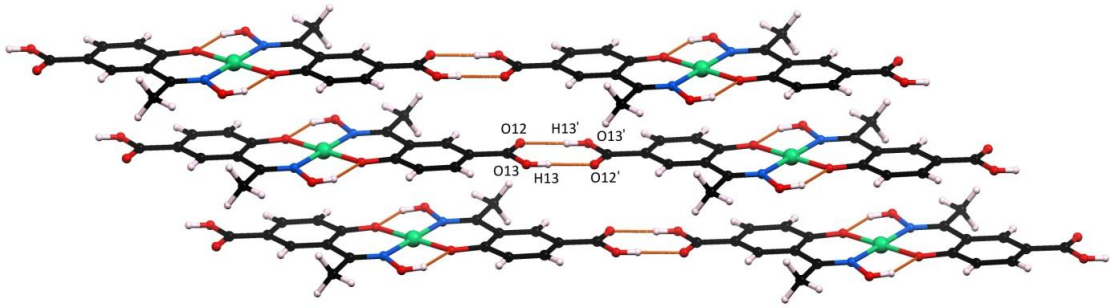

Figure 5.8: *Hydrogen bonding interactions in **5.1**. A centrosymmetric $R_2^2(8)$ head-to-tail hydrogen bonding interaction exists between carboxylic acid groups of complexes.*

The carboxylic acid functional group, which has the potential ability to coordinate to the open metal sites of square planar nickel(II) complexes, did not exhibit any bonding behaviour under the solvothermal conditions used to synthesis **5.1**. This indicates that it should be possible to create framework materials, which commonly use similar synthetic conditions. The fact that the metal adopts a square-planar geometry rather an octahedral geometry with solvent coordinated in the axial positions in this solvent medium is promising in retaining open metal within the framework.

The fact that **5.1** crystallised out of DMF at 100 °C gives an indication of the solubility of the complex. Crystalline samples were unable to be redissolved in common polar solvents with the exception of pyridine, DMSO and aqueous ammonia solutions. The solvent 2,4,6-collidine was not able to solubilise this complex indicating that coordination to the metal ion, rather than deprotonation is required for solubility. Coordination of solvent in axial positions will disrupt the offset π-π stacking interactions.

5.3.2 Synthesis of $[Cu_2(H_2L5.1)_4]\cdot$msi (5.2)

A solution of copper nitrate dissolved in NMP/methanol was layered on top of a NMP/water solution of H_3L**5.1** separated by a buffer layer of pure NMP in a 5 mm NMR tube. Brown crystals grew at the interface of mixing solvents after three weeks. These were carefully removed from the solution with a pipette. The crystals were of sufficient quality for single crystal X-ray diffraction, and the data was solved and refined in the triclinic space group *P*-1 (R-factor 3.27 %). The asymmetric unit contained one copper(II) ion, coordinated, as expected, by two mono-deprotonated H_2**L5.1** ligands with each acting as a bidentate ligand (Figure 5.9). The pseudomacrocyclic ring with two S(5) hydrogen bonding interaction is again observed. A N-methylsuccinimide (msi) molecule was observed between complexes, disordered over an inversion centre. The presence of this solvent molecule can be attributed to the *in situ* oxidation of NMP. Bond lengths and angles of this unexpected molecule are consistent with previous reports.[342]

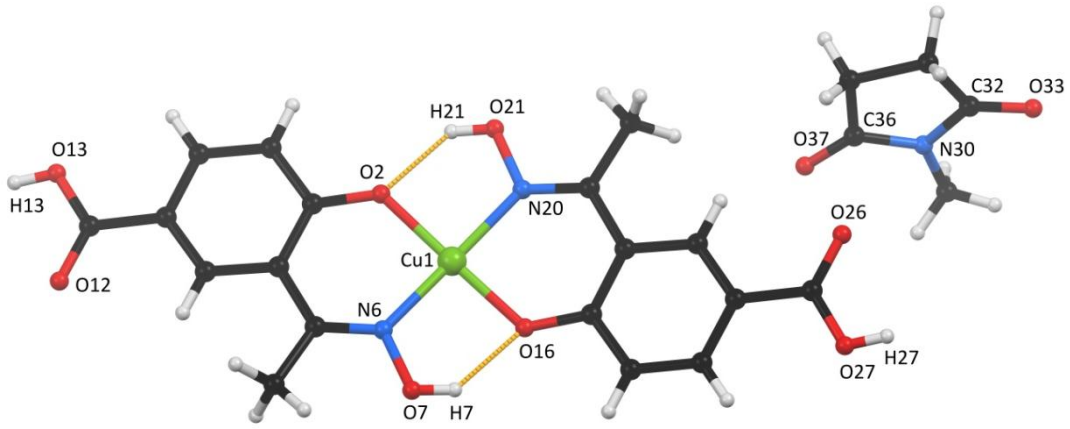

Figure 5.9: *Asymmetric unit of* ***5.2****. Disorder of the N-methylsuccinamide molecule omitted for clarity. Selected bond lengths (Å) and angles(°): Cu1-O2 1.892(2), Cu1-N6 1.958(1), Cu1-O16 1.904(2), Cu1-N20 1.961(1), O2-Cu1-N6 91.66(6), O2-Cu1-N20 88.72(6), N6-Cu1-O16 89.36(6), O16-Cu1-N20 90.29(6).*

In addition to the expected coordination mode, the phenolate oxygen atom O16 coordinates in a μ^2-bridging mode to a symmetry equivalent copper(II) ion to form a dinuclear complex, each half related by an inversion centre (Figure 5.10). The overall five-coordinate copper(II) ion is in an almost perfect square-based pyramidal geometry (τ_5 = 0.08). The bridging behaviour of O16 has the effect of distorting each mono-nuclear complex from planarity, as the middle of the long complexes are pulled together. The aromatic ligand systems in each dimer interact via π-π stacking interactions, (distance between the means planes of ligands in the dinuclear complex is 3.402 Å). Like the copper-halide dimers **2.7** and **2.8** reported in Chapter 2, the dimer of **5.2** is centred over an inversion centre.

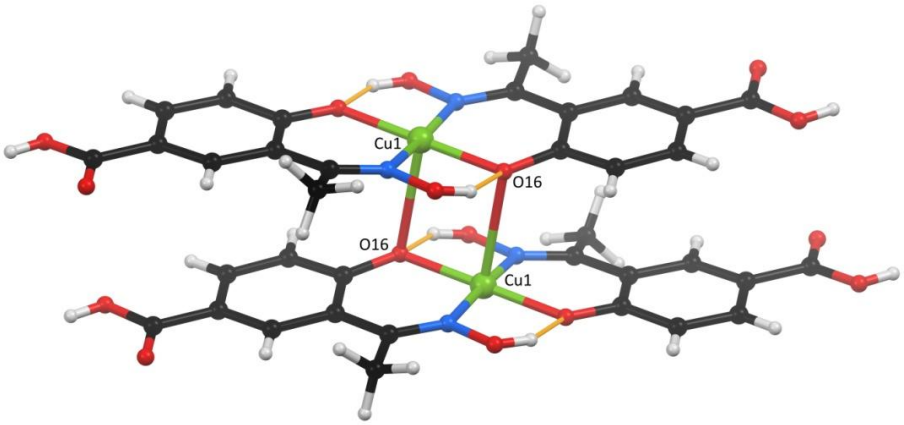

Figure 5.10: *Dinuclear complex of* ***5.2*** *with heteroatomic labeling scheme. Solvent molecule is omitted for clarity. The distance between the mean planes of each theoretical mononuclear complex is 3.402 Å. Selected bond lengths (Å) and angles(°): Cu1-O16' 2.626(1), Cu1-O16-Cu1' 93.53(5), O16-Cu1-O16' 86.47(5).*

Each of the four carboxylic acid groups in the dinuclear complexes of **5.2** interacts with another via the common $R_2^2(8)$ hydrogen bonding carboxylic acid motif in a similar way to **5.1**, however, in this case the interaction is not centred on a symmetry element (Figure 5.11). This again, has the effect of creating a one-dimensional hydrogen bonded polymer. Each hydrogen bonded chain is stacked, albeit offset (metal-metal offset distance 4.013 Å), via close π-π stacking interactions (mean plane distance 3.021 Å). This π-π stacking interaction is closer than the intermolecular equivalent. This is due to a combination of the μ^2-bridging phenolic oxygen and the steric repulsion from the acetyl group.

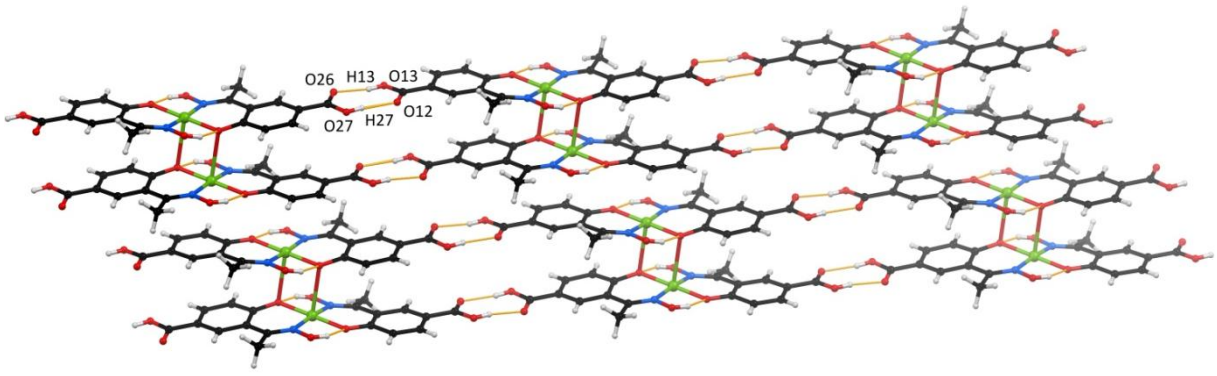

Figure 5.11: *$R_2^2(8)$ hydrogen bonding between dinuclear complexes in* ***5.2*** *create one-dimensional chains. These are stacked in one dimension by off-set π-π stacking interactions.*

The solubility of **5.2** appeared to be slightly lower than that of **5.1**. The brown crystalline product could be redissolved in pyridine, ammonia solutions at room temperature, but only in DMSO at temperatures over 90 °C. Again 2,4,6-collidine was unable to solubilise **5.2** indicating that coordination in the axial sites is important for solubility.

5.3.3 Summary

Two metalloligands based upon phenolic oxime complexes were synthesised and studied by X-ray crystallography. These were based upon H_3**L5.1** and either nickel(II) (**5.1**) or copper(II) (**5.2**). Compound **5.1** formed the expected mononuclear, bis-ligated complex with a square planar coordination geometry. Due to bridging of the phenolic oxygen atom in **5.2**, a dinuclear complex was produced. Dimerisation not only changes the shape of the metalloligand building unit, but also restricts the amount of possible open metal sites within any resultant framework.This complex is not expected to make a good metalloligand and ways to prevent this bridging mode such as use of coordinating solvents which can be removed post synthetically should be investigated.

The close packed nature of **5.1** and **5.2** no doubt contributes to the insolubility in most common laboratory solvents and a decreased solubility of **5.2** with respect to **5.1** is attributed to the formation of dinuclear complexes. Incorporation of bulky substituents in around the phenyl ring is likely to prevent dimerisation by phenolate bridging and π-π stacking interactions of mononuclear complexes and render the resulting complexes more soluble.

5.4 Synthesis of Coordination Polymers

As mentioned previously the 180° divergent arrangement of carboxylate groups in **5.1** and **5.2** render them idea for use as linear linkers in the synthesis of coordination polymers with open metal sites. The insolubility of these complexes however, is a hindrance in their application in the synthesis of porous crystalline frameworks. Both metal complexes are insoluble in water, methanol, acetone, DMF and DEF. However, whilst the nickel complex

dissolves in room temperature NMP and DMSO, the copper analogues require these solvents to be heated for dissolution.

Two strategies were devised to prevent dimerisation in copper(II) phenolic oxime from happening. The first involved the use of coordinating solvents to temporarily block these positions. Pyridine was found to readily dissolve both compounds at room temperature. This was attributed to the formation of octahedral complexes, rather than the square planar complexes preventing π-π stacking accompanied by deprotonation of the carboxylic acid residues preventing hydrogen bonding. This has the advantage of preventing π-π stacking between flat complexes and the solvent can be removed in a post-synthetic activation step.

The second was incorporation of bulky substituents in the 3-position of the ligand. This is likely to prevent dimerisation and π-π stacking interactions of mononuclear complexes, rendering the resulting complexes more soluble, and has the added benefit of potentially no extra coordinated solvent removal step.

5.4.1 Synthesis of $[Cu_2(H_2L5.2)_2(pyridine)_5]\cdot 4pyridine$ (5.3)

When H_3**L5.2** was combined with half an equivalent of copper(II) acetate in pyridine, small plate-like crystals formed over several months. Although very weakly diffracting, they were suitable for single crystal X-ray diffraction. The data were solved and refined in the monoclinic space group *C*2/*c* (R-factor 11.87 %). The structure consists of a one dimensional coordination polymer formed through the linking of the expected bis-phenolic oxime complexes by a copper(II) ion. The asymmetric unit contained two half phenolic oxime complexes of the form [Cu(H**L5.2**)$_2$] linked together by another copper(II) ion (Figure 5.12). Both of the ions in phenolic oxime coordination sites (Cu1 and Cu3) are located on two-fold rotation axes, and have Jahn-Teller distorted octahedral geometries with solvent pyridine co-ligands in the axial sites. Jahn-Teller distortions are typical of copper(II) ions and the metal to pyridine bond lengths are in the range of 2.42(1) - 2.83(1) Å, similar to other reported structures.[343-344] The linking copper(II) ion, Cu2, has square pyrimidal geometry (τ_5= 0.07), with two trans positions of the equitorial plane taken up by monodentate carboxylate groups. The two remaining equatorial and the apical positions are

occupied by pyridine solvent molecules. Four non-coordinating solvent pyridine molecules are also present in the asymmetric unit.

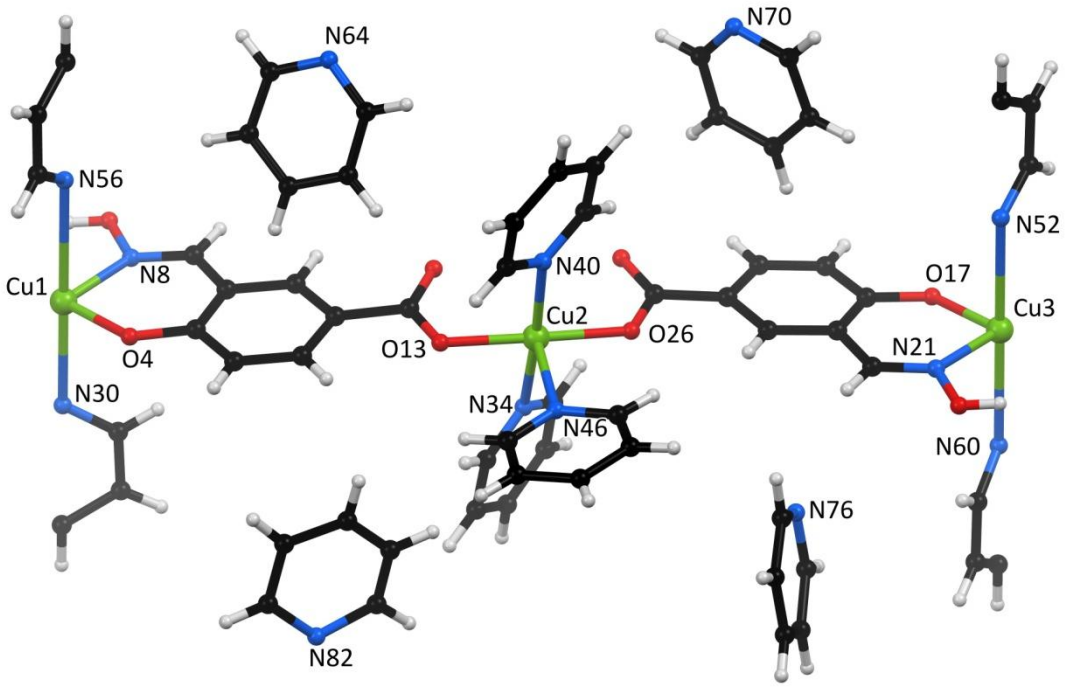

Figure 5.12: *Asymmetric unit of* ***5.3****. Selected bond lengths (Å) and angles(°): Cu1-O4 1.937(6), Cu1-N8 1.952(8), Cu1-N30 2.424(13), Cu1-N56 2.83(1), Cu2-N34 2.047(7), Cu2-O13 1.962(6), Cu2-O26 1.963(6), Cu2-N40 2.055(7), Cu2-N46 2.278(9), Cu3-O17 1.927(7), Cu3-N21 1.942(8), Cu3-N60 2.70(1), Cu3-N52 2.61(1).*

As expected, the copper ions coordinated to the phenolic oxime ligand have octahedral geometries due to the coordination of solvent pyridine molecules.

Each chain interacts with neighbouring chains via non conventional hydrogen bonds centred near the coordination sphere of Cu2 (Figure 5.13). The non-coordinated carboxylate oxygen atoms, O14 and O27, act as hydrogen bond acceptors, and the hydrogen atom at the 4-position of pyridine molecules coordinated to Cu2 acts as a bifurcated hydrogen bond donors in $R_1^2(8)$ type interactions. These added two dimensions are the only major interactions between chains. The space between polymers is comprised of non-coordinated solvent pyridine molecules.

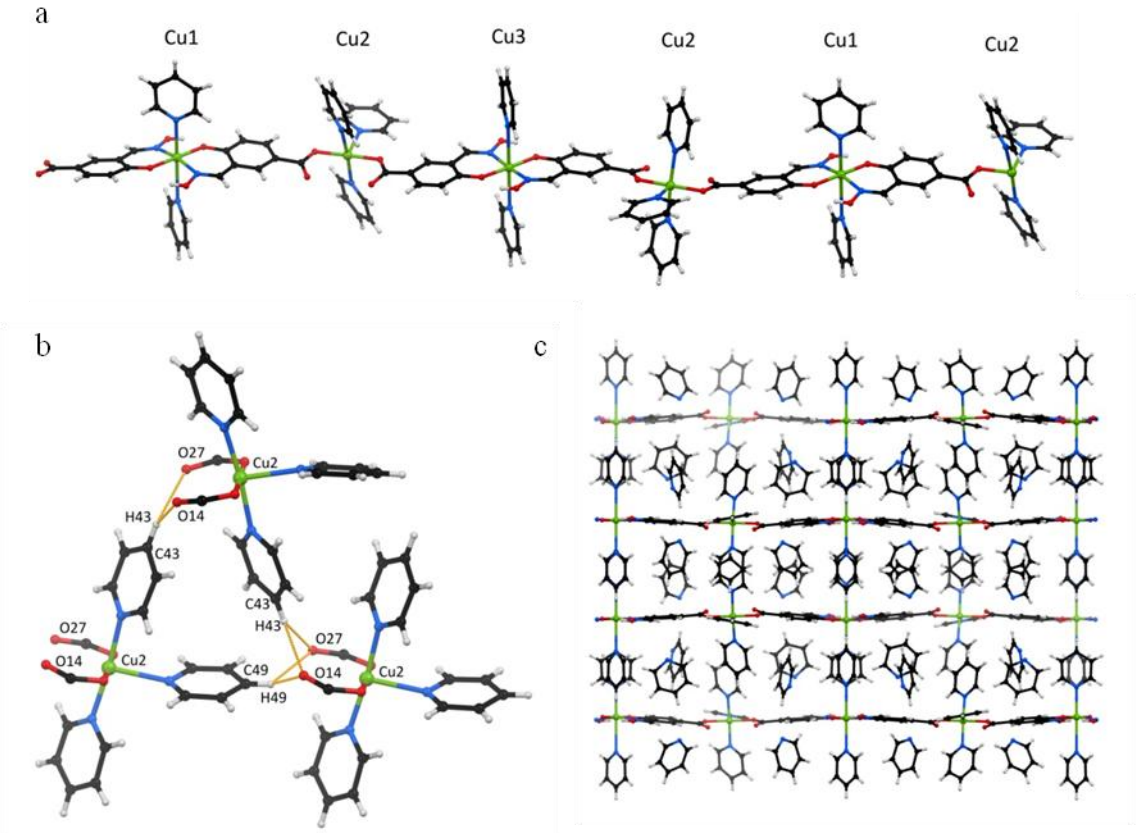

Figure 5.13: *Supramolecular interactions and crystal packing in* ***5.3****. a) Formation of a one-dimensional coordination polymer through coordination of carboxylate groups on [Cu(H****L5.2****)$_2$(pyridine)$_2$] units. b) Hydrogen bonding interactions between one-dimensional coordination polymers. Direction of polymer propagation is perpendicular to the page. c) View down the crystallographic c-axis of* ***5.3*** *showing stacked polymers and the solvent pyridine molecules contained within.*

It was surprising that a polymer with a metal:ligand ratio of 1:1 formed from a 1:2 ratio. However the poor yield indicates that this is not the main product, and the deep green colour of the crystallisation solution indicates that there is still a substantial amount of dissolved copper, most likely in the form of [Cu(**L5.2**)$_2$(pyridine)$_2$] due to the large excess of pyridine.

If the synthesis of coordination polymers based upon phenolic oximes is to be used to make coordination polymers with open metal centres, an activation step to remove the coordinated pyridine ligands would be required. This is likely to require very harsh conditions and therefore a very stable node, such as copper(II) paddlewheels, would be required to survive these conditions.

5.4.2 Synthesis of $[Cu_2(HL5.4)_2(DMF)(H_2O)]$ (5.4)

Copper nitrate and H_3**L5.3** were dissolved in DMF with a little nitric acid and heated at 100 °C for 48 hours. From the resultant precipitate, blue plate-like crystals were isolated. These were suitable for single crystal X-ray diffraction and were solved and refined in the orthorhombic space group *Ibam* (R-factor 11.19 %). Although the diffraction data showed bis-ligated copper(II) complexes linked via paddlewheel secondary building units to create a framework structure, it appears the aldoxime functionality of H_3**L5.3** had hydrolysed then oxidised to a carboxylic acid (new ligand defined as H_3**L5.4**). Despite this, the metalloligand [Cu(H**L5.4**)$_2$] incorporates a lot of the features mentioned previously for phenolic oxime based ligands.

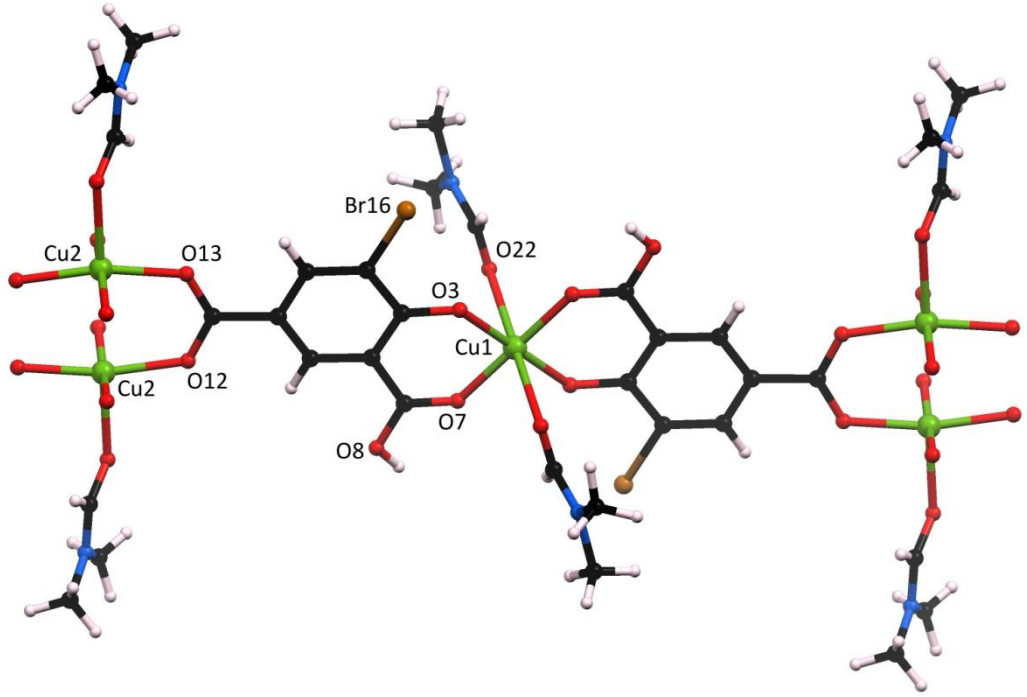

Figure 5.14: *Metalloligand linked to copper(II) paddlewheel secondary building units. Partial occupancy DMF solvent molecules coordinated to Cu1 and DMF/H_2O disorder of axial solvent coordinated to Cu2 shown as DMF molecules for clarity.*

Crystallographically, there was found to be one equivalent of DMF and half an equivalent of water per formula unit. This is due to the assignment of the DMF molecule coordinating to Cu1 being modelled with 25 % occupancy, and the axial position of the paddlewheel secondary building unit containing Cu2 being 50:50 disordered with a water molecule and a

DMF molecule. The 25 % occupancy of the DMF on Cu1 indicated that there is some degree of open metal sites at Cu1.

The partial occupancy of the coordinated DMF molecules do not give any indication of whether Cu1 exists in a five-coordinate square-based pyramid geometry or in a Jahn-Teller distorted octahedral geometry in addition to the square-planar geometry. Although the geometry is not known, it is certain that there is on average one open metal site per copper(II) ion.

As this coordinated solvent molecule has no interactions with the framework itself apart from the coordination to Cu1, post synthetic removal is a potential strategy for removal. Although axial coordination of solvent was not observed in the discrete structures which employed similar solvents (compounds **5.1** and **5.2**) , it was seen here, probably due to the inability to form π-π stacking interactions in the framework. Solvent coordination is one of the biggest barriers to the synthesis of metal-organic frameworks with open metal sites. Through the paddlewheel secondary building units, the overall topology of the resultant framework is that of a two-dimensional regular square grid (**sql**) with internodal distances of 19.007(3) Å (diagonal 27.124(6) Å) (Figure 5.15).

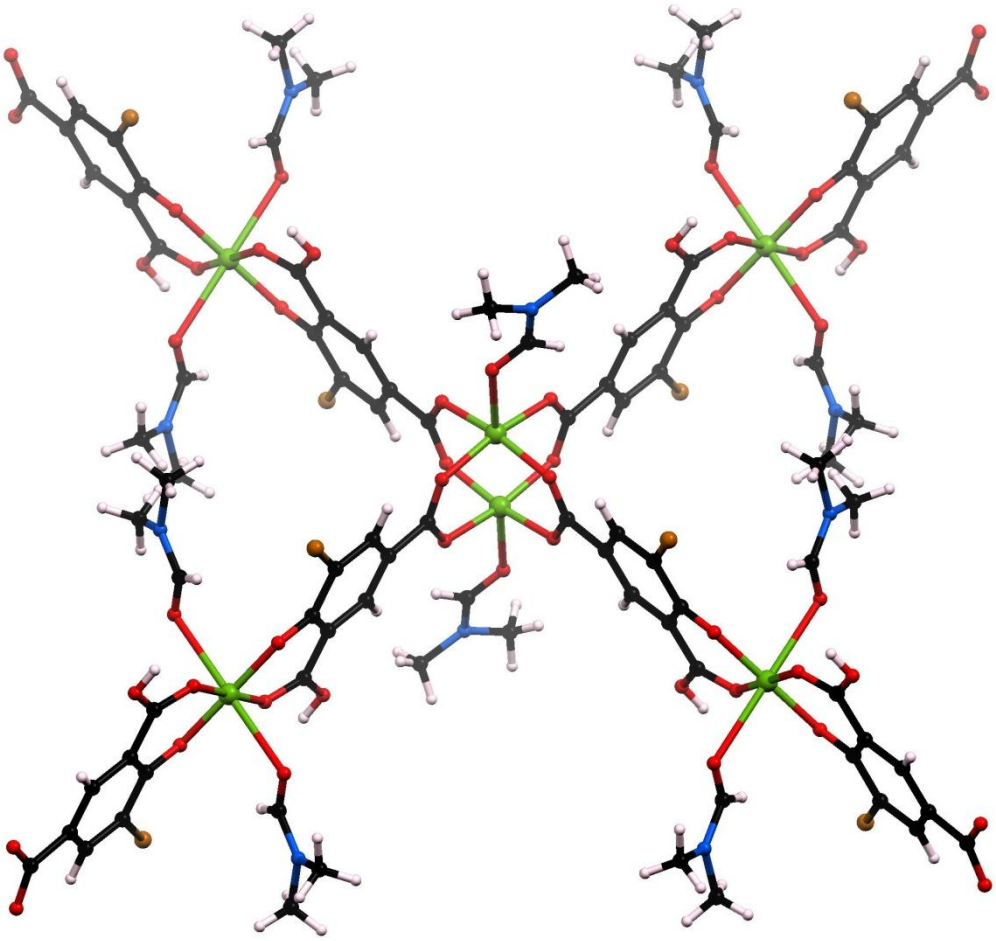

Figure 5.15: *Copper(II) paddlewheel secondary building unit structure of* ***5.4****. The DMF molecule in the apical position of the paddlewheel is disordered with a water molecule (not shown).*

The **sql** framework is interpenetrated and interactions between nets consist of hydrogen bonding between the coordinated monodenate carboxylic acid group and the phenol (Figure 5.16).

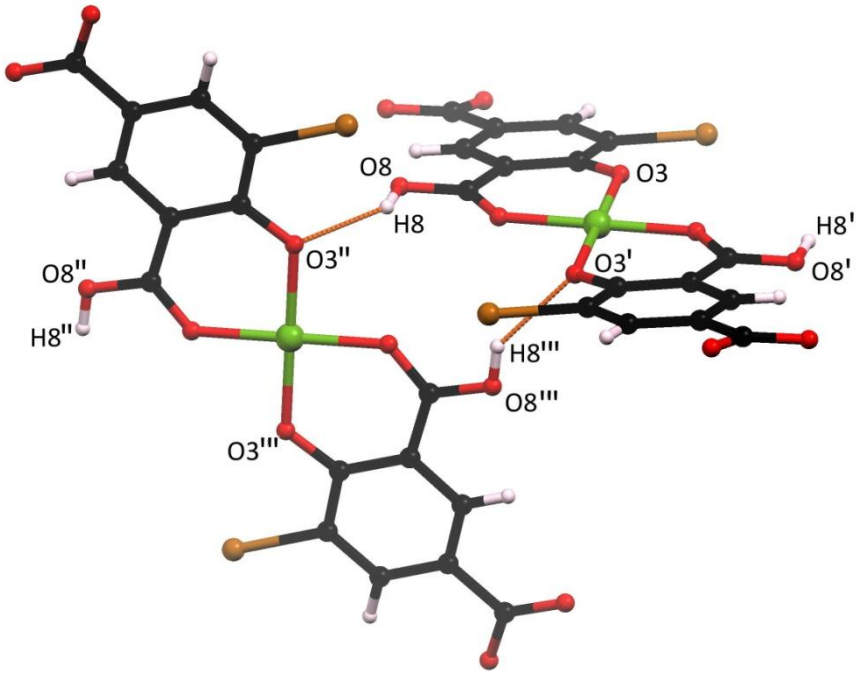

Figure 5.16: *Interactions between interpentrated two-dimensional square grid frameworks in* ***5.4****. Secondary building units and coordinated DMF molecules omitted for clarity.*

Each secondary building unit of the interpenetrated framework is centred in the middle of the square void created by the original framework in a similar way to other interpenetrated square grid type frameworks.[345-346] However, the interpenetrated nets are not perpendicular to each other, but rather have a 56.13° angle between the mean planes of each square grid network (Figure 5.17) allowing for 2D to 3D interpenetration. The dimensions of the **sql** framework and style of interpenetration is similar to that of a previously reported MOF, based upon the linear ligand 9,10-di(4-carboxyphenyl)anthracene and copper paddlewheel SBUs.[347]

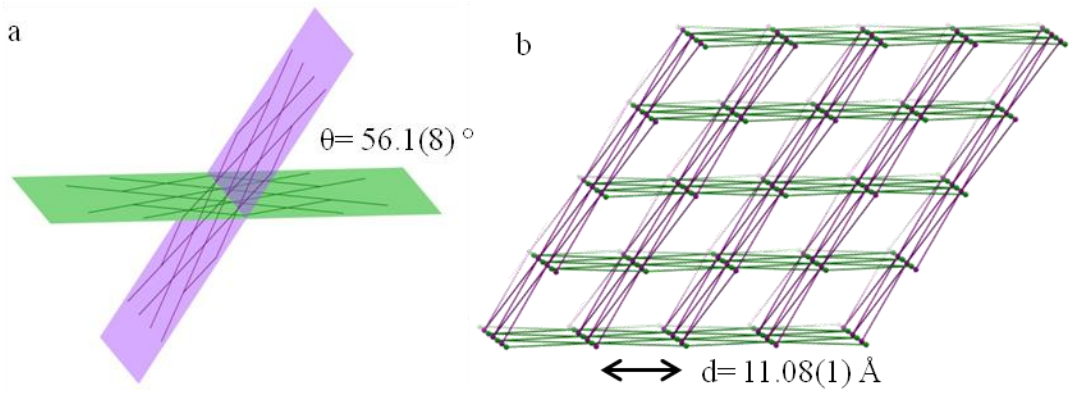

Figure 5.17: *Interpenetration of square grid frameworks in **5.4**. Horizontal grids are shown in green and interpenetrated grids shown in purple. a) Interpenetrated grids are inclined 56.1(8)° relative to each other. b) Packing of grids showing spacing between interpenetrated grids and extended network. Note, the spacing between frameworks is smaller than the internodal distances in the **sql** net.*

Despite the presence of coordinated DMF solvent and interpenetration, the structure remains porous, with a solvent accessible void volume of 813 $Å^3$ per unit cell. As no solvent could be located crystallographically in this region, the OLEX2 Solvent Mask routine (similar to PLATON/SQUEEZE) was used to mask out the disordered density.

The resistance to hydrolysis of related aldehyde derived functional groups is in the order oxime > hydrazone > imine with an approximate thousand fold increase per step.[348] Despite this it seems that under the given conditions the aldoxime of H_2**L5.3** was not stable, and hydrolysed to the aldehyde, followed by oxidation to the carboxylic acid (Scheme 5.2). It is well known in the literature that copper salts in combination with nitric acid under solvothermal conditions are a potent oxidant and the oxidation of an aldehyde to a carboxylic acid is not surprising.[349]

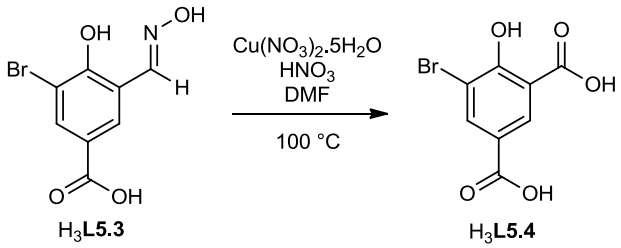

Scheme 5.2: *In situ hydrolysis and oxidation of an aldoxime H_3**L5.3** to a carboxylic acid H_3**L5.4**.*

Several strategies could be used to prevent hydrolysis and oxidation of the oxime functional group. Using a ketoxime based ligand like those in **5.1** and **5.2** would be better to prevent hydrolysis and oxidation under these conditions to retain the stability and properties of the pseudo macrocyclic ring in the framework. Layering techniques for the synthesis of MOFs that do not rely on solvothermal conditions could also be used.[90]

Post synthetic removal of the axial coordinated DMF solvent molecules have been shown to be achievable for other systems and could potentially work for this example.[330] In this case it is likely that removal of solvent would occur from both the metalloligand and the paddlewheel SBUs leading to two different open metal sites in the framework. Due to the yield of the reaction and time constraints, activation and gas sorption analysis of this compound were not performed.

5.5 Conclusions and Future Work

Three novel carboxyl-derivatised phenolic oxime ligands have been synthesised and characterised. From these, several mononuclear and polymeric complexes were synthesised synthesised and studied by X-ray diffraction.

It has been successfully demonstrated that phenolic oxime complexes containing carboxylic acid functional groups do form discrete complexes, proving that they are potentially useful metalloligands for the synthesis of MOFs. The pseudomacrocyclic hydrogen bonding motif around the metal centre was observed in mononuclear complexes of both nickel(II) (**5.1**) and copper(II) (**5.2**). These complexes were trialled as metalloligands in the synthesis of MOFs, however, no crystalline products of their reaction with other metals could be obtained. The poor solubility of such complexes is a contributing factor to this. Due to the insolubility of these metalloligands strongly coordinating solvents such as pyridine and DMF were used in the synthesis of coordination polymers based upon related ligands.

A one-dimensional coordination polymer, **5.3** was formed from copper(II) and H_3**L5.2** in pyridine which indicated that it was possible to form crystalline polymeric species by

coordination of the carboxyl group to additional metal centres. As expected with this solvent, the usually square-planar copper(II) ion in the phenolic oxime complex has a Jahn-Teller distorted octahedral geometry due to the coordination of pyridine solvent molecules.

Complex **5.4** showed that under typical solvothermal reaction conditions hydrolysis and oxidation of the aldoxime functional group is possible. Despite this, a two-dimensional **sql** framework was produced. The new ligand, defined as H_3**L5.4**, coordinated to copper(II) ion in a manner similar to what was expected for H_2**L5.3**. This copper(II) ion includes partial occupancy solvent molecules in its axial coordination sites, probably due to the fact that the open metal sites of the square planar complex are not shielded by equivalent complexes via π-π stacking interactions like those seen in **5.1** and **5.2**. Inclined interpenetration of the resultant **sql** framework lead to a two-dimensional to three-dimensional coordination polymer being produced with potential porosity. Although the oxime had hydrolysed and oxidised, the newly generated ligand coordinated in a similar manner to that expected for phenolic oxime complexes.

Future work should focus on the use of ketoxime based ligands which, despite the added synthetic step, should prove more resistant to hydrolysis and oxidation. Other ketones besides acetyl groups could be appended to 4-hydroxybenzoic acid, which based upon the structure of **5.4**, could control the interpenetration of the resultant framework.

Due to the insolubility of the metalloligands synthesised, appended functional groups that increase the solubility of metalloligands are desired. Further functional groups such as nitro, amino, methylamino, or *tert*-butyl could be incorporated onto the phenyl ring of the ligands to increase their solubility and/or impart other functional groups into the resultant coordination polymers.

Due to the insolubility of the carboxylic acid appended neutral metalloligands **5.1** and **5.2**, another way of including the phenolic oxime coordination group within framework materials could be attempted. The reason for the insolubility of the afore mentioned complexes is due to the phenol deprotonating before the carboxylic acid group, forming a neutral complex which crystallises out of solution. A way around this may be to make the crystallisation step the formation of the phenolic oxime complex, rather than a secondary building unit such as a paddlewheel. This way, the crystallisation of a mononuclear

complex is reduced and the insoluble phase is limited to a polymeric material. Several ligand systems seem ripe for the inclusion of a divergent arrangement of poly-phenolic oxime functional groups and a tetrahedral example is shown in Figure 5.18.

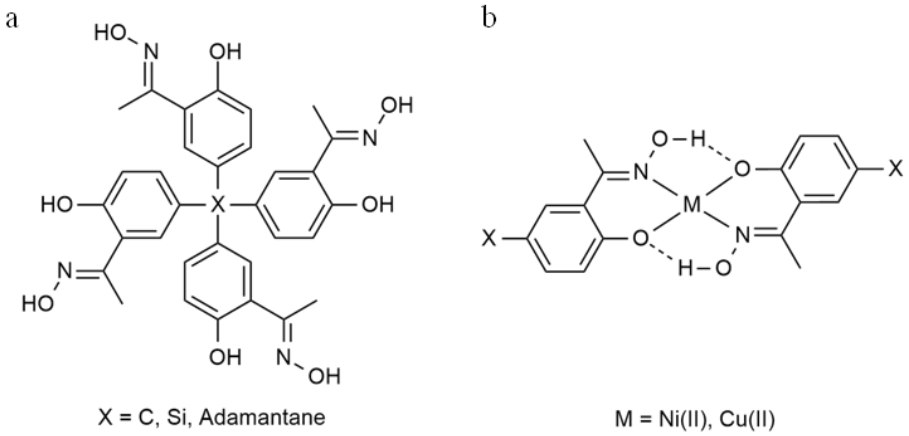

Figure 5.18: *a) Potential tetra-phenolic oxime based ligands for the synthesis of MOFs. The examples shown here would act as tetrahedral shaped nodes. b) Phenolic oxime functional groups in combination with a divalent square planar metal ion would be expected to act as linear linkers between organic nodes with two open metal sites.*

Similar tetrahedral building units to those shown in Figure 5.18, but with different coordination groups have previously been used in the synthesis of MOFs[55,327,350] and covalent-organic frameworks.[351-353]

Chapter 6

Conclusions and Future Work

6.1 Conclusions

The overall aim of this thesis was to design and prepare novel metallosupramolecular assemblies and metal-organic framework materials. This has been achieved through investigation of three families of ligand systems in combination with transition metal salts through solid state analysis. Experiments seeking to determine the effect of modulation of the structural components within these families, whether it be the metal ions, corresponding anions or organic ligands and co-ligands, were performed.

In Chapter 2, a family of ligands containing the N^1-acylamidrazone functional group was synthesised. The hydrogen bonding motifs of complexes of these ligands were analysed with respect to the counter ion and protonation state of the coordinated ligand. The coordinated ligands were demonstrated to be potent hydrogen bond donors, consistent with their squaramide-like arrangement of hydrogen bond donors. Reproducible interactions were seen to form with families of anions.

Chapter 3 sought to examine the coordination behaviour of twofold deprotonated N^1-acylamidrazone functional groups. With zinc(II) carboxylate salts octanuclear metal-organic macrocycles of the general formula $[Zn_8\mathbf{L}_4(RCO_2)_8]$ were observed. The modulation of the carboxylate co-ligand, although observed to alter the crystal packing of discrete macrocycles, did not affect their solubility and all examples remained insoluble in common laboratory solvents. The parent macrocycle with acetate co-ligands, retained crystallinity upon removal from solution and showed luminescence stemming from ligand to metal charge transfer. Two methods were developed in an attempt to use these macrocycles as molecular building blocks or secondary building units in the synthesis of MOFs. The first was reliant on the replacement of mono-carboxylate co-ligands with di-carboxylate equivalents, the second on linking H_2**L2.1** ligands together. Although these ultimately proved unsuccessful, several novel ligands and complexes were synthesised. The lack of MOF formation is attributed to the insolubility of the discrete species.

Chapter 4 introduced a series of terpyridine-4,4"-dicarboxylic acid based ligands. These were synthesised via the Kröhnke methodology and contained a substituent in the 4'-position. When reacted with zinc(II) nitrate in DMF at elevated temperatures a series of isoreticular MOFs based upon the **gis-c** topology were synthesised. These were shown to be

stable with respect to removal of solvent contained within the one-dimensional channel structure. The conserved topology and similarity of channel sizes, means the differences in properties can be attributed to the functional group at the 4'-position of the ligand. Nitrogen, hydrogen, methane and carbon dioxide isotherms were measured at a range of temperatures up to 1 atm. Generally all compounds displayed typical microporous behaviour and were shown to absorb all four gasses. Little variation was seen between MOFs containing different functional groups. An exception to this was compound **4.4** (4-nitrophenyl substituent) which did not adsorb nitrogen or hydrogen. A gating mechanism was proposed for this observation.

Chapter 5 explored the use of phenolic oxime based ligands for the introduction of open metal sites into MOFs. This coordination motif is known to form a pseudomacrocyclic ring around metal ions, with a particular affinity for copper(II) ions. It was thought that carboxylic acid functionalised derivatives of nickel(II) and copper(II) phenolic oxime complexes could be used as metalloligands in the synthesis of MOFs. The insolubility of such complexes hindered this, and several methods to increase solubility such as use of coordinating solvents and functionalisation were trialled. It was found that under solvothermal conditions, the aldoxime functional group was susceptible to hydrolysis and oxidation. Despite this, the newly formed ligand coordinated in a similar manner to that expected for a phenolic oxime ligand and a coordination polymer based upon paddlewheel SBUs was synthesised.

6.2 Future Work

The results presented in Chapters 2-5 are by no means exhaustive studies of the potential metallosupramolecular assemblies that could arise from the use of the applicable ligand system. Several additional avenues of research could be pursued with respect to the work contained within this thesis. Promising areas of further study are identified as follows, and are presented as starting points for future work in this area.

Complexes containing neutral N^1-acylamidrazone functional groups have been shown to be good, reproducible anion binders in the solid state. The use of these complexes to bind anions in solution could be investigated through NMR and UV/Vis titration studies.

The use of twofold deprotonated N^1-acylamidrazone functional groups to form macrocycles has been thoroughly investigated. Although these macrocycles could not be transposed into coordination polymers, the bridging behaviour of this functional groups could be exploited to develop more coordination polymer materials.

One of the most interesting aspects of Chapter 4 was the apparent flexibility in MOF **4.4**. The dynamic processes behind this behaviour are unknown and further work into elucidating this mechanism is suggested. This may include variable pressure X-ray diffractions measurements. The synthesis of derivatives of terpyridine-4,4"-dicarboxylic acid containing electronic or sterically similar functional groups to that of **4.4** such as 4-cyanophenyl or 4-isopropylphenyl may also help determine the basis for this behaviour. The family of terpyridine-4,4"-dicarboxylic acid based ligands could be expanded to contain functional groups tailored to specific applications such as redox active groups, hydrophobic groups or fluorophores. Combinations of these groups could also be included to create multivariate MOFs.

The insolubility of carboxylic acid appended phenolic oxime metalloligands in Chapter 5 limited their applicability in the synthesis of MOFs. To overcome this issue, solubilising functional groups could be appended to the ligand such as tertiary butyl groups. Another strategy involving the use of poly-phenolic oxime based ligands could be used. In this case the phenolic oxime coordination bonds are used to form the framework material so that the insolubility of the discrete species is not an issue.

Chapter 7

Experimental Data and Methods

7.1 Materials and Methods

General Information

Unless otherwise specified, all reagents and starting materials were of reagent grade, purchased from standard suppliers and used as received. Water was purified by reverse osmosis *in-house*. Where anhydrous solvents were required, HPLC-grade solvent was either distilled from standard drying agents or dried by passing over a sealed column of activated alumina. Except where otherwise specified, all reactions were carried out in air.

Nuclear Magnetic Resonance Spectroscopy

All spectra were recorded on a Varian INOVA 500 or an Agilent 400-MR instrument operating at 500 or 400 MHz, respectively, for ^{1}H, and 125 or 101 MHz, respectively, for ^{13}C. All samples were dissolved in commercially available deuterated solvents and spectra were referenced to the residual solvent peak. When required, COSY and HSQC experiments were employed, using standard Varian and Agilent pulse sequences.

Infrared Spectroscopy

IR spectra were measured on a Bruker ALPHA Platinum ATR FT-IR spectrometer in the range 4000-550 cm^{-1}. The following abbreviations were used to describe the signals: s (strong), m (medium), w (weak), br (broad).

Mass Spectrometry

Mass spectra were recorded by Dr. Marie Squire and Dr Amelia Albrett on either a DIONEX Ultimate 3000 or Bruker MaXis 4G spectrometer, operated in high resolution positive ion electrospray mode. Samples were dissolved and diluted to the required concentration in HPLC grade methanol or acetonitrile.

Melting point

Melting points were recorded on an Electrothermal melting point apparatus and are uncorrected.

Elemental Analysis

Elemental analysis was carried out by Campbell Microanalytical Laboratory, University of Otago.

Luminescence Measurements

Emission spectra were recorded on a Horiba Fluorolog-3 spectrometer.

Thermogravimetric Analysis

Thermogravimetric analyses were carried out on an Alphatech SDT Q600 TGA/DSC apparatus. All samples were heated on alumina crucibles under nitrogen flow of 100 mL/min. Heating cycles consist of heating at 1 °C/min to 800 °C.

X-ray Crystallography

X-ray crystallographic data collection and refinement was carried out on a Oxford-Agilent SuperNova instrument with focused microsource Cu Kα (λ = 1.5418 Å) or Mo Kα (λ = 0.71073 Å) radiation and ATLAS CCD area detector. All structures were solved using direct methods with SHELXS[354] or SHELXT[355] and refined on F^2 using all data by full matrix least-squares procedures with SHELXL[356] within OLEX-2.[357] Hydrogen atoms were included in calculated positions or manually assigned from residual electron density where appropriate, with isotropic displacement parameters 1.2 times the isotropic equivalent of their respective carrier atoms. The functions minimized were $\Sigma w(F^2_o-F^2_c)$, with $w=[\sigma^2(F^2_o)+aP_2+bP]^{-1}$, where $P=[\max(F_o)^2+2F^2_c]/3$. Graphical representations of crystallographic data were prepared using Mercury.[358] Crystallographic data for all compounds is included in .cif format as electronic supplementary information. As discussed in the text, where voids containing highly disordered solvent molecules were present, the SQUEEZE routine was carried out[159]. This technique was employed only when sensible explicit modelling of the electron density due to solvent molecules was not possible, and where a considerable benefit to the refinement was gained.

Powder X-ray diffraction

X-Ray Powder Diffraction data were collected using an Oxford-Agilent SuperNova instrument using Cu Kα (λ = 1.5418 Å) radiation and an ATLAS CCD area detector. Samples were prepared by grinding of the applicable compound and packing inside an open glass tube. A baseline correction was manually applied using the baseline feature within the Origin data analysis software.

Gas Sorption

Gas sorption isotherms were carried out at Massey university on a Quantachrome Autosorb iQ2 instrument. Freshly prepared MOF samples were washed with DMF, then soaked in acetone for 48 hours. The acetone was regularly refreshed in this time. The samples were then transferred to a pre-weighed analysis tube. The acetone was then removed by holding the sample at vacuum for 18 hours. Accurate sample masses were calculated by using degassed samples after the activated samples were backfilled with nitrogen. All sorption measurements used ultra-high purity gases.

7.2 Ligand Synthesis

7.2.1 Chapter 2

The compounds 2-pyridylamidrazone[359] and acetylhydrazide,[360] were prepared according to literature methods and all characterisation data was found to be consistent with that provided.

Synthesis of pyridin-2-yl(N^1-acetylamidrazone) (H_2L2.1)

Method 1

2-Pyridylamidrazone (11.58 g, 85.7 mmol) was dissolved in 150 mL of dichloromethane and cooled in an ice bath. Acetyl chloride (8.12 mL, 128.6 mmol) was added dropwise

followed by triethylamine (17.83 mL, 128.6 mmol) and the resulting mixture was allowed to warm to room temperature. The mixture was then refluxed for two hours, before it was cooled back to room temperature, and the white precipitate filtered from the yellow solution. The solid was further washed with ethanol (3 x 50 mL) to afford the desired product as a white solid. Yield 10.80 g (60.6 mmol, 71 %).

Method 2

Pyridine-2-carbonitrile (11.05 g, 106.2 mmol) was added to a sodium methoxide solution, created by adding sodium metal (0.05 g, 2.2 mmol) to dry methanol (25 mL). After stirring for 18 hours, acetylhydrazide was added and the colourless solution was left to stir for a further 18 hours. During this time a precipitate formed which was filtered off and washed with diethyl ether to leave the desired product as a white solid. Yield 12.30 g. (69.1 mmol, 65 %).

Both methods provided analytically pure products.

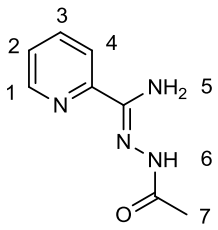

^{1}H NMR (400 MHz, DMSO-d_6) δ/ppm: 1.91 and 2.15 (2s, 3H, H7), 6.57 and 6.60 (2s, 2H, H5), 7.41 (m, 1H, H2), 7.84 (m, 1H, H3), 8.06 (m, 1H, H4), 8.54 (m, 1H, H1), 9.77 and 9.85 (2s, 1H, H6). ^{13}C NMR (101 MHz, DMSO-d_6) δ/ppm: 20.74, 22.09, 120.46, 124.50, 137.22, 148.42, 150.97, 165.14, 171.98. m/z (ESMS) 179.0930 ([M+H$^+$], $C_8H_{11}N_4O$ requires 179.0933). Selected IR (cm^{-1}): 3405(w), 3232(w), 3068(w), 1651(m), 1609(m), 1556(s), 1556(m), 1481(m), 1445(m), 1395(m), 1365(m), 1143(w), 1061(m), 996(m), 796(s), 623(m). m.p 218 °C.

Synthesis of pyridin-2-yl(N^1-amidoamidrazone) (H_2L2.2)

Pyridine-2-carbonitrile (0.98 g, 9.4 mmol) was dissolved in dry methanol (20 mL) with sodium methoxide (0.02 g, 0.4 mmol) and stirred at room temperature for one hour. Semicarbazide hydrochloride (1.05 g, 9.3 mmol) was added, followed by additional sodium methoxide (0.49 g, 9.0 mmol) and stirred at room temperature for 12 hours. The white

suspension that formed during this time was filtered, washed with water, methanol then diethyl ether to obtain the title compound. Yield 1.09 g (6.2 mmol, 66 %).

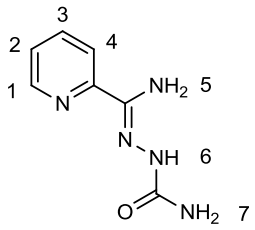

^{1}H NMR (400 MHz, DMSO-d_6) δ/ppm: 6.36 (m, 4H, H5, H7), 7.37 (dd, J=5.1, 2.0 Hz, 1H, H2), 7.77 (dd, J=7.8, 2.0 Hz, 1H, H3), 8.28 (d, J=7.8 Hz, 1H, H4), 8.50 (d, J=5.1 Hz, 1H, H1), 8.71 (s, 1H, H6). ^{13}C NMR (101 MHz, DMSO-d_6) δ/ppm: 120.87, 124.34, 136.92, 140.93, 148.17, 151.09, 158.01. m/z (ESMS) 180.0881 ([M+H$^+$], $C_7H_{10}N_5O$ requires 180.0880). Selected IR (cm^{-1}): 3439(w), 3244(w), 1682(s), 1591(s), 1461(s), 1433(s), 1378(s), 1144(w), 760(m), 624(m). m.p 192 °C.

Synthesis of dipyridin-2-yl(N^1,$N^{1'}$-succinylbisamidrazone) (H_4L2.3)

2-Pyridylamidrazone (0.24 g, 1.73 mmol) was dissolved in 10 mL of dichloromethane and cooled in an ice bath. Succinyl chloride (0.10 mL, 0.87 mmol) was added drop wise followed by triethylamine (1.17 mL, 128.6 mmol) and the resulting mixture was allowed to warm to room temperature. The mixture was stirred at room temperature overnight, filtered, and washed with ethanol (2 x 4 mL) to leave the desired product as a white solid. Yield 0.18 g (0.52 mmol, 60 %).

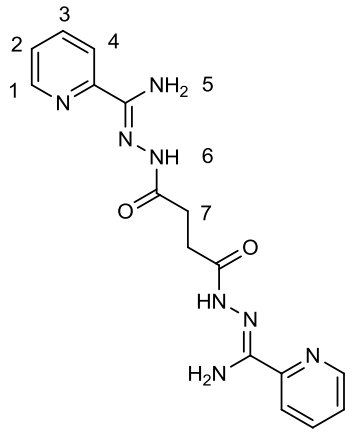

^{1}H NMR (400 MHz, DMSO-d_6) δ/ppm: 2.54 and 2.94 (2s, 4, H7), 6.50 - 6.75 (m, 4H, H5), 7.44 (m, 2H, H2), 7.85 (m, 2H, H3), 8.10 (m, 2H, H4), 8.56 (m, 2H, H1), 9.90 (m, 2H, H6). ^{13}C NMR (101 MHz, DMSO-d_6) δ/ppm: 27.26, 120.92, 124.73, 137.22, 142.47, 148.44, 150.98, 173.78. m/z (ESMS) 355.1627 ([M+H$^+$], $C_{16}H_{18}N_8O_2$ requires 355.1625). Selected IR (cm^{-1}): 3426(w), 3322(w), 3176(w), 1633(s), 1587(s), 1470(s), 14441(s), 1394(s), 1331(m), 1209(s), 997(m), 800(s), 626(m). m.p 210 °C.

Synthesis of pyridin-2-yl(N^1-(4-oxobutanoic acid)amidrazone) (H_3L2.4)

Succinic anhydride (7.66 g, 76.6 mmol) was added to a solution of 2-pyridylamidrazone (5.21 g, 38.3 mmol) in 50 mL of THF. The resulting mixture was heated to reflux for four hours, cooled to room temperature, filtered and washed with cold ethanol to obtain the desired product. Yield 4.34 g (18.5 mmol, 48 %).

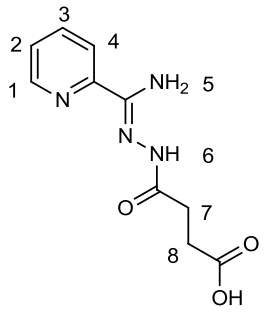

^{1}H NMR (400 MHz, DMSO-d_6) δ/ppm: 2.30-2.42 (m, 2H, H7), 2.83 (m, 2H, H8), 6.58 and 6.62 (2s, 2H, H5), 7.42 (m, 1H, H2), 7.84 (m, 1H, H3), 8.04 (m, 1H, H4), 8.54 (m, 1H, H1), 9.91 (br. s, 1H, H6). ^{13}C NMR (101 MHz, DMSO-d_6) δ/ppm: 27.82, 28.74, 29.61, 120.45, 124.77, 137.25, 148.45, 150.98, 167.25, 173.20, 174.53. m/z (ESMS) 237.0981 ([M+H$^+$], $C_{10}H_{13}N_4O_3$ requires 237.0982). Selected IR (cm^{-1}): 3435(w), 3316(w), 1767(w), 1688(s), 1617(m), 1378(m), 1196(s), 1156(m), 807(m), 656(m), 425(m). m.p 234 °C.

Synthesis of pyrazin-2-yl(N^1-acetylamidrazone) (H_2L2.5)

2-Pyrazinylamidrazone was prepared according to the same procedure as that for 2-pyridylamidrazone,[359] and was used without further characterisation. 2-Pyrazylamidrazone (0.49 g, 3.59 mmol) was dissolved in 18 mL of THF and cooled in an ice bath. Acetyl chloride (0.26 mL, 3.59 mmol) was added drop wise followed by triethylamine (0.50 mL, 3.59 mmol) and stirred at room temperature overnight. The white precipitate was filtered off and washed with ethanol to leave the desired product. (0.36 g, 56 %).

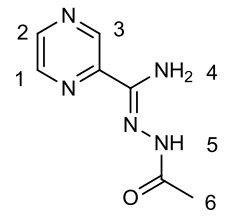

^{1}H NMR (400 MHz, DMSO-d_6) δ/ppm: 1.92 and 2.18 (2s, 3H, H6), 6.62 and 6.68 (2s, 2H, H4), 8.63 (m, 2H, H1, H2), 9.25 (m, 1H, H3), 9.98 (br. m, 1H, H5). ^{13}C NMR (101 MHz, DMSO-d_6) δ/ppm: 20.79, 22.08, 143.10, 144.46, 144.94, 146.46, 165.29, 172.22. m/z (ESMS) 180.0877 ([M+H$^+$], $C_7H_{10}N_5O$ requires 180.0885). Selected IR (cm^{-1}): 3447(w), 3377(w), 1693(m), 1607(s), 1607(m), 1338(s), 1294(m), 1142(m), 1005(m), 861(s), 685(m), 530(s), 458(s). m.p 235 °C.

Synthesis of pyrimidin-2-yl(N^1-acetylamidrazone) (H_2L2.6)

2-Pyrimidylamidrazone was prepared according to the same procedure as that for 2-pyridylamidrazone,[359] and was used without further characterisation. 2-Pyrimidylamidrazone (1.15 g, 8.41 mmol) was dissolved in dry DCM and cooled in an ice bath. Acetyl chloride (0.72 mL, 10.09 mmol) was added drop wise, followed by triethylamine (1.40 mL, 10.09 mmol) and the resulting mixture was stirred overnight. The yellow precipitate was filtered off and washed with ethanol to afford the desired product. Yield 1.14 g (6.34 mmol, 75 %).

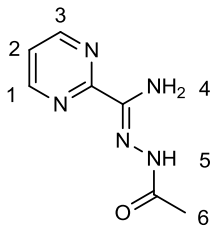

^{1}H NMR (400 MHz, DMSO-d_6) δ/ppm: 1.93 and 2.14 (2s, 3H, H6), 6.57 and 6.60 (2s, 2H, H4), 7.56 (m, 1H, H2), 8.87 (m, 2H, H1, H3), 9.77, 9.85 (2s, 2H, H5). ^{13}C NMR (101 MHz, DMSO-d_6) δ/ppm: 20.79, 22.11, 121.70, 141.68, 144.87, 157.76, 159.02, 172.44. m/z (ESMS) 180.0877 ([M+H^+], $C_7H_{10}N_5O$ requires 180.0885). Selected IR (cm^{-1}): 3390(w), 3127(w), 1643(m), 1543(s), 1455(s), 1387(s), 1287(m), 1066(m), 823(m, 635(s), 439(m). m.p 202 °C.

7.2.2 Chapter 3

4,4'-Bipyridine-2,2'-dicarbonitrile[361] and 1,3-bis(4-pyridyl-2-cyano)propane[362] were prepared according to literature methods, and all characterisation data was found to be consistent with that provided.

Synthesis of 2-cyano-4-*tert*-butylpyridine

2-Cyano-4-*tert*-butylpyridine was synthesised according to a modified preparation of 2-acetyl-4-*tert*-butylpyridine described by Hanan et al.[210] 2-Cyanopyridine (4.20 g, 40.3 mmol) and pivalic acid (12.36 g, 120.9 mmol) were dissolved in a 10 % H_2SO_4 solution. Silver nitrate (1.37 g, 8.0 mmol) was added and the solution was heated at 70 °C until the evolution of CO_2 stopped (circa 15 minutes). At this point, ammonium persulfate (17.5 g, 76.6 mmol) in 40 mL of water was added and the solution was heated at 90 °C for 10 minutes. The solution was cooled to room temperature then basified with a saturated

solution of sodium bicarbonate. The organic layer was extracted with DCM, dried with Na_2SO_4, and the solvent removed in vacuo. The dark brown oily residue was then purified by column chromatography (silica, 7:3 pet. ether:diethyl ether) to afford 2-cyano-4-tert-butylpyridine as a pale yellow oil. Analytical data matches that reported in the literature.[363]

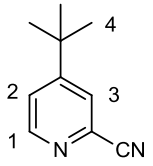

Yield 2.51 g (15.7 mmol, 39 %).

^{1}H NMR (400 MHz, $CDCl_3$) δ/ppm: 1.34 (s, 4 H) 7.49 (dd, J=5.3, 1.9 Hz, 1 H) 7.69 (d, J=1.9 Hz, 1 H) 8.61 (d, J=5.3 Hz, 1 H)

Synthesis of 4-*tert*-butylpyridin-2-yl(N^1-acetylamidrazone) (H_2L3.1)

2-Cyano-4-*tert*-butylpyridine (2.50 g, 15.6 mmol) was then dissolved in a sodium methoxide solution, produced by dissolving 0.05 g of sodium metal in dry methanol (50 ml), and stirred for 12 hours. To this, was added acetylhydrazide and the solution was left to stirr at ambient temperature for a further 12 hours. The white precipitate that formed was collected by suction filtration, and washed with diethyl ether. Yield 2.36 g (10.1 mmol, 65 %).

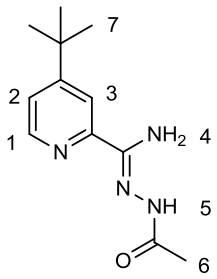

^{1}H NMR (400 MHz, DMSO-d_6) δ/ppm: 1.27 (s, 9H, H7), 1.90 and 2.16 (2s, 3H, H6), 6.56 and 6.61 (2s, 2H, H4), 7.45 (m, 1H, H2), 8.04 (s, 1H, H3), 8.44 (m, 1H, H1), 9.83 (br. s, 1H, H5). ^{13}C NMR (101 MHz, DMSO-d_6) δ/ppm: 20.67, 22.10, 30.56, 35.04, 116.62, 122.03, 142.74, 148.34, 160.35, 165.17, 171.92. m/z (ESMS) 235.1569 ([M+H$^+$], $C_{12}H_{19}N_4O$ requires 235.1559). Selected IR (cm^{-1}): 3424(w), 3327(w), 2953(w), 1644(s), 1583(s), 1543(s), 1439(m), 1377(s), 1304(m), 1269(m), 1056(m), 984(w), 888(m), 842(m), 583(s), 476(s). m.p 205 °C.

Synthesis of 4-phenylpyridin-2-yl(N^1-acetylamidrazone) (H_2L3.2)

2-Cyano-4-phenylpyridine (1.02 g, 5.65 mmol) was dissolved in a sodium methoxide solution, produced by adding 0.03 g sodium metal to 30 mL of dry methanol, and stirred for 12 hours. To this, was added acetylhydrazide (0.63 g, 8.48 mmol) and the solution was left

to stirr at ambient temperature for a further 12 hours. The white precipitate that formed during this time was collected by suction filtration, and washed with diethyl ether. Yield 0.48 g (1.87 mmol, 33 %).

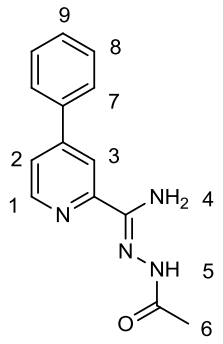

^{1}H NMR (400 MHz, DMSO-d_6) δ/ppm: 1.92 and 2.19 (2s, 3H, H6), 6.64 and 6.68 (2s, 2H, H4), 7.43 - 7.58 (m, 3H, H8, H9), 7.69 - 7.82 (m, 3H, H2, H7), 8.28 (s, 1H, H3), 8.60 (m, 1H, H1), 9.83 and 9.91 (2s, 1H, H5). ^{13}C NMR (101 MHz, DMSO-d_6) δ/ppm: 20.87, 22.11, 117.53, 122.36, 127.28, 129.77, 137.60, 142.55, 148.24, 149.14, 151.78, 165.22, 172.06. m/z (ESMS) 255.1260 ([M+H$^+$], $C_{14}H_{15}N_4O$ requires 255.1246). Selected IR (cm^{-1}): 3430(m), 3348(m), 3218(w), 3041(w, br), 1644(s), 1567(s), 1539(s), 1431(s), 1372(m), 1300(m), 1060(m), 838(m), 764(m), 682(s), 601(s), 573(s). m.p 236 °C.

Synthesis of 4,4'-bis(pyridin-2-yl(N^1-acetylamidrazone)) (H_4L3.3)

4,4'-Bipyridine-2,2'-dicarbonitrile (1.00 g, 4.9 mmol) was dissolved in 150 mL of hot ethanol. Hydrazine hydrate (10 mL, 206.0 mL) was then added, and the mixture was refluxed for two hours. The mixture was then cooled to room temperature and the white solid filtered off. This solid was slurried in DCM to which acetyl chloride (1.42 mL, 20 mmol) was added drop wise followed by triethylamine (2.77 mL, 20 mmol). The resulting mixture was then refluxed for 4 hours, cooled to room temperature and the white solid filtered off and washed with ethanol. Yield 0.53 g (1.5 mmol, 31 %).

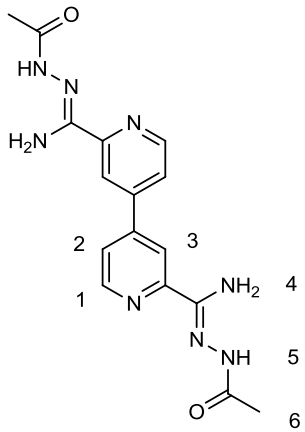

^{1}H NMR (400 MHz, DMSO-d_6) δ/ppm: 1.93 and 2.19 (2s, 6H, H6), 6.67 and 6.70 (2s, 4H, H4), 7.85 (m, 2H, H2), 8.38 (m, 2H, H3), 8.71 (m, 2H, H1), 9.85 and 9.94 (2s, 2H, H5). m/z (ESMS) 355.1627 ([M+H$^+$], $C_{16}H_{19}N_8O_2$ requires 355.1631). Selected IR (cm^{-1}): 3447(w), 3367(w), 1681(m), 1645(s), 1592(m), 1537(m), 1353(s), 1333(s), 1039(m), 993(m),

627(s), 428(m). m.p .300 °C.

Synthesis of 1,3-di(4-(pyridin-2-yl(N^1-acetylamidrazone))propane (H_4L3.4)

1,3-bis(4-pyridyl-2-cyano)propane (0.73 g, 2.95 mmol) was dissolved in a sodium methoxide solution, produced by dissolving 0.03 g of sodium metal in dry methanol (50 ml), and stirred for 9 hours. Acetyl hydrazide (0.53 g, 7.1 mmol) was then added and the resulting solution was stirred at room temperature for 40 hours. After this time, the clear solution was reduced in volume and cooled to 0 °C to allow the product to crystallise out as white needles. Yield 1.00 g (2.53 mmol, 86 %).

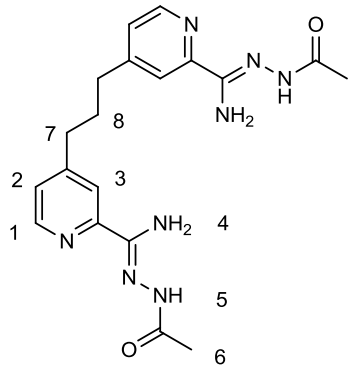

^{1}H NMR (400 MHz, DMSO-d_6) δ/ppm: 1.90 and 2.14 (2s, 6H, H6), 1.92 (m, 2H, H8), 2.66 (m, 4H, H7), 6.54 and 6.58 (2s, 4H, H4), 7.28 (m, 2H, H2), 7.87 (s, 2H, H3), 8.42 (m, 2H, H1), 9.75 - 9.81 (2s, 2H, H5). m/z (ESMS) 397.2095 ([M+H^+], $C_{19}H_{25}N_8O_2$ requires 397.2100). Selected IR (cm^{-1}): 3449(w), 3410(w), 3330(w), 3195(w), 3042(w), 1652(m), 1597(m), 1551(s), 1450(m), 1303(m), 1062(w), 998(w), 834(m), 591(m), 473(s). m.p 248 °C.

Synthesis of 2,5-pyrazinedicarboxylic acid

2,5-dimethylpyrazine 4.8 g (44.3 mmol) was dissolved in 130 mL of water. Potassium permanganate (14.2 g, 88.6 mmol) was added and the mixture was stirred at room temperature for one hour. Additional potassium perganganate (14.2 g, 88.6 mmol) was added and the mixture was refluxed for five hours. Upon cooling the black solid was filtered off and upon acidification of the colourless aqueous filtrate with H_2SO_4 2,5-dicarboxypyrazine crystallised out. Yield 1.02 g (6.1 mmol, 14 %). Analytical data matches that reported in the literature.[364]

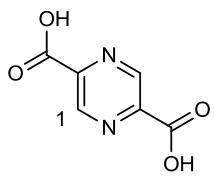

^{1}H NMR (400 MHz, DMSO-d_6) δ/ppm: 9.25 (s, 2H, H1).

Synthesis of 2,5-di(N^1-acetylamidrazone)pyrazine (H_4L3.5)

2,5-Pyrazinedicarboxylic acid was converted to 2,5-pyridinedicarbonitrile according to a literature method.[365] This (0.33 g, 2.56 mmol) was then dissolved in 40 mL of hot ethanol. Hydrazine hydrate (1.0 mL, 20.6 mmol) was added which was followed by the formation of a voluminous white precipitate. This was filtered off then slurried in DCM. Acetyl chloride (0.46 mL, 6.4 mmol) was carefully added to this followed by triethylamine (0.89 mL, 6.4 mmol). The resulting mixture was refluxed for 18 hours, the tan solid collected, then washed with ethanol and diethyl ether. Yield 0.1506 g (0.54 mmol, 21 %).

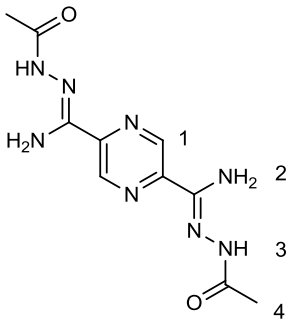

m/z (ESMS) 279.1313 ([M+H^+], $C_{16}H_{19}N_8O_2$ requires 279.1318). Selected IR (cm^{-1}): 3330(w, br), 3051(w, br), 1735(m), 1585(m), 1536(w), 1295(w), 1125(s), 1028(s), 974(s), 764(s), 499(m), 450(m). m.p >300 °C.

7.2.3 Chapter 4

The synthesis of methyl isonicotinate[366] and the purification of aldehydes[255] were performed according to known procedures.

Synthesis of methyl 2-acetylisonicotinate

A modified preparation to that described by Husson et al.[241] for ethyl 2-acetylisonicotinate was used. To solution of methyl isonicotinate (21.30, 0.16 mol) in acetonitrile (300 mL) was added paraldehyde (100 g, 0.76 mol), $FeSO_4.7H_2O$ (0.73 g, 2.6 mmol), trifluoroacetic acid (18 g) and *t*-BuOOH (70 % solution, 39 g, 0.31 mol) at room temperature. The resulting solution was heated at 60 °C for 18 hours. The solvent was then removed under reduced pressure and the dark brown residue was basified with saturated $NaHCO_3$. The organics were then extracted with toluene (3 x 100 mL) and the combined fractions were

dried with $MgSO_4$, filtered and the solvent removed under reduced pressure. The dark tacky residue was then purified by column chromatography (silica, 1:1 diethyl ether:pentane) to afford the desired product as a white solid. Yield 13.41 g (0.10 mol, 65 %). Analytical data matches that reported in the literature.[367]

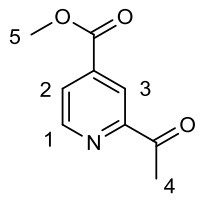

^{1}H NMR (400 MHz, $CDCl_3$) δ/ppm: 2.71 (s, 3H, H4) 3.96 (s, 3H, H5), 7.98 (dd, J=5.1, 1.6 Hz, 1H, H2), 8.51 (d, J=1.6 Hz, 1H, H3), 8.80 (d, J=5.1 Hz, 1H, H1). m.p. 50°C.

Synthesis of 4'-phenyl-2,2':6',2''-terpyridine-4-4''-dicarboxylic acid (H_2L3.1)

To a solution of methyl 2-acetylisonicotinate (3.55 g, 20 mmol) in ethanol (45 mL), was added freshly distilled benzaldehyde (1.1 g, 10 mmol) followed by KOH (1.53 g, 27 mmol). The resulting solution darkened and was allowed to stir until the formation of a visible precipitate (around 30 minutes). To this, a 35% aqueous ammonia solution (21 mL) was added leading to the disappearance of the aforementioned precipitate. Stirring was continued at room temperature, open to the atmosphere, for a further 20 hours after which the newly precipitated K^+/NH_4^+ salt of the final product was precipitated as a brown solid. This was filtered off, washed with ethanol, then re-dissolved in the minimum amount of water and acidified with HCl to pH of 4. This resulting solid was filtered, and washed with water until the washings were neutral. It was then successively washed with with ethanol then diethyl ether and the light brown powder left to air dry. Yield 0.65 g (1.6 mmol, 17 %).

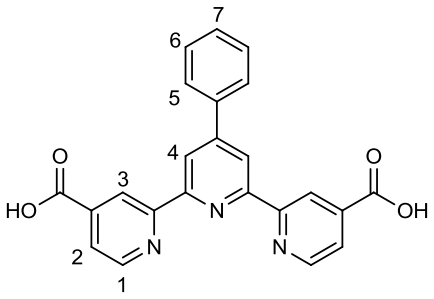

^{1}H NMR (400 MHz, DMSO-d_6) δ/ppm: 7.45 - 7.59 (m, 3H, H6, H7), 7.86 (d, J=6.5 Hz, 2H, H5), 7.90 (d, J=5.1 Hz, 2H, H2), 8.68 (s, 2H, H3), 8.89 (d, J=5.1 Hz, 2H, H1), 8.93 (s, 2H, H4). ^{13}C NMR (101 MHz, DMSO-d_6) δ/ppm: 117.35, 118.31, 122.07, 125.54, 128.01, 128.24, 135.76, 138.22, 148.36, 149.05, 153.66, 154.43, 164.65. m/z (ESMS) 398.1133 ([M+H^+], $C_{23}H_{16}N_3O_4$ requires 398.1140). Selected IR (cm^{-1}): 3028(br), 2781(br), 1714(s), 1593(s), 1550(m), 1361(m), 1276(s), 1221(s), 759(s), 691(s), 665(s). m.p > 330 °C.

Synthesis of 4'-(2-methylphenyl)-2,2':6',2''-terpyridine-4-4''-dicarboxylic acid (H_2L3.2)

The same procedure for the synthesis of H_2**L3.1** was followed using *o*-tolualdehyde (0.97 g, 8.0 mmol) instead of benzaldehyde to yield an off-white solid. Yield 0.75 g (1.8 mmol, 23 %).

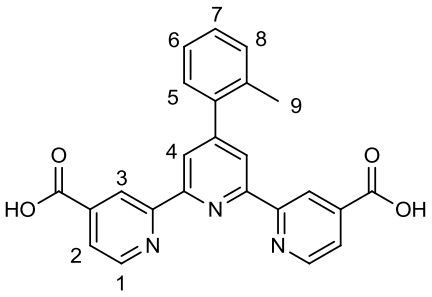

^{1}H NMR (400 MHz, DMSO-d_6) δ/ppm: 2.32 (s, 3H, H9), 7.30 - 7.44 (m, 4H, H5, H6, H7, H8), 7.91 (dd, J=4.9, 1.8 Hz, 2H, H2), 8.43 (s, 2H, H3), 8.90 (d, J=4.9 Hz, 2H, H1), 8.98 (s, 2H, H4). ^{13}C NMR (101 MHz, DMSO-d_6) δ/ppm: 20.40, 120.07, 122.00, 123.89, 126.87, 129.21, 129.58, 131.22, 135.04, 138.99, 140.07, 151.03, 151.85, 154.99, 156.37, 166.52. m/z (ESMS) 412.1298 ([M+H$^+$], C24H18N3O4 requires 412.1292). Selected IR (cm^{-1}): 2778(br), 2476(br), 1714(s), 1594(m), 1564(m), 1543(m), 1459(m), 1365(m), 1281(s), 1224(s), 892(m), 762(s), 673(s). m.p. > 330 °C.

Synthesis of 4'-(4-chlorophenyl)-2,2':6',2''-terpyridine-4-4''-dicarboxylic acid (H_2L3.3)

The same procedure for the synthesis of H_2**L3.1** was followed using *p*-chlorobenzaldehyde (1.37 g, 10 mmol) instead of benzaldehyde to yield a light brown solid. Yield 0.88 g (2.1 mmol, 21 %).

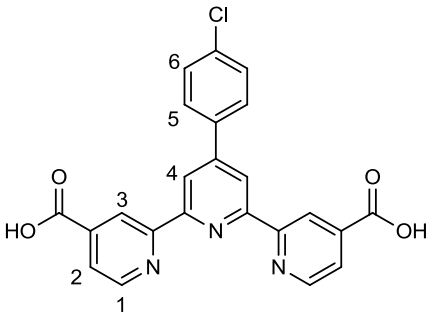

^{1}H NMR (400 MHz, DMSO-d_6) δ/ppm: 7.62 (d, J=8.6 Hz, 2H, H6), 7.92 (dd, J=4.9, 1.8 Hz, 1H, H2), 7.97 (d, J=8.6 Hz, 2H, H5), 8.73 (s, 1H, H3), 8.92 (d, J=4.9 Hz, 2H, H1), 8.96 (s, 2H, H4). m/z (ESMS) 432.0750 ([M+H$^+$], $C_{23}H_{15}N_3O_4Cl$ requires 432.0751). Selected IR (cm^{-1}): 2797(br), 2511(br), 1712(s), 1597(s), 1560(m), 1360(s), 1260(s), 1220(s), 1094(s), 771(s), 664(s). m.p > 330 °C.

Synthesis of 4'-(4-nitrophenyl)-2,2':6',2''-terpyridine-4-4''-dicarboxylic acid (H_2L3.4)

The same procedure for the synthesis of H_2**L3.1** was followed using *p*-nitrobenzaldehyde (1.48 g, 10 mmol) instead of benzaldehyde to yield a brown solid. Yield 0.68 g (1.5 mmol, 15 %).

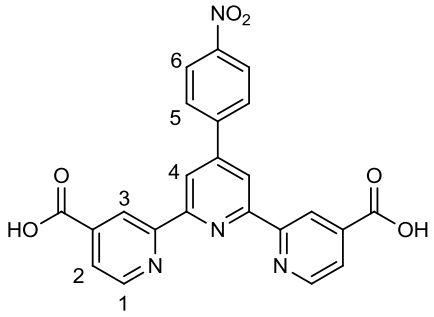

^{1}H NMR (400 MHz, DMSO-d_6) δ/ppm: 7.95 (dd, J=5.0, 1.6 Hz, 2H, H2), 8.24 (d, J=8.7 Hz, 2H, H5), 8.40 (d, J=8.7 Hz, 2H, H6), 8.82 (s, 2H, H3), 8.95 (d, J=5.0 Hz, 2H, H1), 8.99 (s, 2H, H4). m/z (ESMS) 443.0990 ([M+H^+], $C_{23}H_{15}N_4O_6$ requires 443.0991). Selected IR (cm^{-1}): 2989(br), 2791(br), 1715(m), 1591(m), 1517(s), 1345(s), 1258(m), 1220(s), 849(s), 754(m), 665(m). m.p > 330 °C.

Synthesis of 4'-(thiophen-2-yl)-2,2':6',2''-terpyridine-4-4''-dicarboxylic acid (H_2L3.5)

The same procedure for the synthesis of H_2**L3.1** was followed using 2-formylthiophene (1.13 g, 10 mmol) instead of benzaldehyde to yield a brown solid. Yield 1.10 g (2.7 mmol, 27 %).

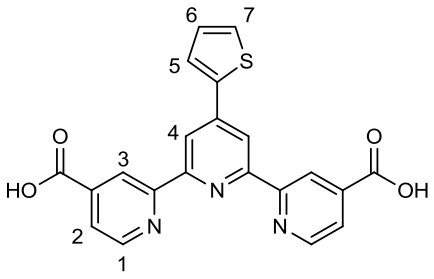

^{1}H NMR (400 MHz, DMSO-d_6) δ/ppm: 7.19 (t, J=4.5 Hz, 1H, H6), 7.73 (d, J=4.5 Hz, 1H, H5), 7.83 - 7.91 (m, 3H, H2, H7), 8.56 (s, 2H, H3) 8.83 - 8.90 (m, 4H, H1, H4). ^{13}C NMR (101 MHz, DMSO-d_6) δ/ppm: 117.19, 120.22, 124.05, 127.46, 129.26, 129.58, 140.20, 140.49, 143.51, 150.63, 155.28, 155.69, 166.36. m/z (ESMS) 404.0697 ([M+H^+], $C_{21}H_{14}N_3O_4S$ requires 404.0705). Selected IR (cm^{-1}): 3341(br), 2827(br), 1690(m), 1593(s), 1509(m), 1314(m), 1227(s), 1008(m), 748(s), 727(m), 666(m). m.p > 330 °C.

Synthesis of 4'-(thiophen-3-yl)-2,2':6',2''-terpyridine-4-4''-dicarboxylic acid (H_2L3.6)

The same procedure for the synthesis of H_2**L3.1** was followed using 3-formylthiophene (1.91 g, 17 mmol) instead of benzaldehyde to yield a light brown solid. Yield 1.67 g (4.1 mmol, 24 %).

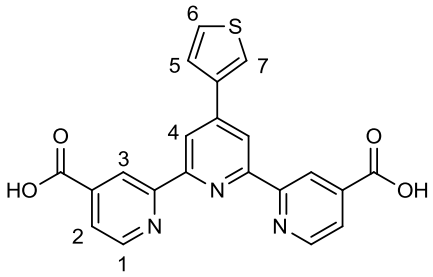

^{1}H NMR (400 MHz, DMSO-d_6) δ/ppm: 7.67 - 7.75 (m, 2H, H5, H6), 7.86 - 7.93 (m, 2H, H2), 8.32 (s, 1H, H7), 8.67 (s, 2H, H3), 8.84 - 8.94 (m, 4H, H1, H4). ^{13}C NMR (101 MHz, DMSO-d_6) δ/ppm: 118.51, 120.25, 123.95, 125.77, 126.32, 128.60, 138.94, 140.17, 144.96, 150.67, 155.25, 156.03, 166.42. m/z (ESMS) 404.0696 ([M+H+], $C_{21}H_{14}N_3O_4S$ requires 404.0705). Selected IR (cm^{-1}): 3368(br), 2517(br), 1714(m), 1595(s), 1552(m), 1273(s), 1227(s), 993(w), 847(w), 768(s), 681(m), 660(m). m.p > 330 °C.

Synthesis of 4'-(pyridin-4-yl)-2,2':6',2''-terpyridine-4-4''-dicarboxylic acid (H_2L3.7)

The same procedure for the synthesis of H_2**L3.1** was followed using 4-pyridinecarboxaldehyde (2.14 g, 20.0 mmol) instead of benzaldehyde to yield an orange solid. Yield 1.02 g (2.6 mmol, 13 %).

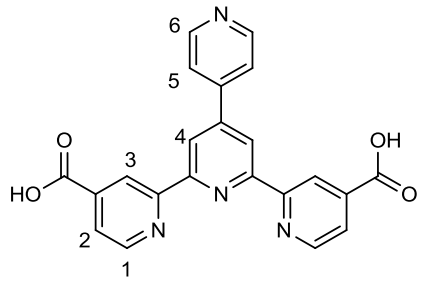

^{1}H NMR (400 MHz, DMSO-d_6) δ/ppm: 7.92 (m, 4H, H2, H5), 8.76 (m, 4H, H3, H6), 8.91 (d, J=5.0 Hz, 2H, H1), 8.95 (s, 2H, H4). m/z (ESMS) 399.1094 ([M+H^+], $C_{22}H_{15}N_4O_4$ requires 399.1093). Selected IR (cm^{-1}): 3035(br), 2850(br), 1701(s), 1590(s), 1542(s), 1362(s), 1217(s), 826(s), 771(s), 669(s), 627(s). m.p > 330 °C.

Synthesis of 4'-furyl-2,2':6',2''-terpyridine-4-4''-dicarboxylic acid (H_2L3.8)

The same procedure for the synthesis of H_2**L3.1** was followed using furfural (5.0 g, 52.0 mmol) instead of benzaldehyde to yield a brown solid. Yield 1.72 g (20 mmol, 38 %).

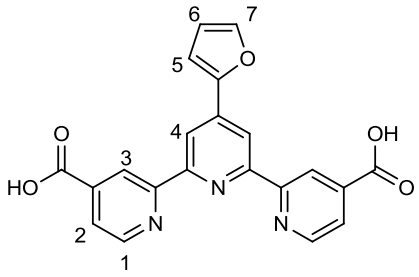

^{1}H NMR (400 MHz, DMSO-d_6) δ/ppm: 6.70 (m, 1H, H6), 7.41 (m, 1H, H5), 7.90 (m, 3H, H2, H7), 8.65 (s, 2H, H3), 8.86 - 8.94 (m, 4H, H1, H4). m/z (ESMS) 388.0931 ([M+H^+], $C_{21}H_{14}N_3O_5$ requires 388.0933). Selected IR (cm^{-1}): 3400(br), 2476(br), 1707(s), 1604(m), 1265(s), 1221(s), 1016(w), 769(m), 664(m). m.p > 330 °C.

Synthesis of 4'-(4-(dimethylamino)phenyl)-2,2':6',2''-terpyridine-4-4''-dicarboxylic acid (H_2L3.9)

The same procedure for the synthesis of H_2**L3.1** was followed using 4-(dimethylamino)benzaldehyde (1.30 g, 9.0 mmol) instead of benzaldehyde to yield a brown solid. Yield 0.98 g (2.2 mmol, 25 %). m.p > 330 °C.

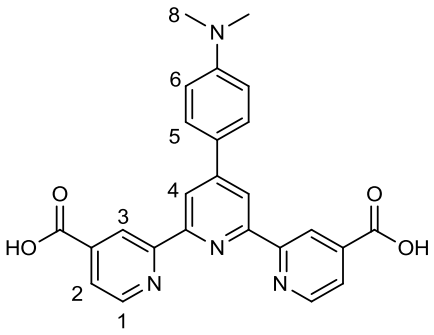

^{1}H NMR (400 MHz, DMSO-d6) δ/ppm: 2.96 (s, 6H, H8), 6.83 (d, J=9.0 Hz, 2H, H6), 7.76 (d, J=9.0 Hz, 2H, H5), 7.89 (dd, J=4.7, 1.2 Hz, 2H, H2), 8.64 (s, 1H, H3), 8.90 (d, J=4.7 Hz, 2H, H1), 8.92 (s, 1H, H4). m/z (ESMS) 441.1567 ([M+H^+], $C_{25}H_{21}N_4O_4$ requires 441.1563). Selected IR (cm^{-1}): 3374(br), 2817(br), 1581(s), 1531(m), 1371(m), 1371(m), 1211(m), 1106(m), 794(m), 615(m), 557(w). m.p > 330 °C.

7.2.4 Chapter 5

Synthesis of 3-acetyl-4-hydroxybenzoic acid

3-Acetyl-4-hydroxybenzoic acid was synthesised according to a modified procedure to that reported in the literature.[368] Acetic anhydride (1.82 mL, 19.3 mmol) and H_2SO_4 (4 drops) were added to 4-hydroxybenzoic acid (2.66 g, 19.3 mmol) and heated at reflux for two hours. Water was then added to the cooled solution, and the product extracted into ethylacetate, dried with $MgSO_4$ and the solvent removed to afford 4-acetoxybenzoic acid. This was mixed with anhydrous $AlCl_3$ and the combined solids were heated at 150 °C for 5 hours before being cooled to room temperature. 2M HCl (100 mL) was added and the product extracted into ethyl acetate, dried with $MgSO_4$ and the solvent removed. The off-white solid was slurried in 60 °C water and filtered whilst hot. After three successive washings of room temperature water, the pale yellow solid was allowed to air dry overnight. Yield 2.01 g (11.2 mmol, 58 %).

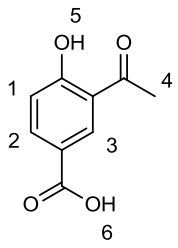

^{1}H NMR (400 MHz, DMSO-d_6) δ/ppm: 2.65 (s, 3H, H4), 7.02 (d, J=8.6 Hz, 1H, H1), 8.00 (d, J=8.6 Hz, 1H, H2), 8.35 (s, 1 H), 12.25 (br. s, 1H, H5), 12.77 (br. s, 1H, H6). ^{13}C NMR (101 MHz, DMSO-d_6) δ/ppm: 28.74, 118.32, 121.25, 122.14, 133.39, 136.76, 164.10, 166.80, 203.68.

Synthesis of 4-hydroxy-3-(1-(hydroxyimino)ethyl)benzoic acid (H_3L5.1)

Hydroxylammonium chloride (0.45 g, 6.5 mmol) was added to a solution of 3-acetyl-4-hydroxybenzoic acid (0.98 g, 5.4 mmol) and triethylamine (0.90 mL, 6.5 mmol) in 30 mL of ethanol and the resulting solution refluxed overnight. This was then reduced in volume and water was added. The white precipitate was then extracted into ethylacetate, dried with $MgSO_4$ and the solvent removed to afford a white powder. Yield 0.84 g (4.3 mmol, 66 %).

^{1}H NMR (400 MHz, DMSO-d_6) δ/ppm: 2.25 (s, 3H, H4), 6.92 (d, J=8.2 Hz, 1H, H1), 7.79 (dd, J=8.2, 2.0 Hz, 1H, H2), 8.00 (d, J=2.0 Hz, 1H, H3), 11.65 (br. s, 1H, H6), 12.12 (br. s, 1H, H5), 12.60 (br. s, 1H, H7).). ^{13}C NMR (101 MHz, DMSO-d_6) δ/ppm: 11.62, 117.12,

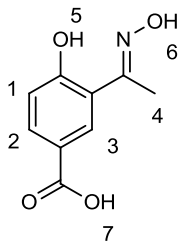

119.94, 121.87, 130.10, 131.91, 157.17, 161.38, 167.27. m/z (ESMS) 196.0614 ([M+H$^+$], $C_9H_{10}NO_4$ requires 196.0610). Selected IR (cm^{-1}): 3352(w), 1698(s), 1605(m), 1513(w), 1321(s), 1267(s), 1123(m), 1039(s), 809(s), 680(s), 639(s), 563(m), 508(m). m.p 262 °C.

Synthesis of 3-formyl-4-hydroxybenzoic acid

4-hydroxybenzoic acid (9.04 g, 65.5 mmol) was suspended in trifluoroacetic acid (20 mL). A solution of hexamine (9.20 g, 65.5 mmol) in trifluoroacetic acid (25 mL) was carefully added and the mixture heated at 90 °C overnight. Upon cooling to room temperature, 100 mL of 4 M HCl was added to the clear yellow solution and the mixture was stirred at room temperature for a further 5 hours. The white precipitate that formed was filtered and washed with water (3 x 100 mL). Yield 6.50 g (39.1 mmol, 60 %). Analytical data matches that reported in the literature.[92]

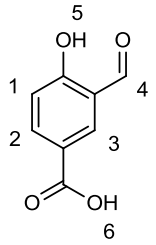

^{1}H NMR (400 MHz, DMSO-d_6) δ/ppm: 7.06 (d, J=8.6 Hz, 1H, H1), 8.01 (dd, J=8.6, 2.7 Hz, 1H, H2), 8.20 (d, J=2.7 Hz, 1H, H3), 10.25 (s, 1H, H4), 11.47 (s, 1H, H5), 12.79 (br. s, 1H, H6).

Synthesis of 4-hydroxy-3-((hydroxyimino)methyl)benzoic acid (H_3L5.2)

3-formyl-4-hydroxybenzoic acid (1.87 g, 11.3 mmol) was dissolved in ethanol (50 mL) to form a pale yellow solution. Triethylamine (1.88 mL, 13.6 mmol) was added followed by hydroxylammonium chloride (0.95 g, 13.6 mmol) and the resulting solution was refluxed overnight. After this period, the solution was cooled then added to 100 mL of 1 M HCl. The product was then extracted with ethylacetate, dried with $MgSO_4$, and the solvent removed to afford the desired product as a white powder. Yield 1.54 g (8.5 mmol, 75 %).

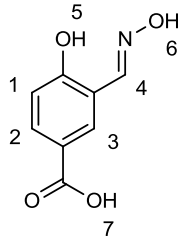

^{1}H NMR (400 MHz, DMSO-d_6) δ/ppm: 6.93 (d, J=8.2 Hz, 1H, H1), 7.77 (dd, J=8.2, 2.3 Hz, 1H, H2), 8.12 (d, J=2.3 Hz, 1H, H3), 8.33 (s,

1H, H4), 10.80 (s, 1H, H6), 11.40 (s, 1H, H5), 12.60 (br. s, 1H, H7). ^{13}C NMR (101 MHz, DMSO-d_6) δ/ppm:116.47, 118.86, 122.36, 129.70, 132.21, 146.69, 160.04, 167.23. m/z (ESMS) 182.0454 ([M+H^+], $C_8H_8NO_4$ requires 182.0453). Selected IR (cm^{-1}): 3418(w), 1668(s), 1621(m), 1583(m), 1495(w), 1238(s), 1137(s), 1011(m), 838(m), 769(s), 687(s), 637(s), 471(s). m.p 246 °C.

Synthesis of 3-Bromo-4-hydroxybenzoic acid

The synthesis of this compound was modified from a literature method.[369] A solution of bromine (2.5 mL, 49.0 mmol) in 20 mL of 1,4-dioxane was added slowly to a stirred solution of 4-hydroxybenzoic acid (6.0 g, 43.4 mmol) dissolved in 30 mL of 1,4-dioxane. The resulting solution was stirred at room temperature for 48 hours. Aqueous sodium thiosulfate was added, and the mixture was extracted with ethyl acetate. The organic layer was then dried with $MgSO_4$ and concentrated under reduced pressure. The solid obtained was recrystallised from ethanol to obtain an analytically pure product. Yield 7.85 g (36.2 mmol, 83 %).

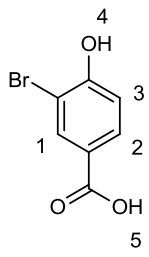

^{1}H NMR (400 MHz, DMSO-d_6) δ/ppm: 6.98 (d, J=8.6 Hz, 1H, H3), 7.74 (dd, J=8.6, 2.0 Hz, 1H, H2), 7.96 (d, J=2.0 Hz, 1H, H1), 11.17 (br. s, 1H, H5). ^{13}C NMR (101 MHz, DMSO-d_6) δ/ppm: 109.48, 116.38, 123.36, 130.88, 134.67, 158.61, 166.48.

Synthesis of 3-bromo-5-formyl-4-hydroxybenzoic acid

Excess hexamine (3.52 g, 25.1 mmol) in 8 mL of trifluoroacetic acid was added to a suspension of 3-bromo-4-hydroxybenzoic acid (0.91 g, 4.2 mmol) in 12 mL of trifluoroacetic acid. The resulting solution was heated at reflux overnight. This solution was allowed to cool to room temperature and 4M HCl was added and stirred for 4 hours. The pale yellow precipitate that formed was filtered and washed with water. Yield 0.62 g (2.5 mmol, 60 %).

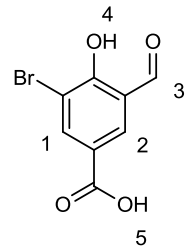

^{1}H NMR (400 MHz, DMSO-d_6) δ/ppm: 8.25 (s, 1H, H1), 8.30 (s, 1H, H2), 10.10 (s, 1H, H3). m/z (ESMS) 244.9441 ([M+H^+], $C_8H_6O_4Br$ requires 244.9449).

Synthesis of 3-bromo-4-hydroxy-5-((hydroxyimino)methyl)benzoic acid (H_3L5.3)

Hydroxylammonium chloride (0.48 g, 6.9 mmol) was added to a solution of 3-bromo-5-formyl-4-hydroxybenzoic acid (1.13 g, 4.6 mmol) and triethylamine (0.96 mL, 6.9 mmol) in 30 mL of ethanol and the resulting solution refluxed overnight. This was then reduced in volume and water was added. The white precipitate was then extracted into ethylacetate, dried with $MgSO_4$ and the solvent removed to afford a white powder. Yield 0.99 g (3.8 mmol, 55 %).

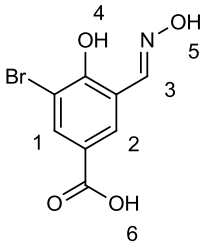

^{1}H NMR (400 MHz, DMSO-d_6) δ/ppm: 8.01 (d, J=2.3 Hz, 1H, H1), 8.05 (d, J=2.3 Hz, 1H, H2), 8.50 (s, 1H, H3), 11.92 (br. s, 1H, H6). ^{13}C NMR (101 MHz, DMSO-d_6) δ/ppm: 110.23, 119.29, 123.89, 134.61, 149.92, 157.11, 166.06. m/z (ESMS) 259.9552 ([M+H^+], $C_8H_7NO_4Br$ requires 259.9558). Selected IR (cm^{-1}): 3439(m), 1687(s), 1613(w), 1576(w), 1461(w), 1412(s), 1280(s), 1219(s), 1183(s), 1017(m), 728(m), 698(s), 672(s), 510(s). m.p 234 °C.

7.3 Complex Synthesis

7.3.1 Chapter 2

All zinc carboxylate salts, apart from zinc acetate which was obtained from a commercial supplier, were synthesised in the following manner; the appropriate carboxylic acid was dissolved in water with one equivalent of sodium hydroxide. To this was added half an equivalent of zinc sulphate dissolved in water. The resulting solution was stirred for several hours until the observation of a white precipitate. This was filtered off, washed with water, and left to air dry.

Synthesis of [Zn(H_2L2.1)(AcO)$_2$] (2.1)

Zinc acetate (49.2 mg, 0.22 mmol) was added to a solution of H_2**L2.1** (40 mg, 0.22 mmol) in methanol (10 mL). The solution was reduced in volume under pressure at 40 °C. Upon standing colourless rod shape crystals formed which were isolated by filtration and air dried Yield 72.9 mg (18.6 mmol, 85%).

Selected IR (cm^{-1}): 3428(w), 3227(w), 3121(w), 1713(w), 1626(m), 1595(m), 1539(s), 1392(s), 1295(s), 1110(m), 1015(m), 799(m), 678(s), 581(br. s). Anal. calcd. for $C_{12}H_{16}N_4O_5Zn+1.5H_2O$: C, 37.08; H, 4.93; N, 14.41 %. Found: C, 37.22; H, 4.93; N, 14.28 %.

Synthesis of [Zn(H_2L2.1)(EtCO$_2$)$_2$]·MeOH (2.2)

2.2 was prepared from H_2**L2.1** (21.5 mg, 0.12 mmol) in an analogous manner to **2.1** except zinc propionate (29.9 mg, 0.12mmol) was used instead of zinc acetate. Yield 11.5 mg (0.03 mmol, 38 %).

Selected IR (cm^{-1}): 3401(w), 3259(w), 1707(w), 1621(m), 1587(m), 1540(s), 1401(m), 1298(s), 1111(m), 1019(m), 814(m), 660(s). Anal. calcd. for $C_{14}H_{20}N_4O_5Zn+1.5H_2O$: C, 40.35; H, 5.56; N, 13.44 %. Found: C, 40.75; H, 5.37; N, 13.43 %.

Synthesis of [Zn(H_2L2.1)(ClAcO)$_2$] (2.3)

Zinc chloroacetate (65.9 mg, 0.24 mmol) and H_2**L2.1** (21.7 mg, 0.13 mmol) were dissolved in methanol (10 mL) to create a pale yellow solution. Upon leaving the solution in a capped vial overnight, white needle like crystals formed which were removed from the colourless solution via suction filtration. Yield 52.1 mg (0.12 mmol, 93 %).

Selected IR (cm^{-1}): 3327(br. w), 3028(w), 1719(w), 1671(m), 1596(m), 1523(s), 1390(s), 1291(s), 1099(m), 1027(m), 770(s), 651(m). Anal. calcd. for $C_{12}H_{14}N_4O_5Cl_2Zn+0.5H_2O$: C, 32.79; H, 3.44; N, 12.75 %. Found: C, 32.68; H, 3.49; N, 12.71 %.

Synthesis of [Zn(H_2L2.1)(BzO)$_2$] (2.4)

2.4 was prepared from H_2**L2.1** (33.3 mg, 0.19 mmol) in an analogous manner to **2.1** except zinc benzoate (128.5 mg, 0.19 mmol) was used instead of zinc acetate. Yield 42.0 mg (0.09 mmol, 46 %).

Selected IR (cm^{-1}): 3340 (br. w), 1709(w), 1594(m), 1542(s), 1384(s), 1304(m), 1069(w), 712(s), 591(m).

Synthesis of [Zn(H_2L2.1)(*p*-MeBzO)$_2$] (2.5)

2.5 was prepared from H_2**L2.1** (25.8 mg, 0.14 mmol) in an analogous manner to **2.1** except zinc *p*-toluate (102.4 mg, 0.14mmol) was used instead of zinc acetate. Yield 27.0 mg (0.05 mmol, 38 %).

Selected IR (cm^{-1}): 3115 (br. w), 1698(w), 1593(m), 1536(s), 1374(s), 1298(s), 1094(w), 766(s), 745(m), 607(s),468(m). Anal. calcd. for $C_{24}H_{24}N_4O_5Zn$: C, 56.10; H, 4.71; N, 10.90 %. Found: C, 55.91; H, 4.58; N, 10.89 %.

Synthesis of [Cd(H_2L2.1)(AcO)$_2$] (2.6)

2.6 was prepared from H_2**L2.1** (10.0 mg, 0.06 mmol) in an analogous manner to **2.1** except cadmium acetate (30.0 mg, 0.11 mmol) was used instead of zinc acetate. Yield 12.0 mg (0.03 mmol, 49 %).

Selected IR (cm^{-1}): 3126(br. w), 1535(s), 1415(s), 1295(m), 1012(m) 802(m), 680(s), 621(m). Anal. calcd. for $C_{12}H_{16}N_4O_5Cd$: C, 35.27; H, 3.95; N, 13.71 %. Found: C, 35.18; H, 4.52; N, 12.92 %.

Synthesis of [Cu_2(H_2L2.1)$_2$$Cl_2$($\mu$-Cl)$_2$] (2.7)

Hot solutions of copper chloride (44.5 mg, 0.26 mmol) in methanol (5 mL) and H_2**L2.1** (46.5 mg, 0.26 mmol) in methanol (5 mL) were combined and left to cool down to room temperature naturally. Large green crystals were isolated from the colourless solution after several hours. Yield 75.4 mg (0.24 mmol, 92 %).

Selected IR (cm^{-1}): 3228(w), 3107(w), 1700(s), 1543(s), 1428(s), 1371(s), 1113(s), 1019(m), 793(m), 711(s), 601(s), 577(s), 542(s). Anal. calcd. for $C_{16}H_{20}N_8O_2Cl_4Cu_2$: C, 30.73; H, 3.22; N, 17.92 %. Found: C, 30.98; H, 3.22; N, 17.98 %.

Synthesis of [Cu_2(H_2L2.1)$_2$$Br_2$($\mu$-Br)$_2$] (2.8)

Hot solutions of copper bromide (39.6 mg, 0.18 mmol) in methanol (5 mL) and H_2**L2.1** (31.6 mg, 0.18 mmol) in methanol (5 mL) were combined and left to cool down to room temperature naturally. Large green crystals were isolated from the pale green solution after several hours. Yield 43.9 mg (0.11 mmol, 61 %).

Selected IR (cm^{-1}): 3263(w), 3117(w), 2856(w), 1698(s), 1538(s), 1425(s), 1370(m), 1111(m), 789(s), 747(m), 677(m), 573(s), 540(s). Anal. calcd. for $C_{16}H_{20}N_4O_2Br_4Cu_2$: C, 23.93; H, 2.51; N, 13.95 %. Found: C, 24.17; H, 2.62; N, 13.93 %.

Synthesis of [Cu(H_2L2.2)Cl_2] (2.9)

Hot solutions of copper chloride (46.7 mg, 0.27 mmol, in methanol (5 mL) and H_2**L2.2** (49.2 mg, 0.27 mmol) in methanol (5 mL) were combined and left to cool to room temperature naturally. Large green crystals were isolated from the pale green solution after several hours. Yield 76.1 mg (0.24 mmol, 90 %).

Selected IR (cm^{-1}): 3360(w), 3204(w), 1709(w), 1650(m), 1635(m), 1530(s), 1378(m), 1125(m), 1105(m), 794(s), 749(m), 648(m). Anal. calcd. for $C_7H_9N_5OCl_2Cu$: C, 26.81; H, 2.89; N, 22.33 %. Found: C, 26.82; H, 3.05; N, 22.11 %.

Synthesis of [Cu(H_2L2.2)Br_2] (2.10)

Hot solutions of copper bromide (64.5 mg, 0.29 mmol) in methanol (5 mL) and H_2**L2.2** (49.6 mg, 0.29 mmol) in methanol (5 mL) were combined and left to cool to room temperature naturally. Large green crystals were isolated from the pale green solution after several hours. Yield 51.1 mg (0.13 mmol, 44 %).

Selected IR (cm^{-1}): 3401(w), 3315(w), 3210(w), 1699(w), 1653(s), 1625(m), 1523(s), 1360(s), 1119(m), 1098(m), 787(s), 746(s), 647(m). Anal. calcd. for $C_7H_9N_5OBr_2Cu$: C, 20.89; H, 2.25; N, 17.40 %. Found: C, 21.14; H, 2.36; N, 17.27 %.

Synthesis of [Cu(H_2L2.1)$_2$](ClO_4)$_2$·H_2O (2.11)

Copper perchlorate (18.3 mg, 0.049 mmol) was added to a solution of H_2**L2.1** (17.6 mmol, 0.098 mmol) in methanol (10 mL). Upon slow evaporation of the solvent, green crystals formed which were removed from the remaining pale green solution by filtration. Yield 11.0 mg (0.017 mmol, 35 %).

Selected IR (cm^{-1}): 3249 (br. w), 1693(w), 1538(s), 1446(m), 1378(m), 1066(br. s), 798(s), 747(m), 621(s). Anal. calcd. for $C_{16}H_{20}N_8O_{10}Cl_2Cu$: C, 31.05; H, 3.26; N, 18.11 %. Found: C, 31.47; H, 3.55; N, 17.78 %.

Synthesis of $[Fe_2(H_4L2.3)_2](ClO_4)_4 \cdot 2MeCN \cdot 0.2H_2O$ (2.12)

Iron perchlorate (31.0 mg, 0.085 mmol) was added to a solution of H_4**L2.3** (30.0 mg, 0.085 mmol) and ascorbic acid (3 mg) in acetonitrile (45 mL) and stirred for 30 minutes. The resulting solution was filtered and *m*-xylene was allowed to diffuse into this solution to afford red needle like crystals. Yield 24mg (0.018 mmol, 43 %).

Selected IR (cm^{-1}): 3425(br. w), 3261(w), 1687(m), 1570(m), 1540(s), 1424(m), 1274(m), 1095(s), 1045(br. s), 792(m), 620(s). Anal. calcd. for $C_{32}H_{36}N_{16}O_{20}Cl_8Fe_2+4H_2O$: C, 29.79; H, 3.44; N, 17.37 %. Found: C, 30.05; H, 3.25; N, 17.33 %.

Synthesis of $[Ni(H_2L2.1)_2]Cl_2 \cdot 2MeOH$ (2.13)

A warm methanolic solution (5 mL) of nickel(II) chloride (29.8 mg, 0.13 mmol) was combined with a warm methanolic solution of H_2**L2.1** (44.6 mg, 0.25mmol). Upon evaporation of the combined solutions green crystals formed and were isolated by suction filtration. Yield 19.7 mg (0.04 mmol, 28 %).

Selected IR (cm^{-1}): 3111(br. m), 2910(br. w), 1693(s), 1542(s), 1422(m), 1301(m), 1098(m), 793(s), 589(m). Anal. calcd. for $C_{16}H_{20}N_8O_2Cl_2Ni$: C, 39.54; H, 4.15; N, 22.06 %. Found: C, 39.32; H, 4.20; N, 22.77 %.

Synthesis of $[Ni(HL2.5)_2]$ (2.14)

A warm methanolic solution (5 mL) of nickel(II) acetate (23.1 mg, 0.10 mmol) was combined with a warm methanolic solution (5 mL) of H_2**L2.5** (34.1 mg, 0.19 mmol). Upon evaporation of the combined solutions orange crystals formed and were isolated via a pipette. Yield 27.0 mg (0.07 mmol, 65 %).

Selected IR (cm^{-1}): 3419(m), 3168(br. w), 1644(m), 1501(m), 1460(m), 1369(s), 1317(s), 1144(m), 1069(s), 974(m), 852(m), 639(m), 505(m), 471(s). Anal. calcd. for $C_{14}H_{16}N_{10}O_2Ni$: C, 40.51; H, 3.89; N, 33.75 %. Found: C, 40.24; H, 3.90; N, 32.85 %.

7.3.2 Chapter 3

All zinc carboxylate salts, apart from zinc acetate which was obtained from a commercial supplier, were synthesised in the following the same procedure as those synthesised in Chapter 2.

Synthesis of $[Zn_8(L2.1)_4(AcO)_8]\cdot 2H_2O$ (3.1)

Zinc acetate (99.0 mg, 0.45 mmol) was added to a warm colourless solution of H_2**L2.1** (40.0 mg, 0.22 mmol) in methanol (10 mL). An immediate colour change to yellow was observed and the resulting solution was filtered after stirring at room temperature for one hour. Diethyl ether was allowed to diffuse into this solution, and yellow crystals could be collected by filtration after approximately a week. Yield 71 mg (0.04 mmol, 74 %).

Selected IR (cm^{-1}): 3371(w), 1610(m), 1589)m), 1554(s), 1391(s), 1340(s), 1218(w), 805(w), 670(m), 618(m). Anal. calcd. for $C_{48}H_{56}N_{16}O_{20}Zn_8+2H_2O$: C, 33.21; H, 3.48; N, 12.91 %. Found C, 33.25; H, 3.20; N, 12.58 %.

Synthesis of $[Zn_8(L2.1)_4(EtCO_2)_8]$ (3.2)

3.2 was prepared from H_2**L2.1** (48.4 mg, 0.27 mmol) in an analogous manner to **3.1** except zinc propionate (134.5 mg, 0.54 mmol) was used instead of zinc acetate. Yield 36.0 mg (0.02 mmol, 29 %).

Selected IR (cm^{-1}): 2985(w), 1610(m), 1586(m), 1538(s), 1405(s), 1347(m), 1223(w), 811(w), 675(m), 606(w). Anal. calcd. for $C_{56}H_{72}N_{16}O_{20}Zn_8$: C, 37.11; H, 4.00; N, 12.37 %. Found C, 37.12; H, 3.95; N, 12.35 %.

Synthesis of $[Zn_8(L2.1)_4(i\text{-}BuCO_2)_8]$ (3.3)

3.3 was prepared from H_2**L2.1** (48.8 mg, 0.27 mmol) in an analogous manner to **3.1** except zinc isovalerate (146.6 mg, 0.55 mmol) was used instead of zinc acetate. Yield 60.4 mg (0.03 mmol, 43 %).

Anal. calcd. for $C_{72}H_{104}N_{16}O_{20}Zn_8$: C, 42.46; H, 5.15; N, 11.00. %. Found C, 42.71; H, 5.09; N, 10.98 %.

Synthesis of $[Zn_8(L2.1)_4(t\text{-}BuCO_2)_8]\cdot 2Et_2O$ (3.4)

3.4 was prepared from H_2**L2.1** (50.4 mg, 0.28 mmol) in an analogous manner to **3.1** except zinc pivalate (151.5 mg, 0.57 mmol) was used instead of zinc acetate. Yield 41.1 mg (0.02 mmol, 29 %).

Selected IR (cm^{-1}): 2957(w), 1602(s), 1591(s), 1483(m), 1416(s), 1348(m), 1225(m), 802(w), 638(m), 605(w). Anal. calcd. for $C_{72}H_{104}N_{16}O_{20}Zn_8+9H_2O$: , 39.33; H, 5.59; N, 10.19. %. Found C, 39.47; H, 5.63; N, 10.10 %.

Synthesis of $[Zn_8(L2.1)_4(n\text{-}PenCO_2)_8]$ (3.5)

3.5 was prepared from H_2**L2.1** (53.4 mg, 0.30 mmol) in an analogous manner to **3.1** except zinc hexanoate (177.3 mg, 0.60 mmol) was used instead of zinc acetate. Yield 31.4 mg (0.01 mmol, 19 %).

Selected IR (cm^{-1}): 2923(w), 1604(s), 1547(s), 1404(s), 1346(m), 1228(w), 799(m), 717(m), 630(m), 589(w). Anal. calcd. for $C_{80}H_{120}N_{16}O_{20}Zn_8+H_2O$: C, 44.34; H, 5.68; N, 10.34. %. Found C, 44.64; H, 5.70; N, 10.23 %.

Synthesis of $[Zn_8(L2.1)_4(p\text{-}MeBzO)_8]$ (3.6)

3.6 was prepared from H_2**L2.1** (48.0 mg, 0.27 mmol) in an analogous manner to **3.1** except zinc *p*-toluate (190.6 mg, 0.54 mmol) was used instead of zinc acetate. Gentle heating was required to dissolve the metal salt in this case. The size and fragility with respect to solvent loss of the crystals prevented collection of bulk sample.

Synthesis of $[Zn_8(L2.1)_4(BnCO_2)_8]$ (3.7)

3.7 was prepared from H_2**L2.1** (51.0 mg, 0.27 mmol) in an analogous manner to **3.1** except zinc phenylacetate (187.8 mg, 0.53 mmol) was used instead of zinc acetate. The size and fragility with respect to solvent loss of the crystals prevented collection of bulk sample.

Synthesis of $[Zn_8(L2.1)_4(p\text{-}ClBnCO_2)_8]$ (3.8)

3.8 was prepared from H_2**L2.1** (51.0 mg, 0.29 mmol) in an analogous manner to **3.1** except zinc *p*-chlorophenylacetate (242.0 mg, 0.57 mmol) was used instead of zinc acetate. The size and fragility with respect to solvent loss of the crystals prevented collection of bulk sample.

Synthesis of $[Zn_8(L2.1)_4(Ph(CH)_2CO_2)_8]\cdot 3Et_2O$ (3.9)

3.9 was prepared from H_2**L2.1** (28.0 mg, 0.16 mmol) in an analogous manner to **3.**1 except zinc cinnamate (119.0 mg, 0.31 mmol) was used instead of zinc acetate. Yield 22 mg (0.01 mmol, 21 %).

Selected IR (cm^{-1}): 1642(m), 1583(m), 1548(s), 1377(s), 1344(m), 972(w), 772(m), 717(m), 590(w). Anal. calcd. for $C_{104}H_{88}N_{16}O_{20}Zn_8$: , 51.94; H, 3.69; N, 9.32. %. Found C, 51.23; H, 3.80; N, 9.05 %.

Synthesis of $[Zn_8(L2.1)_4(Ph(CH_2)_2CO_2)_8]\cdot 6Et_2O$ (3.10)

3.10 was prepared from H_2**L2.1** (54.8 mg, 0.31 mmol) in an analogous manner to **3.1** except zinc cinnamate (234.8 mg, 0.61 mmol) was used instead of zinc acetate. Yield 51.3 mg (0.02 mmol, 45 %).

Selected IR (cm^{-1}): 3137(w), 1651(m), 1596(s), 1532(s), 1379(s), 1350(m), 971(w), 776(w), 729(m), 561(w). Anal. calcd. for $C_{104}H_{104}N_{16}O_{20}Zn_8$: , 51.59; H, 4.33; N, 9.26 %. Found C, 51.64; H, 4.47; N, 9.14 %.

Synthesis of $[Zn_8(L2.1)_4(Cl_3CCO_2)_{0.8}(AcO)_{7.2}]$ (3.11)

Zinc(II) acetate (26.0 mg, 0.12 mmol)and H_2**L2.1** (10.5 mg, 0.06 mmol)were combined in methanol. To this bright yellow solution was added trichloroacetic acid (19.6 mg, 0.12 mmol) and the solution turned colourless. Toluene was then added and then the solvent removed in vacuo to leave a pale yellow oil. Methanol (5 mL) and toluene (5 mL) were then added to the residue, stirred briefly then the solvent removed in vacuo again. Six additional cycles of solvent addition then removal were performed before methanol (8 mL) was added and diethyl ether allowed to diffuse into the solution. After approximately 1 week, small, plate-like crystals formed and were isolated by filtration. Insufficient sample was collected to perform further analysis.

Synthesis of [ZnL2.1]·DMF (3.12)

H_2**L2.1** (14.1 mg, 0.079 mmol) and zinc(II) acetate (34.7 mg, 0.158 mmol) were dissolved in DMF (3 mL) to create a bright yellow solution. This was sealed in a screw capped vial and heated at 100 °C for 24 hours. Colourless needle shaped crystals were removed from the solution by suction filtration. Yield 15.9 mg (0.041 mmol, 52 %).

Synthesis of $[Zn_8(L3.2)_4(AcO)_8]$ (3.13)

3.13 was prepared from zinc(II) acetate in an analogous manner to **3.1** except H_2**L3.2** (10.4 mg, 0.04 mmol)was used instead of H_2**L2.1**. The size and fragility with respect to solvent loss of the crystals prevented collection of bulk sample.

Synthesis of $[Cu_2(H_4L3.3)(H_2O)_2(Me_2CO)_2](ClO_4)_2 \cdot 2(Me_2CO)$ (3.14)

Ligand (10.1 mg, 0.03mmol) was suspended in 6 mL of acetone and copper perchlorate (21.1 mg, 0.06 mmol) was added. The solution was stirred until all of the ligand had dissolved and the resulting green solution was filtered. Diffusion of diethylether afforded green crystals suitable for single crystal X-ray diffraction.

Synthesis of $[Cu_2(H_4L3.3)(MeCN)_4](ClO_4)_2 \cdot 2PhH$ (3.15)

Ligand (11.3 mg, 0.03mmol) was suspended in 6 mL of acetonitrile and copper perchlorate (23.6 mg, 0.06 mmol) was added. The solution was stirred until all of the ligand had dissolved and the resulting green solution was filtered. Diffusion of benzene afforded green crystals suitable for single crystal X-ray diffraction.

Synthesis of $[Zn_2(H_4L3.4)(AcO)_2]$ (3.16)

H_4**L3.4** was suspended in methanol and acetic acid was added until all of the ligand had dissolved. Zinc(II) acetate was added to this and the colourless solution was filtered, and diethyl ether was allowed to diffuse in. After several days, colourless crystals formed.

Synthesis of $[Zn_8(L2.5)_4(BnCO_2)_8] \cdot Et_2O \cdot MeOH$ (3.17)

3.17 was synthesised in an analogous procedure to **3.7** except H_2**L2.5** was used instead of H_2**L2.1**. Orange crystals formed after 1 week. The size and fragility with respect to solvent loss of the crystals prevented collection of bulk sample.

7.3.3 Chapter 4

The activation of MOFs was achieved by washing freshly prepared samples with DMF, then soaking in acetone for 48 hours. The acetone was regularly refreshed in this time. The acetone was then removed by holding the sample at vacuum for 18 hours. Removal of the solvent was confirmed by IR spectroscopy, TGA and elemental analysis.

Synthesis of [Zn(L4.1)] (4.1)

H_2**L4.1** (0.10 g, 0.25 mmol) was dissolved in a solution of DMF (25 mL), water (5 mL) and nitric acid (2.3 mL). To this, zinc nitrate (0.075 g, 0.25 mmol) was added and the orange solution was mixed thoroughly then distributed into 4 mL screw cap vials which were heated to 90°C for 24 hours. Over this time, orange crystals were deposited from the still hot solution. Yield 0.066 g (0.11 mmol, 46 %).

Selected IR (cm^{-1}): 3414(br), 3068(br), 1634(s), 1557(s), 1356(s), 1241(m), 1093(w), 1016(w), 821(w), 786(m), 705(s), 630(w). Anal. calcd. for $C_{23}H_{13}N_3O_4Zn$ $+CH_2O_2+C_3H_7NO$: C, 55.92; H, 3.83; N, 9.66 %. Found: C, 56.32; H, 3.83; N, 9.31%.

Post activation

Selected IR (cm^{-1}): 1607(s), 1553(s), 1478(w), 1359(s), 1240(m), 1015(w), 875(w), 821(w). Anal. calcd. for $C_{23}H_{13}N_3O_4Zn+H_2O$: C, 57.70; H, 3.16; N, 8.78 %. Found: C, 57.72; H, 3.53; N, 8.40 %.

Synthesis of [Zn(L4.2)] (4.2)

H_2**L4.2** (0.10 g, 0.25 mmol) was dissolved in a solution of DMF (28 mL) and nitric acid (2.5 mL). To this, zinc nitrate (0.074 g, 0.25 mmol) was added and the yellow solution was mixed thoroughly then distributed into 4 mL vials which were heated to 90°C for 24 hours. Over this time, colourless crystals were deposited from the still hot solution. Yield 0.080 g (0.13 mmol, 53 %).

Selected IR (cm^{-1}): 3429(br), 3078(br), 1608(s), 1557(s), 1361(s), 1239(m), 1095(w), 1016(w), 824(w), 786(m), 703(s), 632(w). Anal. calcd. for $C_{24}H_{15}N_3O_4Zn$ +CH_2O_2+C_3H_7NO: C, 55.63; H, 4.07; N, 9.43 %. Found: C, 55.90; H, 4.21; N, 9.41%.

Post activation

Selected IR (cm^{-1}): 1606(s), 1556(s), 1462(w), 1360(s), 1240(m), 1016(w), 875(w), 824(w). Anal. calcd. for $C_{24}H_{15}N_3O_4Zn$ +H_2O: C, 58.49; H, 3.48; N, 8.53 %. Found: C, 58.67; H, 3.61; N, 8.49 %.

Synthesis of [Zn(L4.3)] (4.3)

H_2**L4.3** (0.10 g, 0.24 mmol) was dissolved in a solution of DMF (42 mL) and nitric acid (1.7 mL). To this, zinc nitrate (0.074 g, 0.24 mmol) was added and the orange solution was mixed thoroughly then distributed into 4 mL vials which were heated to 90°C for 24 hours. Over this time, orange crystals were deposited from the still hot solution. Yield 0.101 g (0.16 mmol, 69 %).

Selected IR (cm^{-1}): 3385(br), 3084(br), 1610(s), 1557(s), 1361(s), 1241(m), 1094(m), 1011(w), 823(w), 784(m), 706(s). Anal. calcd. for $C_{23}H_{12}N_3O_4ClZn$+CH_2O_2+C_3H_7NO: C, 52.79; H, 3.45; N, 9.12 %. Found: C, 56.69; H, 3.26; N, 8.83%.

Post activation

Selected IR (cm^{-1}): 1610(s), 1556(s), 1478(s), 1359(s), 1241(m), 1094(m), 1011(m), 874(w), 824(m). Anal. calcd. for $C_{23}H_{12}N_3O_4ClZn$+1.5H_2O: C, 52.90; H, 2.89; N, 8.05 %. Found: C, 52.97; H, 2.85; N, 8.01%.

Synthesis of [Zn(L4.4)] (4.4)

H_2**L4.4** (0.11 g, 0.24 mmol) was dissolved in a solution of DMF (44 mL) and nitric acid (1.7 mL). To this, zinc nitrate (0.074 g, 0.24 mmol) was added and the orange solution was mixed thoroughly then distributed into 4 mL vials which were heated to 90°C for 24 hours.

Over this time, orange crystals were deposited from the still hot solution. Yield 0.058 g (0.09 mmol, 38 %).

Selected IR (cm^{-1}): 3429(br), 3076(br), 1609(s), 1557(s), 1516(s), 1343(s), 1240(m), 1094(w), 1013(w), 856(m), 817(w), 784(m), 704(s). Anal. calcd. for $C_{23}H_{12}N_4O_6Zn$ $+CH_2O_2+C_3H_7NO+H_2O$: C, 50.44; H, 3.61; N, 10.89 %. Found: C, 50.40; H, 3.41; N, 10.85%.

Post activation

Selected IR (cm^{-1}): 1609(s), 1555(s), 1515(s), 1479(w), 1342(s), 1239(m), 1013(w), 854(m), 816(m). Anal. calcd. for $C_{23}H_{12}N_4O_6Zn$ $+1.5H_2O$: C, 51.85; H, 2.84; N, 10.52 %. Found: C, 51.75; H, 3.01; N, 10.17 %.

Synthesis of [Zn(L4.5)] (4.5)

H_2**L4.5** (0.11 g, 0.27 mmol) was dissolved in a solution of DMF (40 mL) and nitric acid (1.6 mL). To this, zinc nitrate (0.080 g, 0.27 mmol) was added and the orange solution was mixed thoroughly then distributed into 4 mL vials which were heated to 90°C for 24 hours. Over this time, orange crystals were deposited from the still hot solution. Yield 0.046 g (0.08 mmol, 29 %).

Selected IR (cm^{-1}): 3420(br. w), 3120(br), 1609(s), 1558(s), 1351(s), 1242(m), 1097(w), 1020(w), 824(w), 784(w), 718(s), 671(w). Anal. calcd. for $C_{21}H_{11}N_3O_4SZn$ $+CH_2O_2+C_3H_7NO$: C, 51.25; H, 3.44; N, 9.56 %. Found: C, 50.84; H, 3.45; N, 9.61%.

Post activation

Selected IR (cm^{-1}): 1606(s), 1555(s), 1464(w), 1352(s), 1244(m), 1016(w), 873(w), 825(w). Anal. calcd. for $C_{21}H_{11}N_3O_4SZn$ $+1.25H_2O$: C, 51.55; H, 2.78; N, 8.59 %. Found: C, 51.50; H, 3.08; N, 8.41 %.

Synthesis of [Zn(L4.6)] (4.6)

H_2**L4.6** (0.10 g, 0.26 mmol) was dissolved in a solution of DMF (40 mL) and nitric acid (1.6 mL). To this, zinc nitrate (0.078 g, 0.26 mmol) was added and the orange solution was mixed thoroughly then distributed into 4 mL vials which were heated to 90°C for 24 hours. Over this time, orange crystals were deposited from the still hot solution. Yield 0.036 g (0.07 mmol, 25 %).

Selected IR (cm^{-1}): 3391(br), 3088(br), 1608(s), 1556(s), 1353(s), 1243(m), 1094(w), 1015(w), 823(w), 784(m), 705(s), 660(w). Anal. calcd. for $C_{21}H_{11}N_3O_4SZn$ $+C_3H_7NO+H_2O$: C, 51.67; H, 3.61; N, 10.04 %. Found: C, 51.92; H, 3.51; N, 9.80%.

Post activation

Selected IR (cm^{-1}): 1607(s), 1554(s), 1464(w), 1353(s), 1242(m), 1015(w), 871(w), 823(w). Anal. calcd. for $C_{21}H_{11}N_3O_4SZn$ $+1.25H_2O$: C, 51.55; H, 2.78; N, 8.59 %. Found: C, 51.59; H, 3.16; N, 8.37 %.

Synthesis of [Zn(L4.7)] (4.7)

H_2**L4.7** (0.10 g, 0.25 mmol) was dissolved in a solution of DMF (39 mL) and nitric acid (1.7 mL). To this, zinc nitrate (0.081 g, 0.27 mmol) was added and the orange solution was mixed thoroughly then distributed into 4 mL vials which were heated to 90°C for 24 hours. Over this time, orange crystals were deposited from the still hot solution. Yield 0.066 g (0.10 mmol, 39 %).

Selected IR (cm^{-1}): 3462(br), 3021(br), 1604(s), 1556(s), 1356(s), 1340(s), 1241(m), 1090(w), 1035(w), 820(w), 790(m), 701(m), 621(w). Anal. calcd. for $C_{22}H_{12}N_4O_4Zn$ $+CH_2O_2+2C_3H_7NO+1.5H_2O$: C, 51.30; H, 4.30; N, 12.38 %. Found: C, 51.41; H, 4.34; N, 12.19 %.

Post activation

Selected IR (cm^{-1}): 1597(s), 1547(s), 1464(w), 1359(s), 1239(m), 1015(w), 875(w), 822(w). Anal. calcd. for $C_{22}H_{12}N_4O_4Zn$ +2H_2O: C, 53.08; H, 3.24; N, 11.26 %. Found: C, 53.67; H, 3.36; N, 11.28 %.

7.3.4 Chapter 5

Synthesis of [Ni(H_2L5.1)$_2$] (5.1)

A solution of nickel(II) nitrate (7.9 mg, 27.0 μmol) in DMF (1.7 mL) and H_2O (50 μL) was added to a solution of H_3**L5.1** (10.6 mg, 54.0 μmol) in DMF (2 mL) and the resulting pale orange solution heated at 100 °C for 24 hours. Small green plate-like crystals formed at this temperature and were isolated from the orange solution by suction filtration. Yield 0.0082 g (18.0 μmol, 67 %).

Selected IR (cm^{-1}): 1682(m), 1598(s), 1498(w), 1280(s), 1250(s), 1028(m), 972(m), 765(s), 677(s), 557(m), 499(m). Anal. calcd. for $C_{18}H_{16}N_2O_8Ni$: C, 48.36; H, 3.61; N, 6.27 %. Found: C, 48.07; H, 3.59; N, 6.32 %.

Synthesis of [Cu_2(H_2L5.1)$_4$]·msi (5.2)

H_2**L5.1** (6.1 mg, 31.3 μmol) was dissolved in NMP (0.8 mL) and H_2O (0.2 mL) and the solution was carefully placed in the bottom of a 5 mm NMR tube. Atop this, a 2 cm thick buffer layer of pure NMP was layered followed by a solution of copper(II) nitrate (3.1 mg, 15.7 μmol) in NMP (0.5 mL) and MeOH (0.5 mL). After two months small brown crystals were isolated from the interface of the two layers. Yield 2.0 mg (3.5 μmol, 22 %).

Selected IR (cm^{-1}): 1702(m), 1678(s), 1560(s), 1408(m), 1301(m), 1264(s), 1246(s), 973(m), 825(m), 770(s), 660(s), 544(m), 450(m). Anal. calcd. for $C_{18}H_{16}N_2O_8Cu$ +0.5$C_5H_7NO_2$: C, 48.43; H, 3.87; N, 6.89 %. Found: C, 48.92; H, 4.05; N, 6.92 %.

Synthesis of $[Cu_2(H_2L5.2)_2(pyridine)_5]\cdot 4pyridine$ (5.3)

Copper(II) acetate (7.3 mg, 73.0 μmol) was added to a solution of H_2**L5.2** (13.8 mg, 73.0 μmol) in pyridine (7 mL) and sealed in a capped vial. Upon standing for several months, several small green crystals formed from the green solution. Due to a poor yield, bulk characterisation could not be performed, and the compound was only characterised via single crystal X-ray diffraction.

Synthesis of $[Cu_2(HL5.4)_2(DMF)\ (H_2O)]$ (5.4)

Copper(II) nitrate (10 mg, 39.5 μmol), dissolved in DMF (1 mL) and H_2O (50 μL), was added to a solution of H_3**L5.3** (10.3 mg, 39.5 μmol) in DMF (2 mL) and nitric acid (5 drops). The resulting pale green solution was heated at 100 °C for 24 hours. Blue plate-like crystals formed at this temperature and were isolated from bulk precipitate manually. Due to the presence of the precipitate, bulk characterisation could not be performed, and the compound was only characterised via single crystal X-ray diffraction.

Appendix 1

Chapter 2

Table A1.1: *Crystallographic data for compounds* H_2***L2.1***, H_4***L2.3*** *and* ***2.1***.

Identification code	H_2**L2.1**	H_4**L2.3**	**2.1**
Empirical formula	$C_8H_{10}N_4O$	$C_{16}H_{18}N_8O_2$	$C_{12}H_{16}N_4O_5Zn$
Formula weight	178.2	354.38	361.66
Temperature /K	120.0(1)	120.0(1)	120.0(1)
Crystal system	orthorhombic	monoclinic	monoclinic
Space group	*Pbca*	$P2_1/c$	*Cc*
a/Å	7.9075(5)	5.1538(4)	13.5876(17)
b/Å	14.6595(12)	5.8583(4)	15.6391(13)
c/Å	15.3391(13)	27.048(3)	7.8278(7)
α/°	90	90	90
β/°	90	91.101(8)	93.891(10)
γ/°	90	90	90
Volume /Å^3	1778.1(2)	816.51(11)	1659.6(3)
Z	8	2	4
ρ_{calc} g/cm^3	1.331	1.441	1.447
F(000)	752	372	744
Crystal size/mm^3	0.22 × 0.15 × 0.04	0.13 × 0.08 × 0.04	0.19 × 0.06 × 0.04
Radiation	MoKα (λ = 0.71073)	CuKα (λ = 1.54184)	CuKα (λ = 1.54184)
Reflections collected	5986	2758	2790
Independent reflections	1813	1542	1705
Goodness-of-fit on F^2	1.061	1.075	1.038
Final R indexes [I>=2σ (I)]	R_1 = 0.0563, wR_2 = 0.1095	R_1 = 0.0758, wR_2 = 0.1807	R_1 = 0.0357, wR_2 = 0.0931
Final R indexes [all data]	R_1 = 0.1000, wR_2 = 0.1332	R_1 = 0.1220, wR_2 = 0.2200	R_1 = 0.0378, wR_2 = 0.0950

Table A1.2: *Crystallographic data for compounds* ***2.2-2.4***.

Identification code	**2.2**	**2.3**	**2.4**
Empirical formula	$C_{15}H_{24}N_4O_6Zn$	$C_{12}H_{14}Cl_2N_4O_5Zn$	$C_{22}H_{20}N_4O_5Zn$
Formula weight	421.75	430.54	485.79
Temperature /K	120.0(1)	120.0(1)	120.0(1)
Crystal system	monoclinic	monoclinic	triclinic
Space group	*Cc*	*Cc*	*P*-1
a/Å	13.5855(11)	13.2110(12)	8.0474(5)
b/Å	16.2055(11)	15.4537(11)	9.1344(8)
c/Å	8.4220(8)	9.2256(9)	15.1630(14)
α/°	90	90	82.219(7)
β/°	96.099(7)	99.533(9)	77.594(7)
γ/°	90	90	75.138(7)
Volume /Å^3	1843.7(3)	1857.5(3)	1048.35(16)
Z	4	4	2
ρ_{calc} g/cm^3	1.519	1.54	1.539
F(000)	880	872	500
Crystal size/mm^3	0.15 × 0.05 × 0.027	0.24 × 0.04 × 0.03	0.16 × 0.03 × 0.02
Radiation	CuKα (λ = 1.54184)	CuKα (λ = 1.54184)	MoKα (λ = 0.71073)
Reflections collected	3393	5603	7590
Independent reflections	2081	2463	3656
Goodness-of-fit on F^2	1.019	1.072	0.973
Final R indexes [I>=2σ (I)]	R_1 = 0.0482, wR_2 = 0.1240	R_1 = 0.0627, wR_2 = 0.1700	R_1 = 0.0500, wR_2 = 0.0703
Final R indexes [all data]	R_1 = 0.0507, wR_2 = 0.1272	R_1 = 0.0673, wR_2 = 0.1755	R_1 = 0.0847, wR_2 = 0.0815

Table A1.3: *Crystallographic data for compounds **2.5**-**2.7**.*

Identification code	**2.5**	**2.6**	**2.7**
Empirical formula	$C_{24}H_{24}N_4O_5Zn$	$C_{12}H_{16}CdN_4O_5$	$C_{16}H_{20}Cl_4Cu_2N_8O_2$
Formula weight	513.84	408.69	625.28
Temperature /K	120.0(1)	120.0(1)	120.0(1)
Crystal system	triclinic	triclinic	monoclinic
Space group	*P*-1	*P*-1	$P2_1/c$
a/Å	7.9278(4)	8.8223(6)	10.4678(4)
b/Å	9.7657(6)	8.8373(6)	10.8136(3)
c/Å	15.0781(6)	10.5479(8)	10.7237(4)
α/°	83.181(4)	96.690(6)	90
β/°	88.081(4)	98.129(6)	109.026(4)
γ/°	81.135(5)	107.911(6)	90
Volume /$Å^3$	1145.11(10)	763.40(10)	1147.56(7)
Z	2	2	2
ρ_{calc} g/cm^3	1.49	1.778	1.81
F(000)	532	408	628
Crystal size/mm^3	0.37 × 0.05 × 0.04	0.13× 0.04 × 0.03	0.19 × 0.14 × 0.10
Radiation	CuKα (λ = 1.54184)	MoKα (λ = 0.71073)	CuKα (λ = 1.54184)
Reflections collected	7555	7141	3937
Independent reflections	4308	3360	2014
Goodness-of-fit on F^2	1.014	0.999	1.083
Final R indexes [I>=2σ (I)]	R_1 = 0.0377, wR_2 = 0.0926	R_1 = 0.0356, wR_2 = 0.0628	R_1 = 0.0358, wR_2 = 0.0966
Final R indexes [all data]	R_1 = 0.0453, wR_2 = 0.0970	R_1 = 0.0470, wR_2 = 0.0665	R_1 = 0.0391, wR_2 = 0.1013

Table A1.4: *Crystallographic data for compounds **2.8**-**2.10**.*

Identification code	**2.8**	**2.9**	**2.10**
Empirical formula	$C_{16}H_{20}Br_4Cu_2N_8O_2$	$C_7H_9Cl_2CuN_5O$	$C_7H_9Br_2CuN_5O$
Formula weight	803.12	313.63	402.55
Temperature /K	120.0(1)	120.0(1)	120.0(1)
Crystal system	monoclinic	monoclinic	triclinic
Space group	$P2_1/c$	$P2_1/c$	*P*-1
a/Å	10.8182(2)	9.0730(4)	6.6713(3)
b/Å	10.9277(2)	8.7844(4)	7.7568(3)
c/Å	11.0405(3)	14.0193(5)	12.2149(5)
α/°	90	90	80.936(3)
β/°	109.361(3)	95.139(4)	74.683(4)
γ/°	90	90	68.838(4)
Volume /$Å^3$	1231.38(5)	1112.86(8)	567.17(5)
Z	2	4	2
ρ_{calc} g/cm^3	2.166	1.872	2.357
F(000)	772	628	386
Crystal size/mm^3	0.25 × 0.21 × 0.14	0.09 × 0.0.5 × 0.03	0.38 × 0.13 × 0.03
Radiation	CuKα (λ = 1.54184)	MoKα (λ = 0.71073)	CuKα (λ = 1.54184)
Reflections collected	7900	9078	4062
Independent reflections	2530	4232	2133
Goodness-of-fit on F^2	1.178	1.037	1.072
Final R indexes [I>=2σ (I)]	R_1 = 0.0290, wR_2 = 0.0796	R_1 = 0.0364, wR_2 = 0.0759	R_1 = 0.0320, wR_2 = 0.0919
Final R indexes [all data]	R_1 = 0.0297, wR_2 = 0.0800	R_1 = 0.0529, wR_2 = 0.0844	R_1 = 0.0328, wR_2 = 0.0929

Table A1.5: *Crystallographic data for compounds* ***2.11-2.13****.*

Identification code	**2.11**	**2.12**	**2.13**
Empirical formula	$C_{16}H_{22}Cl_2CuN_8O_{11}$	$C_{36}H_{42}Cl_4Fe_2N_{18}O_{20.2}$	$C_{18}H_{28}Cl_2N_8NiO_4$
Formula weight	636.85	1303.57	550.09
Temperature /K	120.0(1)	120.0(1)	120.0(1)
Crystal system	triclinic	monoclinic	triclinic
Space group	*P*-1	*C*2/*c*	*P*-1
a/Å	7.9570(8)	17.9006(7)	7.9510(3)
b/Å	11.9775(13)	16.5910(7)	12.0117(4)
c/Å	14.5791(16)	18.5282(7)	13.6320(4)
α/°	112.071(10)	90	103.165(3)
β/°	104.972(9)	109.341(4)	99.885(3)
γ/°	91.073(8)	90	101.224(3)
Volume /Å^3	1233.5(2)	5192.1(4)	1211.24(7)
Z	2	4	2
ρ_{calc} g/cm^3	1.715	1.668	1.508
F(000)	650	2662	572
Crystal size/mm^3	0.25 × 0.2 × 0.19	0.26 × 0.05× 0.04	0.13 × 0.10 × 0.05
Radiation	CuKα (λ = 1.54184)	CuKα (λ = 1.54184)	CuKα (λ = 1.54184)
Reflections collected	8796	9825	7684
Independent reflections	4374	4597]	4254
Goodness-of-fit on F^2	1.059	1.033	1.045
Final R indexes [I>=2σ (I)]	R_1 = 0.0338, wR_2 = 0.0884	R_1 = 0.0564, wR_2 = 0.1426	R_1 = 0.0317, wR_2 = 0.0844
Final R indexes [all data]	R_1 = 0.0358, wR_2 = 0.0900	R_1 = 0.0687, wR_2 = 0.1552	R_1 = 0.0348, wR_2 = 0.0870

Table A1.6: *Crystallographic data for compound* ***2.14****.*

Identification code	**2.14**
Empirical formula	$C_{14}H_{16}N_{10}NiO_2$
Formula weight	415.08
Temperature /K	120.0(1)
Crystal system	orthorhombic
Space group	*Pbcn*
a/Å	11.21422(18)
b/Å	8.44489(13)
c/Å	17.2535(3)
α/°	90
β/°	90
γ/°	90
Volume /Å^3	1633.95(5)
Z	4
ρ_{calc} g/cm^3	1.687
F(000)	856
Crystal size/mm^3	0.31 × 0.28 × 0.12
Radiation	MoKα (λ = 0.71073)
Reflections collected	33361
Independent reflections	2029
Goodness-of-fit on F^2	1.169
Final R indexes [I>=2σ (I)]	R_1 = 0.0308, wR_2 = 0.0767
Final R indexes [all data]	R_1 = 0.0330, wR_2 = 0.0777

Chapter 3

Table A1.7: *Crystallographic data for compounds **3.1**-**3.3**.*

Identification code	**3.1**	**3.2**	**3.3**
Empirical formula	$C_{48}H_{64}N_{16}O_{24}Zn_8$	$C_{56}H_{72}N_{16}O_{21.5}Zn_8$	$C_{72}H_{104}N_{16}O_{20}Zn_8$
Formula weight	1772.11	1836.25	2036.67
Temperature /K	120.0(1)	120.0(1)	120.0(1)
Crystal system	tetragonal	tetragonal	monoclinic
Space group	*I*-42*d*	*I*-42*d*	*C*2/*c*
a/Å	27.0867(9)	26.9523(6)	27.9778(10)
b/Å	27.0867(9)	26.9523(6)	27.9456(13)
c/Å	10.1186(6)	10.1609(5)	24.2589(10)
α/°	90	90	90
β/°	90	90	94.151(4)
γ/°	90	90	90
Volume /Å^3	7423.9(7)	7381.2(5)	18917.2(14)
Z	4	4	8
ρ_{calc} g/cm^3	1.586	1.652	1.43
F(000)	3584	3728	8384
Crystal size/mm^3	0.10 × 0.07 × 0.03	0.06 × 0.04 × 0.03	0.08 × 0.06 × 0.03
Radiation	CuKα (λ = 1.54184)	CuKα (λ = 1.54184)	CuKα (λ = 1.54184)
Reflections collected	7637	14114	34693
Independent reflections	3210	3354	17218
Goodness-of-fit on F^2	1.042	1.059	1.036
Final R indexes [I>=2σ (I)]	R_1 = 0.0568, wR_2 = 0.1444	R_1 = 0.0375, wR_2 = 0.0741	R_1 = 0.1290, wR_2 = 0.3286
Final R indexes [all data]	R_1 = 0.0625, wR_2 = 0.1507	R_1 = 0.0557, wR_2 = 0.0854	R_1 = 0.1533, wR_2 = 0.3467

Table A1.8: *Crystallographic data for compounds **3.4**-**3.6**.*

Identification code	**3.4**	**3.5**	**3.6**
Empirical formula	$C_{72}H_{104}N_{16}O_{20}Zn_8$	$C_{80}H_{120}N_{16}O_{20}Zn_8$	$C_{100}H_{98}N_{16}O_{22}Zn_8$
Formula weight	2036.67	2148.87	2398.9
Temperature /K	120.0(1)	120.0(1)	120.0(1)
Crystal system	monoclinic	hexagonal	tetragonal
Space group	*C*2/*c*	$P6_2$	*I*-4
a/Å	38.6299(3)	28.1108(5)	27.6304(4)
b/Å	10.41790(10)	28.1108(5)	27.6304(4)
c/Å	29.2649(2)	24.4881(7)	16.6279(6)
α/°	90	90	90
β/°	124.2130(10)	90	90
γ/°	90	120	90
Volume /Å^3	9739.38(17)	16758.4(8)	12694.4(6)
Z	4	6	4
ρ_{calc} g/cm^3	1.389	1.278	1.255
F(000)	4192	6672	4904
Crystal size/mm^3	0.16 × 0.08 × 0.06	0.04 × 0.02 × 0.02	0.28 × 0.20 × 0.14
Radiation	CuKα (λ = 1.54178)	MoKα (λ = 0.71073)	Mo Kα (λ = 0.71073)
Reflections collected	96687	77995	35984
Independent reflections	10229	19432	15733
Goodness-of-fit on F^2	1.057	1.06	1.055
Final R indexes [I>=2σ (I)]	R_1 = 0.0310, wR_2 = 0.0790	R_1 = 0.0731, wR_2 = 0.1706	R_1 = 0.0453, wR_2 = 0.1145
Final R indexes [all data]	R_1 = 0.0331, wR_2 = 0.0805	R_1 = 0.1016, wR_2 = 0.1932	R_1 = 0.0609, wR_2 = 0.1240
Flack parameter		-0.005(7)	

Table A1.9: *Crystallographic data for compounds **3.7-3.9**.*

Identification code	**3.7**	**3.8**	**3.9**
Empirical formula	$C_{96}H_{88}N_{16}O_{20}Zn_8$	$C_{98}H_{85}Cl_8N_{16}O_{20.5}Zn_8$	$C_{116}H_{118}N_{16}O_{23}Zn_8$
Formula weight	2308.78	2621.38	2627.22
Temperature /K	120.0(1)	120.0(1)	120.0(1)
Crystal system	hexagonal	tetragonal	tetragonal
Space group	$P6_2$	I-4	$I4_1/a$
a/Å	28.6030(8)	27.8603(4)	27.5953(4)
b/Å	28.6030(8)	27.8603(4)	27.5953(4)
c/Å	25.6874(12)	14.0800(3)	17.5147(4)
α/°	90	90	90
β/°	90	90	90
γ/°	120	90	90
Volume /Å^3	18200.1(13)	10928.8(4)	13337.5(5)
Z	6	4	4
ρ_{calc} g/cm^3	1.264	1.593	1.308
F(000)	7056	5300	5400
Crystal size/mm^3	0.07 × 0.04 × 0.03	0.11 × 0.08 × 0.06	0.35 × 0.29 × 0.17
Radiation	CuKα (λ = 1.54184)	MoKα (λ = 0.71073)	Cu Kα (λ = 1.54184)
Reflections collected	68266	62956	26868
Independent reflections	18455	13557	6324
Goodness-of-fit on F^2	1.007	1.019	1.034
Final R indexes [I>=2σ (I)]	R_1 = 0.0636, wR_2 = 0.1396	R_1 = 0.0377, wR_2 = 0.0849	R_1 = 0.0569, wR_2 = 0.1682
Final R indexes [all data]	R_1 = 0.1162, wR_2 = 0.1670	R_1 = 0.0515, wR_2 = 0.0908	R_1 = 0.0610, wR_2 = 0.1749
Flack parameter	-0.035(16)		

Table A1.10: *Crystallographic data for compounds **3.10-3.12**.*

Identification code	**3.10**	**3.11**	**3.12**
Empirical formula	$C_{128}H_{164}N_{16}O_{26}Zn_8$	$C_{48}H_{53.6}Cl_{2.4}N_{16}O_{20}Zn_8$	$C_{19}H_{23}N_9O_3Zn_2$
Formula weight	2865.7	1782.71	556.2
Temperature /K	120.0(1)	120.0(1)	120.0(1)
Crystal system	tetragonal	tetragonal	monoclinic
Space group	$I4_1/a$	I-42d	$P2_1/c$
a/Å	27.33186(7)	26.1792(12)	9.2451(4)
b/Å	27.33186(7)	26.1792(12)	17.2912(3)
c/Å	18.08028(8)	12.105(4)	21.4217(10)
α/°	90	90	90
β/°	90	90	127.039(7)
γ/°	90	90	90
Volume /Å^3	13506.52(9)	8296(3)	2733.5(3)
Z	4	4	4
ρ_{calc} g/cm^3	1.409	1.427	1.352
F(000)	5968	3578	1136
Crystal size/mm^3	0.18 × 0.13 × 0.06	0.16× 0.07 × 0.05	0.12 × 0.04 × 0.03
Radiation	CuKα (λ = 1.54184)	CuKα (λ = 1.54184)	CuKα (λ = 1.54184)
Reflections collected	227466	10597	18837
Independent reflections	6917	3804	5180
Goodness-of-fit on F^2	1.057	0.984	1.045
Final R indexes [I>=2σ (I)]	R_1 = 0.0312, wR_2 = 0.0833	R_1 = 0.0523, wR_2 = 0.1209	R_1 = 0.0450, wR_2 = 0.1155
Final R indexes [all data]	R_1 = 0.0323, wR_2 = 0.0843	R_1 = 0.1034, wR_2 = 0.1518	R_1 = 0.0594, wR_2 = 0.1251

Table A1.11: *Crystallographic data for compounds **3.13**-**3.15**.*

Identification code	**3.13**	**3.14**	**3.15**
Empirical formula	$C_{72}H_{72}N_{16}O_{20}Zn_8$	$C_{28}H_{46}Cl_4Cu_2N_8O_{24}$	$C_{36}H_{42}Cl_4Cu_2N_{12}O_{18}$
Formula weight	2004.41	1147.61	1199.69
Temperature /K	120.0(1)	120.0(1)	120.0(1)
Crystal system	monoclinic	triclinic	monoclinic
Space group	*C*2/*c*	*P*-1	$P2_1/c$
a/Å	26.9495(5)	8.6004(3)	7.82655(14)
b/Å	13.2218(2)	11.9481(5)	34.0319(6)
c/Å	27.5032(5)	12.0237(5)	18.3327(3)
α/°	90	86.841(3)	90
β/°	92.7008(17)	87.761(3)	90.8790(14)
γ/°	90	69.080(4)	90
Volume /Å^3	9789.1(3)	1152.08(8)	4882.38(15)
Z	4	1	4
ρ_{calc} g/cm^3	1.36	1.654	1.632
F(000)	4064	588	2448
Crystal size/mm^3	0.16 × 0.14 × 0.10	0.45 × 0.28 × 0.21	0.24 × 0.18 × 0.05
Radiation	CuKα (λ = 1.54184)	CuKα (λ = 1.54184)	CuKα (λ = 1.54184)
Reflections collected	24661	9550	51242
Independent reflections	8637	4747	9278
Goodness-of-fit on F^2	1.057	1.085	1.033
Final R indexes [I>=2σ (I)]	R_1 = 0.0702, wR_2 = 0.1902	R_1 = 0.0389, wR_2 = 0.1068	R_1 = 0.0573, wR_2 = 0.1609
Final R indexes [all data]	R_1 = 0.0784, wR_2 = 0.1979	R_1 = 0.0397, wR_2 = 0.1078	R_1 = 0.0597, wR_2 = 0.1636

Table A1.12: *Crystallographic data for compounds **3.16**-**3.17**.*

Identification code	**3.16**	**3.17**
Empirical formula	$C_{27}H_{40}N_8O_{12}Zn_2$	$C_{106}H_{128}N_{20}O_{28}Zn_8$
Formula weight	799.41	2653.24
Temperature /K	120.0(1)	120.0(1)
Crystal system	orthorhombic	monoclinic
Space group	$Pna2_1$	*C*2/*c*
a/Å	24.2792(6)	40.0575(15)
b/Å	8.4086(3)	17.6671(4)
c/Å	16.6004(4)	25.0318(10)
α/°	90	90
β/°	90	132.232(7)
γ/°	90	90
Volume /Å^3	3389.05(15)	13116.8(13)
Z	4	4
ρ_{calc} g/cm^3	1.567	1.344
F(000)	1656	5472
Crystal size/mm^3	0.12 × 0.09 × 0.07	0.15 × 0.14 × 0.09
Radiation	CuKα (λ = 1.54184)	CuKα (λ = 1.54184)
Reflections collected	10368	43761
Independent reflections	4743	12439
Goodness-of-fit on F^2	1.057	1.033
Final R indexes [I>=2σ (I)]	R_1 = 0.0743, wR_2 = 0.1652	R_1 = 0.0709, wR_2 = 0.2040
Final R indexes [all data]	R_1 = 0.0895, wR_2 = 0.1762	R_1 = 0.0870, wR_2 = 0.2233

Chapter 4

Table A1.13: *Crystallographic data for compounds* ***4.1-4.3****.*

Identification code	**4.1**	**4.2**	**4.3**
Empirical formula	$C_{23}H_{13}N_3O_4Zn$	$C_{24}H_{15}N_3O_4Zn$	$C_{23}H_{12}ClN_3O_4Zn$
Formula weight	460.73	474.76	495.18
Temperature /K	120.0(1)	120.0(1)	120.0(1)
Crystal system	tetragonal	tetragonal	tetragonal
Space group	$I4_1/acd$	$I4_1/acd$	$I4_1/acd$
a/Å	29.5140(5)	29.4203(3)	29.0435(2)
b/Å	29.5140(5)	29.4203(3)	29.0435(2)
c/Å	26.3488(3)	26.4081(5)	27.2811(2)
α/°	90	90	90
β/°	90	90	90
γ/°	90	90	90
Volume /Å^3	22951.8(8)	22857.6(6)	23012.2(4)
Z	32	32	32
ρ_{calc} g/cm^3	1.067	1.104	1.143
F(000)	7488	7744	8000
Crystal size/mm^3	0.29 × 0.11 × 0.09	0.13 × 0.11 × 0.08	0.50 × 0.15 × 0.12
Radiation	CuKα (λ = 1.54184)	CuKα (λ = 1.54184)	CuKα (λ = 1.54184)
Reflections collected	70713	41314	41447
Independent reflections	5075	5744	5093
Goodness-of-fit on F^2	1.036	1.031	1.091
Final R indexes [I>=2σ (I)]	R_1 = 0.0506, wR_2 = 0.1464	R_1 = 0.0424, wR_2 = 0.1205	R_1 = 0.0449, wR_2 = 0.1260
Final R indexes [all data]	R_1 = 0.0672, wR_2 = 0.1721	R_1 = 0.0562, wR_2 = 0.1327	R_1 = 0.0474, wR_2 = 0.1287

Table A1.14: *Crystallographic data for compounds* ***4.4-4.6***

Identification code	**4.4**	**4.5**	**4.6**
Empirical formula	$C_{23}H_{12}N_4O_6Zn$	$C_{21}H_{11}N_3O_4SZn$	$C_{21}H_{11}N_3O_4SZn$
Formula weight	505.74	466.76	466.76
Temperature /K	120.0(1)	120.0(1)	120.0(1)
Crystal system	tetragonal	tetragonal	tetragonal
Space group	$I4_1/acd$	$I4_1/acd$	$I4_1/acd$
a/Å	28.7087(4)	29.7251(3)	29.7311(4)
b/Å	28.7087(4)	29.7251(3)	29.7311(4)
c/Å	27.7471(4)	26.0789(3)	26.1268(3)
α/°	90	90	90
β/°	90	90	90
γ/°	90	90	90
Volume /Å^3	22868.8(7)	23042.9(6)	23094.5(7)
Z	32	32	32
ρ_{calc} g/cm^3	1.175	1.076	1.074
F(000)	8192	7552	7552
Crystal size/mm^3	0.19 × 0.16 × 0.12	0.64 × 0.25 × 0.18	0.56 × 0.10 × 0.08
Radiation	CuKα (λ = 1.54184)	CuKα (λ = 1.54184)	Cu Kα (λ = 1.54184)
Reflections collected	36343	74057	74910
Independent reflections	5022	5091	5103
Goodness-of-fit on F^2	1.301	1.046	1.096
Final R indexes [I>=2σ (I)]	R_1 = 0.0883, wR_2 = 0.2767	R_1 = 0.0539, wR_2 = 0.1724	R_1 = 0.0494, wR_2 = 0.1622
Final R indexes [all data]	R_1 = 0.1068, wR_2 = 0.3148	R_1 = 0.0591, wR_2 = 0.1809	R_1 = 0.0628, wR_2 = 0.1807

Table A1.15: *Crystallographic data for compound* ***4.7****.*

Identification code	**4.7**
Empirical formula	$C_{22}H_{12}N_4O_4Zn$
Formula weight	461.73
Temperature /K	120.0(1)
Crystal system	tetragonal
Space group	$I4_1/acd$
a/Å	29.6110(5)
b/Å	29.6110(5)
c/Å	25.8589(5)
α/°	90
β/°	90
γ/°	90
Volume /Å^3	22673.4(8)
Z	32
ρ_{calc} g/cm^3	1.082
F(000)	7488
Crystal size/mm^3	0.28 × 0.24 × 0.16
Radiation	CuKα (λ = 1.54184)
Reflections collected	71275
Independent reflections	5014
Goodness-of-fit on F^2	1.047
Final R indexes [I>=2σ (I)]	R_1 = 0.0607, wR_2 = 0.1785
Final R indexes [all data]	R_1 = 0.0794, wR_2 = 0.2105

Chapter 5

Table A1.16: *Crystallographic data for compound* ***5.1-5.3****.*

Identification code	**5.1**	**5.2**	**5.3**
Empirical formula	C18H16N2NiO8	$C_{20.5}H_{19.5}CuN_{2.5}O_9$	$C_{61}H_{55}Cu_2N_{11}O_8$
Formula weight	447.04	508.42	1197.24
Temperature /K	120.0(1)	120.0(1)	120.0(1)
Crystal system	triclinic	triclinic	monoclinic
Space group	*P*-1	*P*-1	*C*2/*c*
a/Å	4.7960(4)	8.2863(2)	38.388(2)
b/Å	8.3182(6)	8.7880(4)	31.7532(15)
c/Å	10.9805(4)	14.9394(4)	9.5637(4)
α/°	79.047(5)	87.395(3)	90
β/°	87.670(5)	84.749(2)	105.976(6)
γ/°	75.215(7)	65.797(3)	90
Volume /Å^3	415.83(5)	988.06(6)	11207.3(10)
Z	1	2	8
ρ_{calc} g/cm^3	1.785	1.709	1.419
F(000)	230	522	4960
Crystal size/mm^3	0.09 × 0.06 × 0.03	0.29 × 0.08 × 0.04	0.08 × 0.06 × 0.03
Radiation	CuKα (λ = 1.54184)	CuKα (λ = 1.54184)	CuKα (λ = 1.54184)
Reflections collected	3354	9102	21705
Independent reflections	1567	3749	9244
Goodness-of-fit on F^2	1.068	1.063	1.085
Final R indexes [I>=2σ (I)]	R1 = 0.0345, wR2 = 0.0886	R_1 = 0.0327, wR_2 = 0.0927	R_1 = 0.1187, wR_2 = 0.3321
Final R indexes [all data]	R1 = 0.0363, wR2 = 0.0904	R_1 = 0.0351, wR_2 = 0.0952	R_1 = 0.1657, wR_2 = 0.3660

Table A1.17: *Crystallographic data for compound* ***5.4****.*

Identification code	**5.4**
Empirical formula	$C_{19}H_{13}Br_2Cu_2NO_{11.5}$
Formula weight	726.2
Temperature /K	120.0(1)
Crystal system	orthorhombic
Space group	*Ibam*
a/Å	12.5302(14)
b/Å	23.503(6)
c/Å	27.124(6)
α/°	90
β/°	90
γ/°	90
Volume /Å^3	7988(3)
Z	8
ρ_{calc} g/cm^3	1.208
F(000)	2832
Crystal size/mm^3	0.08 × 0.08 × 0.04
Radiation	CuKα (λ = 1.54184)
Reflections collected	3600
Independent reflections	3600
Goodness-of-fit on F^2	1.185
Final R indexes [I>=2σ (I)]	R_1 = 0.1119, wR_2 = 0.2974
Final R indexes [all data]	R_1 = 0.1292, wR_2 = 0.3168

Appendix 2

Chapter 4

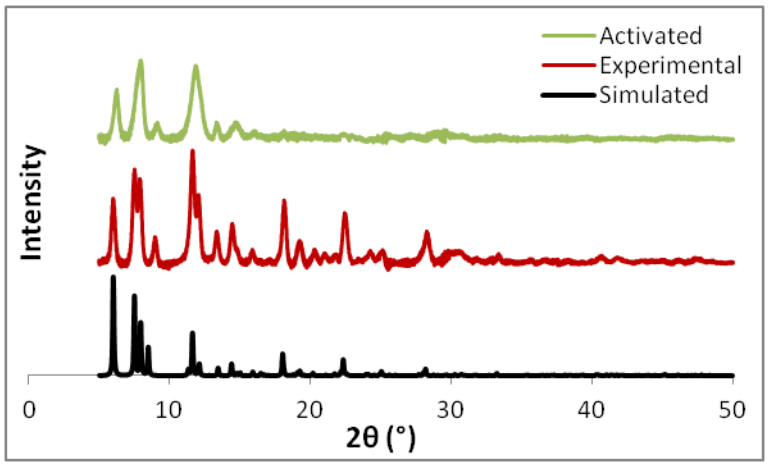

Figure A2.1: *PXRD patterns of* ***4.1*** *simulated from single crystal data, as synthesised and post activation.*

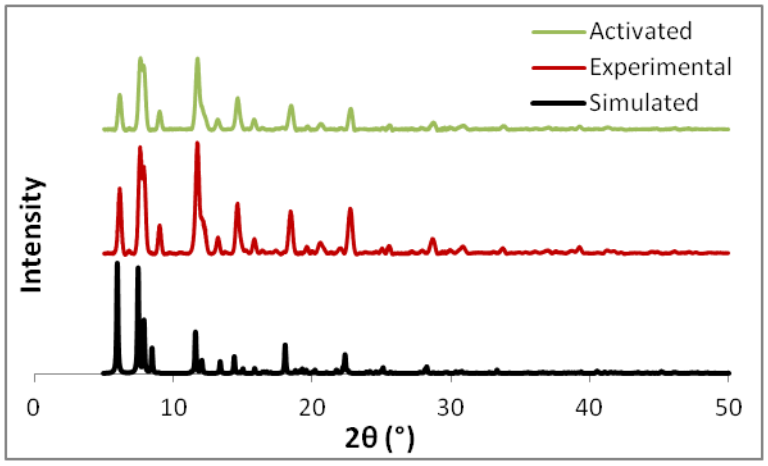

Figure A2.2: *PXRD patterns of* ***4.2*** *simulated from single crystal data, as synthesised and post activation.*

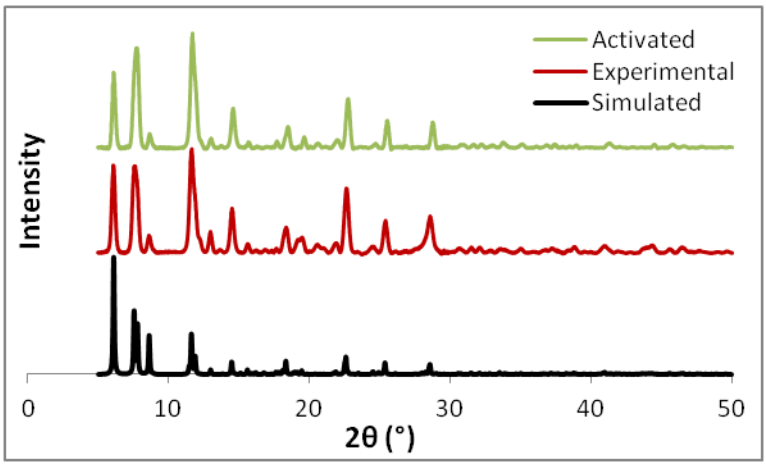

Figure A2.3: *PXRD patterns of* ***4.3*** *simulated from single crystal data, as synthesised and post activation.*

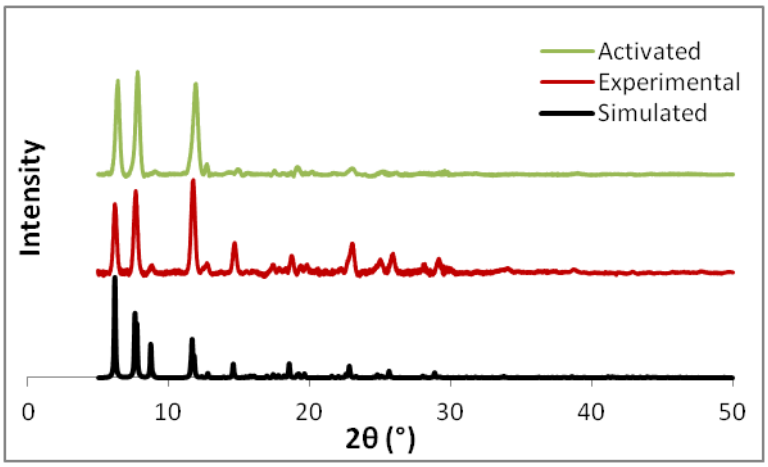

Figure A2.4: *PXRD patterns of* ***4.4*** *simulated from single crystal data, as synthesised and post activation.*

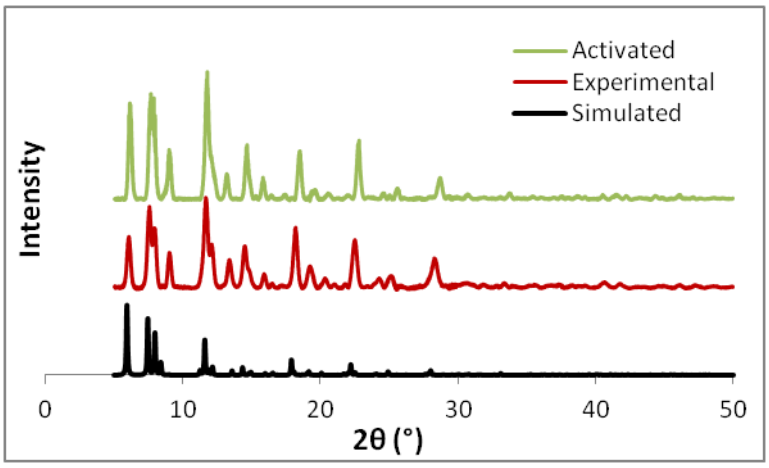

Figure A2.5: *PXRD patterns of* ***4.5*** *simulated from single crystal data, as synthesised and post activation.*

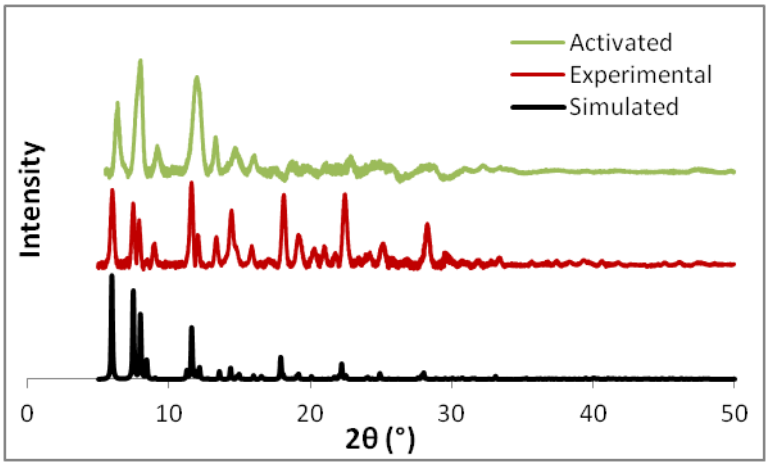

Figure A2.6: *PXRD patterns of* ***4.6*** *simulated from single crystal data, as synthesised and post activation.*

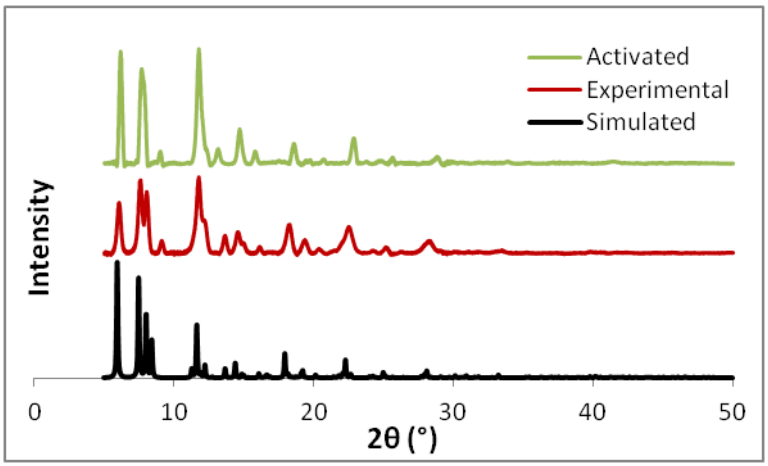

Figure A2.7: *PXRD patterns of* ***4.7*** *simulated from single crystal data, as synthesised and post activation.*

Appendix 3

BET Surface Area Calculations

The surface area of a material is commonly calculated by measuring a nitrogen gas isotherm at 77 K and fitting the data to the BET equation. Although this method was originally derived for multilayer gas adsorption onto flat surfaces, it can be applicable to the determination of surface area in microporous materials in an appropriate pressure range.[370] The appropriate range for microporous materials is at a lower partial pressure than the typical BET pressure range in order to limit problems arising from the false assumptions that adsorption is on a flat surface and there is no limit to the thickness of the adsorbed layer. This range is defined by the following two criteria;[108-109]

1- The isotherm region where $v(1-P/P_0)$ increases versus P/P_0 (where v is the amount of adsorbed gas, P is the pressure of adsorbent in equilibrium with porous material, P_0 is the condensation pressure of adsorbent at the temperature of measurement and P/P_0 the relative pressure).

2- Within this region, points that yield a positive intercept in the plot of $P/P_0/(v(1-P/P_0))$ versus P/P_0. This plot gives a slope a, and intercept b, from which the number of adsorbed molecule in the initial monolayer (v_m) can be calculated according to Equation A3.1

$$v_m = \frac{1}{a+b} \qquad (\textit{Equation A3.1})$$

The surface area can then be calculated according to the following equation:

$$A_{BET} = v_m \sigma_0 N_A / V \qquad (\text{Equation A3.2})$$

Where σ_0 is the cross sectional area of a N_2 gas molecule (16.2 $Å^2$), and V is the molar volume of the adsorbate gas (22414 cm^3).

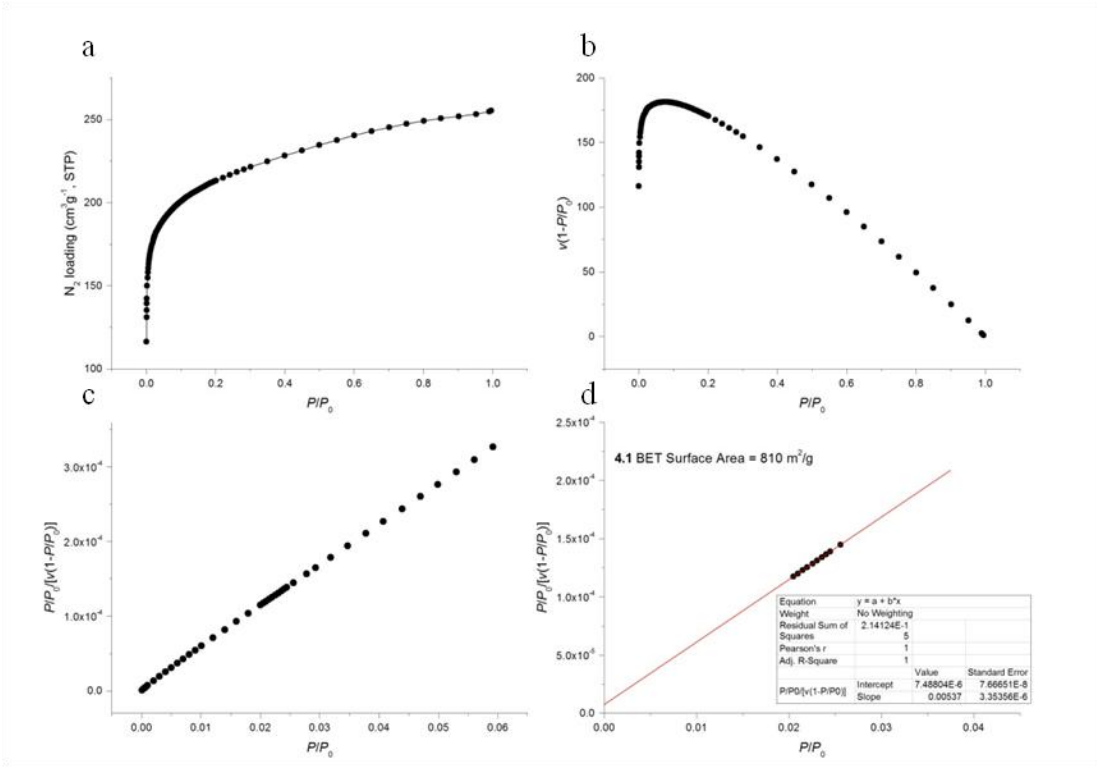

Figure A3.1: *BET surface area calculation for* ***4.1.*** *a) Adsorption isotherm measured at 77 K. b) A plot to find the pressure region that fits the first criterion for analysis of microporous materials by the BET equation. c) A plot to find points that fit the second criterion. d) Final BET plot.*

$$A_{BET} = 1/(7.48804\times10^{-6} + 0.00537)/22414 \times 6.023\times10^{23} \times 0.162\times10^{-18} = 810\ m^2/g$$

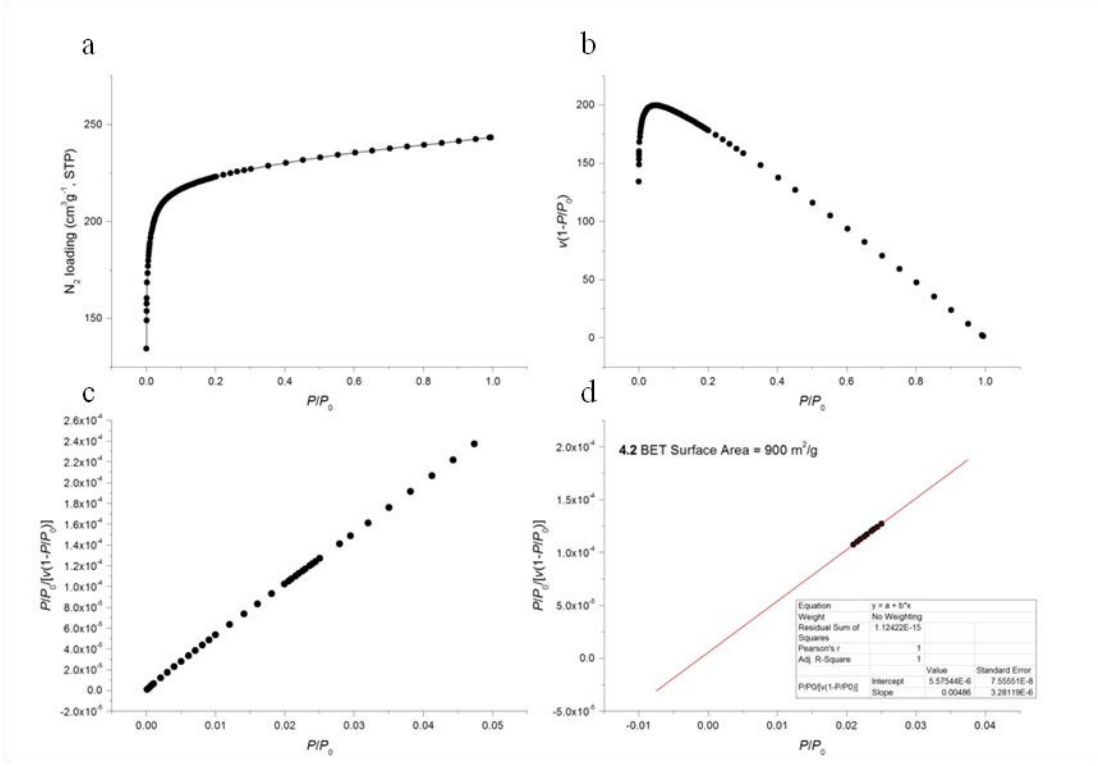

Figure A3.2: *BET surface area calculation for* ***4.2.*** *a) Adsorption isotherm measured at 77 K. b) A plot to find the pressure region that fits the first criterion for analysis of microporous materials by the BET equation. c) A plot to find points that fit the second criterion. d) Final BET plot.*

$$A_{BET} = 1/(5.57544\times10^{-6} + 0.00486)/22414 \times 6.023\times10^{23} \times 0.162\times10^{-18} = 900\ m^2/g$$

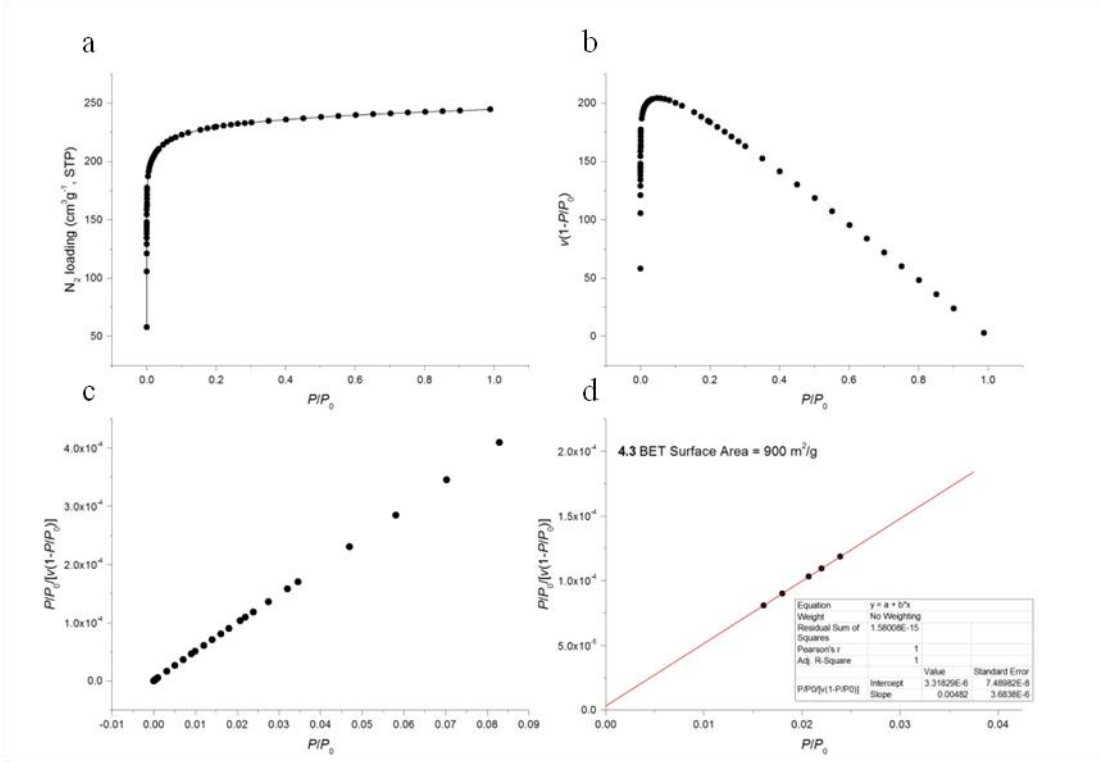

Figure A3.3: *BET surface area calculation for* ***4.3.*** *a) Adsorption isotherm measured at 77 K. b) A plot to find the pressure region that fits the first criterion for analysis of microporous materials by the BET equation. c) A plot to find points that fit the second criterion. d) Final BET plot.*

$$A_{BET} = 1/(3.31829\times10^{-6} + 0.00482)/22414 \times 6.023\times10^{23} \times 0.162\times10^{-18} = 900\ m^2/g$$

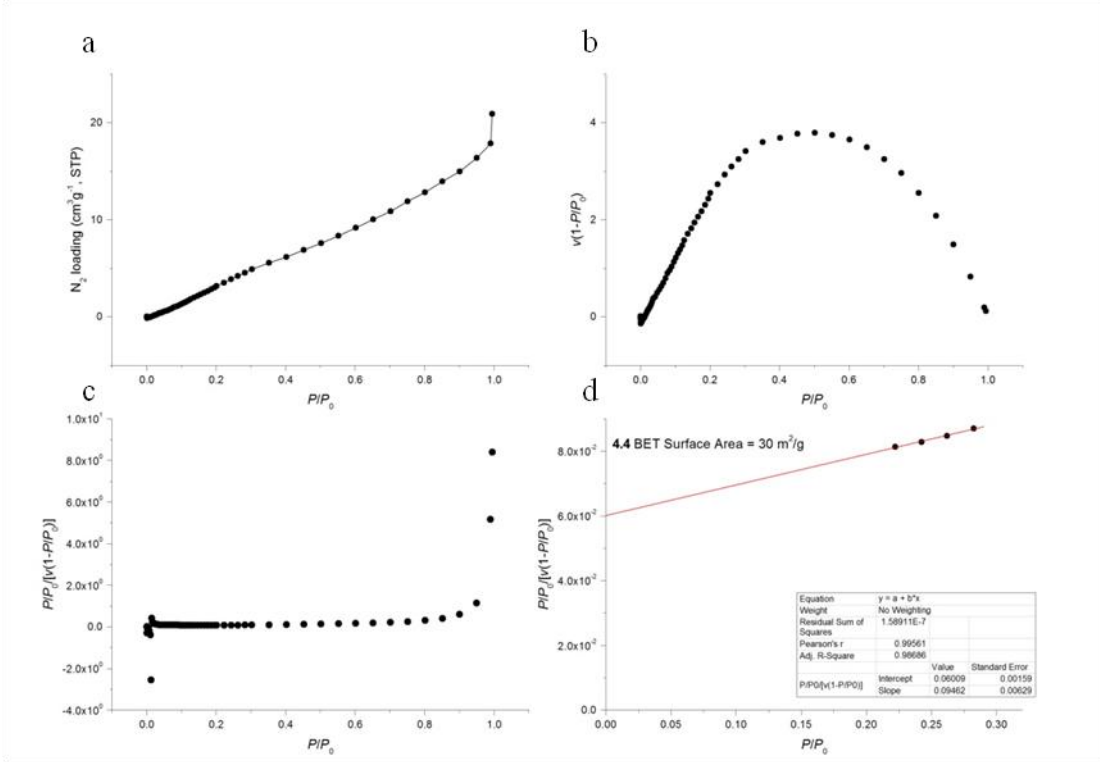

Figure A3.4: *BET surface area calculation for* ***4.4.*** *a) Adsorption isotherm measured at 77 K. b) A plot to find the pressure region that fits the first criterion for analysis of microporous materials by the BET equation. c) A plot to find points that fit the second criterion. d) Final BET plot.*

$$A_{BET} = 1/(0.06009 + 0.09462)/22414 \times 6.023\times10^{23} \times 0.162\times10^{-18} = 30\ m^2/g$$

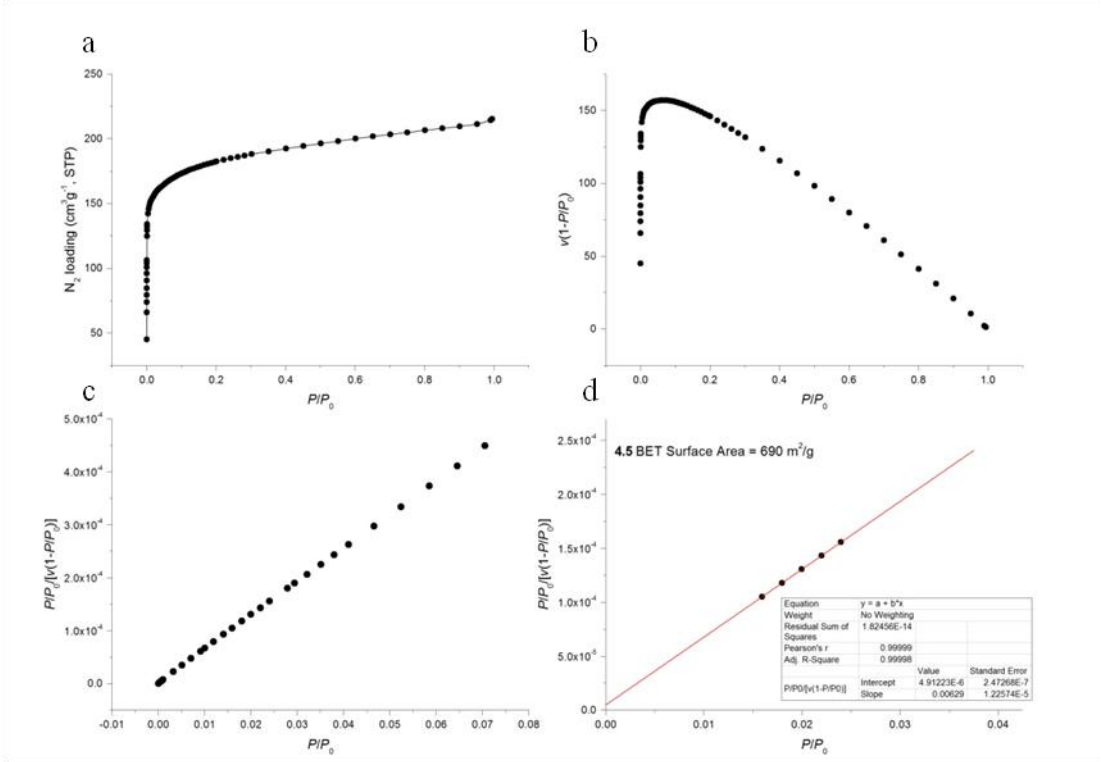

Figure A3.5: *BET surface area calculation for* ***4.5****. a) Adsorption isotherm measured at 77 K. b) A plot to find the pressure region that fits the first criterion for analysis of microporous materials by the BET equation. c) A plot to find points that fit the second criterion. d) Final BET plot.*

$$A_{BET} = 1/(4.91223\times10^{-6} + 0.00629)/22414 \times 6.023\times10^{23} \times 0.162\times10^{-18} = 690\ m^2/g$$

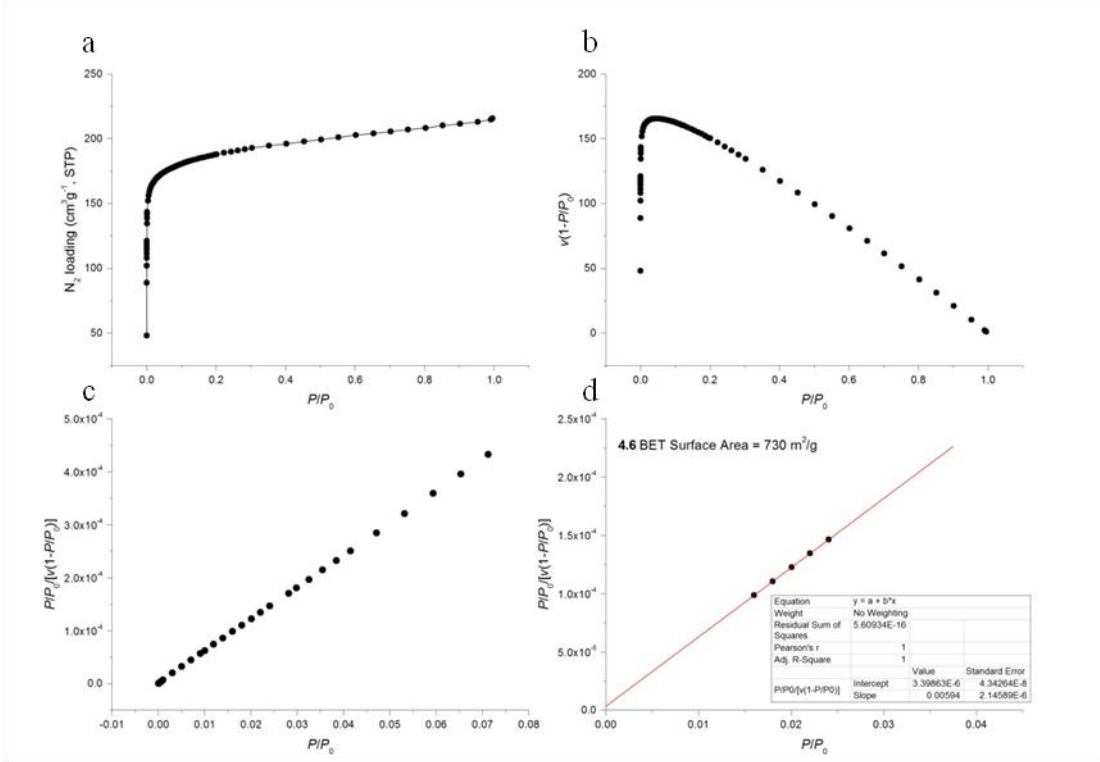

Figure A3.6: *BET surface area calculation for* ***4.6.*** *a) Adsorption isotherm measured at 77 K. b) A plot to find the pressure region that fits the first criterion for analysis of microporous materials by the BET equation. c) A plot to find points that fit the second criterion. d) Final BET plot.*

$$A_{BET} = 1/(3.39863\times10^{-6} + 0.00594)/22414 \times 6.023\times10^{23} \times 0.162\times10^{-18} = 730\ m^2/g$$

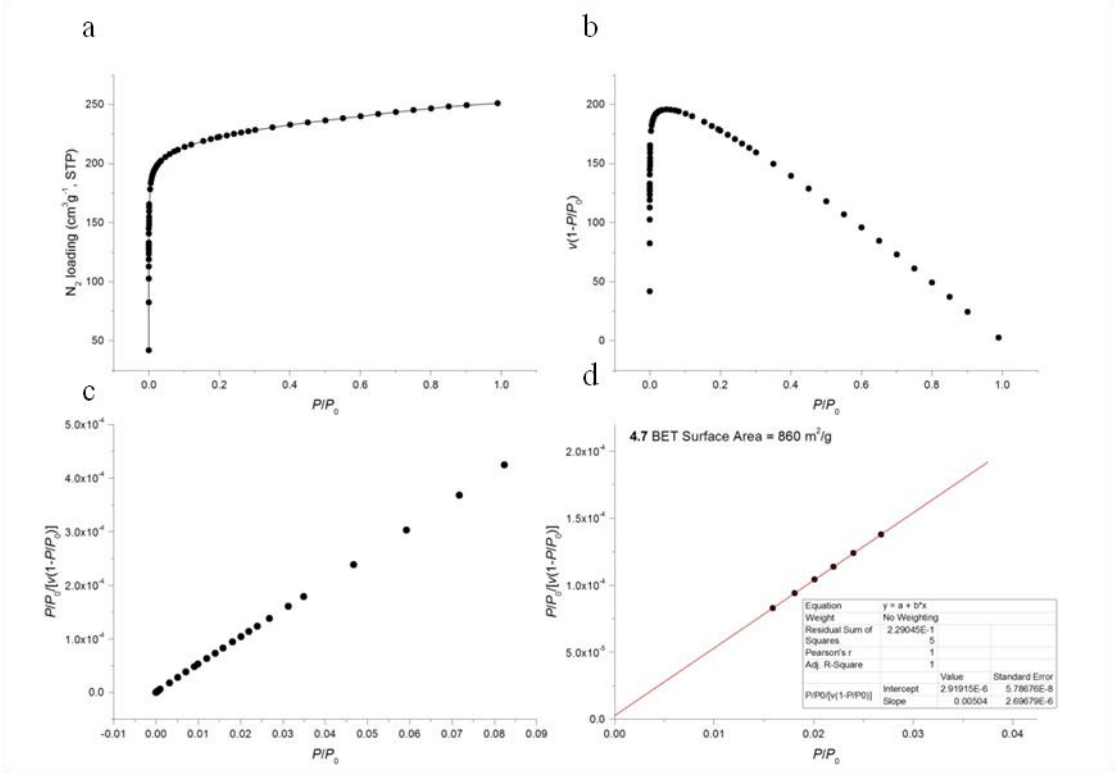

Figure A3.7: *BET surface area calculation for* ***4.7.*** *a) Adsorption isotherm measured at 77 K. b) A plot to find the pressure region that fits the first criterion for analysis of microporous materials by the BET equation. c) A plot to find points that fit the second criterion. d) Final BET plot.*

$$A_{BET} = 1/(2.91915\times10^{-6} + 0.00504)/22414 \times 6.023\times10^{23} \times 0.162\times10^{-18} = 860\ m^2/g$$

Appendix 4

Heat of Adsorption

The heat of adsorption (Q_{st}) is a quantitative measure of the affinity of a material for a given guest molecule. The strength of the interaction between the adsorbate and adsorbent can be calculated by fitting adsorption isotherms at different temperatures. This was done according to the method described in the literature using the virial equation (Equation A4.1);[84]

$$\ln P = \ln N + \frac{1}{T}\sum_{i=0}^{m} a_i N^i + \sum_{i=0}^{n} b_i N^i \qquad (\textit{Equation A4.1})$$

Where *N* is the amount of gas adsorbed at the pressure *P*, *a* and *b* are virial coefficients and *m* and *n* are the number of coefficients require to adequately describe the isotherm. The latter parameters were gradually increased until the contribution of extra coefficients was deemed to be statistically insignificant toward the overall fit. The values of the virial coefficients a_0 through a_m were then used to calculate Q_{st} using the following expression:

$$Q_{st} = -R \sum_{i=0}^{m} a_i N^i \qquad (\textit{Equation A4.2})$$

This equation assumes that the isosteric heat of adsorption does not vary with temperature; however this is only generally true over a narrow temperature range. To limit errors associated with this, isotherms were measured with a 25 K temperature difference.

Methane Adsorption

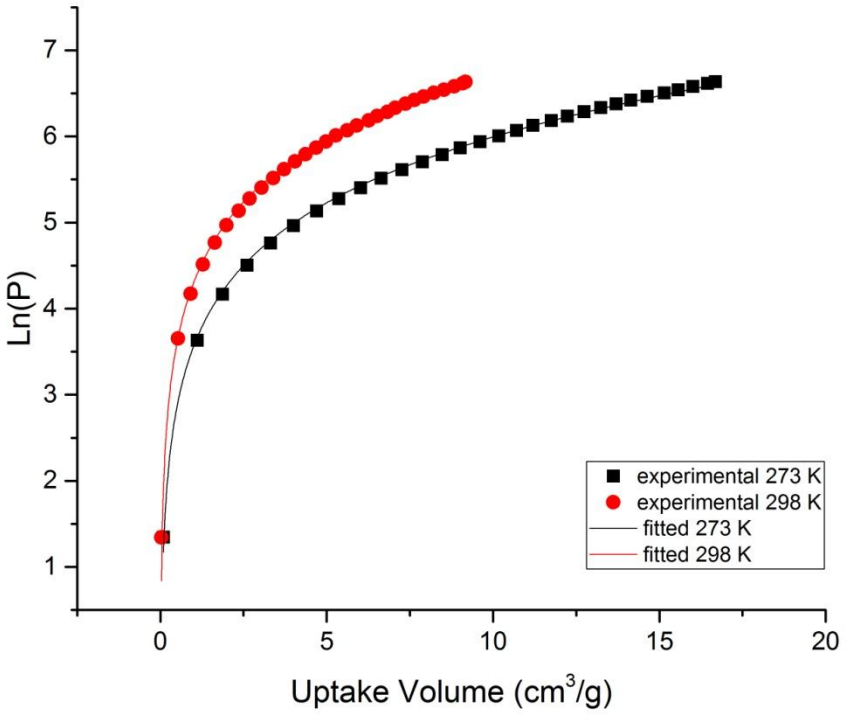

Figure A4.1: *CH_4 adsorption isotherms of* ***4.1*** *at 273and 298 K fitted using the virial equation.*

Equation	ln(x)+1/T*(a0+a1*x+a2*x^2+a3*x^3+a4*x^4+a5*x^5+a6*x^6)+(b0+b1*x+b2*x^2+b3*x^3)		
Reduced Chi-Sqr			0.00559
Adj. R-Square			0.99543
		Value	Standard Error
Ln(P)	a0*	-2406.06	73.94299
	a1*	3.90987	0.67737
	a2*	0	0
	a3*	0	0
	a4*	0	0
	a5*	0	0
	a6*	0	0
	b0*	12.36197	0.25095
	b1*	0	0
	b2*	0	0
	b3*	0	0

Table A4.1: *Parameters used to fit the CH_4 adsorption isotherms of* ***4.1*** *at 273 K and 298 K to the virial equation.*

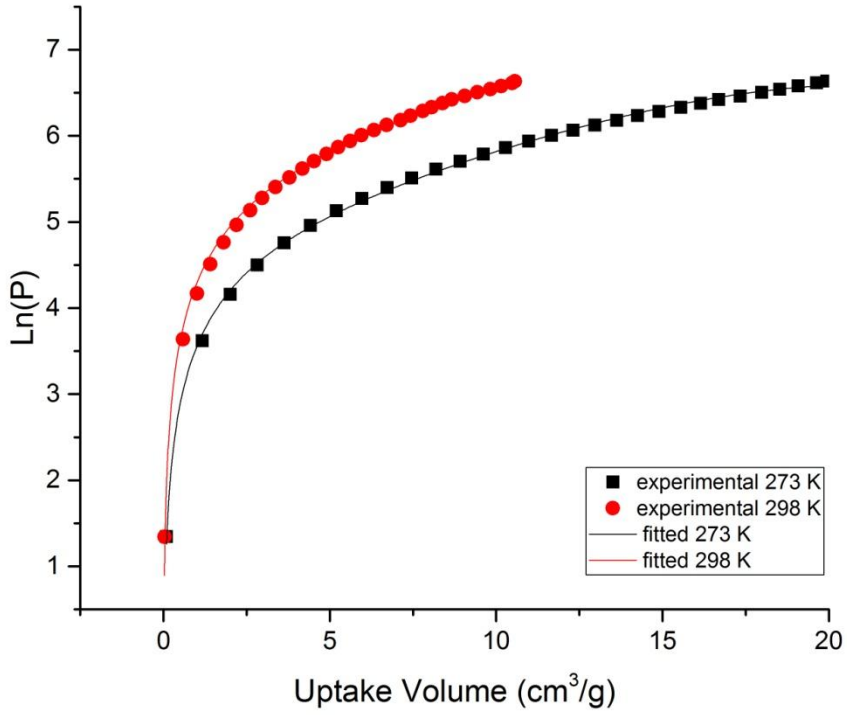

Figure A4.2: *CH_4 adsorption isotherms of* ***4.2*** *at 273and 298 K fitted using the virial equation.*

Equation	ln(x)+1/T*(a0+a1*x+a2*x^2+a3*x^3+a4*x^4+a5*x^5+a6*x^6)+(b0+b1*x+b2*x^2+b3*x^3)		
Reduced Chi-Sqr			0.00563
Adj. R-Square			0.99540
		Value	Standard Error
Ln(P)	a0*	-2388.56201	74.87762
	a1*	-17.31155	4.461
	a2*	2.10943	0.54907
	a3*	-0.0627	0.01844
	a4*	0	0
	a5*	0	0
	a6*	0	0
	b0*	12.35525	0.26046
	b1*	0	0
	b2*	0	0
	b3*	0	0

Table A4.2: *Parameters used to fit the CH_4 adsorption isotherms of* ***4.2*** *at 273 K and 298 K to the virial equation.*

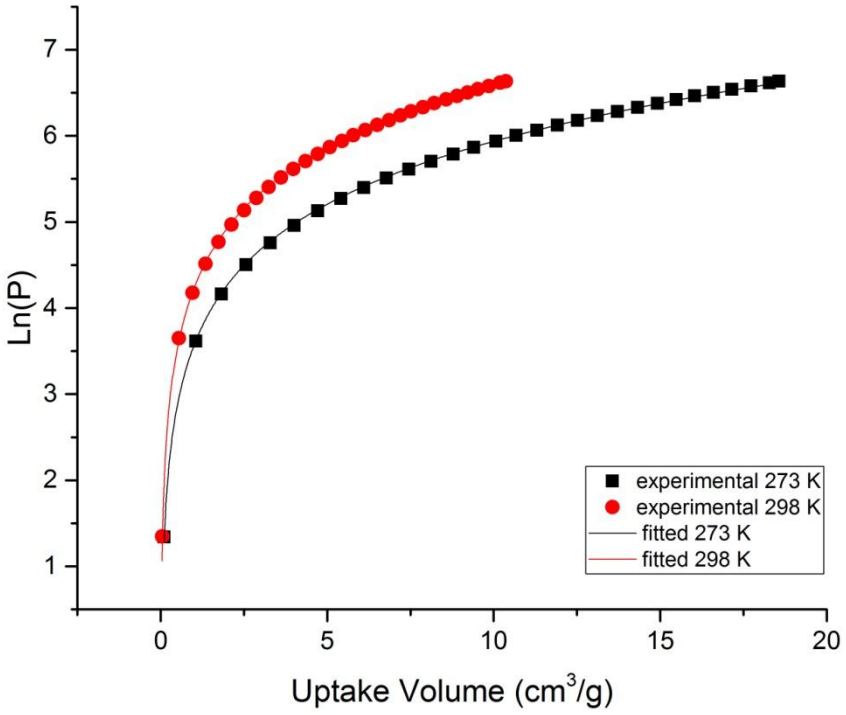

Figure A4.3: *CH_4 adsorption isotherms of **4.3** at 273and 298 K fitted using the virial equation.*

Equation	ln(x)+1/T*(a0+a1*x+a2*x^2+a3*x^3+a4*x^4+a5*x^5+a6*x^6)+(b0+b1*x+b2*x^2+b3*x^3)		
Reduced Chi-Sqr			0.00161
Adj. R-Square			0.99868
		Value	Standard Error
Ln(P)	a0*	-2154.68989	38.87004
	a1*	1.98201	0.32332
	a2*	0	0
	a3*	0	0
	a4*	0	0
	a5*	0	0
	a6*	0	0
	b0*	11.45314	0.13229
	b1*	0	0
	b2*	0	0
	b3*	0	0

Table A4.3: *Parameters used to fit the CH_4 adsorption isotherms of **4.3** at 273 K and 298 K to the virial equation.*

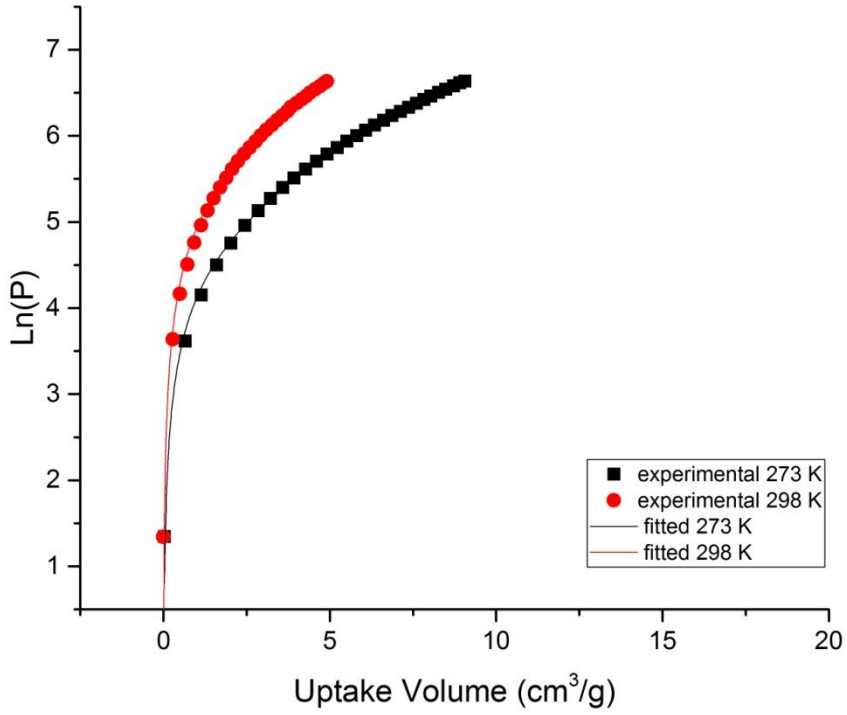

Figure A4.4: *CH_4 adsorption isotherms of **4.4** at 273and 298 K fitted using the virial equation.*

Equation	ln(x)+1/T*(a0+a1*x+a2*x^2+a3*x^3+a4*x^4+a5*x^5+a6*x^6)+(b0+b1*x+b2*x^2+b3*x^3)		
Reduced Chi-Sqr			0.04072
Adj. R-Square			0.96679
		Value	Standard Error
Ln(P)	a0*	-2609.28421	208.54666
	a1*	-49.59437	29.70065
	a2*	13.8578	7.75008
	a3*	-0.88294	0.5593
	a4*	0	0
	a5*	0	0
	a6*	0	0
	b0*	13.81258	0.73165
	b1*	0	0
	b2*	0	0
	b3*	0	0

Table A4.4: *Parameters used to fit the CH_4 adsorption isotherms of **4.4** at 273 K and 298 K to the virial equation.*

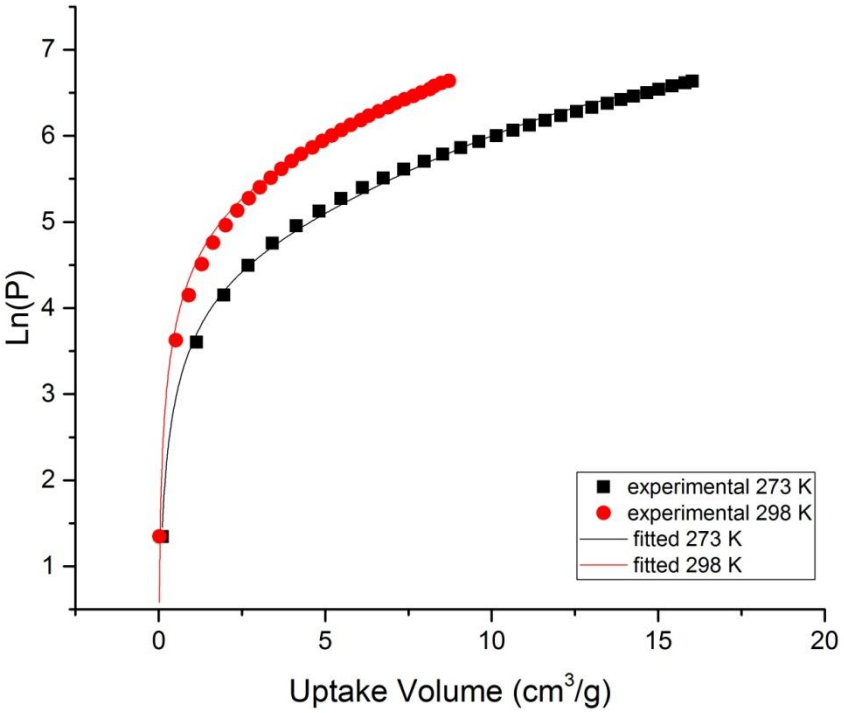

Figure A4.5: *CH_4 adsorption isotherms of **4.5** at 273and 298 K fitted using the virial equation.*

Equation	ln(x)+1/T*(a0+a1*x+a2*x^2+a3*x^3+a4*x^4+a5*x^5+a6*x^6)+(b0+b1*x+b2*x^2+b3*x^3)		
Reduced Chi-Sqr			0.01433
Adj. R-Square			0.98834
		Value	Standard Error
Ln(P)	a0*	-2711.0829	121.73893
	a1*	-29.32846	9.09297
	a2*	4.7347	1.37123
	a3*	-0.17308	0.05673
	a4*	0	0
	a5*	0	0
	a6*	0	0
	b0*	13.60248	0.42335
	b1*	0	0
	b2*	0	0
	b3*	0	0

Table A4.5: *Parameters used to fit the CH_4 adsorption isotherms of **4.5** at 273 K and 298 K to the virial equation.*

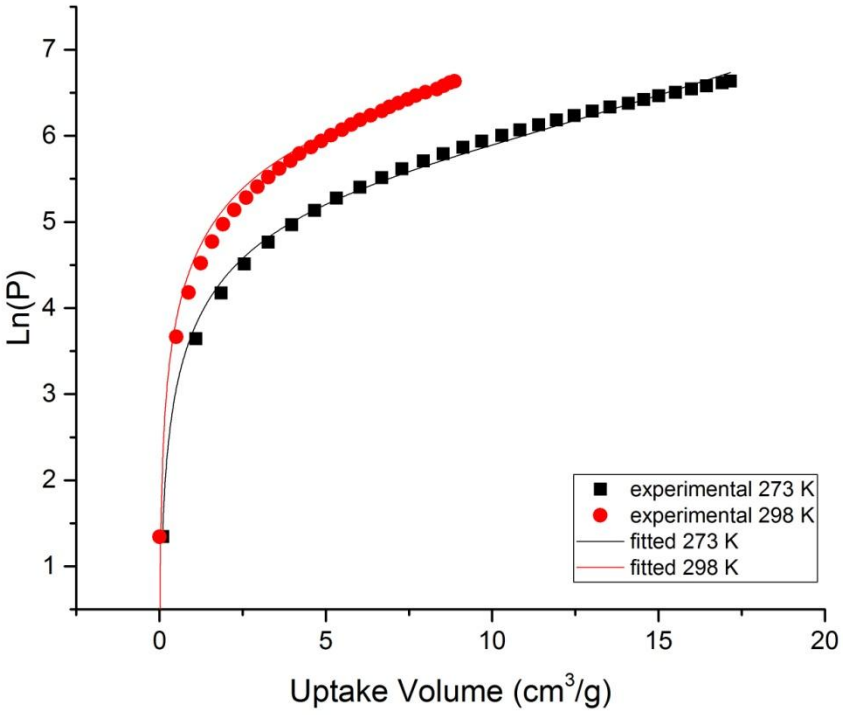

Figure A4.6: *CH_4 adsorption isotherms of* ***4.6*** *at 273and 298 K fitted using the virial equation.*

Equation	ln(x)+1/T*(a0+a1*x+a2*x^2+a3*x^3+a4*x^4+a5*x^5+a6*x^6)+(b0+b1*x+b2*x^2+b3*x^3)		
Reduced Chi-Sqr			0.06286
Adj. R-Square			0.94844
		Value	Standard Error
Ln(P)	a0*	-2612.71	251.8825
	a1*	-14.4454	7.05976
	a2*	0.95528	0.40759
	a3*	0	0
	a4*	0	0
	a5*	0	0
	a6*	0	0
	b0*	13.34022	0.86381
	b1*	0	0
	b2*	0	0
	b3*	0	0

Table A4.6: *Parameters used to fit the CH_4 adsorption isotherms of* ***4.6*** *at 273 K and 298 K to the virial equation.*

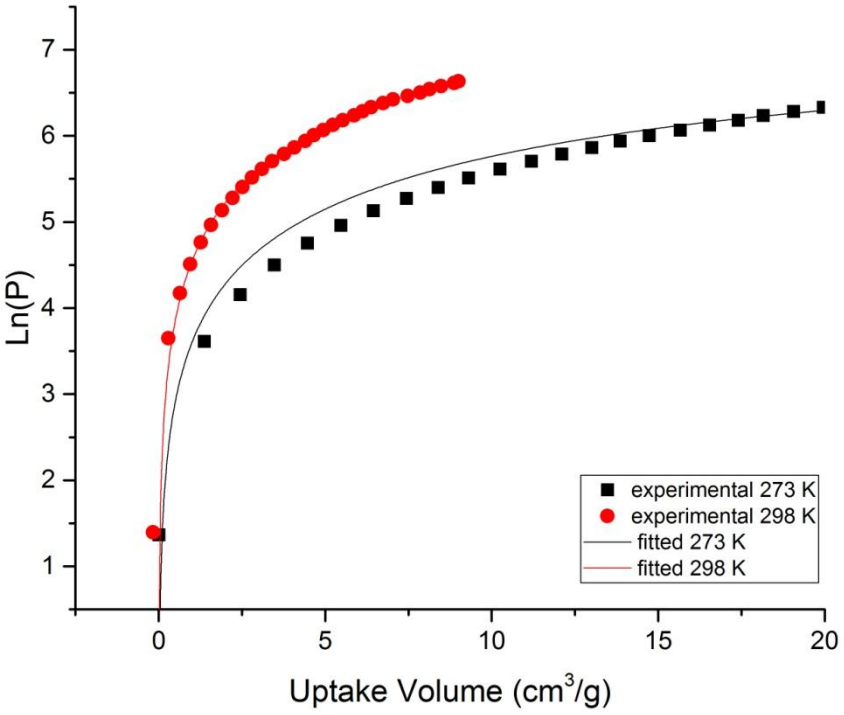

Figure A4.7: *CH_4 adsorption isotherms of **4.7** at 273and 298 K fitted using the virial equation.*

Equation		ln(x)+1/T*(a0+a1*x+a2*x^2+a3*x^3+a4*x^4+a5*x^5+a6*x^6)+(b0+b1*x+b2*x^2+b3*x^3)	
Reduced Chi-Sqr			0.13931
Adj. R-Square			0.88530
		Value	Standard Error
Ln(P)	a0*	-3063.18194	413.11994
	a1*	-4.33998	2.2959
	a2*	0	0
	a3*	0	0
	a4*	0	0
	a5*	0	0
	a6*	0	0
	b0*	14.83881	1.40312
	b1*	0	0
	b2*	0	0
	b3*	0	0

Table A4.7: *Parameters used to fit the CH_4 adsorption isotherms of **4.7** at 273 K and 298 K to the virial equation.*

Carbon Dioxide Adsorption

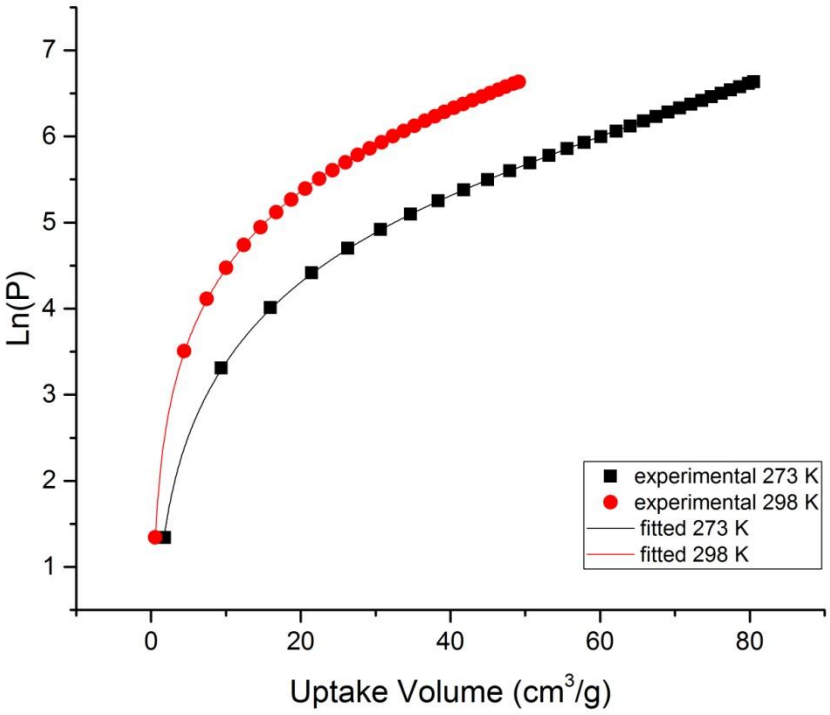

Figure A4.8: *CO_2 adsorption isotherms of* ***4.1*** *at 273and 298 K fitted using the virial equation.*

Equation	ln(x)+1/T*(a0+a1*x+a2*x^2+a3*x^3+a4*x^4+a5*x^5+a6*x^6)+(b0+b1*x+b2*x^2+b3*x^3)		
Reduced Chi-Sqr			1.41162E-4
Adj. R-Square			0.99989
		Value	Standard Error
Ln(P)	a0*	-3682.20988	29.48874
	a1*	16.24772	0.85286
	a2*	-0.23766	0.01987
	a3*	0.00294	3.71993E-4
	a4*	-1.25297E-5	2.26756E-6
	a5*	0	0
	a6*	0	0
	b0*	14.20223	0.10251
	b1*	-0.01625	0.00298
	b2*	0	0
	b3*	0	0

Table A4.8: *Parameters used to fit the CO_2 adsorption isotherms of* ***4.1*** *at 273 K and 298 K to the virial equation.*

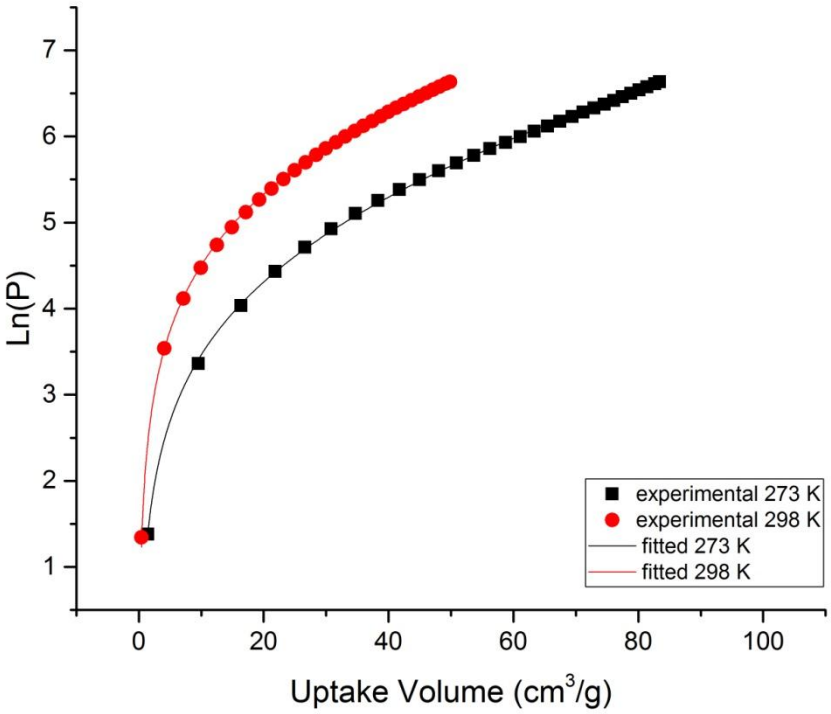

Figure A4.9: *CO_2 adsorption isotherms of* ***4.2*** *at 273and 298 K fitted using the virial equation.*

Equation		ln(x)+1/T*(a0+a1*x+a2*x^2+a3*x^3+a4*x^4+a5*x^5+a6*x^6)+(b0+b1*x+b2*x^2+b3*x^3)	
Reduced Chi-Sqr			4.95118E-4
Adj. R-Square			0.99961
		Value	Standard Error
Ln(P)	a0*	-3443.20097	53.74239
	a1*	6.05184	1.5334
	a2*	-0.00483	0.00203
	a3*	0	0
	a4*	0	0
	a5*	0	0
	a6*	0	0
	b0*	13.6188	0.18424
	b1*	-0.00649	0.00508
	b2*	0	0
	b3*	0	0

Table A4.9: *Parameters used to fit the CO_2 adsorption isotherms of* ***4.2*** *at 273 K and 298 K to the virial equation.*

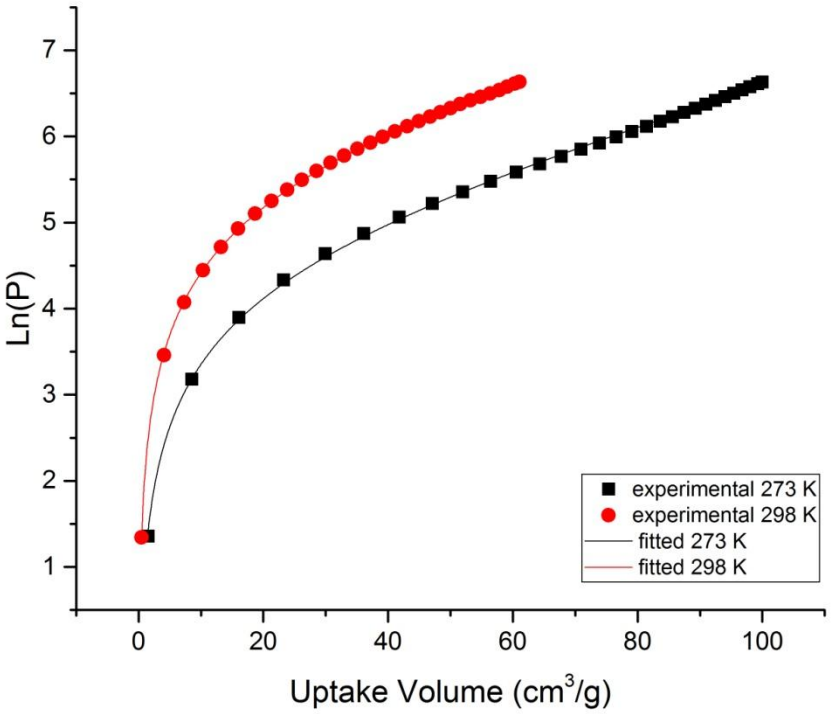

Figure A4.10: *CO_2 adsorption isotherms of **4.3** at 273and 298 K fitted using the virial equation.*

Equation	ln(x)+1/T*(a0+a1*x+a2*x^2+a3*x^3+a4*x^4+a5*x^5+a6*x^6)+(b0+b1*x+b2*x^2+b3*x^3)		
Reduced Chi-Sqr			3.78636E-4
Adj. R-Square			0.99971
		Value	Standard Error
Ln(P)	a0*	-3472.87211	20.7014
	a1*	1.56856	0.09791
	a2*	0.01174	9.34654E-4
	a3*	0	0
	a4*	0	0
	a5*	0	0
	a6*	0	0
	b0*	13.70919	0.07125
	b1*	0	0
	b2*	0	0
	b3*	0	0

Table A4.10: *Parameters used to fit the CO_2 adsorption isotherms of **4.3** at 273 K and 298 K to the virial equation.*

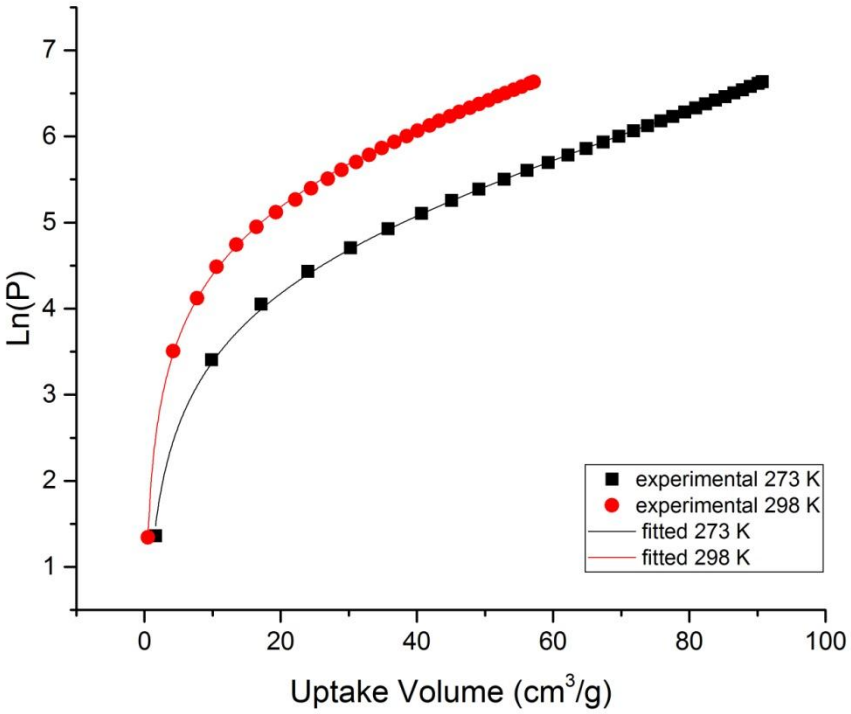

Figure A4.11: *CO_2 adsorption isotherms of* ***4.6*** *at 273and 298 K fitted using the virial equation.*

Equation	ln(x)+1/T*(a0+a1*x+a2*x^2+a3*x^3+a4*x^4+a5*x^5+a6*x^6)+(b0+b1*x+b2*x^2+b3*x^3)		
Reduced Chi-Sqr			5.94777E-4
Adj. R-Square			0.99953
		Value	Standard Error
Ln(P)	a0*	-3310.84112	58.24203
	a1*	2.05993	1.46999
	a2*	-0.00696	0.00901
	a3*	1.51511E-4	6.31171E-5
	a4*	0	0
	a5*	0	0
	a6*	0	0
	b0*	13.10612	0.20063
	b1*	0.00278	0.0048
	b2*	0	0
	b3*	0	0

Table A4.11: *Parameters used to fit the CO_2 adsorption isotherms of* ***4.6*** *at 273 K and 298 K to the virial equation.*

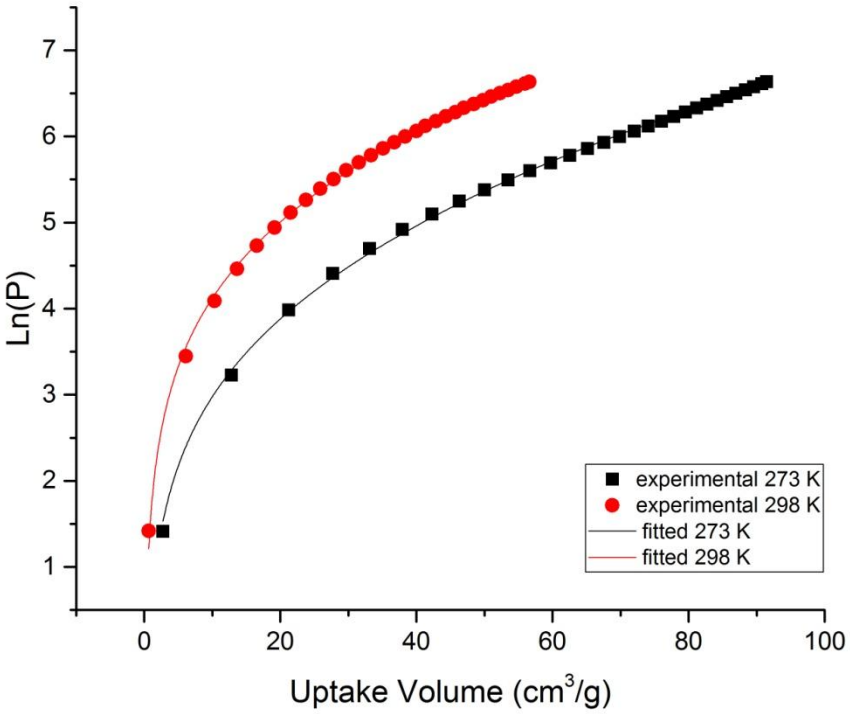

Figure A4.12: *CO_2 adsorption isotherms of* ***4.7*** *at 273and 298 K fitted using the virial equation.*

Equation		ln(x)+1/T*(a0+a1*x+a2*x^2+a3*x^3+a4*x^4+a5*x^5+a6*x^6)+(b0+b1*x+b2*x^2+b3*x^3)	
Reduced Chi-Sqr			0.00195
Adj. R-Square			0.99847
		Value	Standard Error
Ln(P)	a0*	-3783.04493	47.30091
	a1*	6.1757	0.26337
	a2*	-0.01437	0.00266
	a3*	0	0
	a4*	0	0
	a5*	0	0
	a6*	0	0
	b0*	14.30958	0.16211
	b1*	0	0
	b2*	0	0
	b3*	0	0

Table A4.12: *Parameters used to fit the CO_2 adsorption isotherms of* ***4.7*** *at 273 K and 298 K to the virial equation.*

Appendix 5

Carbon Dioxide Adsorption Isotherms

A logarithmic pressure scale can be used to visualise low pressure deviations to typical isotherm behaviour. Carbon dioxide isotherms for compounds **4.1**-**4.7** at 195 K, 273 K and 298 K are presented here.

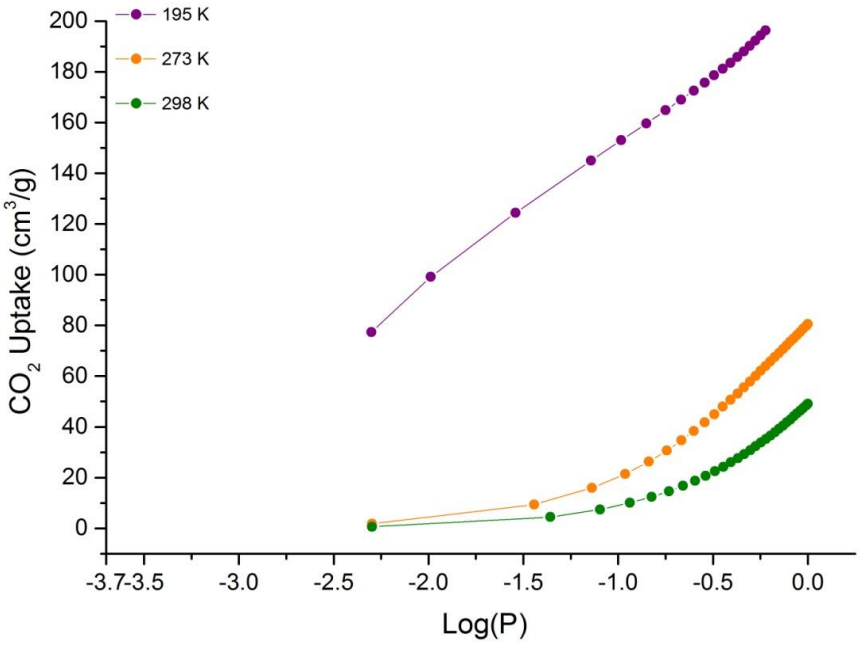

Figure A5.1: *Carbon dioxide adsorption isotherms of* ***4.1*** *at 195, 273 and 298 K with a logarithmic pressure scale.*

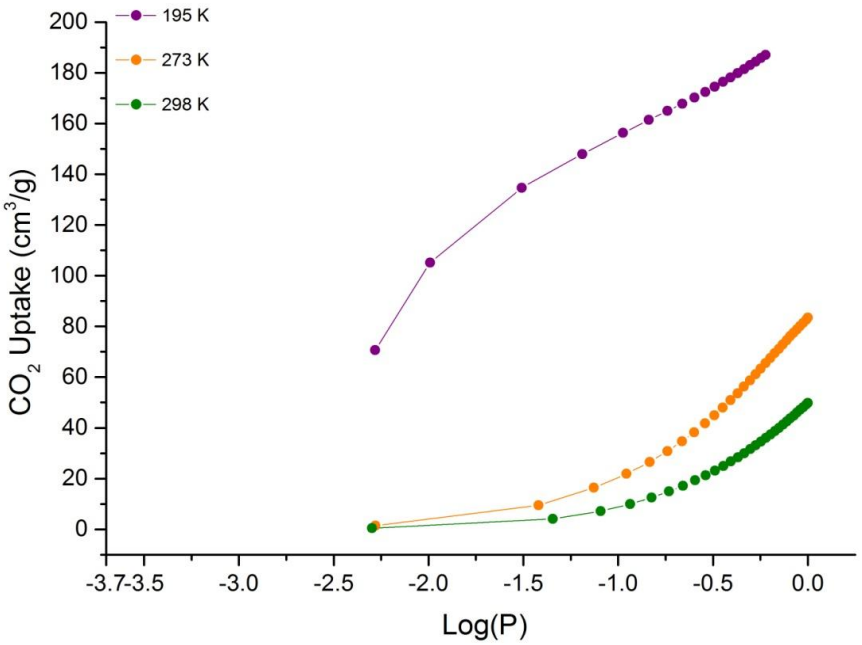

Figure A5.2: *Carbon dioxide adsorption isotherms of* ***4.2*** *at 195, 273 and 298 K with a logarithmic pressure scale.*

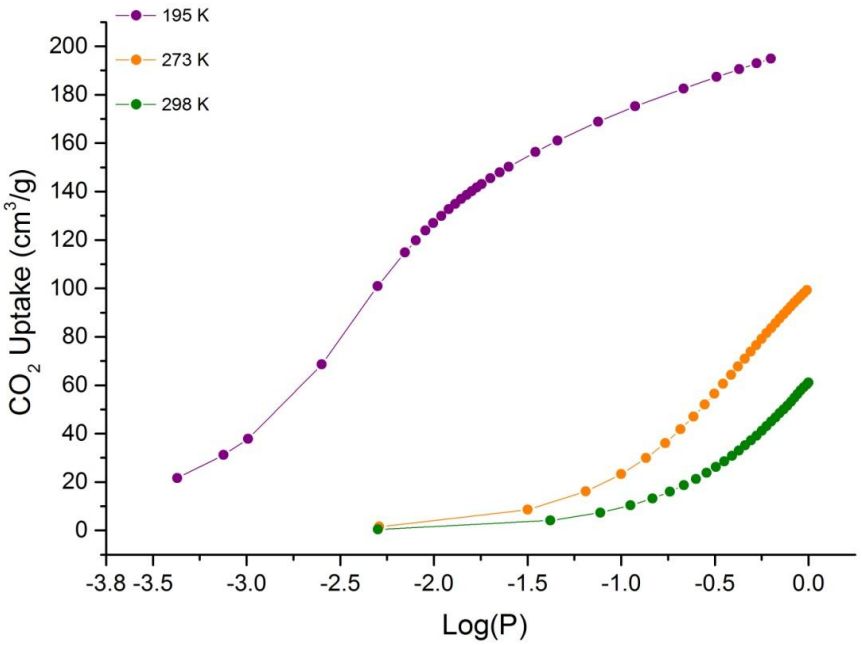

Figure A5.3: *Carbon dioxide adsorption isotherms of* ***4.3*** *at 195, 273 and 298 K with a logarithmic pressure scale.*

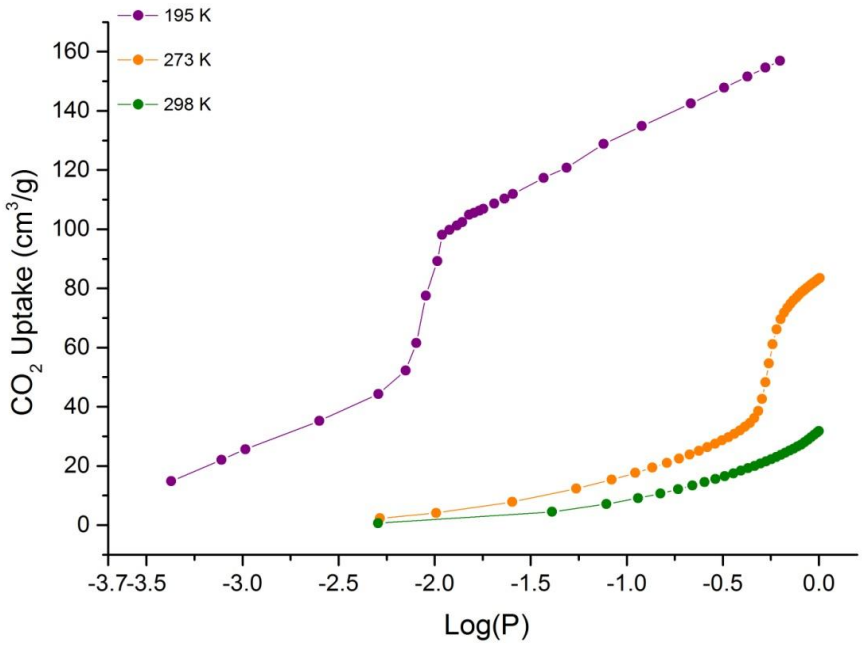

Figure A5.4: *Carbon dioxide adsorption isotherms of* ***4.4*** *at 195, 273 and 298 K with a logarithmic pressure scale.*

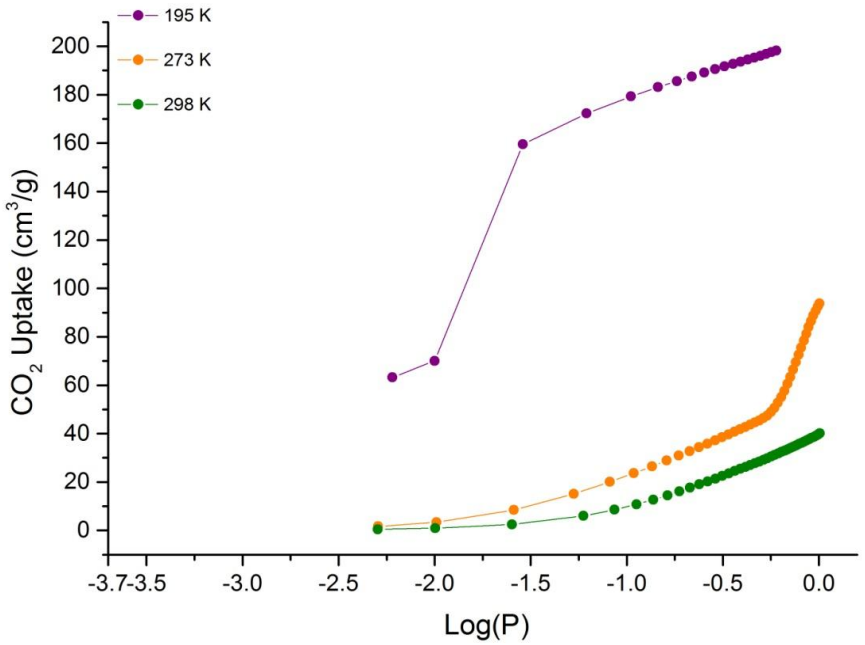

Figure A5.5: *Carbon dioxide adsorption isotherms of* ***4.5*** *at 195, 273 and 298 K with a logarithmic pressure scale.*

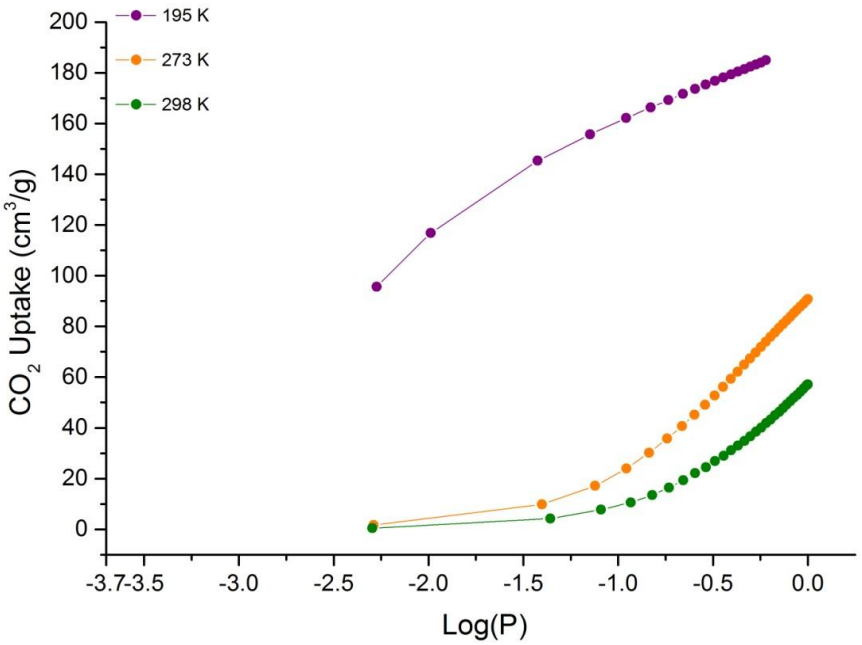

Figure A5.6: *Carbon dioxide adsorption isotherms of* ***4.6*** *at 195, 273 and 298 K with a logarithmic pressure scale.*

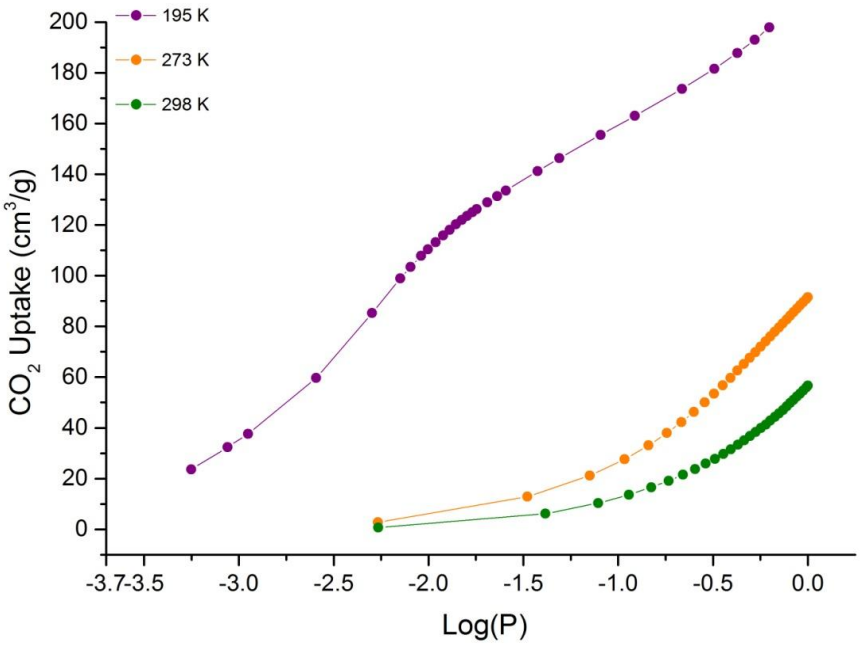

Figure A5.7: *Carbon dioxide adsorption isotherms of* ***4.7*** *at 195, 273 and 298 K with a logarithmic pressure scale.*

References

1. Lehn, J. M., *J. Inclusion Phenom.* **1988,** *6*, 351.

2. Cram, D. J.; Cram, J. M., *Science* **1974,** *183*, 803.

3. Dietrich, B.; Lehn, J. M.; Sauvage, J. P., *Tetrahedron Lett.* **1969**, 2889.

4. Pedersen, C. J., *J. Am. Chem. Soc.* **1967,** *89*, 7017.

5. Chen, J.; Seeman, N. C., *Nature* **1991,** *350*, 631.

6. Gil-Ramírez, G.; Leigh, D. A.; Stephens, A. J., *Angew. Chem. Int. Ed.* **2015,** *54*, 6110.

7. Xue, M.; Yang, Y.; Chi, X.; Yan, X.; Huang, F., *Chem. Rev.* **2015,** *115*, 7398.

8. Piguet, C.; Bernardinelli, G.; Hopfgartner, G., *Chem. Rev.* **1997,** *97*, 2005.

9. Forgan, R. S.; Sauvage, J.-P.; Stoddart, J. F., *Chem. Rev.* **2011,** *111*, 5434.

10. Gale, P. A.; Busschaert, N.; Haynes, C. J. E.; Karagiannidis, L. E.; Kirby, I. L., *Chem. Soc. Rev.* **2014,** *43*, 205.

11. Averill, B.; Eldredge, P., *Chemistry: Principles, Patterns, and Applications*. Pearson Benjamin Cummings: **2007**.

12. Albrecht, M., *Naturwissenschaften* **2007,** *94*, 951.

13. Lindsey, J. S., *New J. Chem.* **1991,** *15*, 153.

14. Schalley, C. A.; Lützen, A.; Albrecht, M., *Chem. Eur. J.* **2004,** *10*, 1072.

15. Desiraju, G. R., *J. Am. Chem. Soc.* **2013,** *135*, 9952.

16. Desiraju, G. R., *Crystal engineering: the design of organic solids*. Elsevier: **1989**.

17. McClellan, A. L., *J. Chem. Educ.* **1967,** *44*, 547.

18. Steed, J. W.; Atwood, J. L., *Supramolecular Chemistry*. Wiley: **2013**.

19. Sarma, J. A. R. P.; Desiraju, G. R., *Acc. Chem. Res.* **1986,** *19*, 222.

20. Desiraju, G. R., *Acc. Chem. Res.* **2002,** *35*, 565.

21. Zerkowski, J. A.; Seto, C. T.; Whitesides, G. M., *J. Am. Chem. Soc.* **1992,** *114*, 5473.

22. Etter, M. C., *Acc. Chem. Res.* **1990,** *23*, 120.

23. Bernstein, J.; Davis, R. E.; Shimoni, L.; Chang, N.-L., *Angew. Chem. Int. Ed.* **1995,** *34*, 1555.

24. Hunter, C. A., *Chem. Soc. Rev.* **1994,** *23*, 101.

25. Janiak, C., *Dalton Trans.* **2000**, 3885.

26. Martinez, C. R.; Iverson, B. L., *Chem. Sci.* **2012,** *3*, 2191.

27. Hunter, C. A.; Sanders, J. K. M., *J. Am. Chem. Soc.* **1990,** *112*, 5525.

28. Steel, P. J., *Chem. N. Z.* **2003,** *67*, 57.

29. Sun, W.-Y.; Yoshizawa, M.; Kusukawa, T.; Fujita, M., *Curr. Opin. Chem. Biol.* **2002,** *6*, 757.

30. McConnell, A. J.; Wood, C. S.; Neelakandan, P. P.; Nitschke, J. R., *Chem. Rev.* **2015,** *115*, 7729.

31. Addison, A. W.; Rao, T. N.; Reedijk, J.; van Rijn, J.; Verschoor, G. C., *J. Chem. Soc., Dalton Trans.* **1984**, 1349.

32. Yang, L.; Powell, D. R.; Houser, R. P., *Dalton Trans* **2007**, 955.

33. Tranchemontagne, D. J.; Ni, Z.; O'Keeffe, M.; Yaghi, O. M., *Angew. Chem. Int. Ed.* **2008,** *47*, 5136.

34. Chakrabarty, R.; Mukherjee, P. S.; Stang, P. J., *Chem. Rev.* **2011,** *111*, 6810.

35. Wells, A. F., *Acta Crystallogr.* **1954,** *7*, 535.

36. Hoskins, B. F.; Robson, R., *J. Am. Chem. Soc.* **1989,** *111*, 5962.

37. Hoskins, B. F.; Robson, R., *J. Am. Chem. Soc.* **1990,** *112*, 1546.

38. Cook, T. R.; Zheng, Y.-R.; Stang, P. J., *Chem. Rev.* **2012,** *113*, 734.

39. Batten, S. R.; Champness, N. R.; Chen, X.-M.; Garcia-Martinez, J.; Kitagawa, S.; Ohrstrom, L.; O'Keeffe, M.; Suh, M. P.; Reedijk, J., *Pure Appl. Chem.* **2013,** *85*, 1715.

40. Prakash, M. J.; Lah, M. S., *Chem. Commun.* **2009**, 3326.

41. Tranchemontagne, D. J.; Mendoza-Cortes, J. L.; O'Keeffe, M.; Yaghi, O. M., *Chem. Soc. Rev.* **2009,** *38*, 1257.

42. Wang, Z.; Hu, K.; Gao, S.; Kobayashi, H., *Adv. Mater.* **2010,** *22*, 1526.

43. de Campos, N. R.; Ribeiro, M. A.; Oliveira, W. X. C.; Reis, D. O.; Stumpf, H. O.; Doriguetto, A. C.; Machado, F. C.; Pinheiro, C. B.; Lloret, F.; Julve, M.; Cano, J.; Marinho, M. V., *Dalton Trans.* **2016**, *45*, 172.

44. O'Keeffe, M.; Peskov, M. A.; Ramsden, S. J.; Yaghi, O. M., *Acc. Chem. Res.* **2008,** *41*, 1782.

45. Jiang, H.-L.; Makal, T. A.; Zhou, H.-C., *Coord. Chem. Rev.* **2013,** *257*, 2232.

46. Kanoo, P.; Matsuda, R.; Higuchi, M.; Kitagawa, S.; Maji, T. K., *Chem. Mater.* **2009,** *21*, 5860.

47. Suh, M. P.; Cheon, Y. E.; Lee, E. Y., *Coord. Chem. Rev.* **2008,** *252*, 1007.

48. Deshpande, R. K.; Minnaar, J. L.; Telfer, S. G., *Angew. Chem. Int. Ed.* **2010,** *49*, 4598.

49. Zhang, J.; Wojtas, L.; Larsen, R. W.; Eddaoudi, M.; Zaworotko, M. J., *J. Am. Chem. Soc.* **2009,** *131*, 17040.

50. Bureekaew, S.; Sato, H.; Matsuda, R.; Kubota, Y.; Hirose, R.; Kim, J.; Kato, K.; Takata, M.; Kitagawa, S., *Angew. Chem. Int. Ed.* **2010,** *49*, 7660.

51. Ferguson, A.; Liu, L.; Tapperwijn, S. J.; Perl, D.; Coudert, F.-X.; Van Cleuvenbergen, S.; Verbiest, T.; van der Veen, M. A.; Telfer, S. G., *Nat. Chem* **2016,** *8*, 250.

52. Ma, L.; Lin, W., *Angew. Chem. Int. Ed.* **2009,** *48*, 3637.

53. Nugent, P.; Belmabkhout, Y.; Burd, S. D.; Cairns, A. J.; Luebke, R.; Forrest, K.; Pham, T.; Ma, S.; Space, B.; Wojtas, L.; Eddaoudi, M.; Zaworotko, M. J., *Nature* **2013,** *495*, 80.

54. Haldar, R.; Sikdar, N.; Maji, T. K., *Mater. Today* **2015,** *18*, 97.

55. Kim, J.; Chen, B.; Reineke, T. M.; Li, H.; Eddaoudi, M.; Moler, D. B.; O'Keeffe, M.; Yaghi, O. M., *J. Am. Chem. Soc.* **2001,** *123*, 8239.

56. Eddaoudi, M.; Kim, J.; Rosi, N.; Vodak, D.; Wachter, J.; O'Keeffe, M.; Yaghi, O. M., *Science* **2002,** *295*, 469.

57. Lu, W.; Wei, Z.; Gu, Z.-Y.; Liu, T.-F.; Park, J.; Park, J.; Tian, J.; Zhang, M.; Zhang, Q.; Gentle Iii, T.; Bosch, M.; Zhou, H.-C., *Chem. Soc. Rev.* **2014,** *43*, 5561.

58. Rosi, N. L.; Kim, J.; Eddaoudi, M.; Chen, B.; O'Keeffe, M.; Yaghi, O. M., *J. Am. Chem. Soc.* **2005,** *127*, 1504.

59. Yaghi, O. M.; O'Keeffe, M.; Ockwig, N. W.; Chae, H. K.; Eddaoudi, M.; Kim, J., *Nature* **2003,** *423*, 705.

60. Rowsell, J. L. C.; Millward, A. R.; Park, K. S.; Yaghi, O. M., *J. Am. Chem. Soc.* **2004,** *126*, 5666.

61. Dietzel, P. D. C.; Blom, R.; Fjellvåg, H., *Eur. J. Inorg. Chem.* **2008,** *2008*, 3624.

62. Zhou, W.; Wu, H.; Yildirim, T., *J. .Am. Chem. Soc.* **2008,** *130*, 15268.

63. Bhattacharjee, S.; Choi, J.-S.; Yang, S.-T.; Choi, S. B.; Kim, J.; Ahn, W.-S., *J. Nanosci. Nanotechnol.* **2010,** *10*, 135.

64. Dietzel, P. D. C.; Morita, Y.; Blom, R.; Fjellvaag, H., *Angew. Chem., Int. Ed.* **2005,** *44*, 6354.

65. Dietzel, P. D. C.; Panella, B.; Hirscher, M.; Blom, R.; Fjellvag, H., *Chem. Commun.* **2006**, 959.

66. Calleja, G.; Sanz, R.; Orcajo, G.; Briones, D.; Leo, P.; Martínez, F., *Catal. Today* **2014,** *227*, 130.

67. Wang, L. J.; Deng, H.; Furukawa, H.; Gándara, F.; Cordova, K. E.; Peri, D.; Yaghi, O. M., *Inorg. Chem.* **2014,** *53*, 5881.

68. Deng, H.; Grunder, S.; Cordova, K. E.; Valente, C.; Furukawa, H.; Hmadeh, M.; Gándara, F.; Whalley, A. C.; Liu, Z.; Asahina, S.; Kazumori, H.; O'Keeffe, M.; Terasaki, O.; Stoddart, J. F.; Yaghi, O. M., *Science* **2012,** *336*, 1018.

69. Kandiah, M.; Nilsen, M. H.; Usseglio, S.; Jakobsen, S.; Olsbye, U.; Tilset, M.; Larabi, C.; Quadrelli, E. A.; Bonino, F.; Lillerud, K. P., *Chem. Mater.* **2010,** *22*, 6632.

70. He, Y.; Zhou, W.; Yildirim, T.; Chen, B., *Energy Environ. Sci.* **2013,** *6*, 2735.

71. Liu, T.-F.; Feng, D.; Chen, Y.-P.; Zou, L.; Bosch, M.; Yuan, S.; Wei, Z.; Fordham, S.; Wang, K.; Zhou, H.-C., *J. Am. Chem. Soc.* **2015,** *137*, 413.

72. Mason, J. A.; Veenstra, M.; Long, J. R., *Chem. Sci.* **2014,** *5*, 32.

73. Kitagawa, S.; Noro, S.-i.; Nakamura, T., *Chem. Commun.* **2006**, 701.

74. Garibay, S. J.; Stork, J. R.; Cohen, S. M., The Use of Metalloligands in Metal-Organic Frameworks. In *Prog. Inorg. Chem.*, John Wiley & Sons, Inc.: **2009**; pp 335.

75. Evans, J. D.; Sumby, C. J.; Doonan, C. J., *Chem. Soc. Rev.* **2014,** *43*, 5933.

76. Wang, X.-L.; Qin, C.; Wu, S.-X.; Shao, K.-Z.; Lan, Y.-Q.; Wang, S.; Zhu, D.-X.; Su, Z.-M.; Wang, E.-B., *Angew. Chem. Int. Ed.* **2009,** *48*, 5291.

77. Ollagnier, C. M.; Nolan, D.; Fitchett, C. M.; Draper, S. M., *Inorg. Chem. Commun.* **2007,** *10*, 1045.

78. Veliks, J.; Tseng, J.-C.; Arias, K. I.; Weisshar, F.; Linden, A.; Siegel, J. S., *Chem. Sci.* **2014,** *5*, 4317.

79. Farha, O. K.; Shultz, A. M.; Sarjeant, A. A.; Nguyen, S. T.; Hupp, J. T., *J. Am. Chem. Soc.* **2011,** *133*, 5652.

80. Song, F.; Wang, C.; Falkowski, J. M.; Ma, L.; Lin, W., *J. Am. Chem. Soc.* **2010,** *132*, 15390.

81. Huang, S.-L.; Jia, A.-Q.; Jin, G.-X., *Chem. Commun.* **2013,** *49*, 2403.

82. Garibay, S. J.; Stork, J. R.; Wang, Z.; Cohen, S. M.; Telfer, S. G., *Chem. Commun.* **2007**, 4881.

83. Peterson, V. K.; Liu, Y.; Brown, C. M.; Kepert, C. J., *J. Am. Chem. Soc.* **2006,** *128*, 15578.

84. Dincă, M.; Dailly, A.; Liu, Y.; Brown, C. M.; Neumann, D. A.; Long, J. R., *J. Am. Chem. Soc.* **2006,** *128*, 16876.

85. Yan, Y.; Telepeni, I.; Yang, S.; Lin, X.; Kockelmann, W.; Dailly, A.; Blake, A. J.; Lewis, W.; Walker, G. S.; Allan, D. R.; Barnett, S. A.; Champness, N. R.; Schröder, M., *J. Am. Chem. Soc.* **2010,** *132*, 4092.

86. Guo, Z.; Wu, H.; Srinivas, G.; Zhou, Y.; Xiang, S.; Chen, Z.; Yang, Y.; Zhou, W.; O'Keeffe, M.; Chen, B., *Angew. Chem. Int. Ed.* **2011,** *50*, 3178.

87. Getzschmann, J.; Senkovska, I.; Wallacher, D.; Tovar, M.; Fairen-Jimenez, D.; Düren, T.; van Baten, J. M.; Krishna, R.; Kaskel, S., *Microporous Mesoporous Mater.* **2010,** *136*, 50.

88. Wu, H.; Simmons, J. M.; Liu, Y.; Brown, C. M.; Wang, X.-S.; Ma, S.; Peterson, V. K.; Southon, P. D.; Kepert, C. J.; Zhou, H.-C.; Yildirim, T.; Zhou, W., *Chem. Eur. J.* **2010,** *16*, 5205.

89. Bloch, E. D.; Murray, L. J.; Queen, W. L.; Chavan, S.; Maximoff, S. N.; Bigi, J. P.; Krishna, R.; Peterson, V. K.; Grandjean, F.; Long, G. J.; Smit, B.; Bordiga, S.; Brown, C. M.; Long, J. R., *J. Am. Chem. Soc.* **2011,** *133*, 14814.

90. Kitaura, R.; Onoyama, G.; Sakamoto, H.; Matsuda, R.; Noro, S.-i.; Kitagawa, S., *Angew. Chem. Int. Ed.* **2004,** *43*, 2684.

91. Song, F.; Wang, C.; Lin, W., *Chem. Commun.* **2011,** *47*, 8256.

92. Eyele-Mezui, S.; Delahaye, E.; Rogez, G.; Rabu, P., *Eur. J. Inorg. Chem.* **2012,** *2012*, 5225.

93. Bhunia, A.; Dey, S.; Moreno, J. M.; Diaz, U.; Concepcion, P.; Van Hecke, K.; Janiak, C.; Van Der Voort, P., *Chem. Commun.* **2016,** *52*, 1401.

94. Shultz, A. M.; Sarjeant, A. A.; Farha, O. K.; Hupp, J. T.; Nguyen, S. T., *J. Am. Chem. Soc.* **2011,** *133*, 13252.

95. Kim, W.-S.; Lee, K. Y.; Ryu, E.-H.; Gu, J.-M.; Kim, Y.; Lee, S. J.; Huh, S., *Eur. J. Inorg. Chem.* **2013,** *2013*, 4228.

96. Shultz, A. M.; Farha, O. K.; Hupp, J. T.; Nguyen, S. T., *J. Am. Chem. Soc.* **2009,** *131*, 4204.

97. Zou, C.; Zhang, T.; Xie, M.-H.; Yan, L.; Kong, G.-Q.; Yang, X.-L.; Ma, A.; Wu, C.-D., *Inorg. Chem.* **2013,** *52*, 3620.

98. Xie, M.-H.; Yang, X.-L.; He, Y.; Zhang, J.; Chen, B.; Wu, C.-D., *Chem. Eur. J.* **2013,** *19*, 14316.

99. Horike, S.; Shimomura, S.; Kitagawa, S., *Nat. Chem.* **2009,** *1*, 695.

100. Kitagawa, S.; Kondo, M., *Bull. Chem. Soc. Jpn.* **1998,** *71*, 1739.

101. Furukawa, S.; Sakata, Y.; Kitagawa, S., *Chem. Lett.* **2013,** *42*, 570.

102. Bourrelly, S.; Llewellyn, P. L.; Serre, C.; Millange, F.; Loiseau, T.; Férey, G., *J. Am. Chem. Soc.* **2005,** *127*, 13519.

103. Llewellyn, P. L.; Bourrelly, S.; Serre, C.; Filinchuk, Y.; Férey, G., *Angew. Chem.* **2006,** *118*, 7915.

104. Norsko, J. K., *Rep. Prog. Phys.* **1990,** *53*, 1253.

105. Bhatia, S. K.; Myers, A. L., *Langmuir* **2006,** *22*, 1688.

106. Morris, R. E.; Wheatley, P. S., *Angew. Chem. Int. Ed.* **2008,** *47*, 4966.

107. Yilmaz, B.; Trukhan, N.; MÜLler, U., *Chinese J. Catal.* **2012,** *33*, 3.

108. Bae, Y.-S.; Yazaydın, A. Ö.; Snurr, R. Q., *Langmuir* **2010,** *26*, 5475.

109. Walton, K. S.; Snurr, R. Q., *J. Am. Chem. Soc.* **2007,** *129*, 8552.

110. Schlapbach, L.; Zuttel, A., *Nature* **2001,** *414*, 353.

111. Xia, Y.; Yang, Z.; Zhu, Y., *J. Mater. Chem. A* **2013,** *1*, 9365.

112. Weitkamp, J.; Fritz, M.; Ernst, S., *Int. J. Hydrogen Energy* **1995,** *20*, 967.

113. Murray, L. J.; Dinca, M.; Long, J. R., *Chem. Soc. Rev.* **2009,** *38*, 1294.

114. Duren, T.; Bae, Y.-S.; Snurr, R. Q., *Chem. Soc. Rev.* **2009,** *38*, 1237.

115. Belof, J. L.; Stern, A. C.; Eddaoudi, M.; Space, B., *J. Am. Chem. Soc.* **2007,** *129*, 15202.

116. He, Y.; Zhou, W.; Qian, G.; Chen, B., *Chem. Soc. Rev.* **2014,** *43*, 5657.

117. Makal, T. A.; Li, J.-R.; Lu, W.; Zhou, H.-C., *Chem. Soc. Rev.* **2012,** *41*, 7761.

118. https://arpa-e-foa.energy.gov/. (accessed 24/07/2016).

119. Zhou, W., *Chem. Rec.* **2010,** *10*, 200.

120. Wilmer, C. E.; Leaf, M.; Lee, C. Y.; Farha, O. K.; Hauser, B. G.; Hupp, J. T.; Snurr, R. Q., *Nat. Chem.* **2012,** *4*, 83.

121. Simon, C. M.; Kim, J.; Gomez-Gualdron, D. A.; Camp, J. S.; Chung, Y. G.; Martin, R. L.; Mercado, R.; Deem, M. W.; Gunter, D.; Haranczyk, M.; Sholl, D. S.; Snurr, R. Q.; Smit, B., *Energy Environ. Sci.* **2015,** *8*, 1190.

122. www.co2.earth/global-co2-emissions. (accessed 2/08/2016).

123. Furukawa, H.; Cordova, K. E.; O'Keeffe, M.; Yaghi, O. M., *Science* **2013,** *341*, 974.

124. Pachfule, P.; Chen, Y.; Jiang, J.; Banerjee, R., *Chem. Eur. J.* **2012,** *18*, 688.

125. Wilmer, C. E.; Farha, O. K.; Bae, Y.-S.; Hupp, J. T.; Snurr, R. Q., *Energy Environ. Sci.* **2012,** *5*, 9849.

126. Wu, T.; Xue, Q.; Ling, C.; Shan, M.; Liu, Z.; Tao, Y.; Li, X., *J. Phys. Chem. C* **2014,** *118*, 7369.

127. Scofield, J. M. P.; Gurr, P. A.; Kim, J.; Fu, Q.; Kentish, S. E.; Qiao, G. G., *J. Membrane Sci.* **2016,** *499*, 191.

128. Rochelle, G. T., *Science* **2009,** *325*, 1652.

129. Burd, S. D.; Ma, S.; Perman, J. A.; Sikora, B. J.; Snurr, R. Q.; Thallapally, P. K.; Tian, J.; Wojtas, L.; Zaworotko, M. J., *J. Am. Chem. Soc.* **2012,** *134*, 3663.

130. Wu, H.; Zhou, W.; Yildirim, T., *J.. Am. Chem. Soc.* **2009,** *131*, 4995.

131. Zhou, W.; Wu, H.; Hartman, M. R.; Yildirim, T., *J. Phys. Chem. C* **2007,** *111*, 16131.

132. Hulvey, Z.; Vlaisavljevich, B.; Mason, J. A.; Tsivion, E.; Dougherty, T. P.; Bloch, E. D.; Head-Gordon, M.; Smit, B.; Long, J. R.; Brown, C. M., *J. Am. Chem. Soc.* **2015,** *137*, 10816.

133. Lüning, U., *Angew. Chem. Int. Ed.* **2013,** *52*.

134. Gale, P. A.; Garcia-Garrido, S. E.; Garric, J., *Chem. Soc. Rev.* **2008,** *37*, 151.

135. Wenzel, M.; Hiscock, J. R.; Gale, P. A., *Chem. Soc. Rev.* **2012,** *41*, 480.

136. Potts, K. T., *Chem. Rev.* **1961,** *61*, 87.

137. Aromí, G.; Barrios, L. A.; Roubeau, O.; Gamez, P., *Coord. Chem. Rev.* **2011,** *255*, 485.

138. Favre, H. A.; Powell, W. H., *Nomenclature of Organic Chemistry: IUPAC Recommendations and Preferred Names **2013***. Royal Society of Chemistry: 2013.

139. Zhu, G.-Z.; Lu, Z.-S.; Shi, H.-L.; Xu, S.-P.; Lu, H.; Wang, X.-S., *ncrs* **2012,** *227*, 533.

140. Hergenrother, P. M., *J. Heterocycl. Chem.* **1969,** *6*, 965.

141. Orselli, E.; Kottas, G. S.; Konradsson, A. E.; Coppo, P.; Froehlich, R.; De, C. L.; van, D. A.; Buechel, M.; Boerner, H., *Inorg. Chem.* **2007**, 11082.

142. Muller, K.; Sun, Y.; Heimermann, A.; Menges, F.; Niedner-Schatteburg, G.; van Wüllen, C.; Thiel, W. R., *Chem. Eur. J.* **2013,** *19*, 7825.

143. Enyedy, E. A.; Primik, M. F.; Kowol, C. R.; Arion, V. B.; Kiss, T.; Keppler, B. K., *Dalton Trans.* **2011,** *40*, 5895.

144. Mendes, I. C.; Botion, L. M.; Ferreira, A. V. M.; Castellano, E. E.; Beraldo, H., *Inorg. Chim. Acta* **2009,** *362*, 414.

145. Graminha, A. E.; Vilhena, F. S.; Batista, A. A.; Louro, S. R. W.; Ziolli, R. L.; Teixeira, L. R.; Beraldo, H., *Polyhedron* **2008,** *27*, 547.

146. Ferraz, K. O.; Wardell, S. M. S. V.; Wardell, J. L.; Louro, S. R. W.; Beraldo, H., *Spectrochim. Acta Mol. Biomol. Spectrosc.* **2009,** *73*, 140.

147. Garcia Santos, I.; Hagenbach, A.; Abram, U., *Dalton Trans.* **2004**, 677.

148. Castineiras, A.; Fernandez-Hermida, N.; Fernandez-Rodriguez, R.; Garcia-Santos, I., *Cryst. Growth Des.* **2012,** *12*, 1432.

149. Bermejo, E.; Castiñeiras, A.; García-Santos, I.; West, D. X., *Z. Anorg. Allg. Chem.* **2005,** *631*, 2011.

150. Gusev, A. N.; Shul'gin, V. F.; Zamnius, E. A.; Ricci, M.; Minin, V. V.; Aleksandrov, G. G.; Eremenko, I. L.; Linert, W., *Inorg. Chim. Acta.* **2015,** *430*, 120.

151. Gusev, A. N.; Shul´gin, V. F.; Efimov, N. N.; Minin, V. V.; Aleksandrov, G. G.; Eremenko, I. L., *Russ. Chem. Bull.* **2015,** *64*, 1891.

152. Russell, M. E.; Hawes, C. S.; Ferguson, A.; Polson, M. I. J.; Chilton, N. F.; Moubaraki, B.; Murray, K. S.; Kruger, P. E., *Dalton Trans.* **2013,** *42*, 13576.

153. Herringer, S. N.; Longendyke, A. J.; Turnbull, M. M.; Landee, C. P.; Wikaira, J. L.; Jameson, G. B.; Telfer, S. G., *Dalton Trans.* **2010,** *39*, 2785.

154. Zhang, L.; Xu, G.-C.; Wang, Z.-M.; Gao, S., *Eur. J. Inorg. Chem.* **2013,** *2013*, 1043.

155. Milway, V. A.; Zhao, L.; Abedin, T. S. M.; Thompson, L. K.; Xu, Z., *Polyhedron* **2003,** *22*, 1271.

156. Zhao, L.; Xu, Z.; Thompson, L. K.; Miller, D. O., *Polyhedron* **2001,** *20*, 1359.

157. Gutowsky, H. S.; Holm, C. H., *J. Chem. Phys.* **1956,** *25*, 1228.

158. Swiegers, G. F.; Malefetse, T. J., *Chem.Rev.* **2000,** *100*, 3483.

159. Van der Sluis, P.; Spek, A. L., *Acta Crystallogr., Sect. A: Found. Crystallogr.* **1990,** *A46*, 194.

160. Fitzmaurice, R. J.; Kyne, G. M.; Douheret, D.; Kilburn, J. D., *J. Chem. Soc., Perkin Trans. 1* **2002**, 841.

161. Sommerer, S. O.; Westcott, B. L.; Jircitano, A. J.; Abboud, K. A., *Inorg. Chim. Acta* **1995,** *238*, 149.

162. Koolhaas, G. J. A. A.; Driessen, W. L.; van, K. P. J.; Reedijk, J.; Spek, A. L., *Dalton Trans.* **1993**, 3803.

163. Stumpe, M. C.; Grubmüller, H., *J. Phys. Chem. B* **2007,** *111*, 6220.

164. Holliday, B. J.; Mirkin, C. A., *Angew. Chem. Int. Ed.* **2001,** *40*, 2022.

165. Taft, K. L.; Lippard, S. J., *J. Am. Chem. Soc.* **1990,** *112*, 9629.

166. Ardizzoia, G. A.; Angaroni, M. A.; La Monica, G.; Cariati, F.; Moret, M.; Masciocchi, N., *Chem. Commun.* **1990**, 1021.

167. Rumberger, E. M.; Shah, S. J.; Beedle, C. C.; Zakharov, L. N.; Rheingold, A. L.; Hendrickson, D. N., *Inorg. Chem.***2005,** *44*, 2742.

168. Tasiopoulos, A. J.; Vinslava, A.; Wernsdorfer, W.; Abboud, K. A.; Christou, G., *Angew. Chem. Int. Ed.* **2004,** *43*, 2117.

169. Thio, Y.; Toh, S. W.; Xue, F.; Vittal, J. J., *Dalton Trans.* **2014,** *43*, 5998.

170. Kumar, A.; Pandey, R.; Kumar, A.; Gupta, R. K.; Dubey, M.; Mohammed, A.; Mobin, S. M.; Pandey, D. S., *Dalton Trans.* **2015,** *44*, 17152.

171. Wang, Q.-Q.; Day, V. W.; Bowman-James, K., *Chem. Commun.* **2013,** *49*, 8042.

172. Moon, M.; Kim, I.; Lah, M. S., *Inorg. Chem.* **2000,** *39*, 2710.

173. Zarrabi, N.; Hayward, J. J.; Clegg, W.; Pilkington, M., *Dalton Trans.* **2014,** *43*, 2352.

174. John, R. P.; Park, M.; Moon, D.; Lee, K.; Hong, S.; Zou, Y.; Hong, C. S.; Lah, M. S., *J. Am. Chem. Soc.* **2007,** *129*, 14142.

175. Fujita, M.; Sasaki, O.; Mitsuhashi, T.; Fujita, T.; Yazaki, J.; Yamaguchi, K.; Ogura, K., *Chem. Commun.* **1996**, 1535.

176. Grancha, T.; Ferrando-Soria, J.; Cano, J.; Lloret, F.; Julve, M.; De Munno, G.; Armentano, D.; Pardo, E., *Chem. Commun.* **2013,** *49*, 5942.

177. John, R. P.; Lee, K.; Kim, B. J.; Suh, B. J.; Rhee, H.; Lah, M. S., *Inorg. Chem.* **2005,** *44*, 7109.

178. Kuhne, I. A.; Mereacre, V.; Anson, C. E.; Powell, A. K., *Chem. Commun.* **2016,** 52 1021.

179. Larsen, F. K.; McInnes, E. J. L.; Mkami, H. E.; Overgaard, J.; Piligkos, S.; Rajaraman, G.; Rentschler, E.; Smith, A. A.; Smith, G. M.; Boote, V.; Jennings, M.; Timco, G. A.; Winpenny, R. E. P., *Angew. Chem. Int. Ed.* **2003,** *42*, 101.

180. Larsen, F. K.; Overgaard, J.; Parsons, S.; Rentschler, E.; Smith, A. A.; Timco, G. A.; Winpenny, R. E. P., *Angew. Chem. Int. Ed.* **2003,** *42*, 5978.

181. Goesten, M.; Kapteijn, F.; Gascon, J., *CrystEngComm* **2013**.

182. Batten, S. R., *J. Solid State Chem.* **2005,** *178*, 2475.

183. Jansen, M.; Schoen, J. C., *Angew. Chem., Int. Ed.* **2006,** *45*, 3406.

184. Serre, C.; Millange, F.; Surblé, S.; Férey, G., *Angew. Chem. Int. Ed.* **2004,** *43*, 6285.

185. Biswas, S.; Tonigold, M.; Volkmer, D., *Z. Anorg. Allg. Chem.* **2008,** *634*, 2532.

186. Deng, J.-J.; Song, B.-Q.; Liang, J.; Jiao, Y.-Q.; Wu, X.-S.; Zhao, L.; Shao, K.-Z.; Su, Z.-M., *Inorg. Chem. Commun.* **2015,** *60*, 82.

187. Chen, Y.-Q.; Qu, Y.-K.; Li, G.-R.; Zhuang, Z.-Z.; Chang, Z.; Hu, T.-L.; Xu, J.; Bu, X.-H., *Inorg. Chem.* **2014,** *53*, 8842.

188. Lan, Y.-Q.; Li, S.-L.; Jiang, H.-L.; Xu, Q., *Chem. Eur. J.* **2012,** *18*, 8076.

189. Schmieder, P.; Denysenko, D.; Grzywa, M.; Baumgartner, B.; Senkovska, I.; Kaskel, S.; Sastre, G.; van Wullen, L.; Volkmer, D., *Dalton Trans.* **2013,** *42*, 10786.

190. Shuvaev, K. V.; Abedin, T. S. M.; McClary, C. A.; Dawe, L. N.; Collins, J. L.; Thompson, L. K., *Dalton Trans.* **2009**, 2926.

191. Cui, Y.; Yue, Y.; Qian, G.; Chen, B., *Chem. Rev.* **2012,** *112*, 1126.

192. Cooke, M. W.; Tremblay, P. M.; Hanan, G. S., *Inorg. Chem. Commun.* **2007,** *10*, 1365.

193. Custelcean, R.; Bonnesen, P. V.; Duncan, N. C.; Zhang, X.; Watson, L. A.; Van Berkel, G.; Parson, W. B.; Hay, B. P., *J. Am. Chem. Soc.***2012,** *134*, 8525.

194. Sun, J.; Weng, L.; Zhou, Y.; Chen, J.; Chen, Z.; Liu, Z.; Zhao, D., *Angew. Chem. Int. Ed.* **2002,** *41*, 4471.

195. Wang, X.-F.; Zhang, Y.-B.; Lin, Y.-Y., *CrystEngComm* **2013,** *15*, 3470.

196. Sidell, N.; Kirma, N.; Morgan, E. T.; Nair, H.; Tekmal, R. R., *Cancer Lett.* **2007,** *251*, 302.

197. Li, H.-H.; Inoue, M.; Nishimura, H.; Mizutani, J.; Tsuzuki, E., *J. Chem. Ecol.* **1993,** *19*, 1775.

198. Sen, S.; Neogi, S.; Rissanen, K.; Bharadwaj, P. K., *Chemical Commun.* **2015,** *51*, 3173.

199. Young, D. C. K., Paul E., *Unpublished results*.

200. Zhang, C.-Z.; Mao, H.-Y.; Wang, Y.-L.; Zhang, H.-Y.; Tao, J.-C., *J. Phys. Chem. Solids* **2007,** *68*, 236.

201. Tanaka, K.; Muraoka, T.; Otubo, Y.; Takahashi, H.; Ohnishi, A., *RSC Adv.* **2016,** *6*, 21293.

202. Mowson, A. M.; Nguyen, T. N.; Abboud, K. A.; Christou, G., *Inorg. Chem.* **2013,** *52*, 12320.

203. Bagai, R.; Christou, G., *Chem. Soc. Rev.* **2009,** *38*, 1011.

204. Chakov, N. E.; Soler, M.; Wernsdorfer, W.; Abboud, K. A.; Christou, G., *Inorg. Chem.* **2005,** *44*, 5304.

205. Park, C.-D.; Jung, D.-Y., *Bull. Korean Chem. Soc.* **2001,** *22*, 611.

206. Bian, G.-Q.; Kuroda-Sowa, T.; Nogami, T.; Sugimoto, K.; Maekawa, M.; Munakata, M.; Miyasaka, H.; Yamashita, M., *Bull. Chem. Soc. Jpn.* **2005,** *78*, 1032.

207. Boskovic, C.; Pink, M.; Huffman, J. C.; Hendrickson, D. N.; Christou, G., *J. Am. Chem. Soc.* **2001,** *123*, 9914.

208. Chakov, N. E.; Wernsdorfer, W.; Abboud, K. A.; Hendrickson, D. N.; Christou, G., *Dalton Trans.* **2003**, 2243.

209. Minisci, F.; Bernardi, R.; Bertini, F.; Galli, R.; Perchinummo, M., *Tetrahedron* **1971,** *27*, 3575.

210. Cooke, M. W.; Tremblay, P.; Hanan, G. S., *Inorg. Chim. Acta* **2008,** *361*, 2259.

211. Ciszewski, J. T.; Mikhaylov, D. Y.; Holin, K. V.; Kadirov, M. K.; Budnikova, Y. H.; Sinyashin, O.; Vicic, D. A., *Inorg. Chem.* **2011,** *50*, 8630.

212. Hayami, S.; Komatsu, Y.; Shimizu, T.; Kamihata, H.; Lee, Y. H., *Coord. Chem. Rev.* **2011,** *255*, 1981.

213. Tessore, F.; Roberto, D.; Ugo, R.; Pizzotti, M.; Quici, S.; Cavazzini, M.; Bruni, S.; De Angelis, F., *Inorg. Chem.* **2005,** *44*, 8967.

214. Campagna, S.; Puntoriero, F.; Nastasi, F.; Bergamini, G.; Balzani, V., Photochemistry and Photophysics of Coordination Compounds: Ruthenium. In *Photochemistry and Photophysics of Coordination Compounds I*, Balzani, V.; Campagna, S., Eds. Springer Berlin Heidelberg: **2007**; Vol. 280, pp 117.

215. Sauvage, J. P.; Collin, J. P.; Chambron, J. C.; Guillerez, S.; Coudret, C.; Balzani, V.; Barigelletti, F.; De Cola, L.; Flamigni, L., *Chem. Rev.* **1994,** *94*, 993.

216. Hofmeier, H.; Schubert, U. S., *Chem. Soc. Rev.* **2004,** *33*, 373.

217. Medlycott, E. A.; Hanan, G. S., *Chem. Soc. Rev.* **2005,** *34*, 133.

218. Dixon, I. M.; Lebon, E.; Sutra, P.; Igau, A., *Chem. Soc. Rev.* **2009,** *38*, 1621.

219. Eryazici, I.; Moorefield, C. N.; Newkome, G. R., *Chem. Rev.* **2008,** *108*, 1834.

220. Sakamoto, R.; Katagiri, S.; Maeda, H.; Nishihara, H., *Coordi. Chem. Rev.* **2013,** *257*, 1493.

221. Pal, A. K.; Hanan, G. S., *Chem. Soc. Rev.* **2014,** *43*, 6184.

222. Cummings, S. D., *Coord. Chem. Rev.* **2009,** *253*, 1495.

223. Cargill Thompson, A. M. W., *Coord. Chem. Rev.* **1997,** *160*, 1.

224. Wild, A.; Winter, A.; Schlutter, F.; Schubert, U. S., *Chem. Soc. Rev.* **2011,** *40*, 1459.

225. Kaes, C.; Katz, A.; Hosseini, M. W., *Chem. Rev.* **2000,** *100*, 3553.

226. Chan, Y.-T.; Li, X.; Yu, J.; Carri, G. A.; Moorefield, C. N.; Newkome, G. R.; Wesdemiotis, C., *J. Am. Chem. Soc.* **2011,** *133*, 11967.

227. Lu, X.; Li, X.; Cao, Y.; Schultz, A.; Wang, J.-L.; Moorefield, C. N.; Wesdemiotis, C.; Cheng, S. Z. D.; Newkome, G. R., *Angew. Chem. Int. Ed.* **2013,** *52*, 7728.

228. Bazzicalupi, C.; Bianchi, A.; Biver, T.; Giorgi, C.; Santarelli, S.; Savastano, M., *Inorg. Chem.* **2014,** *53*, 12215.

229. Breuning, E.; Hanan, G. S.; Romero-Salguero, F. J.; Garcia, A. M.; Baxter, P. N. W.; Lehn, J.-M.; Wegelius, E.; Rissanen, K.; Nierengarten, H.; van Dorsselaer, A., *Chem. Eur. J.* **2002,** *8*, 3458.

230. Yang, J.; Bhadbhade, M.; Donald, W. A.; Iranmanesh, H.; Moore, E. G.; Yan, H.; Beves, J. E., *Chem. Commun.* **2015,** *51*, 4465.

231. Ludlow Iii, J. M.; Xie, T.; Guo, Z.; Guo, K.; Saunders, M. J.; Moorefield, C. N.; Wesdemiotis, C.; Newkome, G. R., *Chemical Commun.* **2015,** *51*, 3820.

232. Schröder, T.; Brodbeck, R.; Letzel, M. C.; Mix, A.; Schnatwinkel, B.; Tonigold, M.; Volkmer, D.; Mattay, J., *Tetrahedron Lett.* **2008,** *49*, 5939.

233. Sauvage, J. P.; Ward, M., *Inorg. Chem.* **1991,** *30*, 3869.

234. Mercer, D. J.; Loeb, S. J., *Dalton Trans.* **2011,** *40*, 6385.

235. Jimenez-Molero, M. C.; Dietrich-Buchecker, C.; Sauvage, J.-P., *Chem. Eur. J.* **2002,** *8*, 1456.

236. Rapenne, G.; Dietrich-Buchecker, C.; Sauvage, J.-P., *J. Am. Chem. Soci.* **1999,** *121*, 994.

237. Sakamoto, R.; Wu, K.-H.; Matsuoka, R.; Maeda, H.; Nishihara, H., *Chem. Soc. Rev.* **2015,** *44*, 7698.

238. C. Constable, E., *Chem. Commun.* **1997**, 1073.

239. Cambridge Structural Database. Version 5.36 (accessed January 2016, 717876 entries).

240. Kruger, P. E., *Chimia* **2013,** *67*, 403.

241. Dehaudt, J.; Husson, J.; Guyard, L., *Green Chem.* **2011,** *13*, 3337.

242. Zhang, J.; Yang, W.; Wu, X.-Y.; Zhang, L.; Lu, C.-Z., *Cryst. Growth Des.* **2016,** *16*, 475.

243. Wang, W.; Xiao, Z.; Lin, H.; Wang, R.; Zhang, L.; Sun, D., *RSC Adv.* **2016,** *6*, 16575.

244. Morgan, G. T.; Burstall, F. H., *J. Chem. Soc.* **1932**, 20.

245. Heller, M.; Schubert, Ulrich S., *Eur. J. Org. Chem.* **2003,** *2003*, 947.

246. Miyaura, N.; Suzuki, A., *Chem. Rev.* **1995,** *95*, 2457.

247. Negishi, E.; King, A. O.; Okukado, N., *J. Org. Chem.* **1977,** *42*, 1821.

248. Stille, J. K., *Angew. Chem.* **1986,** *98*, 504.

249. Kröhnke, F.; Zecher, W.; Curtze, J.; Drechsler, D.; Pfleghar, K.; Schnalke, K. E.; Weis, W., *Angew. Chem. Int. Ed.* **1962,** *1*, 626.

250. Potts, K. T.; Ralli, P.; Theodoridis, G.; Winslow, P., *Org. Synth.* **1986,** *64*, 189.

251. Pabst, G. R.; Sauer, J., *Tetrahedron* **1999,** *55*, 5067.

252. Tohda, Y.; Eiraku, M.; Nakagawa, T.; Usami, Y.; Ariga, M.; Kawashima, T.; Tani, K.; Watanabe, H.; Mori, Y., *Bull. Chem. Soc. Jpn.* **1990,** *63*, 2820.

253. Husson, J.; Dehaudt, J.; Guyard, L., *Nat. Protoc.* **2014,** *9*, 21.

254. Kim, Y.; Huh, S., *CrystEngComm* **2016,** *18*, 3524.

255. Chai, C.; Armarego, W. L. F., *Purification of Laboratory Chemicals*. Elsevier Science: **2003**.

256. Stock, N.; Biswas, S., *Chem. Rev.* **2012,** *112*, 933.

257. Yu, J. Y.; Schreiner, S.; Vaska, L., *Inorg. Chim. Acta* **1990,** *170*, 145.

258. Li, C.-H.; Huang, K.-L.; Chi, Y.-N.; Liu, X.; Han, Z.-G.; Shen, L.; Hu, C.-W., *Inorg. Chem.* **2009,** *48*, 2010.

259. Salinas-Castillo, A.; Calahorro, A. J.; Briones, D.; Fairen-Jimenez, D.; Gandara, F.; Mendicute-Fierro, C.; Seco, J. M.; Perez-Mendoza, M.; Fernandez, B.; Rodriguez-Dieguez, A., *New J. Chem.* **2015,** *39*, 3982.

260. Navarro, J. A. R.; Barea, E.; Rodríguez-Diéguez, A.; Salas, J. M.; Ania, C. O.; Parra, J. B.; Masciocchi, N.; Galli, S.; Sironi, A., *J. Am. Chem. Soc.* **2008,** *130*, 3978.

261. Meek, S. T.; Perry, J. J.; Teich-McGoldrick, S. L.; Greathouse, J. A.; Allendorf, M. D., *Cryst. Growth Des.* **2011,** *11*, 4309.

262. Housecroft, C. E.; Sharpe, A. G., *Inorg. Chem.*. Pearson Prentice Hall: 2008.

263. Angelici, R. J., *Coord. Chem. Rev.* **1990,** *105*, 61.

264. Wong-Foy, A. G.; Matzger, A. J.; Yaghi, O. M., *J. Am. Chem. Soc.* **2006,** *128*, 3494.

265. Cullis, C. F.; Priday, K., *Proc. R. Soc. A.* **1954,** *224*, 308.

266. Kozawa, T.; Onda, A.; Yanagisawa, K.; Kishi, A.; Masuda, Y., *J. Solid State Chem.* **2011,** *184*, 589.

267. Cohen, R.; Zeiri, Y.; Wurzberg, E.; Kosloff, R., *J. Phys. Chem. A* **2007,** *111*, 11074.

268. Pouchert, C. J.; Company, A. C., *The Aldrich Library of Infrared Spectra. Pouchert*. Aldrich Chemical: **1981**.

269. Zeleňák, V.; Vargová, Z.; Györyová, K., *Spectrochim. Acta Mol. Biomol. Spectrosc.* **2007,** *66*, 262.

270. Hyun, S.-m.; Lee, J. H.; Jung, G. Y.; Kim, Y. K.; Kim, T. K.; Jeoung, S.; Kwak, S. K.; Moon, D.; Moon, H. R., *Inorg. Chem.* **2016,** *55*, 1920.

271. Li, D.; Kaneko, K., *Chem. Phys. Lett.* **2001,** *335*, 50.

272. Kitaura, R.; Seki, K.; Akiyama, G.; Kitagawa, S., *Angew. Chem. Int. Ed.* **2003,** *42*, 428.

273. Chen, B.; Wang, X.; Zhang, Q.; Xi, X.; Cai, J.; Qi, H.; Shi, S.; Wang, J.; Yuan, D.; Fang, M., *J. Mater. Chem.* **2010,** *20*, 3758.

274. Zhao, Z.; Li, Z.; Lin, Y. S., *Ind. Eng. Chem. Rev.* **2009,** *48*, 10015.

275. Feldblyum, J. I.; Wong-Foy, A. G.; Matzger, A. J., *Chem. Commun.* **2012,** *48*, 9828.

276. Rowsell, J. L. C.; Yaghi, O. M., *J. Am. Chem. Soc.* **2006,** *128*, 1304.

277. Yan, Y.; Lin, X.; Yang, S.; Blake, A. J.; Dailly, A.; Champness, N. R.; Hubberstey, P.; Schroder, M., *Chem. Commun.* **2009**, 1025.

278. Taft, K. L. http://energy.gov/eere/fuelcells/hydrogen-storage. (accessed 14/05/2016).

279. Kim, H.; Das, S.; Kim, M. G.; Dybtsev, D. N.; Kim, Y.; Kim, K., *Inorg. Chem.* **2011,** *50*, 3691.

280. Gou, Q.; Spada, L.; Vallejo-Lopez, M.; Lesarri, A.; Cocinero, E. J.; Caminati, W., *PCCP* **2014,** *16*, 13041.

281. Wu, X.; Yuan, B.; Bao, Z.; Deng, S., *J. Colloid Interface Sci.* **2014,** *430*, 78.

282. Wu, D.; Guo, X.; Sun, H.; Navrotsky, A., *J. of Phys. Chem. Lett.* **2015,** *6*, 2439.

283. Ferey, G., *New J. Chem.* **2016,** *40*, 3950.

284. Sing, K. S. W., *Pure Appl. Chem.* **1982,** *54*, 2201.

285. Scott, H. S.; Ogiwara, N.; Chen, K.-J.; Madden, D. G.; Pham, T.; Forrest, K.; Space, B.; Horike, S.; Perry Iv, J. J.; Kitagawa, S.; Zaworotko, M. J., *Chem. Sci.* **2016**.

286. Liu, L.; Wang, S.-M.; Han, Z.-B.; Ding, M.; Yuan, D.-Q.; Jiang, H.-L., *Inorg. Chem.* **2016,** *55*, 3558.

287. Chakraborty, A.; Haldar, R.; Maji, T. K., *Cryst. Growth Des.* **2013,** *13*, 4968.

288. Sumida, K.; Rogow, D. L.; Mason, J. A.; McDonald, T. M.; Bloch, E. D.; Herm, Z. R.; Bae, T.-H.; Long, J. R., *Chem. Rev.* **2012,** *112*, 724.

289. Dietzel, P. D. C.; Johnsen, R. E.; Fjellvag, H.; Bordiga, S.; Groppo, E.; Chavan, S.; Blom, R., *Chem. Commun.* **2008**, 5125.

290. Min Wang, Q.; Shen, D.; Bülow, M.; Ling Lau, M.; Deng, S.; Fitch, F. R.; Lemcoff, N. O.; Semanscin, J., *Microporous Mesoporous Mater.* **2002,** *55*, 217.

291. Figueroa, J. D.; Fout, T.; Plasynski, S.; McIlvried, H.; Srivastava, R. D., *IJGGC* **2008,** *2*, 9.

292. Myers, A. L.; Prausnitz, J. M., *AlChE J.* **1965,** *11*, 121.

293. Mason, J. A.; Sumida, K.; Herm, Z. R.; Krishna, R.; Long, J. R., *Energy Environ. Sci.* **2011,** *4*, 3030.

294. Deng, H.; Doonan, C. J.; Furukawa, H.; Ferreira, R. B.; Towne, J.; Knobler, C. B.; Wang, B.; Yaghi, O. M., *Science* **2010,** *327*, 846.

295. Jiang, J.; Zhao, Y.; Yaghi, O. M., *J. Am. Chem. Soc.* **2016,** *138*, 3255.

296. Singh, R. B.; Garg, B. S.; Singh, R. P., *Talanta* **1979,** *26*, 425.

297. Smith, A. G.; Tasker, P. A.; White, D. J., *Coord. Chem. Rev.* **2003,** *241*, 61.

298. Hołyńska, M.; Clérac, R.; Langer, T.; Pöttgen, R.; Dehnen, S., *Polyhedron* **2013,** *52*, 1425.

299. Bill, E.; Krebs, C.; Winter, M.; Gerdan, M.; Trautwein, A. X.; Flörke, U.; Haupt, H.-J.; Chaudhuri, P., *Chem. Eur. J.* **1997,** *3*, 193.

300. Lah, M. S.; Kirk, M. L.; Hatfield, W.; Pecoraro, V. L., *Chem. Commun.* **1989**, 1606.

301. Mason, K.; Gass, I. A.; Parsons, S.; Collins, A.; White, F. J.; Slawin, A. M. Z.; Brechin, E. K.; Tasker, P. A., *Dalton Trans.* **2010,** *39*, 2727.

302. Mason, K.; Gass, I. A.; White, F. J.; Papaefstathiou, G. S.; Brechin, E. K.; Tasker, P. A., *Dalton Trans.* **2011,** *40*, 2875.

303. Raptopoulou, C. P.; Boudalis, A. K.; Sanakis, Y.; Psycharis, V.; Clemente-Juan, J. M.; Fardis, M.; Diamantopoulos, G.; Papavassiliou, G., *Inorg. Chem.* **2006,** *45*, 2317.

304. Raptopoulou, C. P.; Sanakis, Y.; Boudalis, A. K.; Psycharis, V., *Polyhedron* **2005,** *24*, 711.

305. Thorpe, J. M.; Beddoes, R. L.; Collison, D.; Garner, C. D.; Helliwell, M.; Holmes, J. M.; Tasker, P. A., *Angew. Chem. Int. Ed.* **1999,** *38*, 1119.

306. Kalofolias, D. A.; Flamourakis, A. G.; Siczek, M.; Lis, T.; Milios, C. J., *J. Coord. Chem.* **2015,** *68*, 3472.

307. Comar, P.; Rajeshkumar, T.; Nichol, G. S.; Pitak, M. B.; Coles, S. J.; Rajaraman, G.; Brechin, E. K., *Dalton Trans.* **2015,** *44*, 19805.

308. Martínez-Lillo, J.; Cano, J.; Wernsdorfer, W.; Brechin, E. K., *Chem. Eur. J.* **2015,** *21*, 8790.

309. Poole, K. M.; Korabik, M.; Shiddiq, M.; Mitchell, K. J.; Fournet, A.; You, Z.; Christou, G.; Hill, S.; Hołyńska, M., *Inorg. Chem.* **2015,** *54*, 1883.

310. Perivolaris, A.; Fidelli, A. M.; Inglis, R.; Kessler, V. G.; Slawin, A. M. Z.; Brechin, E. K.; Papaefstathiou, G. S., *J. Coord. Chem.* **2014,** *67*, 3972.

311. Martinez-Lillo, J.; Dolan, N.; Brechin, E. K., *Dalton Trans.* **2014,** *43*, 4408.

312. Wu, L.-F.; Wang, Z.-X.; Geng, J.-P.; Xiao, H.-P.; Li, M.-X., *Inorg. Chim. Acta* **2014,** *412*, 1.

313. Nesterova, O. V.; Chygorin, E. N.; Kokozay, V. N.; Omelchenko, I. V.; Shishkin, O. V.; Boca, R.; Pombeiro, A. J. L., *Dalton Trans.* **2015,** *44*, 14918.

314. Curtis, N. F.; Morgan, K. R., *J. Mol. Struct.* **2011,** *1006*, 375.

315. Szymanowski, J., *Hydroxyoximes and Copper Hydrometallurgy*. Taylor & Francis: **1993**.

316. Atwood, R. L.; Miller, J. D., *Trans. Soc. Mining Eng. AIME* **1973,** *254*, 319.

317. Wilson, A. M.; Bailey, P. J.; Tasker, P. A.; Turkington, J. R.; Grant, R. A.; Love, J. B., *Chem. Soc. Rev.* **2014,** *43*, 123.

318. Kordosky, G. A. In *Development of solvent-extraction processes for metal recovery - finding the best fit between the metallurgy and the reagent*, Canadian Institute of Mining, Metallurgy and Petroleum: **2008**; pp 3.

319. Forgan, R. S.; Roach, B. D.; Wood, P. A.; White, F. J.; Campbell, J.; Henderson, D. K.; Kamenetzky, E.; McAllister, F. E.; Parsons, S.; Pidcock, E.; Richardson, P.; Swart, R. M.; Tasker, P. A., *Inorg. Chem.* **2011,** *50*, 4515.

320. Healy, M. R.; Carter, E.; Fallis, I. A.; Forgan, R. S.; Gordon, R. J.; Kamenetzky, E.; Love, J. B.; Morrison, C. A.; Murphy, D. M.; Tasker, P. A., *Inorg. Chem.* **2015,** *54*, 8465.

321. Kudryavtsev, A. B.; Frauendienst, G.; Linert, W., *J. Coord. Chem.* **1998,** *46*, 221.

322. Willis, J. B.; Mellor, D. P., *J. Am. Chem. Soc.* **1947,** *69*, 1237.

323. Basolo, F.; Matoush, W. R., *J. Am. Chem. Soc.* **1953,** *75*, 5663.

324. Romano, V.; Maggio, F.; Pizzino, T., *J. Inorg. Nucl. Chem.* **1971,** *33*, 2611.

325. Li, H.; Eddaoudi, M.; O'Keeffe, M.; Yaghi, M., *Nature* **1999,** *402*, 276.

326. Zhu, C.; Yuan, G.; Chen, X.; Yang, Z.; Cui, Y., *J. Am. Chem. Soc.* **2012,** *134*, 8058.

327. Furukawa, H.; Gándara, F.; Zhang, Y.-B.; Jiang, J.; Queen, W. L.; Hudson, M. R.; Yaghi, O. M., *J. Am. Chem. Soc.* **2014,** *136*, 4369.

328. Bauer, C. A.; Timofeeva, T. V.; Settersten, T. B.; Patterson, B. D.; Liu, V. H.; Simmons, B. A.; Allendorf, M. D., *J.Am. Chem. Soc.* **2007,** *129*, 7136.

329. Chui, S. S. Y.; Lo, S. M. F.; Charmant, J. P. H.; Orpen, A. G.; Williams, I. D., *Science* **1999,** *283*, 1148.

330. Kim, H. K.; Yun, W. S.; Kim, M.-B.; Kim, J. Y.; Bae, Y.-S.; Lee, J.; Jeong, N. C., *J. Am. Chem. Soc.* **2015,** *137*, 10009.

331. Ren, Y.; Cheng, X.; Yang, S.; Qi, C.; Jiang, H.; Mao, Q., *Dalton Trans.* **2013,** *42*, 9930.

332. Cui, H.; Wang, Y.; Wang, Y.; Fan, Y.-Z.; Zhang, L.; Su, C.-Y., *CrystEngComm* **2016,** *18*, 2203.

333. Yang, X.-L.; Xie, M.-H.; Zou, C.; He, Y.; Chen, B.; O'Keeffe, M.; Wu, C.-D., *J. Am. Chem. Soc.* **2012,** *134*, 10638.

334. Queen, W. L.; Hudson, M. R.; Bloch, E. D.; Mason, J. A.; Gonzalez, M. I.; Lee, J. S.; Gygi, D.; Howe, J. D.; Lee, K.; Darwish, T. A.; James, M.; Peterson, V. K.; Teat, S. J.; Smit, B.; Neaton, J. B.; Long, J. R.; Brown, C. M., *Chem. Sci.* **2014,** *5*, 4569.

335. Liu, Y.; Kabbour, H.; Brown, C. M.; Neumann, D. A.; Ahn, C. C., *Langmuir* **2008,** *24*, 4772.

336. Bae, Y.-S.; Lee, C. Y.; Kim, K. C.; Farha, O. K.; Nickias, P.; Hupp, J. T.; Nguyen, S. T.; Snurr, R. Q., *Angew. Chem. Int. Ed.* **2012,** *51*, 1857.

337. Horike, S.; Dincă, M.; Tamaki, K.; Long, J. R., *J. Am. Chem. Soc.* **2008,** *130*, 5854.

338. Horcajada, P.; Serre, C.; Maurin, G.; Ramsahye, N. A.; Balas, F.; Vallet-Regi, M.; Sebban, M.; Taulelle, F.; Ferey, G., *J. Am. Chem. Soc.* **2008,** *130*, 6774.

339. Hinks, N. J.; McKinlay, A. C.; Xiao, B.; Wheatley, P. S.; Morris, R. E., *Microporous Mesoporous Mater.* **2010,** *129*, 330.

340. Bloch, E. D.; Queen, W. L.; Krishna, R.; Zadrozny, J. M.; Brown, C. M.; Long, J. R., *Science* **2012,** *335*, 1606.

341. Błędzka, D.; Gromadzińska, J.; Wąsowicz, W., *Environ.Int.* **2014,** *67*, 27.

342. Tenon, J. A.; Carles, M.; Aycard, J. P., *Acta Crystallogr. Sect. C* **2000,** *56*, 568.

343. Liu, J.-J.; He, X.; Shao, M.; Li, M.-X., *Inorg. Chem. Commun.* **2009,** *12*, 972.

344. Menon, S.; Rajasekharan, M. V., *Polyhedron* **1998,** *17*, 2463.

345. Neville, S. M.; Halder, G. J.; Chapman, K. W.; Duriska, M. B.; Moubaraki, B.; Murray, K. S.; Kepert, C. J., *J. Am. Chem. Soc.* **2009,** *131*, 12106.

346. Ma, S.; Sun, D.; Forster, P. M.; Yuan, D.; Zhuang, W.; Chen, Y.-S.; Parise, J. B.; Zhou, H.-C., *Inorg. Chem.* **2009,** *48*, 4616.

347. Ma, S.; Sun, D.; Forster, P. M.; Yuan, D.; Zhuang, W.; Chen, Y.-S.; Parise, J. B.; Zhou, H.-C., *Inorg. Chem.* **2009,** *48*, 4616.

348. Kalia, J.; Raines, R. T., *Angew. Chem. Int. Ed.* **2008,** *47*, 7523.

349. Kelly, N. R.; Goetz, S.; Hawes, C. S.; Kruger, P. E., *Inorg. Chim.Acta* **2013,** *403*, 102.

350. Patil, K. M.; Dickinson, M. E.; Tremlett, T.; Moratti, S. C.; Hanton, L. R., *Cryst. Growth Des.* **2016,** *16*, 1038.

351. Wang, Z.; Zhang, B.; Yu, H.; Sun, L.; Jiao, C.; Liu, W., *Chem. Commun.* **2010,** *46*, 7730.

352. Beaudoin, D.; Maris, T.; Wuest, J. D., *Nat Chem* **2013,** *5*, 830.

353. Shen, C.; Bao, Y.; Wang, Z., *Chem. Commun.* **2013,** *49*, 3321.

354. Sheldrick, G., *Acta Crystallogr. Sect. A* **2008,** *64*, 112.

355. Sheldrick, G., *Acta Crystallogr. Sect. A* **2015,** *71*, 3.

356. Sheldrick, G., *Acta Crystallogr. Sect. C* **2015,** *71*, 3.

357. Dolomanov, O. V.; Bourhis, L. J.; Gildea, R. J.; Howard, J. A. K.; Puschmann, H., *J. Appl. Crystallogr.* **2009,** *42*, 339.

358. Macrae, C. F.; Bruno, I. J.; Chisholm, J. A.; Edgington, P. R.; McCabe, P.; Pidcock, E.; Rodriguez-Monge, L.; Taylor, R.; van de Streek, J.; Wood, P. A., *J. Appl. Crystallogr.* **2008,** *41*, 466.

359. Weldon, F.; Hammarström, L.; Mukhtar, E.; Hage, R.; Gunneweg, E.; Haasnoot, J. G.; Reedijk, J.; Browne, W. R.; Guckian, A. L.; Vos, J. G., *Inorg. Chem.* **2004,** *43*, 4471.

360. Krackl, S.; Someya, C. I.; Enthaler, S., *Chem. Eur. J.* **2012,** *18*, 15267.

361. Brunner, H.; Störiko, R.; Rominger, F., *Eur. J. Inorg. Chem.* **1998,** *1998*, 771.

362. Deng, D.; Liu, L.; Ji, B.-M.; Yin, G.; Du, C., *Cryst. Growth Des.* **2012,** *12*, 5338.

363. Bell, Z. R.; Motson, G. R.; Jeffery, J. C.; McCleverty, J. A.; Ward, M. D., *Polyhedron* **2001,** *20*, 2045.

364. Zhang, C. Y.; Tour, J. M., *J. Am. Chem. Soc.* **1999,** *121*, 8783.

365. Suenaga, Y.; Kamiya, T.; Kuroda-Sowa, T.; Maekawa, M.; Munakata, M., *Inorg.Chim.Acta* **2000,** *308*, 17.

366. Liu, K.-G.; Cai, X.-Q.; Li, X.-C.; Qin, D.-A.; Hu, M.-L., *Inorg. Chim. Acta* **2012,** *388*, 78.

367. Ishihara, M.; Tsuneya, T.; Shiga, M.; Kawashima, S.; Yamagishi, K.; Yoshida, F.; Sato, H.; Uneyama, K., *J. Agric. Food Chem.* **1992,** *40*, 1647.

368. Tu, Q.-D.; Li, D.; Sun, Y.; Han, X.-Y.; Yi, F.; Sha, Y.; Ren, Y.-L.; Ding, M.-W.; Feng, L.-L.; Wan, J., *Biorg. Med. Chem.* **2013,** *21*, 2826.

369. Yokoyama, A.; Iwashita, K.-i.; Hirabayashi, K.; Aiyama, K.; Yokozawa, T., *Macromolecules* **2003,** *36*, 4328.

370. Rouquerol, J.; Llewellyn, P.; Rouquerol, F., *Stud. Surf. Sci. Catal.*, **2007**, *160*, 49.

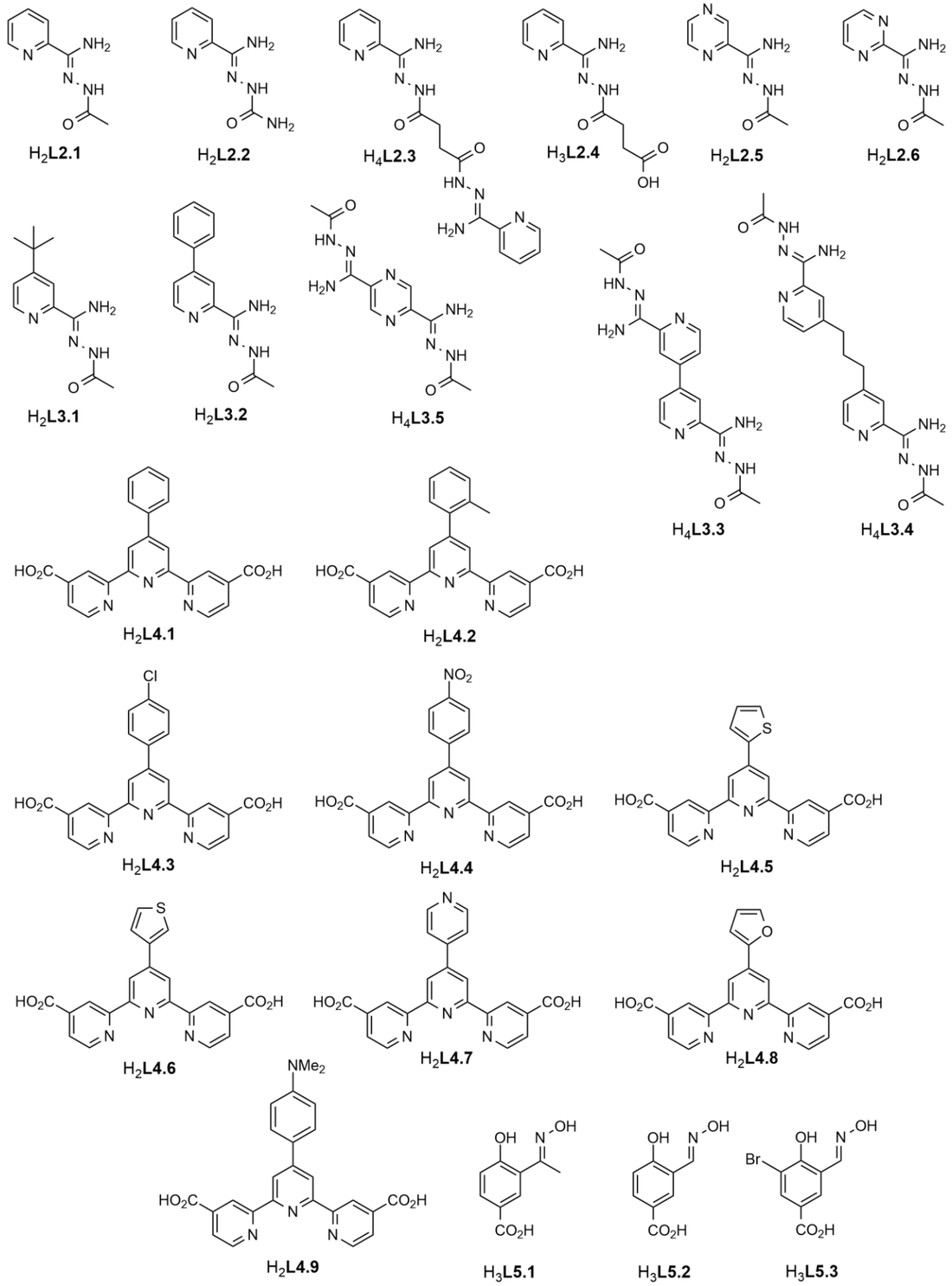
H2L2.1
H2L2.2
H4L2.3
H3L2.4
H2L2.5
H2L2.6
H2L3.1
H2L3.2
H4L3.5
H4L3.3
H4L3.4
H2L4.1
H2L4.2
H2L4.3
H2L4.4
H2L4.5
H2L4.6
H2L4.7
H2L4.8
H2L4.9
H3L5.1
H3L5.2
H3L5.3